

Electronic Thesis and Dissertation Repository

---

10-25-2022 12:30 PM

## Mechanistic Elucidation of M-PR<sub>2</sub>NR'<sub>2</sub> Catalysts for Hydrofunctionalization and Cross Coupling Reactions

Devon E. Chapple

Supervisor: Blacquiere, Johanna M., *The University of Western Ontario*

A thesis submitted in partial fulfillment of the requirements for the Doctor of Philosophy degree in Chemistry

© Devon E. Chapple 2022

Follow this and additional works at: <https://ir.lib.uwo.ca/etd>

---

## Abstract

This thesis attempts to elucidate the mechanistic understanding for metal complexes ligated with 1,5-R-3,7-R'-1,5-diaza-3,7-diphosphacyclooctane ( $P^{R_2}N^{R'_2}$ ) ligands, which were utilized for organic transformations. Alkyne hydrofunctionalization reactions, including hydroamination and hydroalkoxylation, were previously catalyzed with  $[Ru(Cp/Cp^*)(P^{R_2}N^{R'_2})(MeCN)]PF_6$  catalysts. However, validation of the proposed mechanistic pathway for these complexes has not yet been realized. Investigation of these catalysts through substrate studies, intermediate isolation, kinetic analysis, and isotopic labelling was performed in an attempt to better understand the mechanism. Ligand and substrate interactions were identified that stabilized the coordinatively unsaturated complexes. Ligand modification enabled mitigation of a previously observed deactivation species, which enabled investigations for previously problematic hydroalkoxylation reactions. Formation of a new deactivation species was observed, which completely arrested productive catalysis, but gave insight into organic product release steps of the mechanism. Isolation of two vinylidene complexes enabled stoichiometric investigations to assess intermolecular hydroamination. Stoichiometric reactions with the vinylidene complex and amine nucleophiles resulted in the formation of a ruthenium acetylide complex, confirmed via independent synthesis, via deprotonation of  $C_\beta$  instead of the desired nucleophilic attack of  $C_\alpha$ . Formation of the ruthenium acetylide complex was not observed with stoichiometric reactions with aniline which was then targeted for attempted intermolecular hydroamination. Finally, investigation of palladium  $P^{R_2}N^{R'_2}$  complexes were assessed for the Heck coupling of phenyltriflate and styrene, which showed regioselective formation of linear or branched product formation based on the phosphorus R substituent. Investigations into the factors controlling the regioselective product formation were performed through attempted synthesis of reaction intermediates and kinetic studies.

## Keywords

Organometallic • Homogenous Catalysis • MLC Catalysis • Catalysts • Hydrofunctionalization  
• Hydroamination • Hydroalkoxylation • Ligand Design • Intermediate Synthesis • Proton  
Shuttling • Deactivation Species • Mechanism • Variable Time Normalization Analysis •  
Isotopic Labelling

## Summary for Lay Audience

Catalysts are chemicals which make chemical reactions occur more readily. The work in this thesis looks to form a better understanding as to how a particular family of ruthenium and palladium catalysts work. Two of the three reactions that were investigated involved the synthesis of compounds containing nitrogen and oxygen atoms, which are commonly found in high-value chemicals in nature or medicine. The studies established the performance of the catalysts, with slight alterations to its chemical structure. These changes were identified to influence the catalyst performance through helpful interactions that increased stability and reduced catalyst death. The catalysts were further utilized on chemicals that have not previously been looked at, which helped establish previously unsuccessful reactions, and inform on the limitations of the catalysts. Unproductive interactions were also observed which were detrimental to the catalysts and resulted in deactivation of the catalyst. The other reaction that was investigated looked at selective formation of two compounds, which were biased based on the structure of the catalyst used for the reaction. Exploration to determine why a particular catalyst favoured formation of one of the compounds over the other was performed. The aspects of the catalyst that were thought to control the formation were the number of metals per catalyst or how large parts of the catalyst were. Overall, a deeper understanding of the ruthenium and palladium catalysts discussed within was achieved which will be applied to future studies to further improve their performance for established and unestablished chemistry.

## Co-Authorship Statement

This thesis includes work from two previously published manuscripts in Chapters 2 and 3. Manuscripts of the work described in chapters 4 and 5 are in preparation and will be submitted shortly.

Chapter 1 and Chapter 6 were written by DEC and edited by JMB.

The article presented in Chapter 2 was co-authored by: D. E. Chapple, P. D. Boyle, and J. M. Blacquiere.<sup>1</sup> DEC performed all the experimental work and the DFT calculations. PDB collected and solved the X-ray crystallographic data. The manuscript was prepared by DEC and edited by JMB.

The article presented in Chapter 3 was co-authored by: D. E. Chapple, M. A. Hoffer, P. D. Boyle, and J. M. Blacquiere. DEC performed all the synthetic and characterization work except for synthesis of nitrene substrate (ca. 5% of experimental work). PDB collected and solved the X-ray crystallographic data. The manuscript was prepared by DEC and edited by JMB.

Chapter 4 was co-authored by D. E. Chapple, A. M. M. Beardall, N. Henao Ruiz, P. D. Boyle, and J. M. Blacquiere. DEC performed the synthesis and characterization for all the complexes and the attempted cyclization, the stoichiometric reactions were performed by AAMB (ca. 20% of experimental work), and Nick Henao Ruiz performed key preliminary studies (ca. 10% of experimental work). The manuscript was prepared by DEC and edited by JMB. The manuscript is near completion and will be submitted soon.

Chapter 5 describes experimental work performed by D. E. Chapple. The work presented here is ongoing and will be part of a collaborative manuscript co-authored by E. S. Isbrandt, D. E. Chapple, V. Dimakos, J. M. Blacquiere, and S. G. Newman. DEC performed all the experimental work. Contributions by collaborators E. S. Isbrandt, V. Dimakos, and S. G. Newman were summarized in the introduction of chapter 5. The chapter was prepared by DEC and edited by JMB.

## Acknowledgments

First and foremost, I would like to thank Dr. Johanna M. Blacquiere for the opportunity to be part of the Blacquiere group over the past 5 years. Over the years you have pushed me to be a better chemist every day, whether that was through finding one word that was a different font in an entire presentation, edits for manuscripts, or asking questions in the office. Without your support and guidance over the years I would not have been half the person or chemist that I am now. It has been a great experience working with you and learning from you.

To the past and present Blacquiere group that I have had the pleasure of meeting during my time here. I have gotten to work with many amazing people during my time: James who I am glad I only saw in eyeliner once; Scott for turning over my things gently; Ava for being my eternal mortal enemy; Kyle or Kevin who I've been struggling with since 2<sup>nd</sup> year of undergrad; JW for all the memes that you created, Ben for all the afternoon chats downstairs; Meagan for the creation and lifestyle of 5ish; Matt for always being down for sushi, and the new guard Shagana, Megan, and Amrit who are now holding down the fort. I would also like to thank the many undergraduates that have come through the lab over the years.

I would also like to thank the fantastic research staff at Western. Mat Willans (NMR), Paul Boyle (crystals), Aneta Borecki (both), Kristina Jurcic (MALDI), the machine shop crew, and the chembiostores group. Your dedication, help, and friendliness were greatly appreciated.

Lastly, I would also like to thank my partner Sofia Sirohey for her support during my thesis. Whether it was being nervous for me doing a presentation, worrying I won't finish something on time, going climbing in the Glen, or the countless hours of running we did during the lockdown, your work ethic and drive inspired me every day.

# Table of Contents

Abstract.....	ii
Summary for Lay Audience.....	iv
Co-Authorship Statement.....	v
Acknowledgments.....	vi
Table of Contents.....	vii
List of Figures.....	xiv
List of Schemes.....	xxi
List of Tables.....	xxiv
List of Abbreviations.....	xxv
List of Complexes.....	xxviii
Chapter 1.....	1
1 Introduction.....	1
1.1 Importance of Catalysis and Understanding It.....	1
1.2 Hydrofunctionalization to Generate Nitrogen and Oxygen Compounds.....	3
1.2.1 Importance of Nitrogen and Oxygen Compounds.....	3
1.2.2 Ruthenium Catalyzed Hydrofunctionalization to Access <i>N</i> - and <i>O</i> - Compounds.....	5
1.3 Metal Vinylidenes and Their Role in Catalysis.....	9
1.4 Metal-Ligand Cooperativity and Dynamics of $P^{R_2}N^{R'_2}$ Ligands.....	12
1.4.1 Cooperative Ligands and their Role in Catalysis.....	12
1.4.2 $P^{R_2}N^{R'_2}$ Ligands and Their Dynamics.....	13
1.5 Metal- $P^{R_2}N^{R'_2}$ Complexes Utilized for Organic Transformations.....	15
1.5.1 Hydrofunctionalization with Metal $P^{R_2}N^{R'_2}$ Catalysts.....	15
1.5.2 Cross-Coupling with M- $P^{R_2}N^{R'_2}$ Catalysts.....	20
1.6 Scope of Thesis.....	21

1.7	References.....	23
Chapter 2.....		27
2	Origin of Stability and Inhibition of Cooperative Alkyne Hydrofunctionalization Catalysts.....	27
2.1	Introduction.....	27
2.2	Results and Discussion .....	30
2.2.1	Synthesis and Characterization of Catalysts <b>2-1b</b> , <b>2-2b</b> , and <b>2-2c</b> .....	30
2.2.2	Lifetime of Catalysts <b>2-1a-c</b> and <b>2-2a-c</b> .....	31
2.2.3	Preparation of Hydroamination Active Catalysts.....	33
2.2.4	(In)Stability of Pre-Catalysts and Active Catalysts at Elevated Temperature .....	38
2.2.5	(In)Stability of the Cp* Active Catalyst in Halogenated Solvent.....	39
2.2.6	Lifetime of Active Catalysts <b>2-5b</b> and <b>2-6b</b> .....	42
2.2.7	Reaction Rate Comparison of Catalysts <b>2-1a-c</b> and <b>2-2a-c</b> .....	43
2.2.8	Product Inhibition of Catalyst <b>2-1b</b> .....	44
2.2.9	Substrate Modification to Avoid Product Inhibition of Catalyst <b>2-1b</b> .....	46
2.3	Conclusion .....	48
2.4	Experimental Section.....	48
2.4.1	General Procedures, Materials, and Instrumentation.....	48
2.4.2	General Procedure for Synthesis of Pre-Catalysts [Ru(Cp)(P <sup>R</sup> <sub>2</sub> N <sup>R'</sup> <sub>2</sub> )(MeCN)][PF <sub>6</sub> ] ( <b>2-1b</b> , <b>2-2b</b> , <b>2-2c</b> ).....	49
2.4.3	General Procedure for [RuCl(Cp/Cp*)(P <sup>Cy</sup> <sub>2</sub> N <sup>Ph</sup> <sub>2</sub> )] Complex Synthesis. ..	51
2.4.4	General Procedure for [Ru(Cp/Cp*)(P <sup>Cy</sup> <sub>2</sub> N <sup>Ph</sup> <sub>2</sub> )]PF <sub>6</sub> Complex Synthesis. 52	
2.4.5	General Procedure for [RuCl(Cp/Cp*)(P <sup>Cy</sup> <sub>2</sub> N <sup>Ph</sup> <sub>2</sub> )] Halide Abstraction Under Argon Gas. ....	54
2.4.6	Procedure for [RuCl(η <sup>4</sup> -C <sub>5</sub> Me <sub>5</sub> CH <sub>2</sub> Cl)(P <sup>Cy</sup> <sub>2</sub> N <sup>Ph</sup> <sub>2</sub> )] [PF <sub>6</sub> ] Complex Synthesis. ....	55
2.4.7	General Procedure for Intramolecular Hydroamination Catalysis.....	56



2.4.8	General Catalytic Procedure for Product Inhibition Catalysis.....	56
2.4.9	General Procedure for Thermolysis of Complexes 1b, 2b, 5b, and 6b.....	57
2.5	References.....	57
Chapter 3.....		61
3	Alkyne Hydrofunctionalization Mechanism Including an Off-Cycle Alkoxycarbene Deactivation Complex.....	61
3.1	Introduction.....	61
3.2	Results and discussion .....	64
3.2.1	Deployment of Redesigned Catalyst to Suppress Vinylidene Deactivation .....	64
3.2.2	Substrate Investigation.....	66
3.2.3	Evaluation of Catalyst Decomposition and Product Inhibition .....	69
3.2.4	Determination of Substrate and Catalyst Order .....	70
3.2.5	Deuterium Labelling Studies .....	71
3.2.6	Synthesis and Reactivity of Catalytic Intermediates .....	74
3.2.7	Proposed Catalytic Cycle.....	78
3.3	Conclusions.....	80
3.4	Experimental Section.....	81
3.4.1	General Procedure for Hydroalkoxylation of 1a for Catalyst Deactivation or Product Inhibition Studies and Determination of Substrate Order. ....	82
3.4.2	General Procedure for Hydroalkoxylation of <b>3-1a</b> for the Determination of Catalyst Order .....	82
3.4.3	Catalytic Hydroalkoxylation with Alkyne-Labelled Substrate ( <b>3-1a-d1</b> ). 83	
3.4.4	Catalytic Hydroalkoxylation with Alcohol-Labelled Substrate ( <b>3-1a-OD</b> ) .....	83
3.4.5	Synthesis of Alkoxycarbene Complex [Ru(Cp)(P <sup>Cy</sup> <sub>2</sub> N <sup>Ph</sup> <sub>2</sub> )(3,4-Dihydro-2H-furylium)][PF <sub>6</sub> ] ( <b>3-Ru3</b> ) .....	84
3.4.6	<i>In Situ</i> Formation of Vinyl Ether Complex [Ru(Cp)(P <sup>Cy</sup> <sub>2</sub> N <sup>Ph</sup> <sub>2</sub> )(2,3-dihydrofuran)][PF <sub>6</sub> ] ( <b>3-Ru5</b> ) .....	85

3.4.7	General Catalytic Procedure for Hydrofunctionalization Reactions to Obtain <i>In Situ</i> Conversions .....	85
3.5	References.....	86
Chapter 4	.....	89
4	Isolation and Reactivity of Ruthenium Vinylidene Complexes.....	89
4.1	Introduction.....	89
4.2	Results and Discussion .....	92
4.2.1	Synthesis and Characterization of Vinylidene Complexes. ....	92
4.2.2	Stoichiometric Reactions of Primary and Secondary Aliphatic Amines with Vinylidenes. ....	94
4.2.3	Independent Synthesis of <b>Ru4</b> . ....	95
4.2.4	Stoichiometric Reaction with Aniline.....	96
4.2.5	Attempted Intermolecular Hydroamination. ....	97
4.2.6	Conclusion .....	98
4.3	Experimental Section .....	99
4.3.1	General Procedure for the Synthesis of Vinylidene Complexes [Ru(Cp/Cp*)(P <sup>Cy</sup> <sub>2</sub> N <sup>Ph</sup> <sub>2</sub> )(=C=HPh)]PF <sub>6</sub> , <b>4-Ru2a</b> (Cp) and <b>4-Ru2b</b> (Cp*)	99
4.3.2	General Procedure for Stoichiometric Reaction of Vinylidenes with Amine Nucleophiles. ....	100
4.3.3	Procedure for the Independent Synthesis of Acetylide Complex [Ru(Cp)(P <sup>Cy</sup> <sub>2</sub> N <sup>Ph</sup> <sub>2</sub> )(-C≡C-Ph)]PF <sub>6</sub> ( <b>4-Ru4</b> ).....	101
4.3.4	General Procedure for Attempted Catalytic Intermolecular Hydroamination. ....	101
4.4	References.....	102
Chapter 5	.....	104
5	Mechanistic Elucidation of Pd-P <sup>R</sup> <sub>2</sub> N <sup>ArCF<sub>3</sub></sup> <sub>2</sub> Catalysts for Cross Coupling.....	104
5.1	Introduction.....	104
5.2	Results and Discussion .....	107
5.2.1	Synthesis of Pd(P <sup>R</sup> <sub>2</sub> N <sup>ArCF<sub>3</sub></sup> <sub>2</sub> )(MAH) Complexes. ....	107

5.2.2	Structural Confirmation of [Pd(P <sup>Ph</sup> <sub>2</sub> N <sup>ArCF3</sup> <sub>2</sub> )(ABP)] Complexes .....	109
5.2.3	Heck Coupling Reaction with Pd(P <sup>R</sup> <sub>2</sub> N <sup>ArCF3</sup> <sub>2</sub> )(MAH) Complexes. ....	110
5.2.4	Attempted Oxidative Addition with <b>5-3a</b> . ....	111
5.2.5	Oxidative Addition with (P <sup>R</sup> <sub>2</sub> N <sup>ArCF3</sup> <sub>2</sub> )-Pd-G3 Complexes and Phenyl Triflate.....	113
5.2.6	Synthesis of [Pd(Ph)(I)(P <sup>R</sup> <sub>2</sub> N <sup>ArCF3</sup> <sub>2</sub> )] Complexes .....	114
5.2.7	Halide Abstraction of <b>5-5b</b> with AgOTf.....	116
5.2.8	Reaction Order Determination for Palladium. ....	117
5.2.9	Comparison of Catalyst Pocket Steric Congestion. ....	118
5.3	Conclusion .....	121
5.4	Experimental .....	121
5.4.1	General Procedure for the Synthesis of Pd(P <sup>R</sup> <sub>2</sub> N <sup>ArCF3</sup> <sub>2</sub> )(MAH) Complexes. ....	122
5.4.2	General Procedure for the Synthesis of Pd(Ph)(I)(P <sup>R</sup> <sub>2</sub> N <sup>ArCF3</sup> <sub>2</sub> ) Complexes. ....	124
5.4.3	General Procedure for Oxidative Addition of Pd Complexes with Phenyl Triflate.....	125
5.4.4	General Procedure for Independent Synthesis of Oxidative Addition Species <b>5-3b</b> .....	125
5.4.5	General Catalytic Procedure for <b>5-3a</b> and <b>5-3b</b> Assessment. ....	126
5.4.6	General Catalytic Procedure for Catalyst Order Determination. ....	126
5.5	References.....	127
6	Summary, Conclusion, and Future Work.....	129
6.1	Summary and Conclusion.....	129
6.2	Future Work.....	132
	Appendices.....	134
	Appendices A: Supplementary Information for Chapter 2 .....	134
	NMR Data.....	134

IR Spectra.....	149
MALDI Mass Spectra.....	153
Catalytic Data.....	161
Crystallographic Details.....	162
Computational Details .....	168
References.....	182
Appendices B: Supplementary Information for Chapter 3 .....	184
NMR Spectra .....	184
IR Spectra.....	195
MALDI Mass Spectra.....	195
Catalysis Data .....	196
Deuterium Labelling Experiments.....	197
Crystallographic Details.....	199
Computational Details .....	202
References.....	203
Appendices C: Supplementary Information for Chapter 4 .....	204
NMR Spectra .....	204
IR Spectra.....	214
MALDI Mass Spectra.....	215
Crystallographic Details.....	218
References.....	221
Appendices D: Supplementary Information for Chapter 5 .....	222
NMR Spectra .....	222
IR Spectra.....	237
MALDI .....	239
Crystallographic Details.....	243

References.....	250
Appendices E: Copyright Material and Permissions .....	250
Curriculum Vitae .....	258

## List of Figures

- Figure 1-1.** Energy profile of a non-catalyzed reaction (blue) vs catalyzed reaction (green).. 1
- Figure 1-2.** General catalytic cycle with a) one substrate binding to the catalyst and releasing one product, b) general proposed mechanism for a copper free Sonogashira coupling. .... 3
- Figure 1-3.** Examples of a pharmaceutical drug and natural product which contain nitrogen and oxygen heterocycles. .... 4
- Figure 1-4.** Intermolecular hydroamination of phenylacetylene and aniline derivatives. Reaction conditions: <sup>a</sup> 0.1 mol% [Ru<sub>3</sub>(CO)<sub>12</sub>], 0.3 mol% NH<sub>4</sub>PF<sub>6</sub>, 3 h; <sup>b</sup> 0.2 mol% [Ru<sub>3</sub>(CO)<sub>12</sub>], 0.6 mol%, NH<sub>4</sub>PF<sub>6</sub>, 3 h; <sup>c</sup> 1 mol% [Ru<sub>3</sub>(CO)<sub>12</sub>], 3 mol%, HBF<sub>4</sub>/Et<sub>2</sub>O, 12 h; 1 mol% [Ru<sub>3</sub>(CO)<sub>12</sub>], 3 mol%, NH<sub>4</sub>PF<sub>6</sub>, 12 h. <sup>d</sup> 0.7 mol% [Ru<sub>3</sub>(CO)<sub>12</sub>], 2.1 mol%, HBF<sub>4</sub>/Et<sub>2</sub>O, 12 h.. 7
- Figure 1-5.** Intramolecular hydrofunctionalization to generate a variety of nitrogen and oxygen heterocycles. Reaction conditions: 2 mol% [Ru], THF, 70 °C. .... 8
- Figure 1-6.** Intramolecular hydroamination to generate a variety of nitrogen heterocycles catalyzed with a non-MLC ruthenium complex. *NR* means no reaction. .... 9
- Figure 1-7.** Proposed mechanism for the cyclization of 2-ethynylaniline which proceeds through a vinylidene intermediate. .... 11
- Figure 1-8.** Examples of spectator (red) and actor (blue) ligands on a) [Ru(Cp)(Cl)(dppm)] complex **1-1** and b) ruthenium amido complex **1-2** has been identified as cooperative ligands. .... 12
- Figure 1-9.** Rate comparison between non-MLC complexes **1-3** and **1-5** versus MLC complexes **1-4** and **1-6** for a) alkyne hydration and b) alkene isomerization. The cooperative part of the ligand is highlighted in blue. .... 13
- Figure 1-10.** a) Typical route to generate P<sup>R</sup><sub>2</sub>N<sup>R'</sup><sub>2</sub> ligands from readily available phosphines and amines with formaldehyde and b) typical binding mode of P<sup>R</sup><sub>2</sub>N<sup>R'</sup><sub>2</sub> ligands to late transition metal centers. .... 14

<b>Figure 1-11.</b> Ni( $P^R_2N^{R'}_2$ ) complex heterolytic cleavage of H <sub>2</sub> in which the metal center acts as a hydride acceptor and the pendent amine acts as a proton acceptor. The R and R' substituent are not shown for clarity. ....	15
<b>Figure 1-12.</b> a) Attempted hydration of phenylacetylene or 1-octyne catalyzed with [Ru(Cp)(P <sup>tBu</sup> <sub>2</sub> N <sup>Bn</sup> <sub>2</sub> )(MeCN)]PF <sub>6</sub> . b) attempted synthesis of ruthenium vinylidene species resulted in isolation of vinyl ammonium complex. ....	16
<b>Figure 1-13.</b> a) Intramolecular hydroamination catalyzed by [Ru(Cp)(P <sup>R</sup> <sub>2</sub> N <sup>Bn</sup> <sub>2</sub> )(MeCN)]PF <sub>6</sub> and [Ru(Cp)(dppp)(MeCN)]PF <sub>6</sub> complexes. b) Intramolecular hydroamination of 2-ethynylbenzyl alcohol derivative and 4-pentyn-1-ol substrates.....	17
<b>Figure 1-14.</b> General influence of the primary coordination sphere on intramolecular hydrofunctionalization reactions.....	19
<b>Figure 1-15.</b> a) Intramolecular hydroamination catalyzed by Fe-P <sup>R</sup> <sub>2</sub> N <sup>R'</sup> <sub>2</sub> complexes. b) Synthesis of a Fe vinylidene complex. ....	19
<b>Figure 2-1.</b> a) General structure of Ru-P <sup>R</sup> <sub>2</sub> N <sup>R'</sup> <sub>2</sub> intramolecular hydrofunctionalization catalysts; and b) simplified depiction of catalyst conscription by MeCN dissociation to give the donor-free active catalyst.....	28
<b>Figure 2-2.</b> Versatile coordination chemistry of the P <sup>R</sup> <sub>2</sub> N <sup>R'</sup> <sub>2</sub> ligand in donor-free a) ruthenium, <sup>10</sup> and b) manganese <sup>11a</sup> complexes.....	29
<b>Figure 2-3.</b> Cationic ruthenium complexes employed in this study. Yields for newly synthesized complexes shown in parentheses.....	30
<b>Figure 2-4.</b> Displacement ellipsoid plot of complex <b>2-2b</b> . Ellipsoids are given at 30% probability level. H atoms, PF <sub>6</sub> <sup>-</sup> anion, and a molecule of co-crystallized hexanes were omitted for clarity. Selected bond distances (Å): Ru1-N1 = 2.046(4), Ru1-P1 = 2.275(2), Ru1-P2 = 2.262(2). Selected angles (°): P1-Ru1-P2 = 78.80(5), Ru1-N1-C1 = 175.1(4). ....	31
<b>Figure 2-5.</b> Turnover numbers (TON) of Cp (solid) and Cp* (empty) catalysts for intramolecular hydroamination of 2-ethynylaniline. Reaction conditions: 300 mM <b>2-EA</b> , Me-THF, 0.1 mol% [Ru]. Catalysts with R = <i>t</i> -Bu (orange), R = Cy (blue), and R = Ph (green).	

Runs were conducted in duplicate with data points representing the average and the error bars depict the span of individual runs. .... 33

**Figure 2-6.** ORTEP view of solid-state structures of chloro complexes **2-3b** and **2-4b** with ellipsoids at 30% probability level. H atoms and a molecule of co-crystallized DCM in **2-3b** were omitted for clarity. Selected bond distances (Å): **2-3b**, Ru(1)-Cl(1) = 2.4556(6), Ru(1)-P(1) = 2.2616(6), Ru(1)-P(2) = 2.2570(8); **2-4b**, Ru(1A)-Cl(1A) = 2.459(2), Ru(1A)-P(1A) = 2.244(1), Ru(1A)-P(2A) = 2.277(1). Selected Angles (°): **2-3b**, P(1)-Ru(1)-P(2) = 79.20(2); **2-4b**, P(1A)-Ru(1A)-P(2A) = 80.25(3). .... 34

**Figure 2-7.** Two views of the displacement ellipsoid plots for  $\kappa^3$ -(P,P,Ar)-**2-5b** with ellipsoids at 30% probability level. H atoms, [PF<sub>6</sub>]<sup>-</sup>, and a molecule of co-crystallized DCM were omitted for clarity. In the bottom view, the N(2) phenyl substituent was also removed for clarity. Selected bond distances (Å): Ru(1)-Cl(10) = 2.572(2) Ru(1)-C(15) = 2.429(2), Ru(1)-P(1) = 2.2571(8), Ru(1)-P(2) = 2.293(1); Selected Angles (°): P(1)-Ru(1)-P(2) = 81.23(2), Cp(centroid)-Ru(1)-P(centroid) = 144.49°. .... 36

**Figure 2-8.** Calculated energies of ‘donor-free’ complexes **2-5b** and **2-6b** including N<sub>2</sub> adducts, low-coordinate  $\kappa^2$ -(P,P) and  $\kappa^3$ -(P,P,Ar) isomers. .... 37

**Figure 2-9.** Thermal stability of pre-catalysts **2-1b/2-2b** and active catalysts **2-5b/2-6b** after 1 h (filled and empty bar together) and 24 h (filled bar only). % [Ru] values were quantified by <sup>31</sup>P{<sup>1</sup>H} NMR spectroscopy integrals relative to an internal standard. .... 39

**Figure 2-10.** Displacement ellipsoid plot of solid-state structure of [RuCl( $\eta^4$ -C<sub>5</sub>Me<sub>5</sub>CH<sub>2</sub>Cl)(P<sup>Cy</sup><sub>2</sub>N<sup>Ph</sup><sub>2</sub>)] [PF<sub>6</sub>] (**2-7**). Ellipsoids are given at 30% probability level. H atoms, [PF<sub>6</sub>]<sup>-</sup> counterion, a molecule of co-crystallized CH<sub>2</sub>Cl<sub>2</sub>, and a minor component of disorder in the C<sub>5</sub>Me<sub>5</sub>CH<sub>2</sub>Cl ligand were omitted for clarity. Selected bond distances (Å): Ru(1A)-Cl(1A) = 2.364(1), Ru(1A)-P(1A) = 2.2989(8), Ru(1A)-P(2A) = 2.2421(8). Selected Angles (°): P(1A)-Ru(1A)-P(2A) = 77.31(2). .... 41

**Figure 2-11.** TON comparison with 0.1 mol% of donor-free complexes **2-5b** and **2-6b**, and chloro complex **2-3b** toward the intramolecular hydroamination of **2-EA** at 70 °C, in CH<sub>3</sub>NO<sub>2</sub>. TONs were determined after 24 h by GC-FID analysis. Runs were conducted in duplicate with data points representing the average and the error bars depict the span of individual runs.... 43



**Figure 2-12.** Reaction profiles for the intramolecular hydroamination of **2-EA** with a) Cp complexes **2-1a-c** (solid lines); and b) Cp\* complexes **2-2a-c** (dashed lines). Conditions: 300 mM **2-EA**, Me-THF, 70 °C, 0.1 mol% [Ru]; **2-1a** (blue), **2-1b** (orange), **2-1c** (yellow), **2-2a** (blue), **2-2b** (orange), **2-2c** (yellow). Runs were conducted in duplicate with data points representing the average and the error bars depict the span of individual runs. .... 44

Figure 2-13. (top) Intramolecular hydroamination of **2-EA** with catalyst **2-1b** (0.25 mM) to form **2-Ind**. (bottom) Reaction profiles for runs with initial concentrations of: A, 150 mM **2-EA** (●, blue); B, 100 mM **2-EA** (■, orange); and C 100 mM **2-EA** and 50 mM **2-Ind** (▲, green) Solid lines (—) are time-shifted (Run B = orange; Run C = green). Reactions were performed in duplicate and in all cases the error was within ±5%. .... 45

**Figure 2-14.** (top) Intramolecular hydroamination of **2-Me-EA** with catalyst **2-1b** (1.5 mM) to form **2-Me-Ind**. (bottom) Reaction profiles for runs with initial concentrations of: A, 50 mM **2-Me-EA** (●, blue); B, 35 mM **2-EA** (■, orange); and C 35 mM **2-Me-EA** and 15 mM **2-Me-Ind** (▲, green) Solid lines (—) are time-shifted (Run B = orange; Run C = green). Reactions were performed in duplicate and in all cases the error was within ±5%. .... 47

**Figure 3-1.** a) Elucidated mechanism for MLC-catalyzed hydration of alkynes. For simplicity, the involvement of the ligand-centered Brønsted base is not depicted. The box on **3-I** represents an open coordination site. b) oxocycloalkylidene intermediates isolated from hydroalkoxylation catalysts. .... 63

**Figure 3-2.** General structure of hydroalkoxylation catalysts  $[\text{Ru}(\text{Cp})(\text{P}^{\text{R}}_2\text{N}^{\text{R}'_2})(\text{MeCN})][\text{PF}_6]$ , along with  $\kappa^2\text{-P,P};\eta^1\text{-C}_{\text{Ar}}$  stabilized active catalyst **3-C** and vinyl ammonium complex **3-D**. 64

**Figure 3-3.** Displacement ellipsoid plot of **3-Ru2** with ellipsoids at 50% probability level. H atoms,  $[\text{PF}_6]^-$ , and co-crystallized  $\text{Et}_2\text{O}$  were omitted for clarity. Selected bond distances (Å): Ru(1A)-P(1A) = 2.256(1), Ru(1A)-P(2A) = 2.265(1), Ru(1A)-N(1A) = 2.044(3), Ru(1A)-Cp(centroid) = 1.869, Ru(1B)-P(1B) = 2.268(1), Ru(1B)-P(2B) = 2.260(1), Ru(1B)-N(1B) = 2.029(3), Ru(1B)-Cp(centroid) = 1.872. Selected bond angles (°): P(1A)-Ru(1A)-P(2A) = 79.71(3), Ru(1A)-N(1A)-C(6A) = 172.5(3), P(1B)-Ru(1B)-P(2B) = 79.44(3), Ru(1B)-N(1B)-C(6B) = 170.1(3). .... 65

**Figure 3-4.** (top) Hydroalkoxylation of **3-1a** to generate **3-2a** with 0.5 mol% catalyst over 24 hours. (bottom) *In situ* yield of **3-2a** at 40, 54 and 70 °C with catalyst **3-Ru2** (blue) in Me-THF, and **3-Ru1**<sup>2e</sup> (red, 40 and 54 °C) in acetone. Reactions were conducted in duplicate with data points representing the average and the error bars depict the span of individual runs.... 66

**Figure 3-5.** a) Intramolecular hydroalkoxylation of **3-1a** with catalyst **3-Ru2** (7.5 mM) in C<sub>6</sub>D<sub>5</sub>Br (top). b) Reaction profiles for Runs with initial concentrations of: A 150 mM **3-1a** (●, orange); and B 100 mM **3-1a** (■, purple). The Run B data was time-shifted by 40 min (■, blue). Reactions were performed in duplicate with the data points represent the average and the error bars depict the span of values. .... 70

**Figure 3-6.** Time normalized reaction profiles for hydroalkoxylation of **3-1a** at 70 °C in C<sub>6</sub>D<sub>5</sub>Br. a) Variable time normalization with substrate concentration, plotted from reactions conducted with 7.5 mM **3-Ru2** and initial [**3-1a**] of 200 mM (orange), 150 mM (red), and 100 mM (blue). b) Time normalization with catalyst concentration, plotted from reactions conducted with 100 mM **3-1a** and initial [**3-Ru2**] of 7.5 mM (green), 5 mM (purple), and 2.5 mM (grey). Reactions were performed in duplicate and in all cases the error was <±5%. .... 71

**Figure 3-7.** Displacement ellipsoid plot of solid-state structure of alkoxy carbene complex **3-Ru3** with ellipsoids at 50% probability level. H atoms, [PF<sub>6</sub>]<sup>-</sup>, and a disordered Cp ligand (rotational about the Ru – Cp centroid axis by ca. 174°) were omitted for clarity. Selected bond distances (Å): Ru(1)-P(1) = 2.277(2), Ru(1)-P(2) = 2.272(3), Ru(1)-Cp(centroid) = 1.939, Ru(1)-C(34) = 1.949(8), C(34)-O(1) = 1.293(9). Selected bond angles (°): P(1)-Ru(1)-P(2) = 79.6(1)..... 75

**Figure 3-8.** Calculated energy difference between precursor vinylidene complexes (0 kJ/mol) and alkoxy carbene complexes **3-Ru3** and **3-Ru4**. Refer to SI for details regarding calculations. .... 76

**Figure 3-9.** Proposed catalytic cycle for intramolecular hydrofunctionalization with [Ru(Cp)(P<sup>R</sup><sub>2</sub>N<sup>R'</sup><sub>2</sub>)(MeCN)][PF<sub>6</sub>]. Structures are simplified where [Ru]<sup>+</sup> = [Ru(Cp)(P<sup>R</sup><sub>2</sub>N<sup>R'</sup><sub>2</sub>)]<sup>+</sup>, and [PF<sub>6</sub>]<sup>-</sup> is excluded for clarity. .... 80

**Figure 4-1.** Displacement ellipsoid plot of complex **4-Ru2b**. Ellipsoids are given at 30% probability level. H atoms (except H40), the PF<sub>6</sub><sup>-</sup> anion, and a molecule of co-crystallized

hexanes were omitted for clarity. Selected bond distances (Å): Ru(1)-P(1) = 2.2966(9); Ru(1)-P(2) = 2.2815(8); Ru(1)-Cp\*(centroid) = 1.918; Ru(1)-C(39) = 1.851(3); C(39)-C(40) = 1.316(4). Selected Angles (°): P(1)-Ru(1)-P(2) = 78.16(2); Ru(1)-C(39)-C(40) = 176.9..... 94

**Figure 4-2.** (top) Stoichiometric reaction of and **4-Ru2b** under conditions: i) DCM, 25 °C, 30 minutes; and ii) MeCN, C<sub>6</sub>D<sub>5</sub>Br, 2 days, 90 °C. (bottom) <sup>31</sup>P{<sup>1</sup>H NMR spectra stack plot of a) **4-Ru2b** in C<sub>6</sub>D<sub>5</sub>Br and b) after reaction under conditions ii. Orange box highlights MeCN adduct **4-Ru6**. ..... 97

**Figure 5-1.** Previous established organic reactions which employed P<sup>R</sup><sub>2</sub>N<sup>R'</sup><sub>2</sub> ligands. Ru-P<sub>2</sub>N<sub>2</sub> catalysts used were [Ru(Cp/Cp\*)(P<sup>R</sup><sub>2</sub>N<sup>R'</sup><sub>2</sub>)(MeCN)]PF<sub>6</sub>. ..... 106

**Figure 5-2.** Displacement ellipsoid plot of **5-3a** (left) and **5-3b** (right) with ellipsoids at the 50% probability level. **5-3a** had co-crystallized DCM and disordered CF<sub>3</sub> groups that were omitted for clarity. **5-3b** had co-crystallized DCM and disordered aryl-CF<sub>3</sub> substituents that were omitted for clarity. Both complexes had the H atoms omitted for clarity. Selected bond distances (Å): **5-3a**, Pd(1)-P(1) = 2.291(1), Pd(1)-P(2) = 2.2934(8), Pd(1)-C(1) = 2.120(2), Pd(1)-C(2) = 2.125(2), Pd(1)-C(15) = 3.220(2), Pd(1)-C(28) = 3.063(2), C(1)-C(2) = 1.430(3); **5-3b**, Pd(1)-P(1) = 2.302(1), Pd(1)-P(2) = 2.284(1), Pd(1)-C(1) = 2.123(3), Pd(1)-C(2) = 2.113(3), Pd(1)-C(16) = 3.161(3), C(1)-C(2) = 1.430(4). Selected bond angles (°): **5-3a**, P(1)-Pd(1)-P(2) = 85.34(2), C(1)-Pd(1)-C(2) = 39.36(8); **5-3b**, P(1)-Pd(1)-P(2) = 85.67(3), C(1)-Pd(1)-C(2) = 39.5(1). ..... 109

**Figure 5-3.** Displacement ellipsoid plot of **5-2a** representative complex with ellipsoids at 50% probability. H atoms and co-crystallized CH<sub>2</sub>Cl<sub>2</sub> and OMs anion were omitted for clarity. Selected bond distances (Å): Pd(1)-P(1) = 2.246(2), Pd(1)-P(2) = 2.336(3), Pd(1)-N(1) = 2.124(8), Pd(1)-C(1) = 2.029(9). Selected bond angles (°): P(1)-Pd(1)-P(2) = 82.63(8), N(1)-Pd(1)-C(1) = 81.7(3). τ<sub>4</sub> geometry index: 0.03 ..... 110

**Figure 5-4.** (top) Mizoroki-Heck coupling of phenyl triflate and styrene with 1 mol% **5-3a** or **5-3b** over 16 h. (bottom) Conversion to the linear (red) and branched (blue) products with **5-3a** and **5-3b** (solid), and **5-2a** and **5-2b** (outline)..... 111

**Figure 5-5.** (top) Attempted oxidative addition with phenyl triflate in the presence of piperidine at room temperature over 2 h. (bottom) *In situ* monitoring of the reaction with TO

the top NMR spectrum of the stack plot and after 2 h the bottom NMR spectrum of the stack plot. a) Reaction with **5-2a** (SM was not soluble) and b) reaction with **5-2b**..... 114

**Figure 5-6.** Displacement ellipsoid plot of **5-5a** with ellipsoids at 50% probability. H atoms were omitted for clarity. Orientational disorder in the CF<sub>3</sub> group and phenyl substituent were omitted for clarity. The sample was also compositionally disordered between **5-5a** and [Pd(I)<sub>2</sub>(P<sup>Ph</sup><sub>2</sub>N<sup>ArCF<sub>3</sub></sup>)<sub>2</sub>] which was omitted. Selected bond distances (Å): Pd(1)-P(1) = 2.320(2), Pd(1)-P(2) = 2.264(1), Pd(1)-I(1) = 2.634(1), Pd(1)-C(1) = 2.012(7). Selected bond angles (°): P(1)-Pd(1)-P(2) = 83.23(3). τ<sub>4</sub> geometry index: 0.09..... 116

**Figure 5-7.** (top) Halide abstraction of **5-5b** with AgOTf and piperidine. (bottom) <sup>31</sup>P{<sup>1</sup>H} NMR stack plot (DCM-*d*<sub>2</sub>) of: a) starting material (**5-5b**), b) solid from halide abstraction with **5-5b**, c) solid from oxidative addition with **5-2b**. Red box highlights the proposed product. .... 117

**Figure 5-8.** (top) Mizoroki-Heck coupling of phenyl triflate (200 mM) and styrene (200 mM) with catalyst **5-2a** and TMP at 85 °C in toluene-*d*<sub>8</sub>. (bottom) Reaction profiles for runs A) 8 mM catalyst (orange) and B) 4 mM catalyst. Reactions were performed in duplicate and the error bars depicting the span of values. .... 118

**Figure 5-9.** Steric maps of a) **5-3a**, b) **5-3b**, c) **5-5a**, and d) **5-2a**. The horizontal line from y = 0 defines the P-Pd-P plane. .... 120

## List of Schemes

<b>Scheme 1-1.</b> a) Examples of medicine which has the imine functionality. b) Total synthesis of morphine which begins with the asymmetric hydrogenation of an imine. ....	5
<b>Scheme 1-2.</b> General intramolecular (a) and intermolecular (b) hydrofunctionalization reactions. ....	6
<b>Scheme 1-3.</b> a) Tautomerization of a terminal alkyne to a metal free vinylidene. b) Potential pathways for the formation of a metal vinylidene following $\pi$ -coordination of a metal complex. ....	10
<b>Scheme 1-4.</b> First example of hydroamination mediated with $M-P^{R_2}N^{R'_2}$ complexes. Difference in activity based on basicity of pendent nitrogen of the $P^{R_2}N^{R'_2}$ ligand. ....	18
<b>Scheme 1-5.</b> General reaction scheme and conditions for the formation of 2° alcohols via reductive arylation (left) and redox neutral $\alpha$ -arylation (right).....	20
<b>Scheme 1-6.</b> Redox neutral and oxidative ketone synthesis from ketone and primary alcohol substrates, respectively. ....	21
<b>Scheme 2-1.</b> Intramolecular hydroamination of 2-ethynylaniline with Ru catalysts <b>2-1a-c</b> and <b>2-2a-c</b> . ....	31
<b>Scheme 2-2.</b> Halide abstraction under $N_2$ utilizing $TIPF_6$ to generate complexes <b>2-5b-N<sub>2</sub></b> and $k^3$ -(P,P,Ar)- <b>2-5b</b> , and <b>2-6b-N<sub>2</sub></b> . Reactions performed at room temperature in i) $C_6H_5F$ or ii) DCM. ....	35
<b>Scheme 2-3.</b> Deactivation of operationally unsaturated complex <b>2-6b-N<sub>2</sub></b> via reaction with DCM to give Ru-Cl complex <b>2-7</b> .....	40
<b>Scheme 2-4.</b> Benchmark cyclization of 2-ethynylaniline to indole catalyzed using the coordinatively unsaturated complexes <b>2-5b</b> and <b>2-6b</b> , and a control reaction with the complex <b>2-3b</b> . ....	42

<b>Scheme 2-5.</b> Proposed equilibrium between $\kappa^3$ -(P,P,Ar)- <b>2-5b</b> and possible inhibition adducts <b>2-Ru-Ind</b> . Note: samples of <b>2-5b</b> also contain the $\kappa^2$ -(P,P)- <b>2-5b-N<sub>2</sub></b> . [Ru] = [Ru(Cp)(P <sup>Cy</sup> <sub>2</sub> N <sup>Ph</sup> <sub>2</sub> )]PF <sub>6</sub> .....	46
<b>Scheme 3-1.</b> Intramolecular alkyne hydrofunctionalization .....	62
<b>Scheme 3-2.</b> Influence of Substrate Linker on <b>3-Ru2</b> hydroalkoxylation performance. <i>In situ</i> yields were determined by <sup>1</sup> H NMR spectroscopy relative to dimethyl terephthalate ( <b>3-DMT</b> ) as internal standard. Reactions were conducted in duplicate, and values were within $\pm 5\%$ . <sup>[b]</sup> 10 mol% <b>3-Ru2</b> . <sup>[c]</sup> 0.1 mol% <b>3-Ru2</b> . .....	68
<b>Scheme 3-3.</b> Influence of Nucleophile on Ru <sub>2</sub> Hydrofunctionalization Performance. <i>In situ</i> yields were determined by <sup>1</sup> H NMR spectroscopy relative to <b>3-DMT</b> as internal standard. Reactions were conducted in duplicate and all yields were within $\pm 5\%$ . <sup>[b]</sup> 0.1 mol% <b>3-Ru2</b> . .....	69
<b>Scheme 3-4.</b> Parallel isotope experiments for the intramolecular hydroalkoxylation of <b>3-1a</b> and <b>3-1a-d<sub>1</sub></b> .....	72
<b>Scheme 3-5.</b> KIE measurement from parallel reactions of <b>3-Ru2</b> with a) phenylacetylene, and b) phenylacetylene- <i>d</i> <sub>1</sub> .....	73
<b>Scheme 3-6.</b> Parallel isotope experiments for the intramolecular hydroalkoxylation of <b>3-1a</b> and <b>3-1a-OD</b> .....	74
<b>Scheme 3-7.</b> Synthesis of <b>3-Ru3</b> .....	75
<b>Scheme 3-8.</b> a) Attempted deuterium incorporation at C <sub>β</sub> of <b>3-Ru3</b> . b) <b>3-Ru3</b> treated with exogenous bases to deprotonate C <sub>β</sub> . c) Attempted catalytic cyclization of <b>3-1d</b> with 20 mol% base additives. ....	77
<b>Scheme 4-1.</b> Intra- vs Intermolecular hydroamination of terminal alkynes. ....	90
<b>Scheme 4-2.</b> Stoichiometric reactions with vinylidenes and ruthenium catalyzed hydroamination proposed to proceed through vinylidene intermediate. ....	91

<b>Scheme 4-3.</b> Formation of vinyl ammonium and vinylidene complexes. ....	92
<b>Scheme 4-4.</b> Synthesis of <b>4-Ru2a</b> and <b>4-Ru2b</b> .....	93
<b>Scheme 4-5.</b> Stoichiometric reactions of <b>4-Ru2b</b> with amine nucleophiles (50 equiv) which we proposed would generate <b>4-Ru3</b> following nucleophilic attack at C <sub>α</sub> . Alternative reaction pathway was formation of the proposed acetylide complex <b>4-Ru4</b> following deprotonation of C <sub>β</sub> proton. ....	95
<b>Scheme 4-6.</b> Independent synthesis of <b>4-Ru4</b> generated from deprotonation of <b>4-Ru2b</b> with KH in THF at room temperature over 3 h.....	96
<b>Scheme 4-7.</b> Attempted intermolecular hydroamination of phenylacetylene with (top) aniline and (bottom) 2-pyrrolidinone with 2 mol% <b>4-Ru6</b> at 110 °C in C <sub>6</sub> D <sub>6</sub> . ....	98
<b>Scheme 5-1.</b> Competing pathways in the Heck reaction to form linear or branched products. ....	105
<b>Scheme 5-2.</b> a) First established Mizoroki-Heck coupling with Pd <sub>2</sub> dba <sub>3</sub> and P <sup>R</sup> <sub>2</sub> N <sup>R'</sup> <sub>2</sub> ligands. b) optimized conditions for Mizoroki-Heck coupling with <b>5-2a</b> and <b>5-2b</b> . ....	107
<b>Scheme 5-3.</b> Ligand substitution of Leitch complex with P <sup>R</sup> <sub>2</sub> N <sup>ArCF<sub>3</sub></sup> <sub>2</sub> ligands via reaction in THF to give the corresponding [Pd(P <sup>R</sup> <sub>2</sub> N <sup>ArCF<sub>3</sub></sup> <sub>2</sub> )(MAH)] complexes <b>5-3a</b> and <b>5-3b</b> . ....	108
<b>Scheme 5-4.</b> Synthesis of <b>5-5a</b> and <b>5-5b</b> . Reaction conditions i) room temperature for 48 h. ii) 50 °C for 18 h.....	115
<b>Scheme 6-1.</b> a) potential of nucleophiles, such as oxygen, with lower basicity to avoid acetylide formation. b) investigation of internal alkynes for the formation of vinylidenes. ....	132
<b>Scheme 6-2.</b> Cyclization of ynamides to form indole .....	133

## List of Tables

<b>Table 5-1.</b> Attempted oxidative addition of <b>5-3a</b> with aryl (pseudo)halides. ....	112
-----------------------------------------------------------------------------------------------	-----



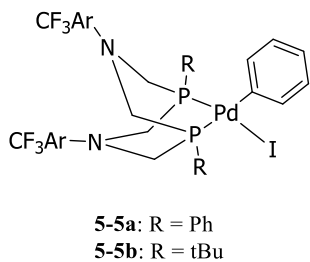
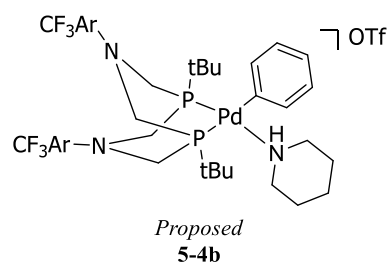
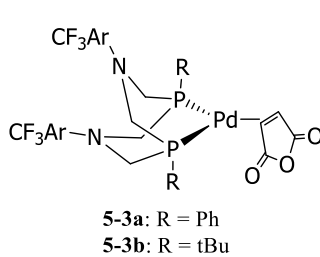
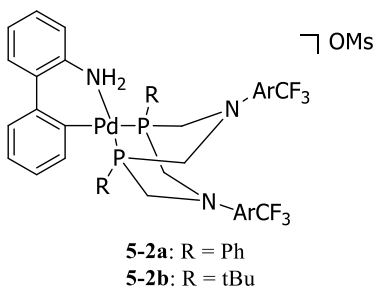
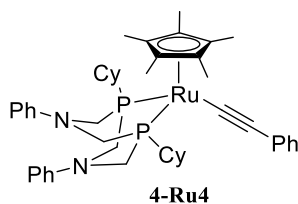
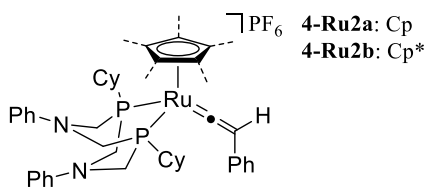
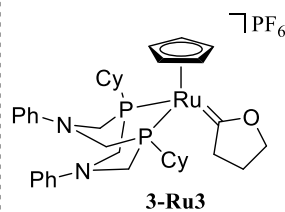
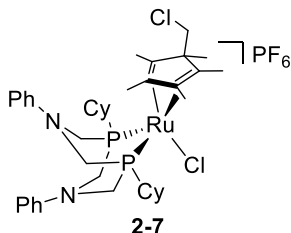
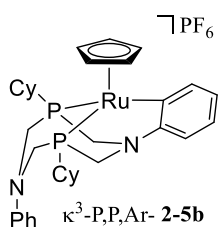
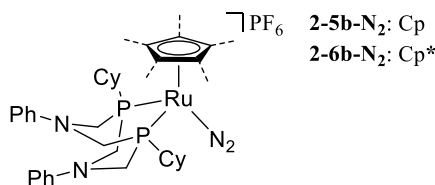
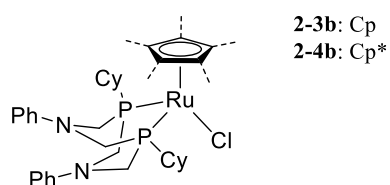
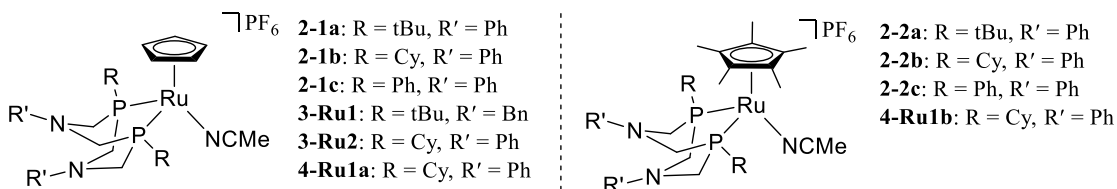
## List of Abbreviations

ABP	2-aminobiphenyl
Ar	Aryl
Bn	Benzyl
C <sub>α</sub>	Alpha carbon
C <sub>β</sub>	Beta carbon
Cp	Cyclopentadienyl
Cp*	Pentamethylcyclopentadienyl
Cy	Cyclohexyl
Conv.	Conversion
COSY	Correlation spectroscopy
Calc.	Calculated
DCM	Dichloromethane
DFT	Density functional theory
DMT	Dimethyl terephthalate
<sup>DMP</sup> DAB	2,6-dimethylphenyl- <i>N,N'</i> -diaryl-diazabutadiene
Equiv	Equivalent
FTIR	Fourier-transform infrared spectroscopy
GC-FID	Gas chromatography flame ionization detector
HMBC	Heteronuclear Multiple Bond Correlation

HSQC	Heteronuclear Single Quantum Coherence
IR	Infrared spectroscopy
IS	Internal standard
$\kappa^2$ -P,P	Kappa two through two phosphorus atoms
$\kappa^3$ -P,P,Ar	Kappa three through two phosphorus atoms and an aryl carbon atom
MAH	Maleic anhydride
MALDI	Matrix Assisted Laser Desorption/Ionization
M	Metal
MLC	Metal ligand cooperative
Non-MLC	Non-metal ligand cooperative
Me	Methyl
Me-THF	2-methyltetrahydrofuran
Min	Minute
NMR	Nuclear magnetic resonance
Obs	Observed
ORTEP	Oak Ridge thermal ellipsoid plot
Ph	Phenyl
$P^{R_2}N^{R'_2}$ or $P_2N_2$	1,5-diaza-3,7-diphosphacyclooctane
Ppm	Parts per million

T0	Initial time point
THF	Tetrahydrofuran
TON	Turnover number
TOF	Turnover frequency
<i>t</i> Bu or t-Bu	<i>Tert</i> -butyl
Tp	hydridotris(pyrazolyl)borate
VTNA	Variable time normalization analysis

# List of Complexes



# Chapter 1

## 1 Introduction

### 1.1 Importance of Catalysis and Understanding It

Catalysis has emerged as one of the most investigated and important fields of chemistry, ubiquitous in industry,<sup>1</sup> pharmaceuticals,<sup>2</sup> and academic research. The role of a catalyst is to increase the rate of chemical reactions, while not being consumed in the process. This is achieved through a decrease in the activation energy of the highest energy step of a reaction (Figure 1-1). The vast importance of catalysis was recognized in 1909 when Ostwald won the Nobel Prize in Chemistry for his contributions to catalysis, chemical equilibria, and rate of reactions.<sup>3</sup> Catalysis has been a contributor to many Nobel Prizes in chemistry since 1909, with one of the most prominent examples being the 2010 Nobel Prize in chemistry on palladium cross-couplings.<sup>4</sup> While the chemistry community can recognize the importance of these awards, a more tangible way to understand the importance can be seen in the global catalyst market, which was valued at \$35.5 billion USD in 2020 and estimated to reach \$57.5 billion by 2030.<sup>1b</sup> Approximately 90% of all chemically obtained industrial goods involve a catalyst at some point during their production.<sup>5</sup>

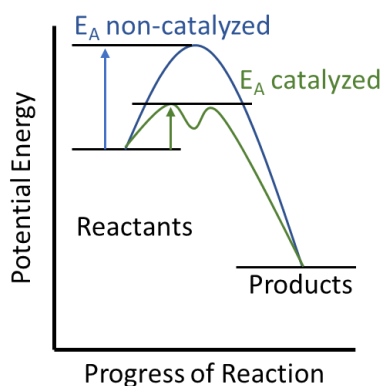


**Figure 1-1.** Energy profile of a non-catalyzed reaction (blue) vs catalyzed reaction (green).

The broad term catalysis can be broken down to include two primary types of catalysis: 1) heterogenous catalysis, which implies the catalyst and substrate(s) are in two separate phases (e.g. liquid/solid); and 2) homogenous catalysis, which indicates the catalyst and

substrate(s) are in the same phase (e.g. liquid/liquid).<sup>6</sup> While both have their advantages and disadvantages this document will focus on homogenous catalysis, which is typically characterized by highly active and well-defined complexes, but can suffer from difficult separations and sensitivities to deactivation.<sup>1b</sup> One of the benefits of homogenous catalysis is being able to apply Michaelis-Menten kinetics, which simply involves reversible binding of the substrate to a catalyst resulting in the formation of a catalyst-substrate complex and irreversible formation of the product and regeneration of the catalyst (Figure 1-2a).<sup>7</sup> Investigations into the catalytic cycle of systems often include many intermediates between substrate coordination and product release, such as the catalytic cycle of a Sonogashira reaction (Figure 1-2b).<sup>8</sup> To further understand how a catalyst works the idea of the catalyst active site must be discussed. The catalytic reaction occurs at a specific site on the catalyst (e.g. an empty coordination site following dissociation of a placeholder ligand) which mediates the reactivity.<sup>9</sup> This was first introduced by H. S. Taylor in the 1920s,<sup>10</sup> however, the idea has been greatly expanded upon since to include steric considerations of the active site and the electronic environment around it.<sup>11</sup> Both the steric and electronic properties of a catalyst have an influence on catalytic performance. The electronic properties of catalysts typically refer to the oxidation state or type of metal centre, while the steric properties are primarily defined by the ligand structure. Catalysts are often assessed through their catalytic lifetime which is typically reported as the catalytic turnover number (TON) and it is the ratio between the consumed mol of starting material and the mol catalyst used, with higher TONs meaning better performance. Catalysts can also be assessed through selectivity, mild reaction conditions, turnover frequency (TOF), atom economy, etc. Due to the variety of ways to assess catalytic systems, continual effort has been put forward to investigate how to make better and more effective catalysts.

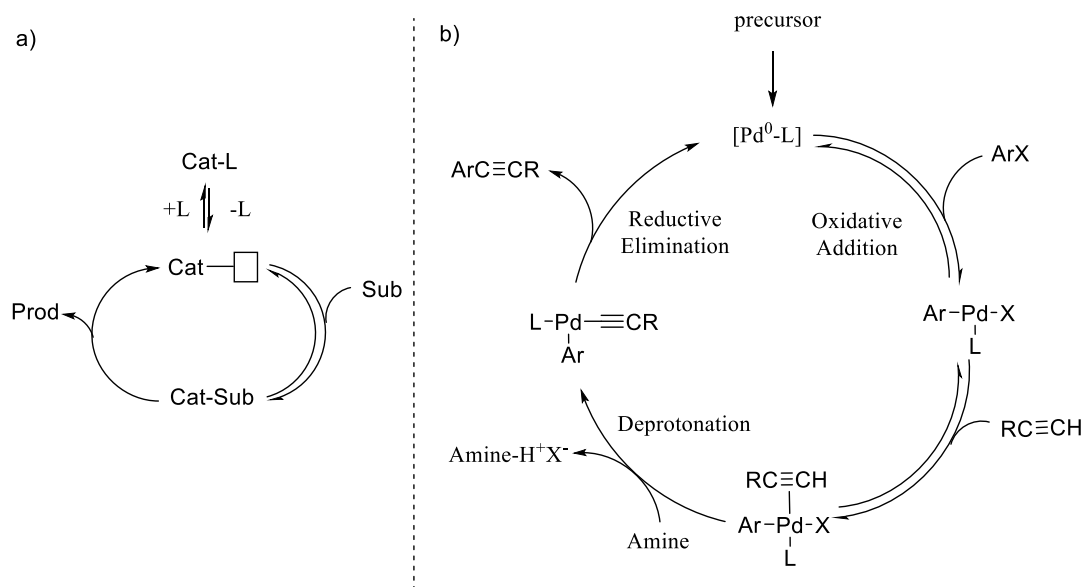


**Figure 1-2.** General catalytic cycle with a) one substrate binding to the catalyst and releasing one product, b) general proposed mechanism for a copper free Sonogashira coupling.

## 1.2 Hydrofunctionalization to Generate Nitrogen and Oxygen Compounds

### 1.2.1 Importance of Nitrogen and Oxygen Compounds

Compounds that possess nitrogen and oxygen heteroatoms are ubiquitous in a variety of academic and industrial settings.<sup>12</sup> Nitrogen compounds, for example, have found prominent use in the pharmaceutical industry, where as much as 84% of US FDA approved small-molecule drugs contain a nitrogen heteroatom.<sup>12c</sup> With a large portion of those drugs bearing nitrogen heterocycle substructures such as piperidine (#1 most frequent) and indole (#9 most frequent). Melatonin, a readily available over-the-counter drug contains an indole core and in 2006 had sales of \$81 million USD<sup>12a</sup> which have been steadily increasing, especially in recent years. In similar regards, oxygen-containing compounds are also of particular interest for chemistry. Oxygen heterocycles are observed in many natural products<sup>13</sup> as well as pharmaceutical drugs.<sup>12b</sup> In FDA approved pharmaceutical drugs oxygen heterocycles were the second most common structural component.<sup>12b</sup> Many

different oxygen heterocycles are found in these drugs such as benzofuran (#16 most frequent) and delta-lactone (#19 most frequent).

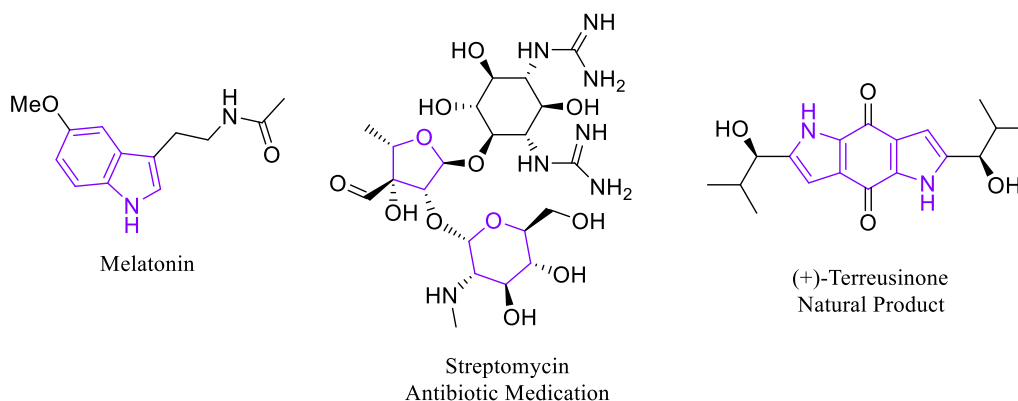
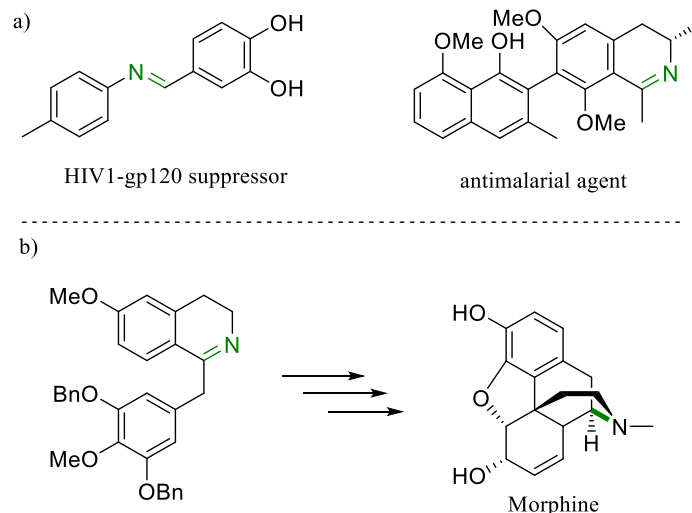


**Figure 1-3.** Examples of a pharmaceutical drug and natural product which contain nitrogen and oxygen heterocycles.

The types of nitrogen-containing functional groups in natural products, pharmaceutical drugs, and commodity chemicals are quite diverse and can include imines, enamines, and enamides. Medicinal drugs with the imine moiety have been used for the treatment of HIV and malaria.<sup>14</sup> These functional groups can also be sites for further chemical manipulation; thus such molecules are powerful building blocks to access a diverse array of other desirable products. Imines and enamines have been utilized in asymmetric hydrogenation reactions to access several natural products, including the synthesis of morphine (Scheme 1-1).<sup>15</sup> Due to the diverse applications of these nitrogen moieties new and improved methods to access them are still actively investigated.

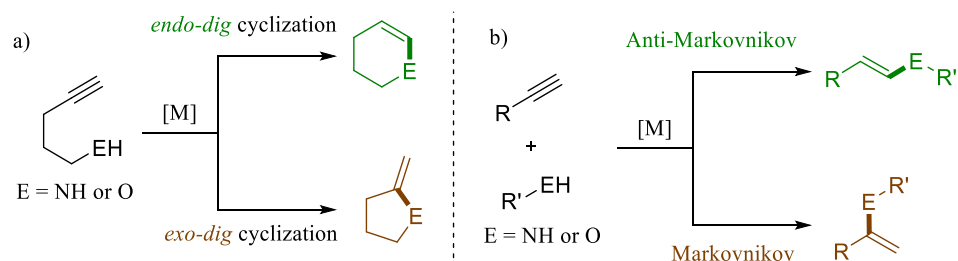




**Scheme 1-1.** a) Examples of medicine which has the imine functionality. b) Total synthesis of morphine which begins with the asymmetric hydrogenation of an imine.

### 1.2.2 Ruthenium Catalyzed Hydrofunctionalization to Access *N*- and *O*-Compounds

Hydrofunctionalization is an attractive method for the generation of compounds that contain nitrogen (hydroamination and hydroamidation)<sup>16</sup> and oxygen (hydroalkoxylation and hydration)<sup>13</sup> containing compounds. These methods involve the activation of a carbon-carbon unsaturated bond and subsequent nucleophilic attack by a heteroatom to form a carbon-nitrogen/oxygen bond. The work presented herein will focus on the hydrofunctionalization of terminal alkynes exclusively. There are a few key advantages to hydrofunctionalization reactions: the reactions can be performed in an intra and intermolecular fashion and generate a variety of compounds (Scheme 1-2a and b); and the reaction is 100% atom-economic, which generates no byproducts. The initial reports of hydroamination with alkynes utilized mercury-based<sup>16-17</sup> catalysts, which were thoroughly investigated until the 1990s when it was set aside due to toxicity concerns. Following the use of mercury, early transition metal<sup>18</sup> and organolanthanide<sup>19</sup> catalysts were investigated. However, the high oxophilicity of both catalyst classes were undesirable, both in terms of catalytic conditions and functional group tolerance.<sup>16</sup> Late transition metals, such as Au<sup>20</sup>, Pt<sup>21</sup>, Ru<sup>22</sup>, and others, have been successfully utilized and avoid issues associated with oxophilicity and functional group tolerance.



**Scheme 1-2.** General intramolecular (a) and intermolecular (b) hydrofunctionalization reactions.

In the last 23 years ruthenium catalysts have begun to be investigated for hydrofunctionalization reactions with alkynes. Wakatsuki *et al.* published the earliest example of ruthenium catalyzed intermolecular hydroamination in 1999, which investigated the reaction between phenylacetylene and aniline at 100 °C catalyzed with the non-metal-ligand-cooperative (non-MLC)  $[\text{Ru}_3(\text{CO})_{12}]$  complex, which performed without solvent (Figure 1-4a).<sup>23</sup> The presence of either acid or ammonium salt was essentially required, with only 1.6% conversion observed without additive present in the reaction versus 52% with  $\text{NH}_4\text{PF}_6$  under analogous conditions. Under optimal conditions of 0.1 mol%  $[\text{Ru}_3(\text{CO})_{12}]$ , 0.3 mol%  $\text{NH}_4\text{PF}_6$ , 100 °C, neat, over 12 h, 84% conversion to the Markovnikov product was achieved. Furthermore, a variety of phenylacetylene and aniline derivatives were also coupled with electron withdrawing substituents, while a sterically hindered aniline required higher catalyst loadings.  $[\text{Ru}_3(\text{CO})_{12}]$  has also been shown to promote intramolecular hydroamination of 6-aminohex-1-yne (Figure 1-4b).<sup>24</sup> Low conversion to the *exo-dig* cyclized product (18%) was observed at 1 mol% in DCM at 40 °C. It must be noted that investigations of  $[\text{Ru}_3(\text{CO})_{12}]$  for intramolecular reactivity did not include-additives as was explored for intermolecular reactivity,<sup>23</sup> which could have resulted in greater conversion. Furthermore, while the intramolecular nucleophilic attack for 6-aminohex-1-yne should be more favourable entropically than intermolecular nucleophilic attack, the flexible nature of the linkage between the alkyne and amine nucleophile would be expected to have a high degree of translational entropy. Therefore, even at low conversion to the cyclized product, this remained a promising result.

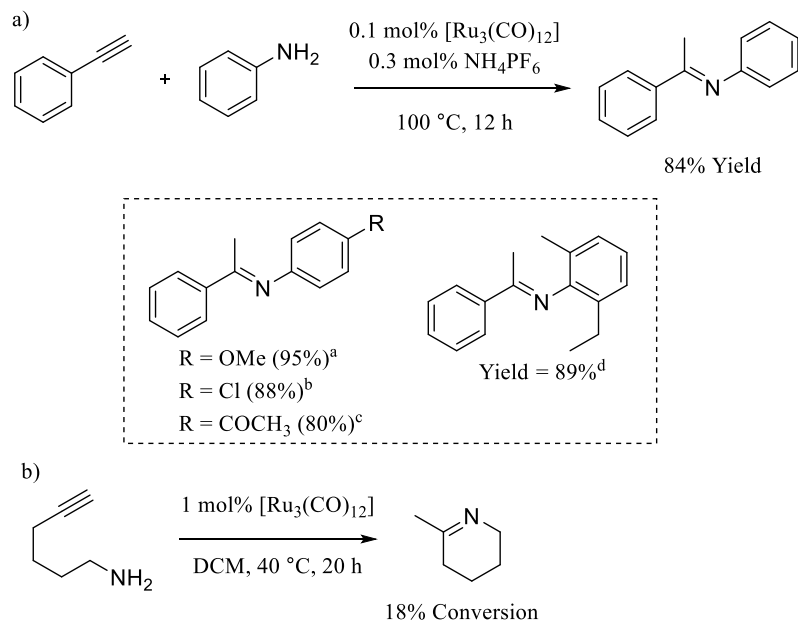


**Figure 1-4.** Intermolecular hydroamination of phenylacetylene and aniline derivatives. Reaction conditions: <sup>a</sup> 0.1 mol%  $[\text{Ru}_3(\text{CO})_{12}]$ , 0.3 mol%  $\text{NH}_4\text{PF}_6$ , 3 h; <sup>b</sup> 0.2 mol%  $[\text{Ru}_3(\text{CO})_{12}]$ , 0.6 mol%,  $\text{NH}_4\text{PF}_6$ , 3 h; <sup>c</sup> 1 mol%  $[\text{Ru}_3(\text{CO})_{12}]$ , 3 mol%,  $\text{HBF}_4/\text{Et}_2\text{O}$ , 12 h; 1 mol%  $[\text{Ru}_3(\text{CO})_{12}]$ , 3 mol%,  $\text{NH}_4\text{PF}_6$ , 12 h. <sup>d</sup> 0.7 mol%  $[\text{Ru}_3(\text{CO})_{12}]$ , 2.1 mol%,  $\text{HBF}_4/\text{Et}_2\text{O}$ , 12 h.

In 2002 Trost and Rhee investigated non-MLC ruthenium catalysts,  $[\text{RuCl}(\text{Cp})(\text{PR}_3)_2]$ , for the formation of oxygen heterocycles via intramolecular alkyne hydroalkoxylation.<sup>25</sup> Cyclization with the  $[\text{RuCl}(\text{Cp})(\text{PR}_3)_2]$  catalysts was achieved with ca. 10 mol% loading, excess ligand, and the inclusion of several additives in stoichiometric amounts. Selectivity was problematic, as a two-component mixture of the lactone and dihydropyran products were obtained even after reaction optimization. In 2010 Grotjahn and coworkers investigated a metal ligand cooperative (MLC) bifunctional ruthenium catalyst for the formation of indole and benzofuran derivatives via intramolecular hydrofunctionalization (Figure 1-5).<sup>22, 26</sup> Cyclization of a variety of indole and phenol derivatives was achieved with 2–5 mol% catalyst loading at 70 °C in acetone. Quantitative conversion from 2-ethynylaniline and 2-ethynylbenzyl alcohol to the *endo-dig* cyclized indole and benzofuran compounds were observed over 17 and 2 h, respectively. A variety of similar 2-ethynylaniline and 2-ethynylbenzyl alcohol derivatives were explored which had excellent

conversion to their corresponding *endo-dig* cyclized heterocycles. The *endo-dig* selectivity observed was proposed to be a result of the mechanism that would involve a vinylidene species, which would direct nucleophilic attack to the highly electrophilic alpha carbon bound to the metal centre (Section 1.3).

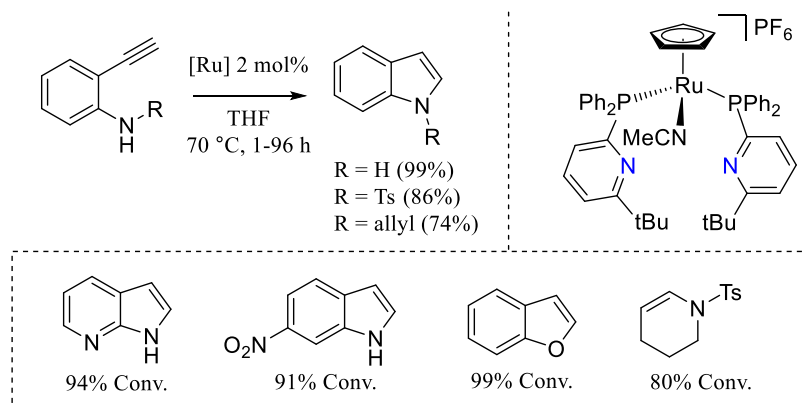


**Figure 1-5.** Intramolecular hydrofunctionalization to generate a variety of nitrogen and oxygen heterocycles. Reaction conditions: 2 mol% [Ru], THF, 70 °C.

In 2011 and 2012, Saa *et al.* investigated the use of  $[\text{RuCl}(\text{Cp})(\text{PPh}_3)_2]$  for intramolecular hydroamination of 2-ethynylaniline and 2-ethynylbenzylamine derivatives.<sup>27</sup> Reaction optimization of the benchmark 2-ethynylaniline cyclization generated 84% indole at 10 mol%  $[\text{Ru}(\text{Cl})(\text{Cp})(\text{PPh}_3)_2]$ , in pyridine at 90 °C for 25 min (Figure 1-6). Excellent conversion was observed for functional groups *para* to the amine with a slight decrease in conversion for electron withdrawing functional groups. Mono-protected 2-ethynylaniline derivatives also showed comparable conversion with sulfonyl protecting groups relative to the unprotected substrate. 2-Ethynylbenzamide derivatives also showed comparable conversion to their respective *endo-dig* cyclized products. Interestingly, cyclization of 2-ethynyl benzylamine showed no cyclization, while analogous derivatives were able to be cyclized. Similar to the MLC bifunctional ruthenium complex, exclusive formation of the *endo-dig* cyclized heterocycles was observed with  $[\text{Ru}(\text{Cl})(\text{Cp})(\text{PPh}_3)_2]$ , which was highly suggestive of a vinylidene intermediate in the catalytic cycle.

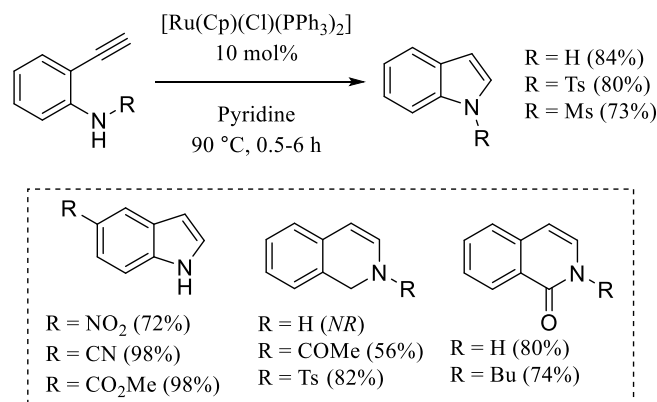


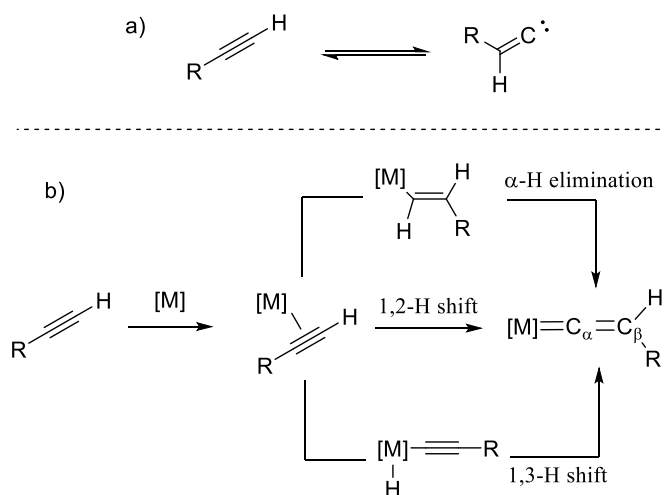
**Figure 1-6.** Intramolecular hydroamination to generate a variety of nitrogen heterocycles catalyzed with a non-MLC ruthenium complex. *NR* means no reaction.

The utilization of ruthenium complexes to promote hydrofunctionalization reactions has in large part focused on the intramolecular cyclization of 5- and 6-membered heterocycles. To date the realization of 4-membered heterocycle formation has not been established for any late transition metal catalysts and 7- and 8-membered heterocycle formation has only been demonstrated a handful of times.<sup>28</sup> While a substantial substrate scope has been established for these ruthenium catalysts, in-depth mechanistic analysis has not been thoroughly investigated.

### 1.3 Metal Vinylidenes and Their Role in Catalysis

In general terms, a vinylidene can be thought of as an isomer of an alkyne, which possess a lone pair on the terminal carbon atom and a C=C double bond. Metal vinylidenes are an example of a unsaturated fisher carbene complex in which the C<sub>α</sub> forms a double bond with the metal center (Scheme 1-3a).<sup>29</sup> The first example of a metal vinylidene was discovered in 1966 from irradiation of benzophenone and iron pentacarbonyl in benzene to afford a bimetallic iron complex bridged by a vinylidene.<sup>30</sup> However, their utilization in catalysis was not realized until 1985, in which a metal vinylidene was determined to be a key intermediate in the polymerization of the terminal alkynes, phenylacetylene and acetylene, with W(CO)<sub>6</sub>.<sup>31</sup> The mechanism for formation of metal vinylidenes (Scheme 1-3b) has been extensively investigated over the last few decades which has found three possible routes to generate the metal vinylidenes: 1) generation of a metal alkenyl intermediate from

a metal-hydride followed by  $\alpha$ -hydrogen elimination;<sup>32</sup> 2) a direct 1,2-hydrogen migration;<sup>33</sup> or 3) formation of a metal hydride via oxidative addition followed by a 1,3-hydrogen migration.<sup>34</sup> A key aspect of transition metal vinylidenes is the extremely electrophilic  $C_\alpha$ . Bonding of a vinylidene to metal involves  $\sigma$  donation from  $C_\alpha$  to the metal center and  $\pi$ -backbonding from the metal center into an empty p-type orbital of  $C_\alpha$ , which is orthogonal to the  $C=C$   $\pi$  bond. However, the  $\pi$  back bond from the metal center can be weak depending on the metal, and in the case of late transition metals this back bonding is not sufficient to satisfy  $C_\alpha$ . For example, molecular orbital analysis of  $[\text{Fe}(\text{Cp})(\text{CO})_2(=\text{C}=\text{CH}_2)]^+$  has indicated that ca. 60% of the LUMO is localized on  $C_\alpha$ .<sup>35</sup>



**Scheme 1-3.** a) Tautomerization of a terminal alkyne to a metal free vinylidene. b) Potential pathways for the formation of a metal vinylidene following  $\pi$ -coordination of a metal complex.

Metal vinylidenes have been utilized in various types of reactions, however, for the purpose of this thesis, the additions of nucleophiles to  $C_\alpha$  will be focused on exclusively. The reactivity of metal vinylidenes in hydrofunctionalization reactions will be discussed. Many ruthenium catalysts utilized for hydrofunctionalization reactions have been proposed to proceed through vinylidene intermediates. In 2011 Saa *et al.* investigated the intramolecular hydroamination of a variety of substrates that could potentially generate either the *endo-dig* or *exo-dig* cyclized *N*-heterocycles.<sup>27a</sup> The catalyst proved regioselective for the *endo-dig* product, which was rationalized through the proposed

mechanism (Figure 1-7). Coordination of the alkyne to the active catalyst **I** resulted in formation of the vinylidene intermediate **II**. Nucleophilic attack at the highly electrophilic C<sub>α</sub> and proton migration mediated by the exogenous base would generate the ruthenium alkenyl complex **III**. Lastly, protonolysis would regenerate the active catalyst **I** and form the observed *endo-dig* cyclized product.

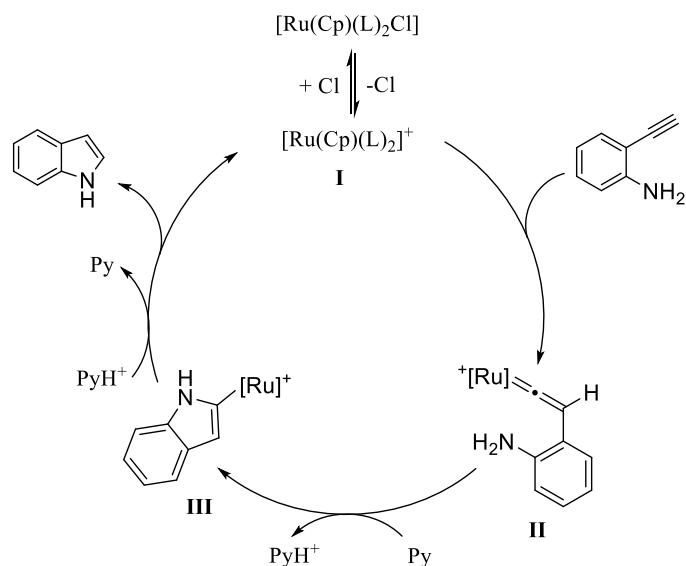


**Figure 1-7.** Proposed mechanism for the cyclization of 2-ethynylaniline which proceeds through a vinylidene intermediate.

To date, many late transition metal catalysts used for hydrofunctionalization reactions have been proposed to proceed through vinylidene intermediates. However, many examples of non-vinylidene involving pathways regarding the mechanisms of Ru-mediated alkyne transformations have also been demonstrated.<sup>36</sup> Therefore, in-depth mechanistic investigations and intermediate isolation to validate these hypotheses must be performed. Whereas much of the current proposals have been based off observed selectivity for the *endo-dig* cyclized product to suggest a vinylidene involving pathway.

## 1.4 Metal-Ligand Cooperativity and Dynamics of $P^{R_2}N^{R'_2}$ Ligands

### 1.4.1 Cooperative Ligands and their Role in Catalysis

Ligands are an integral part of a catalyst structure and have a major impact on the performance and reactivity observed. Ligands can be divided roughly into one of two categories, spectator ligands, which influence reactivity indirectly, through electron density at the metal center and steric properties around the active site.<sup>37</sup> Many ligands fall under this category, bis(diphenylphosphino)methane (dppm) and cyclopentadienyl for example, and have been successfully used to design many effective catalysts, such as the complex **1-1** (Figure 1-8a).<sup>38</sup> The second category of ligands have been commonly referred to multifunctional ligands, which can cooperatively participate in reactivity either through the first or second coordination spheres. Noyori and co-workers have shown the ruthenium complex **1-2** which mediated transfer hydrogenation of ketones through the stepwise transfer of a hydride and proton from the metal centre and ligand, respectively (Figure 1-8b).<sup>39</sup> Complexes bearing these multifunctional ligands working in conjunction with the metal have been referred to as metal-ligand cooperative (MLC) complexes.

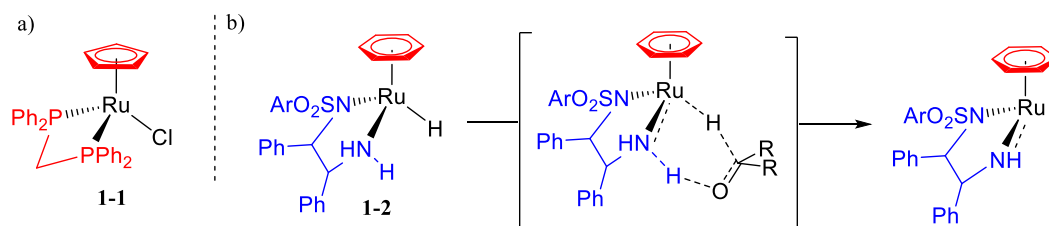


**Figure 1-8.** Examples of spectator (red) and actor (blue) ligands on a) [Ru(Cp)(Cl)(dppm)] complex **1-1** and b) ruthenium amido complex **1-2** has been identified as cooperative ligands.

While cooperative ligands can perform several functions,<sup>40</sup> the main interest for this work will focus on proton shuttling cooperative ligands. These ligands require a functional group incorporated into the ligand framework that is capable of mediating a proton transfer.<sup>40b</sup> Reactions which require the migration of a proton would typically be carried out by an exogenous base, such as a basic solvent or an additive (Figure 1-7). The requirement for



an exogenous base can pose a disadvantage in many cases, either due to limited solvent choices or introduction of undesirable additives. Installation of the base into the ligand framework can remove the need for an exogenous base, which would allow for a wider range of solvents to be utilized and removes the requirement for an additive, which would increase atom-economy. MLC catalysts capable of mediating proton transfer steps have also been shown to have increased performance and rate relative to non-MLC derivatives. Grotjahn investigated the relative rate of two reactions, *anti*-Markovnikov alkyne hydration and alkene isomerization, with both non-MLC and MLC complexes.<sup>41</sup> In both cases the MLC catalysts showed higher rates of reaction over the previous fastest catalysts, with an observed rate 2500 times faster for alkyne hydration with complex **1-4** versus **1-3** (Figure 1-9a) and over 10000 times faster for alkene isomerization with complex **1-6** versus **1-5** (Figure 1-9b).

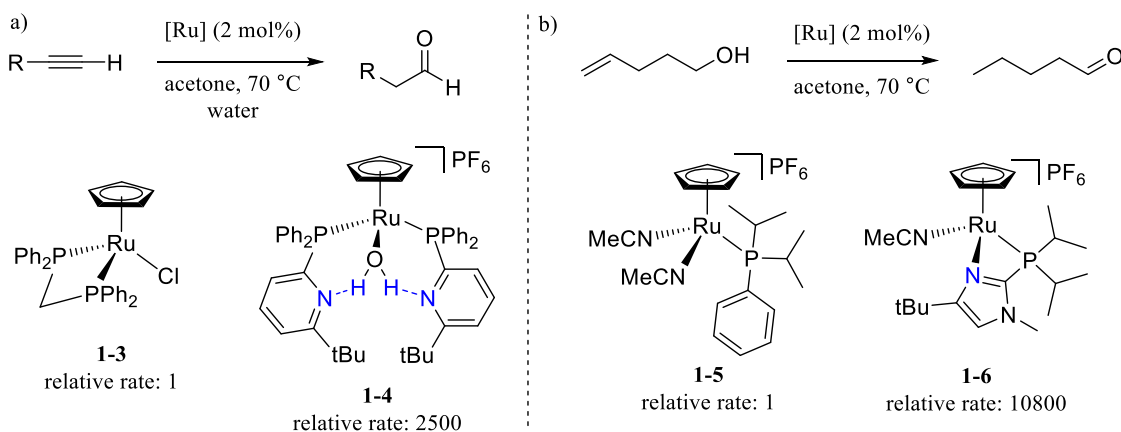


**Figure 1-9.** Rate comparison between non-MLC complexes **1-3** and **1-5** versus MLC complexes **1-4** and **1-6** for a) alkyne hydration and b) alkene isomerization. The cooperative part of the ligand is highlighted in blue.

#### 1.4.2 $P^{R_2}N^{R'_2}$ Ligands and Their Dynamics

The 1,5- $R'$ -3,7- $R$ -1,5-diaza-3,7-diphosphacyclooctane ( $P^{R_2}N^{R'_2}$ ) compounds represent a family of highly tunable cooperative ligands. The first reported synthesis of  $P^{R_2}N^{R'_2}$  ligands was in 1980, which used a phosphorus Mannich reaction with a primary phosphine, formaldehyde, and primary amine to generate the desired ligand (Figure 1-10a).<sup>42</sup> These ligands typically coordinate to the metal through the phosphorus heteroatoms which act as

Lewis bases. The ligand also has a Brønsted base in the ligand framework, in the form of pendent nitrogen heteroatoms, which mediate proton transfer steps and thus qualify  $\text{P}^{\text{R}}_2\text{N}^{\text{R}'_2}$  as cooperative ligands (Figure 1-10b). Due to the variety of primary phosphines and amines available, a diverse array of  $\text{P}^{\text{R}}_2\text{N}^{\text{R}'_2}$  ligands have been synthesized. The modularity of these  $\text{P}^{\text{R}}_2\text{N}^{\text{R}'_2}$  ligands allows for fine tuning of the electronic and steric properties in both the primary and secondary coordination sphere. Due to the tunable nature of these ligands, they are ideal candidates for structure activity relationships to be investigated as well as offering an easily accessible route to possible catalyst improvements.

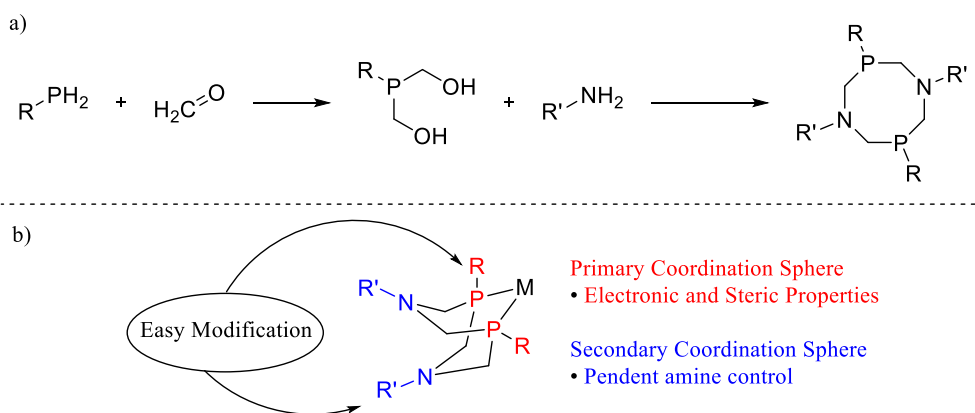


**Figure 1-10.** a) Typical route to generate  $\text{P}^{\text{R}}_2\text{N}^{\text{R}'_2}$  ligands from readily available phosphines and amines with formaldehyde and b) typical binding mode of  $\text{P}^{\text{R}}_2\text{N}^{\text{R}'_2}$  ligands to late transition metal centers.

Initial research performed on complexes bearing  $\text{P}^{\text{R}}_2\text{N}^{\text{R}'_2}$  ligands have focused on electrocatalytic hydrogen production and oxidation.<sup>43</sup> The  $[\text{Ni}(\text{P}^{\text{Ph}}_2\text{N}^{\text{Ph}}_2)_2(\text{CH}_3\text{CN})][\text{BF}_4]_2$  complex was utilized in the generation of  $\text{H}_2$  under electrocatalytic conditions with triflic acid and hydrogen oxidation occurred with the same complex under electrocatalytic conditions with  $\text{Et}_3\text{N}$ .<sup>43c</sup> Furthermore, in subsequent studies, the proposed mechanism for these types of catalytic reactions suggested that the pendent nitrogen atoms act as proton acceptors while the nickel metal center acts as a hydride acceptor based on computations (Figure 1-11).<sup>43c, 43e, 44</sup> Many derivatives of these ligands have been accessed since their discovery, in which both the phosphine substituents (R) and nitrogen substituents (R') play key roles in both the primary and secondary coordination spheres.<sup>45</sup> Another important factor to consider is the conformational flexibility that the  $\text{P}^{\text{R}}_2\text{N}^{\text{R}'_2}$  ligands possess. The

importance of the conformation arises from the proximity of the pendent amine to the metal center which positions it close to the site of reactivity while in the boat conformation (3.1 – 3.4 Å).<sup>45</sup> The most energetically favourable conformation for these ligands, based on DFT calculations, has one of the metallocycles in a boat conformation and the other in a chair conformation.<sup>46</sup> Isomerization between the chair and boat conformers were found to be in the range of  $10^4$ – $10^7$  s<sup>-1</sup>, depending on the amine substituent (Ph > tBu ≈ Bn), which was overall faster relative to catalytic rates of H<sub>2</sub> production and oxidation.<sup>47</sup> In recent years the interest for metal P<sup>R</sup><sub>2</sub>N<sup>R'</sup><sub>2</sub> complexes has expanded beyond electrocatalytic transformations into organic transformations (Section 1.5).

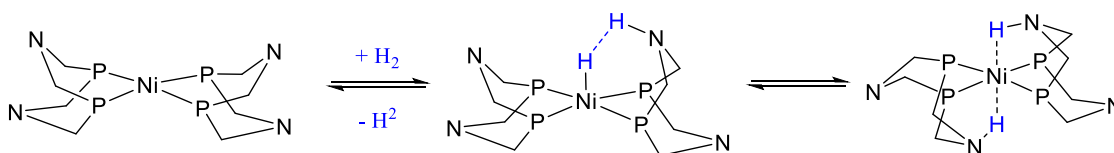


**Figure 1-11.** Ni(P<sup>R</sup><sub>2</sub>N<sup>R'</sup><sub>2</sub>) complex heterolytic cleavage of H<sub>2</sub> in which the metal center acts as a hydride acceptor and the pendent amine acts as a proton acceptor. The R and R' substituent are not shown for clarity.

## 1.5 Metal- P<sup>R</sup><sub>2</sub>N<sup>R'</sup><sub>2</sub> Complexes Utilized for Organic Transformations

### 1.5.1 Hydrofunctionalization with Metal P<sup>R</sup><sub>2</sub>N<sup>R'</sup><sub>2</sub> Catalysts

A particular MLC catalyst family, the [Ru(Cp/Cp\*)(P<sup>R</sup><sub>2</sub>N<sup>R'</sup><sub>2</sub>)(MeCN)]PF<sub>6</sub> complexes, has been a focus for the Blacquiere group. Initial investigation of the [Ru(Cp)(P<sup>tBu</sup><sub>2</sub>N<sup>Bn</sup><sub>2</sub>)(MeCN)]PF<sub>6</sub> complex, **1-7**, for the hydration of phenylacetylene and 1-octyne showed poor conversion (<5%) to the expected aldehyde product (Figure 1-12a).<sup>48</sup> Stoichiometric reaction of phenylacetylene with **1-7** showed conversion to a ruthenium vinylammonium complex **1-9**. The formation of complex **1-9** suggested that formation of the proposed vinylidene complex **1-8** occurred, but nucleophilic attack of the pendent amine deactivated the complex (Figure 1-12b). Attempts to cleave the nitrogen-C<sub>α</sub> bond through heating or addition of strong nucleophiles proved ineffective, which suggested the interaction was strong and corroborates the vinyl ammonium species as an off-cycle

deactivation species. Addition of [HDMF]OTf resulted in quantitative conversion by protonation of the distal pendent amine of the  $P^{R_2}N^{R'_2}$  ligand.

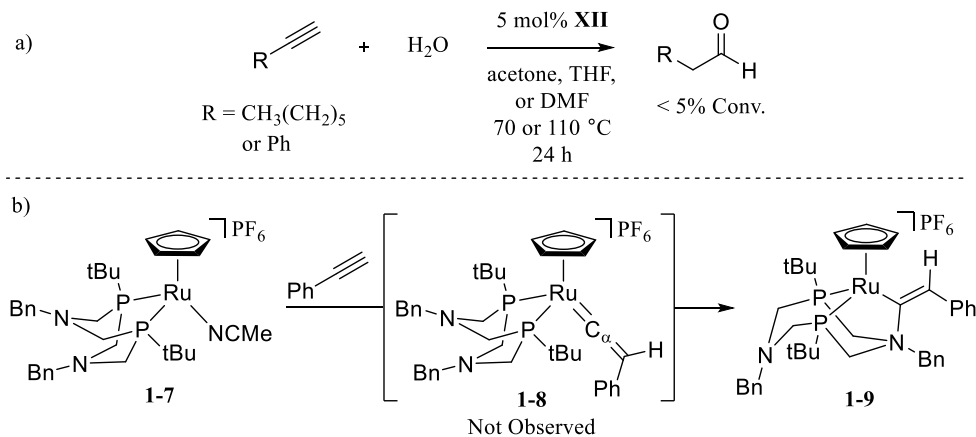


**Figure 1-12.** a) Attempted hydration of phenylacetylene or 1-octyne catalyzed with [Ru(Cp)(P<sup>tBu</sup><sub>2</sub>N<sup>Bn</sup><sub>2</sub>)(MeCN)]PF<sub>6</sub>. b) attempted synthesis of ruthenium vinylidene species resulted in isolation of vinyl ammonium complex.

Two Ru- $P^{R_2}N^{R'_2}$  complexes were assessed for intramolecular hydroalkoxylation of 2-ethynylbenzyl alcohol, methoxy-substituted 2-ethynylbenzyl alcohol derivative, and 4-hexyn-1-ol, with 1 mol% **1-7** or **1-10** in acetone.<sup>49</sup> Successful cyclization of 2-ethynylbenzyl alcohol represented the first catalytic example of the Ru- $P^{R_2}N^{R'_2}$  complexes and no additive was required. Catalyst comparison for the cyclization of 2-ethynylbenzyl alcohol showed that the tBu derivative had greater performance versus the Ph derivative (77% and 42% conv., respectively) under standard reaction conditions at 40 °C. Interestingly, a decrease in conversion of 2-ethynylbenzyl alcohol with **1-7** from 77% to 52% was observed at elevated temperature (54 °C). The reaction was monitored by <sup>31</sup>P{<sup>1</sup>H} NMR over 2 h at both temperatures, which showed that at lower temperatures the major species present was the active catalyst, while at higher temperatures deactivation via vinyl ammonium formation was favoured. Conversion of the methoxy-substituted and alkyl linked substrates with **1-7** at 40 °C showed significantly lower conversion, 22 and 0%, respectively. Furthermore, the importance of the pendent amine was also investigated through catalytic comparisons to [Ru(Cp)(dppp)(MeCN)]PF<sub>6</sub>, **1-11**, for the cyclization of

2-ethynylbenzyl alcohol. For the non-MLC complex **1-11**, no cyclization was observed under analogous conditions, which demonstrated the importance of the pendent base.

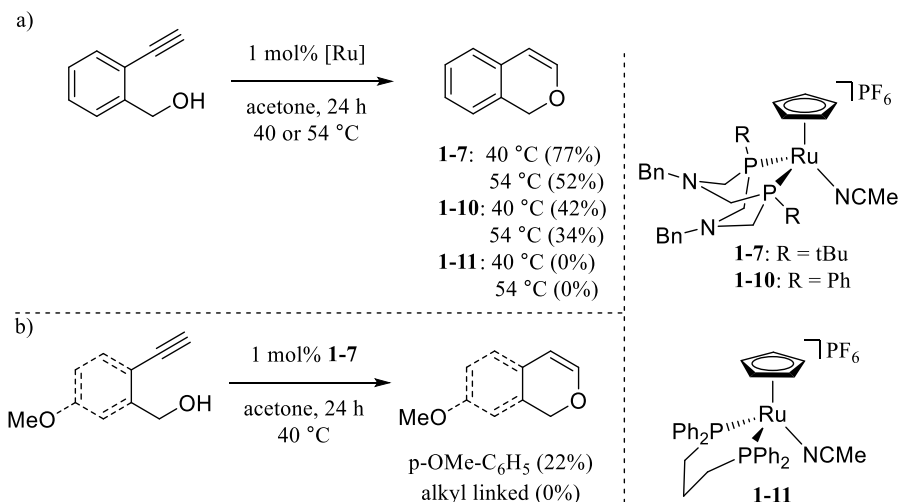
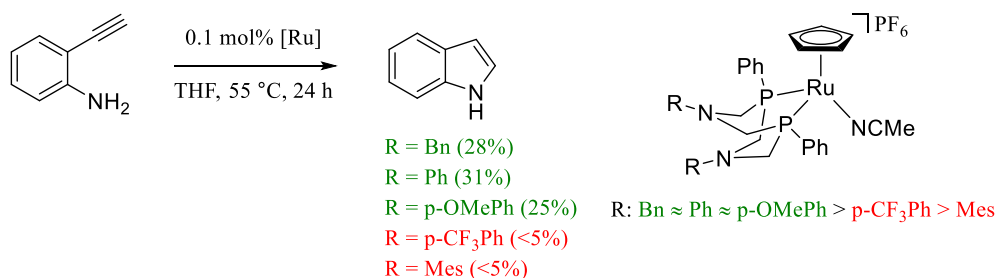


**Figure 1-13.** a) Intramolecular hydroamination catalyzed by  $[\text{Ru}(\text{Cp})(\text{P}^{\text{R}}_2\text{N}^{\text{Bn}}_2)(\text{MeCN})]\text{PF}_6$  and  $[\text{Ru}(\text{Cp})(\text{dppp})(\text{MeCN})]\text{PF}_6$  complexes. b) Intramolecular hydroamination of 2-ethynylbenzyl alcohol derivative and 4-pentyn-1-ol substrates.

A series of  $[\text{Ru}(\text{Cp})(\text{P}^{\text{Ph}}_2\text{N}^{\text{R}'_2})(\text{MeCN})]\text{PF}_6$  complexes, which were previously established to promote intramolecular hydroalkoxylation reactions, were assessed for intramolecular hydroamination reactions.<sup>50</sup> These complexes proved effective catalysts for the cyclization of 2-ethynylaniline to generate indole. Catalyst loadings as low as 0.1 mol% resulted in ca. 20-30% cyclization in THF at 55 °C over 24 h (Scheme 1-4). Structure activity relationship comparisons between these derivatives indicated the basicity of the pendent amine was of particular importance to achieve cyclization. Catalyst derivatives with greater pendent amine basicity ( $\text{R} = \text{Bn}, \text{Ph}, p\text{-OMePh}$ ) showed increased reactivity as compared to derivatives with lower pendent amine basicity ( $\text{R} = p\text{-CF}_3\text{Ph}$ ). This suggested that a minimum basicity, that is similar to the substrate of interest, is required to achieve conversion. The catalytic performance of the  $[\text{Ru}(\text{Cp})(\text{P}^{\text{Ph}}_2\text{N}^{\text{Ph}}_1)(\text{MeCN})]\text{PF}_6$  complex, which possessed one pendent amine, was also investigated which showed negligible conversion of 2-ethynylaniline. The lack of reactivity demonstrated the importance of the second metallocycle of the  $\text{P}^{\text{R}}_2\text{N}^{\text{R}'_2}$  ligand, which bias the position the proximal pendent

amine close to the active site to promote reactivity. Formation of a proposed  $\kappa^3$ -(P,P,N) coordination mode was observed with  $[\text{Ru}(\text{Cp})(\text{P}^{\text{Ph}}_2\text{N}^{\text{Ph}}_1)(\text{MeCN})]\text{PF}_6$  upon removal of MeCN which could deactivate the complex, however, we hypothesize that the nitrogen metal bond should be reversible and likely does not completely explain the lack of reactivity.



**Scheme 1-4.** First example of hydroamination mediated with  $\text{M-P}^{\text{R}}_2\text{N}^{\text{R}'_2}$  complexes. Difference in activity based on basicity of pendent nitrogen of the  $\text{P}^{\text{R}}_2\text{N}^{\text{R}'_2}$  ligand.

To investigate the importance of the primary coordination sphere a series of  $[\text{Ru}(\text{Cp}/\text{Cp}^*)(\text{P}^{\text{R}}_2\text{N}^{\text{R}'_2})(\text{MeCN})]\text{PF}_6$  complexes were assessed for the cyclization of 2-ethynylaniline and 2-ethynylbenzyl alcohol.<sup>51</sup> Comparison of rates between  $[\text{Ru}(\text{Cp})(\text{P}^{\text{tBu}}_2\text{N}^{\text{Ph}}_2)(\text{MeCN})]\text{PF}_6$  and  $[\text{Ru}(\text{Cp}^*)(\text{P}^{\text{tBu}}_2\text{N}^{\text{Ph}}_2)(\text{MeCN})]\text{PF}_6$  for cyclization of both substrates showed the Cp/Cp\* ancillary ligand played a crucial role in catalytic rate of the reaction, with the Cp\* derivative showing greater rate and conversion (Figure 1-14). The lability of MeCN was compared between two catalyst derivatives, which differed only in the ancillary ligand Cp vs Cp\*, which showed a lower barrier for MeCN dissociation for the Cp\* derivative. However, catalytic lifetime of the Cp\* derivatives were notably lower than their Cp analogues at low catalyst loadings for the cyclization of 2-ethynylaniline. The influence of the phosphine substituent was also assessed which showed a large influence on the lifetime of the catalyst. Catalysts with phosphine substituents, Ph and tBu, showed significantly greater catalyst turnover than the Bn derivative for the cyclization of both 2-ethynylaniline and 2-ethynylbenzyl alcohol. Collectively, the optimal catalysts were determined to possess a Cp ancillary ligand and a tBu phosphine substituent.

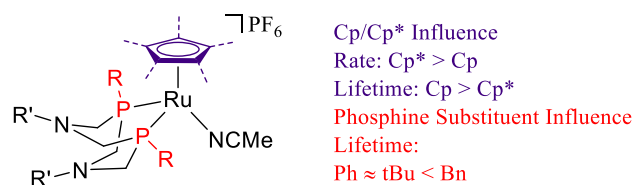


**Figure 1-14.** General influence of the primary coordination sphere on intramolecular hydrofunctionalization reactions.

More recently, the synthesis and utilization of  $[\text{Fe}(\text{Cp}^*)(\text{P}^{\text{R}}_2\text{N}^{\text{R}'})_2(\text{MeCN})]\text{PF}_6$  complexes for hydrofunctionalization of 2-ethynylaniline and 2-ethynylbenzyl alcohol was achieved.<sup>52</sup> These Fe complexes required much harsher conditions as compared to their Ru analogue, in which optimal cyclization of 2-ethynylaniline occurred at 110 °C in anisole at 0.5 mol% catalyst loading after 1 h (Figure 1-15a). Similarly, optimal cyclization of 2-ethynylbenzyl alcohol required an elevated temperature of 110 °C in anisole at 1 mol% after 1 h. By comparison, the iron analogues showed much more rapid conversion to the desired products at the expense of harsher reaction conditions. Selective generation of the *endo-dig* cyclized product with 2-ethynylbenzyl alcohol, was highly suggestive that the reaction proceeded through a vinylidene intermediate. Further corroboration was achieved through independent synthesis of the  $[\text{Fe}(\text{Cp}^*)(\text{P}^{\text{Cy}}_2\text{N}^{\text{Ph}})_2](=\text{C}=\text{CHPh})\text{PF}_6$  complex (Figure 1-15b).

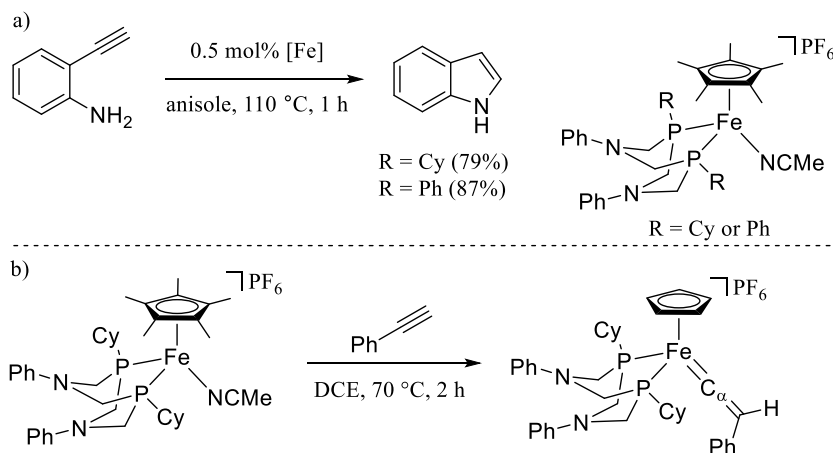
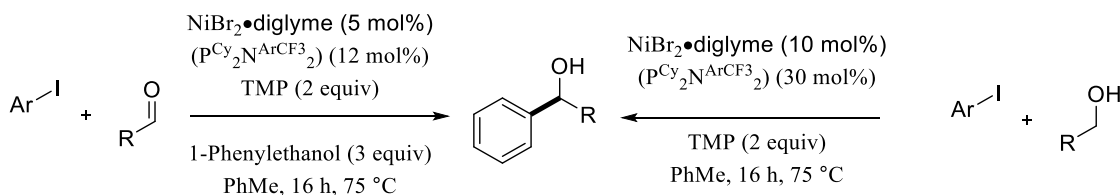


**Figure 1-15.** a) Intramolecular hydroamination catalyzed by  $\text{Fe}-\text{P}^{\text{R}}_2\text{N}^{\text{R}'})_2$  complexes. b) Synthesis of a Fe vinylidene complex.

While we have thoroughly established both the Ru- and Fe- $\text{P}^{\text{R}}_2\text{N}^{\text{R}'_2}$  complexes as effective catalysts for intramolecular hydroamination to generate 5- and 6-membered heterocycles, there remain areas which require investigation. Mechanistic analysis and an expanded substrate scope are of interest to better understand the limitations of these catalysts as well as their potential for improvement. Furthermore, application of these catalysts for intermolecular hydrofunctionalization reactions has not yet been realized.

### 1.5.2 Cross-Coupling with M- $\text{P}^{\text{R}}_2\text{N}^{\text{R}'_2}$ Catalysts

Recently, the first example of a M- $\text{P}^{\text{R}}_2\text{N}^{\text{R}'_2}$  complex was established for the arylation of aldehydes and alcohols.<sup>53</sup> Newman and co-workers explored the *in situ* generation of a Ni- $\text{P}^{\text{Cy}}_2\text{N}^{\text{ArCF}_3}_2$  complex from  $\text{NiBr}_2\cdot\text{diglyme}$  and  $\text{P}^{\text{Cy}}_2\text{N}^{\text{ArCF}_3}_2$ , which promoted reductive 1,2-arylation of a large variety of aryl iodides and aldehydes (Scheme 1-5, left). A substrate scope investigation demonstrated tolerance of the method toward a variety of aryl iodides (containing pyridine, acetanilide, and methyl esters) and aldehydes (containing aryl bromides, hydroxyl, methoxy, and various heterocycles). Substrates which possessed potentially coordinating functionalities showed reduced conversion as compared to substrates without. The redox-neutral  $\alpha$ -arylation of aryl iodides and primary alcohols was also demonstrated with the *in situ* formed Ni- $\text{P}^{\text{Cy}}_2\text{N}^{\text{ArCF}_3}_2$  catalyst (Scheme 1-5, right). A substantial substrate scope was undertaken which demonstrated tolerance of a variety of aryl iodides (containing ethers, esters, carbonyls, halides, and  $\text{OCF}_3$  functionalities) and primary alcohols (containing tertiary amines, halides, and ether functionalities).

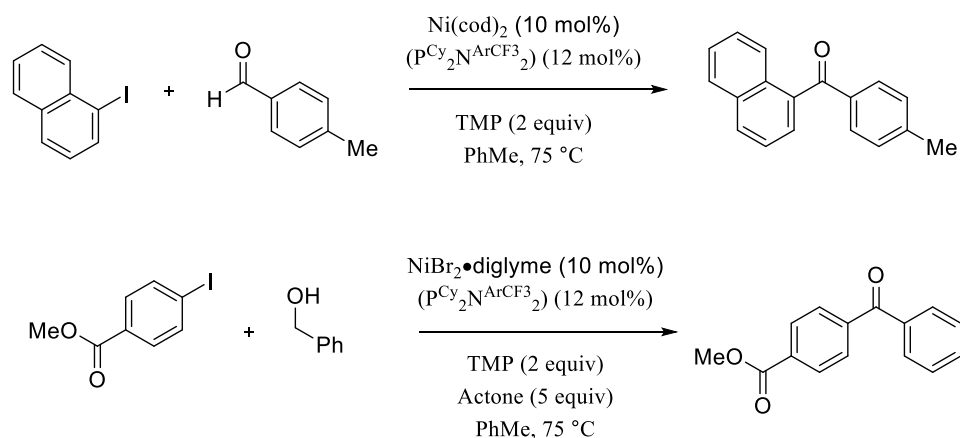


**Scheme 1-5.** General reaction scheme and conditions for the formation of 2° alcohols via reductive arylation (left) and redox neutral  $\alpha$ -arylation (right).

Redox neutral and oxidative ketone synthesis from aryl iodides and aldehydes or alcohols, respectively, was also achieved with an *in situ* formed Ni- $\text{P}^{\text{Cy}}_2\text{N}^{\text{ArCF}_3}_2$  catalyst (Scheme 1-



6).<sup>53</sup> Which demonstrates the potential of these catalysts to access a variety of alcohol and ketone containing compounds. The key to achieve ketone formation was removal of 1-phenylethanol (sacrificial reductant), which forced the proposed nickel alkoxide intermediate to undergo  $\beta$ -hydride elimination to release the ketone product. Generation of the two ketones shown in Scheme 1-6 was achieved in excellent yields, which were previously unsuccessful reactions using a Ni/triphos catalyst system. The success of the *in situ* formed  $\text{Ni-P}^{\text{R}}_2\text{N}^{\text{R}'_2}$  catalysts in mediating difficult reductive, oxidative, and redox neutral cross-coupling reactions demonstrates the potential of  $\text{M-P}^{\text{R}}_2\text{N}^{\text{R}'_2}$  complexes in synthesis. While this represented the first example of cross-coupling mediated with a  $\text{M-P}^{\text{R}}_2\text{N}^{\text{R}'_2}$  complex, the exact role of the ligand to enable these transforms remains unclear.



**Scheme 1-6.** Redox neutral and oxidative ketone synthesis from ketone and primary alcohol substrates, respectively.

## 1.6 Scope of Thesis

Ru- and  $\text{Ni-P}^{\text{R}}_2\text{N}^{\text{R}'_2}$  catalyst systems have been shown to effectively perform hydrofunctionalization and cross-coupling reactions, respectively. However, experimental validation for the proposed mechanisms of the reactions and direct evidence for the role of the  $\text{P}^{\text{R}}_2\text{N}^{\text{R}'_2}$  ligands remains relatively unexplored. To address these gaps the utilization of mechanistic and stoichiometric experiments will be discussed to elucidate proposed reaction mechanisms and identify advantages that the  $\text{P}^{\text{R}}_2\text{N}^{\text{R}'_2}$  ligands provide.

In Chapter 2 new  $[\text{Ru}(\text{Cp}/\text{Cp}^*)(\text{P}^{\text{R}}_2\text{N}^{\text{Ph}}_2)(\text{MeCN})]\text{PF}_6$  complexes ( $\text{R} = \text{Cy}$ ) were synthesized, characterized, and assessed for catalytic performance for the cyclization of 2-ethynylaniline to form indole. Turnover number comparisons compared against previous catalyst derivatives showed the Cy derivatives were comparable to the previous highest lifetime catalyst ( $\text{R} = \text{tBu}$ ). Coordinatively unsaturated active species were synthesized and their relative stability was assessed both experimentally and computationally. Thermolysis demonstrated a significant difference in stability between the Cp and Cp\* derivatives, with the Cp derivative being more stable. Variable time normalization analysis (VTNA) was used to investigate the  $[\text{Ru}(\text{Cp})(\text{P}^{\text{Cy}}_2\text{N}^{\text{Ph}}_2)(\text{MeCN})]\text{PF}_6$  complex, which demonstrated product inhibition which likely contributes to both increased stabilization and reduced reaction rate.

In Chapter 3, mechanistic analysis of  $[\text{Ru}(\text{Cp})(\text{P}^{\text{Cy}}_2\text{N}^{\text{Ph}}_2)(\text{MeCN})]\text{PF}_6$  catalyst for intramolecular hydrofunctionalization reactions was investigated. The complex successfully cyclized 2-ethynylbenzyl alcohol at elevated temperatures, which suggested formation of the vinyl ammonium deactivation complex was mitigated. A variety of substrates were successfully cyclized including alkyl linked substrates and carboxylic acids. The first utilization of  $\text{M}-\text{P}^{\text{R}}_2\text{N}^{\text{R}'}_2$  catalyst for the cyclization of a nitron substrate was also shown which outperformed the previous ruthenium complex. Synthesis of a ruthenium alkoxy carbene was observed upon attempted cyclization of 3-butyn-1-ol which was successfully isolated. A variety of isotopic labelling studies and VTNA experiments were performed, which suggest coordination and formation of the vinylidene intermediate as the rate limiting step.

In Chapter 4, the isolation and characterization of two ruthenium vinylidene complexes was achieved. Stoichiometric reactions with a variety of aliphatic amines were performed, which showed undesirable reactivity via deprotonation of the  $\text{C}_\beta$  proton of the vinylidene to form a ruthenium acetylide complex. Formation of this complex was confirmed through an independent synthesis. Stoichiometric reactions with aniline did not show formation of the ruthenium acetylide complex and promising reactivity was observed under harsher conditions. Attempted intermolecular catalysis was performed with either aniline or 2-

pyrrolidinone and phenylacetylene. No intermolecular hydroamination was observed with either nucleophile.

In Chapter 5, the utilization of  $\text{P}^{\text{R}}_2\text{N}^{\text{ArCF}_3}_2$  (R = Ph or tBu) ligands with palladium complexes were investigated for the Heck coupling of aryl triflates and styrene. The phosphine substituent was observed to have a large influence on the selectivity of the reaction. The synthesis of on-cycle intermediates, stoichiometric reactions, and mechanistic investigations were utilized to provide insight into the selectivity difference observed between the two  $\text{P}^{\text{R}}_2\text{N}^{\text{R}'_2}$  derivatives.

## 1.7 References

1. (a) de Vries, J. G.; Jackson, S. D., *Catalysis Science & Technology* **2012**, 2 (10), 2009-2009; (b) Poovan, F.; Chandrashekhar, V. G.; Natte, K.; Jagadeesh, R. V., *Catalysis Science & Technology* **2022**.
2. (a) Hayler, J. D.; Leahy, D. K.; Simmons, E. M., *Organometallics* **2019**, 38 (1), 36-46; (b) Campeau, L.-C.; Fogg, D. E., *Organometallics* **2019**, 38 (1), 1-2; (c) Brown, D. G.; Boström, J., *J. Med. Chem.* **2016**, 59 (10), 4443-4458.
3. Ertl, G., *Angew. Chem. Int. Ed.* **2009**, 48 (36), 6600-6606.
4. Astruc, D., *Anal. Bioanal. Chem.* **2011**, 399 (5), 1811-1814.
5. Röper, M., *Chem. unserer Zeit* **2006**, 40 (2), 126-135.
6. Farnetti, E.; Di Monte, R.; Kašpar, J., *Inorganic and bio-inorganic chemistry* **2009**, 2 (6), 50-86.
7. Johnson, K. A.; Goody, R. S., *Biochemistry* **2011**, 50 (39), 8264-8269.
8. (a) Soheili, A.; Albaneze-Walker, J.; Murry, J. A.; Dormer, P. G.; Hughes, D. L., *Org. Lett.* **2003**, 5 (22), 4191-4194; (b) Plenio, H., *Angew. Chem. Int. Ed.* **2008**, 47 (37), 6954-6956.
9. Taylor, H. S., *The Journal of Physical Chemistry* **1926**, 30 (2), 145-171.
10. Taylor, H. S.; Armstrong, E. F., *Proceedings of the Royal Society of London. Series A, Containing Papers of a Mathematical and Physical Character* **1925**, 108 (745), 105-111.
11. Boudart, M., *J. Am. Chem. Soc.* **1950**, 72 (2), 1040-1040.

12. (a) Barden, T. C., *Indoles: Industrial, Agricultural and Over-the-Counter Uses*. In *Heterocyclic Scaffolds II: Reactions and Applications of Indoles*, Gribble, G. W., Ed. Springer Berlin Heidelberg: Berlin, Heidelberg, 2010; pp 31-46; (b) Delost, M. D.; Smith, D. T.; Anderson, B. J.; Njardarson, J. T., *J. Med. Chem.* **2018**, *61* (24), 10996-11020; (c) Vitaku, E.; Smith, D. T.; Njardarson, J. T., *J. Med. Chem.* **2014**, *57* (24), 10257-10274.
13. Nanda, S. K.; Mallik, R., *Chemistry – A European Journal* **2021**, *n/a* (n/a).
14. Gutiérrez, R. U.; Hernández-Montes, M.; Mendieta-Moctezuma, A.; Delgado, F.; Tamariz, J., *Molecules* **2021**, *26* (13).
15. Tang, P.; Wang, H.; Zhang, W.; Chen, F.-E., *Green Synthesis and Catalysis* **2020**, *1* (1), 26-41.
16. Huang, L.; Arndt, M.; Gooßen, K.; Heydt, H.; Gooßen, L. J., *Chem. Rev.* **2015**, *115* (7), 2596-2697.
17. Kozlov, N. S.; Dinaburskaya, B.; Rubina, T. J., *Gen. Chem. USSR* **1936**, *6*, 1341.
18. (a) Walsh, P. J.; Baranger, A. M.; Bergman, R. G., *J. Am. Chem. Soc.* **1992**, *114* (5), 1708-1719; (b) McGrane, P. L.; Jensen, M.; Livinghouse, T., *J. Am. Chem. Soc.* **1992**, *114* (13), 5459-5460.
19. (a) Gagne, M. R.; Stern, C. L.; Marks, T. J., *J. Am. Chem. Soc.* **1992**, *114* (1), 275-294; (b) Gagne, M. R.; Nolan, S. P.; Marks, T. J., *Organometallics* **1990**, *9* (6), 1716-1718.
20. Lavallo, V.; Wright II, J. H.; Tham, F. S.; Quinlivan, S., *Angew. Chem. Int. Ed.* **2013**, *52* (11), 3172-3176.
21. Okamoto, N.; Miwa, Y.; Minami, H.; Takeda, K.; Yanada, R., *Angew. Chem. Int. Ed.* **2009**, *48* (51), 9693-6.
22. Nair, R. N.; Lee, P. J.; Grotjahn, D. B., *Top. Catal.* **2010**, *53* (15-18), 1045-1047.
23. Tokunaga, M.; Eckert, M.; Wakatsuki, Y., *Angew. Chem. Int. Ed.* **1999**, *38* (21), 3222-3225.
24. E. Müller, T.; Pleier, A.-K., *J. Chem. Soc., Dalton Trans.* **1999**, (4), 583-588.
25. Trost, B. M.; Rhee, Y. H., *J. Am. Chem. Soc.* **2002**, *124* (11), 2528-2533.
26. Nair, R. N.; Lee, P. J.; Rheingold, A. L.; Grotjahn, D. B., *Chemistry – A European Journal* **2010**, *16* (27), 7992-7995.
27. (a) Varela-Fernández, A.; Varela, J. A.; Saá, C., *Adv. Synth. Catal.* **2011**, *353* (11-12), 1933-1937; (b) Varela-Fernandez, A.; Varela, J. A.; Saá, C., *Synthesis* **2012**, *44* (21), 3285-3295.

28. Cai, T.; Yang, Y.; Li, W.-W.; Qin, W.-B.; Wen, T.-B., *Chemistry – A European Journal* **2018**, *24* (7), 1606-1618.
29. Bruce, M. I., *Chem. Rev.* **1991**, *91* (2), 197-257.
30. Mills, O. S.; Redhouse, A. D., *Chemical Communications (London)* **1966**, (14), 444-445.
31. Landon, S. J.; Shulman, P. M.; Geoffroy, G. L., *J. Am. Chem. Soc.* **1985**, *107* (23), 6739-6740.
32. Arndt, M.; Salih, K. S. M.; Fromm, A.; Goossen, L. J.; Menges, F.; Niedner-Schatteburg, G., *J. Am. Chem. Soc.* **2011**, *133* (19), 7428-7449.
33. (a) Wakatsuki, Y.; Koga, N.; Yamazaki, H.; Morokuma, K., *J. Am. Chem. Soc.* **1994**, *116* (18), 8105-8111; (b) De Angelis, F.; Sgamellotti, A.; Re, N., *Organometallics* **2002**, *21* (26), 5944-5950; (c) De Angelis, F.; Sgamellotti, A.; Re, N., *Dalton Trans.* **2004**, (20), 3225-3230.
34. Höhn, A.; Otto, H.; Dziallas, M.; Werner, H., *J. Chem. Soc., Chem. Commun.* **1987**, (11), 852-854.
35. Kostic, N. M.; Fenske, R. F., *Organometallics* **1982**, *1* (7), 974-982.
36. Chung, L.-H.; Yeung, C.-F.; Wong, C.-Y., *Chemistry – A European Journal* **2020**, *26* (28), 6102-6112.
37. Crabtree, R. H., *The Organometallic Chemistry of the Transition Metals*, 5th ed. John Wiley and Sons: Hoboken, New Jersey, 2009.
38. Suzuki, T.; Tokunaga, M.; Wakatsuki, Y., *Org. Lett.* **2001**, *3* (5), 735-737.
39. (a) z, R.; Hashiguchi, S., *Acc. Chem. Res.* **1997**, *30* (2), 97-102; (b) Dub, P. A.; Ikariya, T., *J. Am. Chem. Soc.* **2013**, *135* (7), 2604-2619.
40. (a) Grützmacher, H., *Angew. Chem. Int. Ed.* **2008**, *47* (10), 1814-1818; (b) Crabtree, R. H., *New J. Chem.* **2011**, *35* (1), 18-23; (c) van der Vlugt, J. I., *Eur. J. Inorg. Chem.* **2012**, *2012* (3), 363-375; (d) Annibale, V. T.; Song, D., *RSC Advances* **2013**, *3* (29), 11432-11449.
41. Grotjahn, D. B., *Pure Appl. Chem.* **2010**, *82* (3), 635-647.
42. Märkl, G.; Jin, G. Y., *Tetrahedron Lett.* **1980**, *21* (36), 3467-3470.
43. (a) Kilgore, U. J.; Roberts, J. A. S.; Pool, D. H.; Appel, A. M.; Stewart, M. P.; DuBois, M. R.; Dougherty, W. G.; Kassel, W. S.; Bullock, R. M.; DuBois, D. L., *J. Am. Chem. Soc.* **2011**, *133* (15), 5861-5872; (b) Gunasekara, T.; Tong, Y.; Speelman, A. L.; Erickson, J. D.; Appel, A. M.; Hall, M. B.; Wiedner, E. S., *ACS Catalysis* **2022**, *12* (5),

2729-2740; (c) Wilson, A. D.; Newell, R. H.; McNevin, M. J.; Muckerman, J. T.; Rakowski DuBois, M.; DuBois, D. L., *J. Am. Chem. Soc.* **2006**, *128* (1), 358-366; (d) Bullock, R. M.; Helm, M. L., *Acc. Chem. Res.* **2015**, *48* (7), 2017-2026; (e) Wiese, S.; Kilgore, U. J.; DuBois, D. L.; Bullock, R. M., *ACS Catalysis* **2012**, *2* (5), 720-727.

44. Shaw, W. J.; Helm, M. L.; DuBois, D. L., *Biochimica et Biophysica Acta (BBA) - Bioenergetics* **2013**, *1827* (8), 1123-1139.

45. Wiedner, E. S.; Appel, A. M.; Raugei, S.; Shaw, W. J.; Bullock, R. M., *Chem. Rev.* **2022**.

46. Raugei, S.; Chen, S.; Ho, M.-H.; Ginovska-Pangovska, B.; Rousseau, R. J.; Dupuis, M.; DuBois, D. L.; Bullock, R. M., *Chemistry – A European Journal* **2012**, *18* (21), 6493-6506.

47. Franz, J. A.; O'Hagan, M.; Ho, M.-H.; Liu, T.; Helm, M. L.; Lense, S.; DuBois, D. L.; Shaw, W. J.; Appel, A. M.; Raugei, S.; Bullock, R. M., *Organometallics* **2013**, *32* (23), 7034-7042.

48. Bow, J.-P. J.; Boyle, P. D.; Blacquiere, J. M., *Eur. J. Inorg. Chem.* **2015**, *2015* (25), 4162-4166.

49. Stubbs, J. M.; Bow, J. P. J.; Hazlehurst, R. J.; Blacquiere, J. M., *Dalton Trans.* **2016**, *45* (43), 17100-17103.

50. Stubbs, J. M.; Chapple, D. E.; Boyle, P. D.; Blacquiere, J. M., *ChemCatChem* **2018**, *10* (17), 4001-4009.

51. Stubbs, J. M.; Bridge, B. J.; Blacquiere, J. M., *Dalton Trans.* **2019**, *48* (22), 7928-7937.

52. Bridge, B. J.; Boyle, P. D.; Blacquiere, J. M., *Organometallics* **2020**, *39* (14), 2570-2574.

53. Isbrandt, E. S.; Nasim, A.; Zhao, K.; Newman, S. G., *J. Am. Chem. Soc.* **2021**, *143* (36), 14646-14656.

## Chapter 2

### 2 Origin of Stability and Inhibition of Cooperative Alkyne Hydrofunctionalization Catalysts

New entries to the  $[\text{Ru}(\text{Cp}/\text{Cp}^*)(\text{P}^{\text{R}}_2\text{N}^{\text{R}'})_2(\text{MeCN})]\text{PF}_6$  catalyst family were synthesized, including a Cp complex ( $\text{R} = \text{Cy}$ ;  $\text{R}' = \text{Ph}$ ) and two Cp\* complexes ( $\text{R} = \text{Cy}, \text{Ph}$ ;  $\text{R}' = \text{Ph}$ ). These and other derivatives were used for the intramolecular hydroamination of 2-ethynylaniline to elucidate trends in catalytic lifetime and rate. The readily accessible  $[\text{Ru}(\text{Cp})(\text{P}^{\text{Cy}}_2\text{N}^{\text{Ph}})_2(\text{MeCN})]\text{PF}_6$  derivative showed comparable lifetime to  $[\text{Ru}(\text{Cp})(\text{P}^{\text{t-Bu}}_2\text{N}^{\text{Ph}})_2(\text{MeCN})]\text{PF}_6$ , the previous optimal catalyst. Donor-free ‘active’ catalysts,  $[\text{Ru}(\text{Cp}/\text{Cp}^*)(\text{P}^{\text{Cy}}_2\text{N}^{\text{Ph}})_2]\text{PF}_6$ , were prepared and their thermal stability was assessed. The relatively high stability of the Cp derivative was explained by the capacity of the  $\text{P}^{\text{Cy}}_2\text{N}^{\text{Ph}}_2$  ligand to coordinate in a  $\kappa^3$ -(P,P,Ar) mode, which protects the low-coordinate species. This coordination mode is inaccessible with the Cp\* derivative. Additionally,  $[\text{Ru}(\text{Cp}^*)(\text{P}^{\text{Cy}}_2\text{N}^{\text{Ph}})_2]\text{PF}_6$  readily activated the C-Cl bond of the solvent dichloromethane. Variable time normalization analysis (VTNA) revealed that the indole product inhibited the catalyst  $[\text{Ru}(\text{Cp})(\text{P}^{\text{Cy}}_2\text{N}^{\text{Ph}})_2(\text{MeCN})]\text{PF}_6$ , which slowed catalytic rates.

#### 2.1 Introduction

Development and improvement of synthetic routes to nitrogen- and oxygen-containing heterocycles is valuable for the preparation of pharmaceutical drugs, agrochemicals, and natural products.<sup>1</sup> An atom-economic route to heterocycles is transition-metal catalyzed intramolecular hydrofunctionalization of alkynes.<sup>2</sup> Depending on the catalyst and substrate structure, alkyne activation by  $\pi$ -coordination can afford either the *exo-dig* or *endo-dig* products. Exclusive selectivity for the latter can be achieved with catalysts that activate the alkyne to give a metal vinylidene, in which the high electrophilicity of  $\text{C}\alpha$  directs nucleophilic attack to that site.<sup>2f, 2g, 3</sup> In the case of ruthenium catalysts, the hydrofunctionalization mechanism<sup>4</sup> involves multiple proton transfer steps, which can be mediated by an exogenous base additive or solvent, such as pyridine.<sup>5</sup> Alternatively,

additive-free methods are possible with cooperative<sup>6</sup> catalysts that contain a Brønsted base as part of a supporting ligand.<sup>7</sup>

We have systematically studied structure-performance relationships of  $[\text{Ru}(\text{Cp}/\text{Cp}^*)(\text{P}^{\text{R}_2}\text{N}^{\text{R}'_2})(\text{MeCN})]\text{PF}_6$  (**2-1**, Cp; **2-2**, Cp<sup>\*</sup>) catalysts that contain the cooperative  $\text{P}^{\text{R}_2}\text{N}^{\text{R}'_2}$  (1,5-R'-3,7-R-1,5-diaza-3,7-diphosphacyclooctane) ligand (Figure 2-1a).<sup>8</sup> The pendent amine groups effectively promote proton transfer steps if the amine is sufficiently basic (i.e. R' = Ph).<sup>8a</sup> Increased basicity with the stronger donor group R' = benzyl leads to undesired vinylidene deactivation.<sup>8d, 9</sup> Steric bulk in the primary coordination sphere with R = *t*-Bu, and Cp<sup>\*</sup> as the spectator ligand (i.e. **2-2a**) promoted facile catalyst conscription, which involves dissociation of the placeholder MeCN ligand to give the on-cycle active catalyst (Figure 2-1b).<sup>8c</sup> This permitted hydrofunctionalization at moderate temperatures, but at the expense of catalyst lifetime as compared to a Cp catalyst analogue (**2-1a**). We hypothesized that the higher MeCN lability gives a higher proportion of the donor-free active catalyst,  $[\text{Ru}(\text{Cp}/\text{Cp}^*)(\text{P}^{\text{R}_2}\text{N}^{\text{R}'_2})]\text{PF}_6$ , a likely vector for decomposition. Thus, understanding the factors that control stability of the active catalyst is of utmost importance to further increase catalyst lifetime.

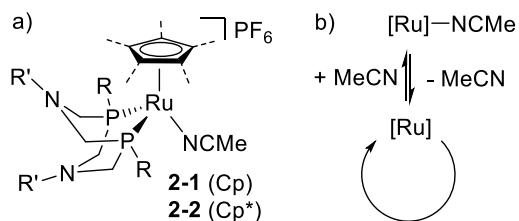


**Figure 2-1.** a) General structure of  $\text{Ru}-\text{P}^{\text{R}_2}\text{N}^{\text{R}'_2}$  intramolecular hydrofunctionalization catalysts; and b) simplified depiction of catalyst conscription by MeCN dissociation to give the donor-free active catalyst.

The donor-free complex  $[\text{Ru}(\text{Cp}^*)(\text{P}^{\text{t-Bu}_2}\text{N}^{\text{Ph}_2})]\text{BAr}^{\text{F}_4}$  (**2-A**) was recently reported by Mock and co-workers as the active catalyst for ammonia oxidation to give  $\text{N}_2$ .<sup>10</sup> Two different isomers of **2-A** were characterized, which differed based on the coordination mode of the  $\text{P}^{\text{t-Bu}_2}\text{N}^{\text{Ph}_2}$  ligand (Figure 2-2a). A low-coordinate isomer  $\kappa^2\text{-(P,P)-2-A}$  with a bidentate  $\text{P}^{\text{t-Bu}_2}\text{N}^{\text{Ph}_2}$  mode was observed in both the solution and solid state. While the open site at the



metal was not stabilized by any close contacts, the boat conformation of the proximal metallocycle may offer steric protection. The second isomer  $\kappa^3$ -(P,P,N)-**2-A**, observed only in the solid-state, is stabilized by coordination of one of the pendent amine nitrogen atoms to ruthenium. Dynamic changes in the coordination mode of the  $P^R_2N^{R'}_2$  ligand do occur in solution with Mn, Mo, Cr, and Ni complexes,<sup>11</sup> which shows that the ligands are structurally responsive.<sup>12</sup> For example, a low-coordinate Mn(I) complex, **2-B**, is stabilized by two different tridentate modes  $\kappa^3$ -(P,P,N) and  $\kappa^3$ -(P,P,agostic), in which the latter includes agostic binding from the benzyl group of the pendent amine substituent (Figure 2-2b).<sup>11a</sup> The  $\kappa^3$ -(P,P,agostic) mode also stabilized  $[Ni(P^{Ph}_2N^{Me}_2)]^{2+}$  by ca. 5.5 kJ/mol relative to the more typical  $\kappa^2$ -(P,P) isomer.<sup>11e</sup> The capacity of the ligand to achieve the higher coordination number competed with substrate binding in electrocatalytic H<sub>2</sub> oxidation catalysis, which slowed catalytic rates.

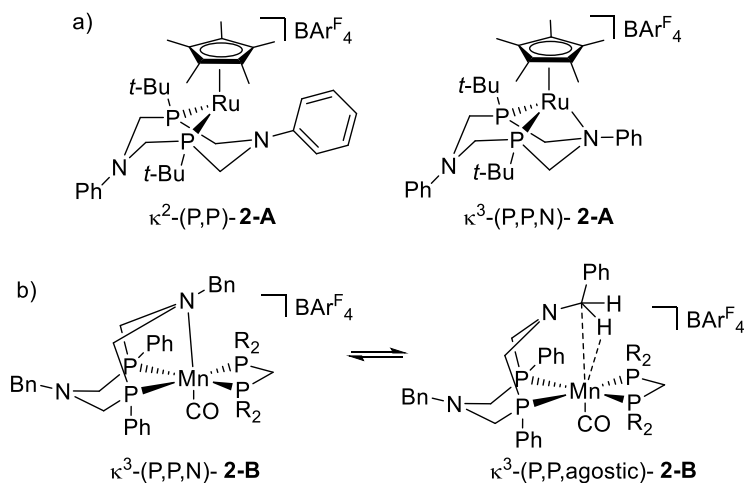


**Figure 2-2.** Versatile coordination chemistry of the  $P^R_2N^{R'}_2$  ligand in donor-free a) ruthenium,<sup>10</sup> and b) manganese<sup>11a</sup> complexes.

Herein, we evaluate the generality of higher catalyst lifetime for Cp vs Cp\* catalysts of the type  $[Ru(Cp/Cp^*)(P^R_2N^{R'}_2)(MeCN)]PF_6$  toward intramolecular alkyne hydroamination. The structure and stability of the donor-free active catalysts is probed, which reveals the

key role of  $P^{R_2}N^{R'_2}$  ligand coordination mode on catalyst lifetime. Product inhibition is also identified as a dominant factor that influences catalytic rates.

## 2.2 Results and Discussion

### 2.2.1 Synthesis and Characterization of Catalysts **2-1b**, **2-2b**, and **2-2c**.

The set of pre-catalysts (**2-1a-c**, **2-2a-c**) used in this study bear the phosphine substituents *t*-Bu, Cy or Ph (**a-c**, respectively) and an ancillary Cp (**2-1**) or Cp\* (**2-2**) ligand (Figure 2-3). Complexes **2-1b**, **2-2b** and **2-2c** were not previously reported, but preparation by  $P^{R_2}N^{R'_2}$  ligand coordination to  $[Ru(Cp/Cp^*)(MeCN)_3]PF_6$  afforded the target complexes in excellent yields. The  $^{31}P\{^1H\}$  NMR signals for **2-1b**, **2-2b**, and **2-2c** were observed at  $\delta_P = 45.9$ , 36.0, and 33.4, respectively. The more upfield shift of the Cp\* complex **2-2b** as compared to the Cp analogue **2-1b** is consistent with related derivatives<sup>8c</sup> and the difference reflects the greater donor strength of Cp\*.

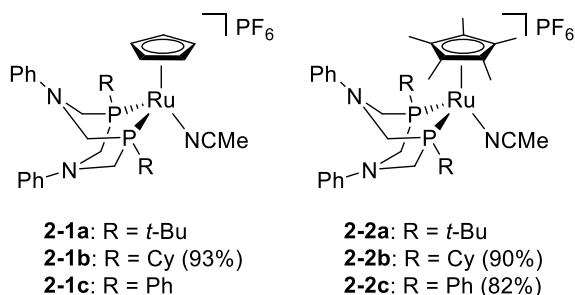


**Figure 2-3.** Cationic ruthenium complexes employed in this study. Yields for newly synthesized complexes shown in parentheses.

Single crystals of the R = Cy complex **2-2b** were obtained and X-ray crystallography confirmed the expected connectivity (Figure 2-4). The Ru(1)-P(1) and Ru(1)-P(2) bond distances were 2.275(2) and 2.262(2) Å, respectively, which were ca. 0.03 - 0.05 Å shorter than the analogous bond distances reported for the *t*-Bu analogue **2-2a**.<sup>8c</sup> The shorter distances for **2-2b** are a consequence of the greater flexibility and lower steric demand of the cyclohexyl substituents as compared to *t*-butyl. The different steric profile allows for slightly wider P(1)-Ru(1)-P(2) bite angle for **2-2b** (78.80(5)°) than **2-2a** (77.75(4)°).

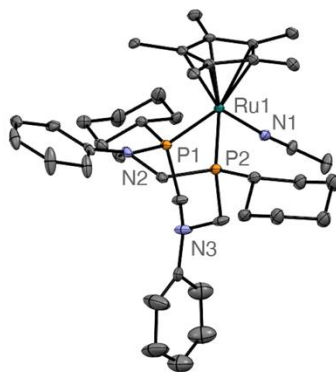
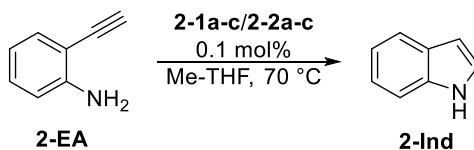


**Figure 2-4.** Displacement ellipsoid plot of complex **2-2b**. Ellipsoids are given at 30% probability level. H atoms,  $\text{PF}_6^-$  anion, and a molecule of co-crystallized hexanes were omitted for clarity. Selected bond distances ( $\text{\AA}$ ): Ru1-N1 = 2.046(4), Ru1-P1 = 2.275(2), Ru1-P2 = 2.262(2). Selected angles ( $^\circ$ ): P1-Ru1-P2 = 78.80(5), Ru1-N1-C1 = 175.1(4).

### 2.2.2 Lifetime of Catalysts **2-1a-c** and **2-2a-c**.

The benchmark substrate 2-ethynylaniline (**2-EA**) was selected to evaluate the catalytic performance of **2-1b-c** and **2-2b-c** toward intramolecular hydroamination. The performance was compared directly to that of  $\text{P}^{t\text{-Bu}}_2\text{N}^{\text{Ph}}_2$  catalysts **2-1a** and **2-2a**, which we reported previously.<sup>8c</sup> Reactions were conducted in Me-THF with a 0.1 mol% catalyst loading (Scheme 2-1). An elevated temperature of 70  $^\circ\text{C}$  was selected to ensure facile MeCN lability so that differences in catalyst initiation have limited impact on the observed activity. All catalytic reactions were monitored over time and the turnover number (TON) was determined at 24 h or once the catalyst conversion reached a plateau (Figure 2-5).



**Scheme 2-1.** Intramolecular hydroamination of 2-ethynylaniline with Ru catalysts **2-1a-c** and **2-2a-c**.

For each of the three  $\text{P}^{\text{R}}_2\text{N}^{\text{Ph}}_2$  ligands, the Cp catalysts (**2-1**) gave superior TONs than the Cp\* (**2-2**) derivatives. The difference was most notable for R = *t*-Bu (**2-1a**, **2-2a**) and R = Cy (**2-1b**, **2-2b**) in which the Cp catalysts exhibited TONs that were 2.2 and 1.7 times

higher than the Cp\* versions, respectively. In contrast, the TONs for R = Ph catalyst **2-1c** are only ca. 1.2 times higher than **2-2c**. While this confirms the previous observation with **2-1a/2-2a** that the TON is enhanced for Cp vs Cp\* derivatives, the magnitude of the difference is dependent on the nature of the R group. The TONs for the Cp catalysts **2-1a-c** were 800, 740 and 560, respectively, giving a performance trend in phosphine substituent (R) of *t*-Bu > Cy > Ph. This trend reasonably tracks with steric properties as judged by %buried volumes (%V<sub>bur</sub>) of AuCl(PR<sub>3</sub>) complexes (38.1, 33.4 and 29.9% for R = *t*-Bu, Cy and Ph, respectively, for M-P = 2.28 Å).<sup>13</sup> The trend in TONs for **2-1a-c** could also be consistent with the donor strength of the phosphine, in which the catalysts with the stronger donors **2-1a** and **2-1b** are superior to **2-1c**. It is notable, that an R = Bn catalyst exhibited very poor activity at 55 °C as compared to R = *t*-Bu or Ph,<sup>8c</sup> which suggest that the benzyl derivative could be highly sensitive to a competing decomposition pathway. The performance trend of phosphine donor substituent is different for the Cp\* catalysts, in which the TONs are similar for all derivatives (**2-2a** = 360; **2-2b** = 430; **2-2c** = 450). We proposed that the greater sensitivity of the Cp\* catalysts to decomposition (*vide infra*) overrides any discernible difference in phosphine substituent properties. The above studies indicate that catalysts **2-1a** and **2-1b** have similar TONs and are the longest lived of the derivatives studied. From a practical perspective, catalyst **2-1b** (R = Cy) is preferred over **2-1a** (R = *t*-Bu) due to the more amenable synthesis of the P<sup>Cy</sup><sub>2</sub>N<sup>Ph</sup><sub>2</sub> ligand that includes both higher synthetic yields and a more economical phosphine precursor (i.e. by ca. 10-fold).<sup>14</sup>

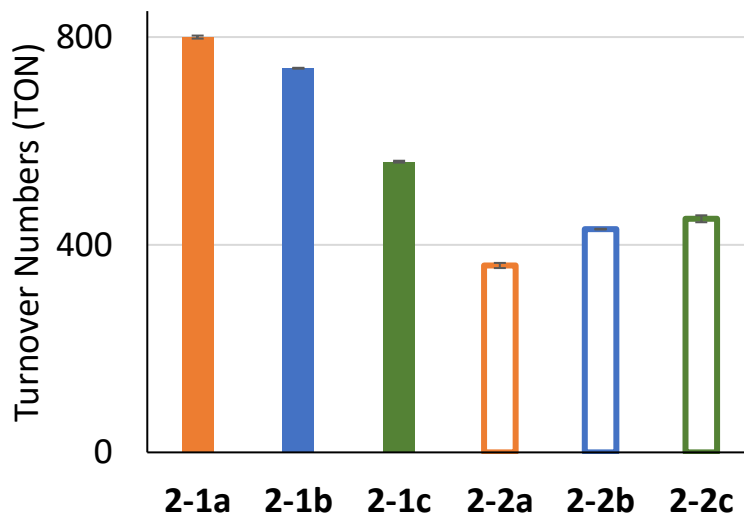


**Figure 2-5.** Turnover numbers (TON) of Cp (solid) and Cp\* (empty) catalysts for intramolecular hydroamination of 2-ethynylaniline. Reaction conditions: 300 mM **2-EA**, Me-THF, 0.1 mol% [Ru]. Catalysts with R = *t*-Bu (orange), R = Cy (blue), and R = Ph (green). Runs were conducted in duplicate with data points representing the average and the error bars depict the span of individual runs.

### 2.2.3 Preparation of Hydroamination Active Catalysts.

Previously, we proposed that the lower lifetime of the Cp\* catalyst **2-2a** vs the Cp derivative **2-1a** was due to decomposition of the active catalyst, which is more accessible for the former as a consequence of higher MeCN lability.<sup>8c</sup> The successful synthesis of **2-A**<sup>10</sup> indicates that the active complexes of **2-1b** and **2-2b** should also be synthetically accessible, which would permit direct stability assessment. To this end, we first synthesized the precursor chloro complexes [RuCl(Cp/Cp\*)(P<sup>Cy</sup><sub>2</sub>N<sup>Ph</sup><sub>2</sub>)] (**2-3b**, Cp; **2-4b**, Cp\*) in very good yields (86 and 86%, respectively) by ligand substitution with [RuCl(Cp/Cp\*)(PPh<sub>3</sub>)<sub>2</sub>]. The <sup>31</sup>P{<sup>1</sup>H} NMR signals corresponding to **2-3b** and **2-4b** were observed at δ<sub>P</sub> = 46.6 and 34.4, respectively. Single crystals of both complexes were obtained, and X-ray crystallography confirmed the expected connectivity (Figure 2-6). Similar Ru-Cl bond distances were observed for **2-3b** and **2-4b** of 2.4556(6) and 2.459(2) Å, respectively. The Ru-P distances were longer for the Cp complex than Cp\* by only ca. 0.02 Å. A slightly

smaller P-Ru-P bite angle of 79.20(2)° was observed for **2-3b** as compared to 80.25(3)° for **2-4b**.

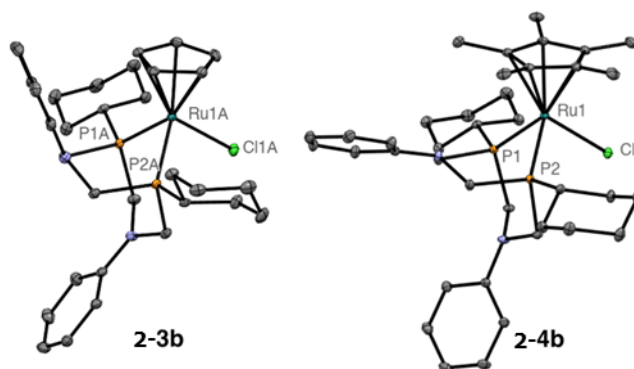
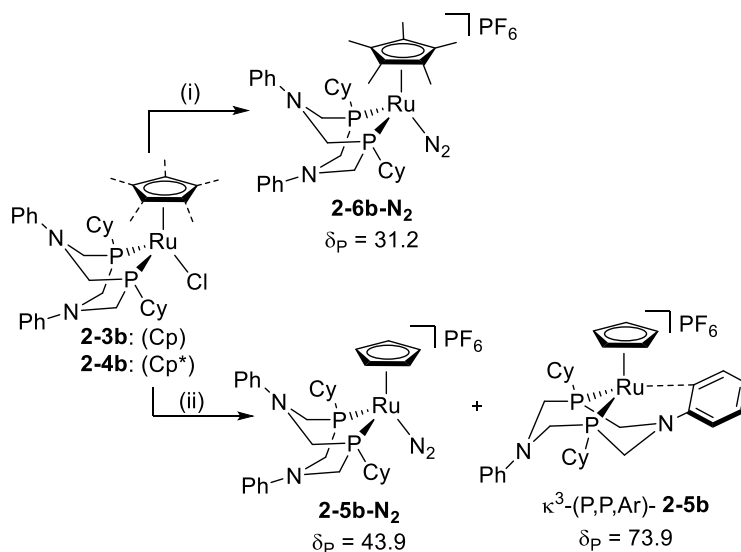


**Figure 2-6.** ORTEP view of solid-state structures of chloro complexes **2-3b** and **2-4b** with ellipsoids at 30% probability level. H atoms and a molecule of co-crystallized DCM in **2-3b** were omitted for clarity. Selected bond distances (Å): **2-3b**, Ru(1)-Cl(1) = 2.4556(6), Ru(1)-P(1) = 2.2616(6), Ru(1)-P(2) = 2.2570(8); **2-4b**, Ru(1A)-Cl(1A) = 2.459(2), Ru(1A)-P(1A) = 2.244(1), Ru(1A)-P(2A) = 2.277(1). Selected Angles (°): **2-3b**, P(1)-Ru(1)-P(2) = 79.20(2); **2-4b**, P(1A)-Ru(1A)-P(2A) = 80.25(3).

Halide abstraction from **2-3b** and **2-4b** give operationally unsaturated products **2-5b-N<sub>2</sub>** and **2-6b-N<sub>2</sub>**, respectively, that are stabilized by a weakly coordinated N<sub>2</sub> ligand (Scheme 2-2). In addition, abstraction from the Cp derivative **2-3b** also affords a product stabilized by a tridentate coordination of the P<sup>Cy</sup><sub>2</sub>N<sup>Ph</sup><sub>2</sub> ligand. Characterization of the simpler case of the Cp\* complex **2-6b-N<sub>2</sub>** will be discussed first. Halide abstraction from **2-4b** resulted in a colour change from yellow to dark red, which is consistent with the formation of an operationally unsaturated<sup>15</sup> product. The <sup>1</sup>H NMR spectrum exhibited one signal for the methyl groups of the Cp\* ligand, concordant with the expected η<sup>5</sup>-coordination mode. None of the P<sup>Cy</sup><sub>2</sub>N<sup>Ph</sup><sub>2</sub> ligand <sup>1</sup>H or <sup>13</sup>C resonances were shifted from the typical ranges found in κ<sup>2</sup>-(P,P) complexes **2-2b** and **2-4b**. Analysis of the <sup>31</sup>P{<sup>1</sup>H} NMR spectrum of **2-6b** revealed a new singlet at δ<sub>P</sub> = 31.2, which is 4.2 ppm upfield of that for **2-4b**. The location is consistent with that observed for κ<sup>2</sup>-(P,P)-**2-A**, which exhibited a <sup>31</sup>P{<sup>1</sup>H} resonance 5.5 ppm upfield of the neutral chloro complex **2-2a**.<sup>10</sup> However, the IR spectrum of **2-6b-N<sub>2</sub>** showed a weak signal at ν = 2160 cm<sup>-1</sup> that is in the range expected for a N≡N

stretch of a terminal Ru-N<sub>2</sub> adduct.<sup>16</sup> Treatment of **2-6b** with MeCN resulted in quantitative conversion to **2-2b** within five minutes, as judged by both <sup>31</sup>P{<sup>1</sup>H} NMR analysis and the near instantaneous colour change from red to yellow. This suggests that the N<sub>2</sub> ligand is labile in solution and readily gives access to the low-coordinate ‘active’ complex. Attempts to obtain X-ray quality crystals of **2-6b-N<sub>2</sub>** were unsuccessful.



**Scheme 2-2.** Halide abstraction under N<sub>2</sub> utilizing TIPF<sub>6</sub> to generate complexes **2-5b-N<sub>2</sub>** and κ<sup>3</sup>-(P,P,Ar)-**2-5b**, and **2-6b-N<sub>2</sub>**. Reactions performed at room temperature in i) C<sub>6</sub>H<sub>5</sub>F or ii) DCM.

Halide abstraction from **2-3b** resulted in a colour change from yellow to orange and the formation of two new singlets in the <sup>31</sup>P{<sup>1</sup>H} NMR spectrum at 73.9 and 43.9 ppm. The ratio of the two compounds was variable, which could be a consequence of minor temperature fluctuations and instability of the more upfield species (*vide infra*). Addition of MeCN to the mixture rapidly gave quantitative formation of **2-1b**, which confirms that both products are operationally unsaturated. The signal at 43.9 ppm is ca. 2 ppm upfield of that for **2-3b**, which is consistent with an N<sub>2</sub> adduct, **2-5b-N<sub>2</sub>**, analogous to **2-6b-N<sub>2</sub>**. The dramatic ca. 30 ppm more downfield shift of the second species is indicative of a difference in chelation of the P<sup>Cy</sup><sub>2</sub>N<sup>Ph</sup><sub>2</sub> ligand from κ<sup>2</sup>-(P,P) to a tridentate mode that forms two 5- or 6-membered metallocycles.<sup>17</sup> The <sup>1</sup>H-<sup>13</sup>C{<sup>1</sup>H} HSQC spectrum revealed a correlation between an aromatic proton to a <sup>13</sup>C signal at 95.8 ppm, a chemical shift that is expected

for an aryl carbon engaged in metal coordination via the  $\pi$ -system.<sup>18</sup> This data suggests that the ruthenium centre in the downfield isomer of **2-5b** is stabilized via a  $\kappa^3$ -(P,P,Ar) coordination mode of the  $\text{P}^{\text{Cy}}_2\text{N}^{\text{Ph}}_2$  ligand. Similar,  $\pi$ -coordination of a ligand aryl substituent is observed in palladium catalysts with dialkyl(biphenyl)phosphine ligands developed extensively by the Buchwald group.<sup>12, 19</sup> Stabilization of Pd via reversible ligand coordination between  $\kappa^2$ -(P,Ar) and  $\kappa^1$ -(P) modes allows for exceptional turnover numbers in Suzuki C-C and Buchwald-Hartwig C-N coupling catalysis.

Single crystals suitable for X-ray diffraction were obtained from a sample containing >95%  $\kappa^3$ -(P,P,Ar)-**2-5b**, and the structure confirmed coordination of ruthenium to the *N*-phenyl substituent (Figure 2-7). A ruthenium pyramidalization angle ( $\text{C}_{\text{pcentroid}}\text{-Ru-PP}_{\text{centroid}}$ )<sup>15a</sup> of  $144.49^\circ$  strongly supports the presence of a stabilizing interaction in the sixth coordination site. The Ru(1)-C(15) distance of  $2.429(2)$  Å is within the range ( $2.26 - 2.46$  Å) observed for similar structures with Ru(II) coordination to the  $\pi$ -system of an aryl group.<sup>16a, 18c, 20</sup> By contrast, the closest distance between Ru and an ortho carbon in  $\kappa^2$ -(P,P)-**2-A** is nearly  $0.2$  Å longer.<sup>10</sup> The capacity of the phenyl group to bind to ruthenium in  $\kappa^3$ -(P,P,Ar)-**2-5b**, is likely due to the small size of the Cp spectator ligand. In line with this hypothesis, complexes **2-A** and **2-6b** with the bulkier Cp\* ligand, do not exhibit this coordination mode. Indeed, this is the first example of this coordination mode with metal complexes of the  $\text{P}^{\text{R}}_2\text{N}^{\text{R}'_2}$  ligand family.

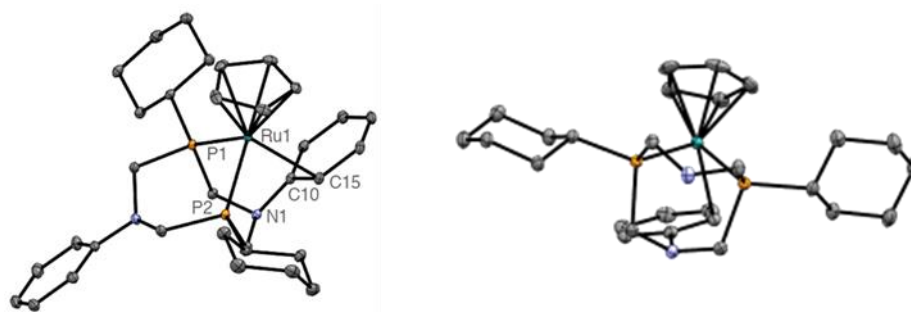


**Figure 2-7.** Two views of the displacement ellipsoid plots for  $\kappa^3$ -(P,P,Ar)-**2-5b** with ellipsoids at 30% probability level. H atoms,  $[\text{PF}_6]^-$ , and a molecule of co-crystallized DCM were omitted for clarity. In the bottom view, the N(2) phenyl substituent was also removed for clarity. Selected bond distances (Å): Ru(1)-Cl(10) =  $2.572(2)$  Ru(1)-C(15) =  $2.429(2)$ ,



Ru(1)-P(1) = 2.2571(8), Ru(1)-P(2) = 2.293(1); Selected Angles (°): P(1)-Ru(1)-P(2) = 81.23(2), Cp(centroid)-Ru(1)-P(centroid) = 144.49°.

Efforts to study the equilibrium between **2-5b-N<sub>2</sub>** and  $\kappa^3$ -(P,P,Ar)-**2-5b** by variable temperature studies were hindered by competing decomposition. Instead, the structures and energetics were validated through computational modelling. Vibrational frequency calculations indicated that the ‘active’ complexes  $\kappa^2$ -(P,P)-**2-5b**,  $\kappa^3$ -(P,P,Ar)-**2-5b**, and **2-5b-N<sub>2</sub>** are all ground state species (Figure 2-8). Relative to the 16e<sup>-</sup> low-coordinate species, the  $\kappa^3$ -P,P,Ar isomer and N<sub>2</sub> adduct are both more stable by 47.7 and 74.5 kJ/mol, respectively. Analogous calculations with the Cp\* complex **2-6b** revealed that a  $\kappa^3$ -P,P,Ar isomer is 63.0 kJ/mol less stable than the  $\kappa^2$ -P,P 16e<sup>-</sup> complex. This is likely due to steric clash of the Cp\* methyl groups with the aryl that would be engaged in metal binding. The high energy of this isomer is consistent with experiments that show no evidence for this isomer. Complex **2-6b-N<sub>2</sub>** was only slightly more stable ( $\Delta G = -5.8$  kJ/mol) than the 16e<sup>-</sup> complex  $\kappa^2$ -(P,P)-**2-6b**, which is in line with experimental indicators that the N<sub>2</sub> ligand is very labile.

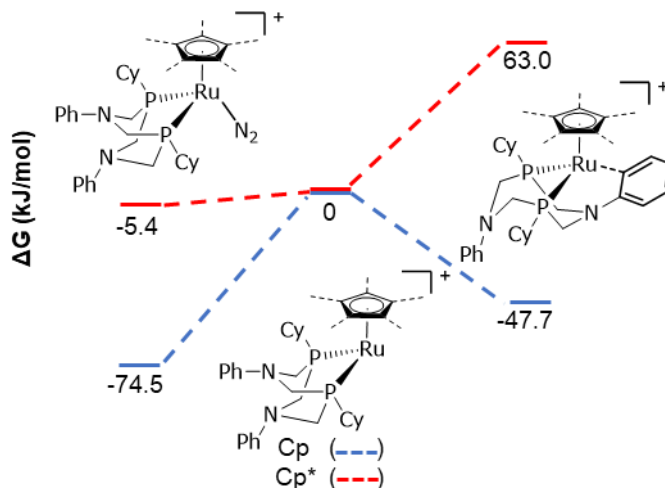


**Figure 2-8.** Calculated energies of ‘donor-free’ complexes **2-5b** and **2-6b** including N<sub>2</sub> adducts, low-coordinate  $\kappa^2$ -(P,P) and  $\kappa^3$ -(P,P,Ar) isomers.

## 2.2.4 (In)Stability of Pre-Catalysts and Active Catalysts at Elevated Temperature

The thermal stability of pre-catalysts **2-1b/2-2b** and active catalysts **2-5b/2-6b** was assessed in nitromethane at 70 °C (Figure 2-9), which is the temperature used in catalytic reactions. Most conventional solvents were precluded for this assessment due to limited solubility of **2-5b** and **2-6b**, as well as competing reactivity with chlorinated solvents (*vide infra*) and competing adduct formation with coordinating solvents. As expected, the pre-catalysts **2-1b/2-2b** were more stable than the active catalysts analogues **2-5b/2-6b**. The Cp pre-catalyst **2-1b** is the most stable structure as is evidenced by 97 and 82% fidelity of speciation at 1 and 24 h, respectively. By contrast the active catalyst **2-5b** is ca. two-fold less stable in which only 54 and 34% of the complex remains at 1 and 24 h, respectively. The speciation of remaining **2-5b** at 70 °C is exclusively the  $\kappa^3$ -(P,P,Ar) isomer, which indicates the N<sub>2</sub> adduct with  $\kappa^2$ -(P,P) ligand coordination is more sensitive to decomposition. The Cp\* pre-catalyst **2-2b** is ca. six-fold more stable than the active complex **2-6b**, however both are much less stable than the Cp analogues. Only 54% of the Cp\* pre-catalyst **2-2b** remains after 1h, which is similar stability to the Cp active catalyst **2-5b** (49% at 1h). Strikingly, less than 10% of the Cp\* active catalyst **2-6b** survives in the same timeframe. These data demonstrates that the Cp complexes are significantly more stable at elevated temperatures than the Cp\* catalysts. We established previously with [Ru(Cp/Cp\*)(P<sup>Ph</sup><sub>2</sub>N<sup>Bn</sup><sub>2</sub>)(MeCN)]PF<sub>6</sub> complexes that MeCN is less labile with Cp as the ancillary ligand as compared to Cp\*.<sup>8c</sup> The lower lability in **2-1b** would give a lower concentration of the more thermally sensitive active catalyst than **2-2b**. While this likely has some contribution to the relative thermal stability of **2-1b** and **2-2b**, the thermal stability of the active catalysts reveals that the Cp\* derivative **2-6b** is intrinsically more sensitive to decomposition than the Cp derivative **2-5b**. We propose that the capacity for the P<sup>Cy</sup><sub>2</sub>N<sup>Ph</sup><sub>2</sub> ligand in **2-5b** to achieve a  $\kappa^3$ -(P,P,Ar) coordination mode stabilizes the active catalyst from decomposition via the five-coordinate  $\kappa^2$ -(P,P) isomer. The thermolysis reactions resulted in the formation of multiple deactivation species (**2-5b** and **2-6b**) or the products were non-observable (**2-1b** and **2-2b**). In all cases, attempts to isolate the decomposition products proved unsuccessful.

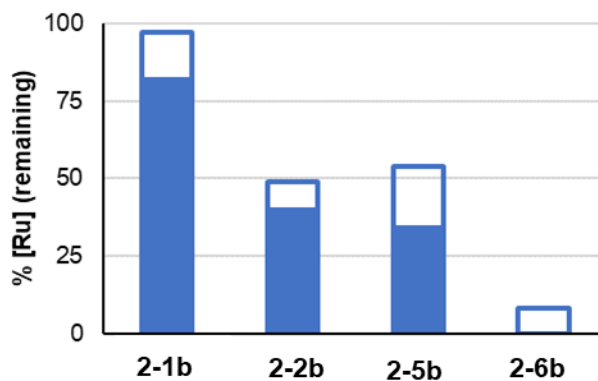
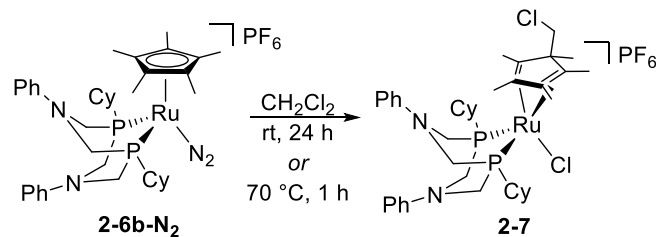


**Figure 2-9.** Thermal stability of pre-catalysts **2-1b/2-2b** and active catalysts **2-5b/2-6b** after 1 h (filled and empty bar together) and 24 h (filled bar only). % [Ru] values were quantified by  $^{31}\text{P}\{^1\text{H}\}$  NMR spectroscopy integrals relative to an internal standard.

### 2.2.5 (In)Stability of the Cp\* Active Catalyst in Halogenated Solvent

Solutions of Cp\* complex **2-6b-N<sub>2</sub>** in CH<sub>2</sub>Cl<sub>2</sub> (or CD<sub>2</sub>Cl<sub>2</sub>) cleanly converted to a single new compound at 70 °C after 1 h or at room temperature after 18 h (Scheme 2-3). By contrast, the Cp analogue **2-5b-N<sub>2</sub>** was stable in CH<sub>2</sub>Cl<sub>2</sub> over 48 h at room temperature. The product of **2-6b-N<sub>2</sub>** decomposition was isolated in 90% yield and identified as **2-7**, which formed by cleavage of a C-Cl bond of the solvent to give a Ru-Cl moiety and a functionalized cyclopentadiene ligand. The product was identified by two doublets in the  $^{31}\text{P}\{^1\text{H}\}$  NMR spectrum at 72.5 and 32.8 ppm, which reflects the lack of symmetry. In the  $^1\text{H}$  NMR spectrum a diagnostic singlet for the Cp\* methyl groups was absent, and instead four singlets were observed around 2 ppm and a fifth was found at 0.8 ppm. The upfield shift of the latter is a consequence of functionalization of one of the carbon atoms of the former Cp\* ligand to give a cyclopentadiene structure. A similar pattern was found in the  $^{13}\text{C}\{^1\text{H}\}$  NMR spectrum that contained four vinylic methyl signals around 12 ppm and one methyl bound to a *sp*<sup>3</sup> carbon at 2.0 ppm. The functionalized quaternary carbon is at  $\delta_{\text{C}} = 1.32$ , which is ca. 9 ppm upfield of the ring carbons of the Cp\* ligand in **2-6b**. A correlation between this carbon and methylene protons at 3.55 and 3.28 ppm in the  $^1\text{H}$ - $^{13}\text{C}\{^1\text{H}\}$  HMBC confirmed that the diene is functionalized with a ‘CH<sub>2</sub>Cl’ unit originating from the solvent.



**Scheme 2-3.** Deactivation of operationally unsaturated complex **2-6b-N<sub>2</sub>** via reaction with DCM to give Ru-Cl complex **2-7**.

Single crystals of **2-7** were obtained and X-ray crystallography unambiguously confirmed the connectivity (Figure 2-10). The C(1A) atom bears four substituents including the ‘CH<sub>2</sub>Cl’ unit from the activated dichloromethane molecule. The C(1A)-C(2A) and C(1A)-C(5A) bond lengths are 1.529 and 1.532 Å, respectively, which are consistent with single bonds. Together, this confirms that the aromaticity of the ring has been broken. The cyclopentadiene ring is bound in an η<sup>4</sup>-coordination mode, in which the Ru(1A) to C(2A)-C(5A) bond lengths are 2.166(2), 2.222(2), 2.339(2), and 2.328(2) Å, respectively. The ca. 0.1 Å shorter distance to C(2A) and C(3A) reflects the stronger backbonding into the alkene trans to the π-donor chloride. The ruthenium centre is pseudo square pyramidal, in which phosphine P(2A) of the P<sup>Cy</sup><sub>2</sub>N<sup>Ph</sup><sub>2</sub> ligand occupies the axial site. This position *trans* to an open coordination site explains the ca. 40 ppm more downfield location of one of the <sup>31</sup>P{<sup>1</sup>H} signals.

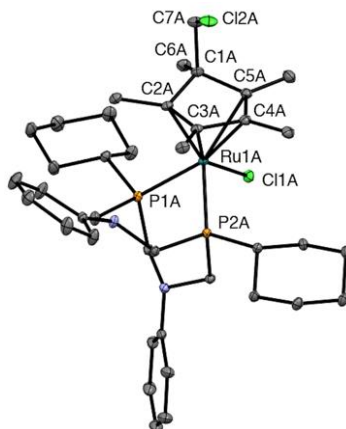
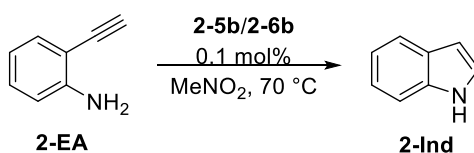


**Figure 2-10.** Displacement ellipsoid plot of solid-state structure of  $[\text{RuCl}(\eta^4\text{-C}_5\text{Me}_5\text{CH}_2\text{Cl})(\text{P}^{\text{Cy}_2\text{N}^{\text{Ph}_2}})][\text{PF}_6]$  (**2-7**). Ellipsoids are given at 30% probability level. H atoms,  $[\text{PF}_6]^-$  counterion, a molecule of co-crystallized  $\text{CH}_2\text{Cl}_2$ , and a minor component of disorder in the  $\text{C}_5\text{Me}_5\text{CH}_2\text{Cl}$  ligand were omitted for clarity. Selected bond distances ( $\text{\AA}$ ):  $\text{Ru}(1\text{A})\text{-Cl}(1\text{A}) = 2.364(1)$ ,  $\text{Ru}(1\text{A})\text{-P}(1\text{A}) = 2.2989(8)$ ,  $\text{Ru}(1\text{A})\text{-P}(2\text{A}) = 2.2421(8)$ . Selected Angles ( $^\circ$ ):  $\text{P}(1\text{A})\text{-Ru}(1\text{A})\text{-P}(2\text{A}) = 77.31(2)$ .

Oxidative addition of the C-Cl bond of dichloromethane is known for other Ru complexes bearing  $\text{Cp}^*$  or Tp ancillary ligands (Tp = hydridotris(pyrazolyl)borate).<sup>21</sup> A similar reaction may occur en route to **2-7**, but no high-valent intermediates were observed. Certainly, the formation of **2-7** from **2-6b** would not be concerted since the Ru-Cl and ‘ $\text{CH}_2\text{Cl}$ ’ fragments are on opposite faces of the cyclopentadiene ligand. Functionalization of Ru-bound Cp/Cp\* ligands can occur via nucleophilic or electrophilic addition.<sup>22</sup> Regardless of the mechanism for  $\text{CH}_2\text{Cl}_2$  activation with **2-6b**, the lack of reactivity with Cp complex **2-5b** is striking. It is compelling to suggest that the  $\kappa^3\text{-(P,P,Ar)}$  isomer contributes to the stability of **2-5b**, it is unlikely however that this is the only factor since the  $\text{N}_2$  adduct is present in significant quantities at room temperature. More likely, the Cp\* ligand gives a sufficiently electron rich metal to achieve C-Cl activation. The facile formation of complex **2-7** reveals the sensitivity of catalyst **2-6b** to side reactions, particularly with alkyl halides.

## 2.2.6 Lifetime of Active Catalysts **2-5b** and **2-6b**

Catalytic intramolecular hydroamination of 2-ethynylaniline was conducted with the Cp and Cp\* active complexes **2-5b** and **2-6b**, respectively (Scheme 2-4). For an additional comparison, the chloro complex **2-3b** was included that requires halide dissociation to enter the catalytic cycle. Reactions were conducted under standard conditions of 0.1 mol% catalyst for 24 h at 70 °C and nitromethane was used to ensure complete solubility of all catalysts. The data below are compared to TON values for **2-1b/2-2b** in Me-THF, but control reactions indicated that the nature of the solvent does not influence the TON values.



**Scheme 2-4.** Benchmark cyclization of 2-ethynylaniline to indole catalyzed using the coordinatively unsaturated complexes **2-5b** and **2-6b**, and a control reaction with the complex **2-3b**.

At 70 °C the TONs for the active complexes **2-5b** and **2-6b** are 220 and 160, respectively (Figure 2-11). The ca. 1.4-fold higher lifetime of the Cp catalyst is consistent with the relative values for the pre-catalyst analogues **2-1b** and **2-2b**. However, the magnitude of the difference is smaller than would be expected based on thermal stability, in which **2-5b** is ca. seven-fold more stable than **2-6b**. This suggests that coordination of the substrate and/or product to ruthenium offers some degree of protection from decomposition, which may be particularly important for the Cp\* analogue that does not benefit from P<sup>Cy</sup><sub>2</sub>N<sup>Ph</sup><sub>2</sub> hemilability for stability. The TONs of the active catalysts **2-5b** and **2-6b** are ca. three times lower than their analogous pre-catalysts **2-1b** and **2-2b**, respectively. Despite the facile initiation of the pre-catalysts to the active catalysts at 70 °C, the equilibrium binding of acetonitrile still offers notable stabilization. The low lability of the chloro ligand in **2-3b**, even at elevated temperature in the relatively polar nitromethane solvent, leads to a poor TON of only 50. Previously, we found that pre-catalysts **2-1a/2-2a** exhibited poor performance at 40 °C due to slow conscription into the catalytic cycle via MeCN dissociation. Since this step is precluded with the active catalysts **2-5b** and **2-6b**, we

anticipated high TONs could be achieved at room temperature. Unfortunately, no conversion was observed for **2-5b**, which indicates that an on-cycle step in the catalytic mechanism has a sufficiently high barrier to prevent catalysis at this temperature.

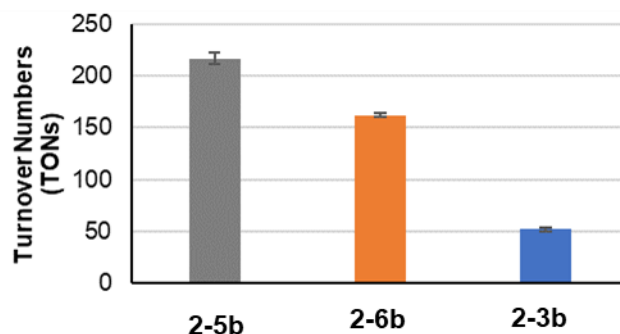


**Figure 2-11.** TON comparison with 0.1 mol% of donor-free complexes **2-5b** and **2-6b**, and chloro complex **2-3b** toward the intramolecular hydroamination of **2-EA** at 70 °C, in CH<sub>3</sub>NO<sub>2</sub>. TONs were determined after 24 h by GC-FID analysis. Runs were conducted in duplicate with data points representing the average and the error bars depict the span of individual runs.

### 2.2.7 Reaction Rate Comparison of Catalysts **2-1a-c** and **2-2a-c**

Hydroamination of **2-EA** under standard conditions with catalysts **2-1a**, **2-1b**, **2-1c**, **2-2a**, **2-2b**, and **2-2c** (Scheme 2-1) was monitored over time by GC-FID (Figure 2-12). Turnover frequencies, calculated at 50% of the maximum conversion, of 1300, 60, and 110 h<sup>-1</sup> for **2-1a**, **2-1b**, and **2-1c**, respectively, revealed that the R = *t*-Bu catalyst is much faster than the R = Cy or Ph derivatives. The TOF of the donor-free complex **2-5b** is ca. 10 h<sup>-1</sup> (Figure A-58), which may suggest that the κ<sup>3</sup>-(P,P,Ar) coordination mode slows catalysis. However, MeCN readily displaces the π-arene interaction, therefore the slow rate may be due to competitive binding of the amine of **2-EA**. The TOFs for **2-2a-c** of 1530, 1330 and 200 h<sup>-1</sup>, respectively, show that in all cases the Cp\* derivatives are faster than the Cp analogues. This is consistent with the prior study of **2-1a** and **2-2a**,<sup>8c</sup> and this confirms the trend is general to other catalyst derivatives. The difference in rate between Cp and Cp\* complexes is likely a consequence of constriction of the pre-catalyst to the κ<sup>2</sup>-(P,P) active

catalyst. This species is likely more prevalent with all Cp\* derivatives due to higher MeCN lability.

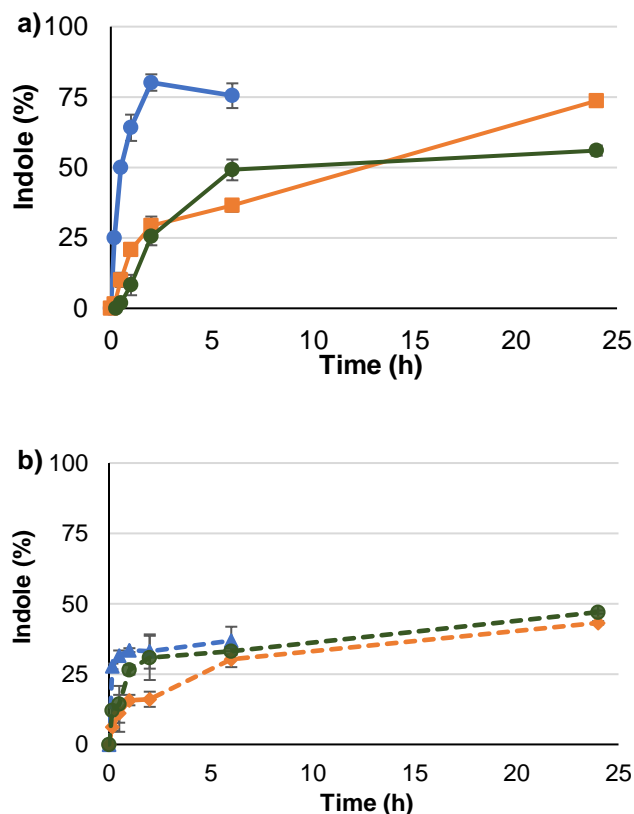


**Figure 2-12.** Reaction profiles for the intramolecular hydroamination of **2-EA** with a) Cp complexes **2-1a-c** (solid lines); and b) Cp\* complexes **2-2a-c** (dashed lines). Conditions: 300 mM **2-EA**, Me-THF, 70 °C, 0.1 mol% [Ru]; **2-1a** (blue), **2-1b** (orange), **2-1c** (yellow), **2-2a** (blue), **2-2b** (orange), **2-2c** (yellow). Runs were conducted in duplicate with data points representing the average and the error bars depict the span of individual runs.

### 2.2.8 Product Inhibition of Catalyst **2-1b**

A qualitative comparison of the reaction profiles (Figure 2-12) reveals that conversion rates with the R = Cy catalysts **2-1b** and **2-2b** slow down considerably after ca. 20% conversion of **2-EA**. This attenuation suggests that the indole product may inhibit catalysis. To evaluate this, Variable Time Normalization Analysis (VTNA)<sup>23</sup> was employed by examining **2-EA** consumption over time (Figure 2-13). Hydroamination was conducted with a consistent concentration of **2-1b** and two different concentrations of **2-EA** (Run A



= 150 and Run B = 100 mM). The starting substrate concentration of Run B corresponds to the amount of **2-EA** remaining after 34% conversion of Run A, which is observed after 50 min. The Run B data was shifted along the time axis so that the first data point aligned with the 50 min data point of Run A. The two lines should overlap if catalyst inhibition is negligible. In this case, Run A and time-shifted Run B data do not overlap and the latter exhibits faster consumption of **2-EA**. A third set of conditions (Run C) was completed with 100 mM **2-EA** and 50 mM indole (**2-Ind**), which corresponds the actual speciation in Run A after 50 min. The data for Run C and A are in close agreement, which indicates that the presence of indole attenuates consumption of **2-EA** due to catalyst inhibition. Given that product formation is not completely arrested, the inhibition process negatively affects only the catalytic rate rather than overall TONs. In fact, as suggested above the indole adduct may offer some catalyst stabilization.

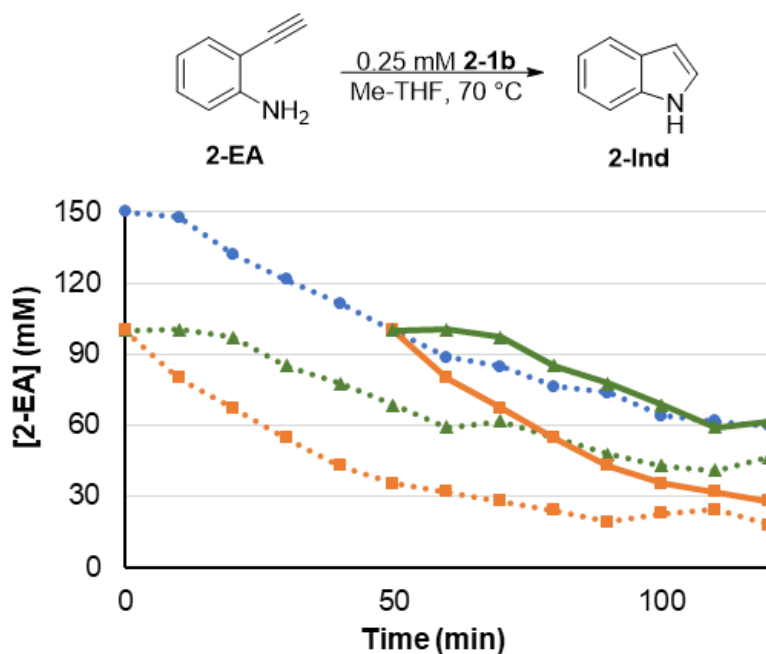
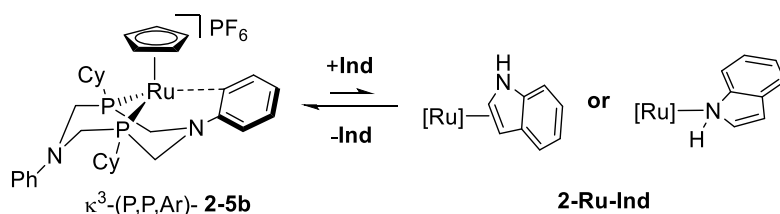


Figure 2-13. (top) Intramolecular hydroamination of **2-EA** with catalyst **2-1b** (0.25 mM) to form **2-Ind**. (bottom) Reaction profiles for runs with initial concentrations of: A, 150 mM **2-EA** (●, blue); B, 100 mM **2-EA** (■, orange); and C 100 mM **2-EA** and 50 mM **2-Ind** (▲, green) Solid lines (—) are time-shifted (Run B = orange; Run C = green). Reactions were performed in duplicate and in all cases the error was within  $\pm 5\%$ .

Catalyst inhibition would result from competitive coordination of either the heterocyclic  $\pi$ -bond or the nitrogen lone pair of indole to the catalyst active site (e.g. **2-Ru-Ind** in Scheme 2-5). Regeneration of the active catalyst would rely on the lability of bound indole. A related  $\kappa^1$ -(N) pyrrolidine adduct,  $[\text{Ru}(\text{Cp})(\text{P}^{\text{Ph}}_2\text{N}^{\text{Bn}}_2)(\text{pyrr})]\text{PF}_6$ , was previously characterized, and in the solid-state it exhibited a hydrogen bond between the Lewis base and the proximal pendent amine of the ligand.<sup>24</sup> Treatment of **2-5b** with 200 equivalent indole resulted in an immediate colour change from dark red to yellow, which is typical for coordinatively-saturated complexes of the type  $[\text{Ru}(\text{Cp}/\text{Cp}^*)(\text{P}^{\text{R}}_2\text{N}^{\text{R}'}_2)(\text{L})]\text{PF}_6$ .<sup>8a-c, 10, 24</sup> Formation of a single new species was not observed. Rather, the  $^{31}\text{P}\{^1\text{H}\}$  NMR signals for the two isomers of **2-5b** were both shifted downfield by ca. 4 ppm, consistent with equilibrium binding of **2-Ind** that strongly favors the active complex structures. In line with this observation, attempts to isolate the **2-Ru-Ind** adduct were unsuccessful. While the formation of **2-Ru-Ind** suppresses the catalytic rate the adduct may protect the active catalyst from decomposition as an off-cycle intermediate.



**Scheme 2-5.** Proposed equilibrium between  $\kappa^3$ -(P,P,Ar)-**2-5b** and possible inhibition adducts **2-Ru-Ind**. Note: samples of **2-5b** also contain the  $\kappa^2$ -(P,P)-**2-5b-N<sub>2</sub>**.  $[\text{Ru}] = [\text{Ru}(\text{Cp})(\text{P}^{\text{Cy}}_2\text{N}^{\text{Ph}}_2)]\text{PF}_6$ .

### 2.2.9 Substrate Modification to Avoid Product Inhibition of Catalyst **2-1b**

We considered that simple modification of the primary amine substrate to a secondary amine, such as 2-ethynyl-*N*-methylaniline (**2-Me-EA**), could prevent catalyst inhibition. VTNA with **2-1b** and **2-Me-EA** was conducted following a similar set of three Runs A-C (Figure 2-14) that were described above with **2-EA**. A 50 mM substrate concentration was used for Run A and 35 mM was used for Runs B and C, which corresponded to the amount of **2-EA** at a reaction time of 30 min in Run A. Run C also included 15 mM **2-Me-Ind** to

directly mimic the speciation of Run A at  $t = 30$  min. A shift in Run B and C data along the time axis shows that all three data sets overlap, which demonstrates that **2-Me-Ind** does not inhibit catalyst **2-1b**. The lack of inhibition could be a consequence of the higher catalyst loading (3 mol%) as compared to that employed above with **2-EA** (0.2 mol%). Indeed, catalysis with **EA** under conditions analogous to those used with **2-Me-Ind** did not lead to inhibition of catalyst **2-1b** (SI, Figure A-57). Adduct formation was instead evaluated by treatment of donor-free complex **2-5b** with 200 equiv. of **2-Me-Ind**. No change in the  $^{31}\text{P}\{^1\text{H}\}$  NMR resonances of **2-5b** were observed nor was there a color change from dark red that would support formation of an adduct. This is contrast to the analogous reaction with **2-Ind** that exhibits both spectroscopic and qualitative color changes indicative of **2-Ru-Ind** (*vide supra*). Thus, coordination of **2-Me-Ind** to the active catalyst **2-5b** is suppressed as compared to **2-Ind** and this could be a consequence of the increased steric clash imposed by the methyl group, lower Lewis basicity, and/or lack of hydrogen bonding capability.

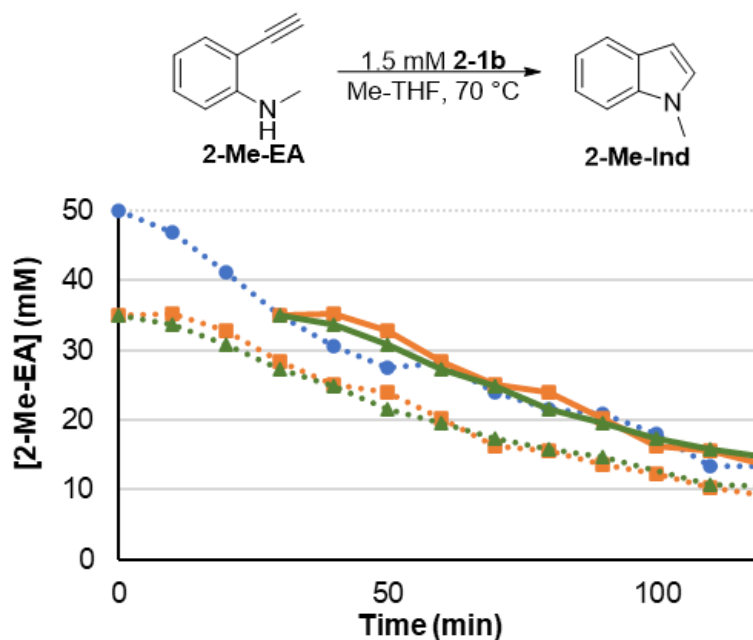


**Figure 2-14.** (top) Intramolecular hydroamination of **2-Me-EA** with catalyst **2-1b** (1.5 mM) to form **2-Me-Ind**. (bottom) Reaction profiles for runs with initial concentrations of: A, 50 mM **2-Me-EA** (●, blue); B, 35 mM **2-EA** (■, orange); and C 35 mM **2-Me-EA** and

15 mM **2-Me-Ind** ( $\blacktriangle$ , green) Solid lines ( $\text{—}$ ) are time-shifted (Run B = orange; Run C = green). Reactions were performed in duplicate and in all cases the error was within  $\pm 5\%$ .

## 2.3 Conclusion

The catalytic lifetime and rate were assessed for a family of  $[\text{Ru}(\text{Cp}/\text{Cp}^*)(\text{P}^{\text{R}}_2\text{N}^{\text{Ph}}_2)(\text{MeCN})]\text{PF}_6$  complexes ( $\text{R} = t\text{-Bu}, \text{Cy}, \text{Ph}$ ). The  $\text{P}^{\text{Cy}}_2\text{N}^{\text{Ph}}_2$  ligand in the donor-free ‘active’ complex  $[\text{Ru}(\text{Cp})(\text{P}^{\text{Cy}}_2\text{N}^{\text{Ph}}_2)(\text{MeCN})]\text{PF}_6$  coordinates to the metal through either a bidentate or tridentate mode. The latter involves coordination of ruthenium to the  $\pi$ -system of the N-Ph substituent, which increases the thermal stability of the Cp active catalyst by seven-fold over the  $\text{Cp}^*$  analogue. Steric clash of the N-phenyl substituent with the methyl groups of  $\text{Cp}^*$  likely precludes  $\text{P}^{\text{Cy}}_2\text{N}^{\text{Ph}}_2$  hemilability in these derivatives. While the Cp derivatives have higher lifetimes, the catalytic rates are slower than the  $\text{Cp}^*$  analogues. The attenuated rates of the Cp derivatives are not likely due to the  $\kappa^3\text{-(P,P,Ar)}$  coordination mode, since the stabilizing interaction is readily displaced by a donor molecule (e.g., MeCN). Rather, the rate is most sensitive to catalyst inhibition by the hydroamination product **Ind**. Despite the attenuated rate, product coordination likely enhances turnover numbers by stabilizing the active catalyst. Therefore, the lifetime of catalyst **2-1b** benefits from both intrinsic ( $\text{P}^{\text{Cy}}_2\text{N}^{\text{Ph}}_2$  hemilability) and extrinsic (reversible MeCN/**2-Ind** coordination) factors. This study shows that with Ru(Cp) complexes the  $\text{P}^{\text{R}}_2\text{N}^{\text{Ph}}_2$  ligand displays two beneficial types of metal-ligand cooperativity: proton-transfer via the pendent tertiary amines, which avoids basic additives; and a change in ligand coordination to stabilize the low-coordinate active catalyst.

## 2.4 Experimental Section

### 2.4.1 General Procedures, Materials, and Instrumentation

All reactions were carried out under an inert atmosphere of Ar or  $\text{N}_2$  using standard Schlenk or glovebox techniques, respectively, unless otherwise stated. All glassware was oven dried ( $150\text{ }^\circ\text{C}$ ) prior to use. All chemicals were obtained from Sigma-Aldrich, Alfa Aesar, or Oakwood, and used without further purification unless otherwise stated.  $\text{CDCl}_3$  (99.8%),  $\text{DCM-}d_2$ , and acetone- $d_6$ , were obtained from Cambridge Isotope Laboratories.  $\text{P}^{\text{Cy}}_2\text{N}^{\text{Ph}}_2$ ,<sup>25</sup>  $[\text{RuCl}(\text{Cp}^*)(\text{PPh}_3)_2]$ ,<sup>26</sup>  $[\text{Ru}(\text{Cp})(\text{P}^{t\text{-Bu}}_2\text{N}^{\text{Ph}}_2)(\text{MeCN})]\text{PF}_6$  (**2-1a**),<sup>8c</sup>  $[\text{Ru}(\text{Cp})(\text{P}^{t\text{-Bu}}_2\text{N}^{\text{Ph}}_2)(\text{MeCN})]\text{PF}_6$

$\text{Bu}_2\text{N}^{\text{Ph}_2}(\text{MeCN})\text{PF}_6$  (**2-1c**),<sup>8c</sup> and  $[\text{Ru}(\text{Cp}^*)(\text{P}^t\text{Bu}_2\text{N}^{\text{Ph}_2})(\text{MeCN})]\text{PF}_6$  (**2-2a**)<sup>8c</sup> were synthesized following literature procedures and the  $^1\text{H}$  and  $^{31}\text{P}\{^1\text{H}\}$  spectroscopic data matched literature values. Dry and degassed tetrahydrofuran (THF), diethyl ether ( $\text{Et}_2\text{O}$ ), and acetonitrile (MeCN) were obtained from an Innovative Technology 400-5 Solvent purification system and stored under  $\text{N}_2$ . These dry and degassed solvents, aside from MeCN, were stored over 4 Å molecular sieves, while MeCN was stored over 3 Å molecular sieves (Fluka and activated at 150 °C in an oven). Absolute ethanol was degassed by bubbling with argon. 2-methyltetrahydrofuran (Me-THF), fluorene, nitromethane, deuterated nitromethane, and  $\text{CDCl}_3$  were dried using 4 Å molecular sieves and degassed by bubbling with argon.

Charge-transfer Matrix Assisted Laser Desorption/Ionization (MALDI) mass spectrometry data were collected on an AB Sciex 5800 TOF/TOF mass spectrometer using pyrene as the matrix in a 20:1 molar ratio to metal complex. Samples were spotted on the target plate as solutions in  $\text{CH}_2\text{Cl}_2$ . NMR spectra were acquired on either an INOVA 400 or 600 MHz, or a Bruker 400 MHz NMR spectrometer.  $^1\text{H}$  NMR spectra acquired were referenced internally against the residual protio-solvent signal to tetramethylsilane at 0 ppm and  $^{13}\text{C}\{^1\text{H}\}$  NMR spectra were referenced internally against the solvent signal to tetramethylsilane at 0 ppm.  $^{31}\text{P}\{^1\text{H}\}$  spectra were referenced externally to 85% phosphoric acid at 0.00 ppm. Infrared spectra were collected on solid samples using a PerkinElmer UATR TWO FTIR spectrometer. Quantification of catalytic conversion of **2-EA**, **2-Ind**, and **2-Me-Ind**, were achieved using an Agilent 7890a gas chromatography with a flame ionization detector (GC-FID), fitted with a HP-5 column, unless otherwise stated. Calibration curves for **2-EA**, **2-Ind**, and **2-Me-Ind**, were prepared to determine the response factor. The amount of each species was quantified, relative to the internal standard (tetralin), using area counts corrected with the response factor.

#### 2.4.2 General Procedure for Synthesis of Pre-Catalysts $[\text{Ru}(\text{Cp})(\text{P}^{\text{R}}_2\text{N}^{\text{R}'_2})(\text{MeCN})][\text{PF}_6]$ (**2-1b**, **2-2b**, **2-2c**).

A 100 mL Schlenk flask was charged with a stir bar,  $[\text{Ru}(\text{Cp})(\text{MeCN})_3][\text{PF}_6]$  or  $[\text{Ru}(\text{Cp}^*)(\text{MeCN})_3][\text{PF}_6]$  (0.21-0.26 mmol, 1 equiv), ligand  $\text{P}^{\text{Cy}}_2\text{N}^{\text{Ph}_2}$  or  $\text{P}^{\text{Ph}_2}_2\text{N}^{\text{Ph}_2}$  (0.23-0.27 mmol, 1.05 equiv, and MeCN/DCM (12 mL, 1:1). The flask was heated under a flow

of argon at 35 °C for 1 h, the solvent was removed *in vacuo*, and the flask with the remaining solid residue was transferred into a glovebox. The solid was dissolved in MeCN and the suspension was then filtered through a microfibre pipette filter to remove insoluble ligand. The solvent of the filtrate was removed *in vacuo* to give an orange/yellow solid, which was triturated and washed with diethyl ether (3 x 5 mL). The solid was further dried *in vacuo* to remove any residual solvent.

**[Ru(Cp)(P<sup>Cy</sup><sub>2</sub>N<sup>Ph</sup><sub>2</sub>)(MeCN)][PF<sub>6</sub>] (2-1b).** Yield = 93%. <sup>1</sup>H NMR (600 MHz, CD<sub>2</sub>Cl<sub>2</sub>): δ 7.36-7.25 (m, Ph-*H*, 4H), 7.05-7.00 (m, Ph-*H*, 2H), 6.99-6.94 (m, Ph-*H*, 1H), 6.91-6.86 (m, Ph-*H*, 3H), 4.83 (s, Ru(C<sub>5</sub>H<sub>5</sub>), 5H), 3.83-3.75 (m, PCH<sub>2</sub>N, 2H), 3.63-3.52 (m, PCH<sub>2</sub>N, 4H), 3.52-3.46 (m, PCH<sub>2</sub>N, 2H), 2.27-2.19 (m, Cy-*H*, 2H), 2.12 (s, NCCH<sub>3</sub>, 3H), 2.11-2.03 (m, Cy-*H*, 2H), 2.03-1.80 (m, Cy-*H*, 8H), 1.63-1.25 (m, Cy-*H*, 10H). <sup>13</sup>C{<sup>1</sup>H} NMR (151 MHz, CD<sub>2</sub>Cl<sub>2</sub>): δ 153.2 (t, <sup>3</sup>J<sub>C-P</sub> = 6.9 Hz, C<sub>Ar</sub>), δ 152.1 (t, <sup>3</sup>J<sub>C-P</sub> = 6.0 Hz, C<sub>Ar</sub>), 130.2 (C<sub>Ar</sub>), 128.0 (C<sub>Ar</sub>), 128.0 (NCCH<sub>3</sub>), 122.1 (C<sub>Ar</sub>), 121.2 (C<sub>Ar</sub>), 118.3 (C<sub>Ar</sub>), 117.3 (C<sub>Ar</sub>), 80.5 (Ru(C<sub>5</sub>H<sub>5</sub>)), 49.7 (X of ABX, N-CH<sub>2</sub>-P), 46.9 (X portion of ABX spin system, N-CH<sub>2</sub>-P), 42.1 (X of ABX, Cy), 28.8 (s, Cy), 28.5 (s, Cy), 27.5 (X of ABX, Cy), 27.1 (X of ABX, Cy), 26.6 (s, Cy), 4.4 (s, NC-CH<sub>3</sub>). <sup>31</sup>P{<sup>1</sup>H} NMR (162 MHz, CD<sub>2</sub>Cl<sub>2</sub>): δ 45.9 (s, Ru-*P*), -144.2 (sept, <sup>1</sup>J<sub>P-F</sub> = 710.0 Hz, PF<sub>6</sub>). IR (neat) ν(cm<sup>-1</sup>): 2924 (m), 2850 (m), 1595 (m), 1493 (m), 1201 (m), 835 (s), 749 (m), 692 (m), 556 (m). MALDI MS (pyrene matrix): Calc. *m/z* = 633.2 [Ru(Cp\*)(P<sub>2</sub><sup>Cy</sup>N<sub>2</sub><sup>Ph</sup>)]<sup>+</sup>, Obs. *m/z* = 633.2.

**[Ru(Cp\*)(P<sup>Cy</sup><sub>2</sub>N<sup>Ph</sup><sub>2</sub>)(MeCN)][PF<sub>6</sub>] (2-2b).** Yield = 90%. <sup>1</sup>H NMR (600 MHz, CD<sub>2</sub>Cl<sub>2</sub>): δ 7.34-7.27 (m, Ph-*H*, 4H), 7.07-6.99 (m, Ph-*H*, 4H), 6.99-6.92 (m, Ph-*H*, 2H), 3.90-3.83 (m, PCH<sub>2</sub>N, 2H), 3.68-3.62 (m, PCH<sub>2</sub>N, 2H), 3.27-3.17 (m, PCH<sub>2</sub>N, 4H), 2.35 (s, NCCH<sub>3</sub>, 3H), 1.74 (t, <sup>4</sup>J<sub>H-P</sub> = 1.5 Hz, Ru(C<sub>5</sub>(CH<sub>3</sub>)<sub>5</sub>), 15H), 2.21-1.80 (m, Cy-*H*, 12H), 1.59-1.25 (m, Cy-*H*, 8H). <sup>13</sup>C{<sup>1</sup>H} NMR (151 MHz, CD<sub>2</sub>Cl<sub>2</sub>): δ 153.3 (t, <sup>3</sup>J<sub>C-P</sub> = 7.2 Hz, C<sub>Ar</sub>), 152.2 (t, <sup>3</sup>J<sub>C-P</sub> = 9.7 Hz, C<sub>Ar</sub>), 129.5 (C<sub>Ar</sub>), 129.4 (C<sub>Ar</sub>), 126.0 (NCCH<sub>3</sub>), 121.9 (C<sub>Ar</sub>), 121.0 (C<sub>Ar</sub>), 118.4 (C<sub>Ar</sub>), 116.8 (C<sub>Ar</sub>), 92.1 (Ru(C<sub>5</sub>(CH<sub>3</sub>)<sub>5</sub>)), 45.8 (X of ABX, N-CH<sub>2</sub>-P), 45.1 (X of ABX, N-CH<sub>2</sub>-P), 39.4 (X of ABX, Cy), 27.6 (Cy), 27.3 (X of ABX, Cy), 27.0 (X of ABX, Cy), 26.9 (X of ABX, Cy), 26.1 (Cy), 10.2 (Ru(C<sub>5</sub>(CH<sub>3</sub>)<sub>5</sub>)), 4.2 (NC-CH<sub>3</sub>). <sup>31</sup>P{<sup>1</sup>H} NMR (243 MHz, CD<sub>2</sub>Cl<sub>2</sub>): δ 36.0 (s, Ru-*P*), -143.9 (sept, <sup>1</sup>J<sub>P-F</sub> = 711.2 Hz, PF<sub>6</sub>). IR (neat) ν(cm<sup>-1</sup>):

2919 (m), 2849 (m), 1655 (m), 1595 (s), 1492 (s), 1192 (s), 840 (s), 739 (m). MALDI MS (pyrene matrix): Calc.  $m/z = 703.3$   $[\text{Ru}(\text{Cp}^*)(\text{P}_2^{\text{Cy}}\text{N}_2^{\text{Ph}})]^+$ , Obs.  $m/z = 703.2$ .

**$[\text{Ru}(\text{Cp}^*)(\text{P}^{\text{Ph}_2}\text{N}^{\text{Ph}_2})(\text{MeCN})][\text{PF}_6]$  (2-2c).** Yield = 82%.  $^1\text{H}$  NMR (600 MHz,  $\text{CD}_2\text{Cl}_2$ ):  $\delta$  7.71-7.58 (m, Ph-*H*, 11H), 7.45-7.38 (t, Ph-*H*, 1H), 7.29-7.20 (m, Ph-*H*, 4H), 7.09-7.04 (t, Ph-*H*, 1H), 6.90-6.83 (m, Ph-*H*, 3H), 4.12-4.02 (m,  $\text{PCH}_2\text{N}$ , 4H), 3.98-3.91 (m,  $\text{PCH}_2\text{N}$ , 2H), 3.88-3.81 (m,  $\text{PCH}_2\text{N}$ , 2H), 2.22 (s,  $\text{CH}_3\text{CN}$ , 3H), 1.36 (s,  $\text{Ru}(\text{C}_5(\text{CH}_3)_5)$ , 15H).  $^{13}\text{C}\{^1\text{H}\}$  NMR (151 MHz,  $\text{CD}_2\text{Cl}_2$ ):  $\delta$  153.7 (t,  $^3J_{\text{C-P}} = 6.9$  Hz,  $\text{C}_{\text{Ar}}$ ), 151.8 (t,  $^3J_{\text{C-P}} = 6.0$  Hz,  $\text{C}_{\text{Ar}}$ ), 132.2 (X of ABX,  $\text{C}_{\text{Ar}}$ ), 131.6 ( $\text{C}_{\text{Ar}}$ ), 130.9 (X of ABX,  $\text{C}_{\text{Ar}}$ ), 130.2 ( $\text{C}_{\text{Ar}}$ ), 130.2 ( $\text{C}_{\text{Ar}}$ ), 130.1 (X of ABX,  $\text{C}_{\text{Ar}}$ ), 127.7 ( $\text{NCCH}_3$ ), 122.8 ( $\text{C}_{\text{Ar}}$ ), 121.1 ( $\text{C}_{\text{Ar}}$ ), 119.0 ( $\text{C}_{\text{Ar}}$ ), 117.4 (s,  $\text{C}_{\text{Ar}}$ ), 93.9 ( $\text{Ru}(\text{C}_5(\text{CH}_3)_5)$ ), 53.3 (X of ABX, N- $\text{CH}_2\text{-P}$ ), 48.4 (X of ABX, N- $\text{CH}_2\text{-P}$ ), 10.1 ( $\text{Ru}(\text{C}_5(\text{CH}_3)_5)$ ), 4.6 (NC- $\text{CH}_3$ ).  $^{31}\text{P}\{^1\text{H}\}$  NMR (162 MHz,  $\text{CD}_2\text{Cl}_2$ ):  $\delta$  31.0 (s, Ru-*P*), -144.2 (sept,  $^1J_{\text{P-F}} = 710.0$  Hz,  $\text{PF}_6$ ). IR (neat)  $\nu(\text{cm}^{-1})$ : 3058 (vs), 2896 (w), 2847 (w), 1659 (m), 1594 (m), 1189 (m), 832 (s), 691 (m), 556 (m). MALDI MS (pyrene matrix): Calc.  $m/z = 691.2$   $[\text{Ru}(\text{Cp}^*)(\text{P}_2^{\text{Cy}}\text{N}_2^{\text{Ph}})]^+$ , Obs.  $m/z = 691.1$ .

### 2.4.3 General Procedure for $[\text{RuCl}(\text{Cp}/\text{Cp}^*)(\text{P}^{\text{Cy}_2}\text{N}^{\text{Ph}_2})]$ Complex Synthesis.

A 100 mL Schlenk flask was charge with a stir bar,  $[\text{RuCl}(\text{Cp})(\text{PPh}_3)_2]$  (0.12 mmol, 1 equiv) or  $[\text{RuCl}(\text{Cp}^*)(\text{PPh}_3)_2]$  (0.12 mmol, 1 equiv),  $\text{P}^{\text{Cy}_2}\text{N}^{\text{Ph}_2}$  ligand (0.12 mmol, 1 equiv), and toluene (20 mL). The flask was refluxed under a flow of argon for 72 h and a colour change from orange to yellow was observed. The solvent was cooled to room temperature and then removed *in vacuo* resulting in a yellow oil. The oil was triturated with hexanes to give a yellow powder which was subsequently washed with hexanes (3 x 5 mL) and dried under reduced pressure.

**$[\text{RuCl}(\text{Cp})(\text{P}^{\text{Cy}_2}\text{N}^{\text{Ph}_2})]$  (2-3b).** Yield = 86%.  $^1\text{H}$  NMR (600 MHz,  $\text{CD}_2\text{Cl}_2$ ):  $\delta$  7.28-7.24 (m, Ph-*H*, 2H), 7.22-7.17 (m, Ph-*H*, 2H), 7.03-6.99 (m, Ph-*H*, 2H), 6.90-6.86 (m, Ph-*H*, 1H), 6.78-6.74 (m, Ph-*H*, 2H), 6.71-6.67 (m, Ph-*H*, 1H), 4.53 (s,  $\text{Ru}(\text{C}_5\text{H}_5)$ , 5H), 4.23-4.16 (m,  $\text{PCH}_2\text{N}$ , 2H), 3.74-3.69 (m,  $\text{PCH}_2\text{N}$ , 2H), 3.52-3.44 (m,  $\text{PCH}_2\text{N}$ , 2H), 3.39-3.33 (m,  $\text{PCH}_2\text{N}$ , 2H), 2.44-2.39 (m, Cy-*H*, 2H), 2.12-2.05 (m, Cy-*H*, 2H), 2.00-1.88 (m, Cy-*H*, 6H), 1.83-1.77 (m, Cy-*H*, 2H), 1.72-1.63 (m, Cy-*H*, 2H), 1.46-1.29 (m, Cy-*H*, 8H).  $^{13}\text{C}\{^1\text{H}\}$

NMR (151 MHz, CD<sub>2</sub>Cl<sub>2</sub>):  $\delta$  154.2 (t,  $^3J_{C-P}$  = 7.0 Hz, C<sub>Ar</sub>), 150.9 (t,  $^3J_{C-P}$  = 4.1 Hz, C<sub>Ar</sub>), 129.3 (C<sub>Ar</sub>), 129.2 (C<sub>Ar</sub>), 120.4 (C<sub>Ar</sub>), 117.9 (C<sub>Ar</sub>), 117.8 (C<sub>Ar</sub>), 114.4 (C<sub>Ar</sub>), 77.6 (Ru(C<sub>5</sub>H<sub>5</sub>)), 46.7 (X of ABX, N-CH<sub>2</sub>-P), 43.6 (X of ABX, N-CH<sub>2</sub>-P), 42.6 (X of ABX, Cy), 28.6 (Cy), 27.9 (Cy), 27.2 (X of ABX, Cy), 26.8 (X of ABX, Cy), 26.4 (Cy).  $^{31}\text{P}\{^1\text{H}\}$  NMR (212 MHz, CD<sub>2</sub>Cl<sub>2</sub>):  $\delta$  46.6 (s, Ru-P). IR (neat)  $\nu(\text{cm}^{-1})$  2923 (m), 2846 (m), 1596 (m), 1499 (m), 1204 (m), 913 (m), 729 (s), 691 (s). MALDI MS (pyrene matrix): Calc.  $m/z$  = 668.2 [RuCl(Cp)(P<sub>2</sub><sup>Cy</sup>N<sup>Ph</sup><sub>2</sub>)]<sup>+</sup>, Obs.  $m/z$  = 668.1.

**[RuCl(Cp\*)(P<sup>Cy</sup><sub>2</sub>N<sup>Ph</sup><sub>2</sub>)] (2-4b)** Yield = 86%.  $^1\text{H}$  NMR (600 MHz, CD<sub>2</sub>Cl<sub>2</sub>):  $\delta$  7.27-7.16 (m, Ph-H, 4H), 7.03-6.97 (m, Ph-H, 2H), 6.96-6.91 (m, Ph-H, 2H), 6.83-6.77 (m, Ph-H, 2H), 4.08-4.00 (m, PCH<sub>2</sub>N, 2H), 3.69-3.57 (m, PCH<sub>2</sub>N, 4H), 3.10-3.03 (m, PCH<sub>2</sub>N, 2H), 2.45-2.37 (m, Cy-H, 2H), 2.26-2.17 (m, Cy-H, 2H), 2.07-2.00 (m, Cy-H, 2H), 1.95-1.88 (m, Cy-H, 4H), 1.81-1.74 (m, Cy-H, 2H), 1.67 (s, Ru(C<sub>5</sub>(CH<sub>3</sub>)<sub>5</sub>), 15H), 1.62-1.21 (m, Cy-H, 8H), 1.12-0.98 (m, Cy-H, 2H).  $^{13}\text{C}\{^1\text{H}\}$  NMR (101 MHz, CD<sub>2</sub>Cl<sub>2</sub>):  $\delta$  154.9 (t,  $^3J_{C-P}$  = 6.5 Hz, C<sub>Ar</sub>), 153.7 (t,  $^3J_{C-P}$  = 8.5 Hz, C<sub>Ar</sub>), 129.7 (C<sub>Ar</sub>), 120.5 (C<sub>Ar</sub>), 119.8 (C<sub>Ar</sub>), 118.0 (C<sub>Ar</sub>), 116.2 (C<sub>Ar</sub>), 89.7 (Ru(C<sub>5</sub>(CH<sub>3</sub>)<sub>5</sub>), 46.0 (X of ABX, N-CH<sub>2</sub>-P), 42.8 (X of ABX, N-CH<sub>2</sub>-P), 41.4 (X of ABX, Cy), 28.6 (Cy), 27.9 (Cy), 27.2 (X of ABX, Cy), 28.4 (Cy), 28.1 (X of ABX, Cy), 27.9 4 (X of ABX, Cy), 27.1 (Cy), 11.0 (Ru(C<sub>5</sub>(CH<sub>3</sub>)<sub>5</sub>)).  $^{31}\text{P}\{^1\text{H}\}$  NMR (162 MHz, CD<sub>2</sub>Cl<sub>2</sub>):  $\delta$  34.4 (Ru-P). IR (neat)  $\nu(\text{cm}^{-1})$ : 2914 (m), 2848 (m), 1590 (m), 1501 (s), 1212 (m), 738 (s), 685 (s). MALDI MS (pyrene matrix): Calc.  $m/z$  = 738.3 [RuCl(Cp\*)(P<sub>2</sub><sup>Cy</sup>N<sub>2</sub><sup>Ph</sup>)]<sup>+</sup>, Obs.  $m/z$  = 738.2.

#### 2.4.4 General Procedure for [Ru(Cp/Cp\*)(P<sup>Cy</sup><sub>2</sub>N<sup>Ph</sup><sub>2</sub>)]PF<sub>6</sub> Complex Synthesis.

TIPF<sub>6</sub> was used in this procedure. Thallium is extremely TOXIC and due care is needed.<sup>27</sup> Solid waste and solution waste contaminated with thallium were placed in a separate containers marked for thallium waste. Glassware contaminated with thallium were heated in water to dissolve residual thallium salts. A 4 mL vial was charged with [RuCl(Cp)(P<sup>Cy</sup><sub>2</sub>N<sup>Ph</sup><sub>2</sub>)] (0.010 – 0.011 mmol, 1 eq) in DCM (3 mL) or [RuCl(Cp\*)(P<sup>Cy</sup><sub>2</sub>N<sup>Ph</sup><sub>2</sub>)] (0.010 – 0.011 mmol, 1 eq) in C<sub>6</sub>H<sub>5</sub>F (3 mL) and TIPF<sub>6</sub> (0.011 mmol, 1.1 eq). The reaction was stirred for 2 h during which precipitation of a white solid, TlCl, and a distinct colour change from light yellow to red was observed. The suspension



was filtered through a microfibre pipette filter to remove the precipitate followed by solvent removal under reduced pressure. Both complexes were isolated as red powders and stored under inert atmosphere.

**[Ru(Cp)( $\kappa^2$ -P<sup>Cy</sup><sub>2</sub>N<sup>Ph</sup><sub>2</sub>)(N<sub>2</sub>)]PF<sub>6</sub> (2-5b-N<sub>2</sub>) and [Ru(Cp)( $\kappa^3$ -P<sup>Cy</sup><sub>2</sub>N<sup>Ph</sup><sub>2</sub>)]PF<sub>6</sub> ( $\kappa^3$ -**(P,P,Ar)-2-5b**). Yield = 82%. IR (neat)  $\nu$ (cm<sup>-1</sup>): 2925 (w), 2851 (w), 1594 (w), 1492 (w), 1194 (w), 833 (s), 743 (m), 853 (m). MALDI MS (pyrene matrix): Calc.  $m/z$  = 633.21 [Ru(Cp\*)(P<sub>2</sub><sup>Cy</sup>N<sub>2</sub><sup>Ph</sup>)]<sup>+</sup>, Obs.  $m/z$  = 633.2.**

**(2-5b-N<sub>2</sub>)**. Mixture of **2-5b-N<sub>2</sub>** and  $\kappa^3$ -(P,P,Ar)-**2-5b**, signals identified via elimination of known  $\kappa^3$ -(P,P,Ar)-**2-5b** signals. Integration of <sup>1</sup>H NMR inaccurate due to mixture of signal overlap. <sup>1</sup>H NMR (400 MHz, CD<sub>3</sub>NO<sub>2</sub>):  $\delta$  7.17-7.07 (m, Ph-*H*, XH), 6.97-6.90 (m, Ph-*H*, XH), 6.86-6.81 (m, Ph-*H*, XH), 6.67-6.61 (m, Ph-*H*, XH), 4.62 (Ru(C<sub>5</sub>H<sub>5</sub>), 5H), 3.77-3.70 (m, PCH<sub>2</sub>N, XH), 3.64-3.60 (m, PCH<sub>2</sub>N, XH), 3.34-3.28 (m, PCH<sub>2</sub>N, XH), 2.41-2.20 (m, Cy-*H*, XH), 1.96-1.80 (m, Cy-*H*, XH), 1.72-1.66 (m, Cy-*H*, XH), 1.44-1.25 (m, Cy-*H*, XH). <sup>13</sup>C{<sup>1</sup>H} NMR (151 MHz, CD<sub>2</sub>Cl<sub>2</sub>):  $\delta$  155.4 (t, <sup>3</sup>J<sub>C-P</sub> = 7.1 Hz, C<sub>Ar</sub>), 152.7 (t, <sup>3</sup>J<sub>C-P</sub> = 5.9 Hz, C<sub>Ar</sub>), 134.5 (C<sub>Ar</sub>), 130.8 (C<sub>Ar</sub>), 130.7 (t, <sup>3</sup>J<sub>C-P</sub> = 3.1 Hz, C<sub>Ar</sub>), 120.2 (C<sub>Ar</sub>), 119.3 (C<sub>Ar</sub>), 119.0 (m, C<sub>Ar</sub>), 116.7 (C<sub>Ar</sub>), 115.6 (s, C<sub>Ar</sub>), 81.4 (Ru(C<sub>5</sub>H<sub>5</sub>)), 48.6 (X of ABX, N-CH<sub>2</sub>-P), 45.5 (X of ABX, N-CH<sub>2</sub>-P), 43.1 (X of ABX, Cy-C), 41.9 (X of ABX, Cy-C), 30.3 (Cy-C), 29.3 (Cy-C), 28.4 (X of ABX, Cy-C), 28.1 (X of ABX, Cy-C), 27.8 (X of ABX, Cy-C), 27.6 (Cy-C), 27.2 (Cy-C), 26.7 (Cy-C), 9.2 (C<sub>5</sub>CH<sub>3</sub>)<sub>5</sub>. <sup>31</sup>P{<sup>1</sup>H} NMR (162 MHz, CD<sub>2</sub>Cl<sub>2</sub>):  $\delta$  43.9 (Ru-*P*,  $\kappa^2$ -P,P), -144.7 (sept, <sup>1</sup>J<sub>P-F</sub> = 708.0 Hz, PF<sub>6</sub>).

**( $\kappa^3$ -(P,P,Ar)-2-5b)**. <sup>1</sup>H NMR (400 MHz, CD<sub>2</sub>Cl<sub>2</sub>):  $\delta$  7.41-7.27 (m, Ph-*H*, 2H), 7.25-7.12 (m, Ph-*H*, 2H), 7.09-6.87 (m, Ph-*H*, 5H), 6.46-6.36 (m, Ph-*H*, 1H), 4.52 (Ru(C<sub>5</sub>H<sub>5</sub>), 5H), 4.17-4.06 (m, PCH<sub>2</sub>N, 2H), 3.67-3.58 (m, PCH<sub>2</sub>N, 2H), 3.47-3.35 (m, PCH<sub>2</sub>N, 2H), 3.31-3.20 (m, PCH<sub>2</sub>N, 2H), 2.27-2.15 (m, Cy-*H*, 4H), 2.06-1.93 (m, Cy-*H*, 8H), 1.90-1.78 (m, Cy-*H*, 4H), 1.52-1.43 (m, Cy-*H*, 8H), 1.38-1.33 (m, Cy-*H*, 2H). <sup>13</sup>C{<sup>1</sup>H} NMR (101 MHz, CD<sub>2</sub>Cl<sub>2</sub>):  $\delta$  152.0 (C<sub>Ar</sub>), 151.3 (C<sub>Ar</sub>), 133.1 (C<sub>Ar</sub>), 129.9 (C<sub>Ar</sub>), 122.4 (C<sub>Ar</sub>), 120.9 (C<sub>Ar</sub>), 118.4 (C<sub>Ar</sub>), 95.8 (C<sub>Ar</sub>), 79.9 (Ru(C<sub>5</sub>H<sub>5</sub>)), 55.6 (P-CH<sub>2</sub>-N), 49.3 (P-CH<sub>2</sub>-N), 40.7 (X of ABX, Cy), 29.1 (X of ABX, Cy), 27.0 (Cy), 25.9 (Cy), 18.8 (Cy). <sup>31</sup>P{<sup>1</sup>H} NMR (162 MHz, CD<sub>2</sub>Cl<sub>2</sub>):  $\delta$  73.6 (s, Ru-*P*,  $\kappa^3$ -P,P,Ar), -144.2 (sept, <sup>1</sup>J<sub>P-F</sub> = 708.0 Hz, PF<sub>6</sub>).

**[Ru(Cp\*)(P<sup>Cy</sup><sub>2</sub>N<sup>Ph</sup><sub>2</sub>)]PF<sub>6</sub> (2-6b).** Yield = 88%. <sup>1</sup>H NMR (400 MHz, CD<sub>3</sub>NO<sub>2</sub>): δ 7.36-7.26 (m, Ph-*H*, 4H), 7.25-7.19 (m, Ph-*H*, 2H), 7.18-7.12 (m, Ph-*H*, 2H), 7.03-6.92 (m, Ph-*H*, 2H), 4.13-4.04 (m, PCH<sub>2</sub>N, 2H), 3.96-3.88 (m, PCH<sub>2</sub>N, 2H), 3.88-3.81 (m, PCH<sub>2</sub>N, 2H), 3.53-3.41 (m, PCH<sub>2</sub>N, 4H), 2.45-2.32 (m, Cy-*H*, 2H), 2.29-2.07 (m, Cy-*H*, 4H), 2.04-1.90 (m, Cy-*H*, 2H), 1.91 (t, <sup>4</sup>J<sub>H-P</sub> = 1.56, Ru(C<sub>5</sub>(CH<sub>3</sub>)<sub>5</sub>, 15H), 1.85-1.76 (m, Cy-*H*, 4H), 1.59-1.45 (m, Cy-*H*, 4H), 1.44-1.20 (m, Cy-*H*, 6H). <sup>13</sup>C{<sup>1</sup>H} NMR (101 MHz, CD<sub>3</sub>NO<sub>2</sub>): δ 153.2 (t, <sup>3</sup>J<sub>C-P</sub> = 7.9 Hz, C<sub>Ar</sub>), 152.4 (t, <sup>3</sup>J<sub>C-P</sub> = 9.9 Hz, C<sub>Ar</sub>), 129.4 (C<sub>Ar</sub>), 129.3 (C<sub>Ar</sub>), 122.2 (C<sub>Ar</sub>), 121.3 (C<sub>Ar</sub>), 119.0 (C<sub>Ar</sub>), 117.4 (C<sub>Ar</sub>), 95.8 (Ru(C<sub>5</sub>(CH<sub>3</sub>)<sub>5</sub>), 45.8 (X of ABX, N-CH<sub>2</sub>-P), 45.5 (X of ABX, N-CH<sub>2</sub>-P), 38.2 (X of ABX, Cy), 27.4 (Cy), 26.7 (X of ABX, Cy), 25.7 (X of ABX, Cy), 9.2 (Ru(C<sub>5</sub>(CH<sub>3</sub>)<sub>5</sub>). <sup>31</sup>P{<sup>1</sup>H} NMR (162 MHz, CD<sub>3</sub>NO<sub>2</sub>): δ 33.5 (s, Ru-*P*), -144.2 (sept, <sup>1</sup>J<sub>P-F</sub> = 706.2 Hz, PF<sub>6</sub>). IR (neat) ν(cm<sup>-1</sup>): 2921 (w), 2580 (w), 1595 (m), 1492 (m), 1192 (m), 834 (vs), 752 (m), 595 (m). MALDI MS (pyrene matrix): Calc. *m/z* = 703.29 [Ru(Cp\*)(P<sub>2</sub><sup>Cy</sup>N<sub>2</sub><sup>Ph</sup>)]<sup>+</sup>, Obs. *m/z* = 703.3.

#### 2.4.5 General Procedure for [RuCl(Cp/Cp\*)(P<sup>Cy</sup><sub>2</sub>N<sup>Ph</sup><sub>2</sub>)] Halide Abstraction Under Argon Gas.

TIPF<sub>6</sub> was used in this procedure. Thallium is extremely TOXIC and due care is needed.<sup>27</sup> Solid waste and solution waste contaminated with thallium were placed in a separate containers marked for thallium waste. Glassware contaminated with thallium were heated in water to dissolve residual thallium salts. A 100 mL Schlenk flask was charged with CH<sub>2</sub>Cl<sub>2</sub> (10 mL) or C<sub>6</sub>H<sub>5</sub>F (10 mL) and degassed with Argon by bubbling Ar through a needle submerged in the solvent. A separate 100 mL Schlenk flask was charge with a stir bar, [RuCl(Cp)(P<sup>Cy</sup><sub>2</sub>N<sup>Ph</sup><sub>2</sub>)] (0.033 mmol, 1 equiv) or [RuCl(Cp\*)(P<sup>Cy</sup><sub>2</sub>N<sup>Ph</sup><sub>2</sub>)] (0.033 mmol, 1 equiv), and TIPF<sub>6</sub> (0.080 mmol, 2.4 equiv). The flask charged with solid material was cycled with argon to ensure displacement of all N<sub>2</sub>. Solvent was canula transferred to dissolve either [RuCl(Cp)(P<sup>Cy</sup><sub>2</sub>N<sup>Ph</sup><sub>2</sub>)] (CH<sub>2</sub>Cl<sub>2</sub>) or [RuCl(Cp\*)(P<sup>Cy</sup><sub>2</sub>N<sup>Ph</sup><sub>2</sub>)] (C<sub>6</sub>H<sub>5</sub>F), both resulting in a yellow solution, and the reaction was allowed to procedure for 2 h at room temperature. After ca. 5 minutes white solids precipitated from solution. The solution was then canula transferred through a filter and the solvent removed *in vacuo* which resulted in a solid powder for both reactions.

## 2.4.6 Procedure for $[\text{RuCl}(\eta^4\text{-C}_5\text{Me}_5\text{CH}_2\text{Cl})(\text{P}^{\text{Cy}}_2\text{N}^{\text{Ph}}_2)][\text{PF}_6]$ Complex Synthesis.

A 20 mL vial was charged with  $[\text{Ru}(\text{Cp}^*)(\text{P}^{\text{Cy}}_2\text{N}^{\text{Ph}}_2)][\text{PF}_6]$  (38 mg, 0.045 mmol, 1 eq) in DCM (5 mL). The reaction was stirred for 1 h at 70 °C or for 18 h at room temperature during which a colour change from light red to dark red occurred. The solvent was removed under reduced pressure and the dark red solid was washed with pentane. The complex was isolated as a red powder and stored under inert atmosphere.

**$[\text{RuCl}(\eta^4\text{-C}_5\text{Me}_5\text{CH}_2\text{Cl})(\text{P}^{\text{Cy}}_2\text{N}^{\text{Ph}}_2)][\text{PF}_6]$  (2-7).** Yield = 90%.  $^1\text{H}$  NMR (600 MHz,  $\text{CD}_2\text{Cl}_2$ ):  $\delta$  7.41-7.33 (m, Ph-*H*, 4H), 7.11-7.05 (m, Ph-*H*, 4H), 7.04-7.00 (m, Ph-*H*, 2H), 4.50-4.44 (m, PCH<sub>2</sub>N, 1H), 4.24-4.19 (m, PCH<sub>2</sub>N, 1H), 4.00-3.93 (m, PCH<sub>2</sub>N, 1H), 3.64-3.57 (m, PCH<sub>2</sub>N, 2H), 3.54 (d,  $^2J_{\text{H-H}} = 11.2$  Hz, C<sub>5</sub>(CH<sub>3</sub>)<sub>5</sub>CH<sub>2</sub>Cl, 1H), 3.50-3.42 (m, PCH<sub>2</sub>N, 1H), 3.30-3.25 (d,  $^2J_{\text{H-H}} = 11.2$  Hz, Ru(C<sub>5</sub>(CH<sub>3</sub>)<sub>5</sub>CH<sub>2</sub>Cl), 1H), 3.24-3.19 (m, PCH<sub>2</sub>N, 1H), 3.04-2.98 (m, PCH<sub>2</sub>N, 1H), 2.67-2.58 (m, Cy-*H*, 1H), 2.45-2.38 (m, Cy-*H*, 1H), 2.38 (s, Ru(C<sub>5</sub>(CH<sub>3</sub>)<sub>5</sub>CH<sub>2</sub>Cl), 3H), 2.26-2.18 (m, Cy-*H*, 2H), 2.08-2.01 (m, Cy-*H*, 2H), 2.04 (s, Ru(C<sub>5</sub>(CH<sub>3</sub>)<sub>5</sub>CH<sub>2</sub>Cl), 3H), 1.98-1.90 (m, Cy-*H*, 4H), 1.97-1.84 (m, Cy-*H*, 1H), 1.82 (d, Ru(C<sub>5</sub>(CH<sub>3</sub>)<sub>5</sub>CH<sub>2</sub>Cl), 3H), 1.68-1.61 (m, Cy-*H*, 2H), 1.64 (s, Ru(C<sub>5</sub>(CH<sub>3</sub>)<sub>5</sub>CH<sub>2</sub>Cl), 3H), 1.52-1.45 (m, Cy-*H*, 2H), 1.39-1.28 (m, Cy-*H*, 6H), 1.17-1.07 (m, Cy-*H*, 1H), 0.80 (s, Ru(C<sub>5</sub>(CH<sub>3</sub>)<sub>5</sub>CH<sub>2</sub>Cl), 3H).  $^{13}\text{C}\{^1\text{H}\}$  NMR (101 MHz,  $\text{CD}_2\text{Cl}_2$ ):  $\delta$  152.8 (t,  $^3J_{\text{C-P}} = 8.8$  Hz, C<sub>Ar</sub>), 150.8 (t,  $^3J_{\text{C-P}} = 10.5$  Hz, C<sub>Ar</sub>), 130.5 (C<sub>Ar</sub>), 130.3 (C<sub>Ar</sub>), 129.3 (X of ABX, Ru(C<sub>5</sub>(CH<sub>3</sub>)<sub>5</sub>CH<sub>2</sub>Cl)), 128.6 (X of ABX, Ru(C<sub>5</sub>(CH<sub>3</sub>)<sub>5</sub>CH<sub>2</sub>Cl)), 124.2 (C<sub>Ar</sub>), 123.2 (C<sub>Ar</sub>), 120.0 (C<sub>Ar</sub>), 117.5 (C<sub>Ar</sub>), 104.0 (Ru(C<sub>5</sub>(CH<sub>3</sub>)<sub>5</sub>CH<sub>2</sub>Cl)), 87.0 (Ru(C<sub>5</sub>(CH<sub>3</sub>)<sub>5</sub>CH<sub>2</sub>Cl)), 53.0 (X of ABX, Ru(C<sub>5</sub>(CH<sub>3</sub>)<sub>5</sub>CH<sub>2</sub>Cl)), 50.8 (X of ABX, Ru(C<sub>5</sub>(CH<sub>3</sub>)<sub>5</sub>CH<sub>2</sub>Cl)), 47.9 (X of ABX, P-CH<sub>2</sub>-P), 46.4 (X of ABX, P-CH<sub>2</sub>-P), 44.6 (X of ABX, P-CH<sub>2</sub>-P), 44.1 (X of ABX, P-CH<sub>2</sub>-P), 40.2 (X of ABX, Cy), 37.8 (X of ABX, Cy), 28.9 (X of ABX, Cy), 28.6 (X of ABX, Cy), 28.1 (X of ABX, Cy), 27.9 (X of ABX, Cy), 27.4 (X of ABX, Cy), 27.3 (X of ABX, Cy), 26.9 (X of ABX, Cy), 26.3 (X of ABX, Cy), 13.2 (Ru(C<sub>5</sub>(CH<sub>3</sub>)<sub>5</sub>CH<sub>2</sub>Cl)), 12.6 (Ru(C<sub>5</sub>(CH<sub>3</sub>)<sub>5</sub>CH<sub>2</sub>Cl)), 12.0 (Ru(C<sub>5</sub>(CH<sub>3</sub>)<sub>5</sub>CH<sub>2</sub>Cl)), 11.0 (Ru(C<sub>5</sub>(CH<sub>3</sub>)<sub>5</sub>CH<sub>2</sub>Cl)), 1.3 (Ru(C<sub>5</sub>(CH<sub>3</sub>)<sub>5</sub>CH<sub>2</sub>Cl)).  $^{31}\text{P}\{^1\text{H}\}$  NMR (212 MHz,  $\text{CD}_2\text{Cl}_2$ ):  $\delta$  71.9 (d,  $^2J_{\text{P-P}} = 75.9$  Hz, Ru-*P*),  $\delta$  31.8 (d, 75.9 Hz, Ru-*P*), -144.2 (sept,  $^1J_{\text{P-F}} = 711$  Hz, PF<sub>6</sub>). IR (neat)  $\nu(\text{cm}^{-1})$ : 2930 (w), 2851 (w), 1596 (w), 1492(w),

1192 (w), 832 (s), 556 (m). MALDI MS (pyrene matrix): Calc.  $m/z = 787.2$   $[\text{RuCl}(\eta^4\text{-C}_5\text{Me}_5\text{CH}_2\text{Cl})(\text{P}^{\text{Cy}}_2\text{N}^{\text{Ph}}_2)]^+$  Obs.  $m/z = 784.2$ .

#### 2.4.7 General Procedure for Intramolecular Hydroamination Catalysis.

In a glovebox, the following stock solutions were prepared: **2-EA** (0.600 M) and tetralin (IS = internal standard) (0.400 M); **2-2a** (0.6 mM); **2-2b** (0.6 mM); **2-1c** (0.6 mM); **2-2c** (0.6 mM) all in Me-THF. Portions of substrate/IS stock solution (300  $\mu\text{L}$ ) and catalyst stock solution (300  $\mu\text{L}$ ) were dispensed into 4 mL screw cap reaction vials containing a stir bar. The final concentration for all reaction vials were 0.300 M in substrate, 0.200 M in tetralin (IS), and 0.3 mM in catalyst. A final 4 mL screw cap vial was charged with 100  $\mu\text{L}$  of both substrate/IS stock solution and 100  $\mu\text{L}$  Me-THF for use as the time = 0 sample, required for accurate quantification of substrate and product. The reaction vials were capped and removed from the glovebox and heated to 70  $^\circ\text{C}$  with stirring. After 0.167, 0.5, 1, 2, 6, and 24 h a vial was removed from heat, exposed to air, and a 20  $\mu\text{L}$  aliquot was removed and diluted with 980  $\mu\text{L}$  MeCN to quench the reaction. This diluted sample was subsequently analyzed by GC-FID. A 20  $\mu\text{L}$  aliquot was also taken from the T0 sample and diluted with 980  $\mu\text{L}$  of MeCN and analyzed by GC-FID. All catalytic runs were run in duplicate and each vial was injected three times and the area of the respective substrate, IS, and product peaks were averaged from the three injections.

#### 2.4.8 General Catalytic Procedure for Product Inhibition Catalysis.

In the glovebox, the following three stock solutions, **a-c** were prepared that contained: **2-EA** (**a** = 0.300 M, **b** = 0.200 M, **c** = 0.200 M), tetralin (**a** = 0.200 M, **b** = 0.135 M, **c** = 0.135 M), and indole (**c** = 100 mM) in Me-THF. A catalyst stock solution was prepared with **2-1b** (0.5 mM) in Me-THF. Screw cap vials (4 mL) containing a stir bar were charged with catalyst stock solution (300  $\mu\text{L}$ ) and either substrate stock solution **a**, **b**, or **c** (300  $\mu\text{L}$ ). A total of 12 reactions vials were used for each reaction **A**, **B**, and **C** (total of 36 vials). The final concentration of the reaction vials were as follows: **A**) 150 mM 2-ethynylaniline, 100 mM IS, 0.25 mM **1b**, **B**) 100 mM 2-ethynylaniline, 68 mM IS, 0.25 mM **2-1b**, **C**) 100 mM 2-ethynylaniline, 68 mM IS, 0.25 mM **1b**, 50 mM indole. Three 4 mL screw cap vials were

charged with 100  $\mu\text{L}$  of either stock solution **a**, **b**, or **c**, and 100  $\mu\text{L}$  Me-THF for use as a time = 0 sample, required for accurate quantification of substrate and product. The vials were capped and removed from the glovebox and heated at 70  $^{\circ}\text{C}$  with stirring. A single reaction vial from each reaction **A**, **B**, and **C**, was removed from the heat every 10 minutes for 2 hours. Aliquots (20  $\mu\text{L}$ ) were taken from each reaction vial and diluted with 980  $\mu\text{L}$  MeCN to quench the reaction. This diluted aliquot was subsequently analyzed by GC-FID. All catalytic runs were run in duplicate and each vial was injected three times and the area of the respective substrate, IS, and product peaks were averaged from the three injections.

#### 2.4.9 General Procedure for Thermolysis of Complexes **1b**, **2b**, **5b**, and **6b**.

An NMR tube was charged with a solution of complex **2-1b** (12 mg, 24 mM), **2-2b** (12 mg, 22 mM), **2-5b** (12 mg, 25 mM), or **2-6b** (12 mg, 24 mM) in  $\text{CH}_3\text{NO}_2$ . A sealed capillary containing the internal standard,  $\text{OPPh}_3$ , was added to the tube. For each sample, an initial (time = 0)  $^{31}\text{P}\{^1\text{H}\}$  NMR spectrum was obtained at 25  $^{\circ}\text{C}$ . The samples were then heated at 70  $^{\circ}\text{C}$  in a mineral oil bath. The samples were periodically removed from the heat, cooled and  $^{31}\text{P}\{^1\text{H}\}$  NMR spectra were obtained at 25  $^{\circ}\text{C}$ . The samples were heated for a total of 18 h and the relative integration of the starting complexes to internal standard were used to quantify decomposition of the complexes over time.

## 2.5 References

- (a) Vitaku, E.; Smith, D. T.; Njardarson, J. T., *J. Med. Chem.* **2014**, *57* (24), 10257-10274; (b) Barden, T. C., Indoles: Industrial, Agricultural and Over-the-Counter Uses. In *Heterocyclic Scaffolds II: Reactions and Applications of Indoles*, Gribble, G. W., Ed. Springer Berlin Heidelberg: Berlin, Heidelberg, 2010; pp 31-46; (c) Cossy, J.; Guérinot, A., Chapter Five - Natural Products Containing Oxygen Heterocycles—Synthetic Advances Between 1990 and 2015. In *Adv. Heterocycl. Chem.*, Scriven, E. F. V.; Ramsden, C. A., Eds. Academic Press: 2016; Vol. 119, pp 107-142.
- (a) Arredondo, V. M.; Tian, S.; McDonald, F. E.; Marks, T. J., *J. Am. Chem. Soc.* **1999**, *121* (15), 3633-3639; (b) Chaisan, N.; Kaewsri, W.; Thongsornkleeb, C.; Tummatorn, J.; Ruchirawat, S., *Tetrahedron Lett.* **2018**, *59* (7), 675-680; (c) Wood, M. C.; Leitch, D. C.; Yeung, C. S.; Kozak, J. A.; Schafer, L. L., *Angew. Chem. Int. Ed.* **2007**, *46* (3), 354-358; (d) Yim, J. C. H.; Schafer, L. L., *Eur. J. Org. Chem.* **2014**, *2014* (31), 6825-6840; (e) Álvarez-Pérez, A.; González-Rodríguez, C.; García-Yebra, C.; Varela, J. A.; Oñate, E.; Esteruelas, M. A.; Saá, C., *Angew. Chem. Int. Ed.* **2015**, *54* (45), 13357-13361;

- (f) Varela, J. A.; González-Rodríguez, C.; Saá, C., Catalytic Transformations of Alkynes via Ruthenium Vinylidene and Allenylidene Intermediates. In *Ruthenium in Catalysis, Top. Organomet. Chem.*, Dixneuf, H. P.; Bruneau, C., Eds. Springer International Publishing: Berlin Heidelberg, 2014; pp 237-287; (g) Varela-Fernández, A.; García-Yebra, C.; Varela, J. A.; Esteruelas, M. A.; Saá, C., *Angew. Chem. Int. Ed.* **2010**, *49* (25), 4278-4281; (h) Varela-Fernandez, A.; Varela, J. A.; Saá, C., *Synthesis* **2012**, *44* (21), 3285-3295.
3. (a) Rigaut, S., *Coord. Chem. Rev.* **2004**, *248* (15-16), 1585-1601; (b) Roh, S. W.; Choi, K.; Lee, C., *Chem. Rev.* **2019**, *119* (6), 4293-4356; (c) Bruneau, C.; Dixneuf, P. H., *Acc. Chem. Res.* **1999**, *32* (4), 311-323.
4. (a) Grotjahn, D. B., *Top. Catal.* **2010**, *53* (15), 1009-1014; (b) Arita, A. J.; Cantada, J.; Grotjahn, D. B.; Cooksy, A. L., *Organometallics* **2013**, *32* (23), 6867-6870; (c) Ogunlana, A. A.; Zou, J.; Bao, X., *J. Organomet. Chem.* **2018**, *864*, 160-168.
5. (a) Trost, B. M.; Rhee, Y. H., *J. Am. Chem. Soc.* **2002**, *124* (11), 2528-2533; (b) Varela-Fernández, A.; Varela Jesús, A.; Saá, C., *Adv. Synth. Catal.* **2011**, *353* (11-12), 1933-1937; (c) Varela-Fernández, A.; González-Rodríguez, C.; Varela, J. A.; Castedo, L.; Saá, C., *Org. Lett.* **2009**, *11* (22), 5350-5353.
6. (a) Crabtree, R. H., *New J. Chem.* **2011**, *35* (1), 18-23; (b) Annibale, V. T.; Song, D., *RSC Advances* **2013**, *3* (29), 11432-11449.
7. (a) Nair, R. N.; Lee, P. J.; Grotjahn, D. B., *Top. Catal.* **2010**, *53* (15-18), 1045-1047; (b) Nair, R. N.; Lee, P. J.; Rheingold, A. L.; Grotjahn, D. B., *Chemistry – A European Journal* **2010**, *16* (27), 7992-7995.
8. (a) Stubbs, J. M.; Chapple, D. E.; Boyle, P. D.; Blacquiere, J. M., *ChemCatChem* **2018**, *10* (17), 4001-4009; (b) Stubbs, J. M.; Bow, J. P. J.; Hazlehurst, R. J.; Blacquiere, J. M., *Dalton Trans.* **2016**, *45* (43), 17100-17103; (c) Stubbs, J. M.; Bridge, B. J.; Blacquiere, J. M., *Dalton Trans.* **2019**, *48* (22), 7928-7937; (d) Stubbs, J. M.; Bow, J. P. J.; Hazlehurst, R. J.; Blacquiere, J. M., *Dalton Trans.* **2016**, *45* (43), 17100-17103.
9. Bow, J.-P. J.; Boyle, P. D.; Blacquiere, J. M., *Eur. J. Inorg. Chem.* **2015**, *2015* (25), 4162-4166.
10. Bhattacharya, P.; Heiden, Z. M.; Chambers, G. M.; Johnson, S. I.; Bullock, R. M.; Mock, M. T., *Angew. Chem. Int. Ed.* **2019**, *58* (34), 11618-11624.
11. (a) Hulley, E. B.; Helm, M. L.; Bullock, R. M., *Chem. Sci.* **2014**, *5* (12), 4729-4741; (b) Zhang, S.; Appel, A. M.; Bullock, R. M., *J. Am. Chem. Soc.* **2017**, *139* (21), 7376-7387; (c) Hulley, E. B.; Kumar, N.; Raugei, S.; Bullock, R. M., *ACS Catalysis* **2015**, *5* (11), 6838-6847; (d) Mock, M. T.; Chen, S.; Rousseau, R.; O'Hagan, M. J.; Dougherty, W. G.; Kassel, W. S.; DuBois, D. L.; Bullock, R. M., *Chem. Commun.* **2011**, *47* (44), 12212-12214; (e) Klug, C. M.; O'Hagan, M.; Bullock, R. M.; Appel, A. M.; Wiedner, E. S., *Organometallics* **2017**, *36* (12), 2275-2284.
12. Blacquiere, J. M., *ACS Catalysis* **2021**, *11* (9), 5416-5437.

13. Clavier, H.; Nolan, S. P., *Chem. Commun.* **2010**, 46 (6), 841-861.
14. Example prices of t-BuPH<sub>2</sub> (CAS: 2501-94-2) and CyPH<sub>2</sub> (CAS: 822-68-4) from Strem Chemicals, Inc. . [https://www.strem.com/catalog/v/15-0966/52/phosphorus\\_2501-94-2](https://www.strem.com/catalog/v/15-0966/52/phosphorus_2501-94-2) and [https://www.strem.com/catalog/v/15-0950/52/phosphorus\\_822-68-4](https://www.strem.com/catalog/v/15-0950/52/phosphorus_822-68-4) (accessed April 21, 2021).
15. (a) Jiménez-Tenorio, M.; Puerta, M. C.; Valerga, P., *Eur. J. Inorg. Chem.* **2004**, 2004 (1), 17-32; (b) Johnson, T. J.; Folting, K.; Streib, W. E.; Martin, J. D.; Huffman, J. C.; Jackson, S. A.; Eisenstein, O.; Caulton, K. G., *Inorg. Chem.* **1995**, 34 (2), 488-499.
16. (a) Aneetha, H.; Jiménez-Tenorio, M.; Puerta, M. C.; Valerga, P.; Mereiter, K., *Organometallics* **2002**, 21 (4), 628-635; (b) Blacquiere, J. M.; Higman, C. S.; Gorelsky, S. I.; Beach, N. J.; Dalgarno, S. J.; Fogg, D. E., *Angew. Chem. Int. Ed.* **2011**, 50 (4), 916-919; (c) Allen, A. D.; Senoff, C. V., *Chem. Commun.* **1965**, (24), 621-622.
17. Garrou, P. E., *Chem. Rev.* **1981**, 81 (3), 229-266.
18. (a) Pregosin, P. S., *Coord. Chem. Rev.* **2008**, 252 (21+22), 2156-2170; (b) Blacquiere, J. M.; Higman, C. S.; McDonald, R.; Fogg, D. E., *J. Am. Chem. Soc.* **2011**, 133 (35), 14054-14062; (c) Feiken, N.; Pregosin, P. S.; Trabesinger, G.; Albinati, A.; Evoli, G. L., *Organometallics* **1997**, 16 (26), 5756-5762.
19. (a) Ingoglia, B. T.; Wagen, C. C.; Buchwald, S. L., *Tetrahedron* **2019**, 75 (32), 4199-4211; (b) Surry, D. S.; Buchwald, S. L., *Chemical Science* **2011**, 2 (1), 27-50; (c) Martin, R.; Buchwald, S. L., *Acc. Chem. Res.* **2008**, 41 (11), 1461-1473; (d) Barder, T. E.; Biscoe, M. R.; Buchwald, S. L., *Organometallics* **2007**, 26 (9), 2183-2192.
20. Pathak, D. D.; Adams, H.; Bailey, N. A.; King, P. J.; White, C., *J. Organomet. Chem.* **1994**, 479 (1), 237-245.
21. (a) Chang, J.; Bergman, R. G., *J. Am. Chem. Soc.* **1987**, 109 (14), 4298-4304; (b) Rondon, D.; He, X.-D.; Chaudret, B., *J. Organomet. Chem.* **1992**, 433 (3), C18-C21; (c) Lo, Y.-H.; Chen, H.-G.; Kuo, T. S., *Dalton Trans.* **2011**, 40 (12), 2711-2715.
22. (a) Kochi, T.; Nomura, Y.; Tang, Z.; Ishii, Y.; Mizobe, Y.; Hidai, M., *J. Chem. Soc., Dalton Trans.* **1999**, (15), 2575-2582; (b) Tanaka, K.; Kushi, Y.; Tsuge, K.; Toyohara, K.; Nishioka, T.; Isobe, K., *Inorg. Chem.* **1998**, 37 (1), 120-126; (c) Basato, M.; Biffis, A.; Tubaro, C.; Graiff, C.; Tiripicchio, A., *Dalton Trans.* **2004**, (24), 4092-4093; (d) Matsuo, Y.; Kuninobu, Y.; Ito, S.; Sawamura, M.; Nakamura, E., *Dalton Trans.* **2014**, 43 (20), 7407-7412.
23. (a) Burés, J., *Angew. Chem. Int. Ed.* **2016**, 55 (52), 16084-16087; (b) Nielsen, C. D. T.; Burés, J., *Chemical Science* **2019**, 10 (2), 348-353.
24. Stubbs, J. M.; Hazlehurst, R. J.; Boyle, P. D.; Blacquiere, J. M., *Organometallics* **2017**, 36 (9), 1692-1698.

25. Orthaber, A.; Karnahl, M.; Tschierlei, S.; Streich, D.; Stein, M.; Ott, S., *Dalton Trans.* **2014**, 43 (11), 4537-4549.
26. Yang, J.; Langis-Barsetti, S.; Parkin, H. C.; McDonald, R.; Rosenberg, L., *Organometallics* **2019**, 38 (17), 3257-3266.
27. Galván-Arzate, S.; Santamaría, A., *Toxicol. Lett.* **1998**, 99 (1), 1-13.



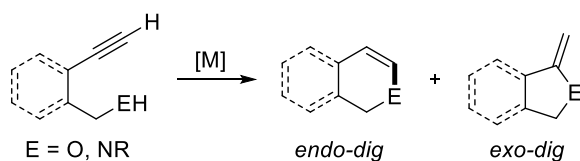
## Chapter 3

### 3 Alkyne Hydrofunctionalization Mechanism Including an Off-Cycle Alkoxy carbene Deactivation Complex

The cooperative  $[\text{Ru}(\text{Cp})(\text{P}^{\text{Cy}}_2\text{N}^{\text{Ph}}_2)(\text{MeCN})][\text{PF}_6]$  (**3-Ru2**) complex was utilized for additive-free hydroalkoxylation of 2-ethynylbenzyl alcohol (**3-1a**) to generate isochromene. The phenyl-substituted pendent amine of the supporting ligand effectively mediated proton transfer steps and mitigated a vinyl ammonium deactivation pathway that was previously favoured with a more nucleophilic *N*-benzyl substituent. A select set of substrates were cyclized to uncover mechanistic opportunities and limitations of **3-Ru2** and related catalysts. Isotopic labelling and kinetic studies, using the variable time normalization analysis (VTNA) method, were utilized to identify vinylidene formation as the most likely rate-limiting step of catalysis. Attempted cyclization of 3-butyn-1-ol afforded an isolable alkoxy carbene complex, the stability of which was investigated both computationally and through stoichiometric reactions. This compound was identified as an off-cycle catalytic species and it reveals a critical competing proton-transfer pathway for this family of cooperative catalysts.

#### 3.1 Introduction

Transition metal catalyzed intramolecular hydrofunctionalization of alkynes has been established as an atom-economic and desirable route to generate a variety of useful heterocycle scaffolds.<sup>1</sup> Selective formation of *endo-dig* products is possible with catalysts that activate the alkyne through a vinylidene intermediate ( $\text{M}=\text{C}=\text{CHR}$ ), which directs nucleophilic attack to the highly electrophilic alpha carbon ( $\text{C}_\alpha$ ).<sup>1c-e</sup> Additive-free methods for intra- or intermolecular additions have been achieved with metal-ligand cooperative (MLC) catalysts, in which the requisite Brønsted base is incorporated into the ligand framework.<sup>2</sup> While MLC catalysts offer simple low-waste protocols to heterocyclic products, further enhancement of activity and scope would benefit from a detailed mechanistic understanding of productive and non-productive catalytic pathways.



**Scheme 3-1.** Intramolecular alkyne hydrofunctionalization

Few mechanistic studies of intramolecular hydrofunctionalization have been conducted. Rather, the mechanism is often presumed based on the closely related and well-studied MLC mechanism for alkyne hydration (Figure 3-1a).<sup>2a-c</sup> Key intermediates involve alkyne isomerization to vinylidene (**3-I** → **3-II**), nucleophilic attack by water and proton transfer to C<sub>β</sub> to give a hydroxycarbene intermediate (**3-II** → **3-III**), and finally proton transfer to C<sub>α</sub> and product release (**3-III** → **3-I**). The pendant Brønsted base assists in all proton transfer steps, including the 1,2-proton shift for vinylidene formation. Depending on the catalyst, either vinylidene formation<sup>2b</sup> or protonolysis at C<sub>α</sub><sup>2c</sup> are the turnover-limiting steps. The mechanism for intramolecular hydroalkoxylation (and by extension other E-H bond additions) should be similar to hydration, except the products are vinyl ER heterocycles rather than terminal aldehydes. The different hybridization of C<sub>β</sub> in the two product types, implies deviation in proton-transfer steps between the two mechanisms. Analogues of the hydroxycarbene **3-III**, were isolated from reactions of hydroalkoxylation catalysts with alkynyl alcohol reagents (**3-A** and **3-B**; Figure 3-1b). The oxocycloalkylidene of type **3-A** were proposed as *on-cycle* intermediates on the grounds that **3-A** exhibited equivalent catalytic performance to the precatalyst.<sup>3</sup> In contrast, **3-B** was assigned as an *off-cycle* intermediate since it was only isolated in the presence of exogenous base, the conjugate acid of which was insufficiently acidic to protonate C<sub>α</sub> and rather gave the C<sub>β</sub> protonated product (**3-B**).<sup>4</sup> This proposal is supported by slower catalysis with **3-B** as compared to the precatalyst.<sup>5</sup>

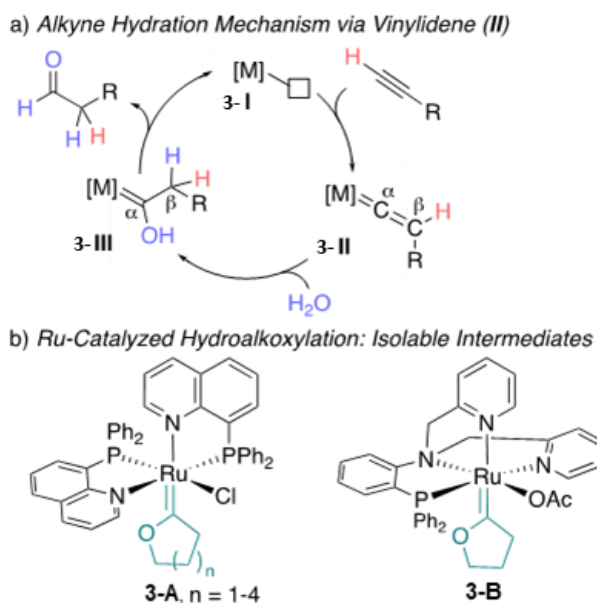


**Figure 3-1.** a) Elucidated mechanism for MLC-catalyzed hydration of alkynes. For simplicity, the involvement of the ligand-centered Brønsted base is not depicted. The box on **3-I** represents an open coordination site. b) oxocycloalkylidene intermediates isolated from hydroalkoxylation catalysts.

We have extensively developed MLC catalysts of the type  $[\text{Ru}(\text{Cp}/\text{Cp}^*)(\text{P}^{\text{R}_2}\text{N}^{\text{R}'_2})(\text{MeCN})][\text{PF}_6]$  (Cp = cyclopentadienyl, Cp\* = pentamethylcyclopentadienyl,  $\text{P}^{\text{R}_2}\text{N}^{\text{R}'_2}$  = 1,5-R'-3,7-R-1,5-diaza-3,7-diphosphacyclooctane) for intramolecular alkyne hydroamination and hydroalkoxylation reactions to generate a variety of 5- and 6-membered *endo-dig* heterocycles.<sup>2e, 6</sup> Two derivatives, **3-Ru1** and **3-Ru2**, are depicted below (Figure 3-2). The Cp catalysts consistently gave higher lifetimes than Cp\* analogues due to stabilization of the active catalyst **3-C** by reversible  $\pi$ -coordination of the pendent amine phenyl substituent.<sup>6a</sup> Related stabilization for Cp\* complexes is precluded by steric clash between the phenyl group and the Cp\* methyl substituents. For all catalyst derivatives, selective formation of the *endo-dig* cyclized products was indicative of a vinylidene mechanism.<sup>2e, 6b</sup> Indeed, a vinylidene intermediate was presumed based on isolation of the vinyl ammonium complex (**3-D**), which formed on addition of phenyl acetylene to **3-Ru1** and nucleophilic attack by the benzyl-substituted pendent amine on the assumed vinylidene  $\text{C}_\alpha$ .<sup>7</sup> The impact of **3-D**

on catalysis was particularly apparent for hydroalkoxylation of 2-ethynylbenzyl alcohol with **3-Ru1**.<sup>2e</sup> Productive catalysis was favoured at low temperatures (40 °C), but deactivation *via* vinyl ammonium formation dominated at elevated temperatures (>55 °C). While these studies have revealed some critical mechanistic features of the [Ru(Cp/Cp\*)(P<sup>R</sup><sub>2</sub>N<sup>R'</sup><sub>2</sub>)(MeCN)][PF<sub>6</sub>] catalyst family, we sought to conduct a more thorough mechanistic analysis. We hypothesize that a P<sup>R</sup><sub>2</sub>N<sup>R'</sup><sub>2</sub> ligand with a less nucleophilic pendent amine could mitigate deactivation and offer a system amenable to mechanistic investigation. Herein, we report the influence of ligand modification on catalyst deactivation through catalytic lifetime comparison. Turnover limiting steps are identified through reaction order determination, kinetic isotope effects, scope analysis and isolation of an off-cycle intermediate.

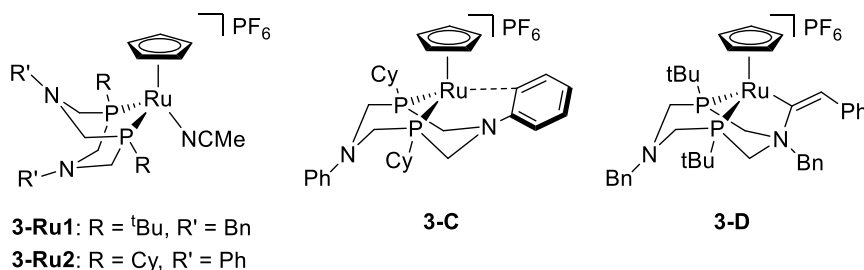


**Figure 3-2.** General structure of hydroalkoxylation catalysts [Ru(Cp)(P<sup>R</sup><sub>2</sub>N<sup>R'</sup><sub>2</sub>)(MeCN)][PF<sub>6</sub>], along with κ<sup>2</sup>-P,P;η<sup>1</sup>-C<sub>Ar</sub> stabilized active catalyst **3-C** and vinyl ammonium complex **3-D**.

## 3.2 Results and discussion

### 3.2.1 Deployment of Redesigned Catalyst to Suppress Vinylidene Deactivation

We reasoned that suppression of vinyl ammonium deactivation (i.e. **3-D**) would permit successful intramolecular hydroalkoxylation of 2-ethynylbenzyl alcohol at elevated temperatures. The formation of **3-D** (and catalytic analogues) was most likely driven by the nucleophilicity of the benzyl-substituted pendent amine in **3-Ru1**. By contrast, the phenyl-substituted amine in **3-Ru2** should have attenuated nucleophilicity as judged by the Mayr nucleophilic parameters of 14.29 and 12.64 for benzylamine and aniline, respectively.<sup>8</sup> While we previously reported the synthesis of **3-Ru2**,<sup>6a</sup> we have since

acquired single crystals suitable for X-ray diffraction (Figure 3-3). Two molecules are found in the unit cell and, since the structural parameters are very similar, only the ‘A’ structure is discussed and depicted below. The structure shows the expected connectivity and the metal ligand bond distances are in good agreement with the Cp\* analogue [Ru(Cp\*)(P<sup>Cy</sup><sub>2</sub>N<sup>Ph</sup><sub>2</sub>)(MeCN)]PF<sub>6</sub>.<sup>6a</sup> The P<sup>Cy</sup><sub>2</sub>N<sup>Ph</sup><sub>2</sub> ligand crystallizes in a chair-boat conformation with a close contact (H(7A)-Ph<sub>centroid</sub> bond distance of 2.730 Å) between the methyl of the acetonitrile ligand and the π-system of the adjacent *N*-phenyl group. A similar C-H/π-interaction<sup>9</sup> was also observed for the close analogue of **3-Ru2** with *t*-Bu phosphine substituents.<sup>10</sup> The interaction in **3-Ru2** causes a slight compression of the Ru(1A)-N(1A)-C(6A) bond angle of 172.5(3)° for **3-Ru2** as compared to 175.1(4)°<sup>6a</sup> for the Cp\* analogue.

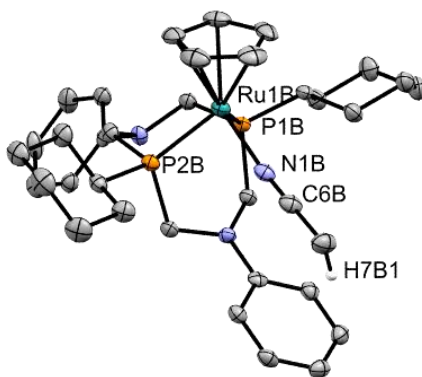


**Figure 3-3.** Displacement ellipsoid plot of **3-Ru2** with ellipsoids at 50% probability level. H atoms, [PF<sub>6</sub>]<sup>-</sup>, and co-crystallized Et<sub>2</sub>O were omitted for clarity. Selected bond distances (Å): Ru(1A)-P(1A) = 2.256(1), Ru(1A)-P(2A) = 2.265(1), Ru(1A)-N(1A) = 2.044(3), Ru(1A)-Cp(centroid) = 1.869, Ru(1B)-P(1B) = 2.268(1), Ru(1B)-P(2B) = 2.260(1), Ru(1B)-N(1B) = 2.029(3), Ru(1B)-Cp(centroid) = 1.872. Selected bond angles (°): P(1A)-Ru(1A)-P(2A) = 79.71(3), Ru(1A)-N(1A)-C(6A) = 172.5(3), P(1B)-Ru(1B)-P(2B) = 79.44(3), Ru(1B)-N(1B)-C(6B) = 170.1(3).

Intramolecular hydroalkoxylation of 2-ethynylbenzyl alcohol (**3-1a**) was conducted with 0.5 mol% **3-Ru2** (Figure 3-4). Isochromene (**3-2a**) was the only observed product and it was formed in 11, 32, and 66% yield at temperatures of 40, 54, and 70 °C, respectively. Thus, catalytic activity with **3-Ru2** increases with increasing temperature, which contrasts with **3-Ru1** that exhibits decreased performance at elevated temperatures.<sup>2e</sup> Methyl-THF

was employed in the present study, rather than acetone, to permit catalytic assessment at elevated temperatures. Prior solvent-effect studies with related catalysts indicate the switch in solvent should have a negligible influence on conversion.<sup>2e, 6b</sup> The trends indicate that vinyl ammonium formation does not compete with catalysis for **3-Ru2** and this should enable reactivity with more challenging substrates, which likely require elevated temperatures to achieve desired reactivity.

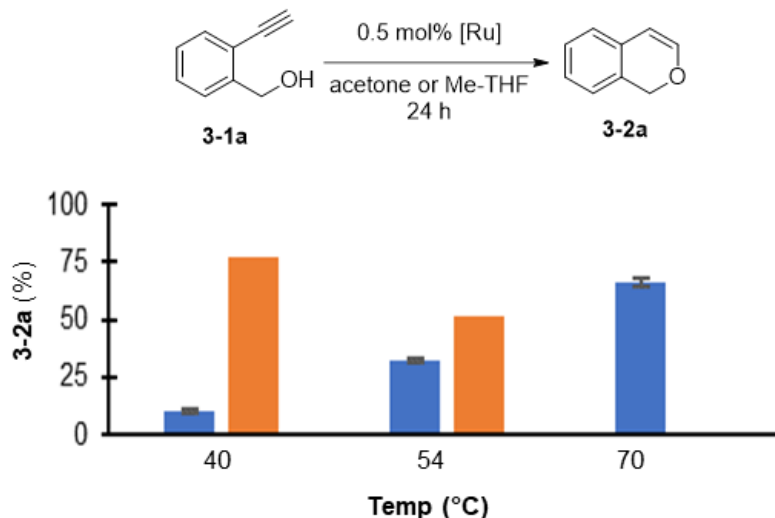
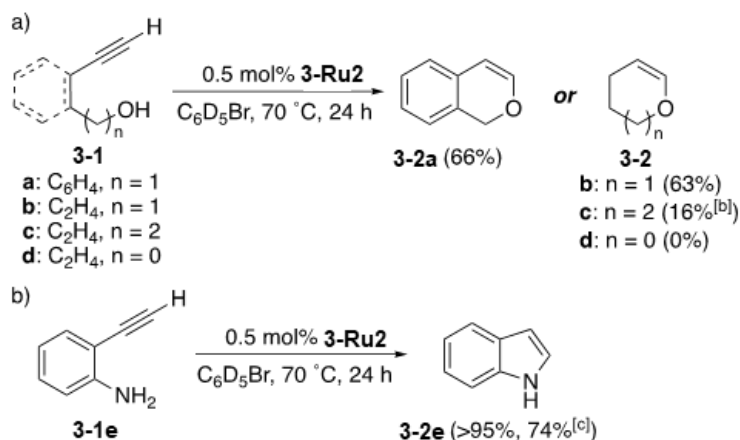


**Figure 3-4.** (top) Hydroalkoxylation of **3-1a** to generate **3-2a** with 0.5 mol% catalyst over 24 hours. (bottom) *In situ* yield of **3-2a** at 40, 54 and 70 °C with catalyst **3-Ru2** (blue) in Me-THF, and **3-Ru1**<sup>2e</sup> (red, 40 and 54 °C) in acetone. Reactions were conducted in duplicate with data points representing the average and the error bars depict the span of individual runs.

### 3.2.2 Substrate Investigation

With the intention of uncovering mechanistic opportunities and limitations of **3-Ru2**, we targeted a select set of substrates for hydrofunctionalization. Previously, the hydroamination of 2-ethynylaniline compounds to give substituted indole products with a derivative of **3-Ru2** (R = *t*-Bu rather than Cy), revealed that the catalyst was tolerant of electron-donating and -withdrawing groups *para* to both the alkyne and amine.<sup>10</sup> Here, we were interested in catalyst evaluation as a function of: the flexibility of the linker between nucleophile and alkyne; the size of the target ring; and the nature of the nucleophile

(Schemes 3-2 and 3-3). A standard set of conditions were used for all substrates to ease comparisons: 0.5 mol% **3-Ru2** in C<sub>6</sub>D<sub>5</sub>Br at 70 °C for 24 h and reactions were monitored by <sup>1</sup>H NMR spectroscopy. C<sub>6</sub>D<sub>5</sub>Br was chosen as the solvent since it is non-coordinating, has a high boiling point (156 °C), and it readily solubilizes **3-Ru2**. Under these conditions, 66% yield of isochromene (**3-2a**) was achieved (Scheme 3-2a). The 1,2-disubstitution of the aryl ring in **3-1a** could facilitate nucleophilic attack by positioning the hydroxyl group near the reactive vinylidene. By contrast, the hydroxyl of **3-1b** would have significantly more rotational freedom due to the flexible propyl linker. Despite this, the pyran product **3-2b** was formed selectively in 63% yield, indicating that nucleophile positioning is not necessary. A computational study showed that isomerization of  $\pi$ -bound alkyne to vinylidene is favoured with electron-poor alkyne substituents.<sup>11</sup> Successful catalysis with **3-1b** indicates that **3-Ru2** is sufficiently electron rich to promote vinylidene formation, despite the inherent reactivity of the alkyl-substituted substrate. Previously, cyclization of **3-1b** was attempted with 1 mol% **3-Ru1** at 40 °C, but no product was observed.<sup>2e</sup> Since the phosphine donor strength is similar for the two catalysts, the much improved performance of **3-Ru2** is likely due to suppression of vinyl ammonium deactivation and thus the ability to employ elevated reaction temperatures. While pyran **3-2b** is accessible, cyclization of the related alkyl linked substrates **3-1c** and **3-1d** was poor, giving 16 and 0% conversion, respectively. In both cases, the balance of materials corresponded to unreacted starting materials. It is unclear if the cause for the low yield of the seven-membered product **3-2c** is a difficult nucleophilic attack step, but we do anticipate that ring strain and increased translational entropy of the linker would hinder this step as compared to formation of the six-membered product **3-2b**. The lack of turnover to give the 5-membered ring product **3-2d** is not likely due to the higher ring strain as compared to the 6-membered product. Rather, analysis of catalytic intermediates (*vide infra*) reveals that the product release step inhibits catalysis. Not all 5-membered products are inaccessible, since we have shown that various catalysts of the type [Ru(Cp/Cp\*)(P<sup>R</sup><sub>2</sub>N<sup>R'</sup><sub>2</sub>)(MeCN)][PF<sub>6</sub>] convert 2-ethynyl aniline (**3-1e**) to indole (**3-2e**). Indeed, under the standard conditions employed here **3-Ru2** gives **3-2e** in quantitative yield and a 74% yield is achieved with 5-fold lower catalyst loading (Scheme 3-2b).

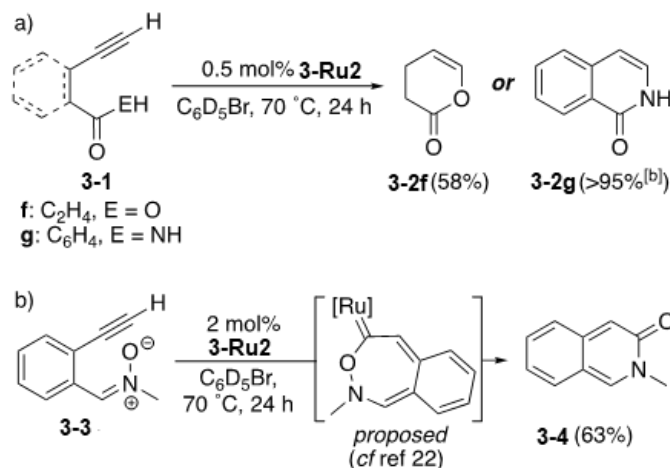


**Scheme 3-2.** Influence of Substrate Linker on **3-Ru2** hydroalkoxylation performance. *In situ* yields were determined by <sup>1</sup>H NMR spectroscopy relative to dimethyl terephthalate (**3-DMT**) as internal standard. Reactions were conducted in duplicate, and values were within ±5%. <sup>[b]</sup> 10 mol% **3-Ru2**. <sup>[c]</sup> 0.1 mol% **3-Ru2**.

We next explored substrates with different types of nucleophilic groups (Scheme 3-3), including carboxylic acid (**3-1f**), amide (**3-1g**) and nitron (**3-3**). The catalyst successfully cyclized **3-1f** to give 3,4-dihydro-2*H*-pyran-2-one (**3-2f**) in 58% yield (Scheme 3-3a). The nearly identical yield to **3-2b** indicates that **3-Ru2** is relatively insensitive to the change in nucleophile from hydroxyl to carboxylic acid. The amide substrate **3-1g** readily reacts with only 0.1 mol% **3-Ru2** to give quantitative conversion to 1-hydroxyisoquinoline (**3-2g**). The nitron of substrate **3-3** also proved to be an effective nucleophile to give 63% isoquinolinone **3-4** (Scheme 3-3b). The performance of **3-Ru2** in this reaction is notably better than the single other reported catalyst [Ru(Tp)(PPh<sub>3</sub>)(MeCN)<sub>2</sub>][SbF<sub>6</sub>] (Tp = trispyrazolylborate), which gave **3-4** in 75% isolated yield with a 10 mol% loading at 90 °C in toluene after 5 h.<sup>12</sup> The mechanism proposed in this prior study includes a carbene intermediate, which forms following nucleophilic attack of the nitron oxygen on C<sub>α</sub> of the vinylidene. Thus, successful formation of **3-4** with **3-Ru2** indirectly indicates that cyclization to give a 7-membered heterocycle is feasible in some cases. Collectively, the selection of substrates reveals that vinylidene formation from aryl or alkyl terminal alkynes occurs readily with **3-Ru2**. Additionally, nucleophilic attack occurs with positioned or non-positioned nucleophiles, to give different ring sizes, and with different types of



nucleophiles. Therefore, the performance of **3-Ru2** is relatively insensitive to the nucleophilic attack step.



**Scheme 3-3.** Influence of Nucleophile on Ru2 Hydrofunctionalization Performance. *In situ* yields were determined by <sup>1</sup>H NMR spectroscopy relative to **3-DMT** as internal standard. Reactions were conducted in duplicate and all yields were within ±5%. <sup>[b]</sup> 0.1 mol% **3-Ru2**.

### 3.2.3 Evaluation of Catalyst Decomposition and Product Inhibition

Previously, we identified that the hydroamination product indole inhibited catalyst **3-Ru2**, which slowed turnover.<sup>6a</sup> To ascertain if the hydroalkoxylation product **3-2a** also inhibits catalyst performance, a ‘same-excess’ experiment<sup>13</sup> was conducted. Hydroalkoxylation was performed with a consistent concentration of **3-Ru2** (7.5 mM) and with two different concentrations of **3-1a**, Run A = 200 and Run B = 150 mM (Figure 3-5). The starting substrate concentration of Run B corresponds to the amount of **3-1a** remaining after 33% conversion of Run A. The Run B data was shifted along the time axis so that the first data point aligned with the time for 33% conversion for Run A (*i.e.* time = 40 min). The two data sets nearly overlap, which indicates that only very minor product inhibition or catalyst deactivation occurs. The negligible catalyst inhibition by isochromene **3-2a** is in contrast to hydroamination of 2-ethynylaniline that was hampered by inhibition of the indole product.<sup>6a</sup> Furthermore, a far greater deviation in the Run A and B data would be expected if **3-Ru2** converted to a deactivated vinyl ammonium species during catalysis. Therefore,

this confirms that the switch from benzyl to phenyl pendent amine substituents successfully mitigated this vinylidene deactivation pathway.

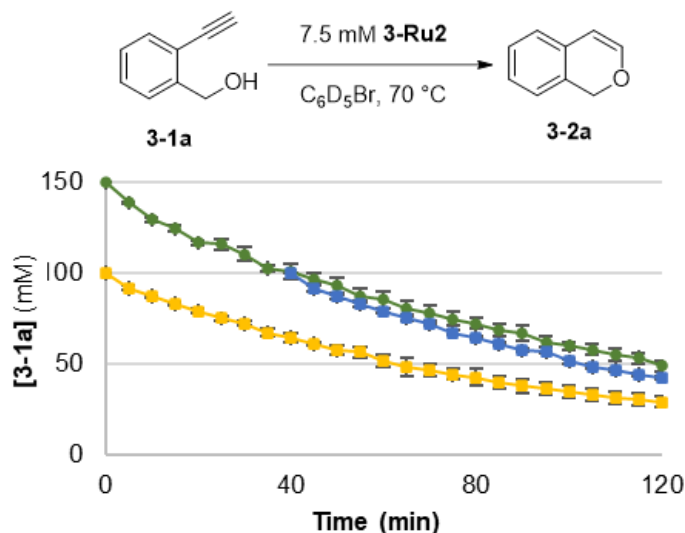


**Figure 3-5.** a) Intramolecular hydroalkoxylation of **3-1a** with catalyst **3-Ru2** (7.5 mM) in  $C_6D_5Br$  (top). b) Reaction profiles for Runs with initial concentrations of: A 150 mM **3-1a** (●, orange); and B 100 mM **3-1a** (■, purple). The Run B data was time-shifted by 40 min (■, blue). Reactions were performed in duplicate with the data points represent the average and the error bars depict the span of values.

### 3.2.4 Determination of Substrate and Catalyst Order

The same-excess experiment revealed that hydroalkoxylation of **3-1a** with **3-Ru2** is well behaved, and therefore suited for kinetic analysis. The reaction order in catalyst and substrate was elucidated using visual kinetic analysis.<sup>13b</sup> The order in substrate was determined from reactions with varying initial amounts of substrate **3-1a** of 200 mM (Run A), 150 mM (Run B), and 100 mM (Run C). Runs A-C all employed 7.5 mM catalyst **3-Ru2** and the reactions were conducted at 70 °C. The reaction order can be extracted by normalization of the time axis to achieve overlap of the three curves and the best overlap corresponded to an order in substrate of 0.7 (Figures 3-5, B-24 and B-25). The order in catalyst was determined with three reactions with varying amounts of **3-Ru2** of 7.5 mM

(Run C), 5 mM (Run D), and 2.5 mM (Run E), and all Runs were conducted with 100 mM **3-1a** at 70 °C. The x-axis of the conversion vs time plots were normalized to achieve overlap of the datasets, which corresponded to an order of 0.7 for the catalyst (Figure 3-6). The same order for both catalyst and substrate indicates a 1:1 ratio of the two in the rate-limiting step. Nucleophilic attack of the hydroxyl on the vinylidene or proton transfer to release product can be eliminated as turnover-limiting, since both steps should give a zero order dependence in substrate. The non-integer order is indicative of a complex rate law, which is common for catalytic mechanisms.<sup>14</sup> Vinylidene formation would be preceded by a reversible reaction of free alkyne with the operationally-unsaturated active catalyst (**3-C**) to give a  $\pi$ -bound alkyne adduct. The rate is likely dictated by the combination of this pre-equilibrium and vinylidene formation.

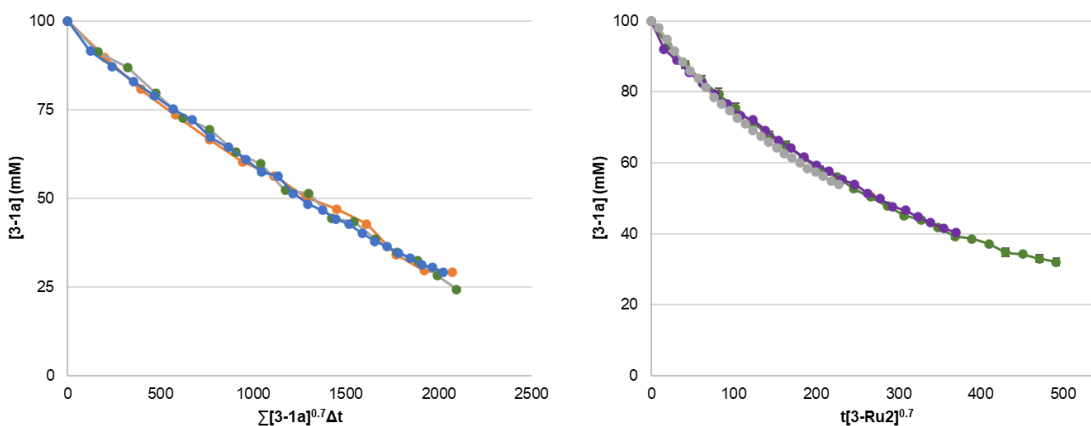


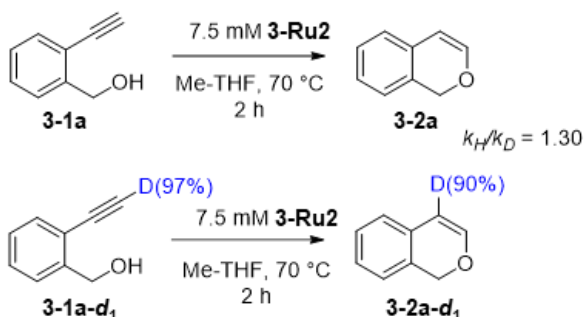
**Figure 3-6.** Time normalized reaction profiles for hydroalkoxylation of **3-1a** at 70 °C in  $C_6D_5Br$ . a) Variable time normalization with substrate concentration, plotted from reactions conducted with 7.5 mM **3-Ru2** and initial [**3-1a**] of 200 mM (orange), 150 mM (red), and 100 mM (blue). b) Time normalization with catalyst concentration, plotted from reactions conducted with 100 mM **3-1a** and initial [**3-Ru2**] of 7.5 mM (green), 5 mM (purple), and 2.5 mM (grey). Reactions were performed in duplicate and in all cases the error was  $\leq \pm 5\%$ .

### 3.2.5 Deuterium Labelling Studies

To further elucidate the mechanistic details, a series of parallel kinetic isotope effect (KIE) experiments were targeted. Two isotopologues of substrate **3-1a** were prepared with

deuterium appended to oxygen (**3-1a-OD**) or at the terminal position of the alkyne (**3-1a-d<sub>1</sub>**). Cyclization of **3-1a** and **3-1a-d<sub>1</sub>** were preformed separately with **3-Ru2** (7.5 mM) at 70 °C in C<sub>6</sub>D<sub>5</sub>Br for 2 h. The <sup>1</sup>H NMR spectrum of the catalytic reaction of **3-1a-d<sub>1</sub>** revealed complete incorporation of deuterium at the C2 carbon in **3-2a** (Figure B-20). This is the expected position for a mechanism that involves alkyne activation to give a vinylidene intermediate with subsequent outersphere nucleophilic attack. Alternatively, deuteration at C<sub>α</sub> would be expected for mechanisms that involve alkyne insertion into Ru-H or Ru-OR intermediates, generated by metal activation of the nucleophile.<sup>15</sup>

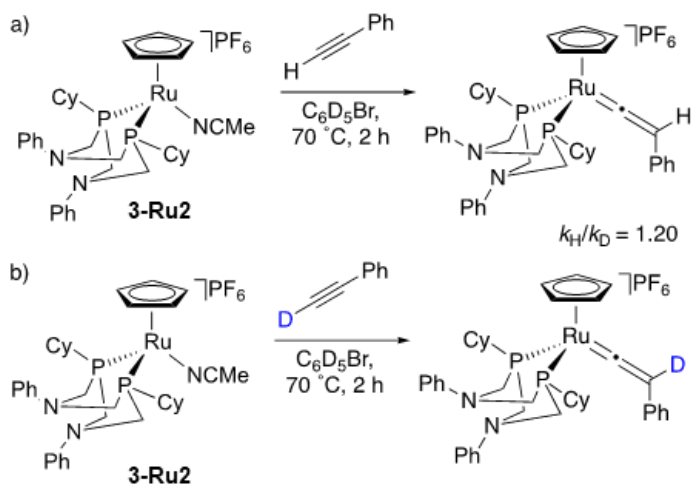
A comparison of the rates for the reactions with **3-1a** and **3-1a-d<sub>1</sub>** revealed a KIE of 1.30 (Scheme 3-4). A kinetic effect due to the terminal C-H bond of the alkyne again discounts nucleophilic attack or product releasing protonolysis as rate limiting. Alkyne coordination to the active catalyst would involve some change in carbon hybridization from sp to sp<sup>2</sup>, which should lead to an inverse isotope effect.<sup>16</sup> A larger primary KIE would be expected for rate-limiting vinylidene formation. In line with related MLC catalysts, this step most likely occurs through 1,2-proton migration promoted by the pendent amine.<sup>2a-c</sup> Therefore, we propose that the observed KIE is a combination of a primary KIE for the 1,2-proton migration step and an inverse EIE due to alkyne coordination, which reduced the magnitude of the KIE. This proposal is consistent with the reaction order studies.



**Scheme 3-4.** Parallel isotope experiments for the intramolecular hydroalkoxylation of **3-1a** and **3-1a-d<sub>1</sub>**.

To corroborate the hypothesis that the observed KIE with **3-1a/3-1a-d<sub>1</sub>** cyclization is due to vinylidene formation, an analogous KIE study was conducted between **3-Ru2** and a

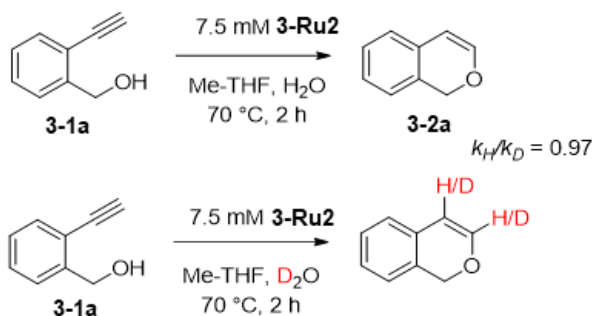
stoichiometric equivalent of phenylacetylene and phenylacetylene- $d_1$  (Scheme 3-5). In both cases, analysis of the reaction solutions by  $^{31}\text{P}\{^1\text{H}\}$  NMR spectroscopy revealed formation of a single new species observed as a singlet at 43.8 ppm. This value is 1 ppm upfield of **3-Ru2**, which is assigned as the expected vinylidene complex. By comparison, the  $\delta_{\text{P}}$  value is significantly different from that for vinyl ammonium complex **3-D**, which is 17 ppm downfield of **3-Ru1**. The rate comparison between the two parallel reactions with phenylacetylene and phenylacetylene- $d_1$  exhibited a KIE of 1.20, which is similar in magnitude to that observed above with **3-1a-d1/3-1a** (Scheme 3-4). The agreement between the values supports the hypothesis that the isotope effect is due to substrate binding and subsequent vinylidene formation.



**Scheme 3-5.** KIE measurement from parallel reactions of **3-Ru2** with a) phenylacetylene, and b) phenylacetylene- $d_1$ .

Parallel reactions of **3-1a** and **3-1a-OD** were performed under the same catalytic conditions to those described above with **3-1a/3-1a-d1**, except **3-1a-OD** was generated *in situ* by adding 20  $\mu\text{L}$  of  $\text{D}_2\text{O}$  to **3-1a**. To exclude the influence of excess water on the observed rates, the reaction with **3-1a** also included 20  $\mu\text{L}$   $\text{H}_2\text{O}$ . Notably, no difference in rate was observed for the cyclization of **3-1a** with or without  $\text{H}_2\text{O}$  (Figure B-29). A  $k_{\text{D}}/k_{\text{H}}$  of 0.97 was observed between **3-1a** and **3-1a-OD**, which suggested a negligible KIE based on deuteration at oxygen (Scheme 3-6). This indicated that proton transfer steps that involve the hydroxy proton are not rate-limiting. We observed deuterium incorporation at both the

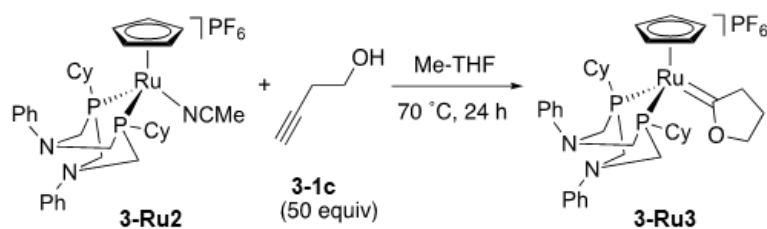
carbons alpha and beta to the oxygen atom, but this is most likely due to scrambling with D<sub>2</sub>O rather than a reflection of the fate of the hydroxyl proton/deuterium (see S.I.).



**Scheme 3-6.** Parallel isotope experiments for the intramolecular hydroalkoxylation of **3-1a** and **3-1a-OD**.

### 3.2.6 Synthesis and Reactivity of Catalytic Intermediates

During our investigations into the reaction scope (*vide supra*) we found that cyclization of 3-butyn-1-ol (**3-1d**) was unsuccessful, but we noted formation of a crystalline product during the course of attempted catalysis. In order to isolate the ruthenium product, a reaction was conducted at higher loading of **3-Ru2** with **3-1d** in Me-THF at 70 °C over 24 h (Scheme 3-7). A singlet was observed by <sup>31</sup>P{<sup>1</sup>H} NMR spectroscopy at 51.6 ppm, which is 5.7 ppm downfield from the pre-catalyst **3-Ru2**. In the <sup>1</sup>H NMR spectrum, a singlet corresponding the Cp ligand was found ca. 0.5 ppm downfield of that for **3-Ru2**. Two triplets and a pentet were observed at  $\delta_{\text{H}} = 4.60, 3.36,$  and 1.95, respectively, the relative integration and multiplicities of which correspond to a non-symmetric propyl group. This assignment was confirmed by <sup>1</sup>H-<sup>1</sup>H COSY NMR spectroscopy. A <sup>1</sup>H-<sup>13</sup>C{<sup>1</sup>H} HMBC experiment revealed a correlation from all three methylene signals to a <sup>13</sup>C resonance at 295.5 ppm (Figure B-7), which is a typical value for related carbenes (296 – 314 ppm; *cf.* **3-A**  $\delta_{\text{C}} = 314,$  **3-B**  $\delta_{\text{C}} = 313$ ).<sup>3-4, 17</sup> Collectively, this data is consistent with quantitative formation of a 2-oxocyclopentylidene complex, **3-Ru3**.



**Scheme 3-7.** Synthesis of **3-Ru3**.

Single crystals suitable for X-ray diffraction were obtained and the solid-state structure confirmed the assignment of **3-Ru3** as an alkoxy-carbene (Figure 3-7). The Ru-P(1)/P(2) bond distances (2.277(2) and 2.272(3) Å, respectively) and P(1)-Ru(1)-P(2) bond angle (79.6(1)) are both in good agreement with **3-Ru2**. A small increase of ca. 0.5 Å for the Cp(centroid)-Ru(1) distance is observed for **3-Ru3** relative to the MeCN adduct **3-Ru2**. This could be due to the increased steric bulk and/or the increased electron donation from the alkoxy-carbene ligand. The C(34)-O(1) bond distance of 1.293 Å suggests a fair amount of double bond character (*cf.* typical C=O bonds *ca.* 1.23 Å). The Ru(1)-C(34) bond distance is 1.949(8) Å. Both of these two distances are consistent with related oxocycloalkylidene complexes, including **3-A** and **3-B**.<sup>3-4, 17b, 17d</sup>

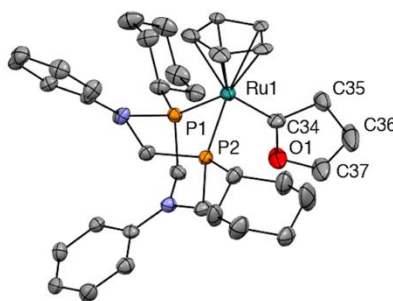


**Figure 3-7.** Displacement ellipsoid plot of solid-state structure of alkoxy-carbene complex **3-Ru3** with ellipsoids at 50% probability level. H atoms, [PF<sub>6</sub>]<sup>-</sup>, and a disordered Cp ligand (rotational about the Ru – Cp centroid axis by ca. 174°) were omitted for clarity. Selected bond distances (Å): Ru(1)-P(1) = 2.277(2), Ru(1)-P(2) = 2.272(3), Ru(1)-Cp(centroid) = 1.939, Ru(1)-C(34) = 1.949(8), C(34)-O(1) = 1.293(9). Selected bond angles (°): P(1)-Ru(1)-P(2) = 79.6(1).

The high yield formation of **3-Ru3** in the presence of excess **3-1d**, explains that catalytic turnover arrests on formation of this complex. By comparison, the analogous 2-oxocyclohexylidene complex **3-Ru4** (see Figure 3-8) is not observed during catalysis with 4-pentyn-1-ol (**3-1b**). Rather, catalytic turnover occurs readily to give the expected six-membered product 3,4-dihydro-2*H*-pyran (**3-2b**). The stark difference in reactivity could be due to different stability of the alkoxy-carbene compounds **3-Ru3** and **3-Ru4**, or possibly intermediate **3-Ru4** is bypassed during catalysis with **3-1b**. To evaluate if **3-Ru3** has a lower ground-state energy that hinders forward reactivity compared to **3-Ru4**, we conducted a computational comparison of the two complexes. The energies of **3-Ru3** and **3-Ru4** were compared to those of the corresponding vinylidene intermediates. In both cases, the reaction to form the alkoxy-carbene is exoergic by 92 to 105 kJ/mol. The 5-membered alkoxy-carbene **3-Ru3** is more stable than the 6-membered complex **3-Ru4**, but only by ca. 13 kJ/mol. Thus, there is no thermodynamic distinction between **3-Ru3** and **3-Ru4** that governs the observed catalysis. Rather, catalytic inhibition by substrate **3-1d**, via formation of **3-Ru3**, is likely governed by a greater kinetic preference (than with substrate **3-1b** via **3-Ru4**) to undergo protonation at C<sub>β</sub> rather than C<sub>α</sub>.

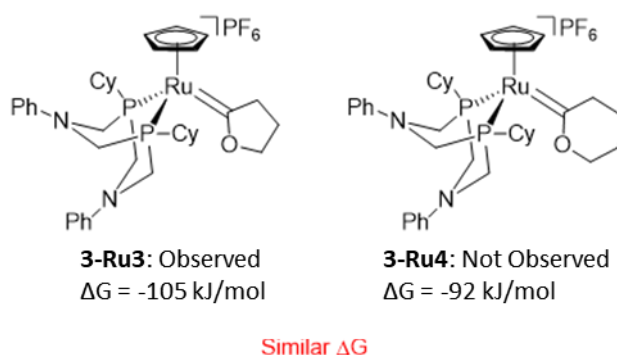
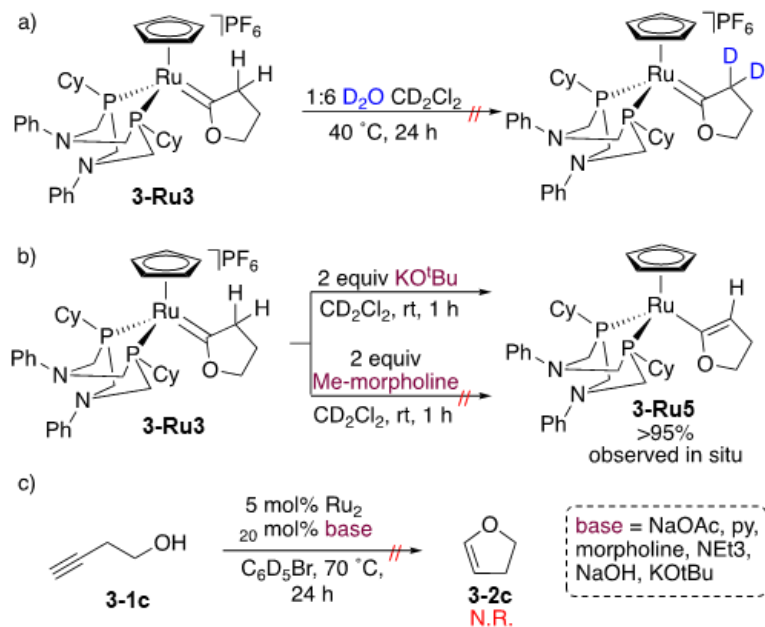


**Figure 3-8.** Calculated energy difference between precursor vinylidene complexes (0 kJ/mol) and alkoxy-carbene complexes **3-Ru3** and **3-Ru4**. Refer to SI for details regarding calculations.

To achieve product release from **3-Ru3**, deprotonation of the C<sub>β</sub> methylene and subsequent protonation of the carbene (C<sub>α</sub>) would be required. Since **3-Ru3** is not catalytically active, we designed a set of experiments to elucidate which step prevents turnover. First, **3-Ru3**



was heated in the presence of D<sub>2</sub>O, (Scheme 3-8a). If the pendent base reversibly deprotonates C<sub>β</sub>, H/D exchange between the resulting ammonium moiety and D<sub>2</sub>O would lead to deuterium incorporation at C<sub>β</sub>. After 24 h at 40 °C, no change in the <sup>1</sup>H NMR spectrum of **3-Ru3** was observed, indicating proton transfer to the pendent amine does not occur. Even heating at 70 °C in (CD<sub>3</sub>)<sub>2</sub>CO did not lead to deuterium incorporation. Based on the solid-state structure of **3-Ru3**, the carbene is oriented such that the C<sub>β</sub> methylene (C35; Figure 3-7) is pointed toward the Cp ligand rather than the pendent amine, which could inhibit deprotonation. However, related ruthenium alkoxycarbene complexes exhibit facile Ru=C rotation at room temperature<sup>17d, 18</sup> and theoretical studies estimate of a 25-46 kJ/mol rotation barrier for such moieties.<sup>19</sup> The low barrier is due to the contribution of resonance structures with single bond character between Ru and C, which will influence the Ru=C bond length. Complexes with facile rotation have lengths in the range of 1.91-2.02 Å,<sup>17d, 18, 20</sup> which is very similar to the observed and calculated values of 1.949(8) and 1.937 Å for **3-Ru3** and **3-Ru4**, respectively. Therefore, it is unlikely that a high barrier carbene rotation prevents C<sub>β</sub> deprotonation in **3-Ru3**.



**Scheme 3-8.** a) Attempted deuterium incorporation at C<sub>β</sub> of **3-Ru3**. b) **3-Ru3** treated with exogenous bases to deprotonate C<sub>β</sub>. c) Attempted catalytic cyclization of **3-1d** with 20 mol% base additives.

Second, **3-Ru3** was treated with the strong exogenous base KO<sup>t</sup>Bu at room temperature for 1 h (Scheme 3-8b). The <sup>31</sup>P{<sup>1</sup>H} NMR spectrum revealed quantitative conversion to a new complex observed as a singlet at 51.2 ppm. Deprotonation at C<sub>β</sub> to give **3-Ru5** was supported by a new triplet at 4.30 ppm in the <sup>1</sup>H NMR spectrum, which corresponded to vinyl ether proton. Deprotonation was also attempted with *N*-Me morpholine, which is expected to have a similar basicity to the pendent amine of **3-Ru3** (p*K*<sub>a(H2O)</sub>: [H(*N*-Me morpholine)]<sup>+</sup> = 7.4; [HNMe<sub>2</sub>Ph]<sup>+</sup> = 5.2).<sup>21</sup> This weaker exogenous base did not induce formation of **3-Ru5**, which indicates that the pendent amine of **3-Ru3** is also insufficiently basic to deprotonate C<sub>β</sub>. Finally, we conducted catalysis of **3-1d** in the presences of several exogenous bases of varying strengths (Scheme 3-8c, p*K*<sub>aH</sub> = 4.8 to 17.0). Even with catalytic loadings 10-fold higher than our optimized conditions, none of the reactions yielded the cyclized product **3-2d**, indicating that proton shuttling by the various bases was not effective. This collection of experiments indicates that product release from **3-Ru3** is prevented by ineffective deprotonation of C<sub>β</sub> by the pendent base of the P<sup>Cy</sup><sub>2</sub>N<sup>Ph</sup><sub>2</sub> ligand.

### 3.2.7 Proposed Catalytic Cycle

The collective experiments described above, combined with prior studies, reveal a mechanistic picture for intramolecular hydrofunctionalization with [Ru(Cp)(P<sup>R</sup><sub>2</sub>N<sup>R'</sup><sub>2</sub>)(MeCN)][PF<sub>6</sub>] catalysts (Figure 3-9). From the pre-catalyst, acetonitrile dissociation occurs readily at elevated temperatures.<sup>6a, 10</sup> The operationally-unsaturated active catalyst **3-IV** is stabilized by a π-interaction for complexes bearing a phenyl substituent on the pendent amine.<sup>6a</sup> Catalysis with **3-1a-d1** gives nearly exclusive incorporation of the C<sub>sp</sub>-D label at C<sub>β</sub> of product **3-2a**, which confirms **3-IV** converts the alkyne to a vinylidene moiety. This was previously implied with the Ru-P<sup>R</sup><sub>2</sub>N<sup>R'</sup><sub>2</sub> catalyst family based on the exclusive *endo* selectivity of the cyclized products and by isolation of vinyl ammonium **3-D**, which is a trapped vinylidene.<sup>2e, 7</sup> The similar KIE values from catalysis with **3-1a-d1/3-1a** and reaction with phenylacetylene-*d*<sub>1</sub>/phenylacetylene is indicative of rate-limiting vinylidene formation during catalysis, which is also supported by a 1:1 reaction order in catalyst and substrate. Together these results indicate that the rate depends on both alkyne coordination and proton migration to give intermediates **3-V** and **3-VI**, respectively. We previously identified that a P<sup>R</sup><sub>2</sub>N<sup>R'</sup><sub>2</sub> ligand with *N*-benzyl

substitution was susceptible to deactivation *via* vinyl ammonium species **3-IX**.<sup>2e</sup> Herein, we established that ligand redesign to include a poorly nucleophilic phenyl-substituted pendent amine suppresses formation of **3-IX**. Rather, productive catalysis occurs by intramolecular nucleophilic attack on C<sub>α</sub> of intermediate **3-VI**. The catalytic reaction was tolerant of substrates with different nucleophilic groups (OH, NH<sub>2</sub>, C(O)OH, C(O)NH<sub>2</sub>, C=N(O)Me) that are linked to the alkyne through either a rigid or flexible linker. Thus, the reaction is relatively insensitive to the nucleophilic attack step (**3-VI** → **3-VII**). From intermediate **3-VIII**, the catalyst likely releases product and regenerates **3-IV** by ligand pendent amine-promoted proton transfer from E to C<sub>α</sub> via intermediate **3-VII**. Product release occurs readily to give 6-membered oxygen and nitrogen heterocycles, and 5-membered indole. However, the 5-membered product 2,3-dihydrofuran (**3-2d**) was inaccessible due to competitive formation of a ruthenium oxocycloalkylidene complex (**3-X**), formed by proton transfer instead to C<sub>β</sub>. The ligand 3° amine proved insufficiently basic to induce proton migration from C<sub>β</sub> to C<sub>α</sub>. This suggests that **3-X** is an off-cycle intermediate for this class of catalysts, which contrasts with related alkyoxycarbene compounds of type **3-A** (see Figure 3-1b) supported by phosphino quinoline ligands. The high retention of the deuterium label of **3-1a-d<sub>1</sub>** at C<sub>β</sub> of **3-2a** further supports the assignment of oxocycloalkylidene **3-X** as off-cycle. If the carbene was instead formed *en route* to **3-VIII** or was in equilibrium with **3-VIII**, then some incorporation of deuterium at C<sub>α</sub> would be anticipated. The five-membered O-heterocycles **3-2d** could not be accessed, while indole forms readily. The lower electronegativity of N or the π-electron delocalization of the alkene moiety defined by C<sub>α</sub> and C<sub>β</sub> to the fused arene of intermediate **3-VII** may lead to preferential protonation at C<sub>α</sub> to give product release, rather than at C<sub>β</sub> to give deactivation product **3-X**. Regardless, identification of **3-X** as a detrimental off-cycle species is a stark contrast to hydration catalysis in which protonation of C<sub>β</sub> is an essential step.

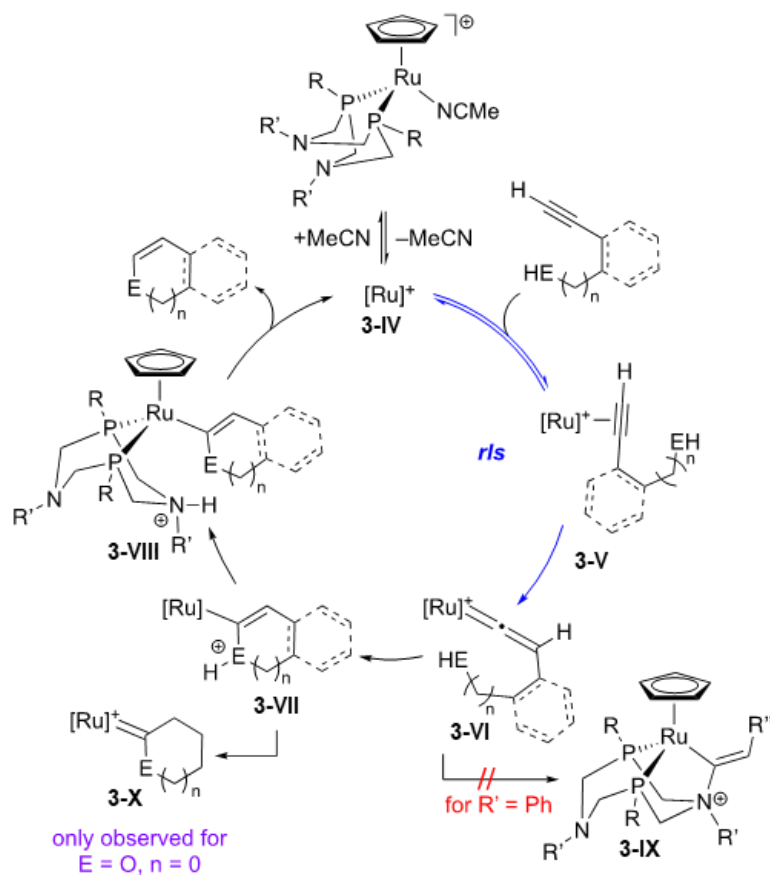


**Figure 3-9.** Proposed catalytic cycle for intramolecular hydrofunctionalization with  $[\text{Ru}(\text{Cp})(\text{P}^{\text{R}}_2\text{N}^{\text{R}'})_2(\text{MeCN})][\text{PF}_6]$ . Structures are simplified where  $[\text{Ru}]^+ = [\text{Ru}(\text{Cp})(\text{P}^{\text{R}}_2\text{N}^{\text{R}'})_2]^+$ , and  $[\text{PF}_6]^-$  is excluded for clarity.

### 3.3 Conclusions

A mechanistic analysis of the  $[\text{Ru}(\text{Cp})(\text{P}^{\text{R}}_2\text{N}^{\text{R}'})_2(\text{MeCN})][\text{PF}_6]$  catalyst family toward the intramolecular hydrofunctionalization of alkynes was conducted. Vinylidene formation was identified as rate-limiting through a series of kinetic and deuterium labelling studies. Deactivation of this key vinylidene intermediate was effectively circumvented through ligand design to include an aryl-substituted pendent amine. A targeted set of substrates revealed that the catalyst is relatively insensitive to the nucleophilic attack step. However, the product of C-E bond formation ( $\text{E} = \text{nucleophile O or N}$ ) is vulnerable to irreversible removal from the catalytic cycle through cycloalkylidene formation. This route represents a limitation of the  $\text{P}^{\text{R}}_2\text{N}^{\text{R}'}$  catalyst family since the pendent tertiary amine is insufficiently

basic to reactivate the intermediate through a C<sub>β</sub> to C<sub>α</sub> proton transfer. Ligand redesign to give a more basic amine is not feasible since this would shuttle the vinylidene intermediate toward a deactivated vinyl ammonium species. Rather, substrate selection to maximize the likelihood of C<sub>α</sub> protonation could favour productive catalysis. This insight will guide future deployment of this catalyst family.

### 3.4 Experimental Section

All reactions were carried out under an inert atmosphere of Argon or N<sub>2</sub>, using standard Schlenk or glovebox techniques, respectively, unless otherwise stated. All glassware was oven dried (150 °C) prior to use. All chemicals were obtained from Sigma-Aldrich, Alfa Aesar, or Oakwood, and used without further purification unless otherwise stated. CDCl<sub>3</sub> (99.8%) and dichloromethane-*d*<sub>2</sub> (99.8%) were obtained from Cambridge Isotope Laboratories. P<sup>Cy</sup><sub>2</sub>N<sup>Ph</sup><sub>2</sub>,<sup>22</sup> [Ru(Cp)(P<sup>Cy</sup><sub>2</sub>N<sup>Ph</sup><sub>2</sub>)(MeCN)][PF<sub>6</sub>],<sup>6a</sup> and were synthesized following literature procedures and the <sup>1</sup>H, <sup>13</sup>C{<sup>1</sup>H}, and <sup>31</sup>P{<sup>1</sup>H} spectroscopic data matched literature values. C<sub>6</sub>D<sub>5</sub>Br,<sup>23</sup> 2-ethynylbenzyl alcohol,<sup>24</sup> 2-ethynyl benzamide,<sup>25</sup> 3-(2-aminophenylthio)prop-1-yne,<sup>26</sup> 2-(prop-2-ynoxy)aniline<sup>27</sup> were prepared following literature procedures. Dry and degassed tetrahydrofuran (THF), diethyl ether (Et<sub>2</sub>O), and acetonitrile (MeCN) were obtained from an Innovative Technology 400-5 solvent purification system and stored under N<sub>2</sub> on 3 Å sieves (Fluka and activated at 150 °C under vacuum). 2-Methyltetrahydrofuran (Me-THF) and bromobenzene-*d*<sub>5</sub> were dried using 3 Å sieves and degassed by bubbling with argon.

Charge-transfer Matrix Assisted Laser Desorption/Ionization (MALDI) mass spectrometry data were collected on an AB Sciex 5800 TOF/TOF mass spectrometer using pyrene as the matrix in a 20:1 molar ratio to metal complex. Samples were spotted on the target plate as solutions in DCM. NMR spectra were acquired on either an INOVA 600 MHz or Bruker 400 MHz NMR spectrometer. <sup>1</sup>H NMR spectra were referenced internally against the residual protio-solvent signal to tetramethylsilane at 0 ppm and <sup>13</sup>C{<sup>1</sup>H} NMR spectra were referenced internally against the solvent signal to tetramethylsilane at 0 ppm. <sup>1</sup>H and <sup>13</sup>C{<sup>1</sup>H} NMR signal assignments were made using a combination of 2D NMR spectra (<sup>1</sup>H-<sup>1</sup>H COSY, <sup>1</sup>H-<sup>13</sup>C{<sup>1</sup>H} HSQC, and <sup>1</sup>H-<sup>13</sup>C{<sup>1</sup>H} HMBC). <sup>31</sup>P{<sup>1</sup>H} NMR spectra were

referenced externally to 85% phosphoric acid at 0.0 ppm. Abbreviations used for multiplicities are as follows: s = singlet, d = doublet, t = triplet, q = quartet, quint = quintet, m = multiplet. Infrared spectra were collected on solid samples using a PerkinElmer UATR TWO FTIR spectrometer. Quantification of catalytic conversion was achieved by  $^1\text{H}$  NMR spectroscopy referenced internally to dimethyl terephthalate (**DMT**) with relative integration.

### 3.4.1 General Procedure for Hydroalkoxylation of **1a** for Catalyst Deactivation or Product Inhibition Studies and Determination of Substrate Order.

In a glovebox, the following three stock solutions, a-c, were prepared: **3-1a** (a = 240 mM, b = 180 mM, c = 120 mM) and **DMT** (a, b, and c = 20 mM) in  $\text{C}_6\text{D}_5\text{Br}$ . A catalyst stock solution was prepared with **3-Ru2** (45 mM) in  $\text{C}_6\text{D}_5\text{Br}$ . An NMR tube was charged with stock a, b, or c (500  $\mu\text{L}$ ) and an initial  $^1\text{H}$  NMR spectrum was obtained as the T0 (time = 0) data point. The NMR instrument probe was then heated to the reaction temperature of 70  $^\circ\text{C}$ . Once the probe had reached the desired temperature the catalyst stock solution (100  $\mu\text{L}$ ) was added to the NMR tube containing either stock a, b, or c and inverted to mix. The final reaction concentrations were as follows: a) 200 mM **3-1a**, 16.7 mM **DMT** and 7.5 mM **Ru2**, b) 150 mM **3-1a**, 16.7 mM **DMT**, and 7.5 mM **Ru2**, and c) 100 mM **3-1a**, 16.7 mM **DMT**, and 7.5 mM **Ru2**. The NMR tube was inserted into the NMR instrument and allowed to reach temperature over 5 minutes before a  $^1\text{H}$  NMR spectral array was obtained with spectra collected every 5 minutes for 2 hours. The resulting spectra were analyzed to quantify the integration of the methylene signal of **1a**, relative to the integral of **DMT** (8.32 ppm) to determine *in situ* conversion. Each catalytic run was performed in duplicate, and the data was averaged, with the error bars representing the span.

### 3.4.2 General Procedure for Hydroalkoxylation of **3-1a** for the Determination of Catalyst Order

In a glovebox, a stock solution of **3-1a** and **DMT** was prepared: **3-1a** (120 mM) and dimethyl terephthalate (**DMT**) (20 mM) in  $\text{C}_6\text{D}_5\text{Br}$ . Three catalyst stock solutions, a-c, were prepared: **3-Ru2** (a = 45 mM, b = 30 mM, and c = 15 mM) in  $\text{C}_6\text{D}_5\text{Br}$ . An NMR tube was charged with stock solution of **3-1a** (500  $\mu\text{L}$ ) and an initial  $^1\text{H}$  NMR spectrum was

obtained and used as T0. The NMR instrument probe was then heated to the reaction temperature of 70 °C. Once the probe had reached the desired temperature catalyst stock solution **a**, **b**, or **c** (100 µL) was added to the NMR tube and inverted to mix. The final reaction concentrations were as follows: a) 100 mM **3-1a**, 16.7 mM **DMT**, and 7.5 mM **Ru2**, b) 100 mM **3-1a**, 16.7 mM **DMT**, and 5 mM **3-Ru2**, and c) 100 mM **3-1a**, 16.7 mM **DMT**, and 2.5 mM **Ru2**. The NMR tubes were inserted into the NMR instrument and allowed to reach temperature over 5 minutes before a <sup>1</sup>H NMR spectral array was obtained with spectra collected every 5 minutes for 2 hours. The resulting NMR spectra were analyzed to quantify the integration of the methylene signal of **3-1a**, relative to the integral of **DMT** (8.32 ppm) to determine *in situ* conversion. Each catalytic run was performed in duplicate, and the data was averaged, with the error bars representing the span.

### 3.4.3 Catalytic Hydroalkoxylation with Alkyne-Labelled Substrate (**3-1a-d<sub>1</sub>**)

In a glovebox, a stock solution of **3-1a-d<sub>1</sub>** and **DMT** was prepared: **3-1a-d<sub>1</sub>** (120 mM) and **DMT** (20 mM) in C<sub>6</sub>D<sub>5</sub>Br. A catalyst stock solution was prepared: **3-Ru2** (45 mM) in C<sub>6</sub>D<sub>5</sub>Br. An NMR tube was charged with the stock solution of **3-1a-d<sub>1</sub>** (500 µL) and an initial <sup>1</sup>H NMR spectrum was obtained and used as T0. The NMR instrument probe was heated to the reaction temperature of 70 °C. Once the probe had reached the desired temperature the catalyst stock solution (100 µL) was added to the NMR tube and inverted to mix. The final concentrations were: 100 mM **3-1a-d<sub>1</sub>**, 16.7 mM **DMT**, and 7.5 mM **3-Ru2**. The NMR tube was inserted into the NMR instrument and allowed to reach temperature over 5 minutes before a <sup>1</sup>H NMR spectral array was obtained with spectra collected every 5 minutes for 2 hours. The resulting NMR spectra were analyzed to quantify the integration of the methylene signal of **3-1a**, relative to the integral of **DMT** (8.32 ppm) to determine *in situ* conversion. Each catalytic run was performed in duplicate, and the data was averaged, with the error bars representing the span.

### 3.4.4 Catalytic Hydroalkoxylation with Alcohol-Labelled Substrate (**3-1a-OD**)

In a glovebox, a stock solution of **3-1a** and **DMT** was prepared: **3-1a** (120 mM) and **DMT** (20 mM) in C<sub>6</sub>D<sub>5</sub>Br. A catalyst stock solution was prepared: **3-Ru2** (90 mM) in C<sub>6</sub>D<sub>5</sub>Br.

An NMR tube was charged with stock solution of **3-1a** (500  $\mu\text{L}$ ) and  $\text{D}_2\text{O}$  (50  $\mu\text{L}$ ) and an initial  $^1\text{H}$  NMR spectrum was obtained and used as T0. This NMR indicated complete exchange of the alcohol proton by deuterium. The NMR instrument probe was then heated to the reaction temperature of 70  $^\circ\text{C}$ . Once the probe had reached the desired temperature the catalyst stock solution (50  $\mu\text{L}$ ) was added to the NMR tube. The final concentrations were: 100 mM **3-1a-OD**, 16.7 mM **DMT**, and 7.5 mM **3-Ru2**. The NMR tube was inserted into the NMR instrument and allowed to reach temperature over 5 minutes before a  $^1\text{H}$  NMR spectral array was obtained with spectra collected every 5 minutes for 2 hours. The resulting NMR spectra were analyzed to quantify the integration of the methylene signal of **3-1a-OD**, relative to the integral of **DMT** (8.32 ppm) to determine *in situ* conversion. Each catalytic run was performed in duplicate, and the data was averaged, with the error bars representing the span.

### 3.4.5 Synthesis of Alkoxy carbene Complex $[\text{Ru}(\text{Cp})(\text{P}^{\text{Cy}}_2\text{N}^{\text{Ph}}_2)(3,4\text{-Dihydro-2H-furylium})][\text{PF}_6]$ (**3-Ru3**)

In the glovebox, a 4 mL vial was charged with **3-Ru2** (21 mg, 0.026 mmol, 1 equiv) and the solid was dissolved in bromobenzene. A second 4 mL vial was charged with 3-butyn-1-ol (90 mg, 1.3 mmol, 50 equiv). The **3-Ru2** solution was transferred to the vial of 3-butyn-1-ol and the mixture was heated to 70  $^\circ\text{C}$  for 24 hours. Colourless X-ray-quality crystals formed over the course of the reaction. The crystals were isolated by removal of bromobenzene (decanted) and were then washed with hexanes ( $3 \times 2$  mL) and dried *in vacuo* to remove any residual solvent. Yield = 93% (17 mg).  $^1\text{H}$  NMR (400 MHz,  $\text{CD}_2\text{Cl}_2$ ):  $\delta$  7.39-7.28 (m, Ph-*H*, 4H), 7.10-6.91 (m, Ph-*H*, 6H), 5.34 (s, Ru( $\text{C}_5\text{H}_5$ ), 5H), 4.60 (t,  $^3J_{\text{H-H}} = 7.3$  Hz, Ru=C- $\text{CH}_2\text{CH}_2\text{CH}_2\text{O}$ , 2H), 3.79-3.72 (m, P $\text{CH}_2\text{N}$ , 2H), 3.67-3.59 (m, P $\text{CH}_2\text{N}$ , 2H), 3.57-3.50 (m, P $\text{CH}_2\text{N}$ , 2H), 3.47-3.40 (m, P $\text{CH}_2\text{N}$ , 2H), 3.36 (t,  $^3J_{\text{H-H}} = 7.7$  Hz, Ru=C= $\text{CH}_2\text{CH}_2\text{CH}_2$ , 2H), 1.95 (quint,  $^3J_{\text{H-H}} = 7.5$  Hz, Ru=C- $\text{CH}_2\text{CH}_2\text{CH}_2\text{O}$ , 2H), 1.93-1.72 (m, Cy-*H*, 10H), 1.42-1.20 (m, Cy-*H*, 10H), 1.12-0.98 (m, Cy-*H*, 2H).  $^{13}\text{C}\{^1\text{H}\}$  NMR (101 MHz,  $\text{CD}_2\text{Cl}_2$ ):  $\delta$  295.5 (Ru=CO $\text{CH}_2\text{CH}_2\text{CH}_2$ ), 154.2 (t,  $^3J_{\text{C-P}} = 8.1$  Hz, C $_{\text{Ar}}$ ), 152.3 (t,  $^3J_{\text{C-P}} = 8.4$  Hz, C $_{\text{Ar}}$ ), 130.2 (C $_{\text{Ar}}$ ), 130.1 (C $_{\text{Ar}}$ ), 123.0 (C $_{\text{Ar}}$ ), 121.7 (C $_{\text{Ar}}$ ), 119.4 (C $_{\text{Ar}}$ ), 117.7 (C $_{\text{Ar}}$ ), 88.6 (Ru( $\text{C}_5\text{H}_5$ )), 80.3 (Ru=C- $\text{CH}_2\text{CH}_2\text{CH}_2\text{O}$ ), 61.7 (Ru=C- $\text{CH}_2\text{CH}_2\text{CH}_2\text{O}$ ), 50.4 (X of ABX, N- $\text{CH}_2\text{-P}$ ), 45.1 (X of ABX, N- $\text{CH}_2\text{-P}$ ), 43.0 (X of ABX, Cy), 29.0 (Cy), 28.7



(Cy), 27.6 (X of ABX, Cy), 27.1 (X of ABX, Cy), 26.4 (Cy), 23.4 (Ru=C=CH<sub>2</sub>CH<sub>2</sub>CH<sub>2</sub>). <sup>31</sup>P{<sup>1</sup>H} NMR (162 MHz, CD<sub>2</sub>Cl<sub>2</sub>): δ 51.6 (Ru-P), -144.2 (sept, <sup>1</sup>J<sub>P-F</sub> = 711 Hz, PF<sub>6</sub>). IR (neat) ν(cm<sup>-1</sup>): 3055 (w), 2931 (w), 2856 (w), 1593 (m), 1503 (m), 1144 (m), 829 (s), 739 (m), 557 (m). MALDI MS (pyrene matrix): calc. *m/z* = 703.3 [Ru(Cp)(P<sup>Cy</sup><sub>2</sub>N<sup>Ph</sup><sub>2</sub>)(=CCH<sub>2</sub>CH<sub>2</sub>CH<sub>2</sub>O)]<sup>+</sup>, Obs. *m/z* = 703.3.

### 3.4.6 *In Situ* Formation of Vinyl Ether Complex [Ru(Cp)(P<sup>Cy</sup><sub>2</sub>N<sup>Ph</sup><sub>2</sub>)(2,3-dihydrofuran)][PF<sub>6</sub>] (**3-Ru5**)

In a glovebox, a 4 mL vial was charge with **3-Ru3** (5 mg, 0.007 mmol, 1 equiv) and dissolved in CD<sub>2</sub>Cl<sub>2</sub>. A second 4 mL vial was charged with KO<sup>t</sup>Bu (2 mg, 0.02 mmol, 2.8 equiv) and the **3-Ru3** solution was added to this vial. The reaction was stirred at room temperature for 18 h. The solution was filtered through Celite and transferred to an NMR tube and analyzed by <sup>1</sup>H NMR spectroscopy. H NMR (400 MHz, CD<sub>2</sub>Cl<sub>2</sub>): δ 7.26-7.16 (m, Ph-H, 4H), 6.96-6.91(m, Ph-H, 2H), 6.83-6.74 (m, Ph-H, 3H), 6.68-6.62 (m, Ph-H, 1H), 4.59 (s, Ru(C<sub>5</sub>H<sub>5</sub>), 5H), 4.30 (t, <sup>3</sup>J<sub>H-H</sub> = 2.0 Hz, Ru-C=CHCH<sub>2</sub>CH<sub>2</sub>O, 1H), 3.88 (t, <sup>3</sup>J<sub>H-H</sub> = 8.9 Hz, Ru-C=CHCH<sub>2</sub>CH<sub>2</sub>, 2H), 3.71-3.64 (m, PCH<sub>2</sub>N, 2H), 3.63-3.51 (m, PCH<sub>2</sub>N, 4H), 3.23-3.16 (m, PCH<sub>2</sub>N, 2H), 2.34 (dt, <sup>3</sup>J<sub>H-H</sub> = 8,8 Hz, <sup>3</sup>J<sub>H-H</sub> = 1.7 Hz, Ru-C=CHCH<sub>2</sub>CH<sub>2</sub>O, 2H), 2.27-2.19 (m, Cy-H, 2H), 2.03-1.74 (m, Cy-H, 8H), 1.62-1.48 (m, Cy-H, 2H), 1.45-1.26 (m, Cy-H, 10H).

### 3.4.7 General Catalytic Procedure for Hydrofunctionalization Reactions to Obtain *In Situ* Conversions

In a glovebox a stock solution of substrate and **DMT** was prepared: Substrate (120 mM) and **DMT** (20 mM) in C<sub>6</sub>D<sub>5</sub>Br. Two catalyst stock solutions, **a** and **b**, were prepared: **3-Ru2** (**a** = 12 mM and **b** = 3 mM) in C<sub>6</sub>D<sub>5</sub>Br. An NMR tube was charged with the substrate/**DMT** stock solution (500 μL) and an initial <sup>1</sup>H NMR spectrum was obtained (Time = 0 for *in situ* yields). Then either catalyst stock solution **a** or **b** (100 μL) was added to the NMR tube and inverted to mix. The final reaction concentrations were as follows: **a**) 100 mM substrate, 16.7 mM **DMT**, and 2 mol% **3-Ru2** or **b**) 100 mM substrate, 16.7 mM **DMT** and 0.5 mol% **Ru2**. The NMR tubes were heated in an oil bath at 70 °C over 24 hours and analyzed by <sup>1</sup>H NMR spectroscopy at the 24 h mark. The resulting NMR spectra

were analyzed by relative integration of the **DMT** signal at 8.32 ppm to a diagnostic signal for the substrate to determine *in situ* conversion.

### 3.5 References

1. (a) Chung, L.-H.; Yeung, C.-F.; Wong, C.-Y., *Chemistry – A European Journal* **2020**, *26* (28), 6102-6112; (b) Huang, L.; Arndt, M.; Gooßen, K.; Heydt, H.; Gooßen, L. J., *Chem. Rev.* **2015**, *115* (7), 2596-2697; (c) Roh, S. W.; Choi, K.; Lee, C., *Chem. Rev.* **2019**, *119* (6), 4293-4356; (d) Trost, B. M.; McClory, A., *Chem. Asian J.* **2008**, *3* (2), 164-194; (e) Bruneau, C.; Dixneuf, P. H., *Acc. Chem. Res.* **1999**, *32* (4), 311-323.
2. (a) Grotjahn, D. B., *Top. Catal.* **2010**, *53* (15), 1009-1014; (b) Arita, A. J.; Cantada, J.; Grotjahn, D. B.; Cooksy, A. L., *Organometallics* **2013**, *32* (23), 6867-6870; (c) Breit, B.; Gellrich, U.; Li, T.; Lynam, J. M.; Milner, L. M.; Pridmore, N. E.; Slattery, J. M.; Whitwood, A. C., *Dalton Trans.* **2014**, *43* (29), 11277-11285; (d) Boeck, F.; Kribber, T.; Xiao, L.; Hintermann, L., *J. Am. Chem. Soc.* **2011**, *133* (21), 8138-8141; (e) Stubbs, J. M.; Bow, J. P. J.; Hazlehurst, R. J.; Blacquiere, J. M., *Dalton Trans.* **2016**, *45* (43), 17100-17103.
3. Cai, T.; Yang, Y.; Li, W.-W.; Qin, W.-B.; Wen, T.-B., *Chemistry – A European Journal* **2018**, *24* (7), 1606-1618.
4. Liu, P. N.; Wen, T. B.; Ju, K. D.; Sung, H. H. Y.; Williams, I. D.; Jia, G., *Organometallics* **2011**, *30* (9), 2571-2580.
5. Liu, P. N.; Su, F. H.; Wen, T. B.; Sung, H. H. Y.; Williams, I. D.; Jia, G., *Chemistry – A European Journal* **2010**, *16* (26), 7889-7897.
6. (a) Chapple, D. E.; Boyle, P. D.; Blacquiere, J. M., *ChemCatChem* **2021**, *13* (17), 3789-3800; (b) Stubbs, J. M.; Chapple, D. E.; Boyle, P. D.; Blacquiere, J. M., *ChemCatChem* **2018**, *10* (17), 4001-4009.
7. Bow, J.-P. J.; Boyle, P. D.; Blacquiere, J. M., *Eur. J. Inorg. Chem.* **2015**, *2015* (25), 4162-4166.
8. (a) Kanzian, T.; Nigst, T. A.; Maier, A.; Pichl, S.; Mayr, H., *Eur. J. Org. Chem.* **2009**, *2009* (36), 6379-6385; (b) Brotzel, F.; Chu, Y. C.; Mayr, H., *J. Org. Chem.* **2007**, *72* (10), 3679-3688.
9. Nishio, M., *CrystEngComm* **2004**, *6* (27), 130-158.
10. Stubbs, J. M.; Bridge, B. J.; Blacquiere, J. M., *Dalton Trans.* **2019**, *48* (22), 7928-7937.
11. Pickup, O. J. S.; Khazal, I.; Smith, E. J.; Whitwood, A. C.; Lynam, J. M.; Bolaky, K.; King, T. C.; Rawe, B. W.; Fey, N., *Organometallics* **2014**, *33* (7), 1751-1761.

12. Pati, K.; Liu, R.-S., *Chem. Commun.* **2009**, (35), 5233-5235.
13. (a) Nielsen, C. D. T.; Burés, J., *Chemical Science* **2019**, *10* (2), 348-353; (b) Burés, J., *Angew. Chem. Int. Ed.* **2016**, *55* (52), 16084-16087; (c) Blackmond, D. G., *Angew. Chem., Int. Ed.* **2005**, *44* (28), 4302-4320.
14. Burés, J., *Top. Catal.* **2017**, *60* (8), 631-633.
15. Arndt, M.; Salih, K. S. M.; Fromm, A.; Goossen, L. J.; Menges, F.; Niedner-Schatteburg, G., *J. Am. Chem. Soc.* **2011**, *133* (19), 7428-7449.
16. (a) Gómez-Gallego, M.; Sierra, M. A., *Chem. Rev.* **2011**, *111* (8), 4857-4963; (b) Bender, B. R., *J. Am. Chem. Soc.* **1995**, *117* (45), 11239-11246.
17. (a) Bruce, M. I.; Swincer, A. G.; Thompson, B. J.; Wallis, R. C., *Aust. J. Chem.* **1980**, *33* (12), 2605-2613; (b) Beddoes, R. L.; Grime, R. W.; Hussain, Z. I.; Whiteley, M. W., *J. Organomet. Chem.* **1996**, *526* (2), 371-378; (c) Gamasa, M. P.; Gimeno, J.; Martín-Vaca, B. M.; Isea, R.; Vegas, A., *J. Organomet. Chem.* **2002**, *651* (1), 22-33; (d) Hansen, H. D.; Nelson, J. H., *Organometallics* **2000**, *19* (23), 4740-4755.
18. Duraczyńska, D.; Nelson, J. H., *Dalton Trans.* **2003**, (3), 449-457.
19. (a) Schilling, B. E. R.; Hoffmann, R.; Lichtenberger, D. L., *J. Am. Chem. Soc.* **1979**, *101* (3), 585-591; (b) Kostic, N. M.; Fenske, R. F., *J. Am. Chem. Soc.* **1982**, *104* (14), 3879-3884; (c) Kostic, N. M.; Fenske, R. F., *Organometallics* **1982**, *1* (7), 974-982.
20. Wong, C.-Y.; Lai, L.-M.; Lam, C.-Y.; Zhu, N., *Organometallics* **2008**, *27* (22), 5806-5814.
21. (a) Hall, H. K., *J. Am. Chem. Soc.* **1957**, *79* (20), 5439-5441; (b) Kaljurand, I.; Lilleorg, R.; Murumaa, A.; Mishima, M.; Burk, P.; Koppel, I.; Koppel, I. A.; Leito, I., *J. Phys. Org. Chem.* **2013**, *26* (2), 171-181.
22. Orthaber, A.; Karnahl, M.; Tschierlei, S.; Streich, D.; Stein, M.; Ott, S., *Dalton Trans.* **2014**, *43* (11), 4537-4549.
23. Wang, P.; Wang, F.-F.; Chen, Y.; Niu, Q.; Lu, L.; Wang, H.-M.; Gao, X.-C.; Wei, B.; Wu, H.-W.; Cai, X.; Zou, D.-C., *Journal of Materials Chemistry C* **2013**, *1* (32), 4821-4825.
24. Wang, L.; Liu, L.; Chang, W.; Li, J., *J. Org. Chem.* **2018**, *83* (15), 7799-7813.
25. Okamoto, N.; Miwa, Y.; Minami, H.; Takeda, K.; Yanada, R., *Angew. Chem., Int. Ed.* **2009**, *48* (51), 9693-9696.
26. Kundu, N. G.; Nandi, B., *J. Org. Chem.* **2001**, *66* (13), 4563-4575.

27. Karunanidhi, S.; Karpoormath, R.; Bera, M.; Rane, R. A.; Palkar, M. B., *J. Heterocycl. Chem.* **2016**, *53* (5), 1611-1616.

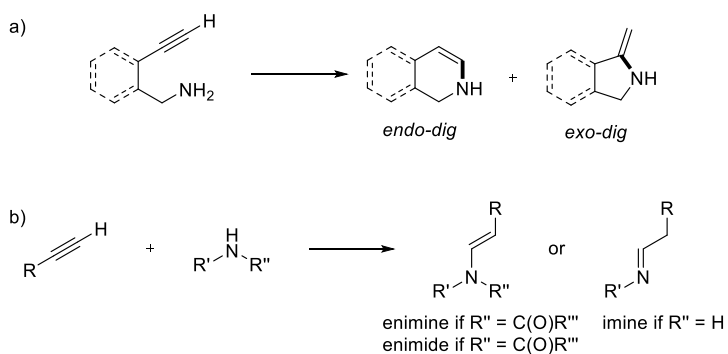
## Chapter 4

### 4 Isolation and Reactivity of Ruthenium Vinylidene Complexes

The synthesis and isolation of  $[\text{Ru}(\text{Cp})(\text{P}^{\text{Cy}}_2\text{N}^{\text{Ph}}_2)(=\text{C}=\text{CHPh})\text{PF}_6$  and  $[\text{Ru}(\text{Cp}^*)(\text{P}^{\text{Cy}}_2\text{N}^{\text{Cy}}_2)(=\text{C}=\text{CHPh})\text{PF}_6$  was successfully accomplished. Utilization of these ruthenium vinylidene complexes for stoichiometric reactions with a variety of alkyl amines was performed. Upon reaction with alkyl amines deprotonation of the  $\text{C}_\beta$  hydrogen resulted in formation of  $[\text{Ru}(\text{Cp})(\text{P}^{\text{Cy}}_2\text{N}^{\text{Ph}}_2)(-\text{C}\equiv\text{CPh})]$  was observed. Independent synthesis of the acetylide complex was performed to confirm formation of the species. Stoichiometric investigation of aniline with  $[\text{Ru}(\text{Cp}^*)(\text{P}^{\text{Cy}}_2\text{N}^{\text{Cy}}_2)(=\text{C}=\text{CHPh})\text{PF}_6$  was also performed which showed distinctly different reactivity as compared to the alkyl amines. Catalytic intermolecular hydroamination of phenylacetylene was attempted with both aniline and 2-pyrrolidinone, which showed no reactivity.

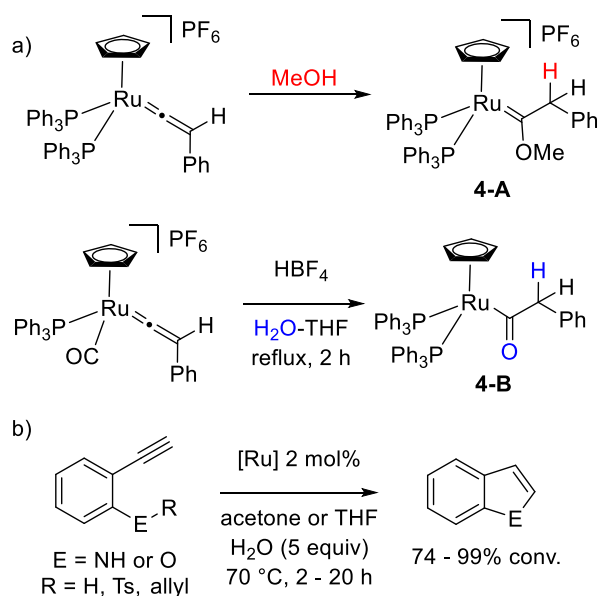
#### 4.1 Introduction

Transition metal catalyzed hydroamination of alkynes has been established as an attractive route to generate a variety of nitrogen containing compounds.<sup>1</sup> Intramolecular hydroamination has garnered much attention due to its ability to generate nitrogen heterocycles (Scheme 4-1a).<sup>2</sup> Intermolecular hydroamination has also been investigated due to the array of enamines, enamides, and imines that are accessible (Scheme 4-1b). The usefulness of enamines, enamides, and imines cannot be understated as they are key reactive intermediates that can be utilized for a variety of subsequent reactions such as: asymmetric hydrogenations<sup>3</sup>, cross-couplings<sup>4</sup>, C-H functionalization<sup>5</sup>, Mannich reactions<sup>6</sup>, and many others.<sup>1b</sup> However, the difficulty associated with intermolecular reactivity lies in the reaction being entropically disfavoured, both from a standpoint of the formation of one product from two and not having close proximity of the nucleophile and electrophile, both of which are circumvented in intramolecular reactivity. Aliphatic amines have continued to be a challenge for late transition metal catalyzed hydroamination reactions due to their prevalence for strong coordination to the catalyst.<sup>1b</sup>



**Scheme 4-1.** Intra- vs Intermolecular hydroamination of terminal alkynes.

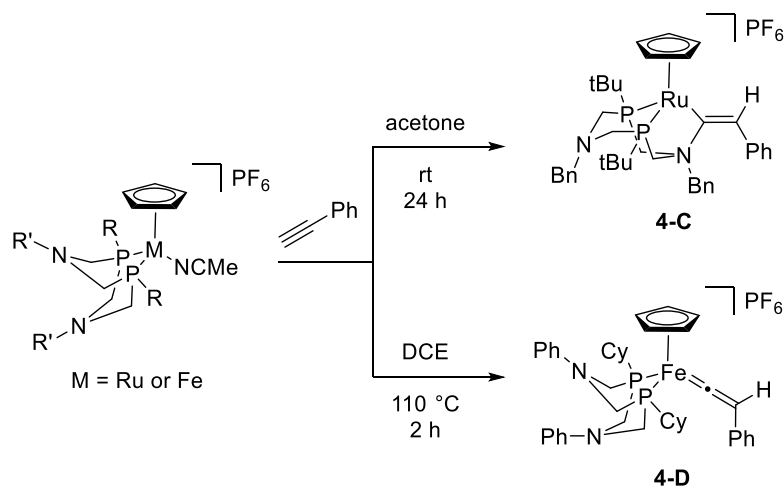
Metal vinylidenes have been established as attractive intermediates for catalytic reactions due to the highly electrophilic nature of the carbon bound to the metal ( $C_\alpha$ ), and the nucleophilic nature of  $C_\beta$ .<sup>1c, 1d, 7</sup> Metal vinylidenes are most easily accessed through coordination of an alkyne and subsequent isomerization to form the vinylidene. Many different transition metal complexes have been shown to form vinylidenes, however, we will specifically focus on ruthenium complexes. The utilization of ruthenium vinylidenes for stoichiometric reactions with various exogenous nucleophiles has previously been investigated. The addition of methanol and water through stoichiometric hydroalkoxylation reactions has previously been established which resulted in the formation of the ruthenium carbene and acyl complexes **4-A** and **4-B**, respectively (Scheme 4-2a).<sup>7c</sup> Certain hydroamination transition metal catalysts have been proposed to proceed through vinylidene intermediates.<sup>8</sup> The benefit of utilizing a catalyst which proceeds through a vinylidene intermediate is increased selectivity for the *endo-dig* cyclized product for intramolecular hydroamination or *anti*-Markovnikov addition for intermolecular hydroamination. Grotjahn *et al.* investigated the use of a bifunctional ruthenium complex for the cyclization of various indole and phenol derivatives (Scheme 4-2b).<sup>8b</sup> The advantageous selectivity achievable through proposed vinylidene intermediates has been suggested in further catalytic investigations by others.<sup>8d, 9</sup>



**Scheme 4-2.** Stoichiometric reactions with vinylidenes and ruthenium catalyzed hydroamination proposed to proceed through vinylidene intermediate.

We have previously investigated a family of  $[\text{Ru}(\text{Cp}/\text{Cp}^*)(\text{P}^{\text{R}}_2\text{N}^{\text{R}'}_2)(\text{MeCN})]\text{PF}_6$  (Cp = cyclopentadienyl, Cp\* = pentamethylcyclopentadienyl,  $\text{P}^{\text{R}}_2\text{N}^{\text{R}'}_2 = 1,5\text{-R}'\text{-}3,7\text{-R-}1,5\text{-diaz-}3,7\text{-diphosphacyclooctane}$ ) complexes for *intramolecular* hydrofunctionalization reactions (hydroamination, hydroamidation, and hydroalkoxylation) to generate a variety of 5- and 6-membered *endo-dig* heterocycles.<sup>10</sup> However, intermolecular hydroamination has not yet been realized for these complexes. A previous attempt to isolate the ruthenium vinylidene species, a key proposed intermediate, from  $[\text{Ru}(\text{Cp})(\text{P}^{\text{tBu}}_2\text{N}^{\text{Bn}}_2)(\text{MeCN})]\text{PF}_6$  was unsuccessful.<sup>11</sup> Instead, formation of the vinylammonium species **4-C**, due to nucleophilic attack of the pendent amine was observed, which we hypothesized was due to its nucleophilic strength and the flexibility of the benzyl substituent (Scheme 3). We recently investigated a catalyst derivative which varied the phosphorus (from R = tBu to Cy) and nitrogen substituents (from R' = Bn to Ph) which avoided this deactivation species, based on catalytic data and variable time normalization analysis.<sup>10e</sup> We hypothesized that the modification of the pendent amine substituent from benzyl to phenyl was paramount in the mitigation of vinyl ammonium formation. The influence of this modification would be two-fold: reduce the nucleophilic strength of the pendent amine and increase steric clash to disfavour nucleophilic attack. This was successfully explored through the isolation of the

iron vinylidene complex **4-D** which possessed a phenyl substituent instead of a benzyl substituent on the pendent amine (Scheme 4-3).<sup>12</sup> We hypothesize that in similar fashion, modification of the nitrogen substituent from Bn to Ph in the ruthenium analog would allow isolation of the ruthenium vinylidene complex. Isolation of the vinylidene species would allow stoichiometric reactivity to be investigated and to better understand the nucleophilic attack, integral to intermolecular hydroamination.



**Scheme 4-3.** Formation of vinyl ammonium and vinylidene complexes.

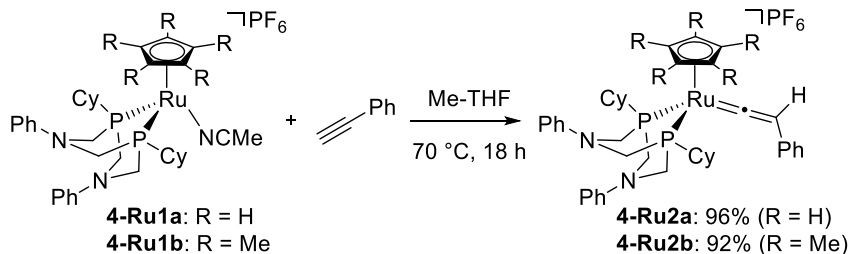
## 4.2 Results and Discussion

### 4.2.1 Synthesis and Characterization of Vinylidene Complexes.

Previously the ruthenium vinylidene species  $[\text{Ru}(\text{Cp})(\text{P}^{\text{Cy}}_2\text{N}^{\text{Ph}}_2)(=\text{C}=\text{CHPh})]\text{PF}_6$  (**4-Ru2a**) was generated *in situ* to evaluate the rate of vinylidene formation. Due to the successful *in situ* formation we attempted the isolation of both **4-Ru2a** and  $[\text{Ru}(\text{Cp}^*)(\text{P}^{\text{Cy}}_2\text{N}^{\text{Ph}}_2)(=\text{C}=\text{CHPh})]\text{PF}_6$  (**4-Ru2b**) from their MeCN adduct analogues **4-Ru1a** and **4-Ru1b**, respectively (Scheme 4-4). The complexes **4-Ru1a-b** were dissolved in Me-THF, charged with phenylacetylene, and heated at 70 °C for 18 h (Scheme 4). The reaction with **4-Ru1a** (Cp) showed quantitative conversion to the new complex **4-Ru2a**, which was observed as a singlet at 45.0 ppm (ca. 1 ppm upfield relative to **4-Ru1a**) in the  $^{31}\text{P}\{^1\text{H}\}$  NMR spectrum. Upon removal of volatiles a solid orange powder was isolated which matched *in situ* formation. Appearance of the diagnostic  $\text{C}_\beta$  proton was observed in the  $^1\text{H}$  NMR spectrum as a triplet at 5.53 ppm.  $^1\text{H}$ - $^{13}\text{C}\{^1\text{H}\}$  HMBC indicated correlation of



the C $_{\beta}$  proton to a significantly downfield carbon signal at 349.6 ppm which matched literature ranges for C $_{\alpha}$  in other vinylidene complexes.<sup>13</sup> The reaction with **4-Ru1b** (Cp\*) also showed quantitative conversion to the new complex **4-Ru2b**, observed as a singlet at 36.8 ppm (ca. 1 ppm downfield shift) in the <sup>31</sup>P{<sup>1</sup>H} NMR spectrum. Removal of volatiles similarly resulted in an orange product, which matched the *in situ* observed <sup>31</sup>P{<sup>1</sup>H} chemical shift of 36.8 ppm when redissolved in solvent. The appearance of the diagnostic C $_{\beta}$  proton was observed at 5.29 ppm, in good agreement with **4-Ru2a**, in the <sup>1</sup>H NMR spectrum. <sup>1</sup>H-<sup>13</sup>C{<sup>1</sup>H} HMBC confirmed correlation to C $_{\alpha}$  346.5 ppm. This data collectively supports the successful isolation of vinylidene complexes **4-Ru2a** and **4-Ru2b**.



**Scheme 4-4.** Synthesis of **4-Ru2a** and **4-Ru2b**.

Single crystals suitable for X-ray diffraction were obtained and confirmed the solid-state structure of **4-Ru2b** (Figure 4-1). The Ru(1)-P(1)/P(2) bond distances (2.2966(9) and 2.2815(8) Å, respectively), and the P(1)-Ru(1)-P(2) bite angle (78.16(2)°) are both similar to the values obtained for **4-Ru1a** and **4-Ru1b**.<sup>10a, 10e</sup> A slight increase of *ca.* 0.5 Å for the Cp\*(centroid)-Ru(1) distance was observed for **4-Ru2b** relative to **4-Ru1b**. This is likely due to the increased steric bulk associated with the vinylidene moiety as compared to a MeCN adduct. Ru(1)-C(39) and C(39)-C(40) bond distances (1.851(3) and 1.316(4) Å, respectively) and Ru(1)-C(39)-C(40) bond angle (176.9(2)°) agree with previously reported Ru-C $_{\alpha}$  (ca. 1.8 Å)/C $_{\alpha}$ -C $_{\beta}$  (ca. 1.3 Å) bond distances and Ru-C $_{\alpha}$ -C $_{\beta}$  (170–176°) bond angles of half sandwich bisphosphine Ru<sup>II</sup>-vinylidene complexes.<sup>13</sup>

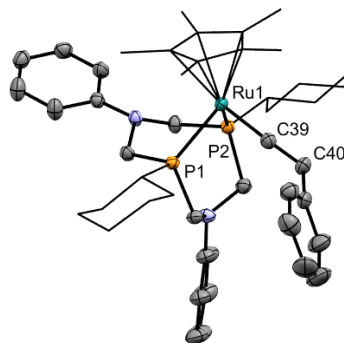
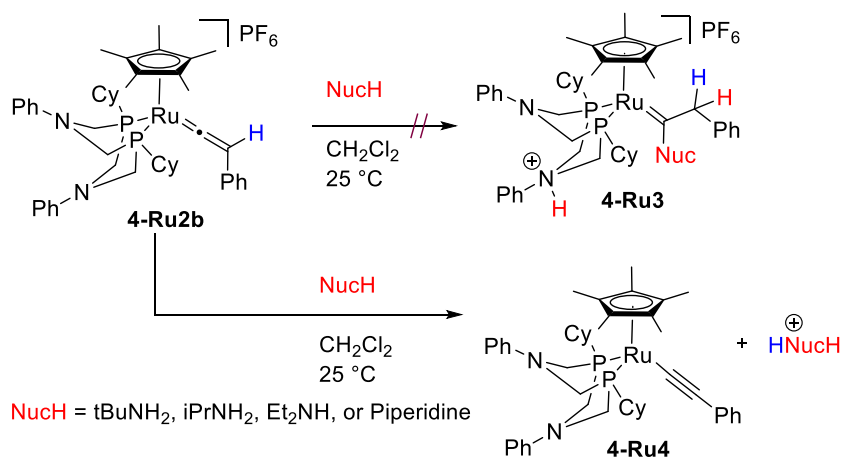


**Figure 4-1.** Displacement ellipsoid plot of complex **4-Ru2b**. Ellipsoids are given at 30% probability level. H atoms (except H40), the  $\text{PF}_6^-$  anion, and a molecule of co-crystallized hexanes were omitted for clarity. Selected bond distances ( $\text{\AA}$ ): Ru(1)-P(1) = 2.2966(9); Ru(1)-P(2) = 2.2815(8); Ru(1)-Cp\*(centroid) = 1.918; Ru(1)-C(39) = 1.851(3); C(39)-C(40) = 1.316(4). Selected Angles ( $^\circ$ ): P(1)-Ru(1)-P(2) = 78.16(2); Ru(1)-C(39)-C(40) = 176.9.

#### 4.2.2 Stoichiometric Reactions of Primary and Secondary Aliphatic Amines with Vinylidenes.

To assess the nucleophilic attack on  $C_\alpha$ , a variety of primary and secondary amines of different nucleophilic strength were targeted. The amines that were investigated were *tert*-butylamine, isopropylamine, diethylamine, and piperidine, which range in nucleophilic strength from 10.5 to 18.1 in Mayr parameter strength.<sup>14</sup> An excess of amine was mixed with **4-Ru2b** in  $\text{CH}_2\text{Cl}_2$  at room temperature and monitored by  $^{31}\text{P}\{^1\text{H}\}$  NMR spectroscopy. We hypothesized that nucleophilic attack by the amine could result in either product release and generation of the coordinatively unsaturated complex or formation of the proposed carbene complex **4-Ru3**, which is analogous to complex **4-A** (Figure 4-5). With all amines tested after 30 minutes a distinct chemical shift change in the  $^{31}\text{P}\{^1\text{H}\}$  NMR spectra was observed from 36.8 ppm to 41.3 ppm. The unknown species at 41.3 ppm did not match the chemical shift value of the previously obtained operationally unsaturated complex.<sup>10a</sup> Although encouraging, it was not expected that the chemical shift for each of these reactions would be identical. We hypothesized that a potential competitive reaction pathway was formation of an acetylide complex **4-Ru4** via deprotonation of  $\text{H}_\beta$ .

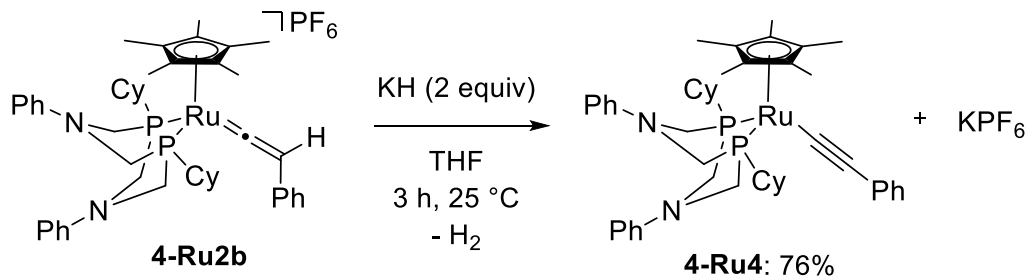


**Scheme 4-5.** Stoichiometric reactions of **4-Ru2b** with amine nucleophiles (50 equiv) which we proposed would generate **4-Ru3** following nucleophilic attack at  $C_\alpha$ . Alternative reaction pathway was formation of the proposed acetylide complex **4-Ru4** following deprotonation of  $C_\beta$  proton.

#### 4.2.3 Independent Synthesis of **Ru4**.

To determine if the acetylide complex, **4-Ru4**, was being generated during the stoichiometric reactions of ruthenium vinylidene with aliphatic amines, an independent synthesis of **4-Ru4** was undertaken. **4-Ru2a** was reacted with KH in THF at room temperature for 3 h (Scheme 4-6). The reaction showed *ca.* 85% conversion to a new species at 40.8 ppm in the  $^{31}\text{P}\{^1\text{H}\}$  NMR spectrum, which was consistent with the species formed during stoichiometric reactions with the aliphatic amines. Isolation of the new species was accomplished by extraction with pentane which dissolved the newly formed product. Disappearance of the  $C_\beta$  hydrogen signal at 5.29 ppm was observed in the  $^1\text{H}$  NMR spectrum, which supports deprotonation of  $\text{H}_\beta$ . Comparison to previously reported half-sandwich ruthenium acetylide complexes shows agreement with the observed  $^{13}\text{C}\{^1\text{H}\}$  NMR chemical shifts for  $C_\alpha$  (131.4 ppm) and  $C_\beta$  (107.5 ppm) to literature ranges of  $C_\alpha$  (128–145 ppm) and  $C_\beta$  (108–116 ppm), respectively.<sup>15</sup> This data collectively supports the formation of the acetylide complex **4-Ru4** which would suggest that **4-Ru2a** in the presence of a stoichiometric base ( $\text{pK}_{\text{aH}} \geq 18$ )<sup>16</sup> will favour deprotonation of  $\text{H}_\beta$  and disfavour nucleophilic attack at  $C_\alpha$ . Formation of **4-Ru4** would shuttle the catalyst off-

cycle, which would be detrimental to hydrofunctionalization catalysis due to either catalyst inhibition or outright deactivation.



**Scheme 4-6.** Independent synthesis of **4-Ru4** generated from deprotonation of **4-Ru2b** with KH in THF at room temperature over 3 h.

#### 4.2.4 Stoichiometric Reaction with Aniline.

We hypothesized that stoichiometric reactions with a less basic amine nucleophile could encourage the desired reactivity. To investigate the proposed hypothesis that an amine with lower basicity could avoid formation of **4-Ru4** the reactivity of **4-Ru2b** with aniline was performed. While the nucleophilic strength of aniline (Mayr parameter strength = 12.6) is similar to that of *tert*-butylamine (Mayr parameter strength = 10.5), the basicity of aniline ( $\text{pK}_{\text{aH}} = 10.56$ ) is significantly lower than *tert*-butylamine ( $\text{pK}_{\text{aH}} = 18.1$ ), which could favour formation of the proposed alkenyl complex **4-Ru5**. An excess of aniline was mixed with **4-Ru2b** in DCM at rt for 30 minutes (Figure 4-2). No reaction was observed by  $^{31}\text{P}\{^1\text{H}\}$  NMR spectroscopy, which was distinctly different from the alkyl amines tested. A second reaction was performed with **4-Ru2b** in  $\text{C}_6\text{D}_5\text{Br}$  with excess aniline and MeCN present. The MeCN was added to stabilize the complex upon organic product release (Figure 4-2). Upon heating the reaction at 90 °C for 2 days three new signals appeared at 39.5, 35.9, and 35.3 ppm along with unreacted vinylidene complex (36.8 ppm). Importantly, no **4-Ru4** was observed and while two of the species formed are unknown, the signal at 35.9 ppm matches the chemical shift of the MeCN adduct, **4-Ru6**, in  $\text{C}_6\text{D}_5\text{Br}$  (Figure 3). One possible explanation could be organic product release, which would result from nucleophilic attack from the amine nucleophile to generate **4-Ru5**. Protonolysis of **4-Ru5** via an intramolecular proton transfer would generate an enamine which would

undergo a tautomerization to form the expected imine product and a coordinatively unsaturated Ru product, which, in the presence of MeCN, would generate **4-Ru6**.

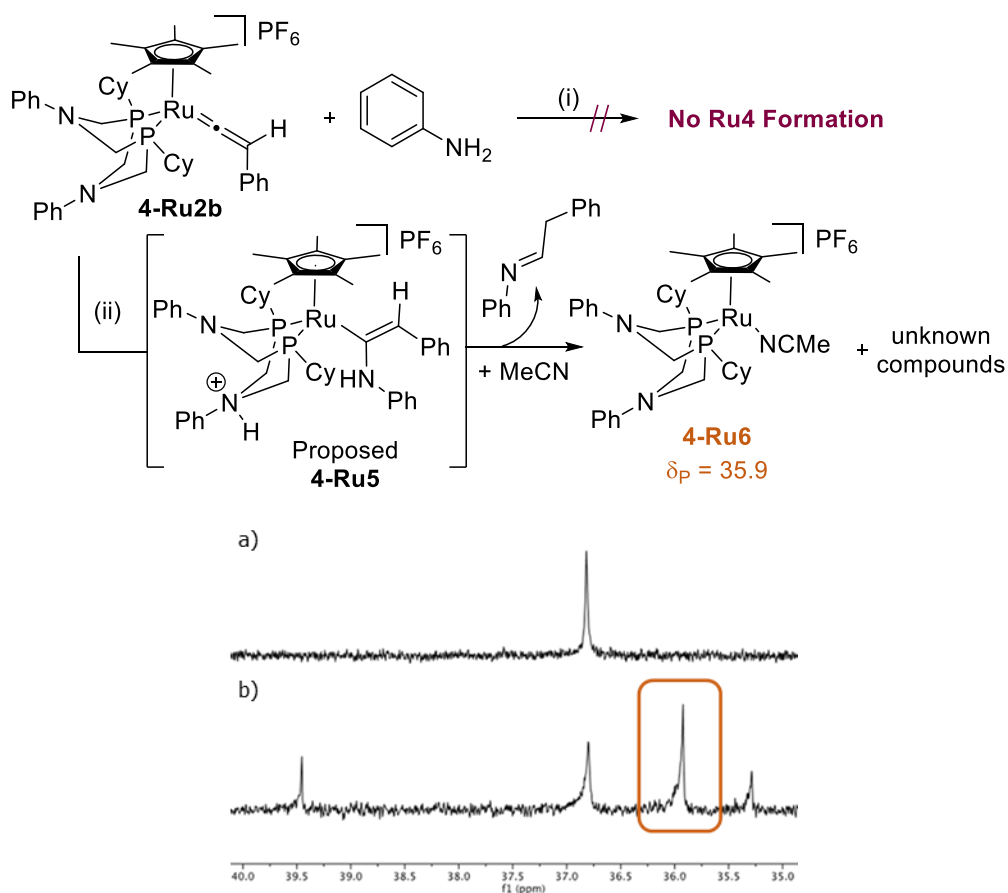
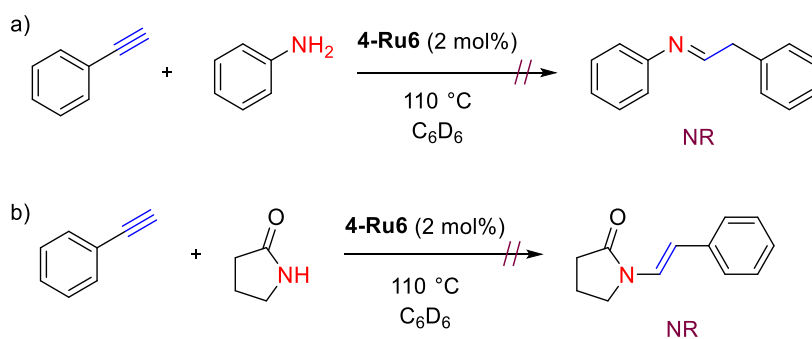


**Figure 4-2.** (top) Stoichiometric reaction of and **4-Ru2b** under conditions: i) DCM, 25 °C, 30 minutes; and ii) MeCN, C<sub>6</sub>D<sub>5</sub>Br, 2 days, 90 °C. (bottom) <sup>31</sup>P{<sup>1</sup>H} NMR spectra stack plot of a) **4-Ru2b** in C<sub>6</sub>D<sub>5</sub>Br and b) after reaction under conditions ii. Orange box highlights MeCN adduct **4-Ru6**.

#### 4.2.5 Attempted Intermolecular Hydroamination.

With the change in stoichiometric reactivity of **4-Ru2b** with aniline as compared to aliphatic amines, an attempt at catalytic intermolecular hydroamination with phenylacetylene and aniline was performed. No intermolecular hydroamination was observed with 2 mol% **4-Ru6** at 110 °C in C<sub>6</sub>D<sub>6</sub> over 24 h (Scheme 4-7a), with negligible consumption of phenylacetylene and no evidence of the desired imine product. The

secondary amide 2-pyrrolidinone was also tested under analogous conditions to the reaction with aniline (Scheme 4-7b). We hypothesized that the reduced basicity of the amide as compared to the aliphatic amines could also disfavor deprotonation of  $H_{\beta}$  of the vinylidene. The reaction was monitored over 24 h, which showed no consumption of either substrate and no evidence of the desired enamide product. The lack of reactivity observed for both aniline and 2-pyrrolidinone could suggest competitive coordination of the nitrogen heteroatom to the metal center. However, these aniline/2-pyrrolidinone adducts should be in equilibrium with the active catalyst as we previously observed product inhibition with indole, which did not deactivate the catalyst.<sup>10a</sup> Therefore, nucleophile inhibition seems unlikely to be the sole cause of unproductive reactivity for these substrates. Another possible reason could be formation of the respective **4-Ru3** carbene complexes. Previous attempted cyclization of 3-butyn-1-ol resulted in complete deactivation of  $[\text{Ru}(\text{Cp})(\text{P}^{\text{Cy}}_2\text{N}^{\text{Ph}}_2)(\text{MeCN})]\text{PF}_6$  and the formation of a ruthenium alkoxy-carbene complex which was irreversible and inhibited intramolecular hydrofunctionalization.<sup>10e</sup>



**Scheme 4-7.** Attempted intermolecular hydroamination of phenylacetylene with (top) aniline and (bottom) 2-pyrrolidinone with 2 mol% **4-Ru6** at 110 °C in  $\text{C}_6\text{D}_6$ .

#### 4.2.6 Conclusion

Two ruthenium vinylidene complexes, **4-Ru2a** and **4-Ru2b**, were successfully isolated and characterized. Stoichiometric reactivity was explored for **4-Ru2b** with a variety of primary and secondary alkyl amines. In all cases the reaction proceeded through an undesirable pathway following deprotonation of the  $\text{C}_{\beta}$  hydrogen, which generated the acetylide complex **4-Ru4**. The identity of **4-Ru4** was confirmed through independent synthesis.

Stoichiometric reactivity with the aromatic amine aniline was also explored, which did not form **4-Ru4** under analogous conditions to the stoichiometric reactions with the aliphatic amines. Upon heating this reaction, the generation of two unknown species along with **4-Ru6** (MeCN adduct) were observed. The generation of **4-Ru6** was suggestive of successful product release, which encouraged investigation into attempted catalysis. Intermolecular hydroamination and hydroamidation was attempted with aniline and 2-pyrrolidinone, respectively, with **4-Ru6** and phenylacetylene, which, in both cases, showed no signs of intermolecular catalysis. We hypothesize that lack of productive reactivity could be due to formation of a Ru-carbene complex which has previously been established as a deactivation pathway.

## 4.3 Experimental Section

### 4.3.1 General Procedure for the Synthesis of Vinylidene Complexes [Ru(Cp/Cp\*)(P<sup>Cy</sup><sub>2</sub>N<sup>Ph</sup><sub>2</sub>)(=C=HPh)]PF<sub>6</sub>, **4-Ru2a** (Cp) and **4-Ru2b** (Cp\*)

A 100 mL Schlenk flask was charged with a stir bar, [Ru(Cp)(P<sup>Cy</sup><sub>2</sub>N<sup>Ph</sup><sub>2</sub>)(MeCN)][PF<sub>6</sub>] or [Ru(Cp\*)(P<sup>Cy</sup><sub>2</sub>N<sup>Ph</sup><sub>2</sub>)(MeCN)][PF<sub>6</sub>] (0.047 mmol), phenylacetylene (0.15 mmol, 3 equiv), and Me-THF. The flask was heated under a flow of argon at 70 °C for 18 h after which quantitative conversion was observed by <sup>31</sup>P{<sup>1</sup>H} NMR spectroscopy. The solvent was then removed *in vacuo* and the solid residue was transferred into a glovebox. The solid was then dissolved in CH<sub>2</sub>Cl<sub>2</sub>, filtered through a microfibre pipette filter, and the solvent was removed *in vacuo*. The solid was washed with diethyl ether (3 x 5 mL) and further dried *in vacuo* to remove any residual solvent.

**[Ru(Cp)(P<sup>Cy</sup><sub>2</sub>N<sup>Ph</sup><sub>2</sub>)(=C=HPh)][PF<sub>6</sub>] (4-Ru2a)**. Yield = 96%. <sup>1</sup>H NMR (600 MHz, CD<sub>2</sub>Cl<sub>2</sub>) δ 7.41–7.26 (m, C<sub>6</sub>H<sub>5</sub>, 6H), 7.19–7.14 (m, C<sub>6</sub>H<sub>5</sub>, 1H), 7.11–6.98 (m, C<sub>6</sub>H<sub>5</sub>, 8H), 5.61 (s, Ru(C<sub>5</sub>H<sub>5</sub>), 5H), 5.52 (t, J<sub>H-P</sub> = 2.6 Hz, Ru=C=CHPh, 1H), 3.78–3.74 (m, PCH<sub>2</sub>N, 4H), 3.74–3.69 (m, PCH<sub>2</sub>N, 2H), 3.63–3.59 (m, PCH<sub>2</sub>N, 2H), 2.03–1.78 (m, C<sub>6</sub>H<sub>11</sub>, 14H), 1.41–1.35 (m, C<sub>6</sub>H<sub>11</sub>, 6H), 1.13–1.04 (m, C<sub>6</sub>H<sub>11</sub>, 2H). <sup>13</sup>C{<sup>1</sup>H} NMR (151 MHz, CD<sub>2</sub>Cl<sub>2</sub>): δ 349.6 (Ru=C=CHPh), 153.2 (t, C<sub>6</sub>H<sub>5</sub>, <sup>3</sup>J<sub>C-P</sub> = 8.6 Hz), 151.5 (t, C<sub>6</sub>H<sub>5</sub>, <sup>3</sup>J<sub>C-P</sub> = 8.6 Hz), 130.5 (s, C<sub>6</sub>H<sub>5</sub>), 130.3 (s, C<sub>6</sub>H<sub>5</sub>), 129.5 (s, C<sub>6</sub>H<sub>5</sub>), 127.5 (s, C<sub>6</sub>H<sub>5</sub>), 127.2 (s, C<sub>6</sub>H<sub>5</sub>), 123.9 (s, C<sub>6</sub>H<sub>5</sub>), 122.6 (s, C<sub>6</sub>H<sub>5</sub>), 119.8 (s, C<sub>6</sub>H<sub>5</sub>), 118.3 (s, C<sub>6</sub>H<sub>5</sub>), 117.7 (s, Ru=C=CHPh), 91.0

(s, Ru(C<sub>5</sub>H<sub>5</sub>)), 49.4 (X of ABX, PCH<sub>2</sub>N), 47.3 (X of ABX, PCH<sub>2</sub>N), 42.0 (X of ABX, C<sub>6</sub>H<sub>11</sub>), 29.4 (s, C<sub>6</sub>H<sub>11</sub>), 28.9 (s, C<sub>6</sub>H<sub>11</sub>), 27.3 (X of ABX, C<sub>6</sub>H<sub>11</sub>), 26.9 (X of ABX, C<sub>6</sub>H<sub>11</sub>), 26.3 (s, C<sub>6</sub>H<sub>11</sub>). <sup>31</sup>P{<sup>1</sup>H} NMR (162 MHz, CD<sub>2</sub>Cl<sub>2</sub>): δ 45.0 (s, Ru-P), -144.2 (sept, <sup>1</sup>J<sub>P-F</sub> = 711 Hz, PF<sub>6</sub>) IR (neat) ν(cm<sup>-1</sup>): 2927 (w), 2853 (w), 1973 (w), 1721 (m), 1593 (m), 1194 (m), 833 (s), 743 (m), 694 (m), 556 (m). MALDI MS (pyrene matrix): Calc. *m/z* = 735.2 [Ru(Cp)(P<sup>Cy</sup><sub>2</sub>N<sup>Ph</sup><sub>2</sub>)(=C=CHPh)]<sup>+</sup>. Obs. *m/z* = 735.3.

**[Ru(Cp\*)(P<sup>Cy</sup><sub>2</sub>N<sup>Ph</sup><sub>2</sub>)(=C=HPh)][PF<sub>6</sub>] (4-Ru2b).** Yield = 92%. <sup>1</sup>H NMR (600 MHz, CD<sub>2</sub>Cl<sub>2</sub>): δ 7.41–7.37 (m, C<sub>6</sub>H<sub>5</sub>, 2H), 7.34–7.28 (m, C<sub>6</sub>H<sub>5</sub>, 4H), 7.18–7.14 (m, C<sub>6</sub>H<sub>5</sub>, 3H), 7.13–7.10 (m, C<sub>6</sub>H<sub>5</sub>, 2H), 7.07–7.03 (m, C<sub>6</sub>H<sub>5</sub>, 1H), 6.98–6.90 (m, C<sub>6</sub>H<sub>5</sub>, 2H), 5.28 (t, *J*<sub>H-P</sub> = 3.6 Hz, Ru=C=CHPh, 1H), 3.89–3.83 (m, PCH<sub>2</sub>N, 2H), 3.82–3.76 (m, PCH<sub>2</sub>N, 2H), 3.72–3.64 (m, PCH<sub>2</sub>N, 2H), 3.40–3.35 (m, PCH<sub>2</sub>N, 2H), 2.06–2.00 (m, C<sub>6</sub>H<sub>11</sub>, 2H), 1.97 (s, Ru(C<sub>5</sub>(CH<sub>3</sub>)<sub>5</sub>), 15H), 1.96–1.88 (m, C<sub>6</sub>H<sub>11</sub>, 5H), 1.85–1.76 (m, C<sub>6</sub>H<sub>11</sub>, 4H), 1.50–1.41 (m, C<sub>6</sub>H<sub>11</sub>, 4H), 1.38–1.30 (m, C<sub>6</sub>H<sub>11</sub>, 2H), 1.28–1.21 (m, C<sub>6</sub>H<sub>11</sub>, 2H), 1.02–0.92 (m, C<sub>6</sub>H<sub>11</sub>, 2H). <sup>13</sup>C{<sup>1</sup>H} NMR (151 MHz, CD<sub>2</sub>Cl<sub>2</sub>): δ 346.5 (Ru=C=CHPh), 153.6 (t, C<sub>6</sub>H<sub>5</sub>, <sup>3</sup>J<sub>C-P</sub> = 7.8 Hz), 152.0 (t, C<sub>6</sub>H<sub>5</sub>, <sup>3</sup>J<sub>C-P</sub> = 10.8 Hz), 130.4 (s, C<sub>6</sub>H<sub>5</sub>), 129.5 (s, C<sub>6</sub>H<sub>5</sub>), 129.3 (s, C<sub>6</sub>H<sub>5</sub>), 128.9 (s, C<sub>6</sub>H<sub>5</sub>), 127.3 (s, C<sub>6</sub>H<sub>5</sub>), 127.1 (s, C<sub>6</sub>H<sub>5</sub>), 123.9 (s, C<sub>6</sub>H<sub>5</sub>), 123.0 (s, C<sub>6</sub>H<sub>5</sub>), 119.8 (s, C<sub>6</sub>H<sub>5</sub>), 118.1 (s, C<sub>6</sub>H<sub>5</sub>), 115.1 (s, Ru=C=CHPh), 104.1 (s, Ru(C<sub>5</sub>(CH<sub>3</sub>)<sub>5</sub>), 46.9 (X of ABX, PCH<sub>2</sub>N), 46.8 (X of ABX, PCH<sub>2</sub>N), 46.6 (X of ABX, PCH<sub>2</sub>N), 46.4 (X of ABX, PCH<sub>2</sub>N), 39.6 (X of ABX, C<sub>6</sub>H<sub>11</sub>), 29.0 (s, C<sub>6</sub>H<sub>11</sub>), 27.7 (X of ABX, C<sub>6</sub>H<sub>11</sub>), 27.5 (X of ABX, C<sub>6</sub>H<sub>11</sub>), 27.3 (X of ABX, C<sub>6</sub>H<sub>11</sub>), 26.3 (s, C<sub>6</sub>H<sub>11</sub>), 11.1 (s, Ru(C<sub>5</sub>(CH<sub>3</sub>)<sub>5</sub>)). <sup>31</sup>P{<sup>1</sup>H} NMR (162 MHz, CD<sub>2</sub>Cl<sub>2</sub>): δ 36.8 (s, Ru-P), -143.9 (sept, <sup>1</sup>J<sub>P-F</sub> = 711 Hz, PF<sub>6</sub>). IR (neat) ν(cm<sup>-1</sup>): 2923 (w), 2852 (w), 1953 (w), 1575 (m), 1491 (m), 1192 (m), 833 (s), 758 (m), 693 (m), 539 (m). MALDI MS (pyrene matrix): Calc. *m/z* = 804.3 [Ru(Cp\*)(P<sup>Cy</sup><sub>2</sub>N<sup>Ph</sup><sub>2</sub>)(=C=CHPh)]<sup>+</sup>. Obs. *m/z* = 803.9.

#### 4.3.2 General Procedure for Stoichiometric Reaction of Vinylidenes with Amine Nucleophiles.

A 4 mL vial was charged with **4-Ru2b** (5 mg, 0.005 mmol) and dissolved in CH<sub>2</sub>Cl<sub>2</sub> (600 μL). The solution was transferred to an NMR tube and a T0 <sup>31</sup>P{<sup>1</sup>H} NMR spectrum was obtained. The NMR tube was then charged with amine (0.026 mmol, 50 equiv) and the



NMR tube was subsequently capped, inverted to mix, and left at room temperature (ca. 25 °C). The reaction was monitored by  $^{31}\text{P}\{^1\text{H}\}$  NMR spectroscopy after 30 minutes.

#### 4.3.3 Procedure for the Independent Synthesis of Acetylide Complex $[\text{Ru}(\text{Cp})(\text{P}^{\text{Cy}}_2\text{N}^{\text{Ph}}_2)(-\text{C}\equiv\text{C}-\text{Ph})]\text{PF}_6$ (**4-Ru4**).

A 4 mL vial was charged with **Ru2b** (15 mg, 0.016 mmol) and dissolved in THF (1 mL). KH (7 mg, 0.17 mmol, 10 equiv) was added as a suspension in THF (1 mL) and the reaction was stirred at room temperature for 3 h. The solution was filtered through Celite, and the filter was subsequently washed with THF until the washings were clear. The filtrate was collected and the solvent removed *in vacuo* to obtain a red solid. The solid was washed with pentane and the yellow tinted pentane was collected in a separate 20 mL vial. The solvent was removed from the collected pentane washes *in vacuo* to obtain the desired product as a yellow solid. Yield = 76%.  $^1\text{H}$  NMR (600 MHz,  $\text{CD}_2\text{Cl}_2$ ):  $\delta$  7.27–7.19 (m,  $\text{C}_6\text{H}_5$ , 4H), 7.10–7.03 (m,  $\text{C}_6\text{H}_5$ , 6H), 6.96–6.92 (m,  $\text{C}_6\text{H}_5$ , 2H), 6.89–6.85 (m,  $\text{C}_6\text{H}_5$ , 1H), 6.84–6.79 (m,  $\text{C}_6\text{H}_5$ , 2H), 4.22–4.16 (m,  $\text{PCH}_2\text{N}$ , 2H), 3.70–3.59 (m,  $\text{PCH}_2\text{N}$ , 4H), 3.04–2.98 (m,  $\text{PCH}_2\text{N}$ , 2H), 2.51–2.43 (m,  $\text{C}_6\text{H}_{11}$ , 2H), 2.07–1.98 (m,  $\text{C}_6\text{H}_{11}$ , 4H), 1.93–1.87 (m,  $\text{C}_6\text{H}_{11}$ , 4H), 1.85 (s,  $\text{Ru}(\text{C}_5(\text{CH}_3)_5)$ , 15H), 1.79–1.73 (m,  $\text{C}_6\text{H}_{11}$ , 2H), 1.56–1.47 (m,  $\text{C}_6\text{H}_{11}$ , 2H), 1.46–1.38 (m,  $\text{C}_6\text{H}_{11}$ , 2H), 1.37–1.29 (m,  $\text{C}_6\text{H}_{11}$ , 4H), 1.13–1.05 (m,  $\text{C}_6\text{H}_{11}$ , 2H).  $^{13}\text{C}\{^1\text{H}\}$  NMR (151 MHz,  $\text{CD}_2\text{Cl}_2$ ):  $\delta$  154.5 (m,  $\text{C}_6\text{H}_5$ ), 153.6 (m,  $\text{C}_6\text{H}_5$ ), 131.4 (s,  $\text{Ru}-\text{C}\equiv\text{CPh}$ ), 129.8 (s,  $\text{C}_6\text{H}_5$ ), 129.1 (s,  $\text{C}_6\text{H}_5$ ), 129.0 (s,  $\text{C}_6\text{H}_5$ ), 127.7 (s,  $\text{C}_6\text{H}_5$ ), 121.9 (s,  $\text{C}_6\text{H}_5$ ), 119.8 (s,  $\text{C}_6\text{H}_5$ ), 119.0 (s,  $\text{C}_6\text{H}_5$ ), 117.3 (s,  $\text{C}_6\text{H}_5$ ), 115.6 (s,  $\text{C}_6\text{H}_5$ ), 107.5 (s,  $\text{Ru}-\text{C}\equiv\text{C}-\text{Ph}$ ), 92.5 (s,  $\text{Ru}(\text{C}_5(\text{CH}_3)_5)$ , 45.6 (X of ABX,  $\text{PCH}_2\text{N}$ ), 43.8 (X of ABX,  $\text{PCH}_2\text{N}$ ), 40.8 (X of ABX,  $\text{C}_6\text{H}_{11}$ ), 27.6 (s,  $\text{C}_6\text{H}_{11}$ ), 27.4 (X of ABX,  $\text{C}_6\text{H}_{11}$ ), 27.3 (X of ABX,  $\text{C}_6\text{H}_{11}$ ), 26.6 (s,  $\text{C}_6\text{H}_{11}$ ), 10.8 (s,  $\text{Ru}(\text{C}_5(\text{CH}_3)_5)$ ).  $^{31}\text{P}\{^1\text{H}\}$  NMR (243 MHz,  $\text{CD}_2\text{Cl}_2$ ):  $\delta$  40.8 ( $\text{Ru}-\text{P}$ ). IR (neat)  $\nu$  ( $\text{cm}^{-1}$ ): 3052 (w), 2948 (w), 2869(w), 1613 (m), 1522 (w), 1330 (s), 1117 (m), 638 (m). MALDI-MS (pyrene matrix): Calc.  $m/z$  = 804.3  $[\text{Ru}(\text{Cp})(\text{P}^{\text{Cy}}_2\text{N}^{\text{Ph}}_2)(-\text{C}\equiv\text{C}-\text{Ph})]^+$ . Obs.  $m/z$  = 803.9.

#### 4.3.4 General Procedure for Attempted Catalytic Intermolecular Hydroamination.

In a glovebox, a substrate stock solution of phenylacetylene, nucleophile (aniline or 2-pyrrolidinone), and IS (dimethyl terephthalate) was prepared with the concentrations of:

phenylacetylene (120 mM), nucleophile (120 mM), and dimethyl terephthalate (20 mM) in C<sub>6</sub>D<sub>6</sub>. A catalyst stock solution was prepared: **4-Ru6** in C<sub>6</sub>D<sub>6</sub> (12 mM). An NMR tube was charged with substrate stock solution (500 μL) and an initial <sup>1</sup>H NMR spectrum was obtained, which was used as the T0 data. The NMR tube was then charged with 100 μL of **4-Ru6** stock solution and inverted to mix. The final reaction concentrations were as follows: phenylacetylene (100 mM), nucleophile (100 mM), dimethyl terephthalate (16.7 mM), and **4-Ru6** (2 mM). The NMR tube was then placed in an oil bath set at 110 °C for 24 h, after which a <sup>1</sup>H NMR spectrum was acquired. The resulting spectra were analyzed to quantify the integration of the terminal alkyne peak of phenylacetylene (δ<sub>H</sub> = 2.60) relative to the integral of dimethyl terephthalate (8.32 ppm) to determine *in situ* conversion.

## 4.4 References

1. (a) Chung, L.-H.; Yeung, C.-F.; Wong, C.-Y., *Chemistry – A European Journal* **2020**, *26* (28), 6102-6112; (b) Huang, L.; Arndt, M.; Gooßen, K.; Heydt, H.; Gooßen, L. J., *Chem. Rev.* **2015**, *115* (7), 2596-2697; (c) Roh, S. W.; Choi, K.; Lee, C., *Chem. Rev.* **2019**, *119* (6), 4293-4356; (d) Bruneau, C.; Dixneuf, P. H., *Acc. Chem. Res.* **1999**, *32* (4), 311-323.
2. (a) Nakamura, I.; Yamamoto, Y., *Chem. Rev.* **2004**, *104* (5), 2127-2198; (b) D'Souza, D. M.; Müller, T. J. J., *Chem. Soc. Rev.* **2007**, *36* (7), 1095-1108.
3. (a) Malkov, A. V.; Liddon, A. J. P. S.; Ramírez-López, P.; Bendová, L.; Haigh, D.; Kočovský, P., *Angew. Chem. Int. Ed.* **2006**, *45* (9), 1432-1435; (b) Tang, W.; Zhang, X., *Chem. Rev.* **2003**, *103* (8), 3029-3070.
4. (a) Mo, J.; Xu, L.; Xiao, J., *J. Am. Chem. Soc.* **2005**, *127* (2), 751-760; (b) Roff, G. J.; Lloyd, R. C.; Turner, N. J., *J. Am. Chem. Soc.* **2004**, *126* (13), 4098-4099; (c) Evano, G.; Gaumont, A.-C.; Alayrac, C.; Wrona, I. E.; Giguere, J. R.; Delacroix, O.; Bayle, A.; Jouvin, K.; Theunissen, C.; Gatignol, J.; Silvanus, A. C., *Tetrahedron* **2014**, *70* (8), 1529-1616.
5. (a) Gigant, N.; Chausset-Boissarie, L.; Belhomme, M.-C.; Poisson, T.; Pannecoucke, X.; Gillaizeau, I., *Org. Lett.* **2013**, *15* (2), 278-281; (b) Pankajakshan, S.; Xu, Y.-H.; Cheng, J. K.; Low, M. T.; Loh, T.-P., *Angew. Chem. Int. Ed.* **2012**, *51* (23), 5701-5705.
6. Hamada, T.; Manabe, K.; Kobayashi, S., *J. Am. Chem. Soc.* **2004**, *126* (25), 7768-7769.

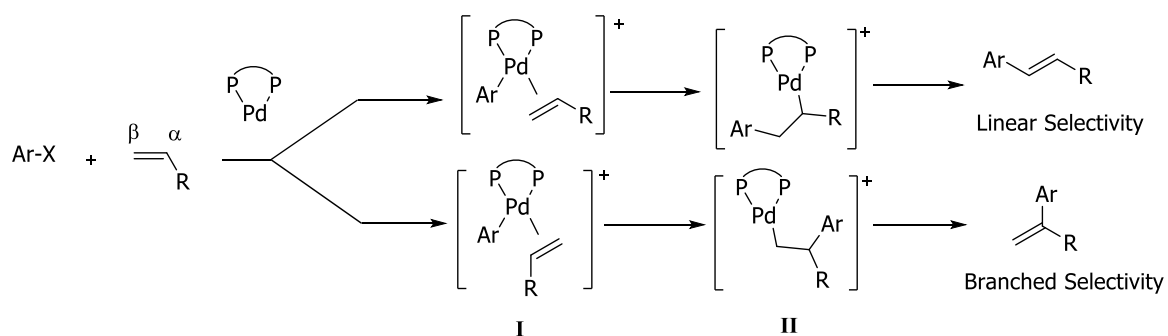
7. (a) Bruneau, C.; Dixneuf, P. H., *Angew. Chem. Int. Ed.* **2006**, *45* (14), 2176-2203; (b) Trost, B. M.; McClory, A., *Chem.--Asian J.* **2008**, *3* (2), 164-94; (c) Roh, S. W.; Choi, K.; Lee, C., *Chem. Rev.* **2019**, *119* (6), 4293-4356.
8. (a) Nair, R. N.; Lee, P. J.; Grotjahn, D. B., *Top. Catal.* **2010**, *53* (15-18), 1045-1047; (b) Nair, R. N.; Lee, P. J.; Rheingold, A. L.; Grotjahn, D. B., *Chemistry – A European Journal* **2010**, *16* (27), 7992-7995; (c) Varela-Fernández, A.; Varela, J. A.; Saá, C., *Adv. Synth. Catal.* **2011**, *353* (11-12), 1933-1937; (d) Varela-Fernandez, A.; Varela, J. A.; Saá, C., *Synthesis* **2012**, *44* (21), 3285-3295; (e) Watanabe, T.; Mutoh, Y.; Saito, S., *J. Am. Chem. Soc.* **2017**, *139* (23), 7749-7752.
9. (a) Varela-Fernández, A.; Varela Jesús, A.; Saá, C., *Adv. Synth. Catal.* **2011**, *353* (11-12), 1933-1937; (b) Alvarez-Perez, A.; González-Rodríguez, C.; García-Yebra, C.; Varela, J. A.; Oñate, E.; Esteruelas, M. A.; Saá, C., *Angew. Chem. Int. Ed.* **2015**, *54* (45), 13357-13361; (c) Kanno, H.; Nakamura, K.; Noguchi, K.; Shibata, Y.; Tanaka, K., *Org. Lett.* **2016**, *18* (7), 1654-1657; (d) Fukumoto, Y.; Asai, H.; Shimizu, M.; Chatani, N., *J. Am. Chem. Soc.* **2007**, *129* (45), 13792-13793; (e) Trost, B. M.; McClory, A., *Angew. Chem. Int. Ed.* **2007**, *46* (12), 2074-2077.
10. (a) Chapple, D. E.; Boyle, P. D.; Blacquiere, J. M., *ChemCatChem* **2021**, *13* (17), 3789-3800; (b) Stubbs, J. M.; Bridge, B. J.; Blacquiere, J. M., *Dalton Trans.* **2019**, *48* (22), 7928-7937; (c) Stubbs, J. M.; Chapple, D. E.; Boyle, P. D.; Blacquiere, J. M., *ChemCatChem* **2018**, *10* (17), 4001-4009; (d) Stubbs, J. M.; Bow, J. P. J.; Hazlehurst, R. J.; Blacquiere, J. M., *Dalton Trans.* **2016**, *45* (43), 17100-17103; (e) Chapple, D. E.; Hoffer, M. A.; Boyle, P. D.; Blacquiere, J. M., *Organometallics* **2022**, *41* (12), 1532-1542.
11. Bow, J.-P. J.; Boyle, P. D.; Blacquiere, J. M., *Eur. J. Inorg. Chem.* **2015**, *2015* (25), 4162-4166.
12. Bridge, B. J.; Boyle, P. D.; Blacquiere, J. M., *Organometallics* **2020**, *39* (14), 2570-2574.
13. (a) Mutoh, Y.; Ikeda, Y.; Kimura, Y.; Ishii, Y., *Chem. Lett.* **2009**, *38* (6), 534-535; (b) Kuwabara, T.; Aoki, Y.; Sakajiri, K.; Deguchi, K.; Takamori, S.; Hamano, A.; Takano, K.; Houjou, H.; Ishii, Y., *Organometallics* **2020**, *39* (5), 711-718.
14. Brotzel, F.; Chu, Y. C.; Mayr, H., *J. Org. Chem.* **2007**, *72* (10), 3679-3688.
15. Fox, M. A.; Roberts, R. L.; Khairul, W. M.; Hartl, F.; Low, P. J., *J. Organomet. Chem.* **2007**, *692* (15), 3277-3290.
16. Tshepelevitsh, S.; Kütt, A.; Lökov, M.; Kaljurand, I.; Saame, J.; Heering, A.; Plieger, P. G.; Vianello, R.; Leito, I., *Eur. J. Org. Chem.* **2019**, *2019* (40), 6735-6748.

## Chapter 5

# 5 Mechanistic Elucidation of Pd- $\text{P}^{\text{R}}_2\text{N}^{\text{ArCF}_3}_2$ Catalysts for Cross Coupling

## 5.1 Introduction

Pd catalyzed cross-coupling reactions have been established as a pillar of synthetic organic chemistry. Transition metal catalyzed C-C coupling reactions has been exploited in pharmaceutical and academic settings for the last 50 years.<sup>1</sup> Some of the most notable cross-coupling reactions, Suzuki-Miyora,<sup>2</sup> Negishi, and Heck cross-couplings, were globally recognized in the 2010 Nobel prize for chemistry.<sup>3</sup> Of these cross-coupling reactions, arguably the most widely utilized is the Suzuki-Miyora reaction.<sup>4</sup> However, the Mizoroki-Heck reaction has historically been underrepresented, specifically in comparison to the Suzuki-Miyora reaction. The Mizoroki-Heck reaction enables the vinylation of aryl(pseudo)halides which is highly desirable.<sup>5</sup> The Mizoroki-Heck reaction does present some challenges with regard to regioselectivity, which can result in C-C bond formation at either the  $\alpha$ - or  $\beta$ -position of the alkene which would result in branched and linear products, respectively (Scheme 5-1).<sup>6</sup> Oxidative addition of ArX to the Pd(0) metal centre followed by  $\pi$ -coordination of the alkene would generate intermediate **I**. Selectivity of the products would be influenced based on the orientation of the coordinated alkene in **I**, which would then undergo an insertion to generation intermediate **II**, followed by product release. It should also be noted that formation of 5-coordinate  $\pi$ -intermediates have been proposed upon coordination of the alkene, however, theoretical and experimental data suggest that direct migratory insertion from the 5-coordinate intermediates is unlikely due to high activation energies.<sup>7</sup> Control of selectivity is especially difficult in unbiased alkenes and have generally been achieved with activated olefins with electron bias.<sup>8</sup> The development of new ligands has been an attractive route to explore, which can potentially improve upon the regioselectivity issue while also improving reaction scope, conditions, and catalyst performance.



**Scheme 5-1.** Competing pathways in the Heck reaction to form linear or branched products.

1,5-*R'*-3,7-*R*-1,5-Diaza-3,7-diphosphacyclooctane ( $P^{R_2}N^{R'_2}$ ) (**5-1**) ligands have been established for C-N and C-O bond forming reactions via intramolecular hydrofunctionalization,<sup>9</sup> as well they have been employed for acceptorless dehydrogenation<sup>10</sup> reactions (Figure 5-1a/b). These ligands are attractive due to the modularity of the phosphorus and nitrogen substituents which can influence the steric and electronic parameters of the primary and secondary coordination sphere. Furthermore, the ligands have been demonstrated as cooperative due to the Lewis basic pendent amine. The typical binding mode for these ligands occurs through bidentate phosphorus coordination to the metal center (Figure 5-1c).<sup>11</sup> Recently, Newman and co-workers have demonstrated the first use of  $P^{R_2}N^{R'_2}$  ligands in C-C bond forming reactions via the arylation of alcohols and ketones with Ni (Figure 5-1d).<sup>12</sup> In this publication the ligands were shown to be highly effective for these C-C coupling reactions and utilized for previously difficult coupling reactions. This demonstrated the potential of these ligands in other C-C bond forming reactions.

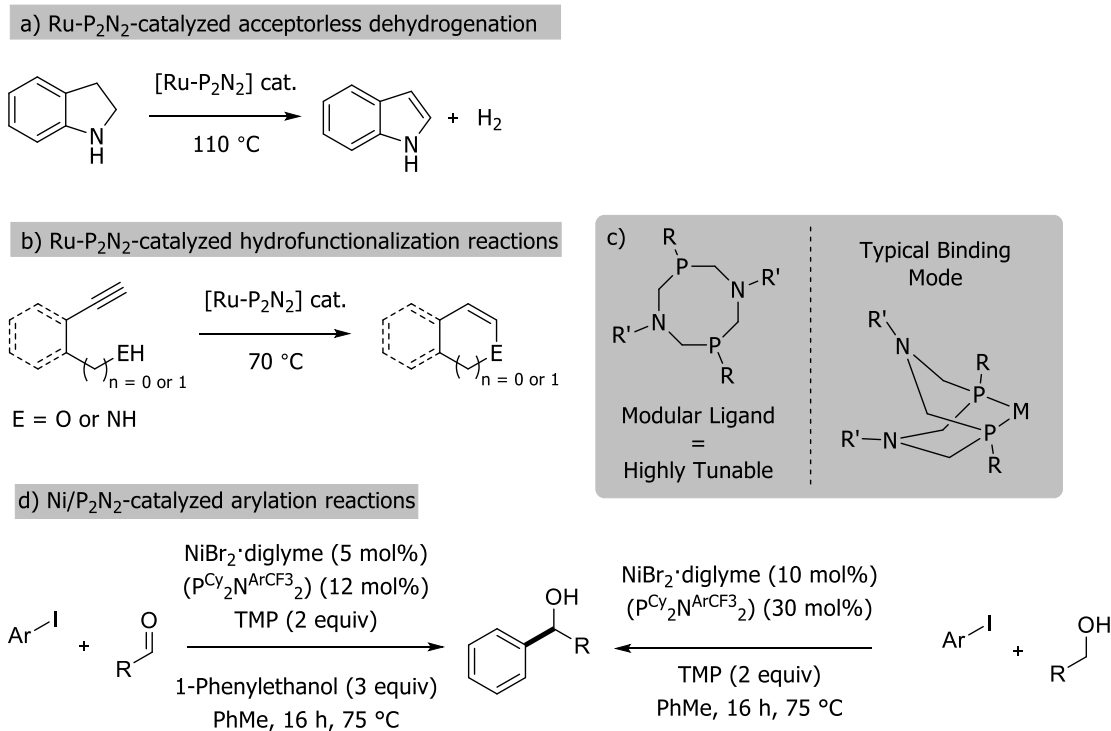
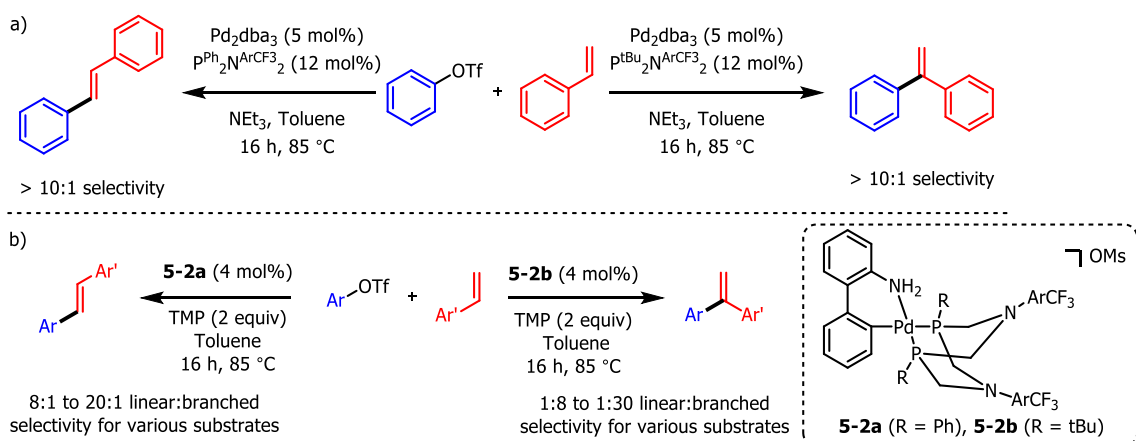


**Figure 5-1.** Previous established organic reactions which employed P<sup>R</sup><sub>2</sub>N<sup>R'</sup><sub>2</sub> ligands. Ru-P<sub>2</sub>N<sub>2</sub> catalysts used were [Ru(Cp/Cp\*)(P<sup>R</sup><sub>2</sub>N<sup>R'</sup><sub>2</sub>)(MeCN)]PF<sub>6</sub>.

The Newman group have recently investigated the efficacy of P<sup>R</sup><sub>2</sub>N<sup>R'</sup><sub>2</sub> ligands as compared to other previously used ligands for the Mizoroki-Heck coupling of phenyl triflate and styrene with Pd<sub>2</sub>dba<sub>3</sub> as a precatalyst (Scheme 5-2a). Reactions with P<sup>Ph</sup><sub>2</sub>N<sup>ArCF<sub>3</sub></sup><sub>2</sub> (**5-1a**) and P<sup>tBu</sup><sub>2</sub>N<sup>ArCF<sub>3</sub></sup><sub>2</sub> (**5-1b**) ligands provided comparable yield to the other ligands. Interestingly, the P<sup>R</sup><sub>2</sub>N<sup>ArCF<sub>3</sub></sup><sub>2</sub> ligands enabled highly regioselective formation of the linear and branched coupled products with **5-1a** and **5-1b**, respectively. Synthesis and assessment of the well defined Pd catalysts, [Pd(P<sup>R</sup><sub>2</sub>N<sup>ArCF<sub>3</sub></sup><sub>2</sub>)(ABP)]OMs (ABP = 2-aminobiphenyl, Oms = methanesulfonate) (**5-2**) showed higher activity and the same regioselectivity as compared to *in situ* catalyst formation from Pd<sub>2</sub>dba<sub>3</sub>. Optimized conditions with **5-2a** (R = Ph) and **5-2b** (R = tBu) were utilized to couple a variety of aryl triflates and aryl alkenes (Scheme 5-2b) However, the exact reason for the difference in regioselectivity is not fully understood, which initiated a collaboration between the Newman and Blacquiere groups. We hypothesize two potential reasons for the observed selectivity, a switch in mechanism occurs with the two derivatives (potentially mononuclear and dinuclear pathways), or a

substantial steric difference in the catalyst pocket exists which controls the selectivity. Herein, a mechanistic evaluation was conducted, we report the synthesis and characterization of well-defined monometallic Pd precatalysts, which were accessed for the Mizoroki-Heck coupling of phenyl triflate and styrene. Stoichiometric reactions to isolate reaction intermediates were performed as well as visual kinetic analysis to corroborate a mononuclear or dinuclear pathway. Calculations of the steric congestion of the catalyst pocket were also performed to access the difference in steric influence between the  $P^{R_2}N^{R'_2}$  ligands.



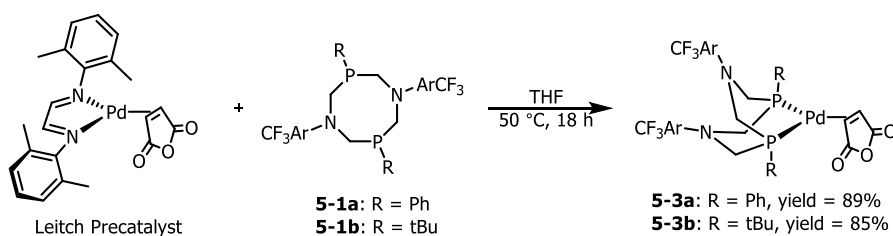
**Scheme 5-2.** a) First established Mizoroki-Heck coupling with  $Pd_2dba_3$  and  $P^{R_2}N^{R'_2}$  ligands. b) optimized conditions for Mizoroki-Heck coupling with **5-2a** and **5-2b**.

## 5.2 Results and Discussion

### 5.2.1 Synthesis of $Pd(P^{R_2}N^{ArCF_3}_2)(MAH)$ Complexes.

To assess catalyst performance and regioselectivity, we targeted a well-defined mononuclear Pd(0) catalyst with the  $P^{R_2}N^{ArCF_3}_2$  ligand coordinated, instead of *in situ* formation of the catalyst. Synthesis of the Leitch precatalyst,  $^{DMP}DAB$ -Pd-MAH ( $^{DMP}DAB$  = 2,6-dimethylphenyl-*N,N'*-diaryl-diazabutadiene, MAH = maleic anhydride), was performed and was subsequently ligated with either **5-1a** or **5-1b**. Coordination of the  $P^{R_2}N^{R'_2}$  ligands were attempted via ligand substitution of the Leitch precatalyst with **5-1a** or **5-1b** in THF at 50 °C over 18 h (Scheme 5-3). A singlet was observed by  $^{31}P\{^1H\}$  NMR spectroscopy at 9.6 and 30.3 ppm for the Ph and tBu derivatives, respectively. The 20 ppm

difference in chemical shift between the Ph and *t*Bu derivative was consistent with Ru complexes that differed only in the phosphine substituent.<sup>9c, 9e</sup> Furthermore, disappearance of the diagnostic imine signal of the <sup>DMP</sup>DAB ligand at 8.56 ppm was observed by <sup>1</sup>H NMR spectroscopy for both derivatives. A significant downfield shift of the MAH proton signals was observed by <sup>1</sup>H NMR spectroscopy, from 2.30 ppm to 3.50 and 3.70 ppm for the Ph and *t*-Bu derivatives, respectively. Collectively, this data was consistent with successful coordination of the P<sup>R</sup><sub>2</sub>N<sup>R'</sup><sub>2</sub> ligands to form P<sup>Ph</sup><sub>2</sub>N<sup>ArCF<sub>3</sub></sup><sub>2</sub>-Pd-MAH (**5-3a**) and P<sup>*t*Bu</sup><sub>2</sub>N<sup>ArCF<sub>3</sub></sup><sub>2</sub>-Pd-MAH (**5-3b**).



**Scheme 5-3.** Ligand substitution of Leitch complex with P<sup>R</sup><sub>2</sub>N<sup>ArCF<sub>3</sub></sup><sub>2</sub> ligands via reaction in THF to give the corresponding [Pd(P<sup>R</sup><sub>2</sub>N<sup>ArCF<sub>3</sub></sup><sub>2</sub>)(MAH)] complexes **5-3a** and **5-3b**.

Single crystals of both **5-3a** and **5-3b** were obtained and X-ray crystallography unambiguously confirmed the connectivity (Figure 5-2). Similar Pd(1)-P(1)/P(2) bond distances of ca. 2.29 Å were observed for **5-3a** and **5-3b**. Pd(1)-C(1)/C(2) bond distances of ca. 2.12 Å and C(1)-C(2) bond distances of ca. 1.43 Å were observed for both complexes. P(1)-Pd(1)-P(2) bond angles of 85.3 and 85.7° were observed for both **5-3a** and **5-3b**, respectively. These bond distances and angles were in close agreement with each other, and previously synthesized diphosphine Pd-MAH complexes.<sup>13</sup> The conformation of **5-3a** was of interest due to the boat-boat configuration of the P<sup>Ph</sup><sub>2</sub>N<sup>ArCF<sub>3</sub></sup><sub>2</sub> ligand, which is atypical for similar Ni-P<sub>2</sub>N<sub>2</sub> complexes<sup>14</sup> or other M-P<sub>2</sub>N<sub>2</sub> complexes.<sup>10, 15</sup> We postulated that a Pd-C(ipso) interaction was present, which has been shown by Buchwald and co-workers in a variety of (biaryl)phosphine-Pd complexes and is evidenced by Pd-C(arene) bond distances of 2.35–2.86 Å.<sup>16</sup> This type of M-C(arene) interaction has also been demonstrated by Blacquiere and co-workers for P<sup>Cy</sup><sub>2</sub>N<sup>Ph</sup><sub>2</sub> ligands in Ru complexes.<sup>9e</sup> Pd-C(ipso) bond distances of 3.063(2) and 3.220(2) Å were observed between the two ArCF<sub>3</sub> substituents of **5-3a**, which fell outside the expect range for similar Pd-C(arene)



interactions (2.35–2.86 Å). Furthermore, no elongation of the aryl C-C bond lengths were observed which would be expected if a Pd-C(arene) interaction was present. Therefore, it appears that no interaction between the nitrogen substituents and Pd centre were present.

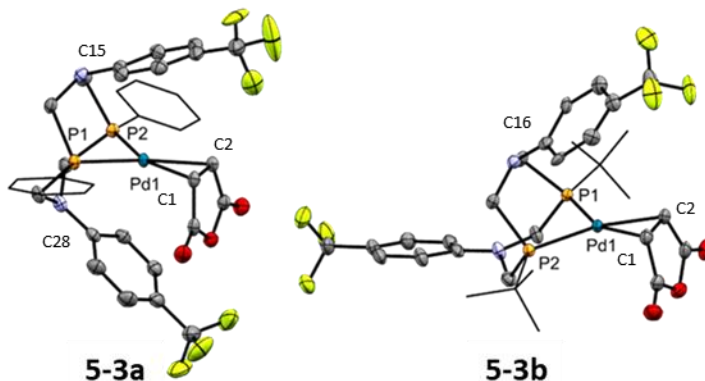


**Figure 5-2.** Displacement ellipsoid plot of **5-3a** (left) and **5-3b** (right) with ellipsoids at the 50% probability level. **5-3a** had co-crystallized DCM and disordered CF<sub>3</sub> groups that were omitted for clarity. **5-3b** had co-crystallized DCM and disordered aryl-CF<sub>3</sub> substituents that were omitted for clarity. Both complexes had the H atoms omitted for clarity. Selected bond distances (Å): **5-3a**, Pd(1)-P(1) = 2.291(1), Pd(1)-P(2) = 2.2934(8), Pd(1)-C(1) = 2.120(2), Pd(1)-C(2) = 2.125(2), Pd(1)-C(15) = 3.220(2), Pd(1)-C(28) = 3.063(2), C(1)-C(2) = 1.430(3); **5-3b**, Pd(1)-P(1) = 2.302(1), Pd(1)-P(2) = 2.284(1), Pd(1)-C(1) = 2.123(3), Pd(1)-C(2) = 2.113(3), Pd(1)-C(16) = 3.161(3), C(1)-C(2) = 1.430(4). Selected bond angles (°): **5-3a**, P(1)-Pd(1)-P(2) = 85.34(2), C(1)-Pd(1)-C(2) = 39.36(8); **5-3b**, P(1)-Pd(1)-P(2) = 85.67(3), C(1)-Pd(1)-C(2) = 39.5(1).

## 5.2.2 Structural Confirmation of [Pd(P<sup>Ph</sup><sub>2</sub>N<sup>Ar</sup>CF<sub>3</sub><sub>2</sub>)(ABP)] Complexes

Complexes **5-2a** and **5-2b** were determined to be the preferred well-defined catalysts, based on the catalytic studies (Section 5.2.3, and data obtained by the Newman group). Single crystals of **5-2a** complex were obtained and X-ray crystallography unambiguously confirmed the expected connectivity (Figure 5-3). Pd(1)-P(1)/P(2) bond distances of ca. 2.29 Å and P(1)-Pd(1)-P(2) bond angle of 82.6° were similar to those observed with complexes **5-3a** and **5-3b**. Pd(1)-N(1)/C(1) bond distances of 2.12 and 2.03 Å, respectively, and the N(1)-Pd(1)-C(1) bond angle of 81.7° were observed which were close to those

observed with a similar Pd(diphosphine)(ABP) complex.<sup>18</sup> The complex had very little distortion in the square planar geometry, with a  $\tau_4$  value of 0.03, which is different from **5-3a** and **5-3b** which had much more distortion in the geometry, likely caused by the small bite angle of the MAH ligand (ca. 39°) as compared to the bite angle of the ABP ligand (ca. 82°). The boat-boat conformation of the  $\text{P}^{\text{Ph}}_2\text{N}^{\text{ArCF}_3}_2$  ligand of **5-2a** matched the observed conformation of complex **5-3a**. The Pd-C(arene) bond distances observed (ca 3.1 Å) again fell outside the range expected range (2.35–2.86 Å) for a Pd-C(arene) interaction.

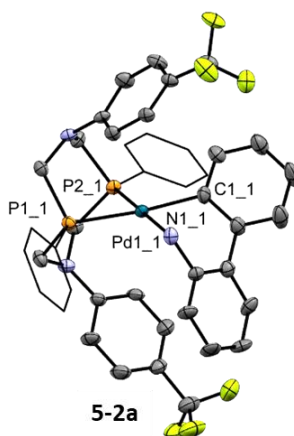


**Figure 5-3.** Displacement ellipsoid plot of **5-2a** representative complex with ellipsoids at 50% probability. H atoms and co-crystallized  $\text{CH}_2\text{Cl}_2$  and OMs anion were omitted for clarity. Selected bond distances (Å): Pd(1)-P(1) = 2.246(2), Pd(1)-P(2) = 2.336(3), Pd(1)-N(1) = 2.124(8), Pd(1)-C(1) = 2.029(9). Selected bond angles (°): P(1)-Pd(1)-P(2) = 82.63(8), N(1)-Pd(1)-C(1) = 81.7(3).  $\tau_4$  geometry index: 0.03

### 5.2.3 Heck Coupling Reaction with $\text{Pd}(\text{P}^{\text{R}}_2\text{N}^{\text{ArCF}_3}_2)(\text{MAH})$ Complexes.

The Pd(0) complexes **5-3a** and **5-3b**, were assessed for the Heck-coupling coupling of phenyl triflate and styrene and the data was compared to that obtained with the Pd(II) precatalysts **5-2a** and **5-2b**, respectively (Figure 5-4). Reactions were conducted in toluene with 1 mol% catalyst loading at 85 °C over 16 h. Turnover number (TON) determination of **5-3a** and **5-3b** showed values of 9 and 4, respectively. A TON comparison of **5-3a** to **5-2a** was 9 and 20, respectively, while a TON comparison of **5-3b** to **5-2b** was 4 and 22, respectively. Thus complexes **5-3a** and **5-3b** are catalytic, however, the complexes give ca.

2–5 times lower conversion as compared to **5-2a** and **5-2b**. With complex **5-3a**, selective formation of the linear product with negligible formation of the branched product was observed. Complex **5-3b** promoted selective formation of the branched product with negligible formation of the linear product. The selectivity observed with **5-3a** and **5-3b** matched the observed selectivity seen with the other mononuclear complexes **5-2a** and **5-2b**, as well as from *in situ* catalyst formation from Pd<sub>2</sub>dba<sub>3</sub>. Collectively, the fact that both the well-defined mononuclear Pd catalysts, **5-2** and **5-3** showed the same selectivity is suggestive of a monometallic pathway. However, the possibility that formation of a bimetallic complex following precatalyst activation cannot be dismissed completely.

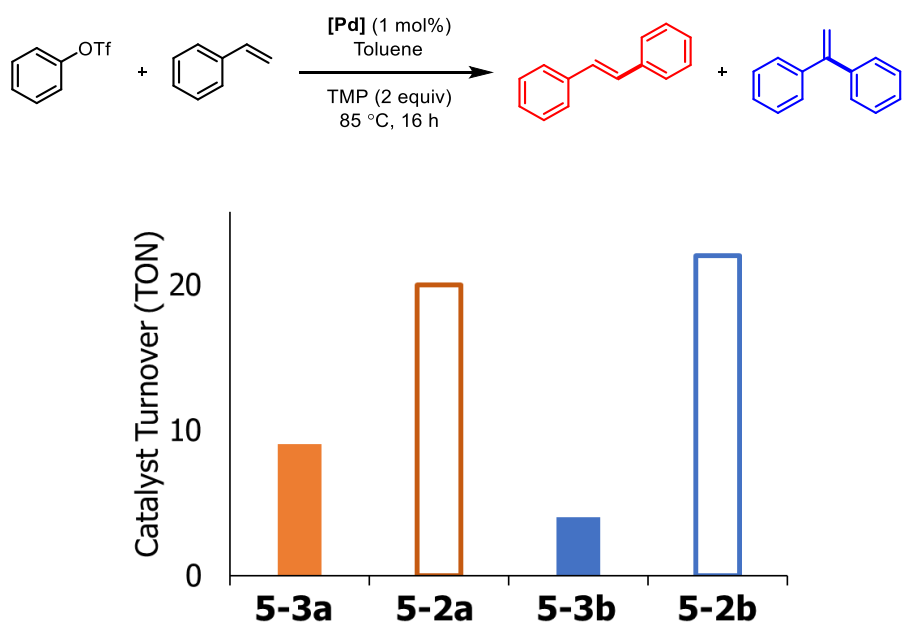


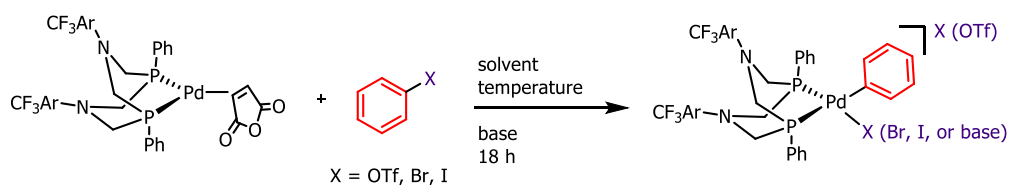
**Figure 5-4.** (top) Mizoroki-Heck coupling of phenyl triflate and styrene with 1 mol% **5-3a** or **5-3b** over 16 h. (bottom) Conversion to the linear (red) and branched (blue) products with **5-3a** and **5-3b** (solid), and **5-2a** and **5-2b** (outline).

#### 5.2.4 Attempted Oxidative Addition with **5-3a**.

To determine if a bimetallic species is formed following precatalyst activation and provide further elucidation of the mechanism, isolation of potential reactive intermediates was investigated. While **5-3a** and **5-3b** were shown to have low reactivity, we attempted to use these complexes to access the likely reaction intermediate following oxidative addition of

phenyl triflate. Complex **5-3a** was reacted with an aryl (pseudo)halide (2 equiv) and base (2 equiv) over 18 h under a variety of conditions (Table 5-1). Reactions with phenyl triflate at 85 °C, the typical temperature for catalysis, showed no signs of reactivity with or without a base present (Entries 1–3). The reaction temperature was increased to 110 °C and performed in 1,4-dioxane in an attempt to promote MAH dissociation. Qualitative observation of Pd black was observed along with the appearance of multiple species by  $^{31}\text{P}\{^1\text{H}\}$  NMR spectroscopy that suggest decomposition of the complex (Entry 4). The aryl halides, phenyl iodide and phenyl bromide, were also tested which also did not result in any oxidative addition (Entries 5–6). Collectively, these results suggests that dissociation of the MAH ligand is not facile with these complexes, which stops oxidative addition. While they do promote the Heck-coupling under analogous catalytic conditions these complexes were deemed unsuitable for further stoichiometric studies.

**Table 5-1.** Attempted oxidative addition of **5-3a** with aryl (pseudo)halides.



Entry	Aryl-X <sup>a</sup>	Solvent	Temp (°C)	Base	Reaction <sup>b</sup>
1	PhOTf	THF	85	None	No
2	PhOTf	THF	85	TMP	No
3	PhOTf	THF	85	Piperidine	No
4	PhOTf	1,4-dioxane	110	TMP	Decomp
5	PhI	THF	85	None	No
6	PhBr	DCM	40	None	No

<sup>a</sup> 2 equiv of aryl-X. <sup>b</sup>Reaction monitored by  $^{31}\text{P}\{^1\text{H}\}$  NMR spectroscopy.

### 5.2.5 Oxidative Addition with $(\text{P}^{\text{R}}_2\text{N}^{\text{ArCF}_3}_2)\text{-Pd-G3}$ Complexes and Phenyl Triflate.

Due to both the low activity of **5-3a** and **5-3b** and their inability to access the oxidative addition products, **5-2a** and **5-2b** were investigated instead. It must be noted that complexes **5-2a** and **5-2b** first undergo reductive elimination of carbazole to generate the active Pd(0) complex ligated with **5-1a** and **5-1b**, respectively. Complexes **5-2a** and **5-2b** were reacted with phenyl triflate (2 equiv) and piperidine (2 equiv) at 85 °C in THF over 2 h (Figure 5-5). The excess of phenyl triflate and piperidine is consistent with catalytic conditions where they would be in extreme excess. The reaction with **5-2a** was analyzed by  $^{31}\text{P}\{^1\text{H}\}$  NMR spectroscopy, which showed conversion to a new species that appeared as two doublets at 3.1 and -7.1 ppm ( $^2J_{\text{PP}} = 49.5$  Hz). The reaction with **5-2b** showed the evolution of a new major species observed by  $^{31}\text{P}\{^1\text{H}\}$  NMR spectroscopy as two doublets at 24.2 and 11.7 ppm ( $^2J_{\text{PP}} = 10.8$  Hz). It must be noted that a substantial difference in coupling constants was observed, ca. 38 Hz difference, which could be indicative of a difference in structure between the two complexes. However, the exact cause of this difference is still under investigation. The new species were proposed to be the oxidative addition products **5-4a** and **5-4b**. However, complete isolation of the proposed oxidative addition complexes **5-4a** and **5-4b** from these reactions proved difficult due to competitive formation of minor unknown species and incomplete conversion to products.

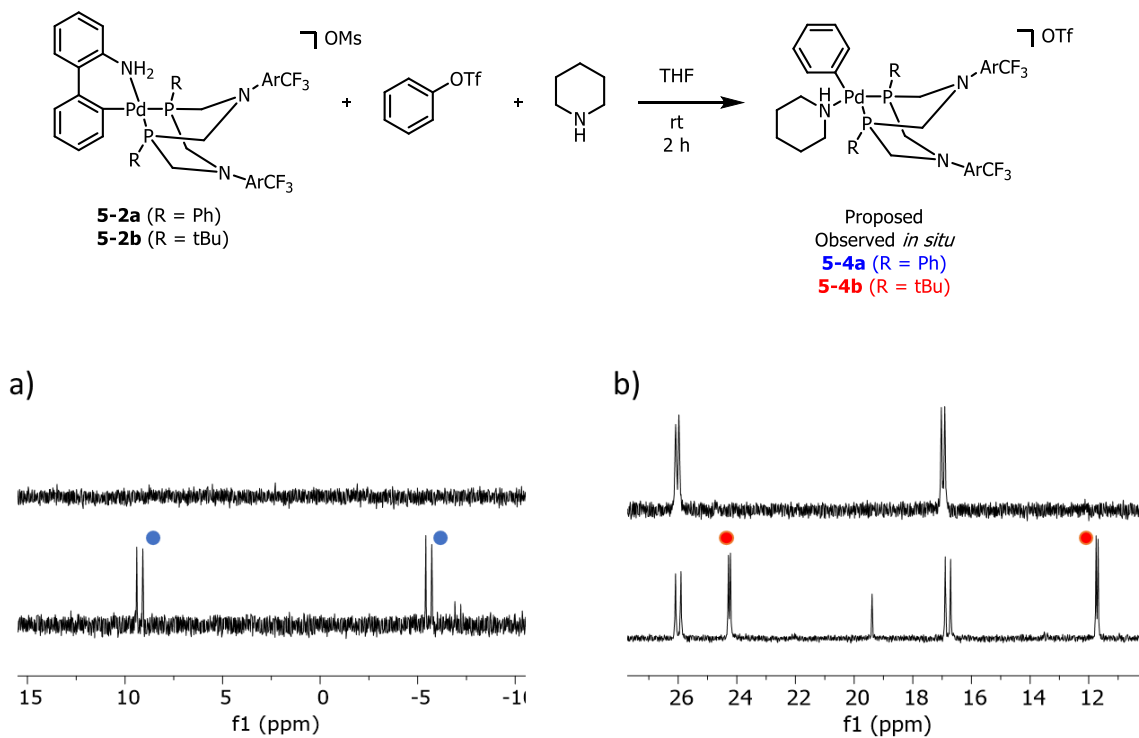
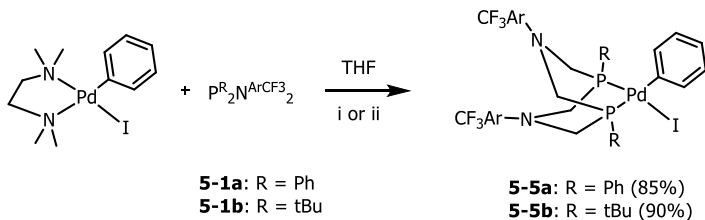


**Figure 5-5.** (top) Attempted oxidative addition with phenyl triflate in the presence of piperidine at room temperature over 2 h. (bottom) *In situ* monitoring of the reaction with T0 the top NMR spectrum of the stack plot and after 2 h the bottom NMR spectrum of the stack plot. a) Reaction with **5-2a** (SM was not soluble) and b) reaction with **5-2b**.

### 5.2.6 Synthesis of [Pd(Ph)(I)(P<sup>R</sup><sub>2</sub>N<sup>ArCF<sub>3</sub><sub>2</sub>)] Complexes</sup>

In an effort to confirm the identity of the oxidative addition intermediates, the independent syntheses of **5-4a** and **5-4b** were investigated. Initial synthesis of Pd(II) complexes [Pd(Ph)(I)(P<sup>R</sup><sub>2</sub>N<sup>ArCF<sub>3</sub><sub>2</sub>)] **5-5a** (R = Ph) and **5-5b** (R = tBu) was performed (Scheme 5-4). [Pd(Ph)(I)(TMEDA)] and **5-1a** were stirred at room temperature in THF over 48 h. A new species was observed by <sup>31</sup>P{<sup>1</sup>H} NMR spectroscopy as two doublets at 4.2 and -20.9 ppm (<sup>2</sup>J<sub>PP</sub> = 60.1 Hz). Diagnostic signals for the P<sup>Ph</sup><sub>2</sub>N<sup>ArCF<sub>3</sub><sub>2</sub> methylene signals were observed by <sup>1</sup>H NMR spectroscopy between 4.7–4.1 ppm, which correlated to the phosphorus signals based on <sup>1</sup>H-<sup>31</sup>P HMBC. In similar fashion, the reaction of [Pd(Ph)(I)(TMEDA)] and **5-1b** was stirred at 50 °C in THF over 18 h. Observation of two doublets at 15.2 and -2.7 ppm (<sup>2</sup>J<sub>PP</sub> = 47.8 Hz) by <sup>31</sup>P{<sup>1</sup>H} NMR spectroscopy were suggestive of coordination of **5-1b**. Diagnostic signals for the P<sup>tBu</sup><sub>2</sub>N<sup>ArCF<sub>3</sub><sub>2</sub> methylene signals and tBu substituents were</sup></sup></sup>

observed between 4.3–3.7 ppm, at 1.64 and 0.95 ppm, respectively, by  $^1\text{H}$  NMR spectroscopy. Collectively, this data suggests the successful coordination of **5-1a** and **5-1b** to form **5-5a** and **5-5b**.



**Scheme 5-4.** Synthesis of **5-5a** and **5-5b**. Reaction conditions i) room temperature for 48 h. ii) 50 °C for 18 h.

Single crystals of **5-5a** were obtained and X-ray crystallography unambiguously confirmed the expected connectivity (Figure 5-6). Pd(1)-P(1)/P(2) bond distances of 2.32 and 2.26 Å, respectively were observed along with a P(1)-Pd(1)-P(2) bond angle of 83.2°. These bond distances and angles were in a similar range as compared to the previously obtained bond distances/angle observed for **5-3a**, **5-3b**, and **5-2a**. Pd(1)-I(1) and Pd(1)-C(1) bond distances of 2.63 and 2.01 Å, respectively, were observed which were similar in value to comparable diphosphine-Pd(Ph)(I) complexes.<sup>19</sup> Similar to **5-2a**, there was little distortion of the square planar geometry, with a  $\tau_4$  value of 0.09. Interestingly, the conformation of the  $\text{P}^{\text{Ph}}_2\text{N}^{\text{ArCF}_3}_2$  ligand was in a chair-boat conformation, which is different from the boat-boat conformer observed for **5-3a** and **5-2a**. This could be suggestive that there is little bias toward either of the conformers and in solution, interconversion between the conformers readily occurs. Studies with  $\text{Ni-P}^{\text{R}}_2\text{N}^{\text{R}'_2}$  complexes showed that chair/boat isomerization readily occurs in solution, with a barrier of ca. 16–42 kJ/mol for isomerization, depending on phosphorus and nitrogen substituents.<sup>20</sup>

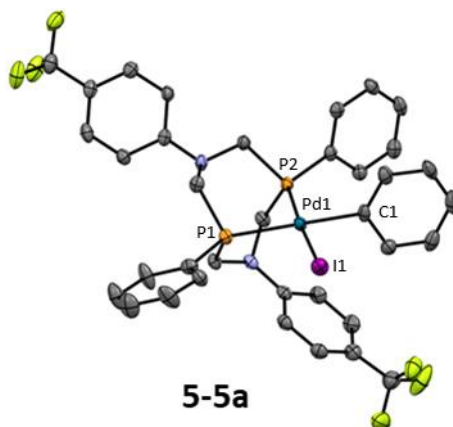


**Figure 5-6.** Displacement ellipsoid plot of **5-5a** with ellipsoids at 50% probability. H atoms were omitted for clarity. Orientational disorder in the CF<sub>3</sub> group and phenyl substituent were omitted for clarity. The sample was also compositionally disordered between **5-5a** and [Pd(I)<sub>2</sub>(P<sup>Ph</sup><sub>2</sub>N<sup>Ar</sup>CF<sub>3</sub>)<sub>2</sub>] which was omitted. Selected bond distances (Å): Pd(1)-P(1) = 2.320(2), Pd(1)-P(2) = 2.264(1), Pd(1)-I(1) = 2.634(1), Pd(1)-C(1) = 2.012(7). Selected bond angles (°): P(1)-Pd(1)-P(2) = 83.23(3).  $\tau_4$  geometry index: 0.09.

### 5.2.7 Halide Abstraction of **5-5b** with AgOTf.

Halide abstraction from **5-5b** with AgOTf in THF at room temperature was initially attempted with no base present, which resulted in formation of black precipitate (Pd black) that was indicative of decomposition. We hypothesized that halide abstraction in the presence of a base would help stabilize the resulting oxidative addition species. Halide abstraction of **5-5b** with AgOTf and piperidine in THF at room temperature was analyzed after 2 h (Figure 5-7). Analysis of the resulting solid by <sup>31</sup>P{<sup>1</sup>H} NMR spectroscopy showed the formation of several minor species (ca. 25% total) and a major species (ca. 75%) (Figure 5-7, NMR b). Efforts to isolate the species through crystallization, filtration, and solvent washes proved ineffective, as well reduced reaction times lead to incomplete conversion. The major species was observed as two doublets at 19.4 and 7.3 ppm (<sup>2</sup>J<sub>PP</sub> = 15.0 Hz) by <sup>31</sup>P{<sup>1</sup>H} NMR spectroscopy. This major product appeared at the same chemical shift and had the same coupling constant as the proposed oxidative addition product **5-4b** (Figure 5-7, NMR c). A substantial decrease in the coupling constant by ca. 33 Hz was observed for the major species as compared to **5-5b**. The reason for the decrease



in coupling constant is currently under investigation. These results collectively support the proposed assignment of **5-4b** as the monoligated  $[\text{Pd}(\text{Ph})(\text{piperidine})(\text{P}^{\text{tBu}}_2\text{N}^{\text{ArCF}_3}_2)]$  complex. Halide abstraction with **5-5a** is currently under investigation as well as isolation and characterization of both halide abstraction products to validate the proposed structure.

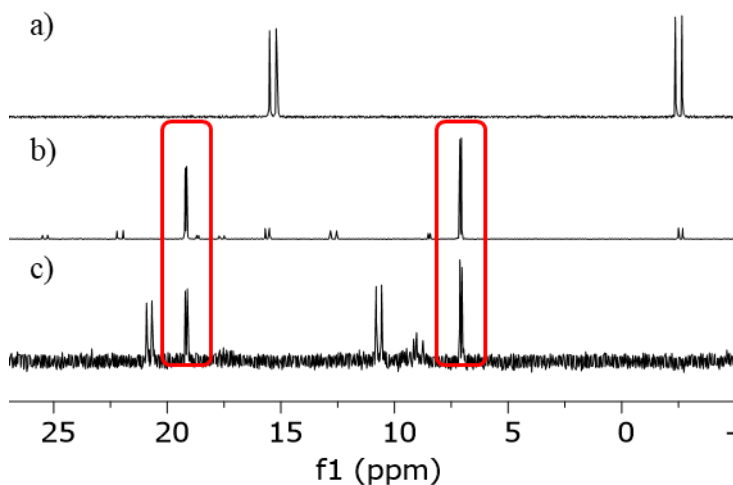
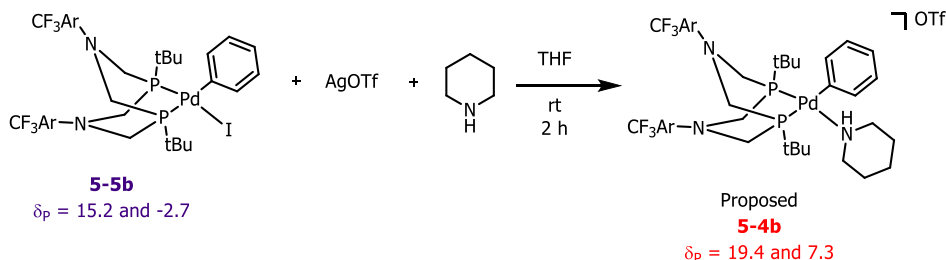


**Figure 5-7.** (top) Halide abstraction of **5-5b** with AgOTf and piperidine. (bottom)  $^{31}\text{P}\{^1\text{H}\}$  NMR stack plot (DCM- $d_2$ ) of: a) starting material (**5-5b**), b) solid from halide abstraction with **5-5b**, c) solid from oxidative addition with **5-2b**. Red box highlights the proposed product.

### 5.2.8 Reaction Order Determination for Palladium.

To further elucidate the likelihood of a mononuclear vs binuclear pathway the order in **5-2a** was investigated. For a mononuclear pathway a catalyst order of 1 would be expected, whereas a binuclear pathway a catalyst order of 2 would be observed, since it would take 2 mononuclear precatalysts to form a binuclear active catalyst. To evaluate this, variable time normalization analysis (VTNA) was employed which allowed for the determination

of reaction components based on reaction profiles (Figure 5-8). The order in **5-2a** was determined from two reactions with varying amounts of catalyst of 4 mM (run A) and 8 mM (run B), with both runs conducted with 200 mM phenyl triflate and 200 mM styrene, under reaction conditions of 85 °C in toluene-*d*<sub>8</sub>. The x-axis of the conversion vs time plots was normalized to achieve overlap of the datasets, which corresponded to an order of 1 for **5-2a**. This suggests that for the Ph derivative the reaction pathway proceeds through a monometallic mechanism. The corresponding study with **5-2b** is currently ongoing to determine if both species proceed through a mononuclear pathway.

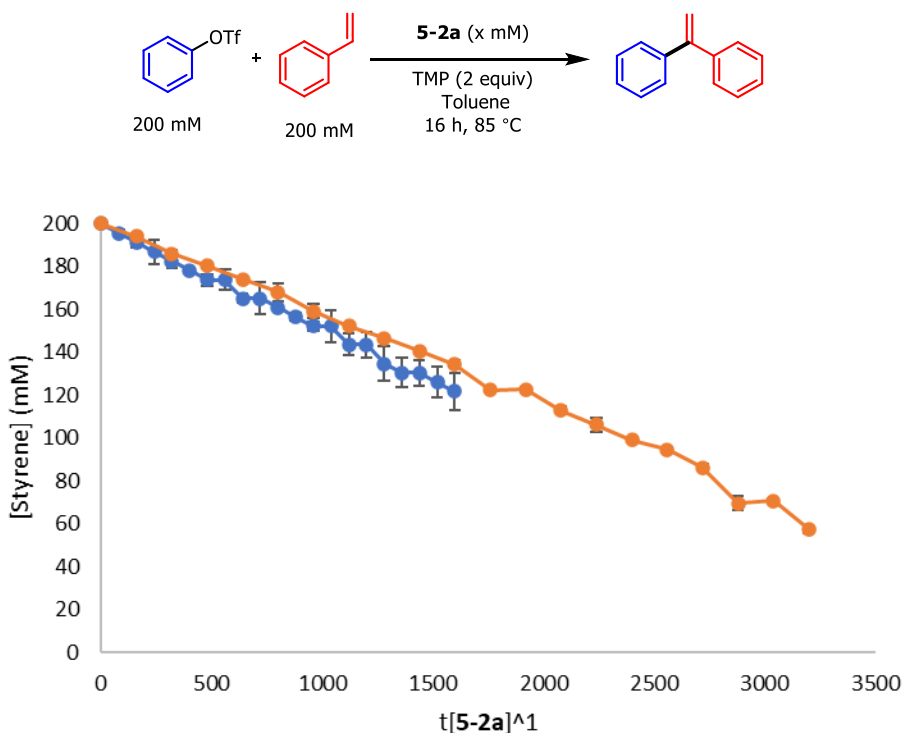


**Figure 5-8.** (top) Mizoroki-Heck coupling of phenyl triflate (200 mM) and styrene (200 mM) with catalyst **5-2a** and TMP at 85 °C in toluene-*d*<sub>8</sub>. (bottom) Reaction profiles for runs A) 8 mM catalyst (orange) and B) 4 mM catalyst. Reactions were performed in duplicate and the error bars depicting the span of values.

### 5.2.9 Comparison of Catalyst Pocket Steric Congestion.

To investigate the steric difference of the binding pocket of (P<sup>Ph</sup><sub>2</sub>N<sup>ArCF<sub>3</sub>2</sup>)<sub>2</sub>-Pd complexes, analysis with SambVca 2.1 Web program was performed (Figure 5-9).<sup>21</sup> Calculations were

performed using metrical parameters obtained from X-ray crystal structures of the following complexes: **5-3a**, **5-3b**, **5-5a**, and **5-2a**. A comparison between the steric pockets of the Pd(P<sup>R</sup><sub>2</sub>N<sup>ArCF<sub>3</sub>2</sup>)(MAH) complexes **5-3a** (R = Ph) and **5-3b** (R = tBu) were performed, which differed structurally by the phosphorus substituent, Ph vs tBu, respectively. The binding pocket of **5-3a** was more congested (% V<sub>Bur</sub> = 64.3%) as compared to **5-3b** (% V<sub>Bur</sub> = 56.6%), however, the conformation of the P<sup>R</sup><sub>2</sub>N<sup>ArCF<sub>3</sub>2</sup> differed in **5-3a** (boat-boat) and **5-3b** (chair-boat). This conformational difference likely greatly increased the steric congestion of **5-3a** due to both pendent amines being positioned toward the binding pocket whereas in **5-3b** only one pendent amine is positioned toward the binding pocket. A comparison between **5-3a** (boat-boat) and **5-5a** (boat-chair) assessed the difference in steric congestion due to P<sup>Ph</sup><sub>2</sub>N<sup>ArCF<sub>3</sub>2</sup> conformation, as both complexes possessed Ph as the phosphorus substituent. Complex **5-5a** was found to be less congested (% V<sub>Bur</sub> of 50.2%) as compared to **5-3a** (% V<sub>Bur</sub> = 64.3%) by ca. 14%, which demonstrated the significant influence conformation plays on steric congestion of the binding pocket. The oxidation state of the Pd in **5-3a** (Pd<sup>0</sup>) and **5-5a** (Pd<sup>II</sup>) could account for some difference in the calculated steric congestion, however, no significant differences in Pd-P bond lengths were observed for any of the complexes, with all distances between 2.26–2.32 Å.

A comparison between **5-3b** (R = tBu) and **5-5a** (R = Ph) was performed, in which both complexes have the P<sup>R</sup><sub>2</sub>N<sup>ArCF<sub>3</sub>2</sup> ligands in the chair-boat conformation. Complex **5-3b** (% V<sub>Bur</sub> = 56.6%) was more congested as compared to **5-5a** (% V<sub>Bur</sub> = 50.2) by ca. 6%. This result suggests that the tBu substituent has increased steric congestion of the binding pocket relative to the Ph substituent. The increased steric bulk of the tBu substituent could result in a disfavoured transition state during migratory insertion to formation the linear product, which would result in increased selectivity for the branched product. The Ph substituents in complex **5-3b** have the Ph substituents co-planar with the square plane, which represents the conformation with the most steric congestion, however, rotation of the Ph substituents to be perpendicular would decrease the steric congestion further. A comparison of **5-3a** (co-planar Ph substituents) and **5-2a** (one Ph substituent perpendicular), which differ only in the rotation of the Ph substituents, showed less congestion for **5-2a** (% V<sub>Bur</sub> = 58.7%) as compared to **5-3a** (% V<sub>Bur</sub> = 64.3%) by ca. 6%. It must be noted that part of the decreased congestion of **5-2a** could be due to the ABP ligand

which positions the proximal pendent amine further from the steric pocket, however, visual comparison of the steric maps of the Ph locations show less congestion for the perpendicular Ph substituent.

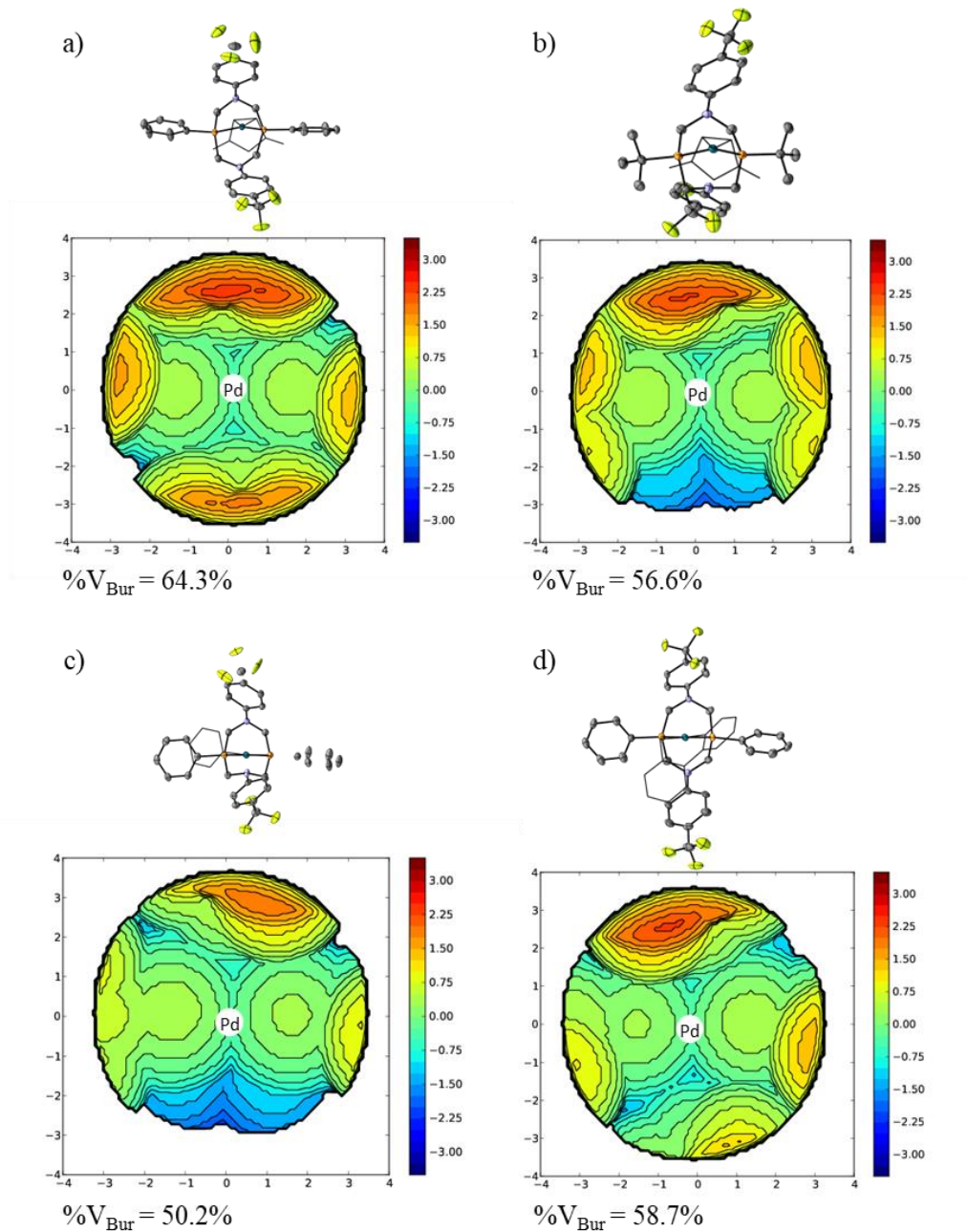


**Figure 5-9.** Steric maps of a) **5-3a**, b) **5-3b**, c) **5-5a**, and d) **5-2a**. The horizontal line from  $y = 0$  defines the P-Pd-P plane.

## 5.3 Conclusion

In conclusion, the first demonstration of Pd- $\text{P}^{\text{R}}_2\text{N}^{\text{ArCF}_3}_2$  for Mizoriki-Heck coupling was shown. Catalyst formation *in situ* from  $\text{Pd}_2\text{dba}_3$  and  $\text{P}^{\text{R}}_2\text{N}^{\text{ArCF}_3}_2$  as well as several mononuclear palladium precatalysts, **5-2a**, **5-2b**, **5-3a**, and **5-3b**, were assessed and successfully mediated the C-C coupling of phenyl triflate and styrene. Importantly, modification of the phosphorus substituent of the  $\text{P}^{\text{R}}_2\text{N}^{\text{ArCF}_3}_2$  ligand allowed for regioselective control of the coupling, which could favour linear (R = Ph) or branched (R = tBu) product formation. Elucidation of the reaction mechanism is still ongoing to determine the cause of regioselectivity. We initially hypothesized that the difference in selectivity could be due to a change in mechanism between the derivative (Ph vs tBu) or a steric influence of the phosphine substituents could be controlling regioselectivity. Stoichiometric reactions to access key intermediates were performed and the proposed mononuclear complex **5-4b** was observed from two separate reactions, oxidative addition from **5-2b** and halide abstraction from **5-5b**. However, isolation and complete characterization of this species and **5-5a** are currently ongoing to validate their formation. Catalyst order determination of **5-2a** showed an order of 1, which was also suggestive of a mononuclear pathway. Efforts to elucidate the catalyst order for **5-2b** will be explored. Investigations into the steric congestion of the binding pocket suggest an increased congestion from the tBu substituents as compared to the Ph substituents. Continued efforts to elucidate if the increased steric bulk influences the difference in selectivity are ongoing.

## 5.4 Experimental

All reactions were carried out under an inert atmosphere of Ar or  $\text{N}_2$ , using standard Schlenk or glovebox techniques, respectively, unless otherwise stated. All glassware was oven-dried (150 °C) prior to use. All chemicals were obtained from Sigma-Aldrich, Alfa Aesar, or Oakwood and used without further purification unless otherwise stated. Chloroform ( $\text{CDCl}_3$ , 99.8%), dichloromethane- $d_2$  ( $\text{CD}_2\text{Cl}_2$ , 99.8%), and toluene- $d_8$  ( $\text{C}_6\text{D}_5\text{CD}_3$ , 99.6%) were obtained from Cambridge Isotope Laboratories and used following drying over 4 Å sieves. *N,N'*-diaryldiazabutadiene,  $^{\text{DMP}}\text{DAB-Pd-MAH}^{22}$  and  $\text{Pd}(\text{Ph})(\text{I})(\text{TMEDA})^{22}$  were synthesized following literature procedures and the  $^1\text{H}$  and  $^{31}\text{P}\{^1\text{H}\}$  spectroscopic data matched literature values. Dry and degassed tetrahydrofuran

(THF), diethyl ether (Et<sub>2</sub>O), acetonitrile (MeCN), pentane, and hexanes were obtained from an Innovative Technology 400-5 solvent purification system and stored under a N<sub>2</sub> atmosphere on 4 Å sieves, besides MeCN which was on 3 Å sieves (Fluka and activated at 150 °C under vacuum).

Charge-transfer matrix assisted laser desorption/ionization (MALDI) mass spectrometry data were collected on an AB Sciex 5800 TOF/TOF mass spectrometer using pyrene as the matrix in a 20:1 molar ratio to metal complex. Samples were spotted on the target plate as solutions in DCM. NMR spectra were acquired on either an INOVA 600 MHz, Bruker 400 MHz, or Bruker 600 MHz NMR spectrometer. <sup>1</sup>H NMR spectra were referenced internally against the residual protio-solvent signal to tetramethylsilane at 0 ppm and <sup>13</sup>C{<sup>1</sup>H} NMR signal assignments were made using a combination of two-dimensional (2D) NMR spectra (<sup>1</sup>H-<sup>1</sup>H COSY, <sup>1</sup>H-<sup>13</sup>C{<sup>1</sup>H} heteronuclear single quantum coherence (HSQC), and <sup>1</sup>H-<sup>13</sup>C{<sup>1</sup>H} HMBC). <sup>31</sup>P{<sup>1</sup>H} NMR spectra were referenced externally to 85% phosphoric acid at 0.0 ppm. Abbreviations used for multiplicities are as follows: s = singlet, d = doublet, t = triplet, q = quartet, quint = quintet, sept = septet, and m = multiplet. Infrared spectra were collected on solid samples using a PerkinElmer UATR TWO FTIR spectrometer. Quantification of catalytic conversion was achieved using either: <sup>1</sup>H NMR spectroscopy referenced internally to dimethyl terephthalate (DMT) with relative integration or an Agilent 7890a gas chromatography with a flame ionization detector (GC-FID), fitted with a HP-5 column with calibration curves prepared to determine the response factor. The amount of each species was quantified, relative to a constant amount of internal standard (IS), 1,3,5-trimethoxybenzene, using area counts corrected with the response factor.

#### 5.4.1 General Procedure for the Synthesis of Pd(P<sup>R</sup><sub>2</sub>N<sup>ArCF<sub>3</sub><sub>2</sub>)<sub>2</sub>(MAH) Complexes.</sup>

A 20 mL vial with a stir bar was charged with <sup>DMP</sup>DAB-Pd-MAH (145 mg, 0.309 mmol) and either P<sup>Ph</sup><sub>2</sub>N<sup>ArCF<sub>3</sub><sub>2</sub> or P<sup>tBu</sup><sub>2</sub>N<sup>ArCF<sub>3</sub><sub>2</sub> (0.323 mmol, 1.05 equiv) and dissolved in THF (ca. 10 mL). The reaction was stirred at room temperature for 3 h during which a colour change from red to yellow was qualitatively observed. The solvent was removed *in vacuo* and the resulting solid was dissolved in a minimal amount of THF and filtered through Celite. Et<sub>2</sub>O</sup></sup>

was added to the filtrate which resulted in a pale yellow solid to precipitate out of solution. The suspension was left at -20 °C for 1 hour before the solvent was decanted. The solids were washed with Et<sub>2</sub>O (5 x 2 mL) until the washings were colourless and the residual solvent was removed *in vacuo* to afford an off-white solid.

**Pd(P<sup>Ph</sup><sub>2</sub>N<sup>ArCF<sub>3</sub>2</sup>)(MAH) (5-3a).** Yield = 89%. <sup>1</sup>H NMR (600 MHz, CD<sub>2</sub>Cl<sub>2</sub>): δ 7.89–7.82 (m, P-C<sub>6</sub>H<sub>6</sub>, 4H), 7.70–7.63 (m, P-C<sub>6</sub>H<sub>6</sub>, 6H), 7.38 (d, <sup>3</sup>J<sub>H-H</sub> = 9.0 Hz, N-C<sub>6</sub>H<sub>4</sub>-CF<sub>3</sub>, 2H), 7.30 (d, <sup>3</sup>J<sub>H-H</sub> = 8.8 Hz, N-C<sub>6</sub>H<sub>4</sub>-CF<sub>3</sub>, 2H), 6.47 (d, <sup>3</sup>J<sub>H-H</sub> = 8.6 Hz, N-C<sub>6</sub>H<sub>4</sub>-CF<sub>3</sub>, 2H), 6.40 (d, <sup>3</sup>J<sub>H-H</sub> = 8.6 Hz, N-C<sub>6</sub>H<sub>4</sub>-CF<sub>3</sub>, 2H), 4.49–4.43 (m, PCH<sub>2</sub>N, 2H), 4.32–4.23 (m, PCH<sub>2</sub>N, 6H), 3.51–3.48 (m, C<sub>4</sub>H<sub>2</sub>O<sub>3</sub>, 2H). <sup>13</sup>C{<sup>1</sup>H} NMR (243 MHz, CD<sub>2</sub>Cl<sub>2</sub>): δ 171.8 (s, (CH)<sub>2</sub>(CO)<sub>2</sub>O), 150.7 (s, N-C<sub>6</sub>H<sub>4</sub>CF<sub>3</sub>), 150.2 (s, N-C<sub>6</sub>H<sub>4</sub>CF<sub>3</sub>), 133.5 (X of ABX, P-C<sub>6</sub>H<sub>6</sub>), 132.3 (s, P-C<sub>6</sub>H<sub>6</sub>), 130.4 (X of ABX, P-C<sub>6</sub>H<sub>6</sub>), 127.3 (q, <sup>3</sup>J<sub>C-F</sub> = 3.8 Hz, N-C<sub>6</sub>H<sub>4</sub>CF<sub>3</sub>), 126.4 (q, <sup>3</sup>J<sub>C-F</sub> = 3.7 Hz, N-C<sub>6</sub>H<sub>4</sub>CF<sub>3</sub>), 115.8 (s, N-C<sub>6</sub>H<sub>4</sub>CF<sub>3</sub>), 115.1 (s, N-C<sub>6</sub>H<sub>4</sub>CF<sub>3</sub>), 56.0 (X of ABX, PCH<sub>2</sub>N), 55.8 (X of ABX, PCH<sub>2</sub>N), 50.7 (X of ABX, PCH<sub>2</sub>N). <sup>19</sup>F NMR (565 MHz, CD<sub>2</sub>Cl<sub>2</sub>): δ -61.7 (s, N-C<sub>6</sub>H<sub>4</sub>CF<sub>3</sub>), -61.8 (s, N-C<sub>6</sub>H<sub>4</sub>CF<sub>3</sub>). <sup>31</sup>P{<sup>1</sup>H} NMR (243 MHz, CD<sub>2</sub>Cl<sub>2</sub>): δ 9.6 (s, Pd-P). IR (neat) ν(cm<sup>-1</sup>): 3060 (w), 2944 (w), 1791 (m), 1751 (s), 1324 (s), 1109 (s), 1058 (s), 811 (m), 694 (m). MALDI MS (pyrene matrix): Simulated *m/z* [Pd(P<sup>Ph</sup><sub>2</sub>N<sup>ArCF<sub>3</sub>2</sup>)]<sup>+</sup> = 696.0, Obs. *m/z* = 695.8.

**Pd(P<sup>tBu</sup><sub>2</sub>N<sup>ArCF<sub>3</sub>2</sup>)(MAH) (5-3b).** Yield = 85%. <sup>1</sup>H NMR (400 MHz, CDCl<sub>3</sub>): δ 7.57 (d, <sup>3</sup>J<sub>H-H</sub> = 8.6 Hz, N-C<sub>6</sub>H<sub>4</sub>-CF<sub>3</sub>, 2H), 7.46 (d, <sup>3</sup>J<sub>H-H</sub> = 8.5 Hz, N-C<sub>6</sub>H<sub>4</sub>-CF<sub>3</sub>, 2H), 6.91 (d, <sup>3</sup>J<sub>H-H</sub> = 8.5 Hz, N-C<sub>6</sub>H<sub>4</sub>-CF<sub>3</sub>, 2H), 6.81 (d, <sup>3</sup>J<sub>H-H</sub> = 8.7 Hz, N-C<sub>6</sub>H<sub>4</sub>-CF<sub>3</sub>, 2H), 4.12–4.04 (m, PCH<sub>2</sub>N, 2H), 3.88–3.72 (m, PCH<sub>2</sub>N, 6H), 3.70 (m, C<sub>4</sub>H<sub>2</sub>O<sub>3</sub>, 2H), 1.37 (m, P-C(CH<sub>3</sub>)<sub>3</sub>, 18H). <sup>13</sup>C{<sup>1</sup>H} NMR (101 MHz, CD<sub>2</sub>Cl<sub>2</sub>): δ 172.1 (s, (CH)<sub>2</sub>(CO)<sub>2</sub>O), 152.2 (s, N-C<sub>6</sub>H<sub>4</sub>CF<sub>3</sub>), 151.0 (s, N-C<sub>6</sub>H<sub>4</sub>CF<sub>3</sub>), 127.5 (q, <sup>3</sup>J<sub>C-F</sub> = 3.8 Hz, N-C<sub>6</sub>H<sub>4</sub>CF<sub>3</sub>), 126.4 (q, <sup>3</sup>J<sub>C-F</sub> = 3.5 Hz, N-C<sub>6</sub>H<sub>4</sub>CF<sub>3</sub>), 114.9 (s, N-C<sub>6</sub>H<sub>4</sub>CF<sub>3</sub>), 114.7 (s, N-C<sub>6</sub>H<sub>4</sub>CF<sub>3</sub>), 48.5 (X of ABX, PCH<sub>2</sub>N), 46.6 (X of ABX, PCH<sub>2</sub>N), 46.4 (X of ABX, PCH<sub>2</sub>N), 32.5 (X of ABX, P-C(CH<sub>3</sub>)<sub>3</sub>), 27.2 (X of ABX, P-C(CH<sub>3</sub>)<sub>3</sub>). <sup>19</sup>F NMR (376 MHz, CD<sub>2</sub>Cl<sub>2</sub>): δ -61.59 (s, N-C<sub>6</sub>H<sub>4</sub>CF<sub>3</sub>), -61.64 (s, N-C<sub>6</sub>H<sub>4</sub>CF<sub>3</sub>). <sup>31</sup>P{<sup>1</sup>H} NMR (162 MHz, CD<sub>2</sub>Cl<sub>2</sub>): δ 30.3 (s, Pd-P). IR (neat) ν(cm<sup>-1</sup>): 2942 (w), 2898 (w), 1782 (m), 1715 (m), 1610 (m), 1322 (m), 1195 (m), 1106 (s), 1070 (m), 818 (m). MALDI MS (pyrene matrix): Simulated *m/z* [Pd(P<sup>tBu</sup><sub>2</sub>N<sup>ArCF<sub>3</sub>2</sup>)]<sup>+</sup> = 656.1, Obs. *m/z* = 655.9.

## 5.4.2 General Procedure for the Synthesis of Pd(Ph)(I)(P<sup>R</sup><sub>2</sub>N<sup>ArCF<sub>3</sub><sub>2</sub>) Complexes.</sup>

A 100 mL Schlenk flask with a stir bar was charged with Pd(Ph)(I)(TMEDA) (106 mg, 0.248 mmol) and either P<sup>Ph</sup><sub>2</sub>N<sup>ArCF<sub>3</sub><sub>2</sub> or P<sup>tBu</sup><sub>2</sub>N<sup>ArCF<sub>3</sub><sub>2</sub> (0.251 mmol, 1.05 equiv) and dissolved in THF (ca. 25 mL). The reaction with **5-1a** was stirred at room temperature for 48 h, while the reaction with **5-1b** was stirred at 50 °C for 24 h. The solvent was removed *in vacuo*, the solid was redissolved in a minimal amount of THF and filtered through Celite. The filter was subsequently washed with THF until the washings were colourless. The volume of the filtrate was reduced *in vacuo* and Et<sub>2</sub>O was added to the filtrate which resulted in an orange solid to precipitate out of solution. The solvent was decanted off, the solid washed with Et<sub>2</sub>O (5 x 2 mL) until the washings were colourless, and the residual solvent removed *in vacuo* to afford an orange solid.</sup></sup>

**Pd(Ph)(I)(P<sup>Ph</sup><sub>2</sub>N<sup>ArCF<sub>3</sub><sub>2</sub>) (5-5a).</sup>** Yield = 87%. <sup>1</sup>H NMR (600 MHz, CD<sub>2</sub>Cl<sub>2</sub>): δ 8.07 (m, P-C<sub>6</sub>H<sub>6</sub>, 2H), 7.67–7.59 (m, P-C<sub>6</sub>H<sub>6</sub> and N-C<sub>6</sub>H<sub>4</sub>CF<sub>3</sub>, 6H), 7.33–7.25 (m, P-C<sub>6</sub>H<sub>6</sub>, 2H), 7.20–7.14 (m, P-C<sub>6</sub>H<sub>6</sub>, 2H), 7.08–6.98 (m, P-C<sub>6</sub>H<sub>6</sub> and N-C<sub>6</sub>H<sub>4</sub>CF<sub>3</sub>, 6H), 6.53–6.46 (m, Pd-C<sub>6</sub>H<sub>6</sub>, 2H), 6.46–6.42 (m, Pd-C<sub>6</sub>H<sub>6</sub>, 1H), 6.30–6.25 (m, Pd-C<sub>6</sub>H<sub>6</sub>, 2H), 4.61–4.56 (m, Pd-PCH<sub>2</sub>N, 2H), 4.41–4.35 (m, Pd-PCH<sub>2</sub>N, 2H), 4.31–4.25 (m, Pd-PCH<sub>2</sub>N, 2H), 4.22–4.17 (m, Pd-PCH<sub>2</sub>N, 2H). <sup>13</sup>C{<sup>1</sup>H} NMR (400 MHz, CD<sub>2</sub>Cl<sub>2</sub>): δ 153.0 (Pd-C<sub>6</sub>H<sub>6</sub>), 151.9 (s, N-C<sub>6</sub>H<sub>4</sub>CF<sub>3</sub>), 137.6 (Pd-C<sub>6</sub>H<sub>6</sub>), 133.8 (d, <sup>3</sup>J<sub>C-P</sub> = 8.4 Hz, P-C<sub>6</sub>H<sub>6</sub>), 131.4 (d, J<sub>C-P</sub> = 7.9 Hz, P-C<sub>6</sub>H<sub>6</sub>), 129.8 (d, J = 9.2 Hz, P-C<sub>6</sub>H<sub>6</sub>), 129.4 (d, J = 9.8 Hz, P-C<sub>6</sub>H<sub>6</sub>), 127.8 (q, <sup>3</sup>J<sub>C-F</sub> = 2.8 Hz, N-C<sub>6</sub>H<sub>4</sub>CF<sub>3</sub>), 127.4 (s, Pd-C<sub>6</sub>H<sub>6</sub>), 122.9 (N-C<sub>6</sub>H<sub>4</sub>CF<sub>3</sub>), 122.6 (s, Pd-C<sub>6</sub>H<sub>6</sub>), 117.1 (s, N-C<sub>6</sub>H<sub>4</sub>CF<sub>3</sub>), 52.7 (P-CH<sub>2</sub>-N), 52.5 (P-CH<sub>2</sub>-N), 51.3 (P-CH<sub>2</sub>-N), 51.2 (P-CH<sub>2</sub>-N). <sup>19</sup>F NMR (565 MHz, CD<sub>2</sub>Cl<sub>2</sub>): δ -61.9 (s, N-C<sub>6</sub>H<sub>4</sub>CF<sub>3</sub>). <sup>31</sup>P{<sup>1</sup>H} NMR (243 MHz, CD<sub>2</sub>Cl<sub>2</sub>): δ 4.2 (d, <sup>2</sup>J<sub>P-P</sub> = 60.1 Hz, P-Pd-P), -20.9 (d, <sup>2</sup>J<sub>P-P</sub> = 60.1 Hz, P-Pd-P). IR (neat) ν(cm<sup>-1</sup>): 3033 (w), 1612 (m), 1325 (s), 1107 (s), 1070 (s), 812 (m), 727 (m), 690 (m). MALDI MS (pyrene matrix): Simulated *m/z* for [Pd(Ph)(I)(P<sup>Ph</sup><sub>2</sub>N<sup>ArCF<sub>3</sub><sub>2</sub>)]<sup>+</sup> - 3F = 843.0, Obs. *m/z* = 843.8.</sup>

**Pd(Ph)(I)(P<sup>tBu</sup><sub>2</sub>N<sup>ArCF<sub>3</sub><sub>2</sub>) (5-5b).</sup>** Yield = 90%. <sup>1</sup>H NMR (400 MHz, CD<sub>2</sub>Cl<sub>2</sub>): δ 7.64 (d, <sup>3</sup>J<sub>H-H</sub> = 8.5 Hz, N-C<sub>6</sub>H<sub>4</sub>CF<sub>3</sub>, 4H), 7.09 (d, <sup>3</sup>J<sub>H-H</sub> = 8.7 Hz, N-C<sub>6</sub>H<sub>4</sub>CF<sub>3</sub>, 4H), 6.78 (ddd, <sup>3</sup>J<sub>H-H</sub> = 7.6 Hz, <sup>4</sup>J<sub>H-H</sub> = 6.6 Hz, <sup>5</sup>J<sub>H-H</sub> = 1.3 Hz, Pd-C<sub>6</sub>H<sub>6</sub>, 2H), 6.67 (ddd, <sup>3</sup>J<sub>H-H</sub> = 7.6 Hz, <sup>4</sup>J<sub>H-H</sub> = 5.3 Hz, <sup>5</sup>J<sub>H-H</sub> = 1.1 Hz, Pd-C<sub>6</sub>H<sub>6</sub>, 1H), 6.47 (ddd, <sup>3</sup>J<sub>H-H</sub> = 7.9 Hz, <sup>4</sup>J<sub>H-H</sub> = 2.7 Hz, <sup>5</sup>J<sub>H-H</sub> = 1.2 Hz,



Pd-C<sub>6</sub>H<sub>6</sub>, 2H), 4.29–4.21 (m, PCH<sub>2</sub>N, 2H), 4.14–4.06 (m, PCH<sub>2</sub>N, 2H), 3.84–3.75 (m, PCH<sub>2</sub>N, 4H), 1.64 (d, <sup>3</sup>J<sub>H-P</sub> = 13.8 Hz, P-C(CH<sub>3</sub>)<sub>3</sub>, 9H), 0.95 (d, <sup>3</sup>J<sub>H-P</sub> = 14.2 Hz, P-C(CH<sub>3</sub>)<sub>3</sub>, 9H). <sup>13</sup>C{<sup>1</sup>H} NMR (101 MHz, CD<sub>2</sub>Cl<sub>2</sub>): δ 151.8 (s, N-C<sub>6</sub>H<sub>4</sub>CF<sub>3</sub>), 145.2 (Pd-C<sub>6</sub>H<sub>6</sub>), 139.9 (dd, <sup>3</sup>J<sub>C-P</sub> = 4.3 Hz, 1.7 Hz, Pd-C<sub>6</sub>H<sub>6</sub>), 127.5 (q, <sup>3</sup>J<sub>C-F</sub> = 3.8 Hz, N-C<sub>6</sub>H<sub>4</sub>CF<sub>3</sub>), 127.0 (dd, <sup>4</sup>J<sub>C-P</sub> = 4.3, 1.7 Hz, Pd-C<sub>6</sub>H<sub>6</sub>), 123.0 (s, Pd-C<sub>6</sub>H<sub>6</sub>), 123.8 (s, N-C<sub>6</sub>H<sub>4</sub>CF<sub>3</sub>), 122.2 (s, N-C<sub>6</sub>H<sub>4</sub>CF<sub>3</sub>), 116.5 (s, N-C<sub>6</sub>H<sub>4</sub>CF<sub>3</sub>), 49.3 (dd, <sup>1</sup>J<sub>C-P</sub> = 13.2 Hz, <sup>3</sup>J<sub>C-P</sub> = 4.2 Hz, PCH<sub>2</sub>N), 47.7 (dd, <sup>1</sup>J<sub>C-P</sub> = 8.2 Hz, <sup>3</sup>J<sub>C-P</sub> = 2.3 Hz, PCH<sub>2</sub>N), 34.7 (dd, <sup>1</sup>J<sub>C-P</sub> = 10.2 Hz, <sup>3</sup>J<sub>C-P</sub> = 1.7 Hz, P-C(CH<sub>3</sub>)<sub>3</sub>), 34.2 (d, <sup>1</sup>J<sub>C-P</sub> = 5.9 Hz, P-C(CH<sub>3</sub>)<sub>3</sub>), 27.8 (d, <sup>2</sup>J<sub>C-P</sub> = 1.7 Hz, P-C(CH<sub>3</sub>)<sub>3</sub>), 27.1 (s, P-C(CH<sub>3</sub>)<sub>3</sub>). <sup>19</sup>F NMR (376 MHz, CD<sub>2</sub>Cl<sub>2</sub>): δ -61.8 (s, N-C<sub>6</sub>H<sub>4</sub>CF<sub>3</sub>). <sup>31</sup>P{<sup>1</sup>H} NMR (162 MHz, CD<sub>2</sub>Cl<sub>2</sub>): δ 15.2 (d, <sup>2</sup>J<sub>P-P</sub> = 47.8 Hz, P-Pd-P), -2.7 (d, <sup>2</sup>J<sub>P-P</sub> = 47.8 Hz, P-Pd-P). IR (neat) ν(cm<sup>-1</sup>): 3051 (w), 2956 (w), 2869 (w), 1612 (m), 1326 (s), 1110 (s), 1070 (s), 810 (m). MALDI MS (pyrene matrix): Simulated *m/z* for [Pd(Ph)(I)(P<sup>t</sup>Bu<sub>2</sub>N<sup>Ar</sup>CF<sub>3</sub><sub>2</sub>)]<sup>+</sup> - 3F = 803.1, Obs. *m/z* = 803.9.

#### 5.4.3 General Procedure for Oxidative Addition of Pd Complexes with Phenyl Triflate.

A 4 mL vial was charged with a Pd precatalyst, either **5-3a**, **5-3b**, **5-2a**, or **5-2b** (10 mg, 0.010–0.014 mmol), phenyl triflate (0.020–0.022 mmol, 2 equiv), and a base (either TMP, piperidine, or pyridine; 0.020–0.022 mmol, 2 equiv) in THF, DCM, or 1,4-dioxane (2 mL). The reactions with **5-3a** and **5-3b** were stirred for 18 h at 85 °C during which no reaction was observed by <sup>31</sup>P{<sup>1</sup>H} NMR spectroscopy or by visual inspection. The reactions with the G3 complexes were stirred for 3 h at 85 °C during which a colour change from colourless to red was observed. The reactions with the G3 complexes were filtered through Celite and the solvent removed under reduced pressure. The red powders were analyzed by <sup>31</sup>P{<sup>1</sup>H} NMR spectroscopy in DCM-*d*<sub>2</sub> which showed a major species which was proposed as the respective oxidative addition intermediates **5-5a** and **5-5b**.

#### 5.4.4 General Procedure for Independent Synthesis of Oxidative Addition Species **5-3b**.

A 4 mL vial was charged with either **5-3a** or **5-3b** (10 mg, 0.010–0.011 mmol), silver trifluoromethanesulfonate (0.011 mmol, 1 equiv), and piperidine (0.011 mmol, 1 equiv) in THF (2 mL). The reactions were stirred for 2 h at room temperature during which

precipitation of a brown solid was observed. The reactions were filtered through Celite and the solvent removed under reduced pressure. The resulting yellow solids were dissolved in DCM- $d_2$  and analyzed by  $^{31}\text{P}\{^1\text{H}\}$  NMR spectroscopy.

#### 5.4.5 General Catalytic Procedure for **5-3a** and **5-3b** Assessment.

In a glovebox, the following stock solutions were prepared: phenyl acetylene (0.400 M), styrene (0.440 M), and TMP (0.800 M); **5-3a** (0.004 M) or **5-3b** (0.004 M); and 1,3,5-trimethoxybenzene (IS = internal standard) (0.200 M) all in either toluene and Me-THF. Portions of substrate stock solution (500  $\mu\text{L}$ ) and catalyst stock solution (500  $\mu\text{L}$ ) were dispensed into 4 mL screw cap reaction vials containing a stir bar. The final concentration for all reaction vials were 0.200 M in phenyl triflate, 0.220 M in styrene, and 0.002 M in catalyst. The reaction vials were capped and removed from the glovebox and heated to 85  $^\circ\text{C}$  with stirring. After 16 h the vials were removed from heat, exposed to air, and 500  $\mu\text{L}$  was diluted with with 500  $\mu\text{L}$  of IS stock solution. This diluted sample was subsequently analyzed by GC-FID.

#### 5.4.6 General Catalytic Procedure for Catalyst Order Determination.

In a glovebox, the following two catalyst solutions were prepared: **5-2a** (**a** = 0.024 M, **b** = 0.012 M) in DCM. A substrate stock solution was prepared with phenyl triflate (0.300 M), styrene (0.300 M), TMP (0.600 M), and dimethyl terephthalate (IS) (0.030 M) in toluene- $d_8$ . A sealable NMR tube was charged with either catalyst stock solution **a** or **b** (200  $\mu\text{L}$ ) and the solvent pumped off *in vacuo*. Once the volatiles were removed the NMR tube was charged with 200  $\mu\text{L}$  toluene- $d_8$  and 400  $\mu\text{L}$  substrate stock solution and inverted to mix. An initial  $^1\text{H}$  NMR spectrum was obtained and used as T0. The NMR instrument probe was then heated to the reaction temperature of 85  $^\circ\text{C}$  and the NMR tube was inserted after it reached the desired temperature. The final concentration of the reactions **A** and **B** were as follows: **A**) 200 mM phenyl triflate, 200 mM styrene, 400 mM TMP, 8 mM catalyst, **B**) 200 mM phenyl triflate, 200 mM styrene, 400 mM TMP, 4 mM catalyst. The NMR tubes were inserted into the NMR instrument and allowed to reach the reaction temperature over 5 min before a  $^1\text{H}$  NMR spectral array was obtained with spectra collected every 20 min

for 7 h. The resulting NMR spectra were analyzed to quantify the integration of the terminal alkene signal of styrene relative to the integral of DMT (8.32 ppm) to determine *in situ* consumption. Each catalytic run was performed in duplicate, and the data averaged, with the error bars representing the span.

## 5.5 References

1. (a) L. Budarin, V.; S. Shuttleworth, P.; H. Clark, J.; Luque, R., *Curr. Org. Synth.* **2010**, *7* (6), 614-627; (b) Devendar, P.; Qu, R.-Y.; Kang, W.-M.; He, B.; Yang, G.-F., *J. Agric. Food. Chem.* **2018**, *66* (34), 8914-8934; (c) Xu, S.; Kim, E. H.; Wei, A.; Negishi, E.-i., *Science and Technology of Advanced Materials* **2014**, *15* (4), 044201.
2. Kadu, B. S., *Catalysis Science & Technology* **2021**, *11* (4), 1186-1221.
3. Suzuki, A., *Angew. Chem. Int. Ed.* **2011**, *50* (30), 6722-6737.
4. Brown, D. G.; Boström, J., *J. Med. Chem.* **2016**, *59* (10), 4443-4458.
5. (a) Heck, R. F., *J. Am. Chem. Soc.* **1969**, *91* (24), 6707-6714; (b) Heck, R. F.; Nolley, J. P., *J. Org. Chem.* **1972**, *37* (14), 2320-2322; (c) Mizoroki, T.; Mori, K.; Ozaki, A., *Bull. Chem. Soc. Jpn.* **1971**, *44* (2), 581-581; (d) Heck, R. F., *J. Am. Chem. Soc.* **1968**, *90* (20), 5518-5526; (e) Fujiwara, Y.; Moritani, I.; Danno, S.; Asano, R.; Teranishi, S., *J. Am. Chem. Soc.* **1969**, *91* (25), 7166-7169; (f) Moritanl, I.; Fujiwara, Y., *Tetrahedron Lett.* **1967**, *8* (12), 1119-1122.
6. Shen, J.; Xu, B.; Zhang, M.; Su, W., *Eur. J. Org. Chem.* **2018**, *2018* (22), 2768-2773.
7. Dounay, A. B.; Overman, L. E., *Chem. Rev.* **2003**, *103* (8), 2945-2964.
8. Nilsson, P.; Olofsson, K.; Larhed, M., *The Mizoroki–Heck Reaction* **2009**, 133-162.
9. (a) Stubbs, J. M.; Bow, J. P. J.; Hazlehurst, R. J.; Blacquiere, J. M., *Dalton Trans.* **2016**, *45* (43), 17100-17103; (b) Stubbs, J. M.; Chapple, D. E.; Boyle, P. D.; Blacquiere, J. M., *ChemCatChem* **2018**, *10* (17), 4001-4009; (c) Stubbs, J. M.; Bridge, B. J.; Blacquiere, J. M., *Dalton Trans.* **2019**, *48* (22), 7928-7937; (d) Bridge, B. J.; Boyle, P. D.; Blacquiere, J. M., *Organometallics* **2020**, *39* (14), 2570-2574; (e) Chapple, D. E.; Boyle, P. D.; Blacquiere, J. M., *ChemCatChem* **2021**, *13* (17), 3789-3800; (f) Chapple, D. E.; Hoffer, M. A.; Boyle, P. D.; Blacquiere, J. M., *Organometallics* **2022**, *41* (12), 1532-1542.
10. Stubbs, J. M.; Hazlehurst, R. J.; Boyle, P. D.; Blacquiere, J. M., *Organometallics* **2017**, *36* (9), 1692-1698.
11. Wiedner, E. S.; Appel, A. M.; Raugei, S.; Shaw, W. J.; Bullock, R. M., *Chem. Rev.* **2022**.

12. Isbrandt, E. S.; Nasim, A.; Zhao, K.; Newman, S. G., *J. Am. Chem. Soc.* **2021**, *143* (36), 14646-14656.
13. Huang, J.; Isaac, M.; Watt, R.; Becica, J.; Dennis, E.; Saidaminov, M. I.; Sabbers, W. A.; Leitch, D. C., *ACS Catalysis* **2021**, *11* (9), 5636-5646.
14. Kilgore, U. J.; Roberts, J. A. S.; Pool, D. H.; Appel, A. M.; Stewart, M. P.; DuBois, M. R.; Dougherty, W. G.; Kassel, W. S.; Bullock, R. M.; DuBois, D. L., *J. Am. Chem. Soc.* **2011**, *133* (15), 5861-5872.
15. (a) Tronic, T. A.; Kaminsky, W.; Coggins, M. K.; Mayer, J. M., *Inorg. Chem.* **2012**, *51* (20), 10916-10928; (b) Zhang, S.; Appel, A. M.; Bullock, R. M., *J. Am. Chem. Soc.* **2017**, *139* (21), 7376-7387.
16. Barder, T. E.; Biscoe, M. R.; Buchwald, S. L., *Organometallics* **2007**, *26* (9), 2183-2192.
17. Yang, L.; Powell, D. R.; Houser, R. P., *Dalton Trans.* **2007**, (9), 955-964.
18. Bruno, N. C.; Tudge, M. T.; Buchwald, S. L., *Chemical Science* **2013**, *4* (3), 916-920.
19. Hayashi, Y.; Wada, S.; Yamashita, M.; Nozaki, K., *Organometallics* **2012**, *31* (3), 1073-1081.
20. Franz, J. A.; O'Hagan, M.; Ho, M.-H.; Liu, T.; Helm, M. L.; Lense, S.; DuBois, D. L.; Shaw, W. J.; Appel, A. M.; Raugei, S.; Bullock, R. M., *Organometallics* **2013**, *32* (23), 7034-7042.
21. Falivene, L.; Cao, Z.; Petta, A.; Serra, L.; Poater, A.; Oliva, R.; Scarano, V.; Cavallo, L., *Nature Chem.* **2019**, *11* (10), 872-879.
22. Witte, F.; Zucker, S. P.; Paulus, B.; Tzschucke, C. C., *Organometallics* **2021**, *40* (5), 591-599.

## 6 Summary, Conclusion, and Future Work

### 6.1 Summary and Conclusion

The utilization of M-P<sub>2</sub>N<sub>2</sub> catalysts for catalytic reactions was investigated through substrate scope studies, stoichiometric reactions, and mechanistic studies. Ru-P<sub>2</sub>N<sub>2</sub> and Pd-P<sub>2</sub>N<sub>2</sub> complexes were applicable catalysts for alkyne hydrofunctionalization and Heck coupling reactions, respectively. Elucidation of structural factors and interactions that influenced catalyst lifetime, pathways for catalyst deactivation, and selectivity were identified and, in some cases, mitigated.

In chapter two, new entries into the Ru-P<sub>2</sub>N<sub>2</sub> catalyst family, [Ru(Cp)(P<sup>Cy</sup><sub>2</sub>N<sup>Ph</sup><sub>2</sub>)(MeCN)]PF<sub>6</sub> and [Ru(Cp\*)(P<sup>Cy</sup><sub>2</sub>N<sup>Ph</sup><sub>2</sub>)(MeCN)]PF<sub>6</sub>, were synthesized and their performance assessed for intramolecular hydroamination to form *N*-heterocycles. The ligand structure, specifically the phosphine substituent and ancillary Cp/Cp\* ligand, was found to play a crucial role in both catalyst lifetime and reaction rate. Investigations into the active operationally unsaturated catalysts provided insight into their inherent stability differences. Stabilization through a previously unseen κ<sup>3</sup>-(P,P,Ar) binding mode with the P<sup>Cy</sup><sub>2</sub>N<sup>Ph</sup><sub>2</sub> ligand was observed exclusively with the Cp derivative, which likely contributes to the higher catalytic lifetime. Product inhibition was also observed, which may further contribute to catalyst stabilization at the expense of reduced reaction rate. A deactivation pathway was also observed through undesired reactivity with halogenated solvents for the Cp\* derivative whereas the Cp derivative was stable under analogous conditions. These findings showed that choice of the ancillary Cp/Cp\* ligand is fundamental to achieve a long lifetime catalysis. While complexes furnished with the Cp ligand showed slower catalytic rate, the reduced risk of deactivation through undesired reactivity (Cp\* functionalization) and the observed stabilization via the P<sub>2</sub>N<sub>2</sub> ligand (hemilability) with Cp derivatives, are highly desirable. Consideration should also be given to unproductive coordination between the catalysts and substrates/products, which can have both a positive (stabilization) and negative (reduced rate) influence on reactivity.

In chapter three, [Ru(Cp)(P<sup>Cy</sup><sub>2</sub>N<sup>Ph</sup><sub>2</sub>)(MeCN)]PF<sub>6</sub> was accessed for various hydrofunctionalization reactions to explore mechanistic opportunities and limitations.

Experimental data which corroborated the proposed mechanistic pathway, beyond selective formation of *endo-dig* cyclized products, was thoroughly investigated for the first time for these Ru-P<sup>R</sup><sub>2</sub>N<sup>R'</sup><sub>2</sub> complexes. Ligand modification of the pendent amine (from Bn to Ph) enabled alkyne hydroalkoxylation cyclization without problematic deactivation that was previously observed. This result demonstrated the power of ligand modification from a more nucleophilic pendent amine to a less nucleophilic analogue, which mitigated formation of the vinyl ammonium deactivation pathway. Vinylidene formation was determined to be rate-limiting for these catalysts. Further elucidation of the benchmark 2-ethynylbenzyl alcohol cyclization was performed, which validated and identified previously proposed and new aspects of the mechanism. A new deactivation pathway via formation of a highly stable off-cycle ruthenium species was identified via protonation of C<sub>β</sub>, instead of productive C<sub>α</sub> protonation. Substrates which preferentially protonate C<sub>β</sub> would be incompatible with these catalysts, however, identifying which substrates this includes is still unclear.

In chapter four, the successful implementation of the findings enabled the isolation of ruthenium vinylidene complexes [Ru(Cp/Cp\*)(P<sup>Cy</sup><sub>2</sub>N<sup>Ph</sup><sub>2</sub>)(=C=HPh)]PF<sub>6</sub>. Ligand modification proved essential to achieve isolation of the vinylidene complexes, which required a less nucleophilic pendent amine. The isolation of these vinylidene complexes supported the proposal that these species are likely intermediates in intramolecular hydrofunctionalization reactions and allow systematic investigation into intermolecular chemistry as a proposed on-cycle intermediate. Isolation of the vinylidene complexes allowed stoichiometric studies to be attempted with various amine nucleophiles to investigate the applicability of these catalysts for intermolecular reactivity. However, the stoichiometric studies of nucleophiles with high basicity (pK<sub>aH</sub> ≥ 18) showed undesirable reactivity, which resulted in the formation of the ruthenium acetylide complex [Ru(Cp\*)(P<sup>Cy</sup><sub>2</sub>N<sup>Ph</sup><sub>2</sub>)(-C≡C-Ph)]. Stoichiometric reactions with an amine nucleophile, aniline, with a lower basicity (pK<sub>aH</sub> ≈ 10) avoided formation of the ruthenium acetylide complex and showed potential of organic product release. Attempts at intermolecular hydroamination were performed with two amine nucleophiles of lower basicity were unsuccessful. We hypothesize that potential formation of a ruthenium-carbene complex, via protonation of C<sub>β</sub> could deactivate the complex, which would only be problematic for

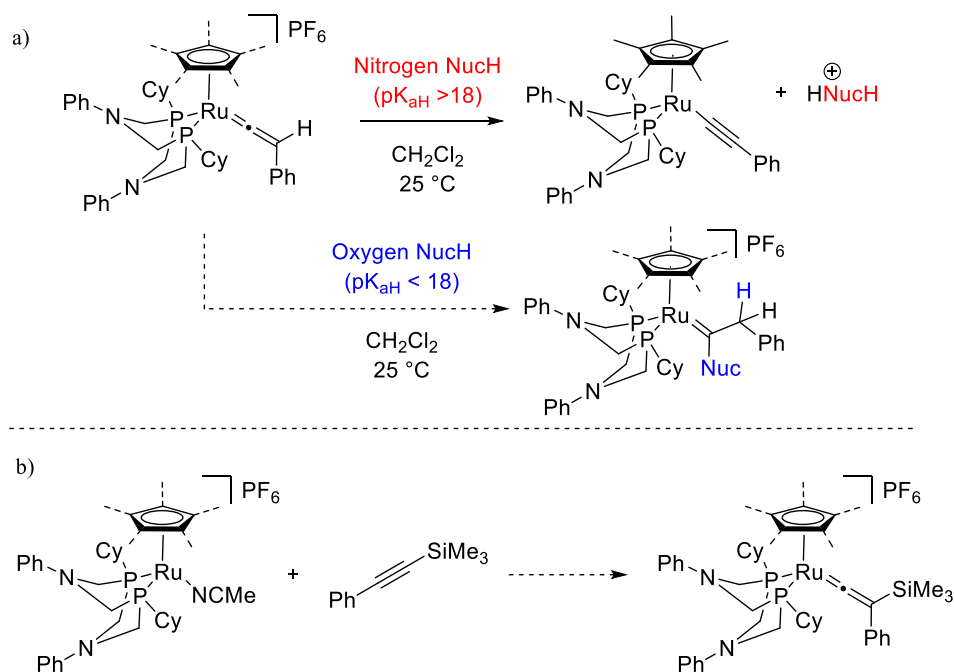
*anti*-Markovnikov product formation, specifically catalysts, which proceed through a vinylidene intermediate.

In chapter five, the second example of C-C coupling with  $M-P^R_2N^{ArCF_3}_2$  complexes was realized through collaboration with the Newman group (UOttawa).  $Pd-P^R_2N^{ArCF_3}_2$  complexes were investigated for the Heck-coupling of phenyl triflate and styrene. Complexes with  $R = Ph$  resulted in high selectivity for the linear product while complexes with  $R = tBu$  had high selectivity for the branched product. The content of Chapter 5 focuses on the cause of differing selectivity through intermediate synthesis, kinetic analysis, and ligand steric considerations. Currently, the findings from intermediate synthesis and kinetic analysis suggest the difference in selectivity is likely due to a steric difference in the phosphorus substituents and further investigations to corroborate this hypothesis are currently ongoing. The steric congestion of the catalyst pocket was investigated computationally, which demonstrated more steric hindrance for the  $tBu$  derivative versus the  $Ph$  derivative. The location of the increased steric bulk should theoretically influence the preferred orientation of the styrene which results in branched product formation for more sterically bulky phosphorus substituents. This represents the one of the first instances of selective product formation with complexes ligated with  $P^R_2N^{R'}_2$  ligands.

Overall, contributions to the mechanistic understanding and future potential of  $M-P_2N_2$  catalysts for organic transformations was performed. Validation of previous proposed mechanistic pathways was achieved through experimental methods. Modification of the nitrogen substituent of the  $P^R_2N^{R'}_2$  ligand influenced catalyst stability through stabilization of the low-coordinate active species and avoidance of deactivation. Phosphorus substituent choice was also shown to influence catalyst performance and was also essential in product selectivity in cross-coupling. Choice of ancillary ligand was shown to influence interactions between the  $P^R_2N^{R'}_2$  ligand and the metal center, which have significant impact on performance and stability. Advances to the scope of organic transformations was achieved, which demonstrate the potential of  $M-P^R_2N^{R'}_2$  catalysts for previously unrealized transformations and improved performance on already established reactions.

## 6.2 Future Work

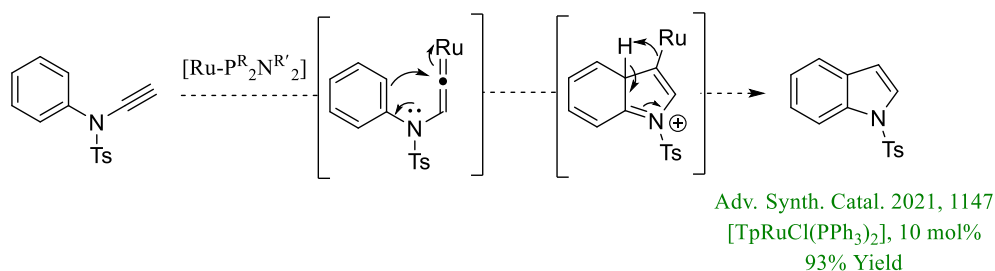
Intermolecular hydrofunctionalization has not yet been realized for the Ru-P<sub>2</sub>N<sub>2</sub> complexes. In chapter four nucleophiles with pK<sub>aH</sub> above 18 led to C<sub>β</sub> deprotonation while aniline (pK<sub>aH</sub> ca. 10) did not result in deprotonation (Scheme 6-1a). Therefore, future stoichiometric studies should focus on nucleophiles with a pK<sub>aH</sub> < 18 to determine when deprotonation becomes problematic and avoid it (Scheme 6-1a). Oxygen nucleophiles, while less nucleophilic than amine nucleophiles, would possess lower basicity which should avoid formation of the acetylide species. Furthermore, while the stoichiometric investigations with the ruthenium vinylidene complexes were focused on the Cp\* derivative, nucleophilic experiments with the Cp analogue should also be investigated. The Cp complexes possess greater stability due to ligand interactions that stabilize the low coordinate active complex. Investigations into internal alkyne vinylidene formation, such as trimethylsilylethynylbenzene, would also be an interesting route to explore and has been demonstrated with other catalysts (Scheme 6-1b. Internal alkynes would avoid possible formation of acetylide formation due to the lack of C<sub>β</sub> deprotonation.



**Scheme 6-1.** a) potential of nucleophiles, such as oxygen, with lower basicity to avoid acetylide formation. b) investigation of internal alkynes for the formation of vinylidenes.



Indole formation from ynamides has recently been established with similar half-sandwich ruthenium diphosphine complexes via vinylidene formation and subsequent C-C bond formation (Scheme 6-2). However, the catalyst loadings required under the optimal conditions for cyclization was found to be 10 mol%, which could be greatly improved. The successful cyclization of the nitron substrate, which involved an electronic rearrangement for product release, is similar to the proposed mechanism for the release of indole from ynamides. The  $\text{Ru-P}^{\text{R}_2}\text{N}^{\text{R}'_2}$  should be assessed for the cyclization of *N*-phenyl-*N*-tosylynamide and other derivatives. Furthermore, precedent for  $\text{M-P}^{\text{R}_2}\text{N}^{\text{R}'_2}$  catalysts in C-C couplings with Ni and Pd based catalysts been demonstrated which establishes the potential of these ligands for other C-C bond forming reactions.



**Scheme 6-2.** Cyclization of ynamides to form indole

## Appendices

### Appendices A: Supplementary Information for Chapter 2

#### NMR Data

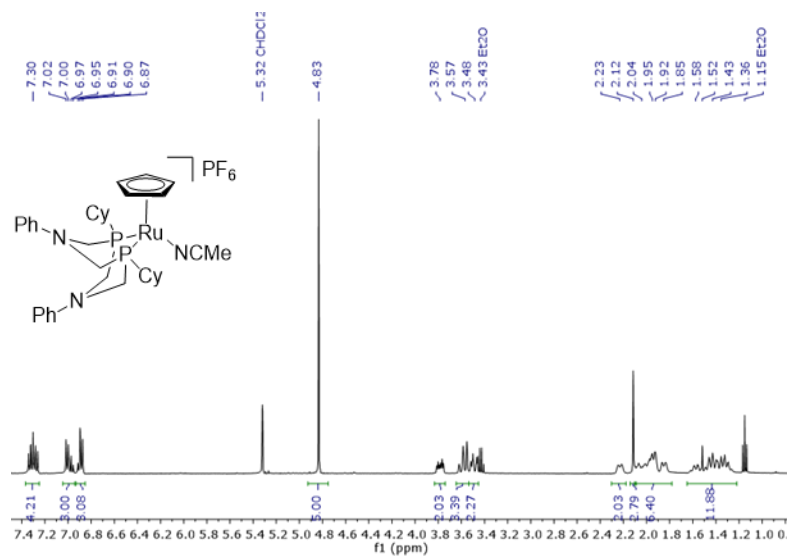


**Figure A-1.**  $^1\text{H}$  NMR spectrum of  $[\text{Ru}(\text{Cp})(\text{P}^{\text{Cy}}_2\text{N}^{\text{Ph}}_2)(\text{MeCN})]\text{PF}_6$  (**2-1b**) (600 MHz,  $\text{CD}_2\text{Cl}_2$ ).

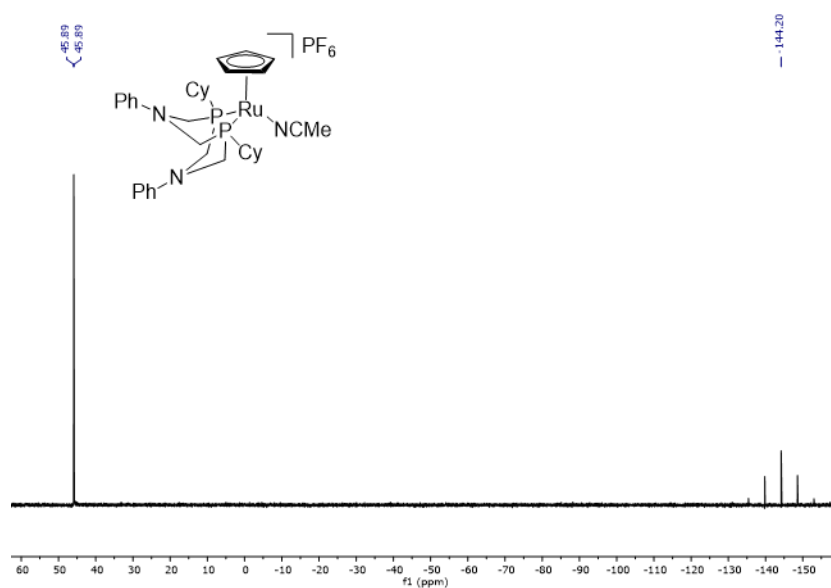


**Figure A-2.**  $^{31}\text{P}\{^1\text{H}\}$  NMR spectrum of **2-1b** (243 MHz,  $\text{CD}_2\text{Cl}_2$ ).

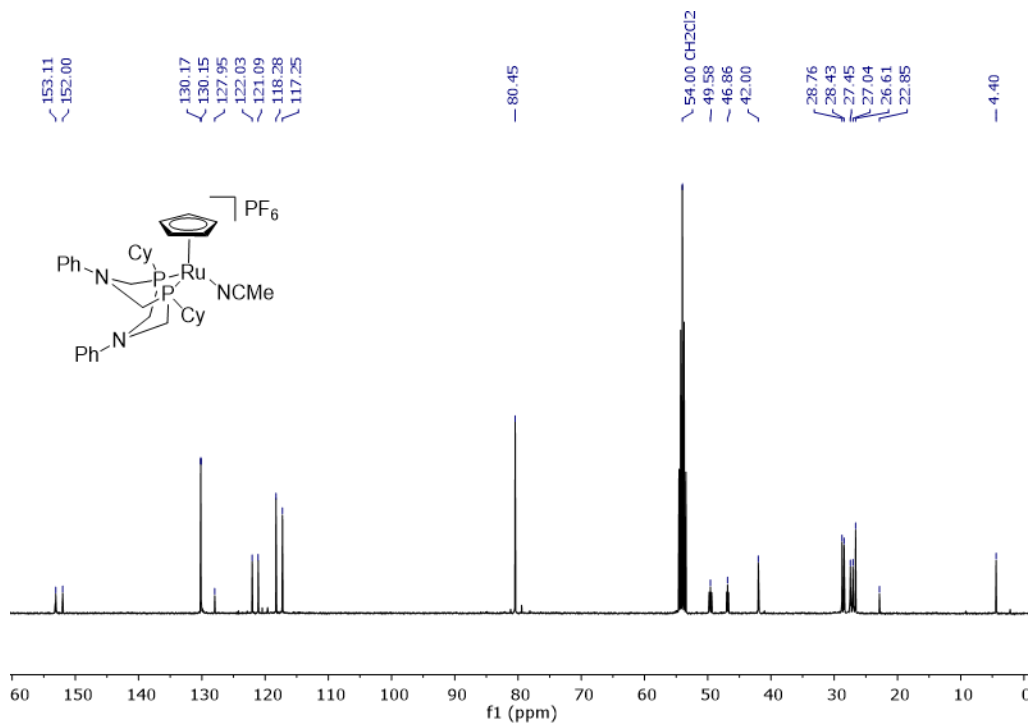


**Figure A-3.**  $^{13}\text{C}\{^1\text{H}\}$  NMR spectrum of **2-1b** (151 MHz,  $\text{CD}_2\text{Cl}_2$ ).

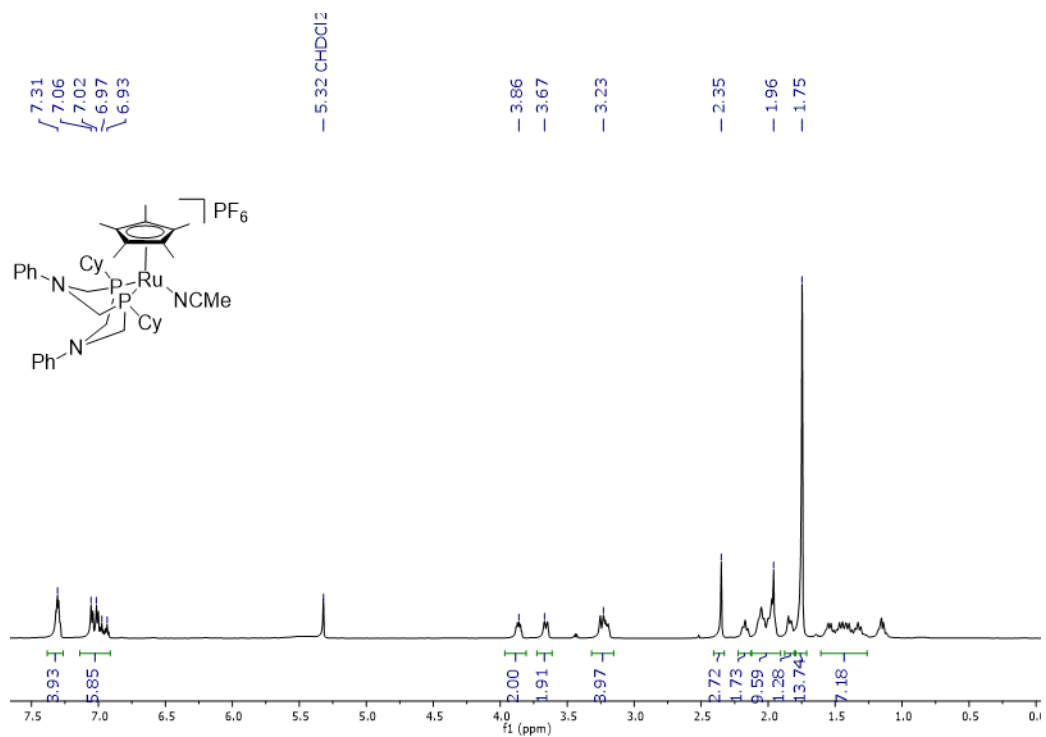


**Figure A-4.**  $^1\text{H}$  NMR spectrum of  $[\text{Ru}(\text{Cp}^*)(\text{P}^{\text{Cy}}_2\text{N}^{\text{Ph}}_2)(\text{NCMe})]\text{PF}_6$  (**2-2b**) (600 MHz,  $\text{CD}_2\text{Cl}_2$ ).

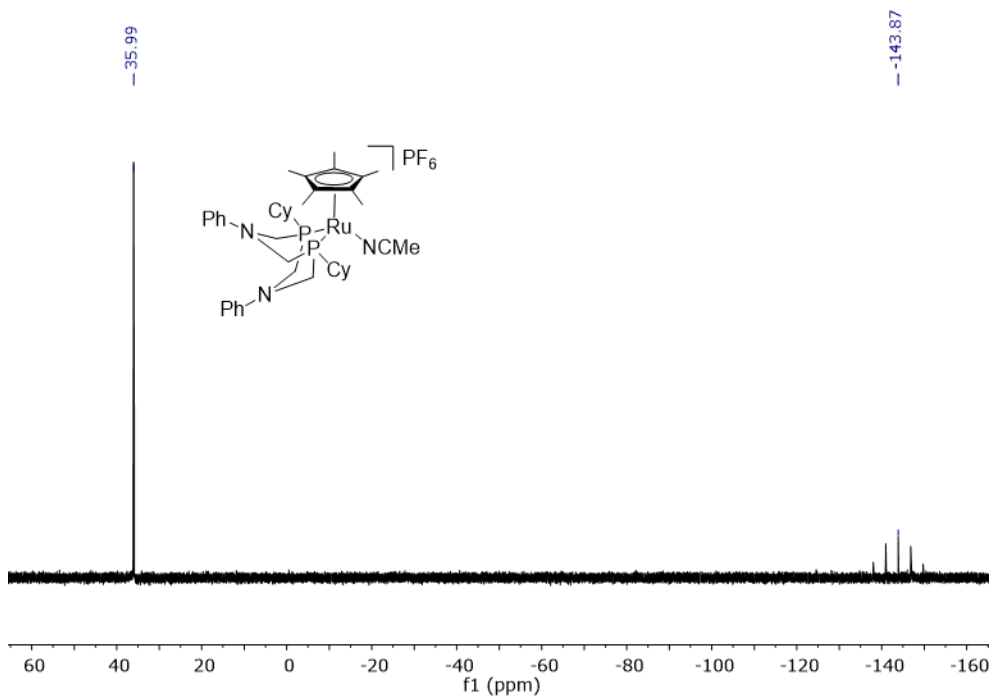


**Figure A-5.**  $^{31}\text{P}\{^1\text{H}\}$  NMR spectrum of **2-2b** (243 MHz,  $\text{CD}_2\text{Cl}_2$ ).

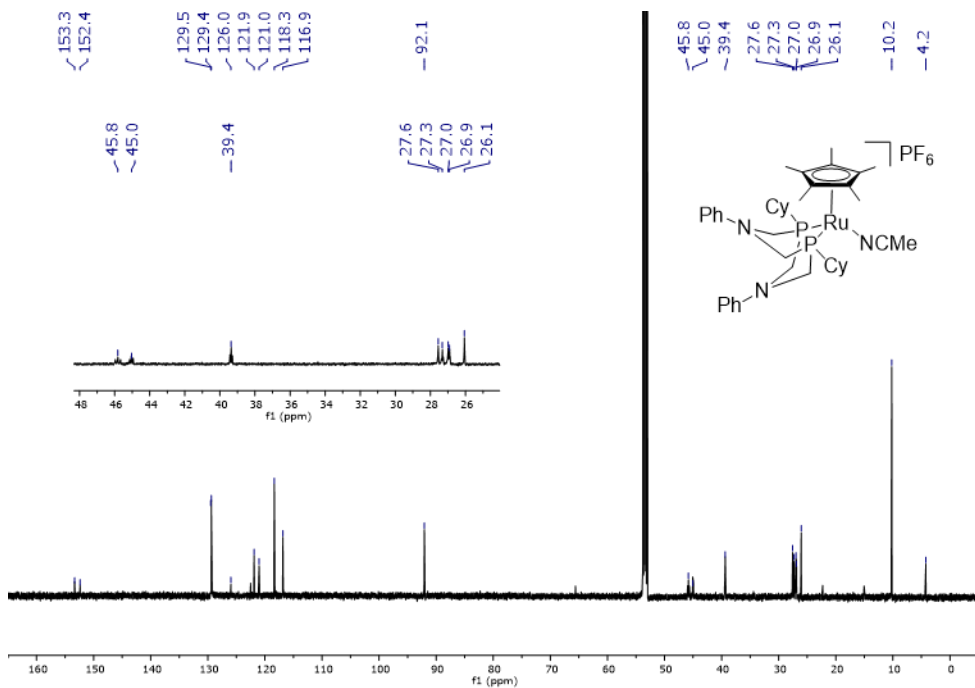


**Figure A-6.**  $^{13}\text{C}\{^1\text{H}\}$  NMR spectrum of **2-2b** (151 MHz,  $\text{CD}_2\text{Cl}_2$ ).

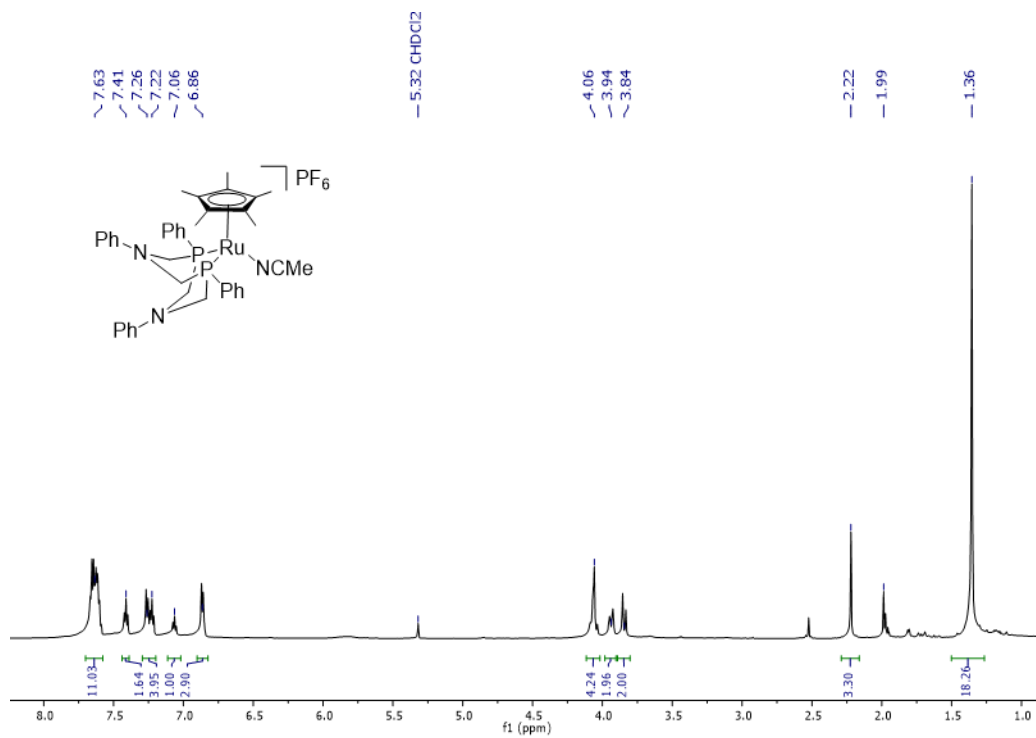


**Figure A-7.**  $^1\text{H}$  NMR spectrum of  $[\text{Ru}(\text{Cp}^*)(\text{P}^{\text{Ph}}_2\text{N}^{\text{Ph}}_2)(\text{MeCN})]\text{PF}_6$  (**2-2c**) (600 MHz,  $\text{CD}_2\text{Cl}_2$ ).

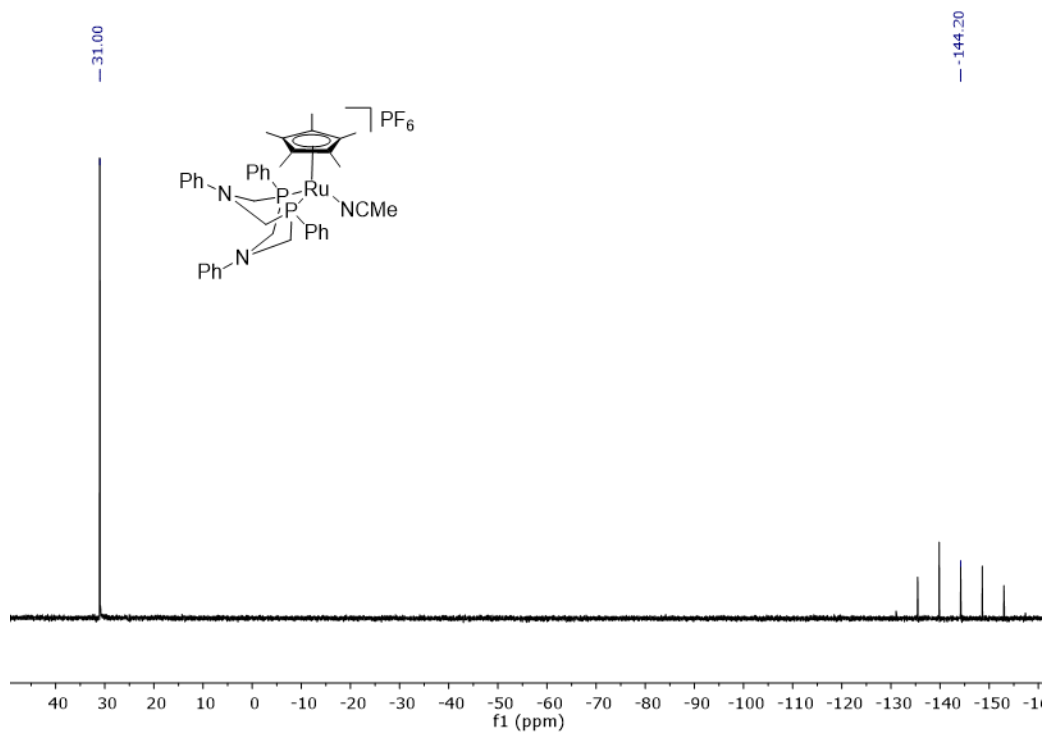


**Figure A-8.**  $^{31}\text{P}\{^1\text{H}\}$  NMR spectrum of **2-2c** (243 MHz,  $\text{CD}_2\text{Cl}_2$ ).

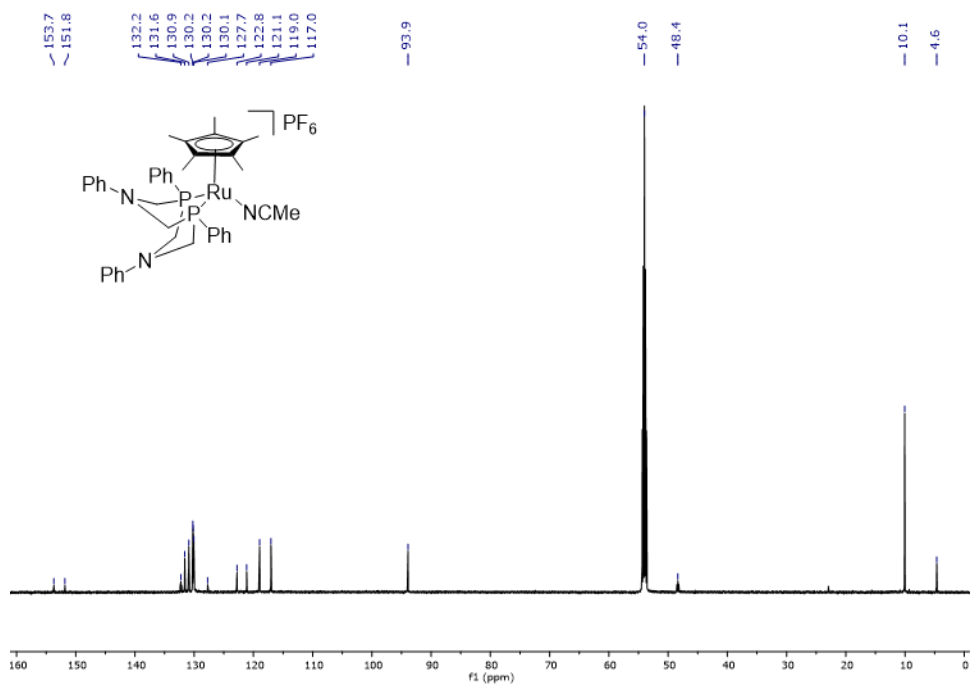


**Figure A-9.** <sup>13</sup>C{<sup>1</sup>H} NMR spectrum of **2-2c** (151 MHz, CD<sub>2</sub>Cl<sub>2</sub>).

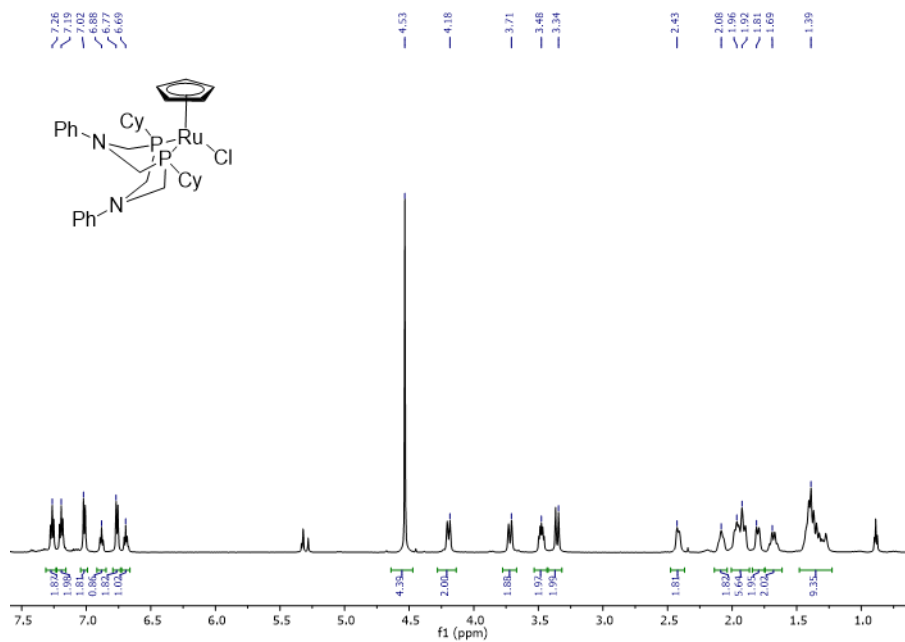


**Figure A-10.** <sup>1</sup>H NMR spectrum of [RuCl(Cp)(P<sup>Cy</sup><sub>2</sub>N<sup>Ph</sup><sub>2</sub>)] (**2-3b**) (600 MHz, CD<sub>2</sub>Cl<sub>2</sub>).

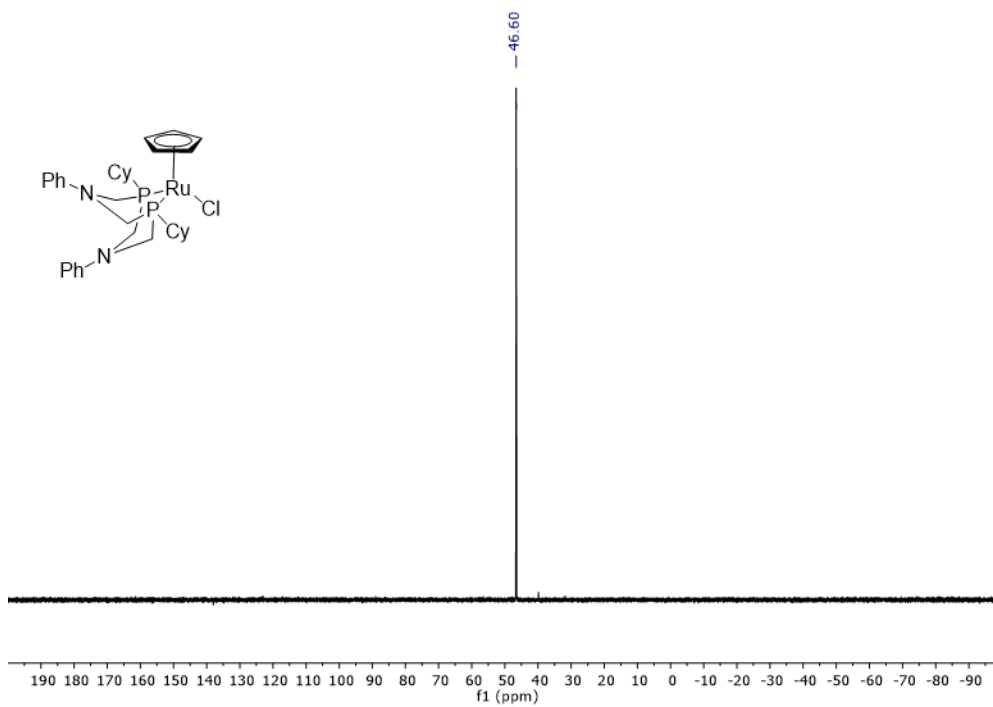


**Figure A-11.**  $^{31}\text{P}\{^1\text{H}\}$  NMR spectrum of **2-3b** (243 MHz,  $\text{CD}_2\text{Cl}_2$ ).

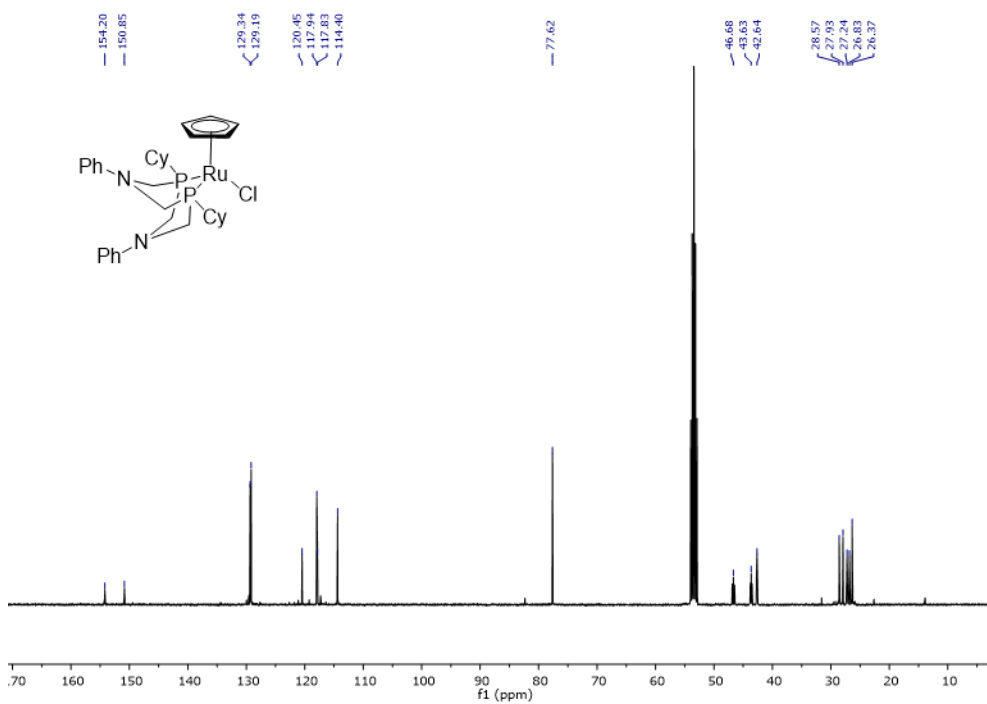


**Figure A-12.**  $^{13}\text{C}\{^1\text{H}\}$  NMR spectrum of **2-3b** (151 MHz,  $\text{CD}_2\text{Cl}_2$ ).

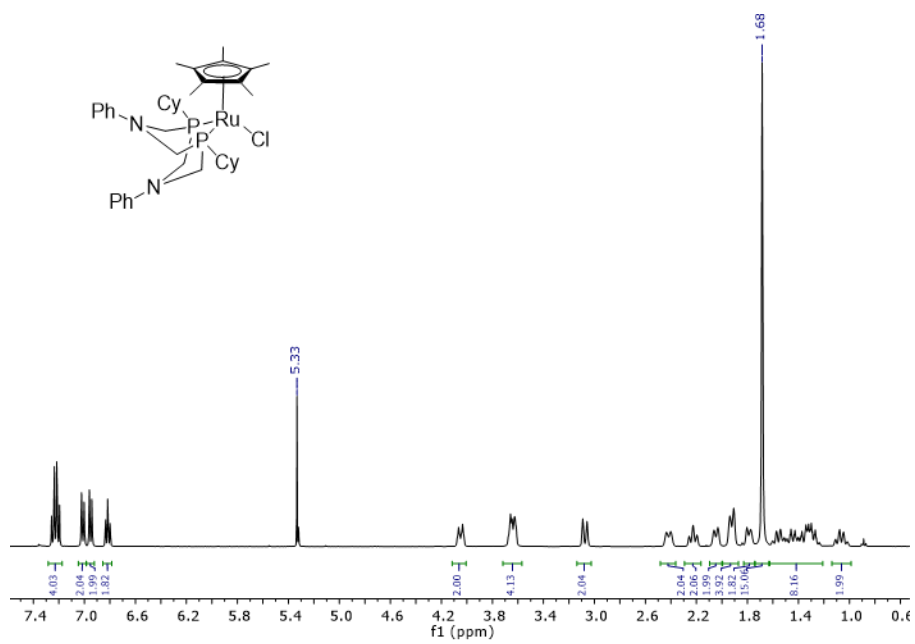


**Figure A-13.**  $^1\text{H}$  NMR spectrum of  $[\text{RuCl}(\text{Cp}^*)(\text{P}^{\text{Cy}}_2\text{N}^{\text{Ph}}_2)]$  (**2-4b**) (400 MHz,  $\text{CD}_2\text{Cl}_2$ ).

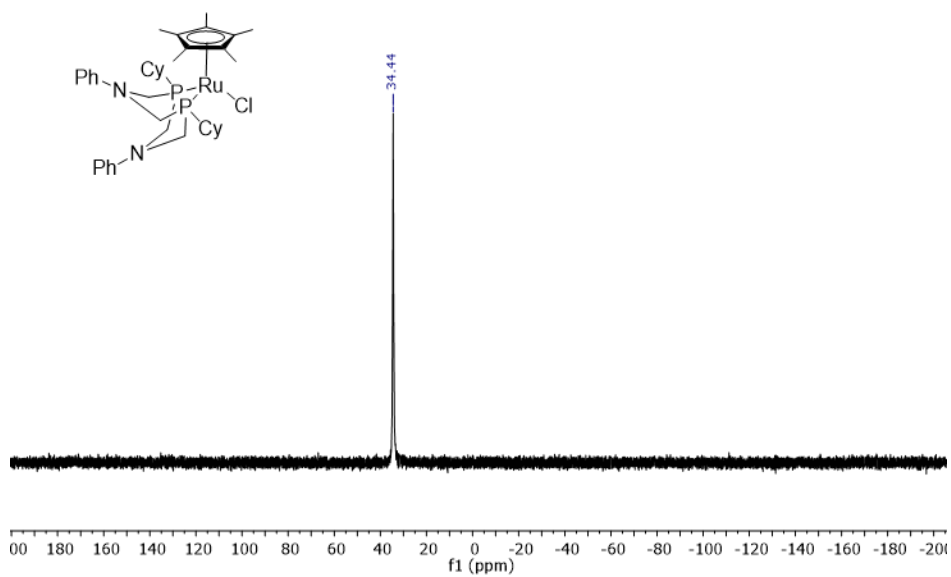


**Figure A-14.**  $^{31}\text{P}\{^1\text{H}\}$  NMR spectrum of **2-4b** (162 MHz,  $\text{CD}_2\text{Cl}_2$ ).



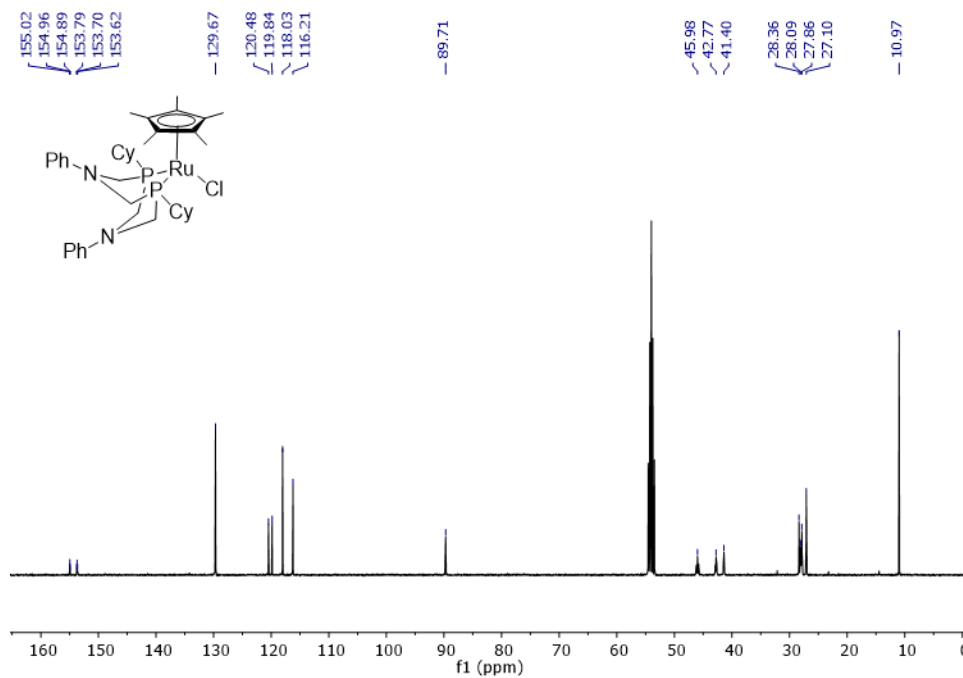


**Figure A-15.**  $^{13}\text{C}\{^1\text{H}\}$  NMR spectrum of **2-4b** (101 MHz,  $\text{CD}_2\text{Cl}_2$ ).

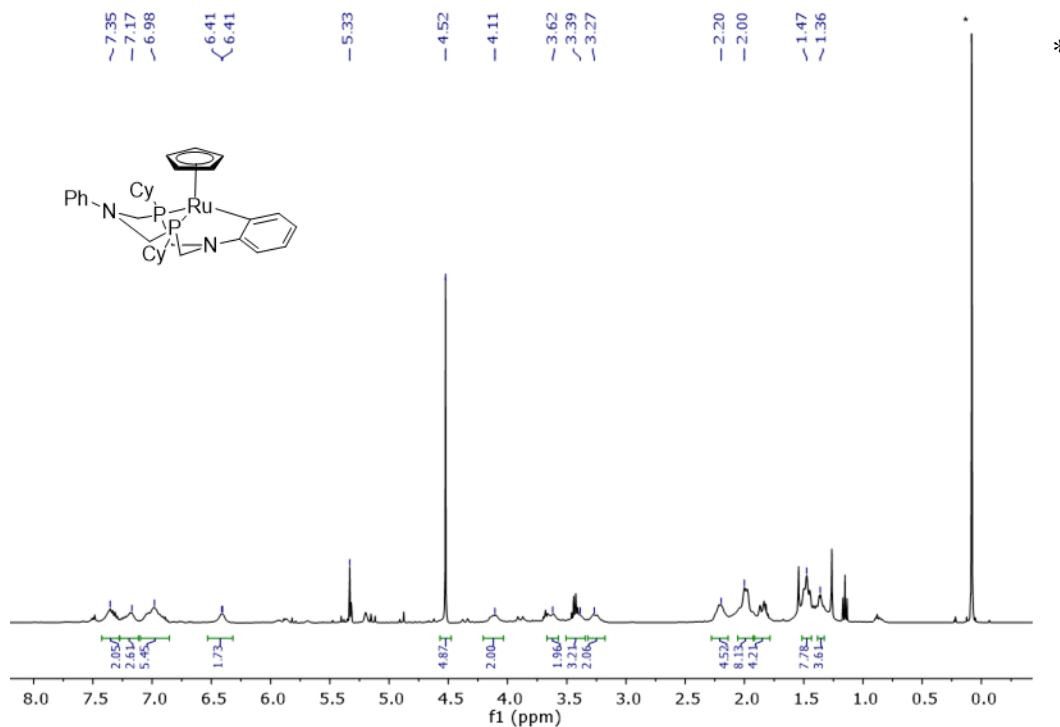


**Figure A-16.**  $^1\text{H}$  NMR spectrum of  $[\text{Ru}(\text{Cp})(\kappa^3\text{-P}^{\text{Cy}}_2\text{N}^{\text{Ph}}_2)][\text{PF}_6]$  (**2- $\kappa^3$ -(P,P,Ar)-5b**) (400 MHz,  $\text{CD}_2\text{Cl}_2$ ). \* indicates H grease impurity.

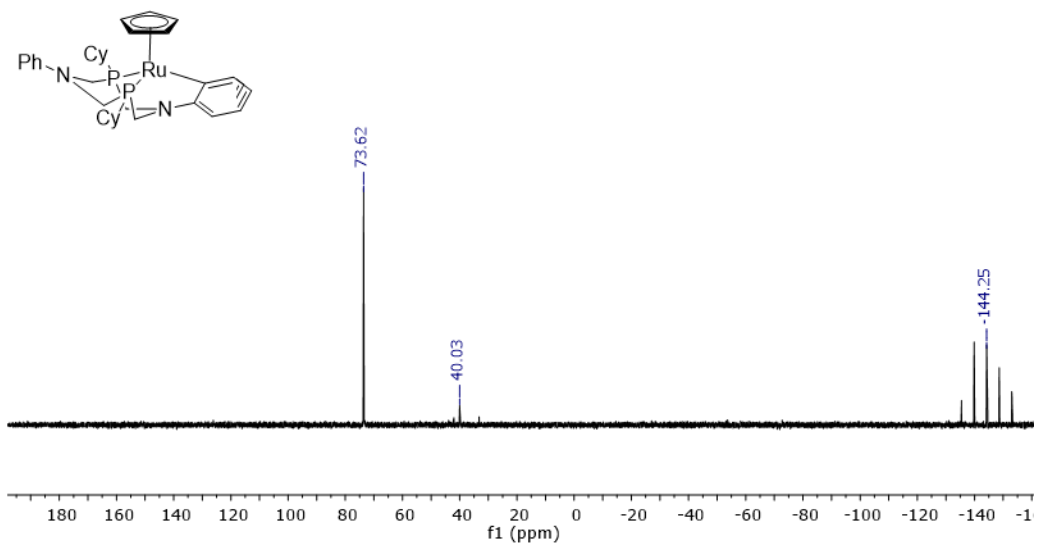


**Figure A-17.**  $^{31}\text{P}\{^1\text{H}\}$  NMR spectrum of  $2-\kappa^3-(P,P,Ar)-5b$  (162 MHz,  $\text{CD}_2\text{Cl}_2$ ).

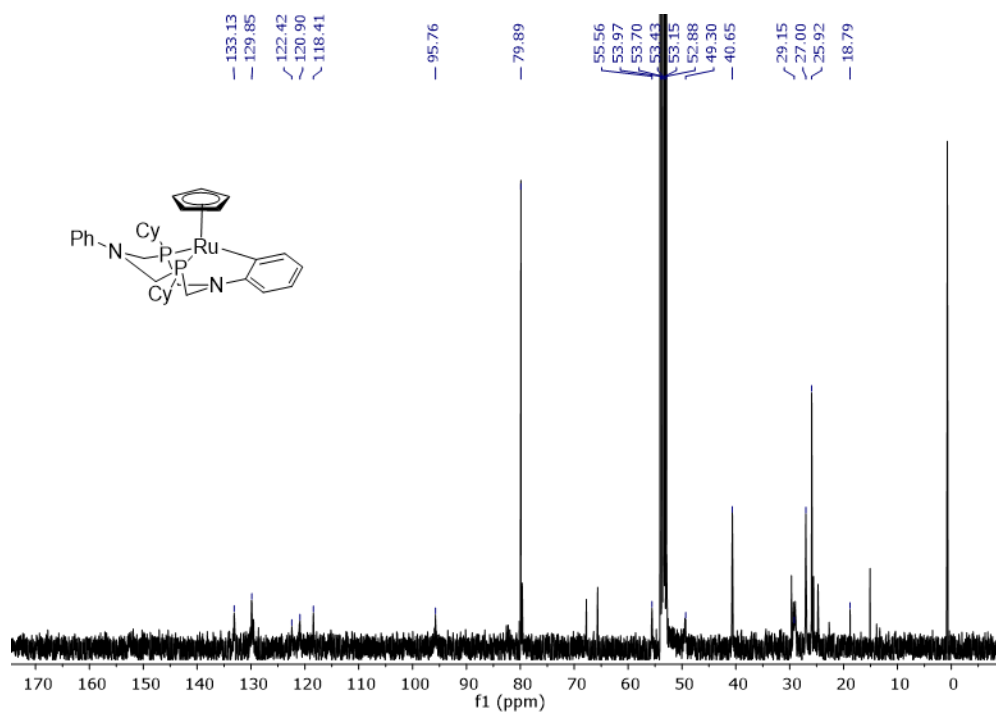


**Figure A-18.**  $^{13}\text{C}\{^1\text{H}\}$  NMR spectrum of  $2-\kappa^3-(P,P,Ar)-5b$  (101 MHz,  $\text{CD}_2\text{Cl}_2$ ).

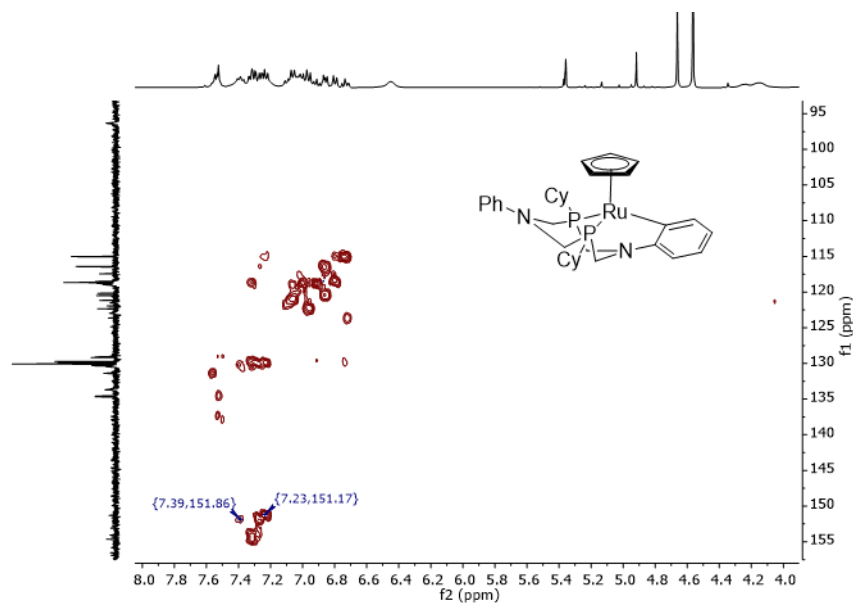


**Figure A-19.**  $^1\text{H}$ - $^{13}\text{C}\{^1\text{H}\}$  HMBC spectrum of **2-5b-N<sub>2</sub>** and **2- $\kappa^3$ -(P,P,Ar)-5b** (400 MHz,  $\text{CD}_2\text{Cl}_2$ ). Signals highlighted represents the correlation between the ipso carbons of the phenyl substituents and proton signals for **2- $\kappa^3$ -(P,P,Ar)-5b**.

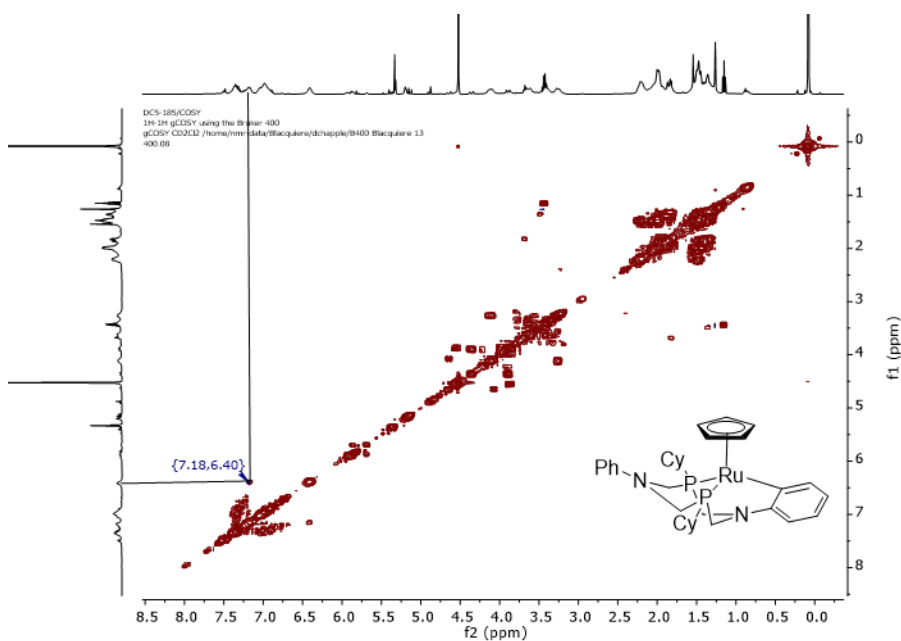


**Figure A-20.**  $^1\text{H}$ - $^1\text{H}$  COSY spectrum of **2- $\kappa^3$ -(P,P,Ar)-5b** (400 MHz,  $\text{CD}_2\text{Cl}_2$ ). Signal highlighted represents an upfield shifted hydrogen due to aryl interaction with ruthenium.

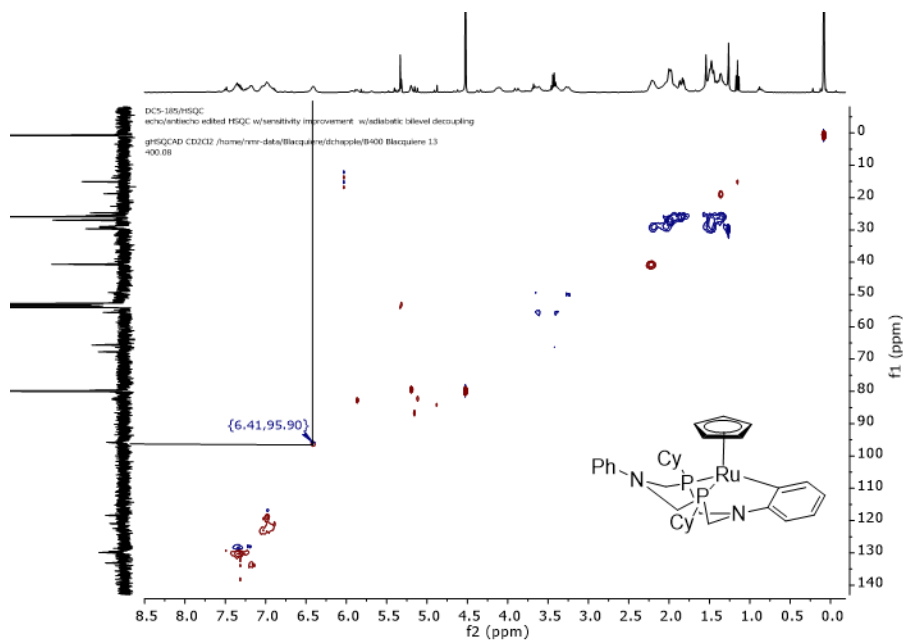


**Figure A-21.**  $^1\text{H}$ - $^{13}\text{C}\{^1\text{H}\}$  HSQC spectrum of **2- $\kappa^3$ -(P,P,Ar)-5b** (400 MHz,  $\text{CD}_2\text{Cl}_2$ ). Signal highlighted shows correlation of upfield shifted carbon atom (interaction with ruthenium) correlates to upfield shifted hydrogen.

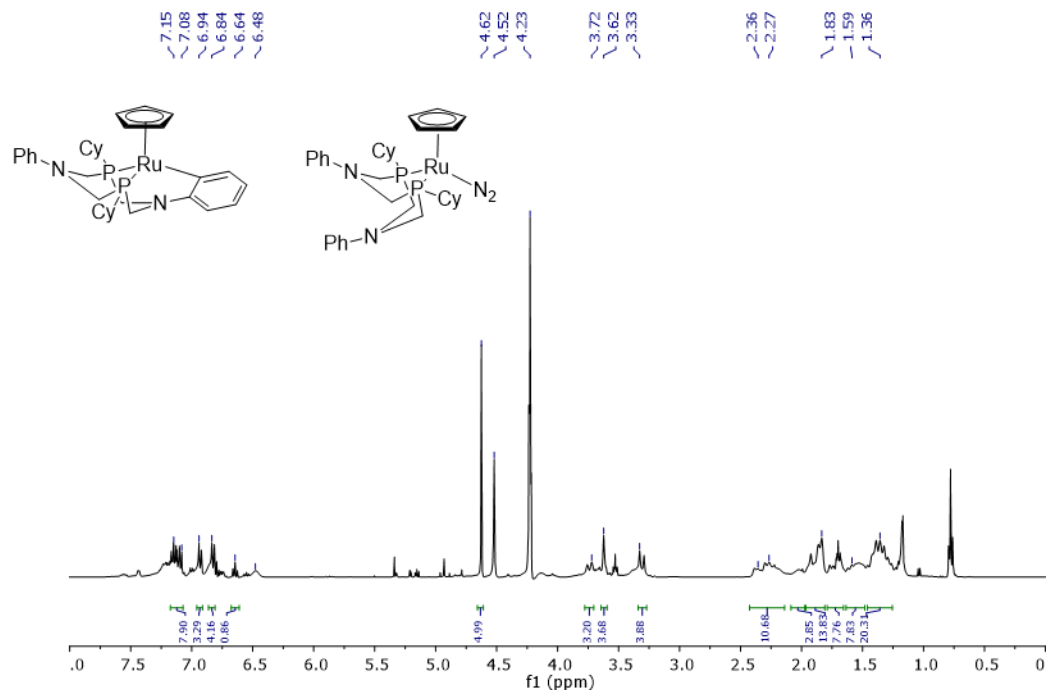


**Figure A-22.**  $^1\text{H}$  NMR spectrum of mixture of  $[\text{Ru}(\text{Cp})(\kappa^2\text{-P}^{\text{Cy}}_2\text{N}^{\text{Ph}}_2)(\text{N}_2)][\text{PF}_6]$  (**2-5b-N<sub>2</sub>**) and **2- $\kappa^3$ -(P,P,Ar)-5b** (400 MHz,  $\text{CD}_3\text{NO}_2$ ).

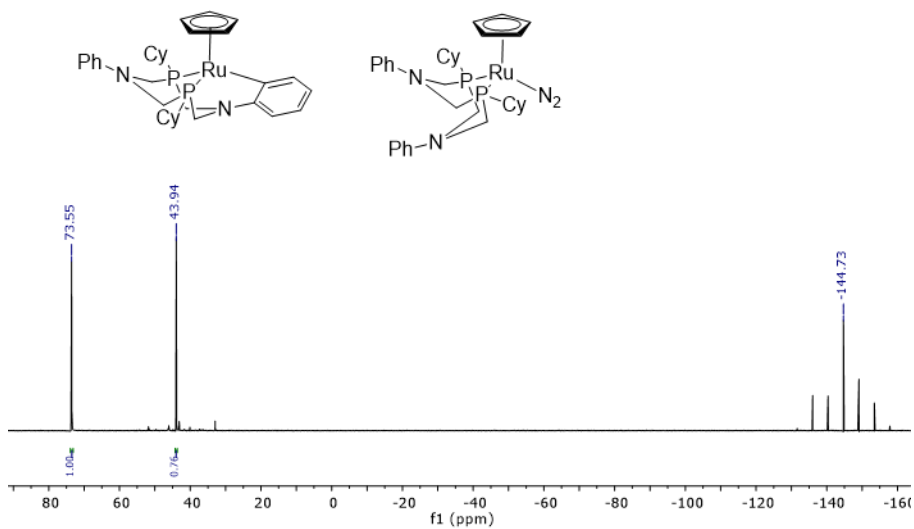


**Figure A-23.**  $^{31}\text{P}\{^1\text{H}\}$  NMR spectrum of **2-5b-N<sub>2</sub>** and **2-κ<sup>3</sup>-(P,P,Ar)-5b** (162 MHz,  $\text{CD}_3\text{NO}_2$ ).

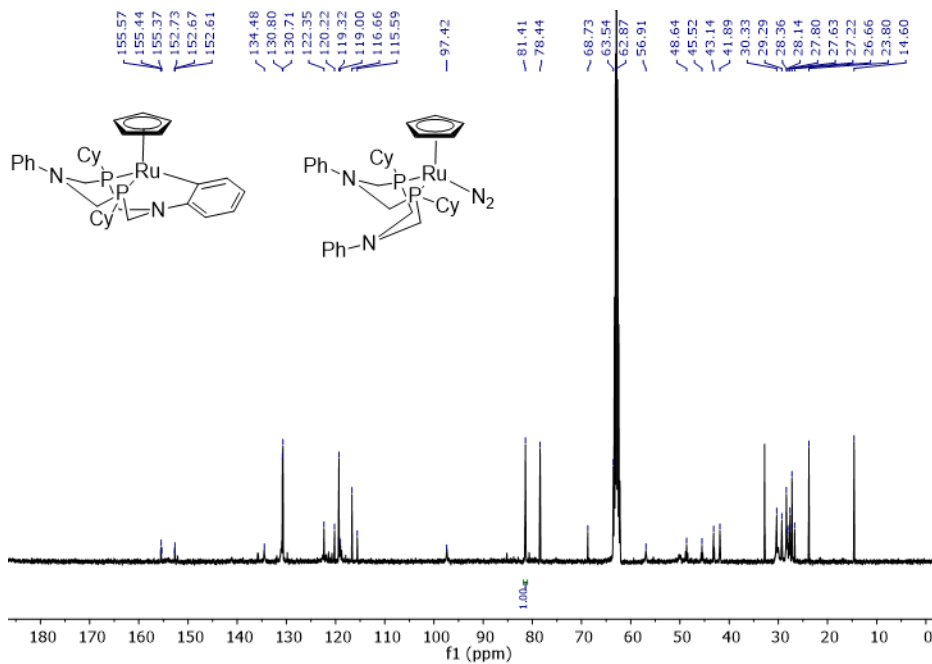


**Figure A-24.**  $^{13}\text{C}\{^1\text{H}\}$  NMR spectrum of **2-5b-N<sub>2</sub>** and **2-κ<sup>3</sup>-(P,P,Ar)-5b** (101 MHz,  $\text{CD}_3\text{NO}_2$ ).

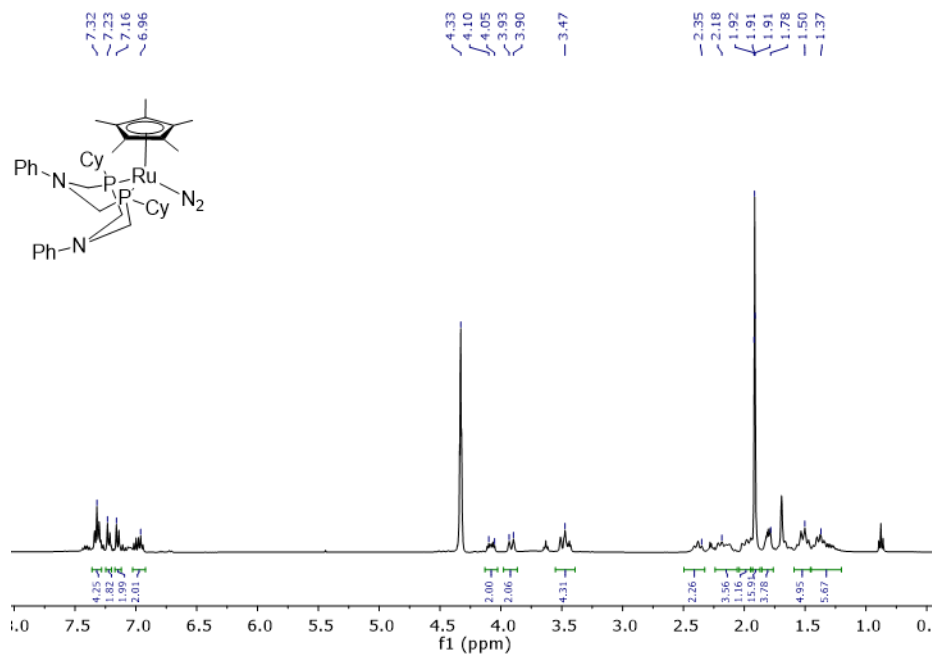


**Figure A-25.**  $^1\text{H}$  NMR spectrum of  $[\text{Ru}(\text{Cp}^*)(\text{P}^{\text{Cy}}_2\text{N}^{\text{Ph}}_2)(\text{N}_2)][\text{PF}_6]$  (**2-6b-N<sub>2</sub>**) (400 MHz,  $\text{CD}_3\text{NO}_2$ ).

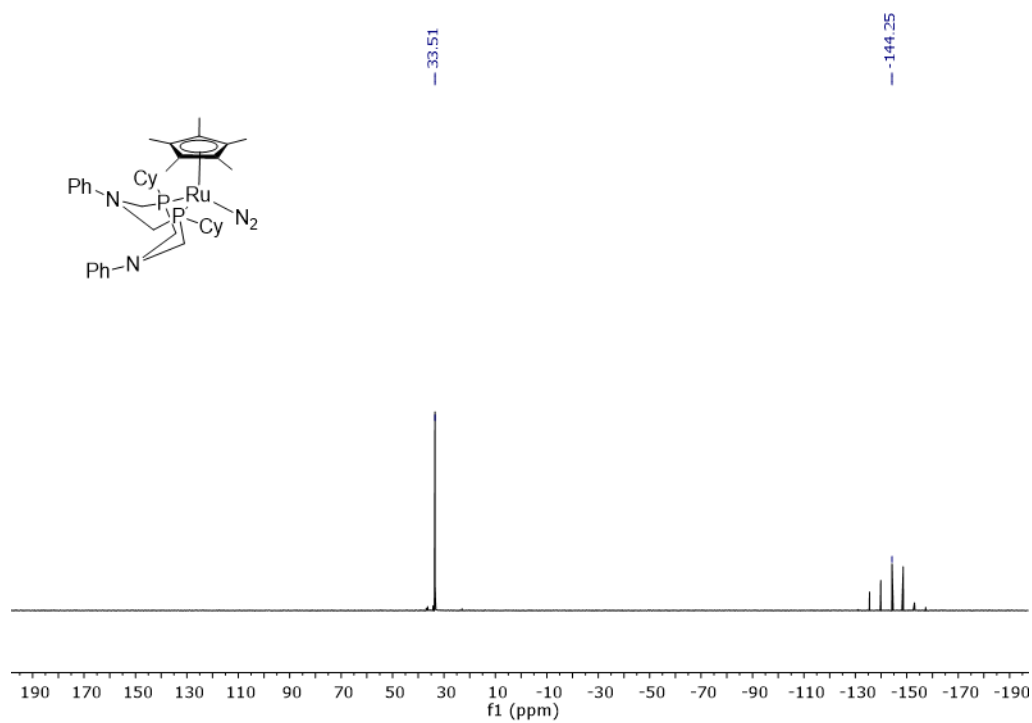


**Figure A-26.**  $^{31}\text{P}\{^1\text{H}\}$  NMR spectrum of **2-6b-N<sub>2</sub>** (162 MHz,  $\text{CD}_3\text{NO}_2$ ).

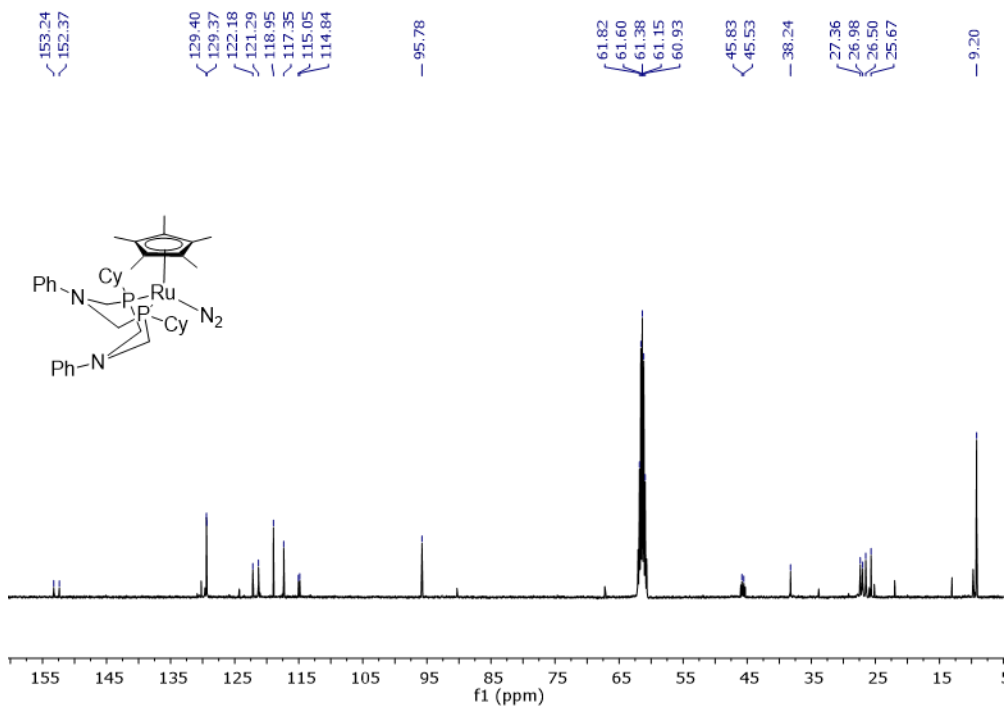


**Figure A-27.**  $^{13}\text{C}\{^1\text{H}\}$  NMR spectrum of **2-6b-N<sub>2</sub>** (101 MHz,  $\text{CD}_3\text{NO}_2$ ).

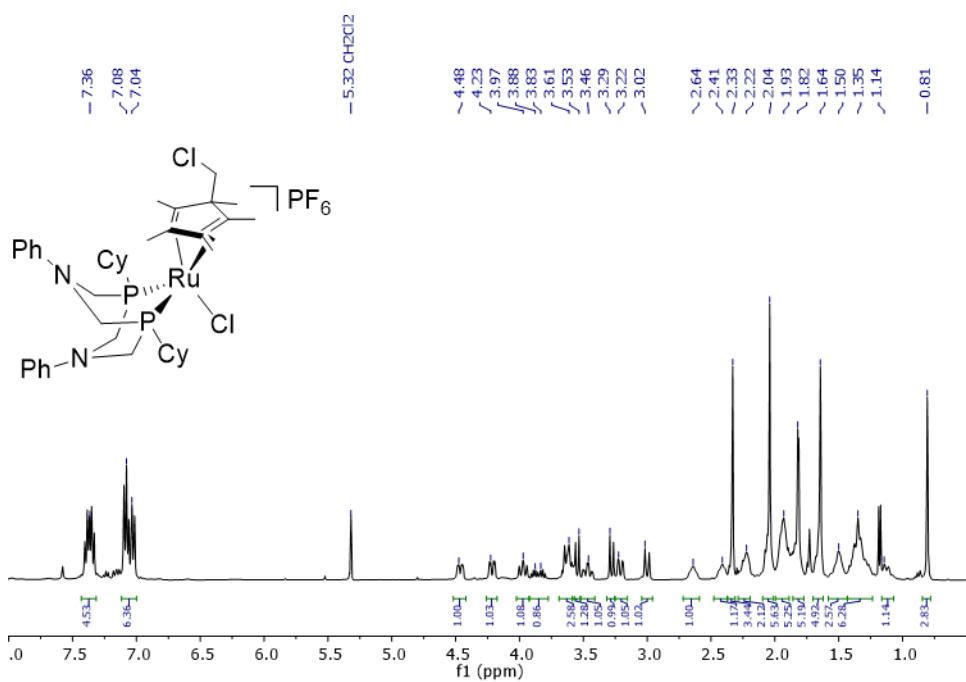


**Figure A-28.**  $^1\text{H}$  NMR spectrum of  $[\text{RuCl}(\eta^4\text{-C}_5(\text{CH}_3)_5\text{CH}_2\text{Cl})(\text{P}^{\text{Cy}}_2\text{N}^{\text{Ph}}_2)][\text{PF}_6]$  (**2-7**) (400 MHz,  $\text{CD}_2\text{Cl}_2$ ).

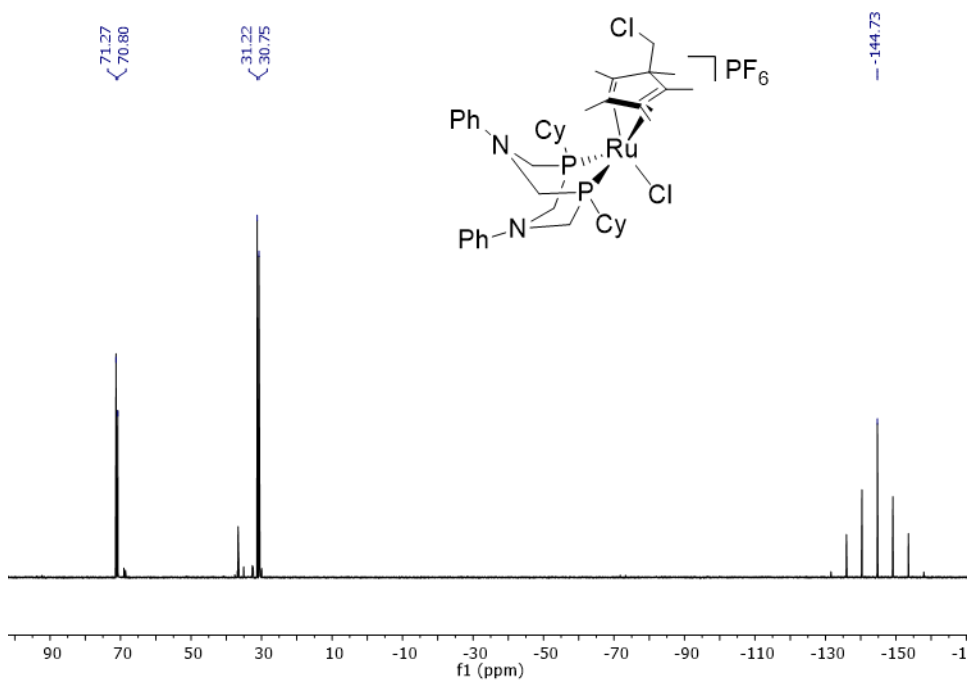


**Figure A-29.**  $^{31}\text{P}\{^1\text{H}\}$  NMR spectrum of 2-7 (162 MHz,  $\text{CD}_2\text{Cl}_2$ ).

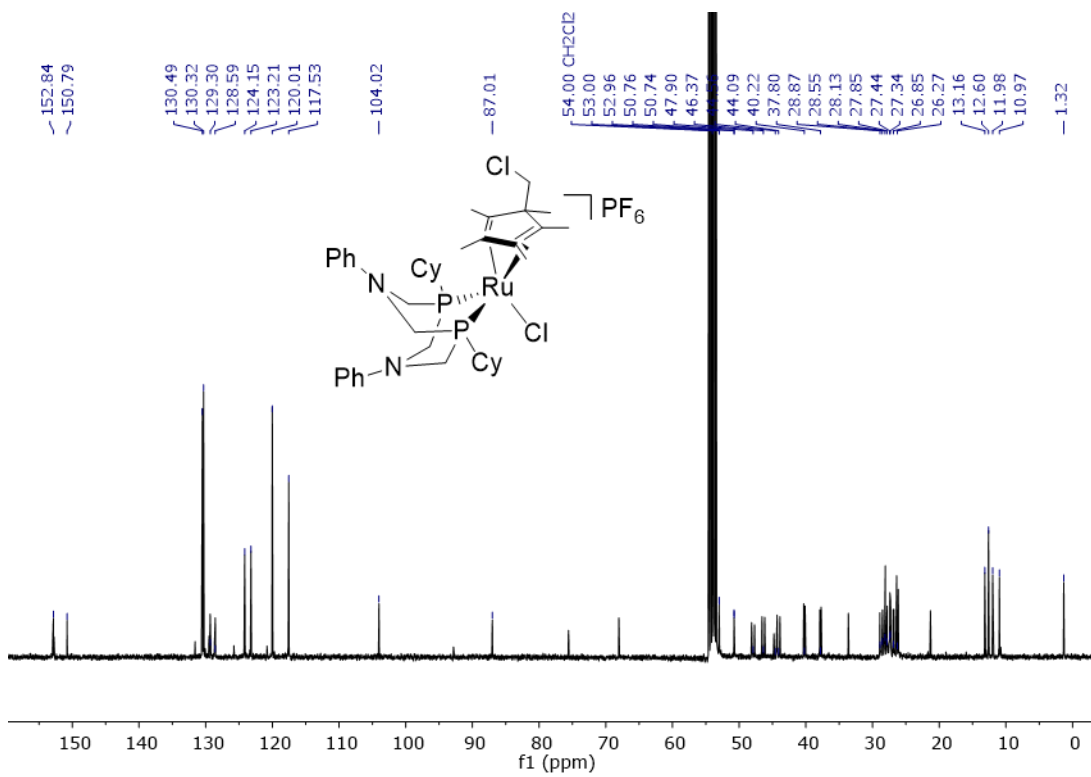


**Figure A-30.**  $^{13}\text{C}\{^1\text{H}\}$  NMR spectrum of 2-7 (101 MHz,  $\text{CD}_2\text{Cl}_2$ ).



## IR Spectra

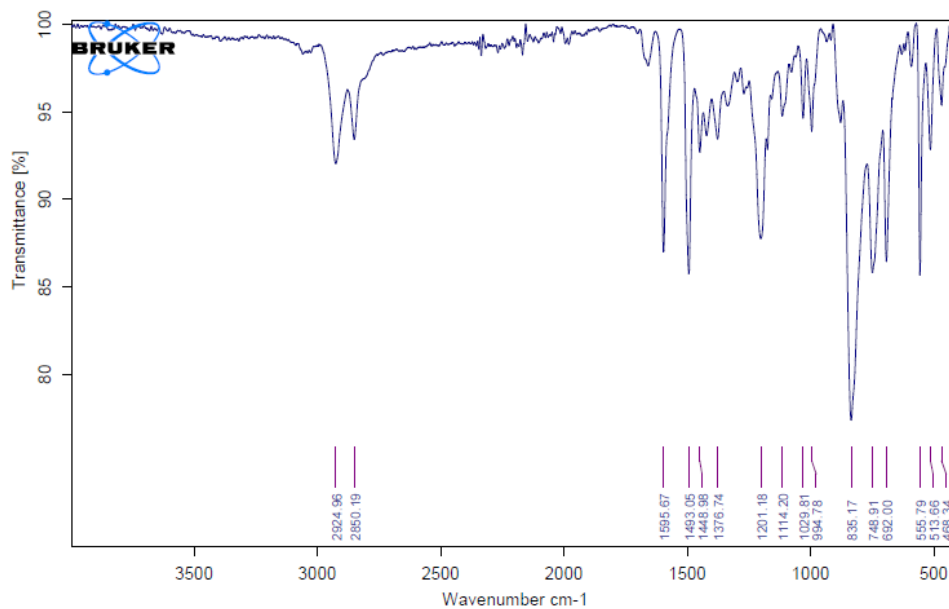


**Figure A-31.** ATR-FTIR spectrum of solid **2-1b** collected following general procedure.

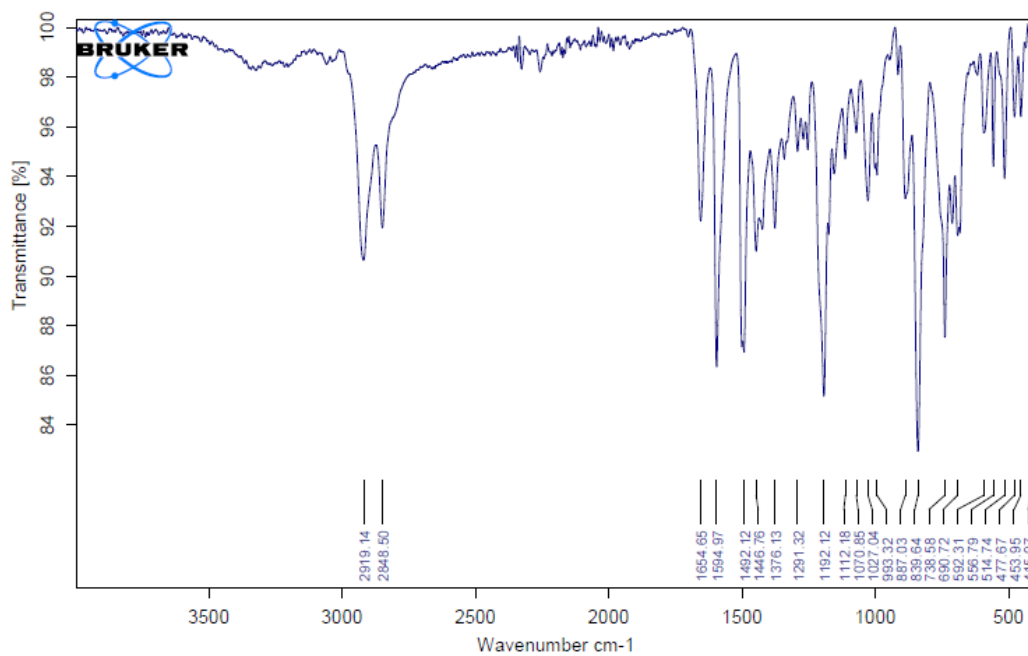


**Figure A-32.** ATR-FTIR spectrum of solid **2-2b** collected following general procedure.

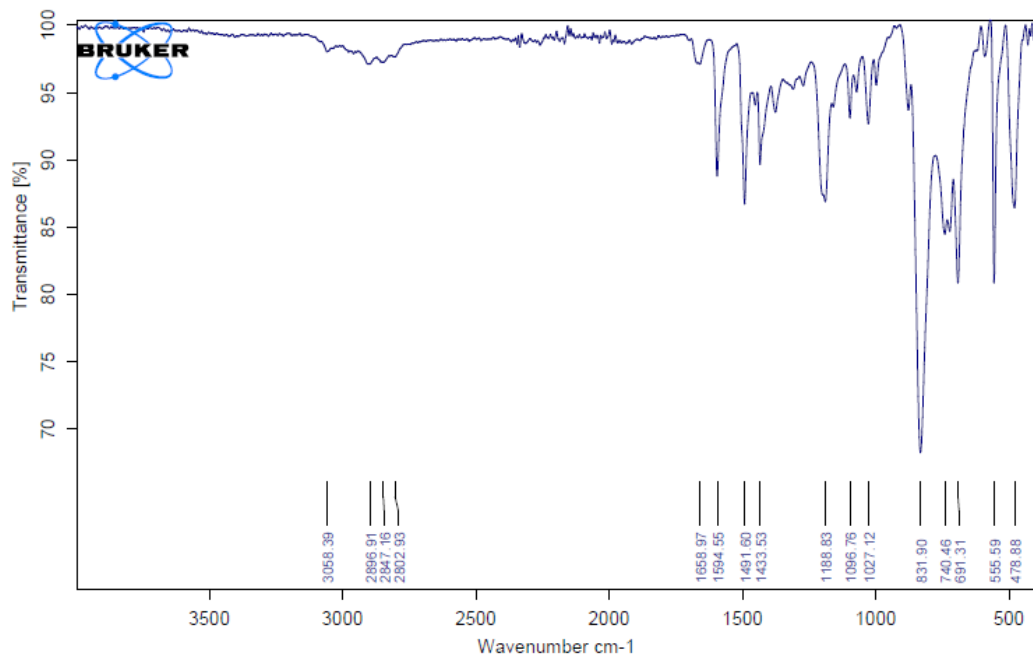


**Figure A-33.** ATR-FTIR spectrum of solid **2-2c** collected following general procedure.

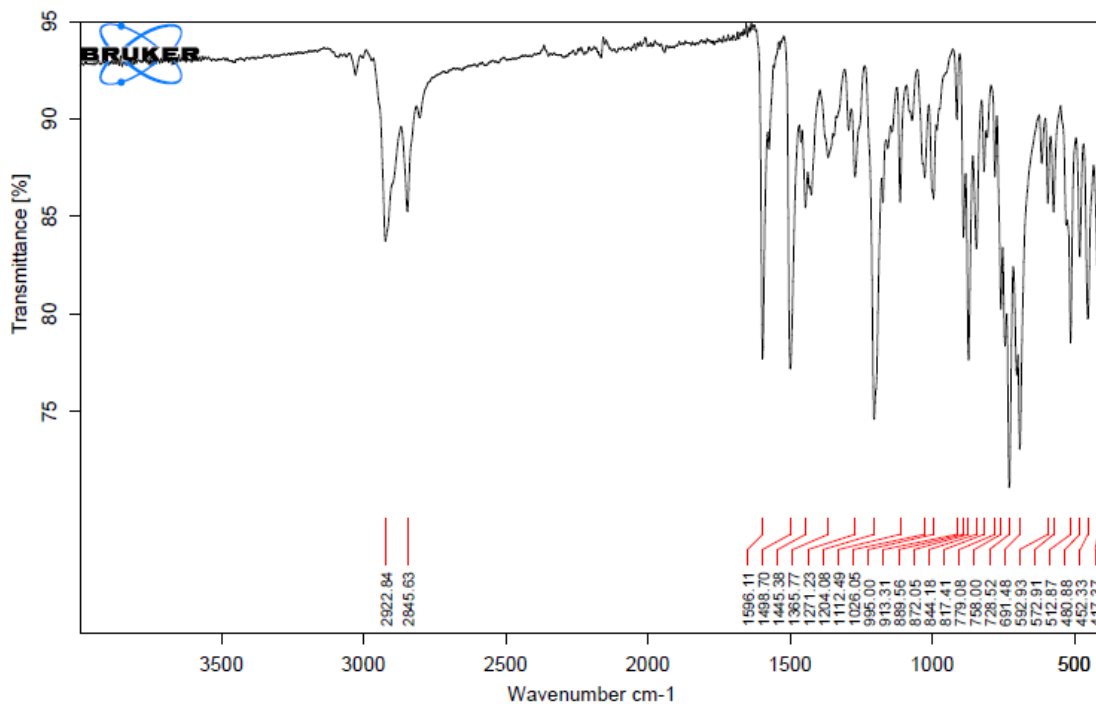


**Figure A-34.** ATR-FTIR spectrum of solid **2-3b** collected following general procedure.

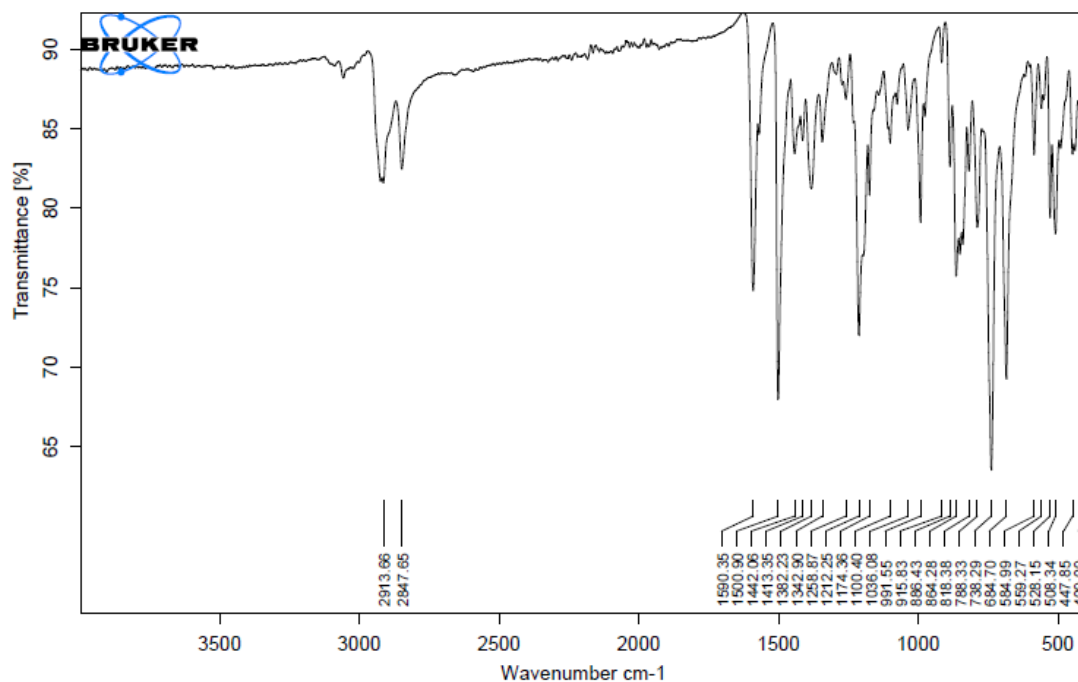


**Figure A-35.** ATR-FTIR spectrum of solid **2-4b** collected following general procedure

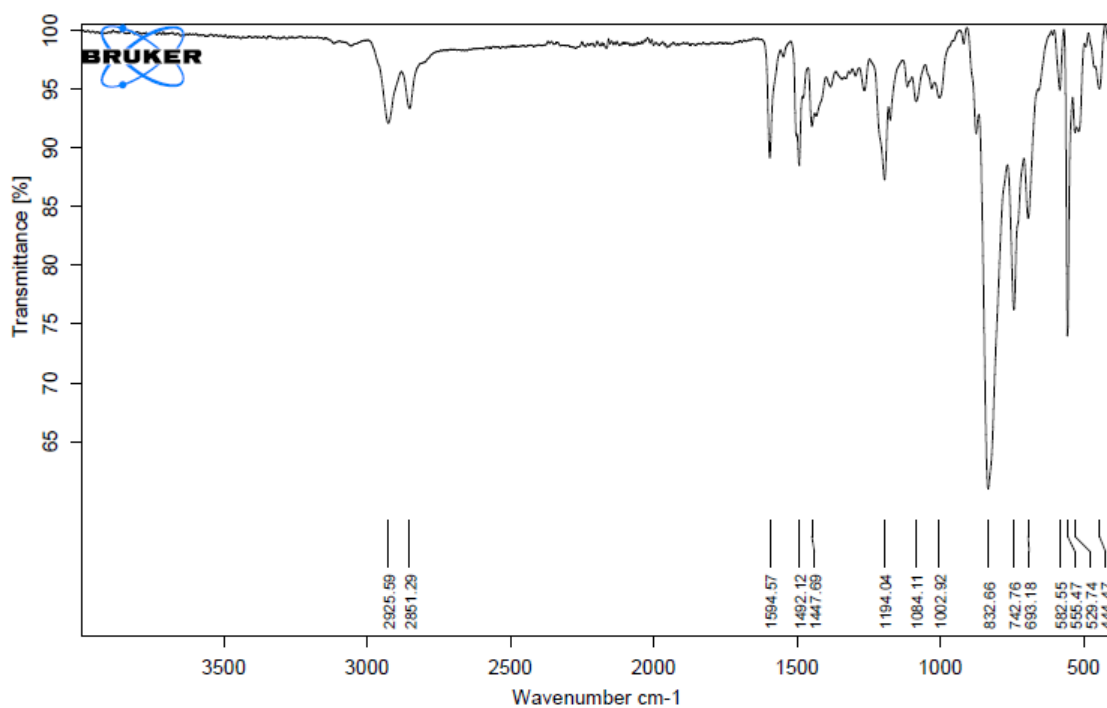


**Figure A-36.** ATR-FTIR spectrum of solid **2-5b-N<sub>2</sub>** and **2-κ<sup>3</sup>-(P,P,Ar)-5b** collected following general procedure.

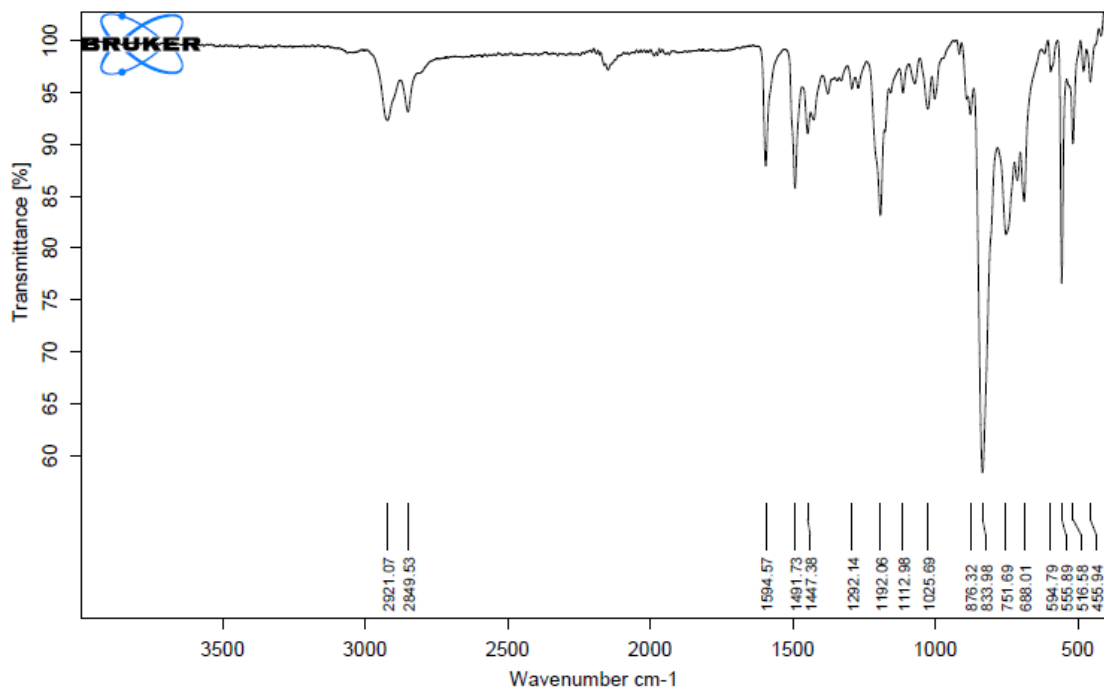


**Figure A-37.** ATR-FTIR spectrum of solid **2-6b-N<sub>2</sub>** collected following general procedure.

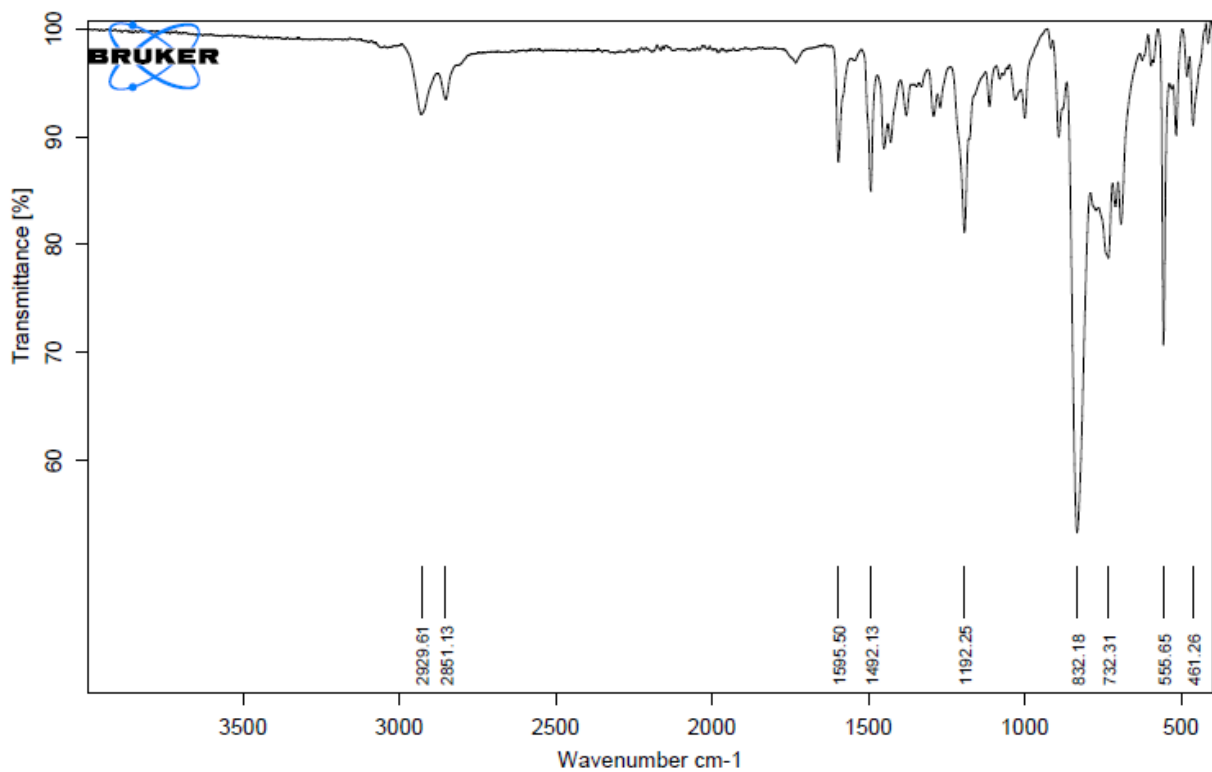


**Figure A-38.** ATR-FTIR spectrum of solid **2-7** collected following general procedure.

## MALDI Mass Spectra

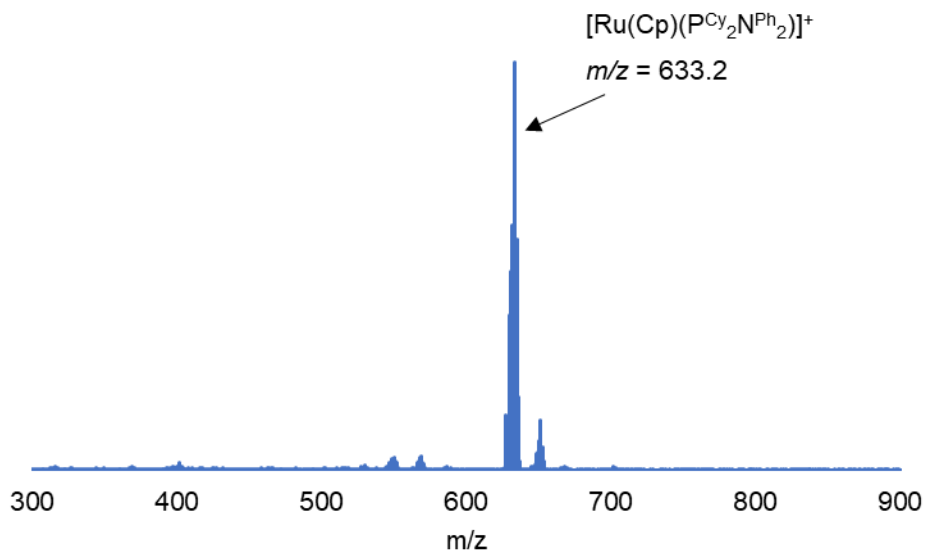


**Figure A-39.** MALDI -TOF mass spectrum of **2-1b** with pyrene as the matrix (1:20 ratio).

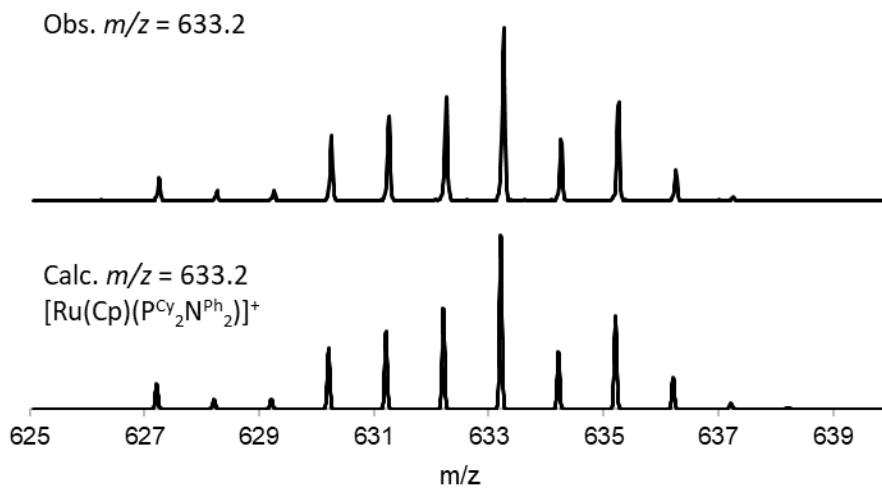


**Figure A-40.** Zoom in (top) of the observed signal with  $m/z = 633.2$  in the MALDI-TOF mass spectrum of **2-1b**; and simulation<sup>1</sup> (bottom) of the isotope pattern for the fragmentation  $[\text{Ru}(\text{Cp})(\text{P}^{\text{Cy}}_2\text{N}^{\text{Ph}}_2)]^+$  with  $m/z = 633.2$ .

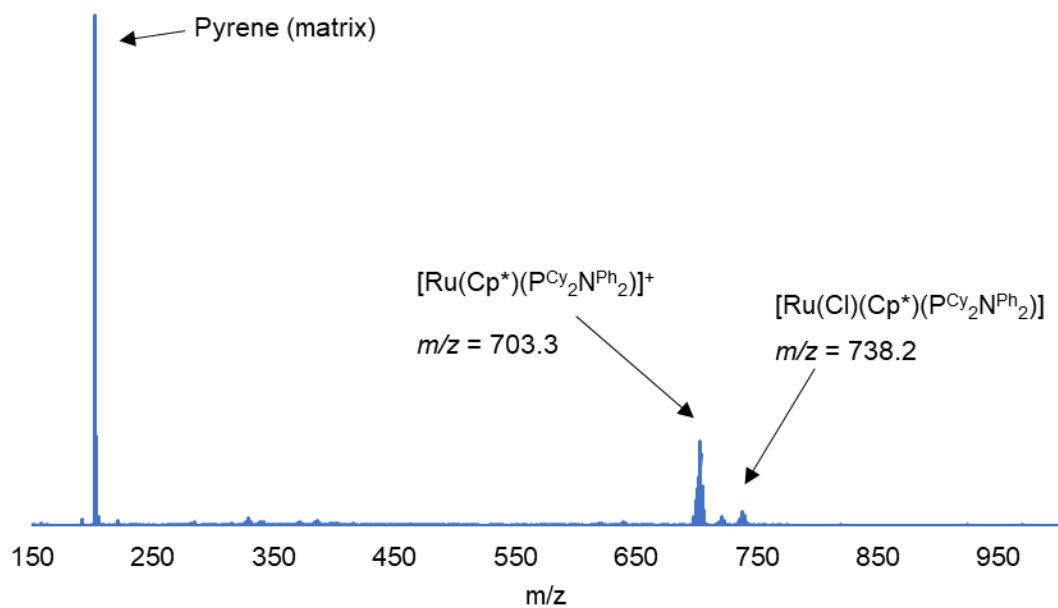


**Figure A-41.** MALDI -TOF mass spectrum of **2-2b** with pyrene as the matrix (1:20 ratio).

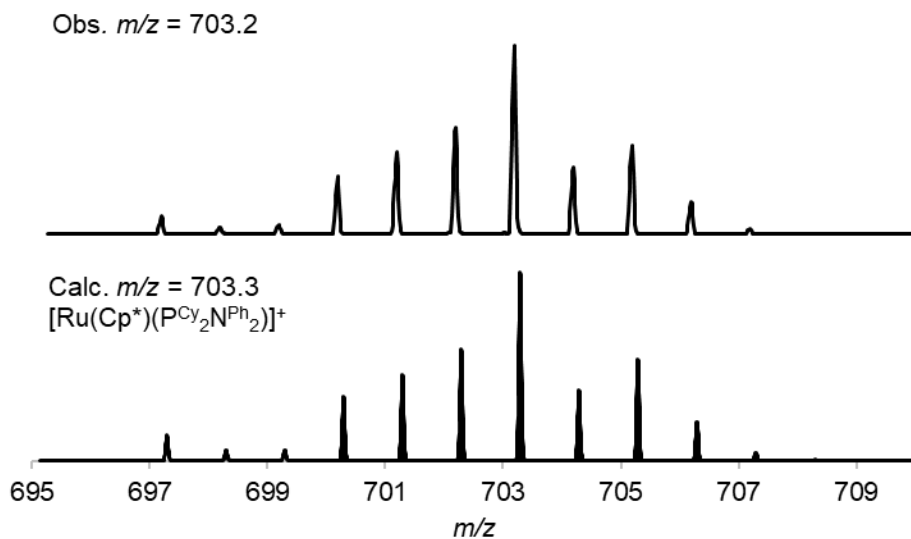


**Figure A-42.** Zoom in (top) of the observed signal with  $m/z = 703.2$  in the MALDI-TOF mass spectrum of **2-2b**; and simulation<sup>1</sup> (bottom) of the isotope pattern for the fragmentation  $[\text{Ru}(\text{Cp}^*)(\text{PCy}_2\text{NPh}_2)]^+$  with  $m/z = 703.3$ .

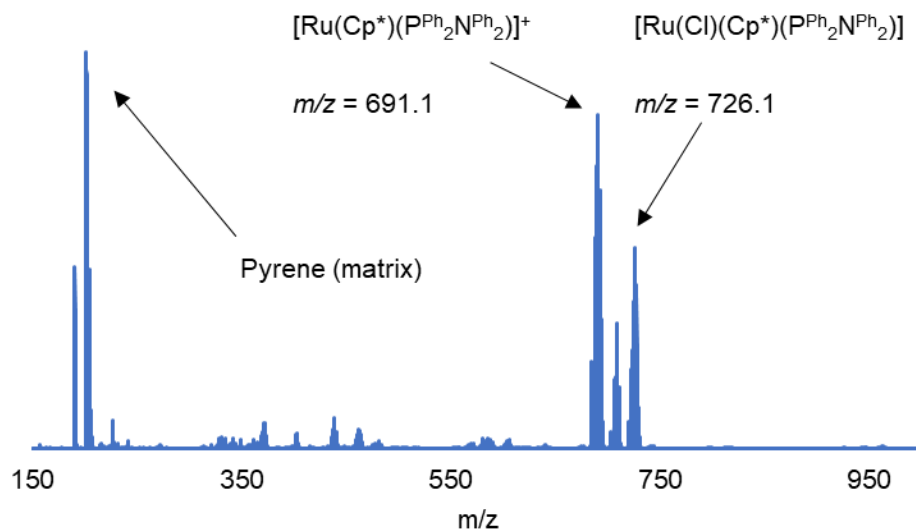


**Figure A-43.** MALDI -TOF mass spectrum of **2-2c** with pyrene as the matrix (1:20 ratio).

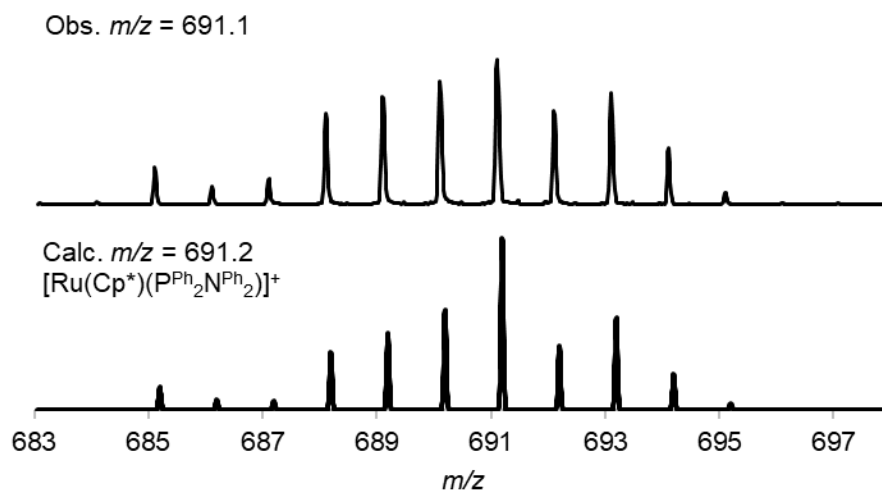


**Figure A-44.** Zoom in (top) of the observed signal with  $m/z = 691.1$  in the MALDI-TOF mass spectrum of **2-2c**; and simulation<sup>1</sup> (bottom) of the isotope pattern for the fragmentation  $[\text{Ru}(\text{Cp}^*)(\text{P}^{\text{Ph}}_2\text{N}^{\text{Ph}}_2)]^+$  with  $m/z = 691.2$ .

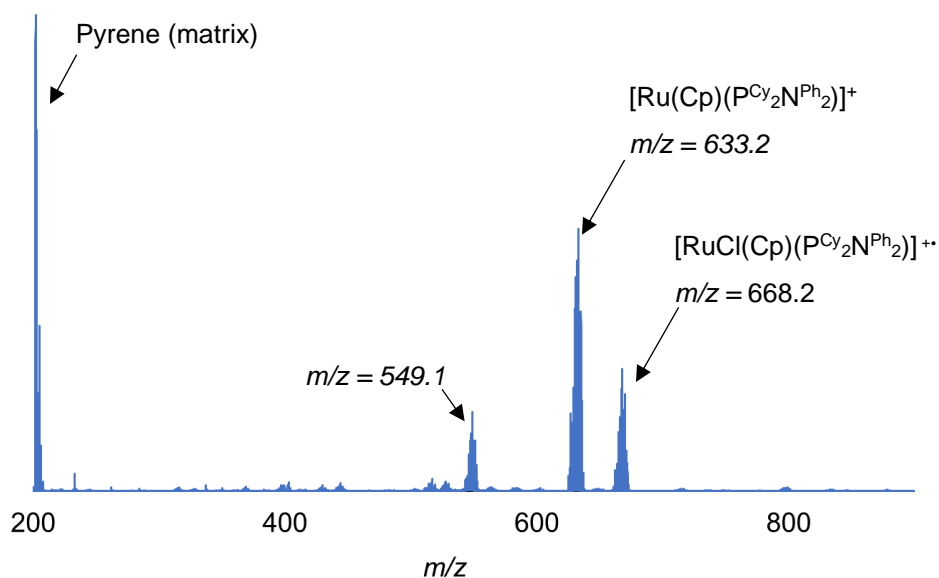


**Figure A-45.** MALDI -TOF mass spectrum of **2-3b** with pyrene as the matrix (1:20 ratio).

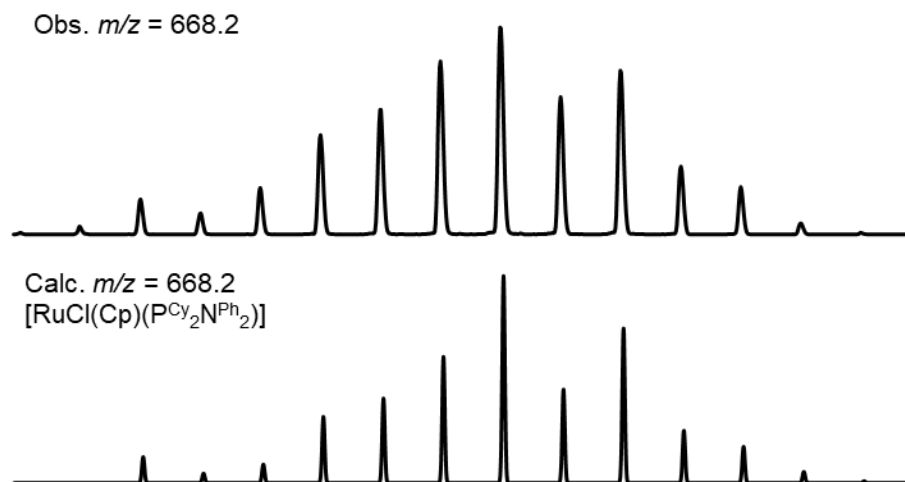


**Figure A-46.** Zoom in (top) of the observed signal with  $m/z = 668.2$  in the MALDI-TOF mass spectrum of **2-3b**; and simulation<sup>1</sup> (bottom) of the isotope pattern for charged  $[\text{RuCl}(\text{Cp})(\text{PCy}_2\text{N}^{\text{Ph}}_2)]^{+\bullet}$  with  $m/z = 668.2$ .



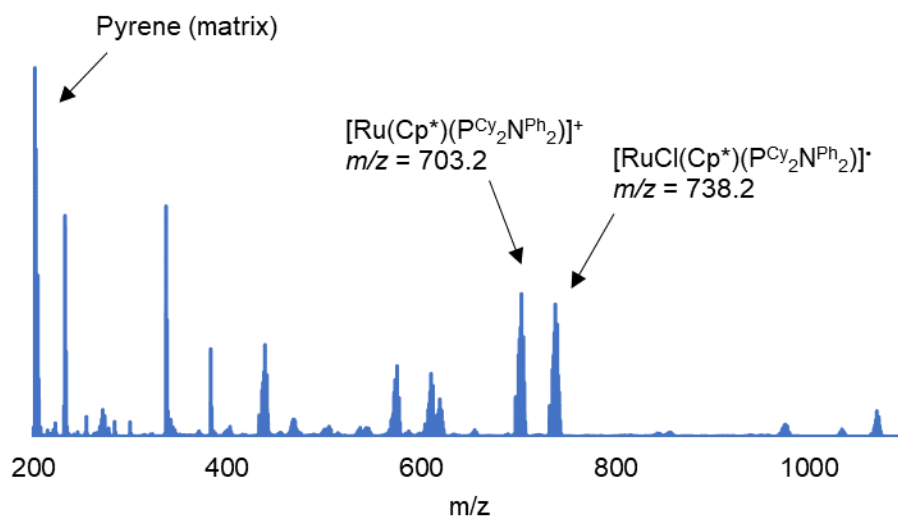


**Figure A-47.** MALDI -TOF mass spectrum of **2-4b** with pyrene as the matrix (1:20 ratio).

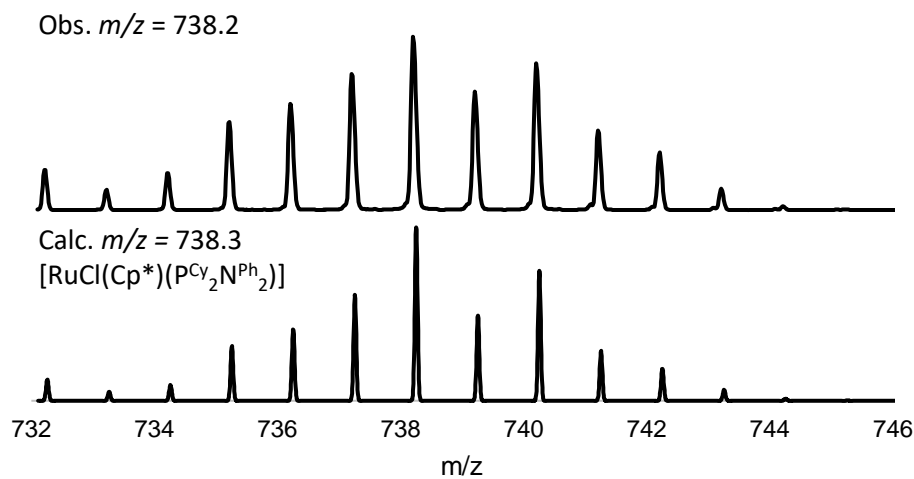


**Figure A-48.** Zoom in (top) of the observed signal with  $m/z = 738.2$  in the MALDI-TOF mass spectrum of **2-4b**; and simulation<sup>2</sup> (bottom) of the isotope pattern for complex **2-4b** with  $m/z = 738.3$ .

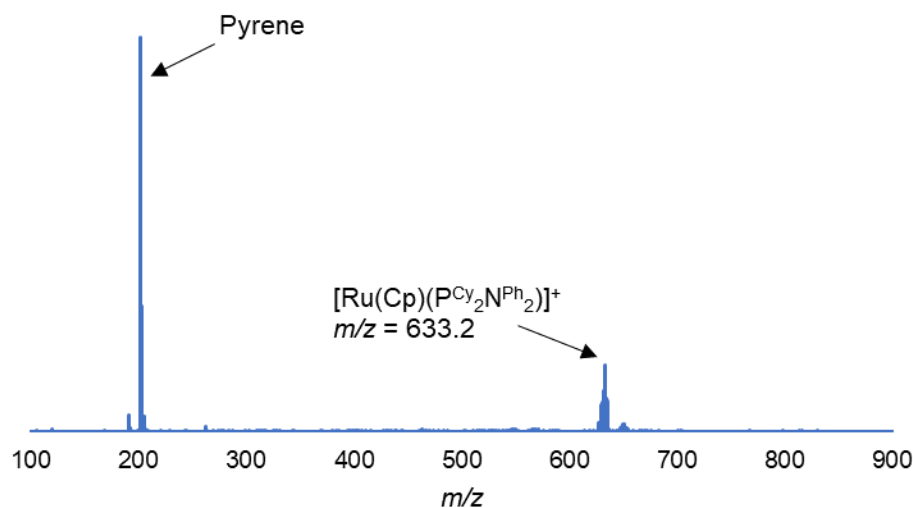


**Figure A-49.** MALDI -TOF mass spectrum of **2-5b-N<sub>2</sub>** and **2-κ<sup>3</sup>-(P,P,Ar)-5b** with pyrene as the matrix (1:20 ratio).

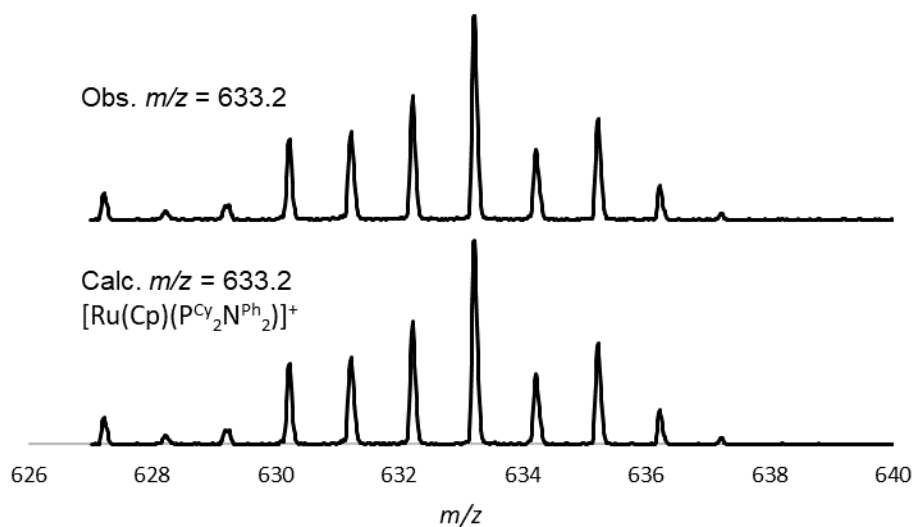


**Figure A-50.** Zoom in (top) of the observed signal with  $m/z = 633.2$  in the MALDI-TOF mass spectrum of **2-5b-N<sub>2</sub>** and **2-κ<sup>3</sup>-(P,P,Ar)-5b**; and simulation<sup>1</sup> (bottom) of the isotope pattern for the cationic fragment  $[\text{Ru}(\text{Cp})(\text{P}^{\text{Cy}}_2\text{N}^{\text{Ph}}_2)]^+$  complex with  $m/z = 633.2$ .

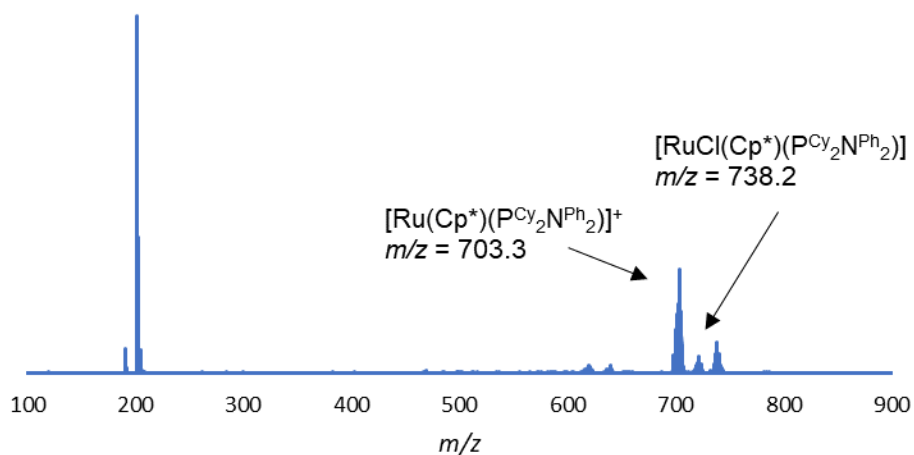


**Figure A-51.** MALDI -TOF mass spectrum of **2-6b-N<sub>2</sub>** with pyrene as the matrix (1:20 ratio).

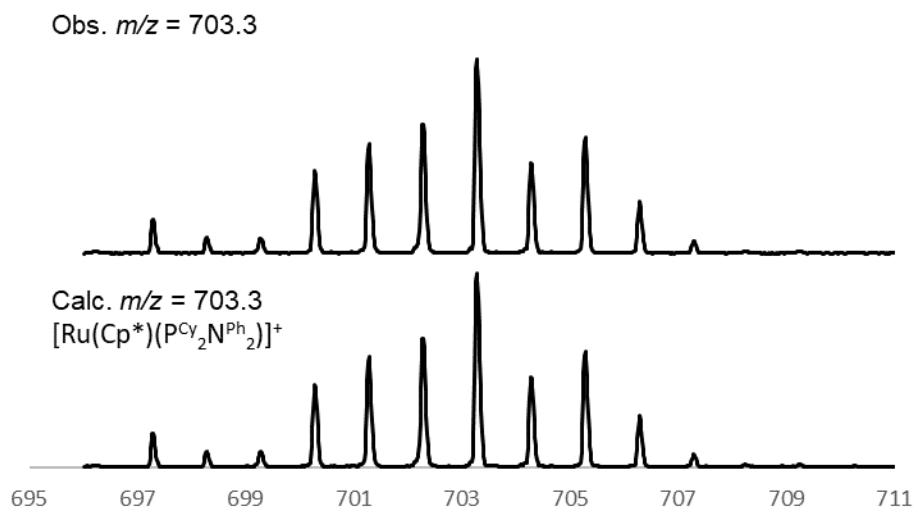


**Figure A-52.** Zoom in (top) of the observed signal with  $m/z = 703.3$  in the MALDI-TOF mass spectrum of **2-6b-N<sub>2</sub>**; and simulation<sup>2</sup> (bottom) of the isotope pattern for the cationic fragment  $[\text{Ru}(\text{Cp}^*)(\text{PCy}_2\text{N}^{\text{Ph}}_2)]^+$  with  $m/z = 703.3$ .

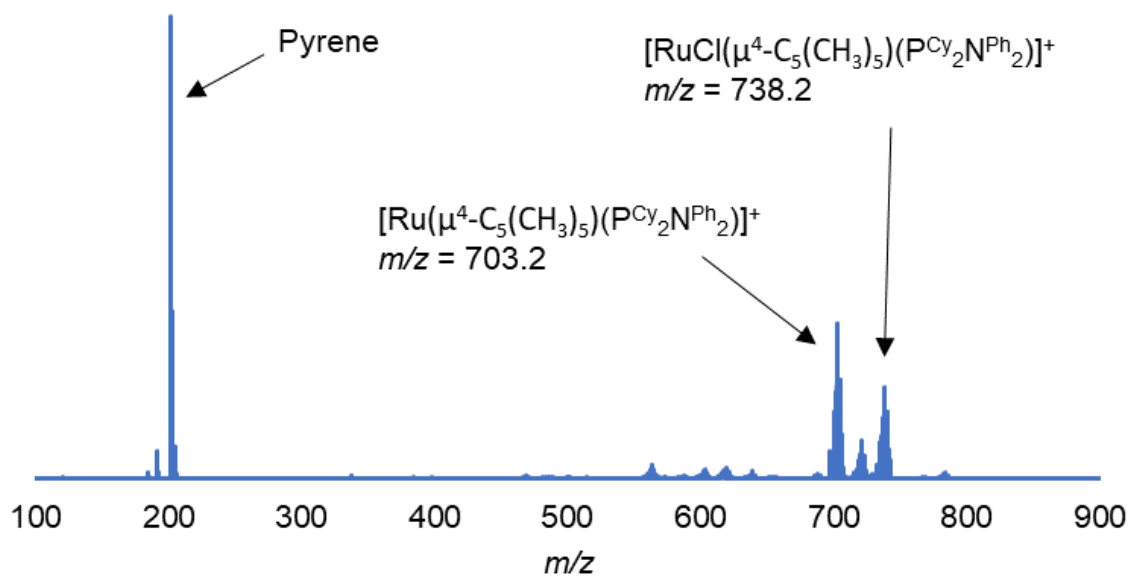


**Figure A-53.** MALDI -TOF mass spectrum of **2-7** with pyrene as the matrix (1:20 ratio).

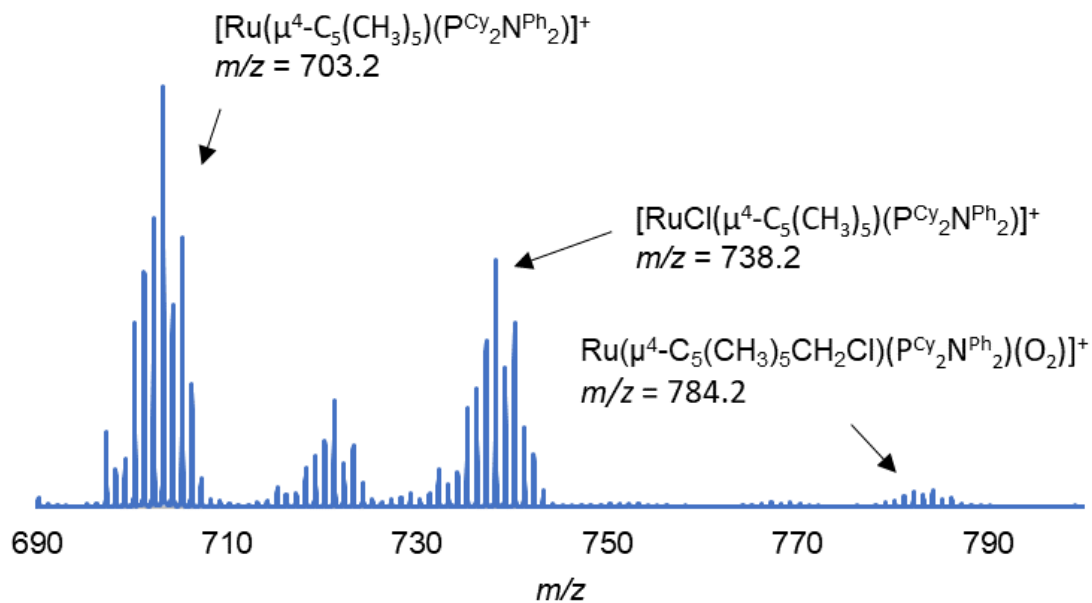


**Figure A-54.** Zoom in of  $m/z$  from 690 to 800 in the MALDI-TOF mass spectrum of **2-7**.

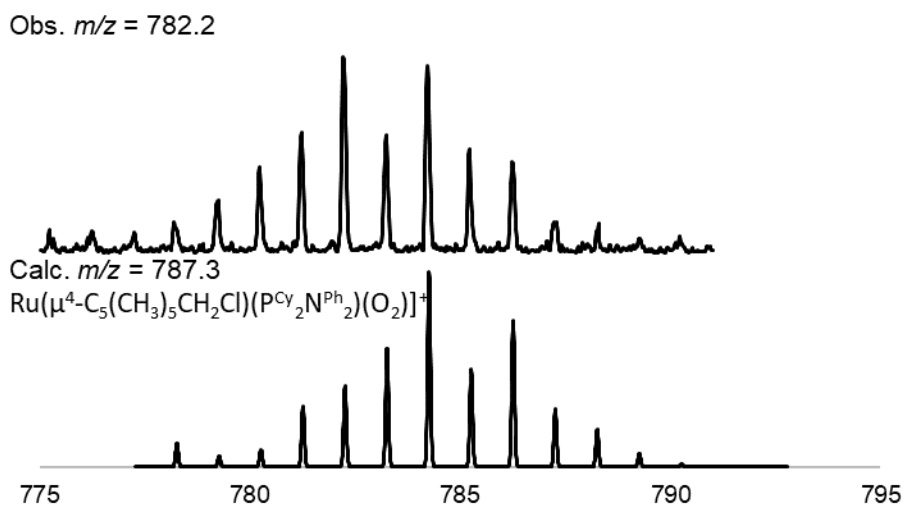


**Figure A-55.** Zoom in (top) of the observed signal with  $m/z = 782.2$  in the MALDI-TOF mass spectrum of **2-7**; and simulation<sup>2</sup> (bottom) of the isotope pattern for the cationic complex  $[\text{Ru}(\mu^4\text{-C}_5(\text{CH}_3)_5\text{CH}_2\text{Cl})(\text{P}^{\text{Cy}}_2\text{N}^{\text{Ph}}_2)(\text{O}_2)]^+$  with  $m/z = 784.3$ .

### Catalytic Data

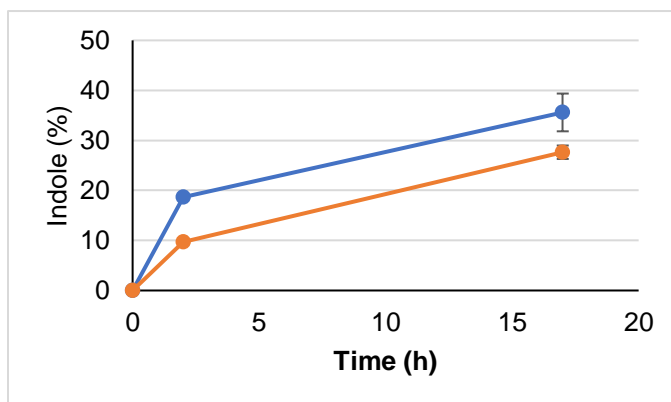


**Figure A-56.** Intramolecular hydroamination of 2-ethynylaniline (**2-EA**) catalyzed with **2-1b** in Me-THF (blue) and  $\text{CH}_3\text{NO}_2$  (orange) for solvent comparison. Conditions: 300 mM **2-EA**, Me-THF or  $\text{CH}_3\text{NO}_2$ , 70 °C, 0.1 mol% **2-1b**. Data points represent an average of the two runs and the error bars give the span of the conversion values of each data set.

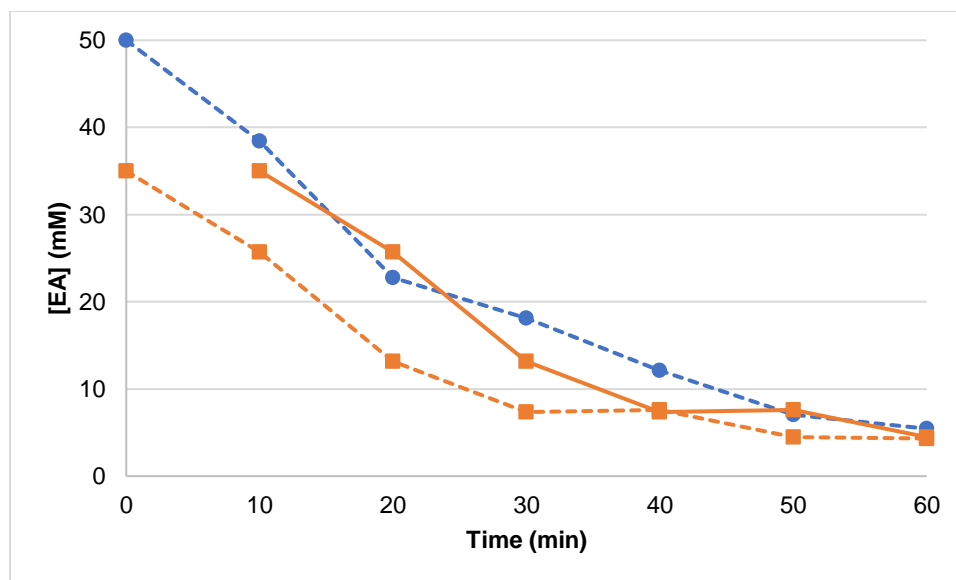


**Figure A-57.** Reaction profiles for runs with initial concentrations of: A, 50 mM **2-EA** (●, blue) and B, 35 mM **2-EA** (■, orange). Solid lines (—) are time-shifted (Run B = orange; Run C = green). Reactions were performed in duplicate and in all cases the error was within  $\pm 5\%$ .

## Crystallographic Details

Data Collection and Processing. Samples of **2-2b**, **2-3b**, **2-4b**, **2-5b**, and **2-7**, were mounted on a Mitegen polyimide micromount with a small amount of Paratone N oil. All X-ray measurements were made on a Bruker Kappa Axis Apex2 diffractometer at a temperature of 110 K. The unit cell dimensions were determined from a symmetry constrained fit with reflections and dimensions listed in Table S1. The data collection strategy was a number of  $\omega$  and  $\phi$  scans which collected data up to  $2\theta_{\max}$  as listed in Table S1. The frame integration was performed using SAINT.<sup>3</sup> The resulting raw data was scaled and absorption corrected using a multi-scan averaging of symmetry equivalent data using SADABS.<sup>4</sup>

Structure Solution and Refinement. The structure for **2-2b** was solved by using a dual space methodology using the SHELXT program.<sup>5</sup> All non-hydrogen atoms were obtained from the initial solution. The hydrogen atoms were introduced at idealized positions and were allowed to ride on the parent atom. The structural model was fit to the data using full matrix least-squares based on  $F^2$

. The calculated structure factors included corrections for anomalous dispersion from the usual tabulation. The structure was refined using the SHELXL program from the SHELX suite of crystallographic software.<sup>6</sup> Graphic plots were produced using the SHELXL XP program suite.<sup>7</sup>,

Structure Solution and Refinement. The structure for **2-3b**, **2-4b**, **2-5b**, and **2-7**, was solved by using a dual space methodology using the SHELXT program.<sup>8</sup> All non-hydrogen atoms were obtained from the initial solution. The hydrogen atoms were introduced at idealized positions and were allowed to ride on the parent atom. The structural model was fit to the data using full matrix least-squares based on  $F^2$ . The calculated structure factors included corrections for anomalous dispersion from the usual tabulation. The structure was refined using the SHELXL program from the SHELX suite of crystallographic software.<sup>8</sup> Graphic plots were produced using the Mercury program.<sup>9</sup>

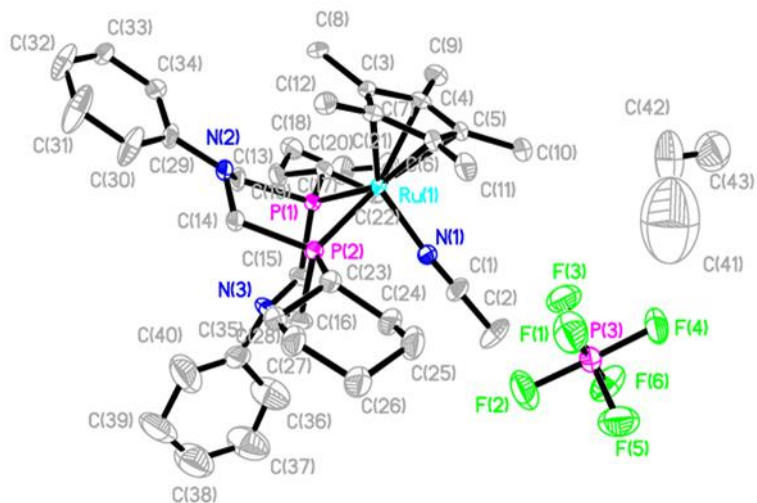


**Figure A-58.** ORTEP drawing of **2-2b** showing naming and numbering scheme. Ellipsoids are at the 50% probability level and hydrogen atoms were omitted for clarity.

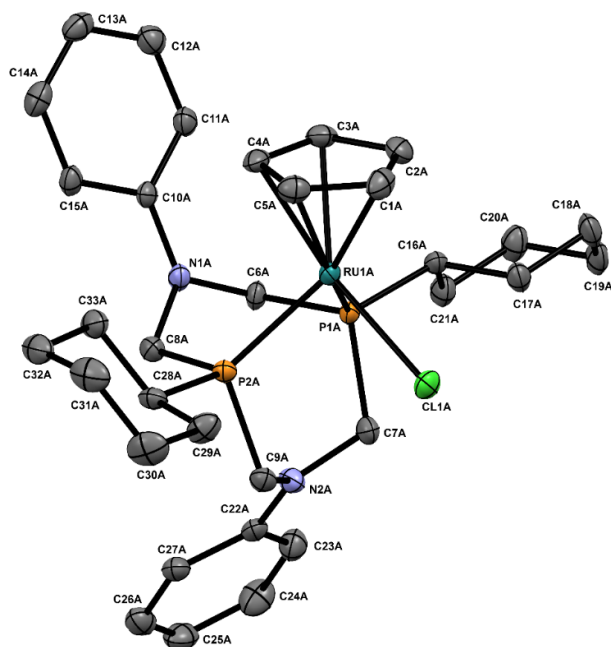


**Figure A-59.** ORTEP drawing of **2-3b** showing naming and numbering scheme. Ellipsoids are at the 50% probability level and hydrogen atoms were omitted for clarity.

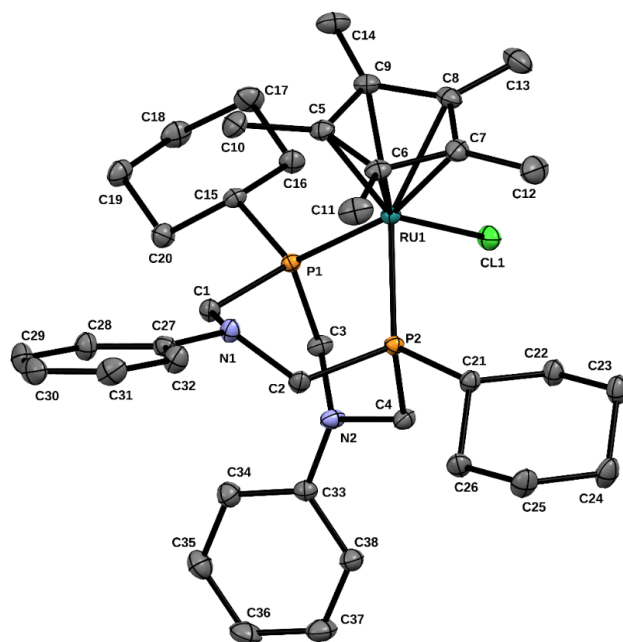


**Figure A- 60.** ORTEP drawing of **2-4b** showing naming and numbering scheme. Ellipsoids are at the 50% probability level and hydrogen atoms were omitted for clarity. The  $\text{CH}_2\text{Cl}_2$  of solvation was also omitted for clarity.



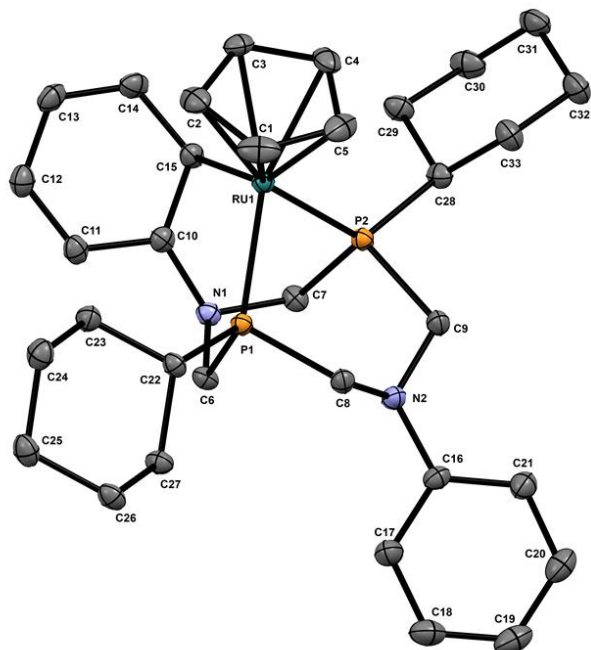


**Figure A-61.** ORTEP drawing of **2- $\kappa^3$ -5b** cation showing naming and numbering scheme. Ellipsoids are at the 50% probability level and hydrogen atoms were omitted for clarity.

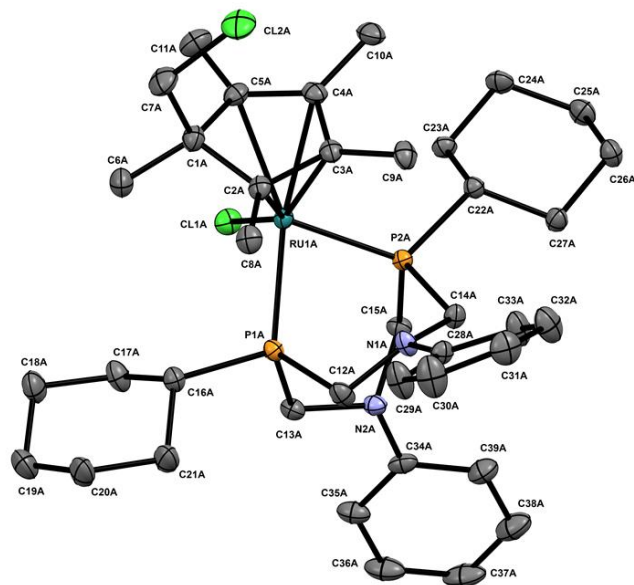


**Figure A-62.** ORTEP drawing of **2-7** cation showing naming and numbering scheme. Ellipsoids are at the 50% probability level and hydrogen atoms were omitted for clarity. A minor component of disorder was omitted for clarity.

**Table A-1.** Summary of Crystal Data for **2-2b**, **2-3b**, **2-4b**, **2-5b**, and **2-7**.

Compound	<b>2b</b>	<b>3b</b>	<b>4b</b>	<b>5b</b>	<b>7</b>
Formula	C <sub>43</sub> H <sub>65</sub> F <sub>6</sub> N <sub>3</sub> P <sub>3</sub> Ru	C <sub>33</sub> H <sub>45</sub> ClN <sub>2</sub> P <sub>2</sub> Ru	C <sub>39</sub> H <sub>57</sub> Cl <sub>3</sub> N <sub>2</sub> P <sub>2</sub> Ru	C <sub>34</sub> H <sub>47</sub> Cl <sub>2</sub> F <sub>6</sub> N <sub>2</sub> P <sub>3</sub> Ru	C <sub>40</sub> H <sub>59</sub> Cl <sub>4</sub> F <sub>6</sub> N <sub>2</sub> P <sub>3</sub> Ru
CCDC	2077208	2077207	2077206	2077205	2077059
Formula Weight (g/mol)	931.96	668.17	823.22	862.61	1017.67
Crystal Dimensions (mm)	0.174 × 0.163 × 0.109	0.293 × 0.223 × 0.045	0.275 × 0.204 × 0.109	0.212 × 0.177 × 0.030	0.298 × 0.243 × 0.161
Crystal Color and Habit	orange prism	yellow plate	yellow prism	red prism	red prism
Crystal System	monoclinic	monoclinic	monoclinic	monoclinic	monoclinic
Space Group	P 2 <sub>1</sub> /c	P 2 <sub>1</sub> /c	P 2 <sub>1</sub> /n	P 2 <sub>1</sub> /n	P 2 <sub>1</sub> /n
Temperature, K	110	110	110	110	110
<i>a</i> , Å	17.271(12)	27.093(14)	11.565(2)	9.728(3)	21.004(7)
<i>b</i> , Å	12.730(7)	19.205(11)	27.874(6)	34.572(9)	19.798(7)
<i>c</i> , Å	20.815(14)	13.194(7)	12.377(2)	11.458(3)	22.578(9)
$\alpha$ , °	90	90	90	90	90
$\beta$ , °	109.709(14)	95.189(12)	102.246(13)	112.886(8)	109.970(18)
$\gamma$ , °	90	90	90	90	90
<i>V</i> , Å <sup>3</sup>	4308(5)	6837(6)	3898.8(14)	3549.9(16)	8824(6)
Number of reflections to determine final unit cell	8884	9858	9917	9957	9391

Min and Max 2 $\theta$ for cell determination, °	5.02, 47.86	5.0, 52.12	4.64, 72.2	4.68, 59.04	5.02, 61.02
Z	4	8	4	4	8
F(000)	1948	2784	1720	1768	4192
$\rho$ (g/cm <sup>3</sup> )	1.437	1.298	1.402	1.614	1.532
$\lambda$ , Å, (MoKa)	0.71073	0.71073	0.71073	0.71073	0.71073
$\mu$ , (cm <sup>-1</sup> )	0.536	0.653	0.720	0.788	0.764
Diffractometer Type	Bruker Kappa Axis Apex2	Bruker Kappa Axis Apex2	Bruker Kappa Axis Apex2	Bruker Kappa Axis Apex2	Bruker Kappa Axis Apex2
Scan Type(s)	$\phi$ and $\omega$ scans	$\phi$ and $\omega$ scans	$\phi$ and $\omega$ scans	$\phi$ and $\omega$ scans	$\phi$ and $\omega$ scans
Max 2 $\theta$ for data collection, °	48.496	54.264	75.73	63.282	71.47
Measured fraction of data	0.999	0.999	0.998	0.998	0.999
Number of reflections measured	71281	258434	164988	162390	707850
Unique reflections measured	6946	15102	20968	11899	40951
R <sub>merge</sub>	0.0718	0.1072	0.0827	0.0936	0.0768
Number of reflections included in refinement	6946	15102	20968	11899	40951

Cut off	I > 2θ(I)	I > 2θ(I)	I > 2θ(I)	I > 2θ(I)	I > 2θ(I)
Threshold Expression					
Structure refined using	full matrix least-squares using F <sup>2</sup>	full matrix least-squares using F <sup>2</sup>	full matrix least-squares using F <sup>2</sup>	full matrix least-squares using F <sup>2</sup>	full matrix least-squares using F <sup>2</sup>
Weighting Scheme	w=1/[σ <sup>2</sup> (Fo <sup>2</sup> )+(0.1088P) <sup>2</sup> +11.4443P] where P=(Fo <sup>2</sup> +2Fc <sup>2</sup> )/3	w=1/[σ <sup>2</sup> (Fo <sup>2</sup> )+(0.0238P) <sup>2</sup> +14.5649P] where P=(Fo <sup>2</sup> +2Fc <sup>2</sup> )/3	w=1/[σ <sup>2</sup> (Fo <sup>2</sup> )+(0.0343P) <sup>2</sup> +0.1929P] where P=(Fo <sup>2</sup> +2Fc <sup>2</sup> )/3	w=1/[σ <sup>2</sup> (Fo <sup>2</sup> )+(0.0368P) <sup>2</sup> +0.8914P] where P=(Fo <sup>2</sup> +2Fc <sup>2</sup> )/3	w=1/[σ <sup>2</sup> (Fo <sup>2</sup> )+(0.02415P) <sup>2</sup> +9.2415P] where P=(Fo <sup>2</sup> +2Fc <sup>2</sup> )/3
Number of parameters in least-squares	513	703	429	454	1126
R <sub>1</sub>	0.0593	0.0429	0.0374	0.0352	0.0373
wR <sub>2</sub>	0.1713	0.0841	0.0788	0.0773	0.0796
R <sub>1</sub> (all data)	0.0719	0.0607	0.0572	0.0494	0.0531
wR <sub>2</sub> (all data)	0.1829	0.0895	0.0852	0.0818	0.0858
GOF	1.107	1.057	1.050	1.044	1.064
Maximum shift/error	0.001	0.001	0.003	0.001	0.003
Min & Max peak heights on final DF Map (e <sup>-</sup> /Å)	-0.867, 2.761	-0.776, 0.990	-0.909, 0.608	-0.786, 0.549	-1.558, 1.505

Where:

$$R_1 = \frac{\sum (|F_o| - |F_c|)}{\sum F_o}$$

$$wR_2 = \left[ \frac{\sum (w(F_o^2 - F_c^2))^2}{\sum (w F_o^4)} \right]^{1/2}$$

$$GOF = \left[ \frac{\sum (w(F_o^2 - F_c^2))^2}{(\text{No. of reflns.} - \text{No. of params.})} \right]^{1/2}$$

## Computational Details

All computational structures were optimized using ORCA 4.2.1<sup>10</sup> without symmetry constraints using the hybrid GGA functional B3LPY<sup>11</sup> with D3 dispersion corrections with Becke-Johnson damping,<sup>12</sup> and the def2-TZVP basis set with effective core potential (ECP)<sup>13</sup> for Ru and the def2-

SVP basis set<sup>14</sup> for all the remaining atoms with the def2/J auxiliary basis set.<sup>15</sup> Each stationary point was confirmed by a frequency calculation at the same level of theory to be a real local minimum on the potential energy surface without an imaginary frequency. The lowest energy ground state species for each structure are described here. All reported free energy are for THF solutions at the standard state ( $T = 298.25$  K,  $P = 1$  atm of  $N_2$ ,  $1$  mol  $L^{-1}$  concentration of all species in THF) as modeled by the universal solvation model (SMD)<sup>16</sup> with standard correction for (harmonic) vibrational, rotational, and translational thermal free energy contributions.

**Sample input file for single point energy calculations, geometry optimizations, and frequency calculations, with Orca 4.2.1**

```
! B3LYP def2-SVP def2/J RIJCOSX D3BJ TightSCF OPT FREQ pal4
```

```
%basis
```

```
newgto Ru "def2-TZVP" end
```

```
end
```

```
%cpcm
```

```
SMD true
```

```
SMDsolvent "THF"
```

```
end
```

```
%freq Temp 298, 323, 343
```

```
end
```

```
*xyz 1 1
```

```
coordinates
```

```
*
```

**xyz coordinates for DFT structures**

**$N_2$**

```
* xyz 0 1
```

```
N -5.31287 0.45097 -0.06402
```

```
N -4.19811 0.39924 -0.15916
```

```
*
```

## 2-5b-κ<sup>2</sup>-P,P

\*xyz 1 1

Ru	10.49435	2.62213	7.49610
P	11.72695	4.49484	7.88429
P	9.60530	3.33641	9.44900
N	12.24130	3.37472	10.40527
N	10.09516	6.05312	9.43920
C	12.11302	1.11642	7.50904
C	11.72083	1.31756	6.13539
C	10.36432	0.92802	6.02173
C	9.89805	0.48119	7.28957
C	10.99395	0.59704	8.22232
H	13.51868	1.20426	8.03028
H	12.64750	1.63708	4.99492
H	9.55663	0.92165	4.76173
H	8.57645	-0.17949	7.53647
H	11.04299	0.07638	9.62340
C	10.84028	3.38873	10.83049
H	10.68208	4.20757	11.36351
H	10.68361	2.61160	11.42273
C	12.69466	4.40458	9.46272
H	13.64441	4.23318	9.24152
H	12.64777	5.28566	9.91250
C	10.77506	6.06330	8.14393
H	11.39393	6.83495	8.10370
H	10.10690	6.16724	7.42178
C	8.99613	5.08436	9.48427
H	8.39597	5.23610	8.71115
H	8.46899	5.22919	10.31021
C	12.98773	5.03344	6.63899
H	13.56440	4.23991	6.44789
C	14.93029	6.49357	5.98450
H	15.52005	5.71046	5.84610
H	15.49383	7.25582	6.26744
C	13.93071	6.18041	7.06813
H	13.39530	6.98980	7.26635
H	14.41026	5.92095	7.89429
C	9.86861	7.71183	11.19497
H	10.32985	7.13124	11.78948
C	9.36825	8.99756	11.77696
H	9.48957	9.23551	12.68853
C	8.71572	9.80465	10.86968

H	8.30672	10.60179	11.18780
C	8.62469	9.50804	9.50387
H	8.20138	10.11698	8.90993
C	9.15521	8.33051	9.02574
H	9.15050	8.15471	8.09271
C	9.74868	7.30702	9.99180
C	14.55408	3.01319	11.16166
H	14.86698	3.24041	10.29365
C	15.47073	2.65039	12.15124
H	16.39841	2.64988	11.94873
C	15.05390	2.29522	13.41123
H	15.67844	2.03484	14.07746
C	13.71115	2.32577	13.67381
H	13.40334	2.08550	14.54016
C	12.78332	2.70258	12.70579
H	11.85939	2.72103	12.92814
C	13.17915	3.04756	11.43208
C	7.78020	2.80824	11.62020
H	8.56729	2.68727	12.20863
H	7.50884	3.75893	11.66166
C	6.64374	1.93623	12.11205
H	6.38772	2.21869	13.02677
H	6.94989	0.99582	12.16011
C	5.41750	2.01898	11.20085
H	5.03446	2.93116	11.24394
H	4.72876	1.38078	11.51183
C	5.80154	1.69309	9.75273
H	6.07791	0.74484	9.69205
H	5.01425	1.82155	9.16737
C	6.93967	2.58164	9.27068
H	6.63983	3.52547	9.26306
H	7.18371	2.33043	8.34483
C	8.16079	2.44416	10.17208
H	8.40025	1.47347	10.17835
C	12.27569	5.39879	5.32413
H	11.72022	4.63579	5.02604
H	11.67763	6.17306	5.47566
C	13.28531	5.74505	4.23657
H	13.80685	4.93588	4.00440
H	12.80301	6.03977	3.42339
C	14.23099	6.83728	4.67747
H	13.72580	7.68095	4.79023

H 14.91257 6.98328 3.97305

\*

**2-κ<sup>3</sup>-(P,P,Ar)-5b**

\* xyz 1 1

Ru	2.89776	28.80919	7.06336
P	4.48935	29.27626	5.48871
P	3.42134	30.94298	7.71804
N	2.63724	31.20400	5.06352
N	5.94285	31.29769	6.66761
C	3.71813	26.80782	7.40189
H	4.46350	26.47195	6.91679
C	2.36372	26.63876	7.04763
H	2.03195	26.19196	6.27754
C	1.58687	27.26521	8.06523
H	0.63822	27.30182	8.08799
C	2.44142	27.81767	9.02520
H	2.17772	28.27734	9.81362
C	3.78596	27.56426	8.60317
H	4.57698	27.84923	9.04532
C	3.89681	30.73762	4.46805
H	4.57171	31.46173	4.48239
H	3.75057	30.46246	3.52830
C	2.84224	31.99846	6.27355
H	1.99360	32.44634	6.51699
H	3.51618	32.70048	6.09225
C	6.06224	29.90720	6.23429
H	6.30362	29.34319	7.01136
H	6.79073	29.83488	5.56771
C	5.19057	31.46467	7.90309
H	5.22232	32.41543	8.17762
H	5.61529	30.92739	8.61794
C	1.71805	30.13088	5.19948
C	1.42961	29.34506	4.03800
H	1.98315	29.42530	3.27012
C	0.37183	28.48214	4.01625
H	0.19308	27.97539	3.23282
C	-0.45864	28.33694	5.14797
H	-1.19142	27.73272	5.12471
C	-0.21058	29.06122	6.27165
H	-0.77945	28.96145	7.02594
C	0.89078	29.97012	6.33858



H	1.06539	30.45855	7.13447
C	7.07014	32.13467	6.45786
C	7.61661	32.21419	5.16538
H	7.25241	31.68206	4.46757
C	8.68380	33.06259	4.89800
H	9.04864	33.09864	4.02126
C	9.21642	33.85221	5.89238
H	9.94185	34.43758	5.70639
C	8.67829	33.78030	7.17177
H	9.03789	34.32657	7.86071
C	7.62537	32.92326	7.45836
H	7.28198	32.87562	8.34300
C	5.20308	28.01819	4.32312
H	5.82568	27.44775	4.85875
C	4.17198	27.07506	3.68807
H	3.66157	26.61287	4.39966
H	3.53314	27.59976	3.14262
C	4.87575	26.03825	2.80210
H	5.45324	25.46501	3.36585
H	4.19648	25.45948	2.37349
C	5.72403	26.70168	1.72359
H	5.13857	27.20592	1.10501
H	6.19752	26.00658	1.20077
C	6.74292	27.65069	2.34956
H	7.38215	27.13235	2.89974
H	7.25286	28.10610	1.63370
C	6.05011	28.69165	3.22107
H	5.46639	29.25794	2.65665
H	6.73118	29.27585	3.64004
C	2.76211	31.77443	9.23800
H	3.07941	32.72223	9.20381
C	1.23883	31.82975	9.32298
H	0.87499	30.91072	9.37602
H	0.87552	32.25931	8.50843
C	0.81169	32.62629	10.56068
H	1.13817	33.55742	10.48274
H	-0.17723	32.65149	10.61091
C	1.36585	32.00053	11.82666
H	0.98933	31.09160	11.93776
H	1.09391	32.54287	12.60921
C	2.88555	31.91791	11.76860
H	3.21991	31.45748	12.57855
H	3.26337	32.83282	11.75862

C	3.35578	31.15940	10.52098
H	3.07994	30.21105	10.58918
H	4.34432	31.18785	10.47230

\*

## 2-5b-N<sub>2</sub>

\* xyz 1 1

Ru	10.72806	2.68809	7.97804
P	11.67283	4.78749	8.03084
P	9.50996	3.60466	9.71302
N	11.99156	4.30378	10.78299
N	9.51254	6.25576	8.96193
C	12.63774	1.55256	8.00610
C	12.00859	1.31113	6.74196
C	10.76894	0.64275	7.01184
C	10.63520	0.46177	8.41301
C	11.79500	1.04206	9.03809
H	13.60767	2.01893	8.15828
H	12.41583	1.54680	5.76147
H	10.03644	0.34438	6.26287
H	9.81765	-0.04447	8.92262
H	12.02400	1.02561	10.09894
C	10.58211	4.31205	11.10441
H	10.25647	5.34157	11.31029
H	10.37841	3.74171	12.01329
C	12.37484	5.22891	9.73999
H	13.46477	5.30185	9.66467
H	12.01465	6.23477	10.00391
C	10.35656	6.10641	7.79496
H	10.81611	7.05722	7.51408
H	9.74517	5.79322	6.93552
C	8.59073	5.16094	9.19238
H	8.02794	4.93650	8.27304
H	7.85556	5.42543	9.95420
C	12.97129	5.23443	6.77928
H	13.75928	4.47220	6.91818
C	14.66137	6.89652	5.89341
H	15.49767	6.18685	6.02961
H	15.08213	7.90624	6.03148
C	13.60004	6.62681	6.96999
H	12.81688	7.40160	6.89813
H	14.05014	6.72303	7.97060

C	8.66322	7.58113	10.85438
H	7.93529	6.81664	11.12098
C	8.69005	8.74767	11.62165
H	7.97646	8.85183	12.44370
C	9.60580	9.77033	11.35777
H	9.61332	10.68372	11.95638
C	10.51614	9.58738	10.31317
H	11.25749	10.35885	10.08582
C	10.50091	8.42797	9.53580
H	11.24005	8.34272	8.74180
C	9.55386	7.39808	9.76662
C	14.09353	3.04503	10.61503
H	14.45747	3.68856	9.81570
C	14.90322	1.98319	11.02212
H	15.86992	1.84308	10.53116
C	14.49217	1.09734	12.02171
H	15.12901	0.26627	12.33187
C	13.24434	1.30798	12.61612
H	12.89260	0.64020	13.40751
C	12.42222	2.36043	12.21457
H	11.46065	2.46753	12.71222
C	12.82009	3.25787	11.19225
C	7.44036	3.25780	11.64848
H	8.10818	3.70302	12.40306
H	6.87378	4.09082	11.19794
C	6.44882	2.30072	12.32119
H	5.85901	2.85110	13.07309
H	7.01174	1.52191	12.86765
C	5.52363	1.63698	11.29734
H	4.87870	2.40766	10.83536
H	4.85063	0.92270	11.80071
C	6.32281	0.93514	10.19635
H	6.89133	0.09388	10.63427
H	5.64529	0.50061	9.44266
C	7.30339	1.89755	9.51843
H	6.73416	2.69191	9.00241
H	7.88936	1.37670	8.74649
C	8.24271	2.54036	10.55143
H	8.84726	1.74050	11.01837
C	12.39066	5.07958	5.36137
H	11.96390	4.07248	5.23594
H	11.55757	5.79317	5.23025
C	13.45122	5.35841	4.29153

H	14.23677	4.58328	4.35020
H	12.99495	5.27220	3.29073
C	14.08913	6.73964	4.48055
H	13.32576	7.52025	4.30636
H	14.87962	6.90665	3.72996
N	8.51483	3.44572	5.85235
N	9.32732	3.27959	6.66175

\*

## 2-6b- $\kappa^2$ -P,P

\*xyz 1 1

Ru	10.84097	2.79877	7.95371
P	11.88744	4.81942	8.14250
P	9.54227	3.63154	9.63537
N	11.88932	4.43070	10.92596
N	9.55138	6.25309	8.71689
C	12.43971	1.37036	6.76997
C	11.21141	1.06532	6.14127
C	10.29618	0.50432	7.13960
C	10.96964	0.48342	8.38692
C	12.28241	1.09973	8.19589
C	13.72906	1.76737	6.12462
C	10.85755	1.23969	4.70082
C	8.95318	-0.06798	6.80764
C	10.50870	-0.15048	9.65955
C	13.43478	0.99836	9.14099
C	10.45755	4.47187	11.06008
H	10.13339	5.51889	11.11159
H	10.14485	4.00861	12.00188
C	12.43798	5.28500	9.89911
H	13.53146	5.22791	9.89163
H	12.16924	6.33590	10.09037
C	10.57297	6.11792	7.70543
H	11.05403	7.07560	7.48545
H	10.10979	5.78135	6.76504
C	8.66624	5.11799	8.82750
H	8.33528	4.80740	7.82409
H	7.75823	5.36670	9.38501
C	13.29414	5.28419	7.02504
H	14.06980	4.52325	7.22340
C	15.05543	6.94480	6.29334
H	15.87474	6.23072	6.49259
H	15.46643	7.95223	6.47210
C	13.91094	6.67208	7.28087

H	13.14006	7.45302	7.15857
H	14.28433	6.75385	8.31359
C	8.52431	7.41910	10.61955
H	7.79138	6.62630	10.76285
C	8.47364	8.51331	11.48582
H	7.69485	8.53828	12.25343
C	9.39559	9.55933	11.38785
H	9.34685	10.41451	12.06591
C	10.38244	9.47991	10.40070
H	11.12541	10.27636	10.29884
C	10.44548	8.39364	9.52574
H	11.24297	8.38546	8.78468
C	9.50648	7.33610	9.60163
C	14.03327	3.46442	11.62453
H	14.58601	4.30105	11.19640
C	14.74713	2.46928	12.29111
H	15.83546	2.55714	12.35569
C	14.09781	1.38218	12.88887
H	14.66706	0.60807	13.40815
C	12.70493	1.31693	12.80774
H	12.16260	0.47961	13.25550
C	11.97852	2.30505	12.13893
H	10.89712	2.19321	12.08451
C	12.62302	3.40927	11.53314
C	7.33254	3.43878	11.43096
H	7.96024	3.87649	12.22230
H	6.83412	4.27976	10.91640
C	6.25895	2.53843	12.05442
H	5.64222	3.12846	12.75266
H	6.75531	1.75314	12.65324
C	5.37742	1.88478	10.98624
H	4.79426	2.66807	10.46721
H	4.64593	1.20832	11.45930
C	6.21714	1.12656	9.95366
H	6.71511	0.26880	10.44261
H	5.57469	0.70905	9.16106
C	7.28325	2.03329	9.33212
H	6.78796	2.83980	8.76207
H	7.89774	1.47759	8.61276
C	8.17712	2.65259	10.41573
H	8.69741	1.83485	10.94605
C	12.83416	5.15030	5.56236
H	12.39106	4.15695	5.39263
H	12.03408	5.88478	5.36624
C	13.98269	5.41690	4.58780
H	14.75717	4.63865	4.71362
H	13.61134	5.33367	3.55231
C	14.60415	6.79702	4.83625

H	13.85766	7.57818	4.60285
H	15.45471	6.96663	4.15556
H	8.30953	0.65873	6.28773
H	8.42388	-0.41952	7.70339
H	9.06174	-0.93713	6.13500
H	9.41363	-0.22086	9.71629
H	10.86745	0.40803	10.53318
H	10.91208	-1.17523	9.74153
H	14.08971	1.87846	9.08358
H	14.04887	0.11441	8.88627
H	13.10572	0.89123	10.18050
H	13.58433	2.20626	5.12819
H	14.37827	0.88225	6.00256
H	14.28763	2.48659	6.73898
H	10.01447	1.93999	4.57800
H	10.53704	0.28101	4.25852
H	11.70322	1.61886	4.11066

\*

### 2-κ<sup>3</sup>-(P,P,Ar)-6b

\*xyz 1 1

Ru	3.01922	28.75596	7.16176
P	4.70556	29.16708	5.57929
P	3.64795	30.89320	7.88503
N	3.09897	31.34628	5.18178
N	6.31746	30.91595	7.00899
C	3.70305	26.70753	7.55597
C	4.90950	25.97842	7.05814
C	2.36394	26.59808	7.05959
C	1.85795	25.75976	5.92747
C	1.50321	27.26508	8.00846
C	0.01256	27.22773	7.96821
C	2.28242	27.77503	9.07774
C	1.72428	28.23451	10.38927
C	3.67328	27.49137	8.77327
C	4.82613	27.64953	9.71139
C	4.31519	30.76932	4.63573
H	5.13797	31.48874	4.71585
H	4.20207	30.53982	3.57077
C	3.29912	32.06206	6.42754
H	2.40675	32.65357	6.67306
H	4.12375	32.77312	6.29866
C	6.33513	29.59483	6.42799
H	6.48392	28.84456	7.22117
H	7.16714	29.47638	5.72900
C	5.49766	31.05294	8.18917
H	5.71698	31.99571	8.70168
H	5.75362	30.24661	8.89455

C	1.97238	30.51708	5.08062
C	1.73345	29.77849	3.88793
H	2.43592	29.84745	3.05922
C	0.58152	29.02466	3.72921
H	0.42545	28.48036	2.79464
C	-0.39430	28.97364	4.74083
H	-1.31014	28.39732	4.59420
C	-0.18159	29.68578	5.91133
H	-0.93980	29.69862	6.69616
C	1.00268	30.42303	6.11162
H	1.05635	31.05505	6.98952
C	6.90283	32.02116	6.38511
C	7.82720	31.87200	5.32307
H	8.12039	30.88510	4.96872
C	8.40176	32.98388	4.70486
H	9.11198	32.81936	3.88989
C	8.08394	34.28354	5.10938
H	8.53429	35.14713	4.61589
C	7.17218	34.44511	6.15669
H	6.89008	35.44577	6.49610
C	6.59055	33.34334	6.78492
H	5.87390	33.53134	7.58244
C	5.29603	27.95995	4.28218
H	5.85845	27.20882	4.86184
C	4.14941	27.24801	3.55644
H	3.43420	26.84436	4.28030
H	3.59157	27.98119	2.95180
C	4.68988	26.14869	2.63560
H	5.18553	25.37457	3.24991
H	3.85537	25.65113	2.11415
C	5.69005	26.71792	1.62379
H	5.15031	27.39532	0.93604
H	6.11345	25.91084	1.00299
C	6.81450	27.49249	2.31829
H	7.43583	26.78928	2.90293
H	7.48019	27.95678	1.57133
C	6.26704	28.57399	3.25861
H	5.73574	29.33205	2.65794
H	7.10405	29.09069	3.75031
C	2.97947	31.84513	9.35270
H	3.28996	32.89054	9.16649
C	1.44597	31.79261	9.41829
H	1.11973	30.74213	9.39102
H	1.01000	32.28193	8.53420
C	0.88813	32.47133	10.67477
H	1.07401	33.55949	10.60808
H	-0.20623	32.33361	10.70215
C	1.52717	31.93720	11.95814
H	1.25906	30.87353	12.09043
H	1.12345	32.47427	12.83196
C	3.04780	32.07664	11.90062

H	3.51482	31.65604	12.80659
H	3.31687	33.14846	11.87648
C	3.63397	31.38075	10.66713
H	3.49387	30.29470	10.77307
H	4.71905	31.55963	10.63854
H	0.88131	28.92898	10.27462
H	2.48248	28.71118	11.02171
H	1.34133	27.36157	10.94741
H	-0.37012	27.14992	6.94343
H	-0.44084	28.10708	8.44335
H	-0.34195	26.33824	8.51956
H	2.67448	25.27083	5.38086
H	1.27082	26.35107	5.20869
H	1.19828	24.96064	6.30889
H	4.79250	25.63657	6.02262
H	5.07747	25.08337	7.68115
H	5.82388	26.58417	7.12520
H	5.78865	27.63241	9.18026
H	4.84241	26.82062	10.44235
H	4.77243	28.58433	10.28422

\*

## 2-6b-N<sub>2</sub>

\*xyz 1 1

Ru	10.83108	2.73598	7.95206
P	11.71892	4.88885	8.03965
P	9.47670	3.62929	9.77026
N	11.93946	4.34063	10.73468
N	9.51611	6.24679	8.95983
C	12.47292	1.55864	7.96947
C	12.00743	1.15240	6.79031
C	10.83269	0.59086	7.04026
C	10.71604	0.40232	8.33629
C	11.80459	0.88684	8.90656
C	13.75885	2.07449	8.12349
C	12.54494	1.55246	5.58301
C	9.86020	0.24933	6.15583
C	9.68938	-0.17849	8.99293
C	11.98423	0.90506	10.22253
C	10.55248	4.32874	11.11948
H	10.24423	5.35464	11.34314
H	10.32571	3.77524	12.00983
C	12.39161	5.27279	9.72835
H	13.46292	5.34132	9.65261
H	12.03988	6.26651	10.00924
C	10.36710	6.10246	7.77369
H	10.80834	7.03071	7.46842
H	9.74893	5.81333	6.91523



C	8.57960	5.13705	9.19192
H	8.00725	4.93454	8.27637
H	7.84334	5.38408	9.92597
C	12.99160	5.25715	6.77154
H	13.77499	4.48906	6.90751
C	14.66768	6.89371	5.89678
H	15.50061	6.17469	6.02930
H	15.08212	7.91337	6.02935
C	13.60016	6.63885	6.96577
H	12.81895	7.41192	6.88737
H	14.05669	6.72312	7.97109
C	8.66135	7.60665	10.86685
H	7.93038	6.87554	11.16137
C	8.68665	8.75139	11.62970
H	7.98114	8.85795	12.44458
C	9.60600	9.76886	11.35753
H	9.61662	10.67000	11.95137
C	10.51917	9.59600	10.31360
H	11.25365	10.36154	10.09423
C	10.49661	8.45447	9.54872
H	11.25131	8.39683	8.78283
C	9.54695	7.40464	9.76080
C	14.18478	3.16889	10.76314
H	14.59300	3.74371	9.95557
C	14.97153	2.02536	11.09932
H	15.88412	1.84529	10.54756
C	14.51422	1.12958	12.05965
H	15.11578	0.25981	12.31623
C	13.28901	1.33675	12.69336
H	12.89690	0.62960	13.40538
C	12.47701	2.45234	12.33776
H	11.50802	2.42828	12.77286
C	12.91949	3.34426	11.34185
C	7.42608	3.26938	11.65523
H	8.10799	3.70090	12.41189
H	6.85224	4.08781	11.20258
C	6.45188	2.29824	12.32732
H	5.85295	2.85252	13.07667
H	7.02036	1.51247	12.86459
C	5.51908	1.64246	11.29461
H	4.87931	2.41887	10.82933
H	4.84951	0.91771	11.80298
C	6.32460	0.93258	10.19769
H	6.89977	0.09195	10.64154
H	5.63861	0.50099	9.43954
C	7.28049	1.92482	9.52414
H	6.71841	2.70946	9.00202
H	7.82213	1.41480	8.71301
C	8.22079	2.55254	10.58256

H	8.81711	1.76923	11.08267
C	12.38683	5.12703	5.36018
H	11.88985	4.18701	5.18266
H	11.55424	5.82302	5.22854
C	13.45642	5.35798	4.29132
H	14.24357	4.57735	4.35922
H	12.99434	5.27696	3.28504
C	14.08529	6.74522	4.48025
H	13.31400	7.52390	4.31268
H	14.88421	6.90362	3.72711
N	8.38944	3.37949	5.72530
N	9.32090	3.45408	6.69171
H	8.97302	-0.45129	8.25733
H	9.37853	0.57389	9.65196
H	10.18649	-0.97839	9.50276
H	12.90982	1.31035	10.23696
H	12.10805	-0.09466	10.49252
H	11.16730	1.49665	10.63841
H	14.14854	2.36868	7.18419
H	14.34330	1.29727	8.62847
H	13.40300	2.91942	8.62083
H	11.92670	1.35985	4.78055
H	13.43308	0.98330	5.57540
H	12.68503	2.57229	5.69778
H	10.12370	0.48236	5.17090
H	9.01906	0.86358	6.43724
H	9.84000	-0.81080	6.28468

\*

## References

1. Patiny, L.; Borel, A., *J. Chem. Inf. Model.* 2013, 53, 1223-1228.
2. Loos, M.; Gerber, C.; Corona, F.; Hollender, J.; Singer, H., *Anal. Chem.* 2015, 87, 5738-5744.
3. Bruker-Nonius; SAINT; version; 2013.8, 2013, Bruker-Nonius, Madison, WI 53711, USA
4. Bruker-Nonius; SADABS; version; 2012.1, 2012, Bruker-Nonius, Madison, WI 53711, USA.
5. Sheldrick, G. M., *Acta Crystallogr. Sect. A* 2008, A64, 112-122.182
6. Burla, M. C.; Caliandro, R.; Camalli, M.; Carrozzini, B.; Cascarano, G. L.; Giacovazzo, C.; Mallamo, M.; Mazzone, A.; Polidori, G.; Spagna, R., *J. Appl. Cryst.* 2012, 45, 357-361.
7. Gabe, E. J.; Le Page, Y.; Charland, J. P.; Lee, F. L.; White, P. S., *J. Appl. Cryst.* 1989, 22, 384-387.
8. Sheldrick, G., *Acta Crystallogr. Sect. C* 2015, C71, 3-8.
9. Macrae, C. F.; Bruno, I. J.; Chisholm, J. A.; Edgington, P. R.; McCabe, P.; Pidcock, E.; Rodriguez-Monge, L.; Taylor, R.; van de Streek, J.; Wood, P. A., *J. Appl. Cryst.* 2008, 41, 466-470.

10. Neese, F., WIREs Comput. Mol. Sci. 2018, 8, e1327.
11. (a) Becke, A. D., J. Chem. Phys. 1993, 98, 5648-5652; (b) Lee, C.; Yang, W.; Parr, R. G., Phys. Rev. B 1988, 37, 785-789; (c) Vosko, S. H.; Wilk, L.; Nusair, M., Can. J. Phys. 1980, 58, 1200-1211; (d) Stephens, P. J.; Devlin, F. J.; Chabalowski, C. F.; Frisch, M. J., J. Phys. Chem. 1994, 98, 11623-11627.
12. (a) Grimme, S.; Ehrlich, S.; Goerigk, L., J. Comput. Chem. 2011, 32, 1456-1465; (b) Grimme, S.; Antony, J.; Ehrlich, S.; Krieg, H., J. Chem. Phys. 2010, 132, 154104.
13. Andrae, D.; Häußermann, U.; Dolg, M.; Stoll, H.; Preuß, H., Theoret. Chim. Acta 1990, 77, 123-141.
14. Weigend, F.; Ahlrichs, R., Phys. Chem. Chem. Phys. 2005, 7, 3297-3305.
15. Weigend, F., Phys. Chem. Chem. Phys. 2006, 8, 1057-1065.
16. Marenich, A. V.; Cramer, C. J.; Truhlar, D. G., J. Phys. Chem. B 2009, 113, 6378-6396.

Appendices B: Supplementary Information for Chapter 3  
 NMR Spectra

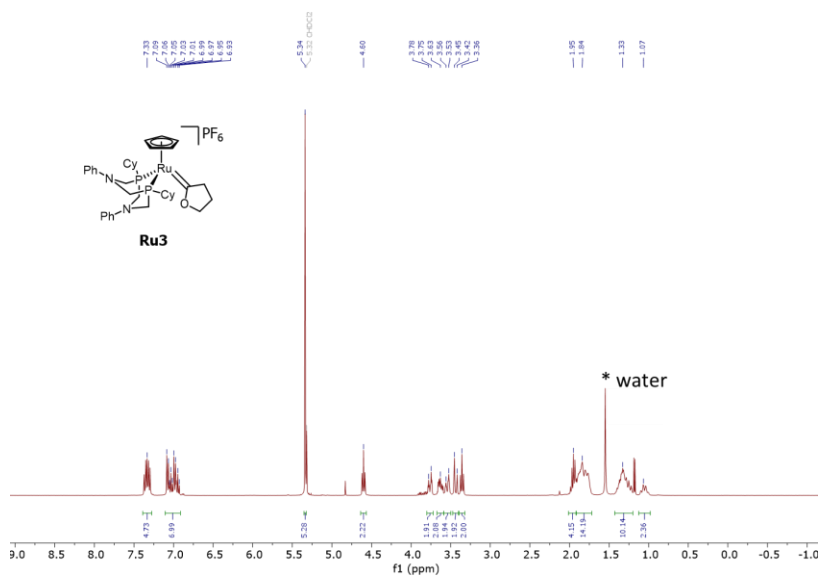


**Figure B-1.**  $^1\text{H}$  NMR spectrum of  $[\text{Ru}(\text{Cp})(\text{P}^{\text{Cy}}_2\text{N}^{\text{Ph}}_2)(3,4\text{-Dihydro-}2H\text{-furylium})][\text{PF}_6]$  (**3-Ru3**) (400 MHz,  $\text{CD}_2\text{Cl}_2$ ).

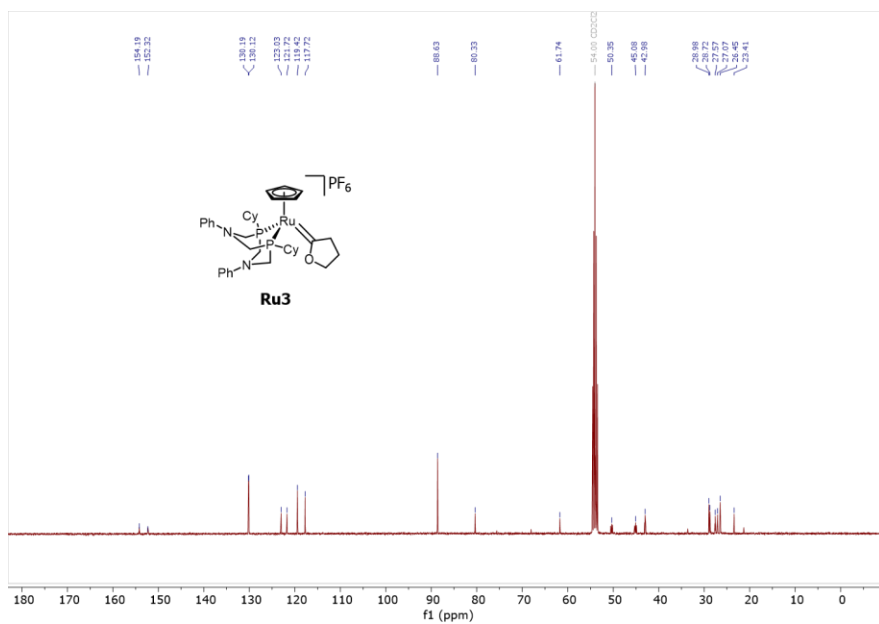


**Figure B-2.**  $^{13}\text{C}\{^1\text{H}\}$  NMR spectrum of **3-Ru3** (101 MHz,  $\text{CD}_2\text{Cl}_2$ ).

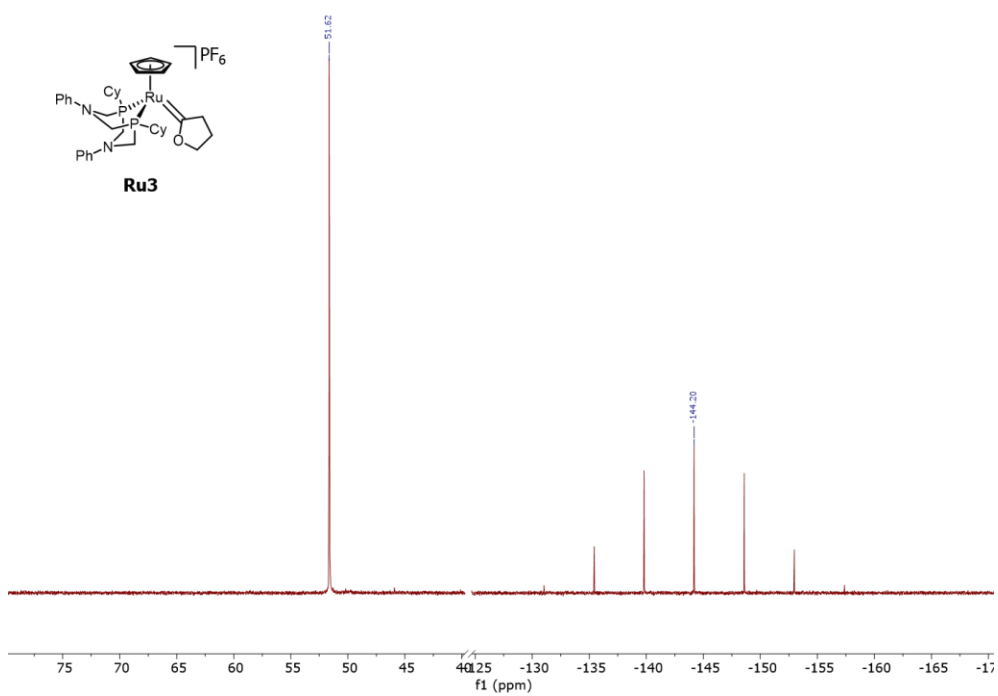


**Figure B-3.**  $^{31}\text{P}\{^1\text{H}\}$  NMR spectrum of **3-Ru3** (162 MHz,  $\text{CD}_2\text{Cl}_2$ ).

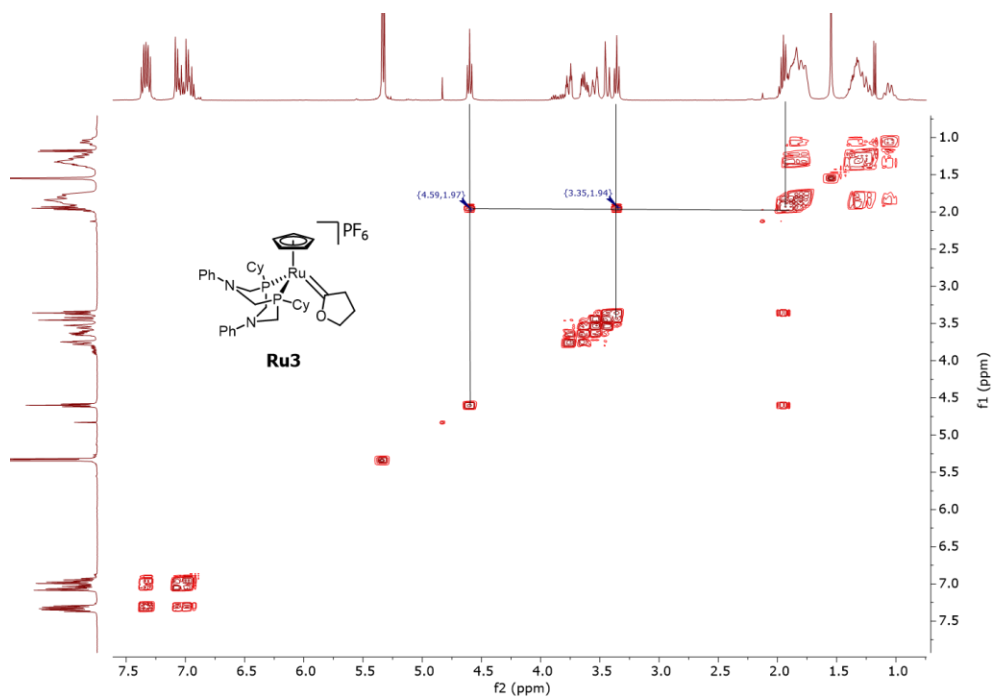


**Figure B-4.**  $^1\text{H}$ - $^1\text{H}$  COSY spectrum of **3-Ru3** (400 MHz,  $\text{CD}_2\text{Cl}_2$ ) showing the correlation of the alkoxy carbene ring.

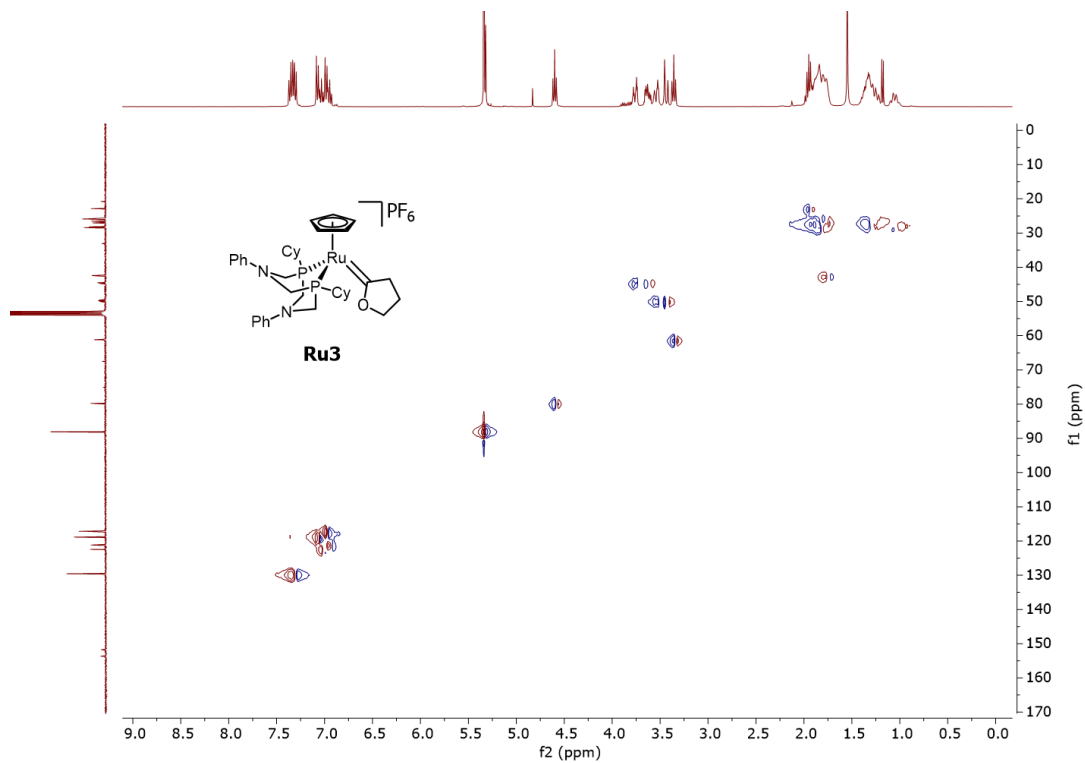


**Figure B-5.**  $^1\text{H}$ - $^{13}\text{C}\{^1\text{H}\}$  HSQC spectrum of **3-Ru3** (400 MHz,  $\text{CD}_2\text{Cl}_2$ ).

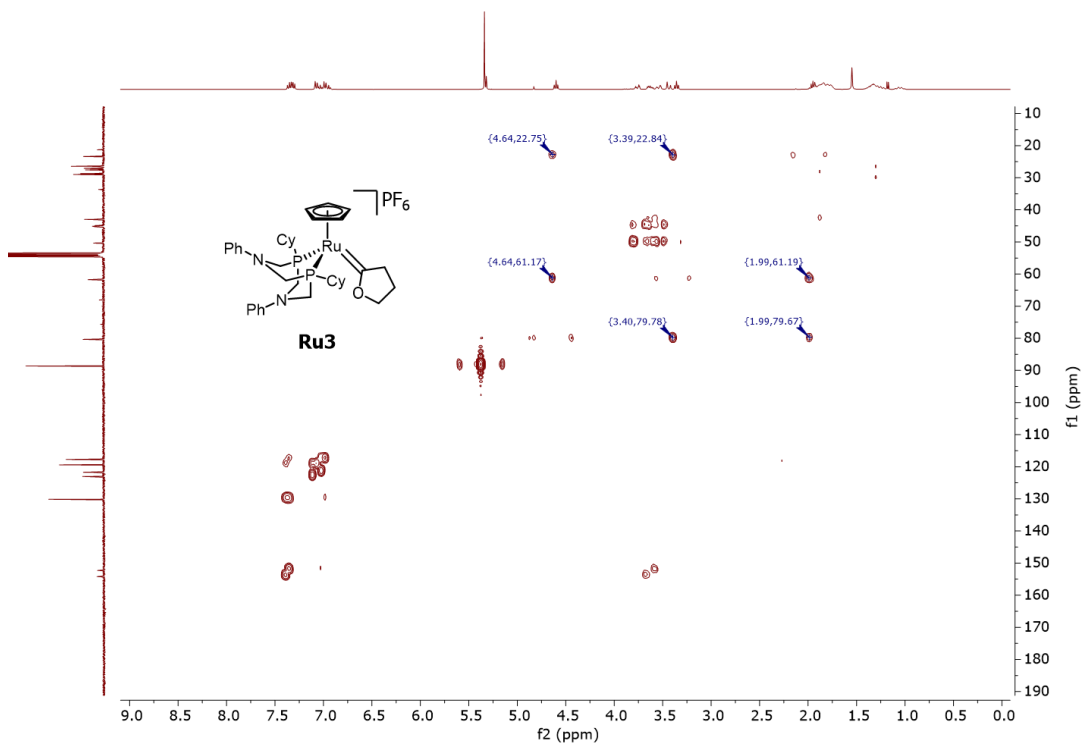


**Figure B-6.**  $^1\text{H}$ - $^{13}\text{C}\{^1\text{H}\}$  HMBC spectrum of **3-Ru3** (400 MHz,  $\text{CD}_2\text{Cl}_2$ ).

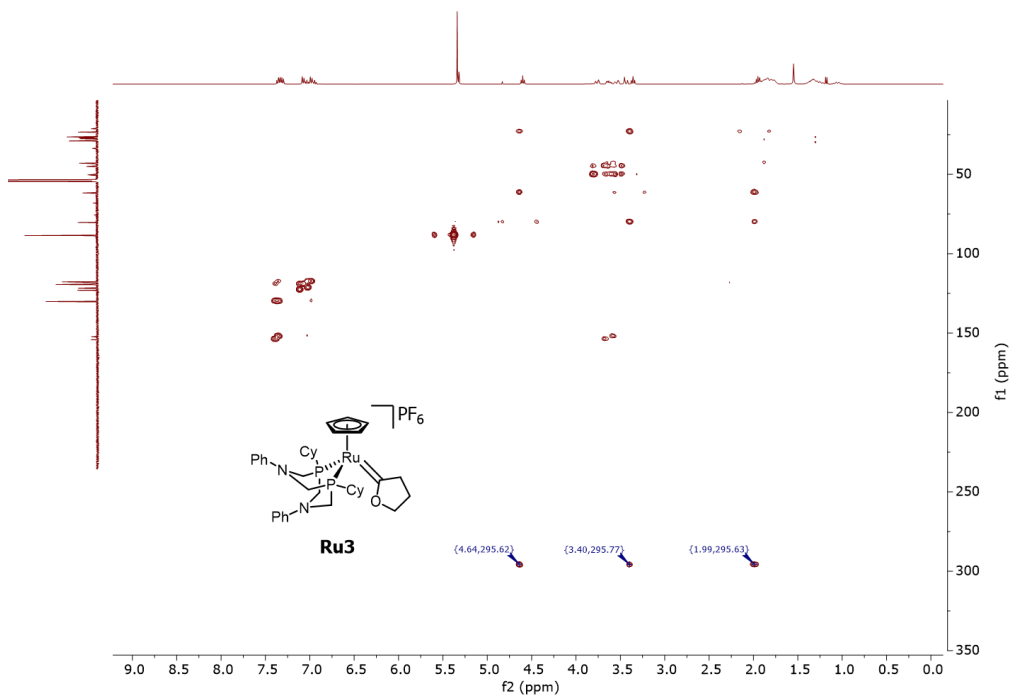


**Figure B-7.**  $^1\text{H}$ - $^{13}\text{C}\{^1\text{H}\}$  HMBC spectrum of **3-Ru3** (400 MHz,  $\text{CD}_2\text{Cl}_2$ ) showing correlations to  $\text{Ru}=\text{C}$  ( $\delta_{\text{C}} = 295.6$ ).

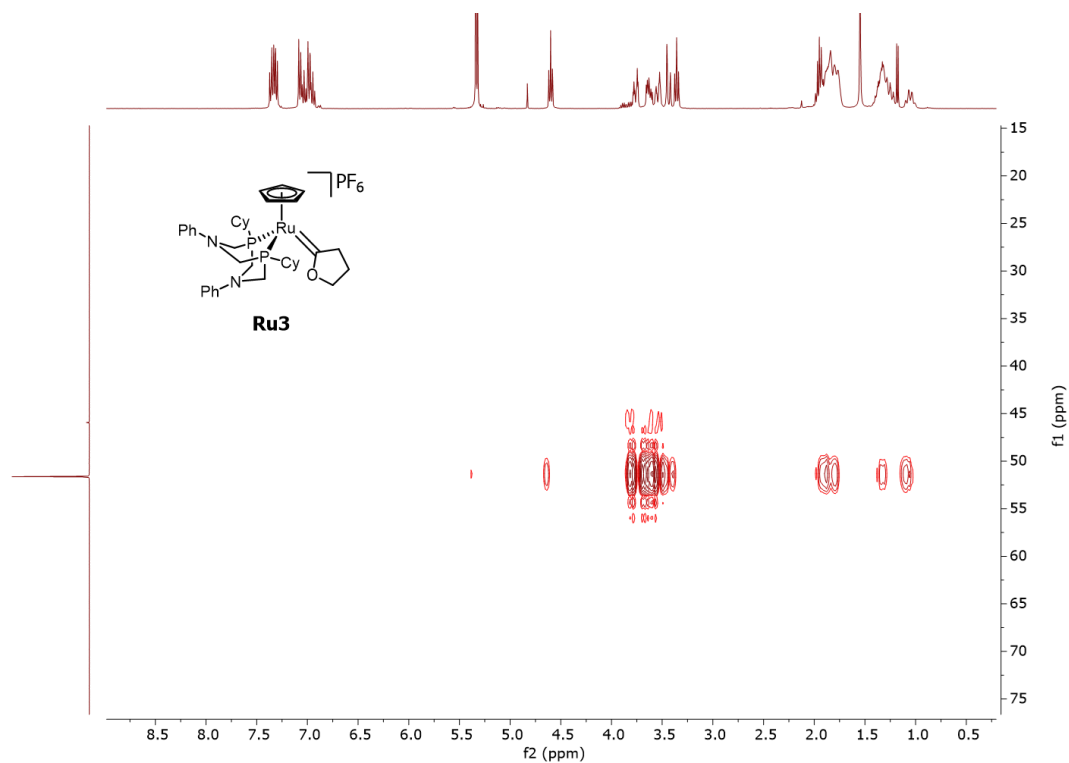


**Figure B-8.**  $^1\text{H}$ - $^{31}\text{P}$  HMBC spectrum of **3-Ru3** (400 MHz,  $\text{CD}_2\text{Cl}_2$ ).

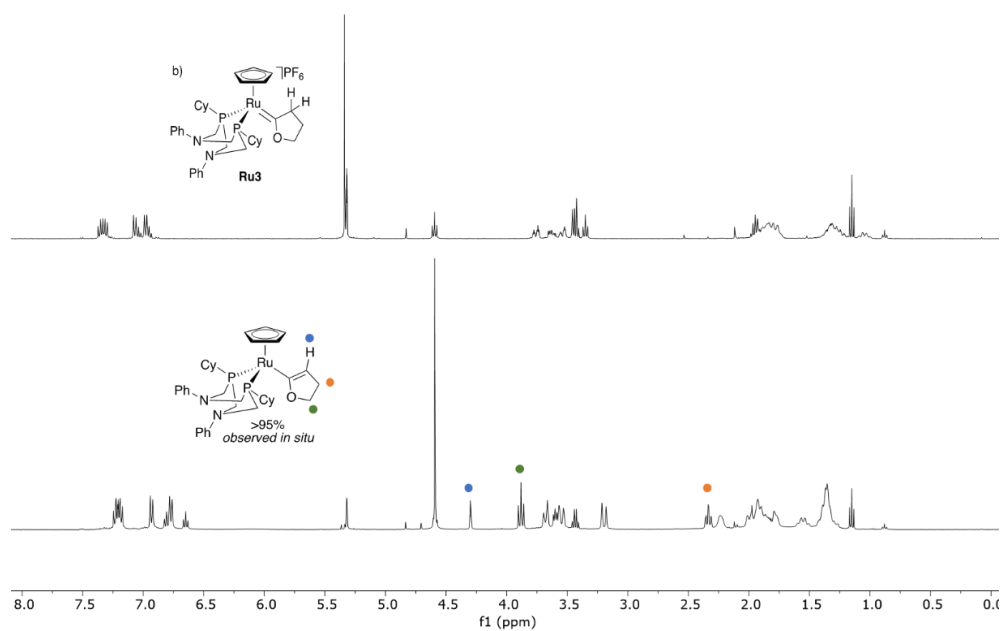


**Figure B-9.**  $^1\text{H}$  NMR spectra of a) **3-Ru3**; and b) vinyl ether complex **3-Ru5** generated *in situ* from the deprotonation of **3-Ru3** by  $\text{KO}^t\text{Bu}$  (600 MHz,  $\text{CD}_2\text{Cl}_2$ ).



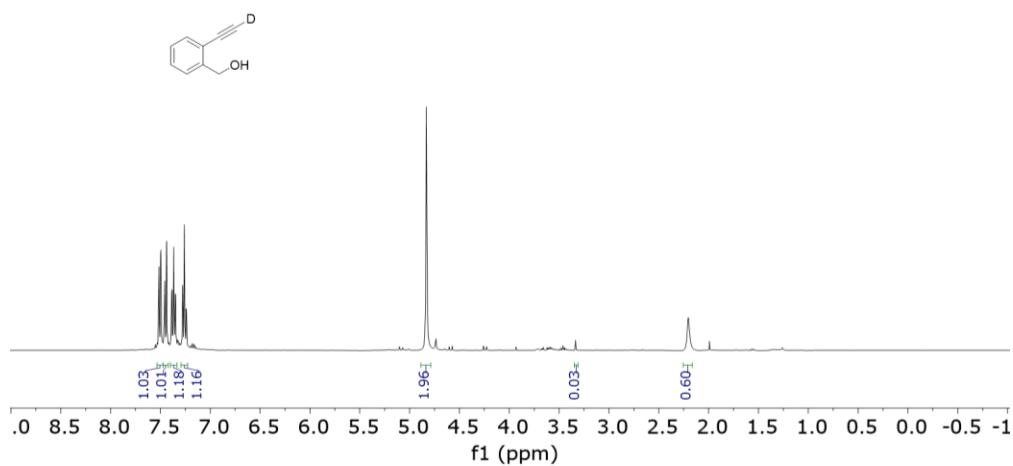


**Figure B-10.** <sup>1</sup>H NMR spectrum of 2-ethynyl benzylalcohol-*d*<sub>1</sub>, **3-1a-*d*<sub>1</sub>** (600 MHz, CDCl<sub>3</sub>).

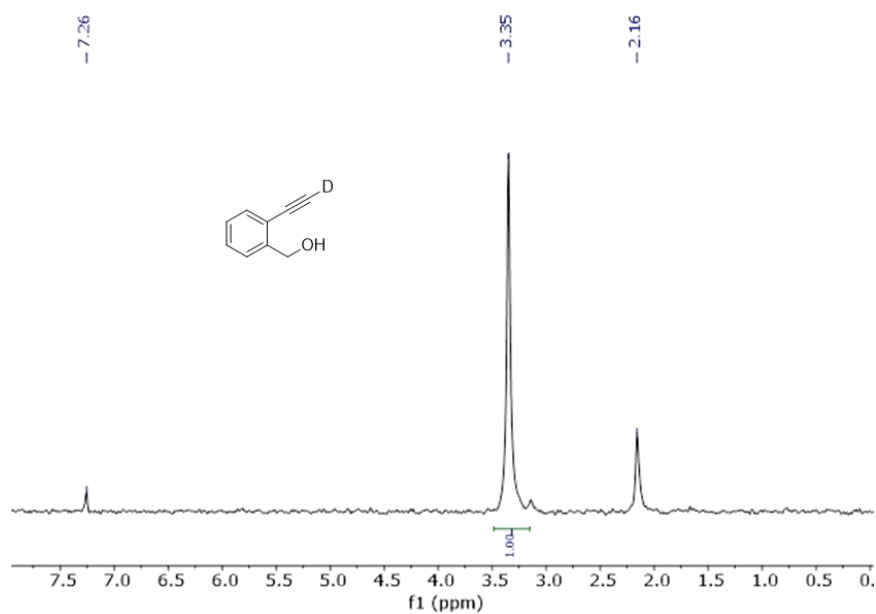


**Figure B-11.** <sup>2</sup>H NMR spectrum of 2-ethynyl benzylalcohol-*d*<sub>1</sub>, **3-1a-*d*<sub>1</sub>** (92 MHz, CDCl<sub>3</sub>). Minor deuterium incorporation of alcohol which is subsequently protonated upon addition of substrate to reaction solvent.

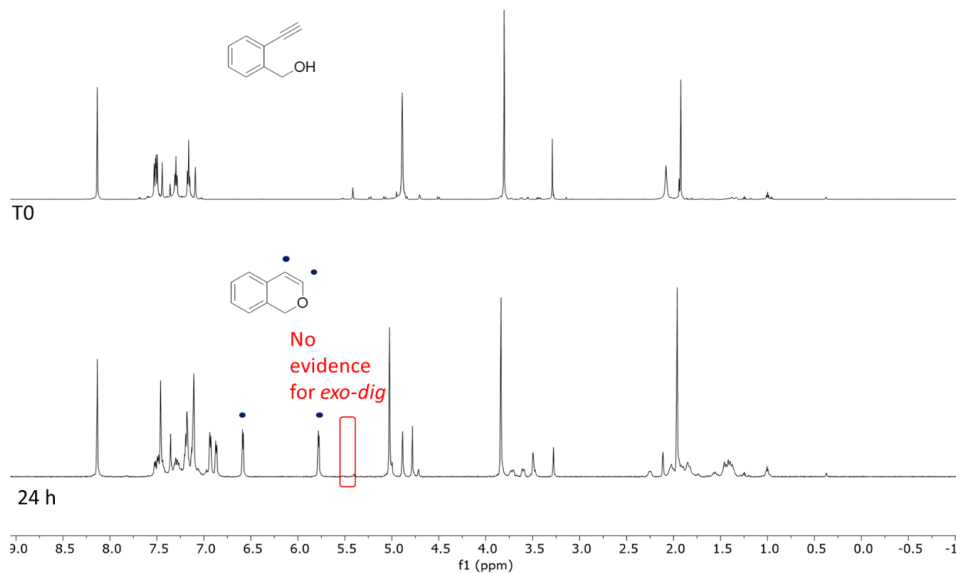


**Figure B-12.**  $^1\text{H}$  NMR stack plot for conversion of **3-1a** to **3-2a** (400 MHz,  $\text{C}_6\text{D}_5\text{Br}$ ). (top) T0 NMR spectrum (bottom) 24 h *in situ* NMR spectrum. Reaction conditions: 0.5 mol% **3-Ru2**, 70 °C, 24 h.

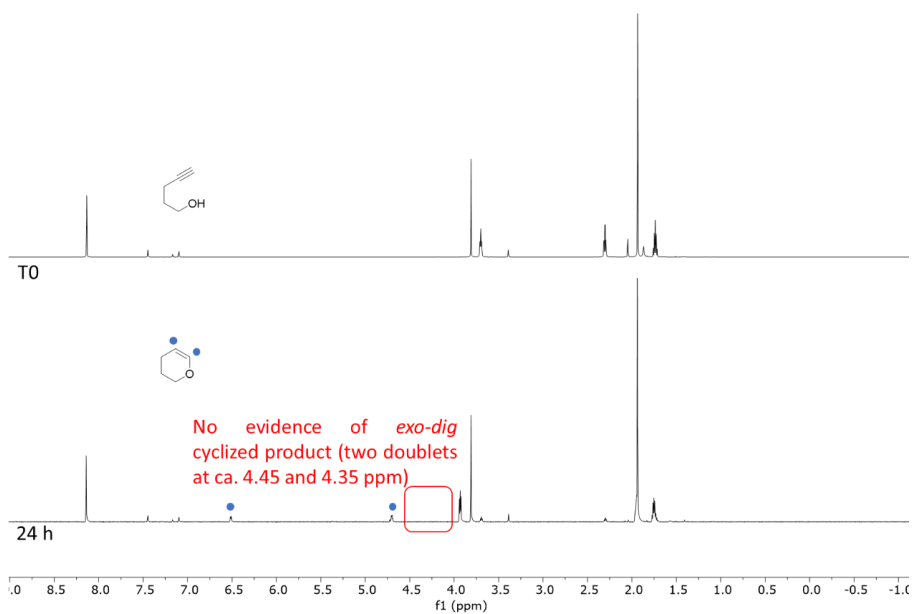


**Figure B-13.**  $^1\text{H}$  NMR stack plot for conversion of **3-1b** to **3-2b** (400 MHz,  $\text{C}_6\text{D}_5\text{Br}$ ). (top) T0 NMR spectrum (bottom) 24 h *in situ* NMR spectrum. Reaction conditions: 0.5 mol% **3-Ru2**, 70 °C, 24 h.

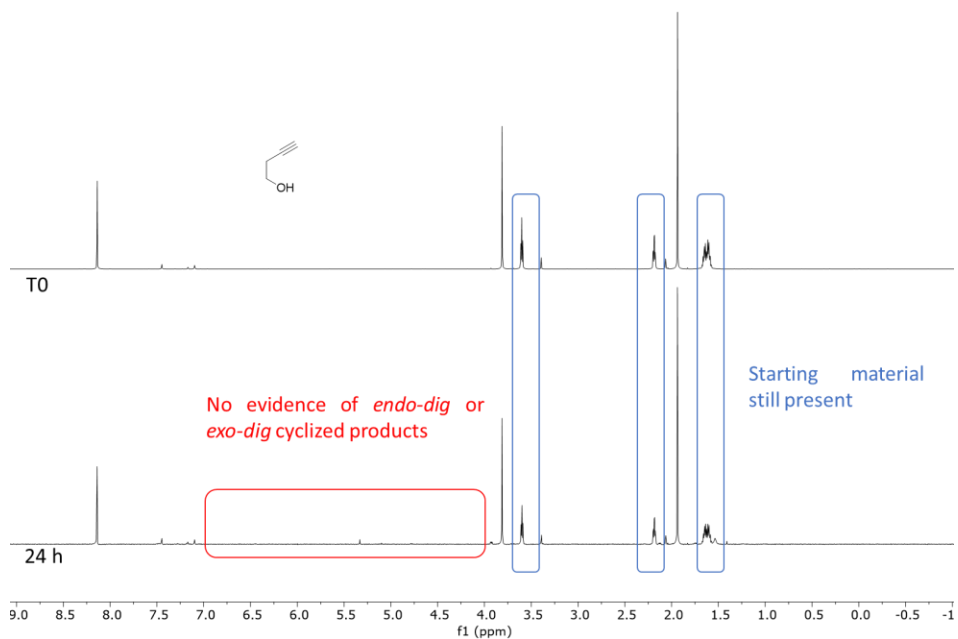


**Figure B-14.**  $^1\text{H}$  NMR stack plot for conversion of **3-1d** to **3-2d** (400 MHz,  $\text{C}_6\text{D}_5\text{Br}$ ). (top) T0 NMR spectrum (bottom) 24 h *in situ* NMR spectrum. Reaction conditions: 0.5 mol% **3-Ru2**, 70  $^\circ\text{C}$ , 24 h.

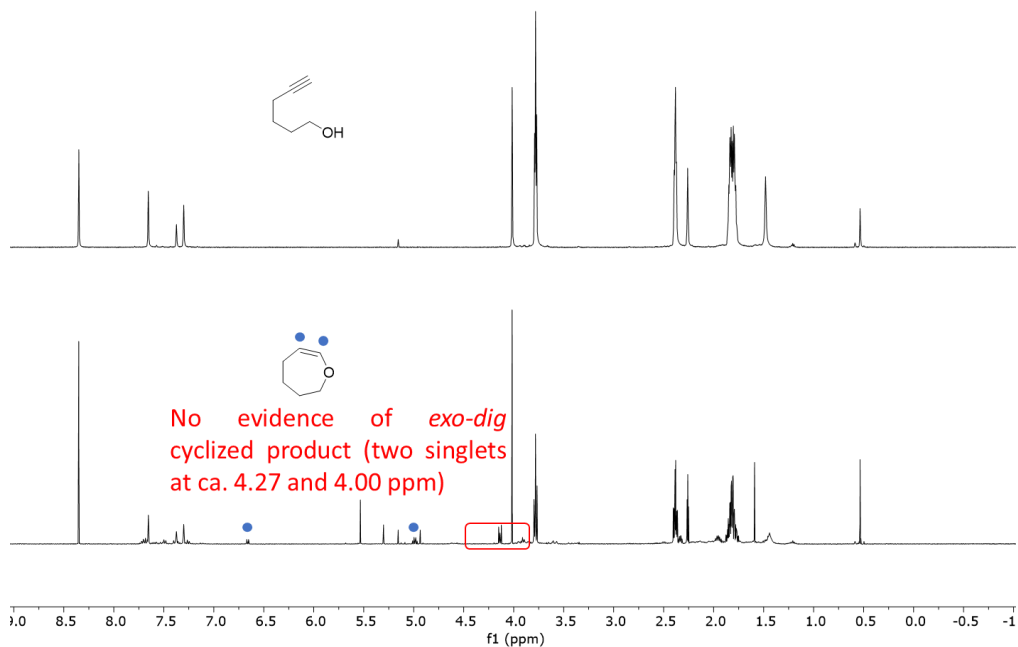


**Figure B-15.**  $^1\text{H}$  NMR stack plot for conversion of **3-1c** to **3-2c** (400 MHz,  $\text{C}_6\text{D}_5\text{Br}$ ). (top) T0 NMR spectrum (bottom) 24 h *in situ* NMR spectrum. Reaction conditions: 10 mol% **3-Ru2**, 70  $^\circ\text{C}$ , 24 h.

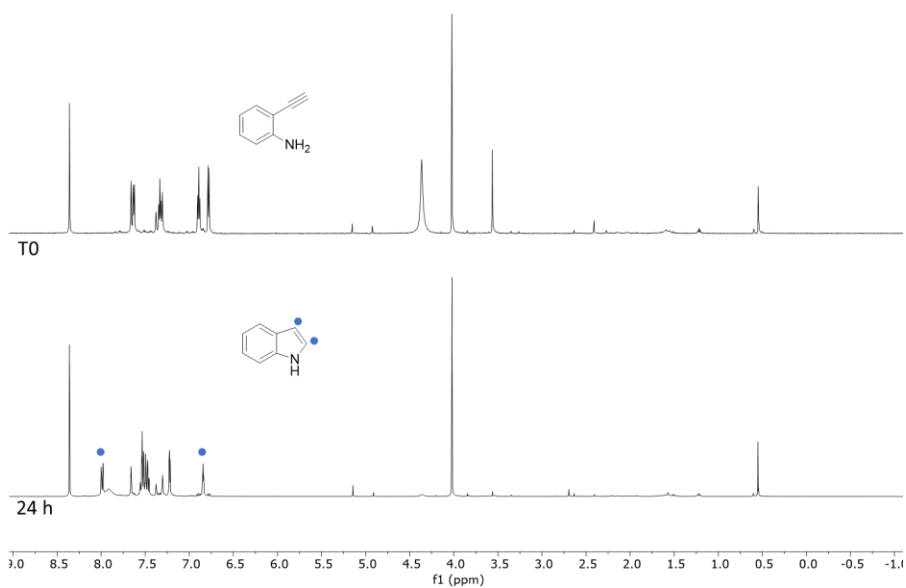


**Figure B-16.**  $^1\text{H}$  NMR stack plot for conversion of **3-1e** to **3-2e** (400 MHz,  $\text{C}_6\text{D}_5\text{Br}$ ). (top) T0 NMR spectrum (bottom) 24 h *in situ* NMR spectrum.

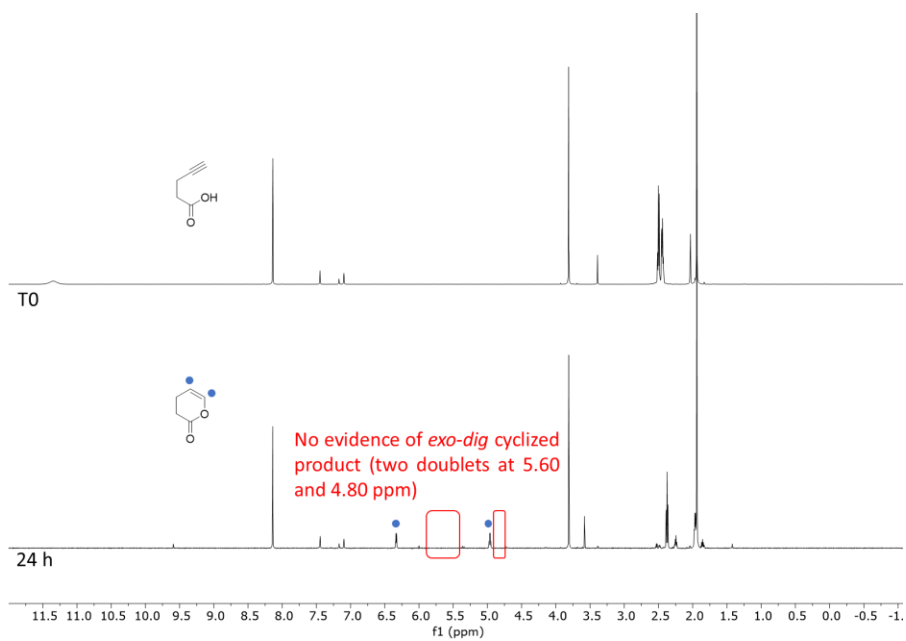


**Figure B-17.**  $^1\text{H}$  NMR stack plot for conversion of **3-1f** to **3-2f** (400 MHz,  $\text{C}_6\text{D}_5\text{Br}$ ). (top) T0 NMR spectrum (bottom) 24 h *in situ* NMR spectrum. Reaction conditions: 0.5 mol% **3-Ru2**, 70 °C, 24 h.

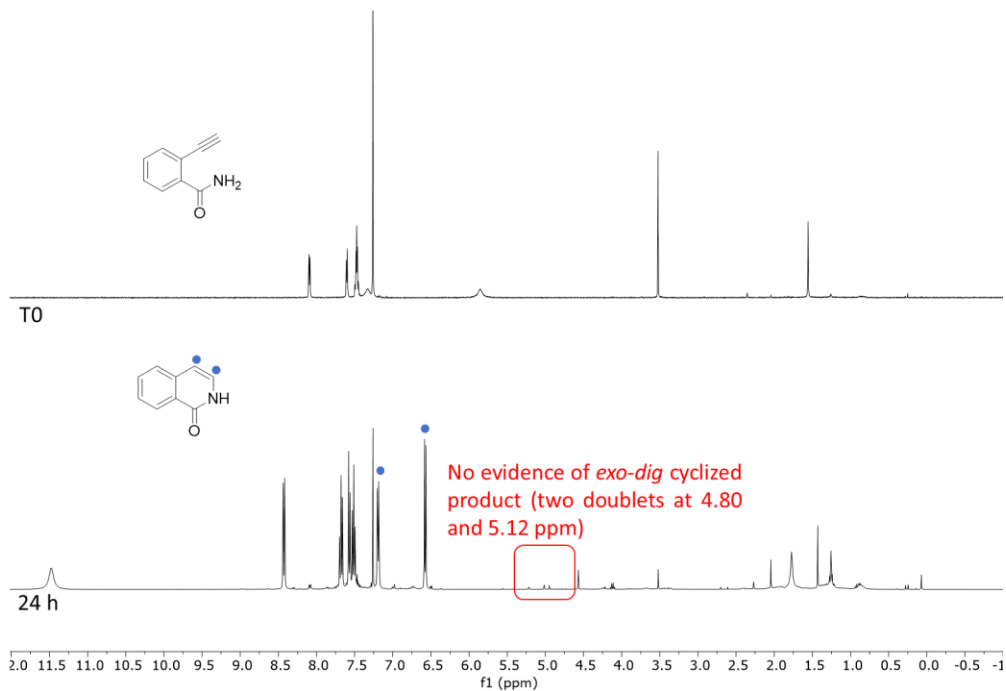


**Figure B-18.**  $^1\text{H}$  NMR stack plot for conversion of **3-1g** to **3-2g** (400 MHz,  $\text{C}_6\text{D}_5\text{Br}$ ). (top) T0 NMR spectrum (bottom) 24 h *in situ* NMR spectrum

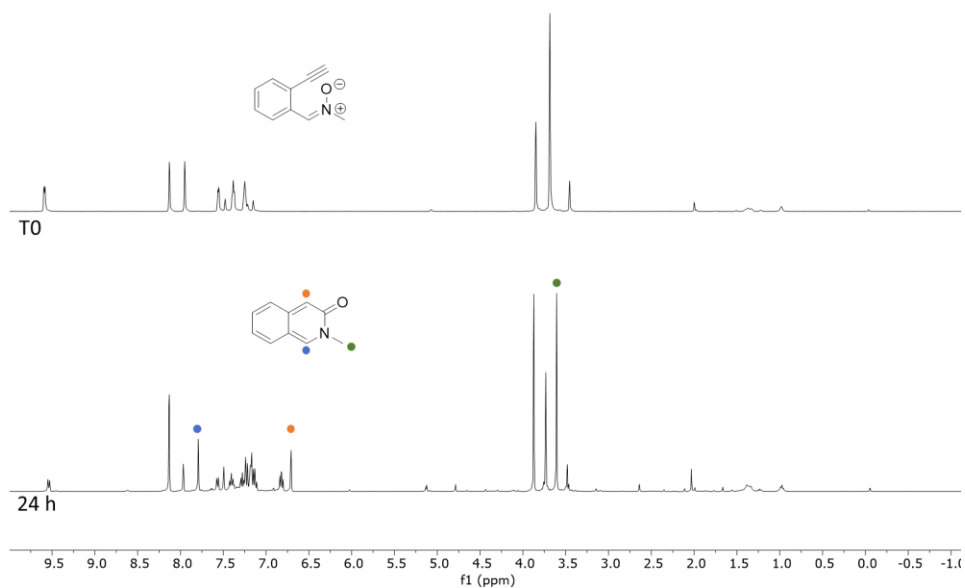


**Figure B-19.**  $^1\text{H}$  NMR stack plot for conversion of **3-3** to **3-4** (400 MHz,  $\text{C}_6\text{D}_5\text{Br}$ ). (top) T0 NMR spectrum (bottom) 24 h *in situ* NMR spectrum. Reaction conditions: 2 mol% **3-Ru2**, 70 °C, 24 h.

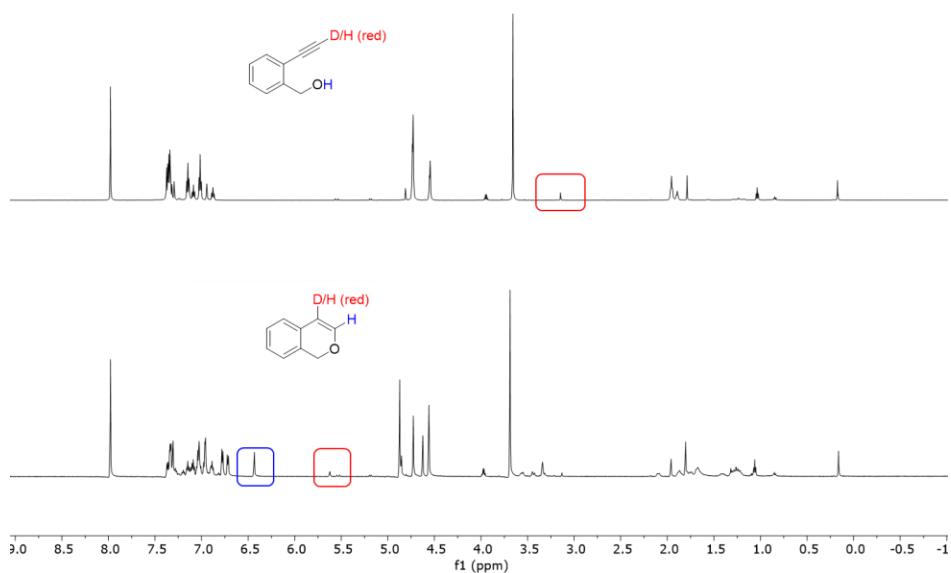


**Figure B-20.**  $^1\text{H}$  NMR stacked spectrum of **3-1a- $d_1$**  cyclization to form C2-labelled isochromene (600 MHz,  $\text{C}_6\text{D}_5\text{Br}$ ). Reaction conditions: 7.5 mM **3-Ru2**, 70 °C, 2 h. 90% deuterium incorporation at C2.

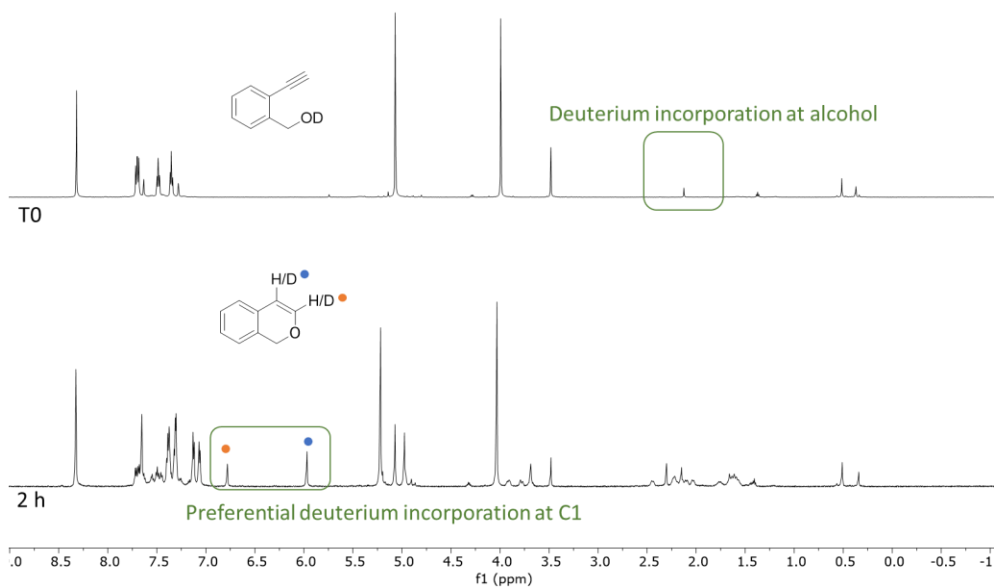


**Figure B-21.**  $^1\text{H}$  NMR stacked spectrum of **3-1a-OD** cyclization to form C1/C2-labelled isochromene (600 MHz,  $\text{C}_6\text{D}_5\text{Br}$ ).

## IR Spectra

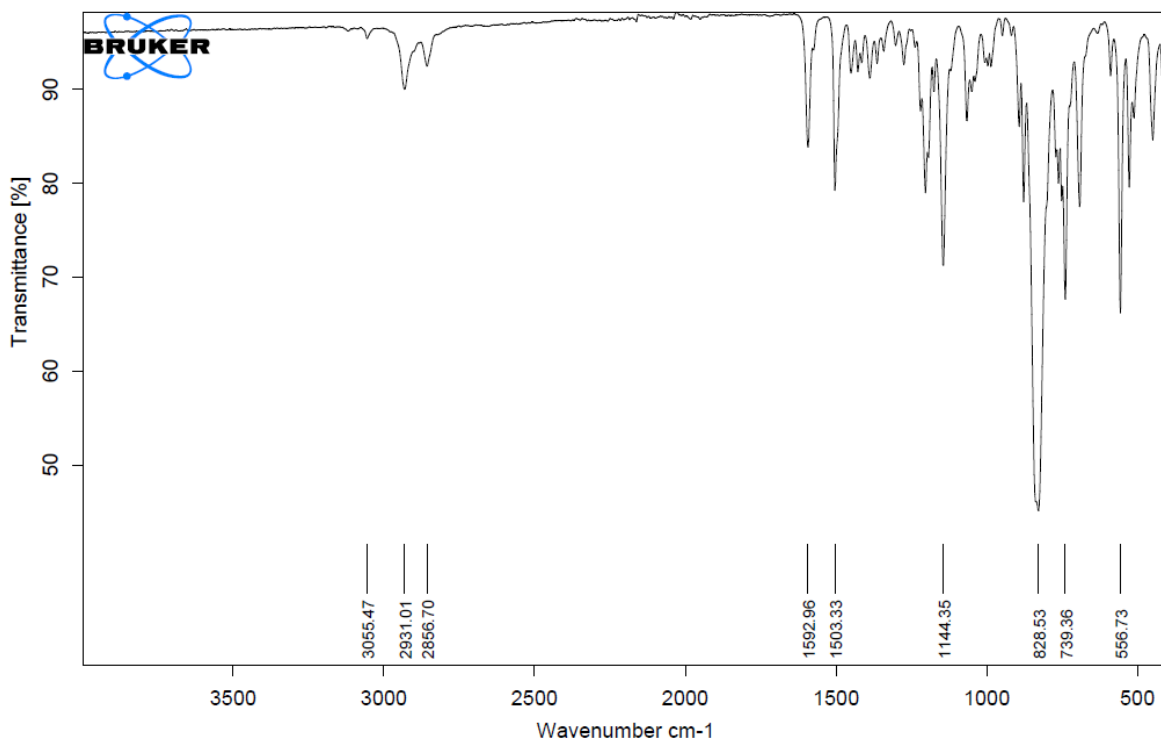


**Figure B-22.** ATR-FTIR spectrum of solid **3-Ru3**.

## MALDI Mass Spectra

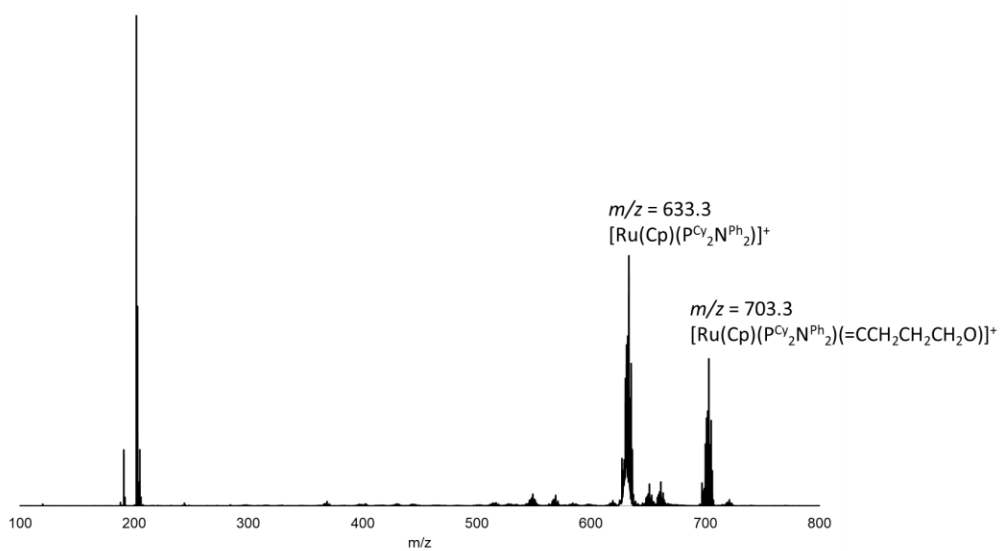


**Figure B-23.** MALDI-TOF mass spectrum of **3-Ru3** with pyrene as the matrix (1:20 molar ratio).

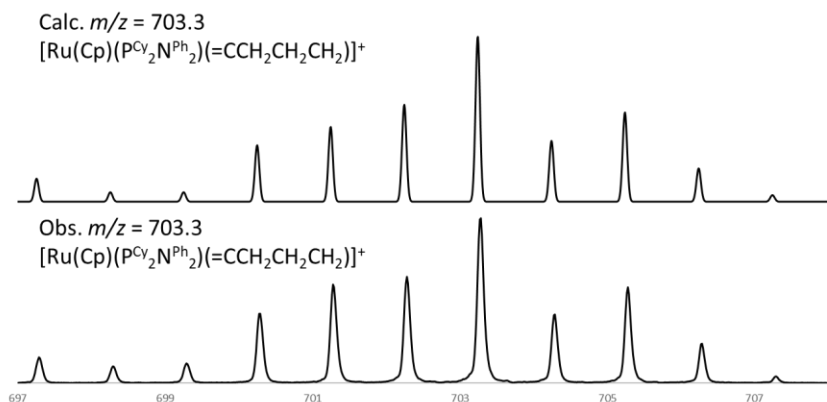


**Figure B-24.** Calculated signal (top) with  $m/z = 703.3$  for  $[\text{Ru}(\text{Cp})(\text{P}^{\text{Cy}}_2\text{N}^{\text{Ph}}_2)(=\text{CCH}_2\text{CH}_2\text{CH}_2\text{O})]^+$ ; and zoom-in of the observed MALDI-TOF mass spectrum signal of **3-Ru3** (bottom) at  $m/z$  703.3.

## Catalysis Data

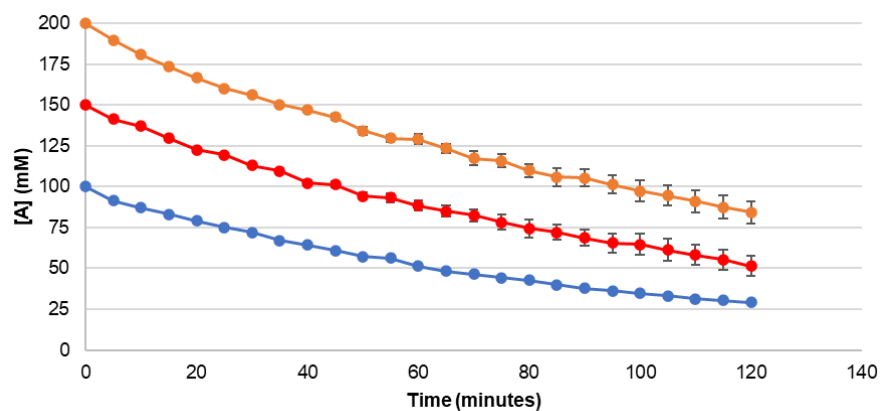


**Figure B-25.** Untreated concentration vs time reaction profiles used to determine order in substrate. Reaction conditions: 7.5 mM **3-Ru2**,  $\text{C}_6\text{D}_5\text{Br}$ , 70 °C, 2 h, and initial **[3-1a]** of 200 mM (orange), 150 mM (red), and 100 mM (blue). Data points are an average of two runs with the error bars the individual values of one of the runs.



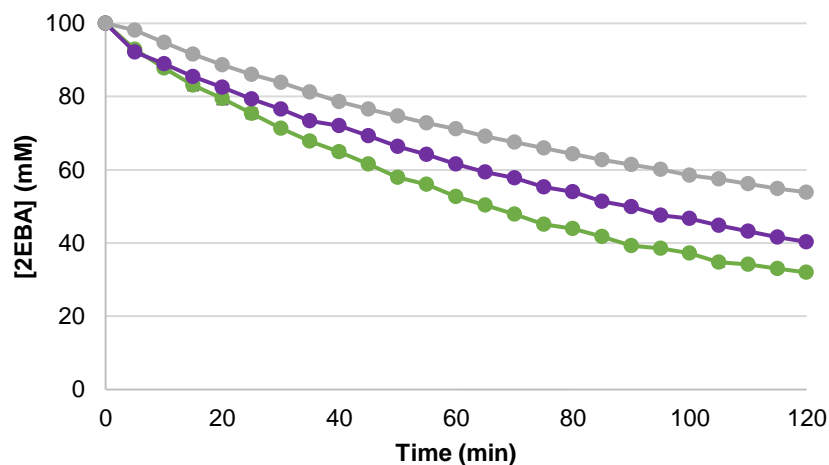


**Figure B-26.** Untreated concentration vs time reaction profiles used to determine order in catalyst. 100 mM **3-1a** and initial [**3-Ru2**] of 7.5 mM (green), 5 mM (purple), and 2.5 mM (grey). Data points are an average of two runs with the error bars the individual values of one of the runs.

## Deuterium Labelling Experiments

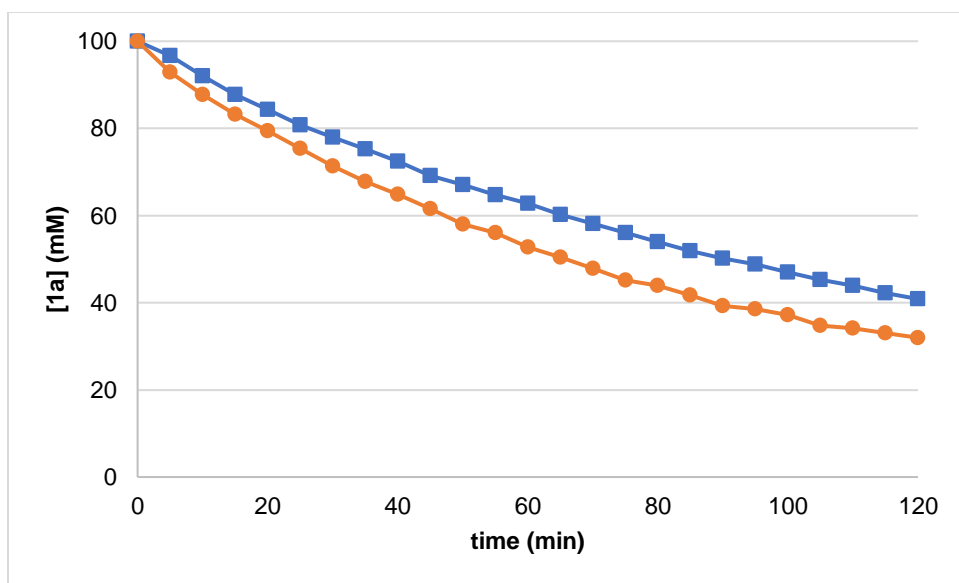


**Figure B-27.** Concentration vs time reaction progress for hydroalkoxylation of **3-1a** with the protio-substrate (●, orange) and the deutero-substrate (■, blue). Reaction conditions: 7.5 mM **3-Ru2**, 100 mM **3-1a**,  $C_6D_5Br$ , and 70 °C, monitored over 2 h. Reactions were analyzed by  $^1H$  NMR spectroscopy and they were performed in duplicate with errors < 5%.

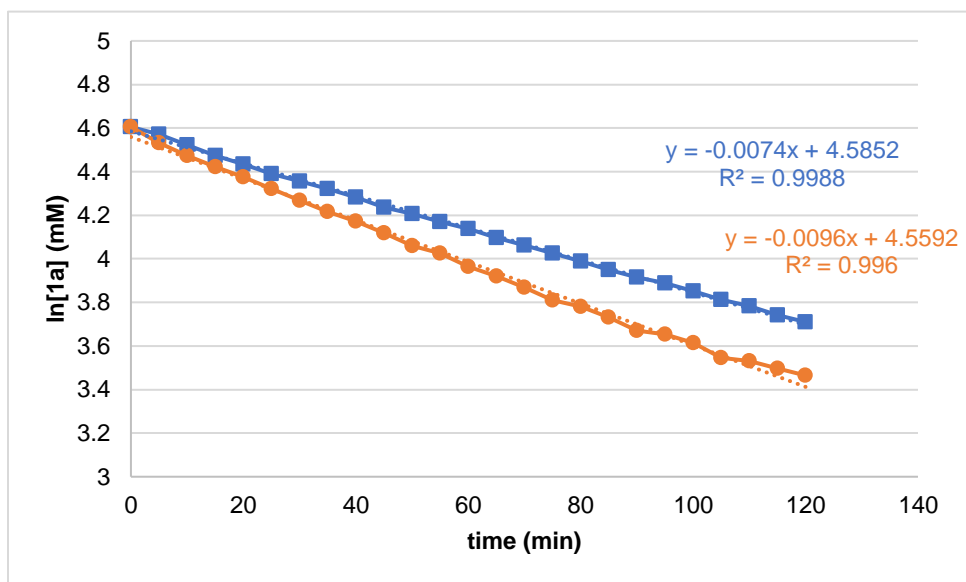


**Figure B-28.**  $\ln[3-1a]$  vs time data sets for hydroalkoxylation of **3-1a** with the protio-substrate (●, orange) and the deutero-substrate (■, blue). This result suggested a first order reaction with respect to **1a** and the slope generated represents the rate of reaction ( $k_{obs}$ ).

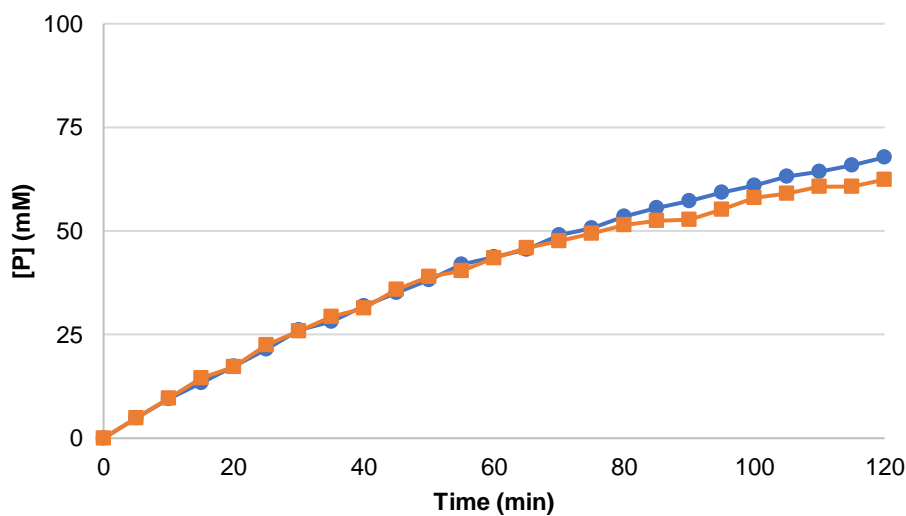


**Figure B-29.** Concentration vs time reaction progress for hydroalkoxylation of **3-1a** with (■, orange) and without (●, blue)  $H_2O$  as an additive. Reaction conditions were 7.5 mM **3-Ru2**, 100 mM **3-1a**,  $C_6D_5Br$ , 20  $\mu L$   $H_2O$ , and 70  $^{\circ}C$ , monitored over 2 h. Reactions were performed in duplicate with errors < 5%.

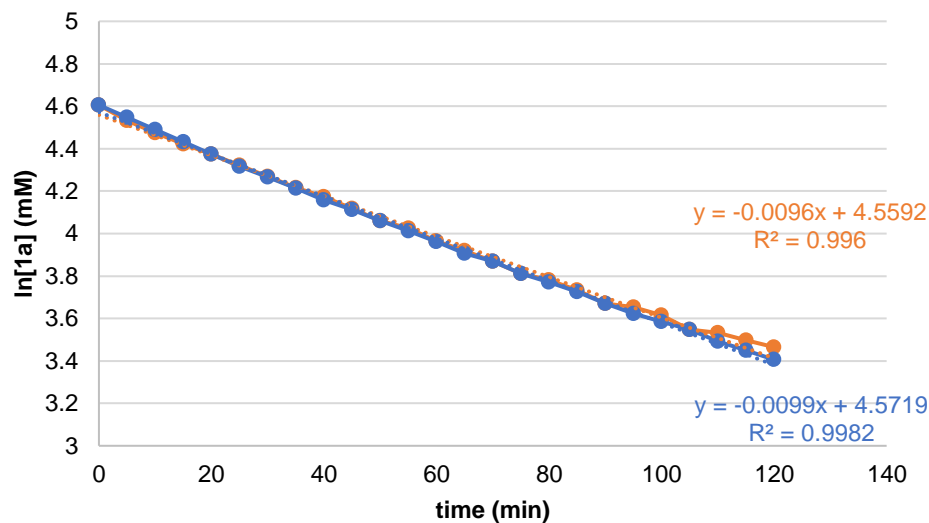


**Figure B-30.**  $\ln[3-1a]$  vs time data sets for hydroalkoxylation of **3-1a** with the protio-substrate (orange) and the deuterio-substrate (blue). This result suggested a first order reaction with respect to 1a and the slope generated represents the rate of reaction ( $k_{\text{obs}}$ ).

## Crystallographic Details

*Data Collection and Processing.* Samples of **3-Ru2** and **3-Ru3** were mounted on a Mitegen polyimide micromount with a small amount of Paratone N oil. All X-ray measurements were made on a Bruker Kappa Axis Apex2 diffractometer at a temperature of 110 K. The unit cell dimensions were determined from a symmetry constrained fit with reflections and dimensions listed in Table SX. The data collection strategy was a number of  $\omega$  and  $\phi$  scans which collected data up to  $2\theta_{\text{max}}$  as listed in Table SX. The frame integration was performed using SAINT.<sup>1</sup> The resulting raw data was scaled and absorption corrected using a multi-scan averaging of symmetry equivalent data using SADABS.<sup>2</sup>

*Structure Solution and Refinement.* The structure for **3-Ru2** was solved by using a dual space methodology using the SHELXT program.<sup>3</sup> All non-hydrogen atoms were obtained from the initial solution. The hydrogen atoms were introduced at idealized positions and were allowed to ride on the parent atom. The diethyl ether of solvation was disordered. The occupancy of the primary site refined to a value of 0.661(9). The structural model was fit to the data using full matrix least-squares based on  $F^2$ . The calculated structure factors included corrections for anomalous dispersion from the usual tabulation. The structure was refined using the SHELXL program from the SHELX suite of crystallographic software.<sup>4</sup> Graphic plots were produced using the Mercury program.<sup>5</sup>

*Structure Solution and Refinement.* The structure for **3-Ru3** was solved by using a dual space methodology using the SHELXT program.<sup>3</sup> All non-hydrogen atoms were obtained from the initial solution. The hydrogen atoms were introduced at idealized positions and were allowed to ride on the parent atom. The structure exhibited disordered in both the cation and the anion. The Cp ligand

of the cation was disordered by approximate  $174(3)^\circ$  rotation about the Ru – Centroid(C1-C2-C3-C4-C5) axis. The  $\text{PF}_6^-$  anion was disordered over two orientations. The normalized occupancies for the predominant orientations for the disordered groups were refined to values of 0.620(13) for the Cp ligand and 0.512(16) for the  $\text{PF}_6^-$  anion. The structure also exhibited a small amount of twinning by pseudo-merohedry. The twin law was determined by the COSET program<sup>6</sup> to be a  $180^\circ$  rotation about the [110] axis. The minor component of the twin fraction refined to a value of 0.0294(20). The Flack parameter for the absolute structure was determined using the Parsons' method<sup>7</sup> to be -0.015(18) from 2527 selected quotients. The structural model was fit to the data using full matrix least-squares based on  $F^2$ . The calculated structure factors included corrections for anomalous dispersion from the usual tabulation. The structure was refined using the SHELXL program from the SHELX suite of crystallographic software.<sup>4</sup> Graphic plots were produced using the Mercury program.<sup>5</sup>

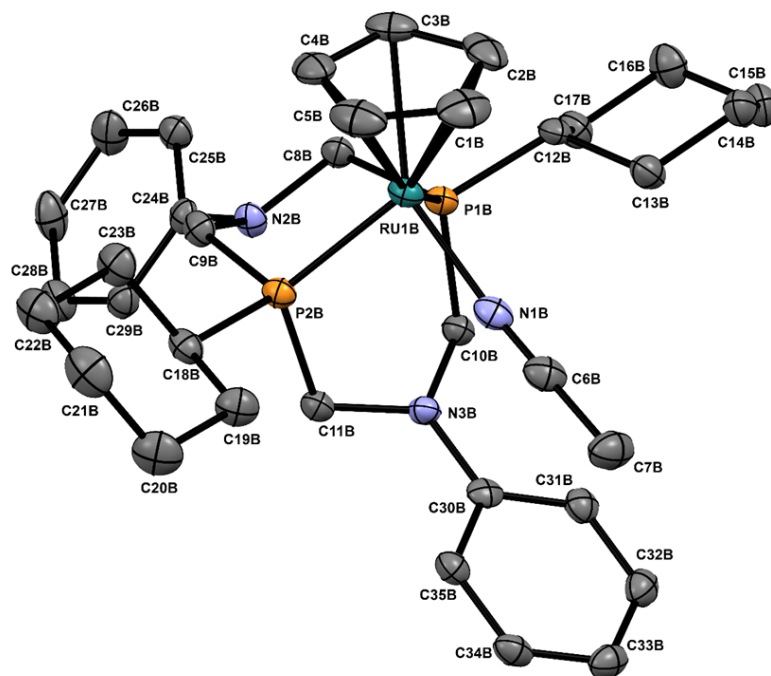


**Figure B-31.** ORTEP drawing of **3-Ru2** showing the naming and numbering scheme. Ellipsoids are at 50% probability level and hydrogen atoms were omitted for clarity.

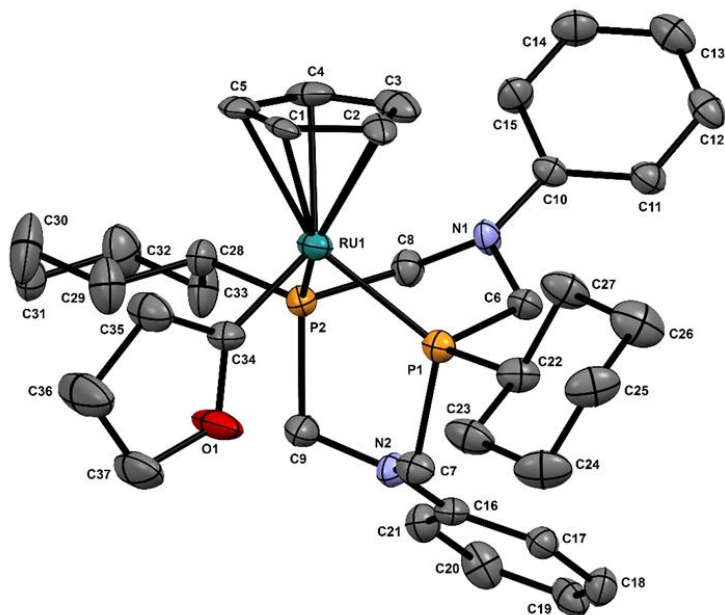


**Figure B-32.** ORTEP drawing of **3-Ru3** showing the naming and numbering scheme. Ellipsoids are at 50% probability level and hydrogen atoms were omitted for clarity.

**Table B-1.** Summary of Crystal Data for **3-Ru2** and **3-Ru3**.

Compound	<b>3-Ru2</b>	<b>3-Ru3</b>
CCDC	2159300	2159301
Formula	C <sub>37</sub> H <sub>53</sub> F <sub>6</sub> N <sub>3</sub> O <sub>0.50</sub> P <sub>3</sub> Ru	C <sub>55.50</sub> H <sub>76.50</sub> F <sub>9</sub> N <sub>3</sub> O <sub>1.50</sub> P <sub>4.50</sub> Ru <sub>1.50</sub>
Formula Weight ( <i>g/mol</i> )	855.80	1271.66
Crystal Dimensions ( <i>mm</i> )	0.189 × 0.178 × 0.064	0.209 × 0.077 × 0.050
Crystal Color and Habit	yellow plate	colourless prism
Crystal System	orthorhombic	hexagonal
Space Group	P b c a	P 6 <sub>5</sub>
Temperature, K	110	110
<i>a</i> , Å	20.009(8)	11.214(3)
<i>b</i> , Å	22.111(9)	11.214
<i>c</i> , Å	35.538(17)	49.775(12)
$\alpha$ , °	90	90
$\beta$ , °	90	90
$\gamma$ , °	90	120
<i>V</i> , Å <sup>3</sup>	15722(12)	5420(3)
Number of reflections to determine final unit cell	9848	9289
Min and Max 2 $\theta$ for cell determination, °	4.68, 41.14	4.86, 48.04
<i>Z</i>	16	4

F(000)	7088	2628
$\rho$ (g/cm <sup>3</sup> )	1.446	1.558
$\lambda$ , Å, (MoK $\alpha$ )	0.71073	0.71073
$\mu$ , (cm <sup>-1</sup> )	0.581	0.632
Diffractometer Type	Bruker Kappa Axis Apex2	Bruker Kappa Axis Apex2
Scan Type(s)	$\phi$ and $\omega$ scans	$\phi$ and $\omega$ scans
Max $2\theta$ for data collection, °	48.276	51.404
Measured fraction of data	0.997	0.995
Number of reflections measured	330134	87159
Unique reflections measured	12505	6737
$R_{\text{merge}}$	0.1110	0.0841
Number of reflections included in refinement	12505	6737
Cut off Threshold Expression	$I > 2\sigma(I)$	$I > 2\sigma(I)$
Structure refined using	full matrix least-squares using $F^2$	full matrix least-squares using $F^2$
Weighting Scheme	$w=1/[\sigma^2(F_o^2)+(0.0327P)^2+18.8583P]$ where $P=(F_o^2+2F_c^2)/3$	$w=1/[\sigma^2(F_o^2)+(0.0483P)^2+9.1357P]$ where $P=(F_o^2+2F_c^2)/3$
Number of parameters in least-squares	958	505
$R_1$	0.0334	0.0481
$wR_2$	0.0741	0.1038
$R_1$ (all data)	0.0484	0.0572
$wR_2$ (all data)	0.0800	0.1074
GOF	1.043	1.065
Maximum shift/error	0.003	0.000
Min & Max peak heights on final $\Delta F$ Map (e/Å)	-0.530, 0.538	-0.516, 0.999

Where:

$$R_1 = \frac{\sum (|F_o| - |F_c|)}{\sum F_o}$$

$$wR_2 = \left[ \frac{\sum (w(F_o^2 - F_c^2)^2)}{\sum (wF_o^4)} \right]^{1/2}$$

$$GOF = \left[ \frac{\sum (w(F_o^2 - F_c^2)^2)}{(\text{No. of reflns.} - \text{No. of params.})} \right]$$

## Computational Details

All computational structures were optimized using ORCA 5.0.1<sup>8</sup> without symmetry constraints using the hybrid GGA functional B3LPY<sup>9</sup> with D3 dispersion corrections with Becke-Johnson damping,<sup>10</sup> and the def2-TZVP basis set with effective core potential (ECP)<sup>11</sup> for Ru and the def2-SVP basis set<sup>12</sup> for all the remaining atoms with the def2/J auxiliary basis set.<sup>13</sup> Each stationary point was confirmed by a frequency calculation at the same level of theory to be a real local minimum on the potential energy surface without an imaginary frequency. The lowest energy ground state species for each structure are described here. All reported free energy are at the standard state (T = 298.25 K, P = 1 atm of N<sub>2</sub>) with standard correction for (harmonic) vibrational, rotational, and translational thermal free energy contributions.

## References

1. Bruker-AXS, SAINT version 2013.8, **2013**, Bruker-AXS, Madison, WI 53711, USA
2. Bruker-AXS, SADABS version 2012.1, **2012**, Bruker-AXS, Madison, WI 53711, USA
3. Sheldrick, G. M., *Acta Cryst.* **2015**, *A71*, 3-8
4. Sheldrick, G. M., *Acta Cryst.* **2015**, *C71*, 3-8
5. Macrae, C. F.; Bruno, I. J.; Chisholm, J. A.; Edington, P. R.; McCabe, P.; Pidcock, E.; Rodriguez-Monge, L.; Taylor, R.; van de Streek, J. and Wood, P. A. *J. Appl. Cryst.*, **2008**, *41*, 466-470
6. Boyle, P. D. *J. Appl. Cryst.*, **2014**, *47*, 467-470
7. Parsons, S.; Flack, H. D. and Wagner, T. *Acta Cryst.* **2013**, *B69*, 249-259
8. Neese, F.; Wennmohs, F.; Becker, U.; Riplinger, C., *The Journal of Chemical Physics* **2020**, *152* (22), 224108.
9. (a) Becke, A. D., *J. Chem. Phys.* 1993, *98*, 5648-5652; (b) Lee, C.; Yang, W.; Parr, R. G., *Phys. Rev. B* 1988, *37*, 785-789; (c) Vosko, S. H.; Wilk, L.; Nusair, M., *Can. J. Phys.* 1980, *58*, 1200-1211; (d) Stephens, P. J.; Devlin, F. J.; Chabalowski, C. F.; Frisch, M. J., *J. Phys. Chem.* 1994, *98*, 11623-11627.
10. (a) Grimme, S., Ehrlich, S., Goerigk, L., *J. Comput. Chem.* **2011**, *32*, 1456-1465. (b) Grimme, S., Antony, J., Ehrlich, S., Krieg, H., *J. Chem. Phys.* **2010**, *132*, 154104.
11. Andrae, D.; Häußermann, U.; Dolg, M.; Stoll, H.; Preuß, H., *Theoret. Chim. Acta* 1990, *77*, 123-141.
12. Weigend, F.; Ahlrichs, R., *Phys. Chem. Chem. Phys.* 2005, *7*, 3297-3305.
13. Weigend, F., *Phys. Chem. Chem. Phys.* 2006, *8*, 1057-1065.

## Appendices C: Supplementary Information for Chapter 4

### NMR Spectra

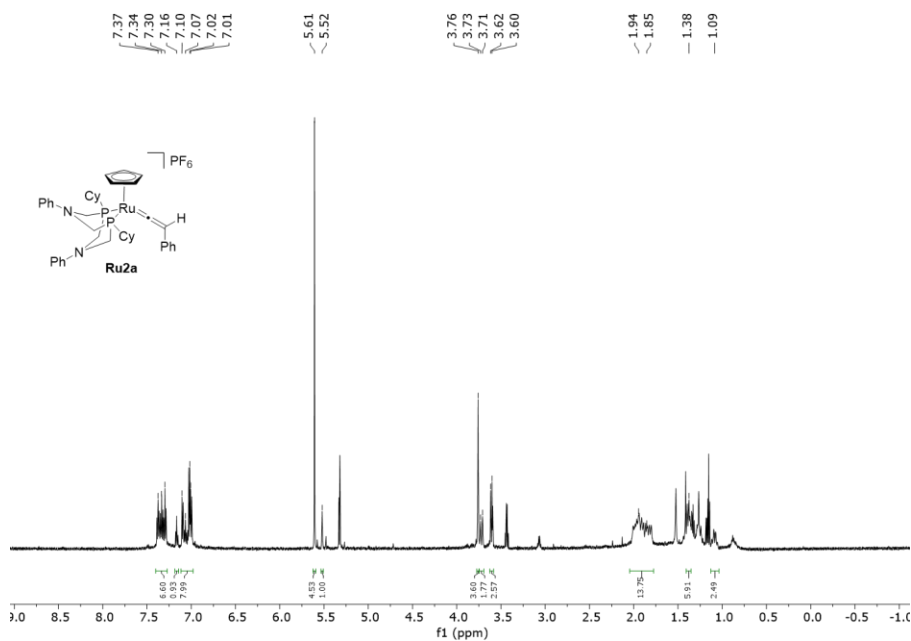


**Figure C-1.** <sup>1</sup>H NMR spectrum of [Ru(Cp)(P(Cy)<sub>2</sub>NPh<sub>2</sub>)(=C=CHPh)]PF<sub>6</sub> (**4-Ru2a**) (600 MHz, CD<sub>2</sub>Cl<sub>2</sub>).



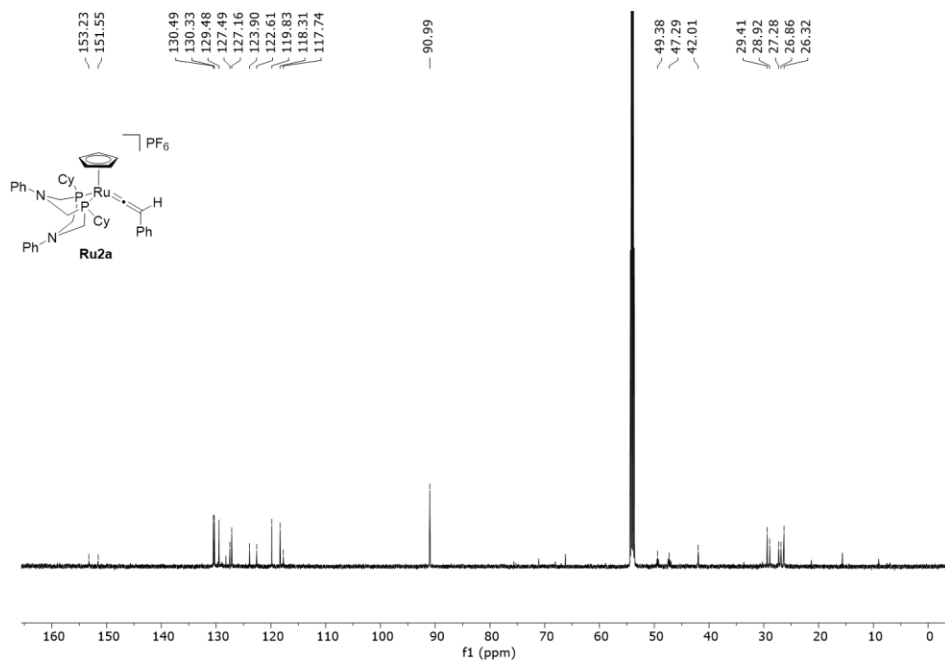


**Figure C-2.**  $^{13}\text{C}\{^1\text{H}\}$  NMR spectrum of **4-Ru2a** (151 MHz,  $\text{CD}_2\text{Cl}_2$ ).

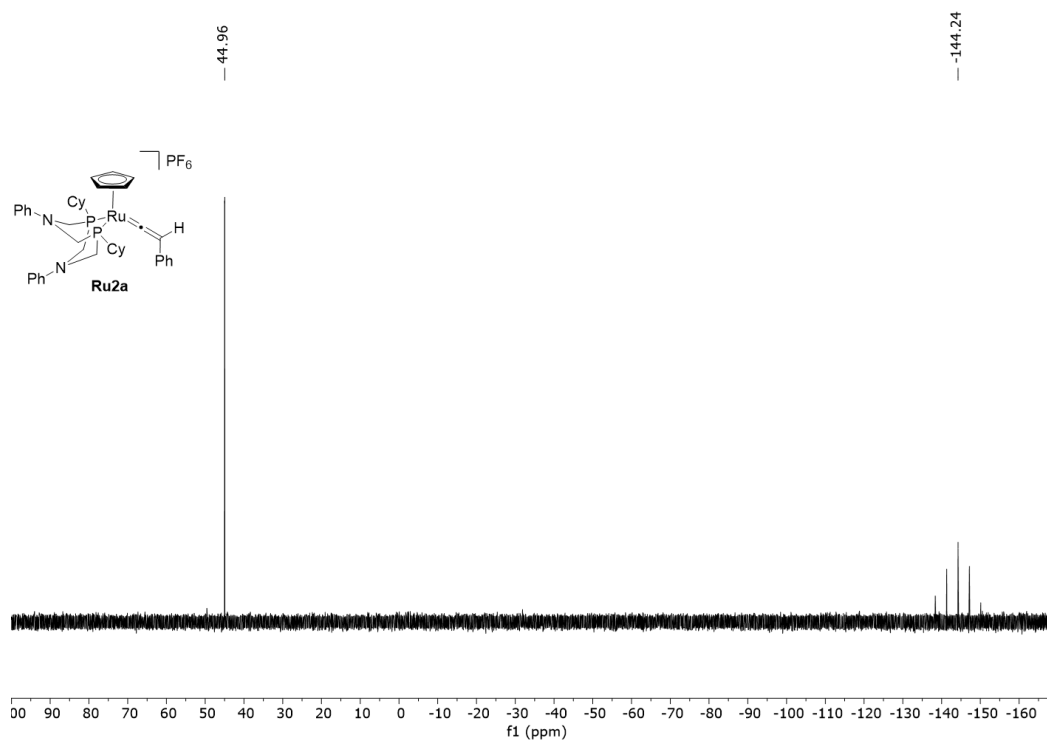


**Figure C-3.**  $^{31}\text{P}\{^1\text{H}\}$  NMR spectrum of **4-Ru2a** (243 MHz,  $\text{CD}_2\text{Cl}_2$ ).

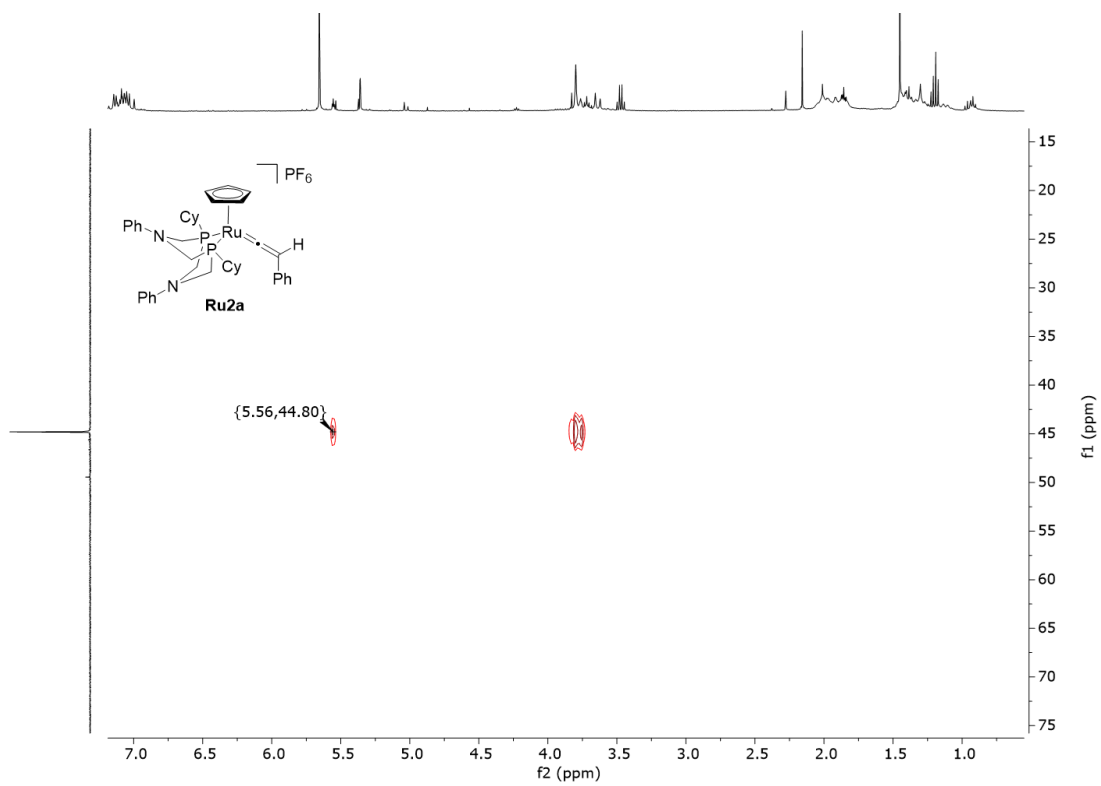


**Figure C-4.**  $^1\text{H}$ - $^{31}\text{P}$  HMBC spectrum of **4-Ru2a** (400 MHz,  $\text{CD}_2\text{Cl}_2$ ).

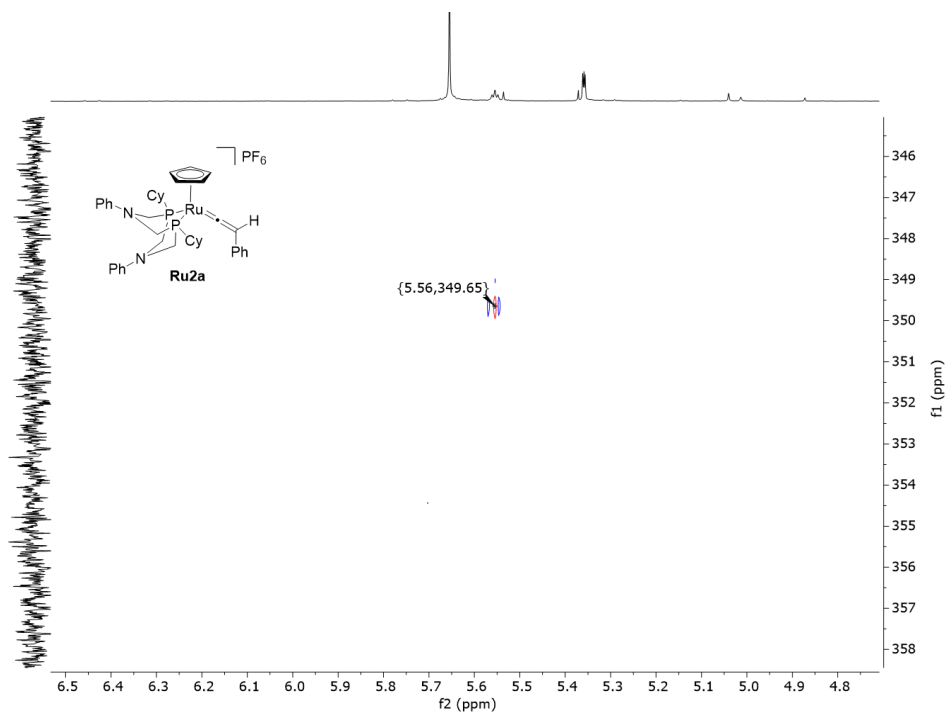


**Figure C-5.**  $^1\text{H}$ - $^{13}\text{C}\{^1\text{H}\}$  HMBC spectrum of **4-Ru2a** (600 MHz,  $\text{CD}_2\text{Cl}_2$ ) which shows correlation of  $\text{H}_\beta$  proton to  $\text{C}_\alpha$  of the vinylidene.

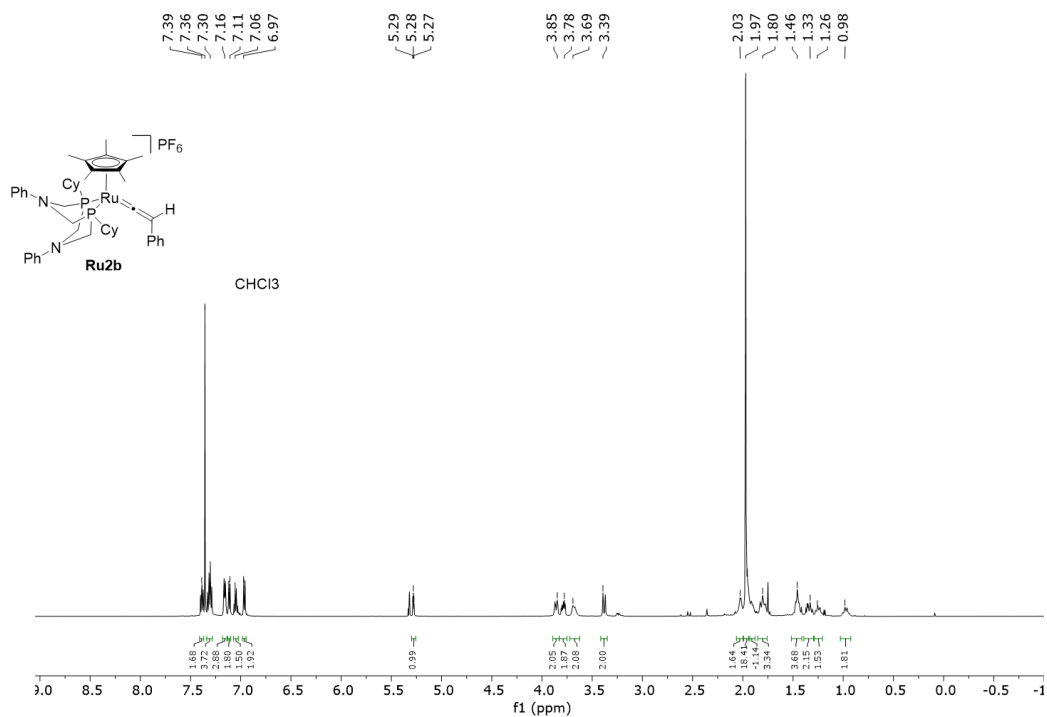


**Figure C-6.**  $^1\text{H}$  NMR spectrum of  $[\text{Ru}(\text{Cp}^*)(\text{PCy}_2\text{NPh}_2)(=\text{C}=\text{CHPh})]\text{PF}_6$  (**4-Ru2b**) (600 MHz,  $\text{CD}_2\text{Cl}_2$ ).

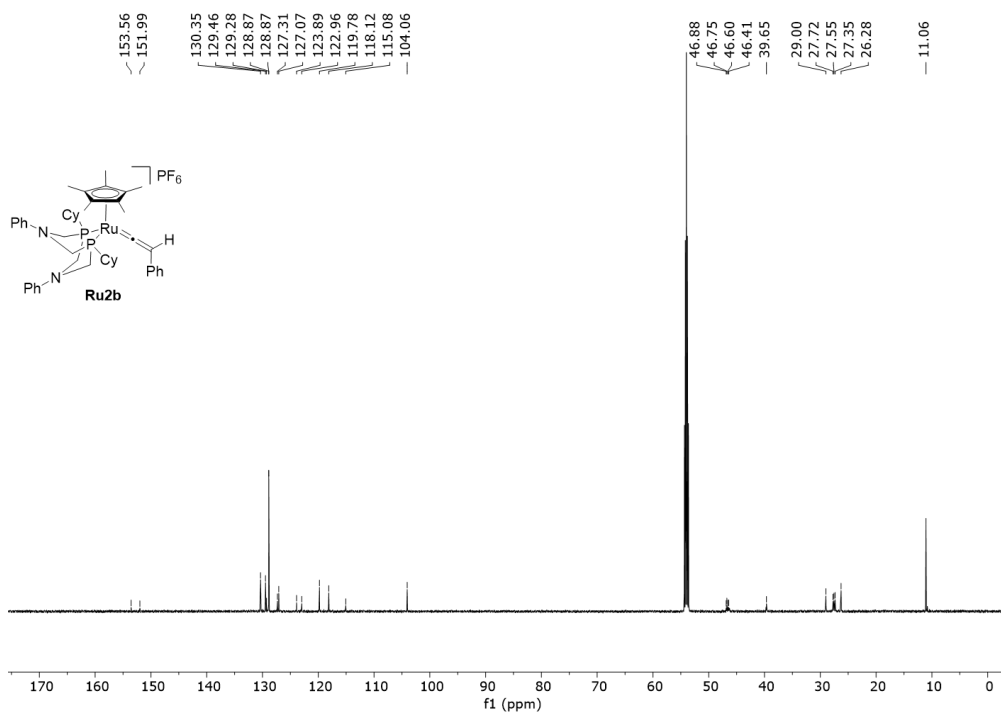


**Figure C-7.**  $^{13}\text{C}\{^1\text{H}\}$  NMR spectrum of **4-Ru2b** (151 MHz,  $\text{CD}_2\text{Cl}_2$ ).

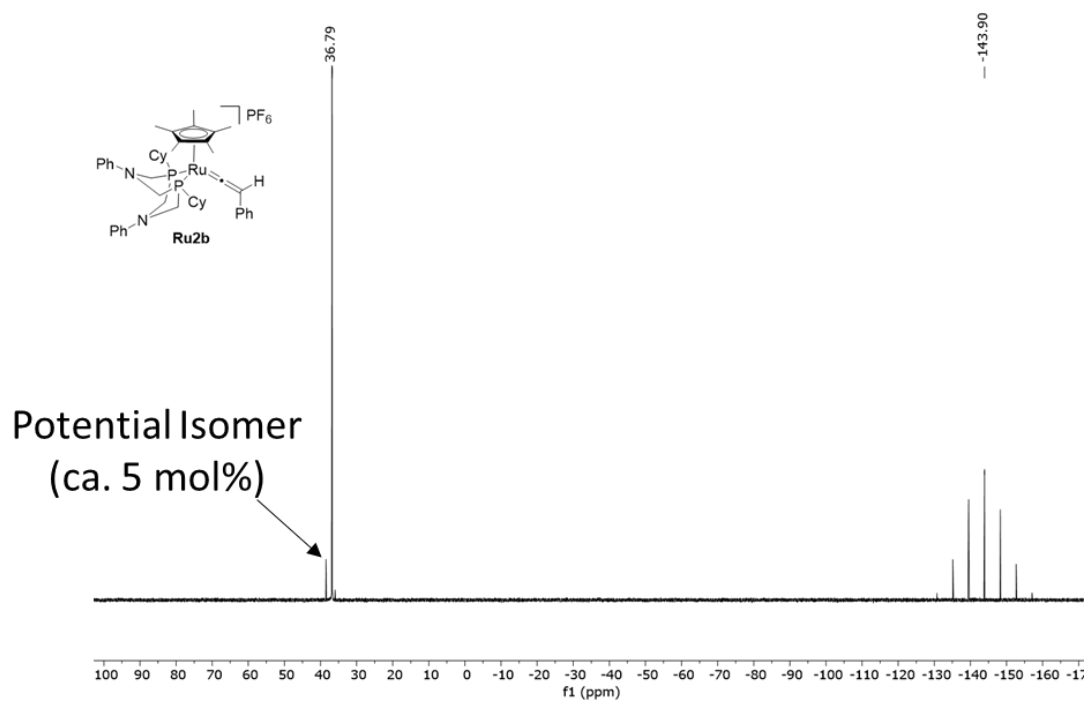


**Figure C-8.**  $^{31}\text{P}\{^1\text{H}\}$  NMR spectrum of **4-Ru2b** (243 MHz,  $\text{CD}_2\text{Cl}_2$ ).

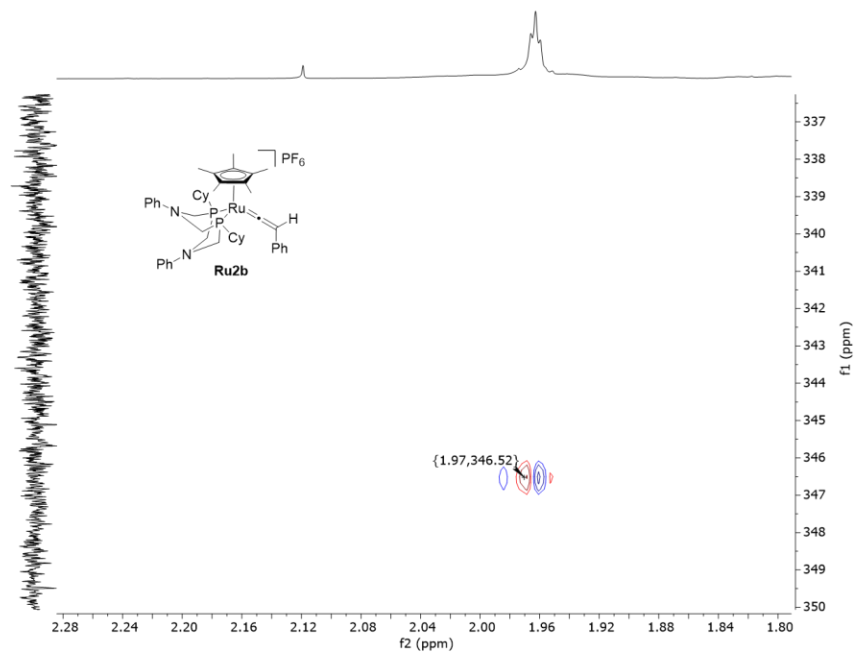


**Figure C-9.**  $^1\text{H}$ - $^{13}\text{C}\{^1\text{H}\}$  HMBC spectrum of **4-Ru2b** (400 MHz,  $\text{CD}_2\text{Cl}_2$ ) which shows correlation of Cp\* protons to  $\text{C}_\alpha$  of the vinylidene.

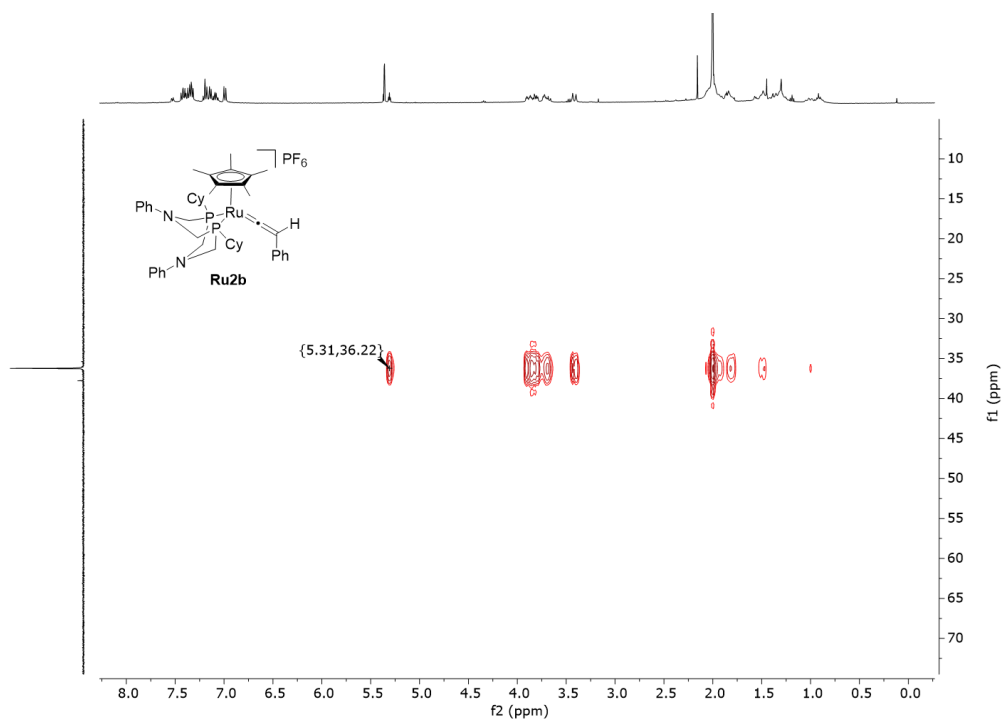


**Figure C-10.**  $^1\text{H}$ - $^{31}\text{P}$  HMBC spectrum of **4-Ru2b** (400 MHz,  $\text{CD}_2\text{Cl}_2$ ).

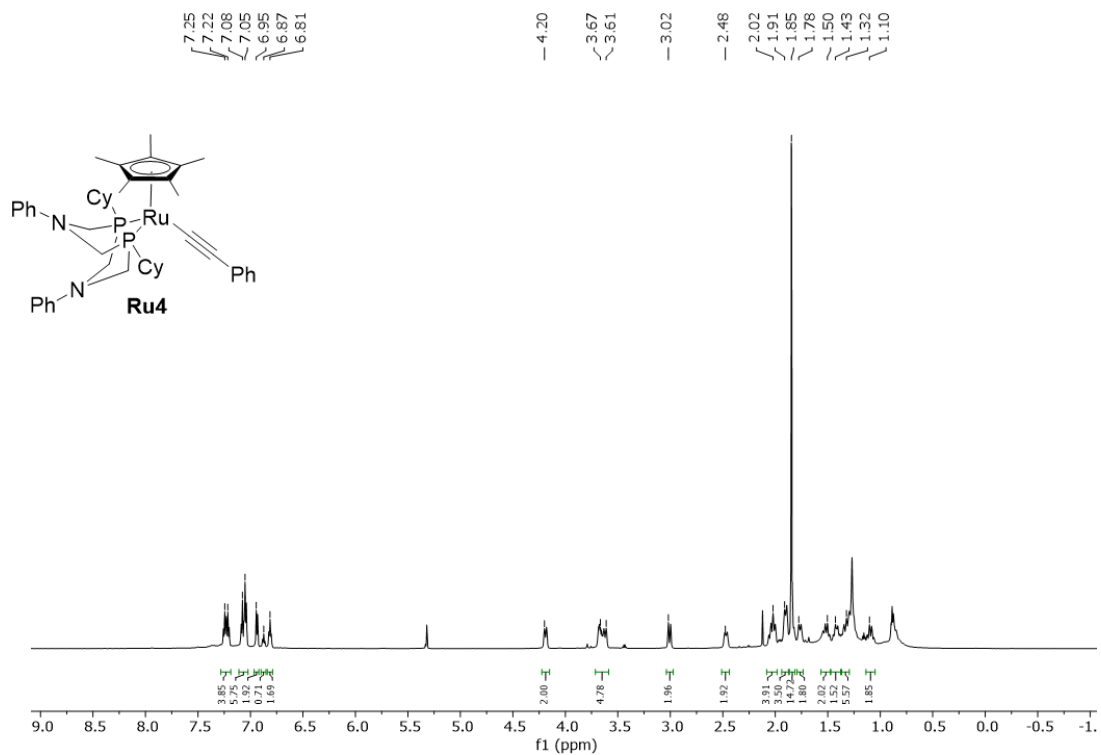


**Figure C-11.**  $^1\text{H}$  NMR spectrum of Ru(Cp\*)(P(Cy)<sub>2</sub>N(Ph)<sub>2</sub>)(-CC-Ph) (**4-Ru4**) (600 MHz, CD<sub>2</sub>Cl<sub>2</sub>).

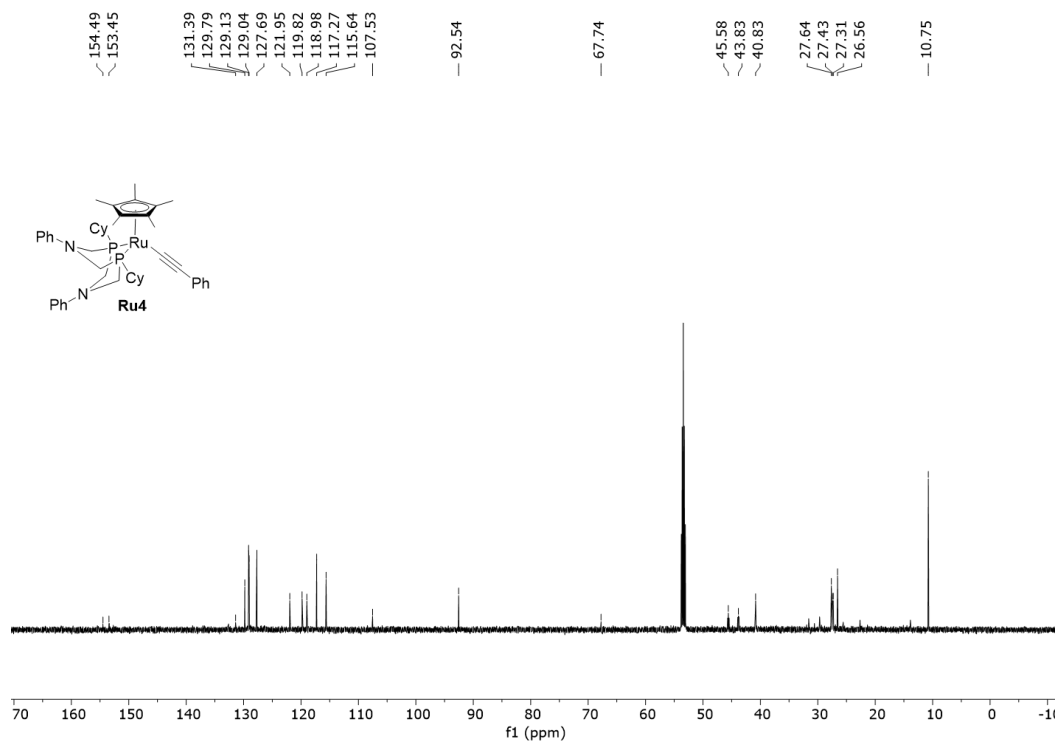


**Figure C-12.**  $^{13}\text{C}\{^1\text{H}\}$  NMR spectrum of **4-Ru4** (151 MHz, CD<sub>2</sub>Cl<sub>2</sub>).

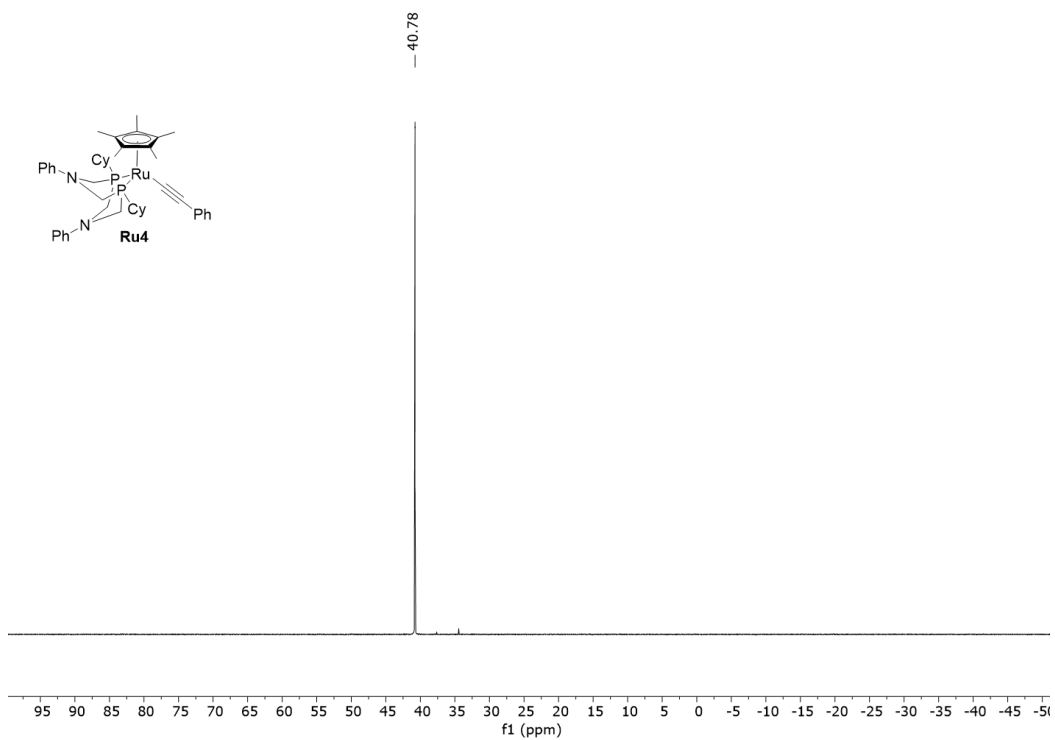


**Figure C-13.**  $^{31}\text{P}\{^1\text{H}\}$  NMR spectrum of **4-Ru4** (243 MHz,  $\text{CD}_2\text{Cl}_2$ ).

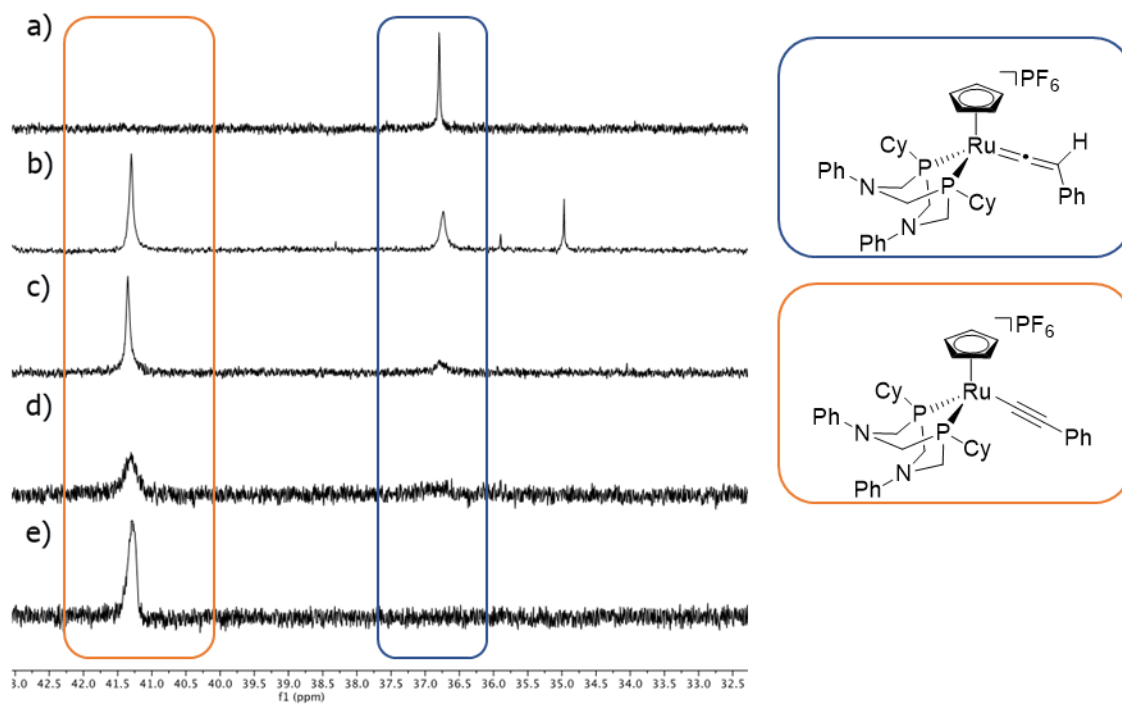


**Figure C-14.**  $^{31}\text{P}\{^1\text{H}\}$  NMR spectra stack plot (243 MHz,  $\text{CD}_2\text{Cl}_2$ ) of: a) **4-Ru2b**; and reaction of **4-Ru2b** with 5 equiv b) *tert*-butylamine, c) isopropylamine, d) diethylamine, e) piperidine.

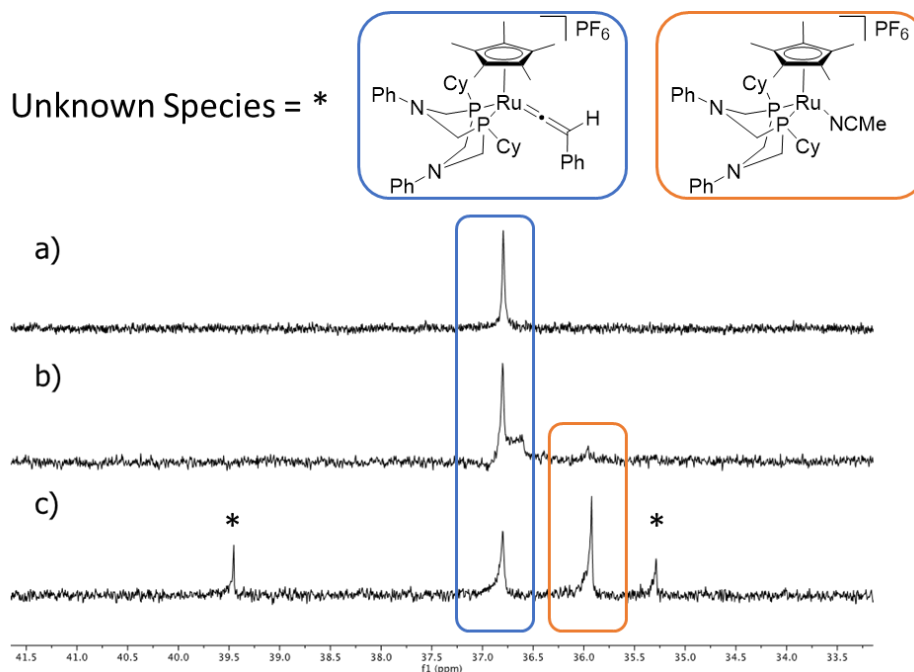


**Figure C-15.**  $^{31}\text{P}\{^1\text{H}\}$  NMR spectra stack plot (243 MHz,  $\text{C}_6\text{D}_5\text{Br}$ ) of: a) **4-Ru2b**; and reaction of **4-Ru2b** with 5 equiv aniline and excess MeCN after b) 2 h at 50 °C and c) 50 h at 90 °C.

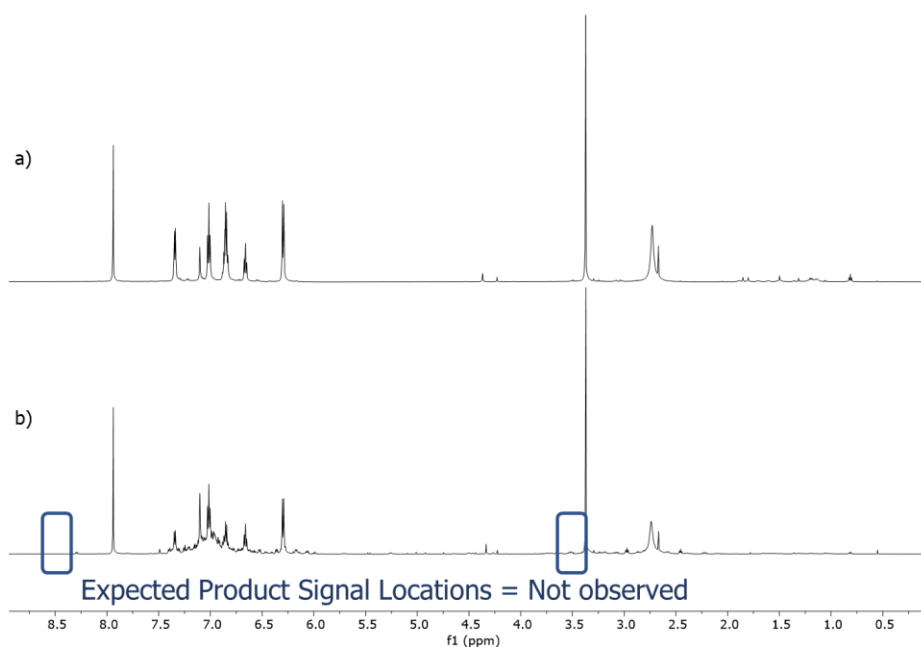


**Figure C-16.**  $^1\text{H}$  NMR (600 MHz) spectra stack plot of attempted hydroamination of phenylacetylene (100 mM) with aniline (100 mM) catalyzed by **4-Ru6** (2 mol%), and dimethyl terephthalate (16 mM) as the internal standard in  $\text{C}_6\text{D}_6$  at 110 °C: a) T0 (no **4-Ru6** added); and b) 24 h time point.



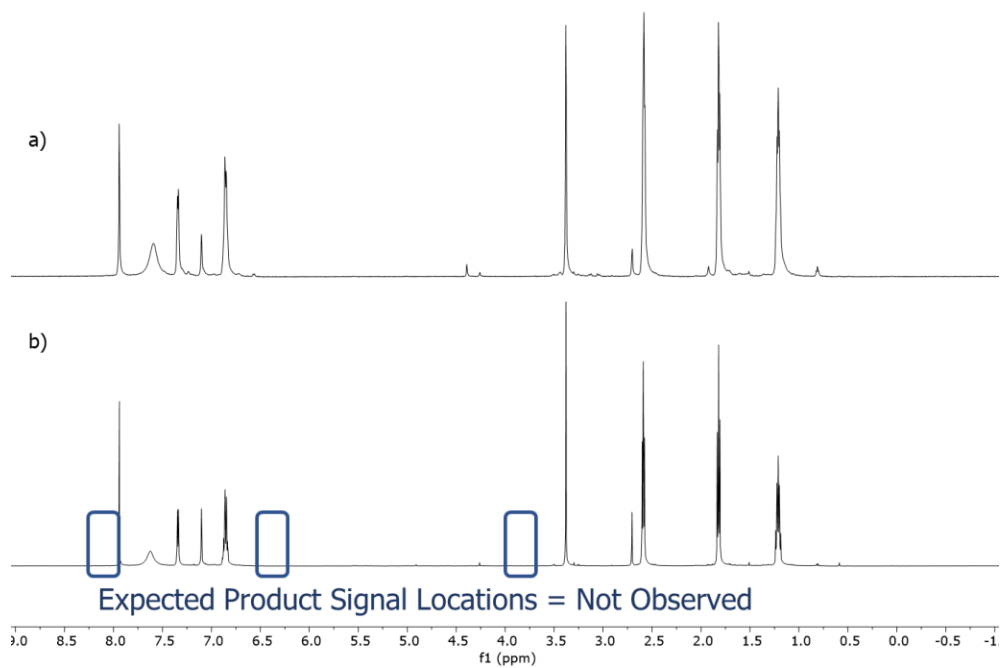


**Figure C-17.**  $^1\text{H}$  NMR (600 MHz) spectra stack plot of attempted hydroamidation of phenylacetylene (100 mM) with 2-pyrrolidinone (100 mM) catalyzed by **4-Ru6** (2 mol%), and dimethyl terephthalate (16 mM) as the internal standard in  $\text{C}_6\text{D}_6$  at 110  $^\circ\text{C}$ . a) T0 (no **4-Ru6** added); and b) 24 h time point.

## IR Spectra

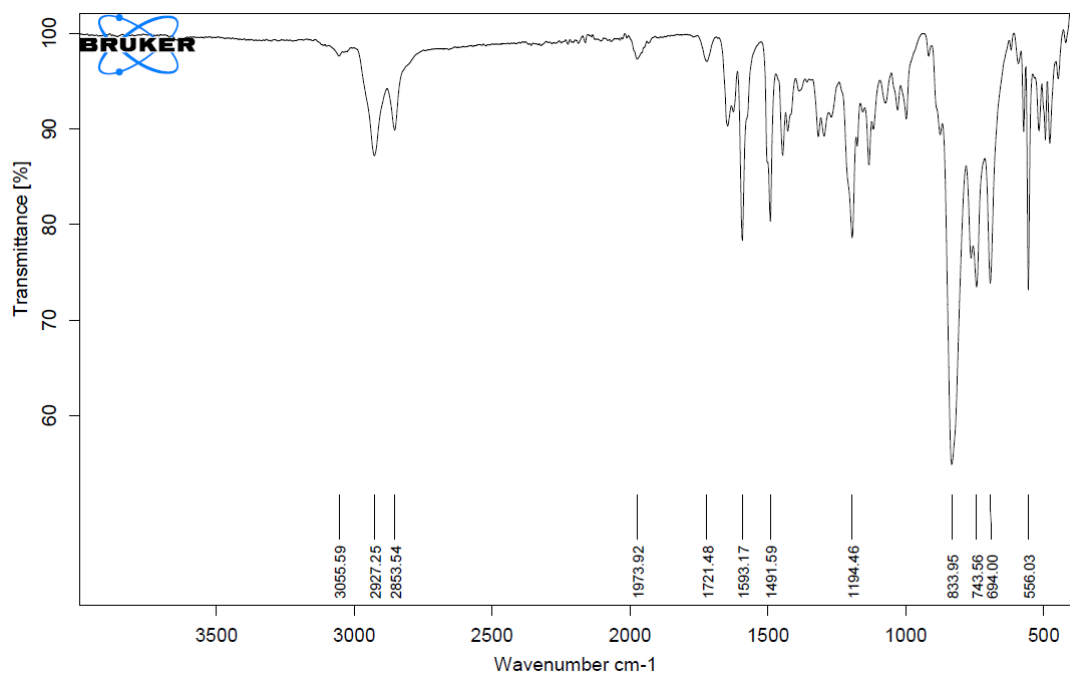


**Figure C-18.** ATR-FTIR spectrum of solid **4-Ru2a**.

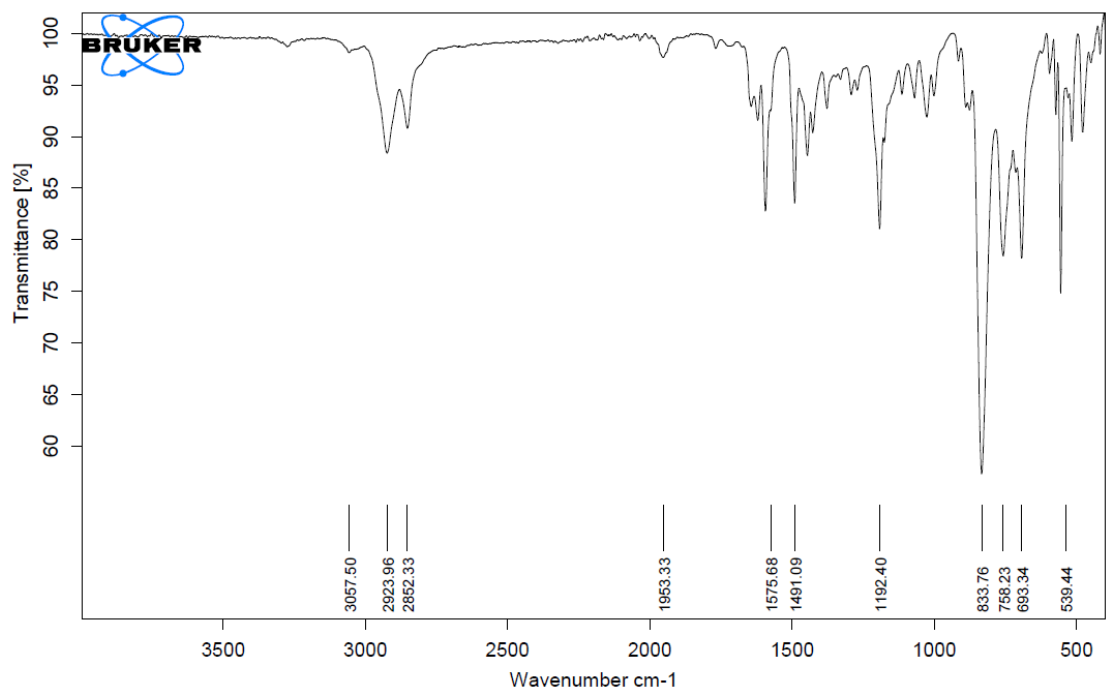


**Figure C-19.** ATR-FTIR spectrum of solid **4-Ru2b**.

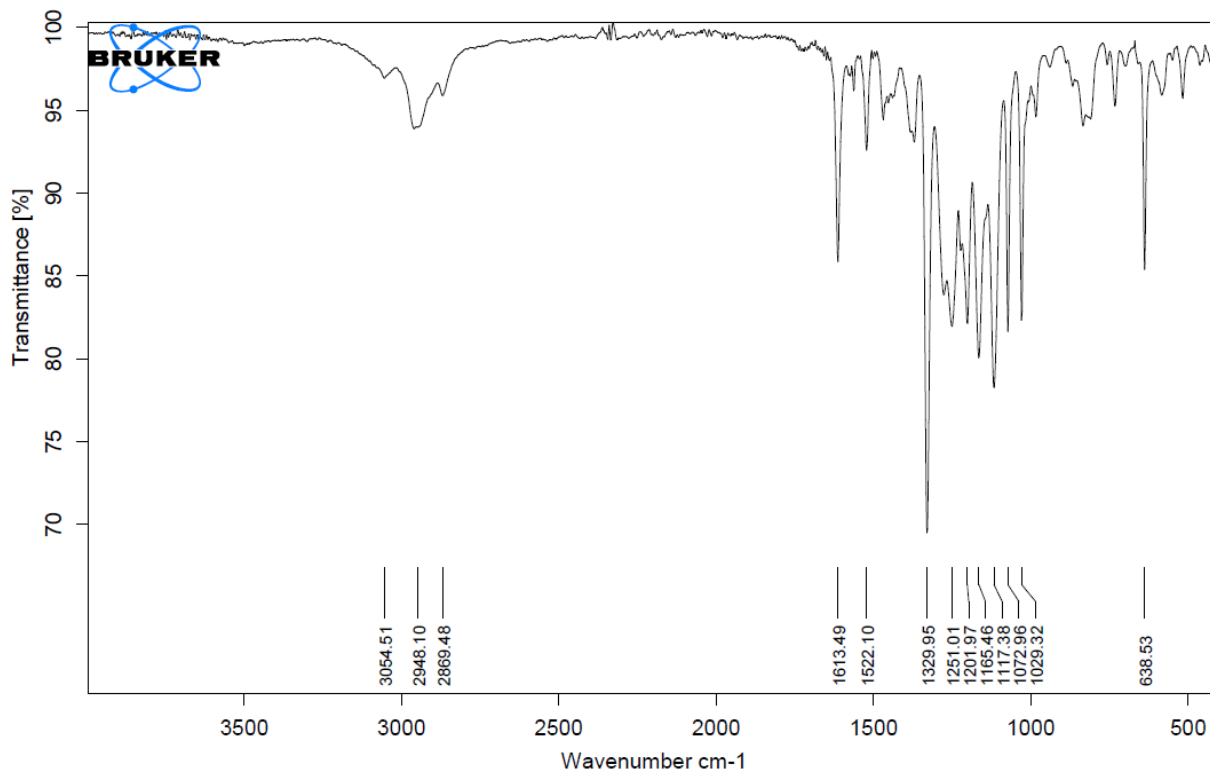


Figure C-20. ATR-FTIR spectrum of solid **4-Ru4**.

### MALDI Mass Spectra

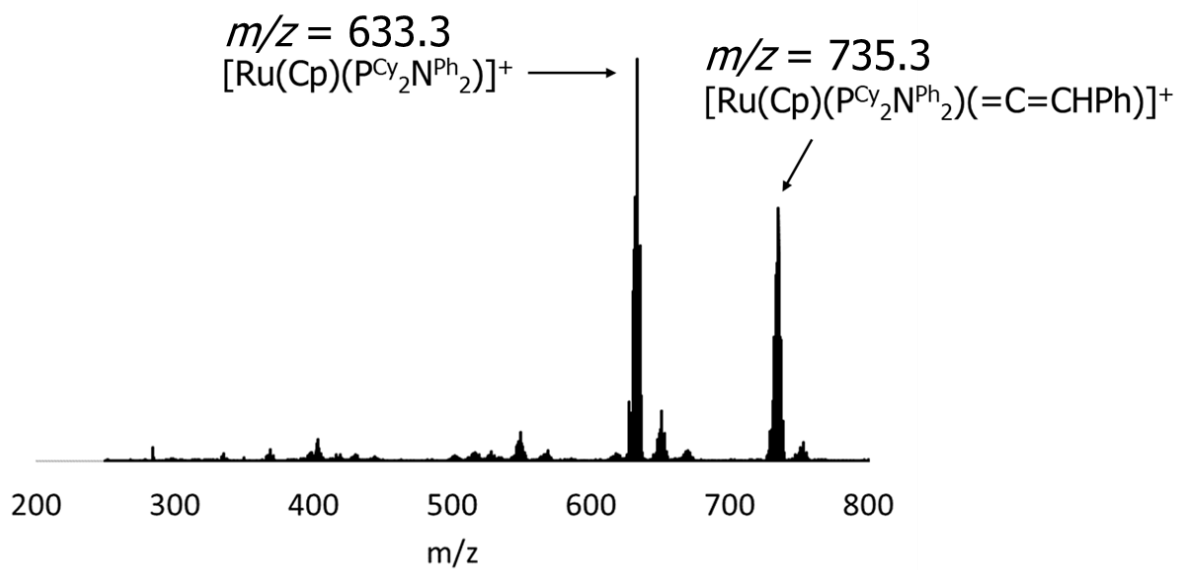
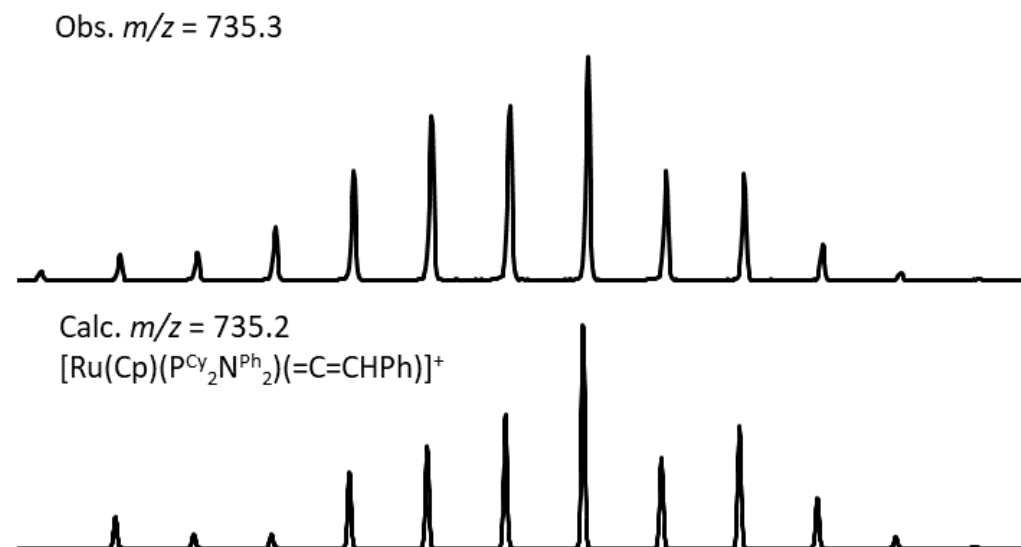
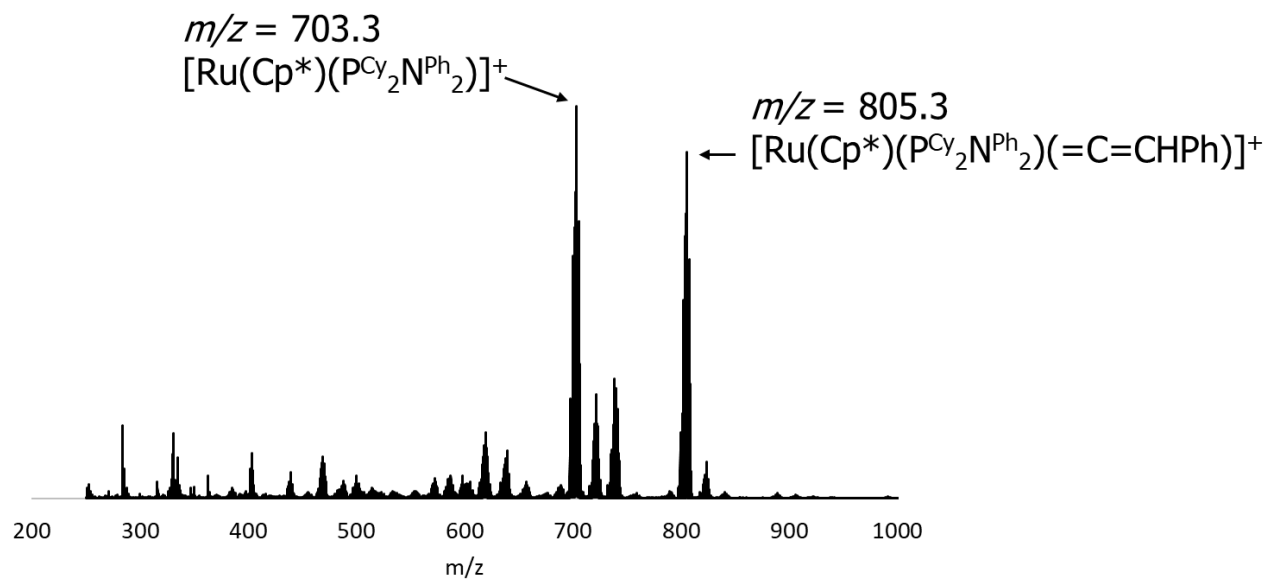


Figure C-21. MALDI-TOF mass spectrum of **4-Ru2a** with pyrene as the matrix (1:20 molar ratio).



**Figure C-22.** (top) Zoom-in of the observed MALDI-TOF mass spectrum signal of **4-Ru2a** at  $m/z = 735.3$ ; and (bottom) simulated signal with  $m/z = 735.2$  for  $[\text{Ru}(\text{Cp})(\text{P}^{\text{Cy}}_2\text{N}^{\text{Ph}}_2)(=\text{C}=\text{CHPh})]^+$ .



**Figure C-23.** MALDI-TOF mass spectrum of **4-Ru2b** with pyrene as the matrix (1:20 molar ratio).

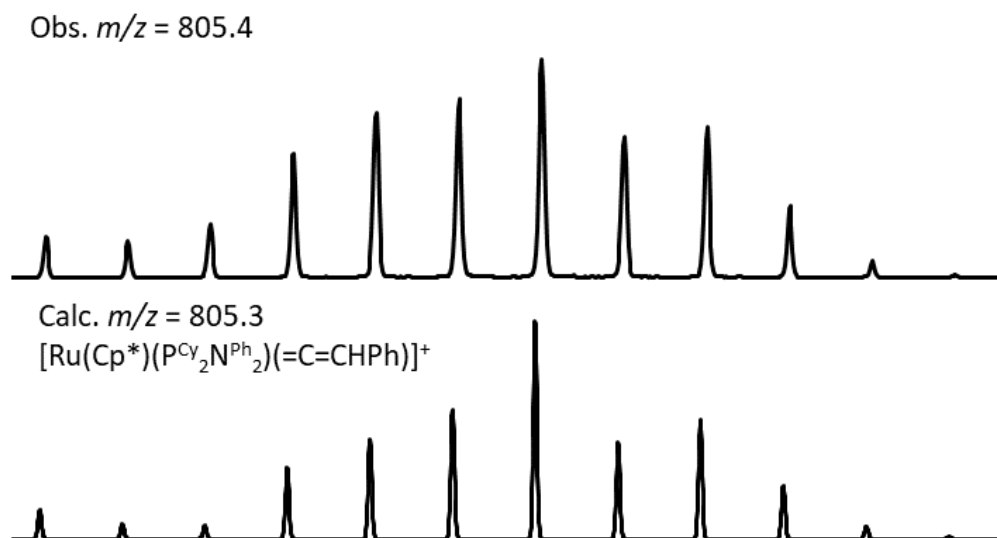


**Figure C-24.** (top) Zoom-in of the observed MALDI-TOF mass spectrum signal of **4-Ru2b** at  $m/z = 805.4$ ; and (bottom) simulated signal with  $m/z = 805.3$  for  $[\text{Ru}(\text{Cp}^*)(\text{P}^{\text{Cy}}_2\text{N}^{\text{Ph}}_2)(=\text{C}=\text{CHPh})]^+$ .

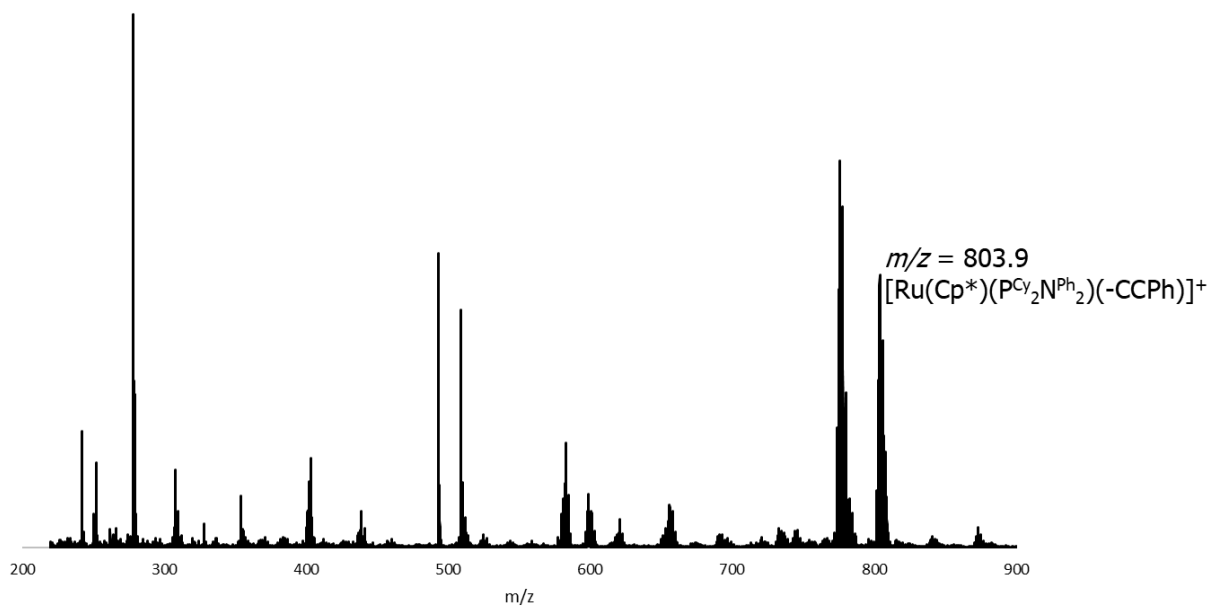


**Figure C-25.** MALDI-TOF mass spectrum of **4-Ru4** with pyrene as the matrix (1:20 molar ratio).

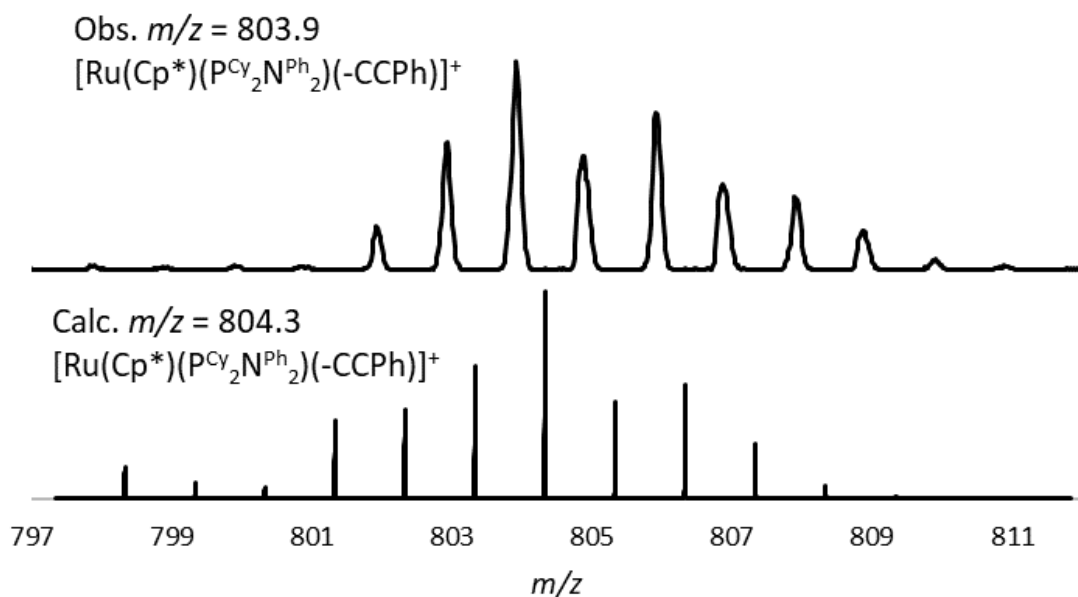


**Figure C-26.** Zoom in of the observed signal (top) with  $m/z$  value = 803.9 for  $[\text{Ru}(\text{Cp}^*)(\text{PCy}_2\text{N}^{\text{Ph}}_2)(-\text{CCPh})]^+$ ; and simulated signal (bottom) with  $m/z = 804.3$ .

## Crystallographic Details

*Data Collection and Processing.* Samples of **4-Ru2b** were mounted on a Mitegen polyimide micromount with a small amount of Paratone N oil. All X-ray measurements were made on a Bruker Kappa Axis Apex2 diffractometer at a temperature of 110 K. The unit cell dimensions were determined from a symmetry constrained fit with reflections and dimensions listed in Table SX. The data collection strategy was a number of  $\omega$  and  $\varphi$  scans which collected data up to  $2\theta_{\text{max}}$  as listed in Table SX. The frame integration was performed using SAINT.<sup>1</sup> The resulting raw data was scaled and absorption corrected using a multi-scan averaging of symmetry equivalent data using SADABS.<sup>2</sup>

*Structure Solution and Refinement for 4-Ru2b.* The structure was solved by using a dual space methodology using the SHELXT program.<sup>3</sup> All non-hydrogen atoms were obtained from the initial solution. The hydrogen atoms were introduced at idealized positions and were allowed to ride on the parent atom. The  $\text{PF}_6^-$  anion was disordered over two orientations which led to distinct positions for all F atoms. The normalized occupancy factor converged to a value of 0.605(12) for the predominant orientation. The structural model was fit to the data using full matrix least-squares based on  $F^2$ . The calculated structure factors included corrections for anomalous dispersion from

the usual tabulation. The structure was refined using the SHELXL program from the SHELXTL suite of crystallographic software.<sup>4</sup> Graphic plots were produced using the NRCVAX program suite.<sup>5</sup> Additional information and other relevant literature references can be found in the reference section of this website (<http://xray.chem.uwo.ca>).

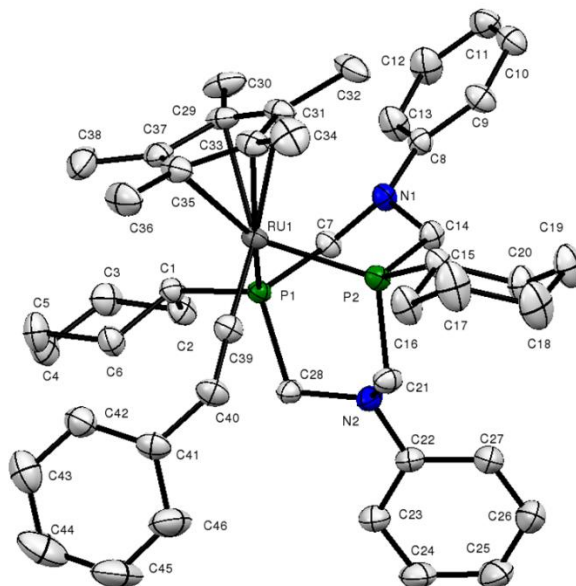


**Figure C-27.** ORTEP drawing of **4-Ru2b** showing the naming and numbering scheme. Ellipsoids are at 50% probability level and hydrogen atoms were omitted for clarity.

**Table C-1.** Summary of Crystal Data for **4-Ru2b**.

Compound	<b>4-Ru2b</b>
CCDC	
Formula	$C_{46}H_{61}F_6N_2P_3Ru$
Formula Weight ( <i>g/mol</i> )	949.94
Crystal Dimensions ( <i>mm</i> )	$0.476 \times 0.386 \times 0.109$
Crystal Color and Habit	yellow Prism
Crystal System	orthorhombic
Space Group	$P b c a$
Temperature, K	110

$a$ , Å	18.588(5)
$b$ , Å	19.108(7)
$c$ , Å	24.585(9)
$\alpha$ , °	90
$\beta$ , °	90
$\gamma$ , °	90
$V$ , Å <sup>3</sup>	8732(5)
Number of reflections to determine final unit cell	9332
Min and Max $2\theta$ for cell determination, °	5.4, 60.56
$Z$	8
$F(000)$	3952
$\rho$ (g/cm <sup>3</sup> )	1.445
$\lambda$ , Å, (MoK $\alpha$ )	0.71073
$\mu$ , (cm <sup>-1</sup> )	0.530
Diffractionmeter Type	Bruker Kappa Axis Apex2
Scan Type(s)	$\varphi$ and $\omega$ scans
Max $2\theta$ for data collection, °	61.092
Measured fraction of data	0.999
Number of reflections measured	313325
Unique reflections measured	13343



R <sub>merge</sub>	0.0386
Number of reflections included in refinement	13343
Cut off Threshold Expression	I > 2 σ (I)
Structure refined using	full matrix least-squares using F <sup>2</sup>
Weighting Scheme	w=1/[σ <sup>2</sup> (Fo <sup>2</sup> )+(0.0527P) <sup>2</sup> +17.1315 P] where P=(Fo <sup>2</sup> +2Fc <sup>2</sup> )/3
Number of parameters in least-squares	583
R <sub>1</sub>	0.0451
wR <sub>2</sub>	0.1127
R <sub>1</sub> (all data)	0.0634
wR <sub>2</sub> (all data)	0.1298
GOF	1.106
Maximum shift/error	0.002
Min & Max peak heights on final ΔF Map (e <sup>-</sup> /Å)	-1.497, 1.845

Where:

$$R_1 = \frac{\sum (|F_o| - |F_c|)}{\sum F_o}$$

$$wR_2 = \left[ \frac{\sum (w(F_o^2 - F_c^2)^2)}{\sum (w F_o^4)} \right]^{1/2}$$

$$GOF = \left[ \frac{\sum (w(F_o^2 - F_c^2)^2)}{(\text{No. of reflns.} - \text{No. of params.})} \right]$$

## References

1. Bruker-AXS, SAINT version 2013.8, **2013**, Bruker-AXS, Madison, WI 53711, USA
2. Bruker-AXS, SADABS version 2012.1, **2012**, Bruker-AXS, Madison, WI 53711, USA
3. Sheldrick, G. M., *Acta Cryst.* **2015**, *A71*, 3-8
4. Sheldrick, G. M., *Acta Cryst.* **2015**, *C71*, 3-8
5. Gabe, E. J.; Le Page, Y.; Charland, J. P.; Lee, F. L. and White, P. S. *J. Appl. Cryst.* **1989**, *22*, 384-3

## Appendices D: Supplementary Information for Chapter 5

### NMR Spectra

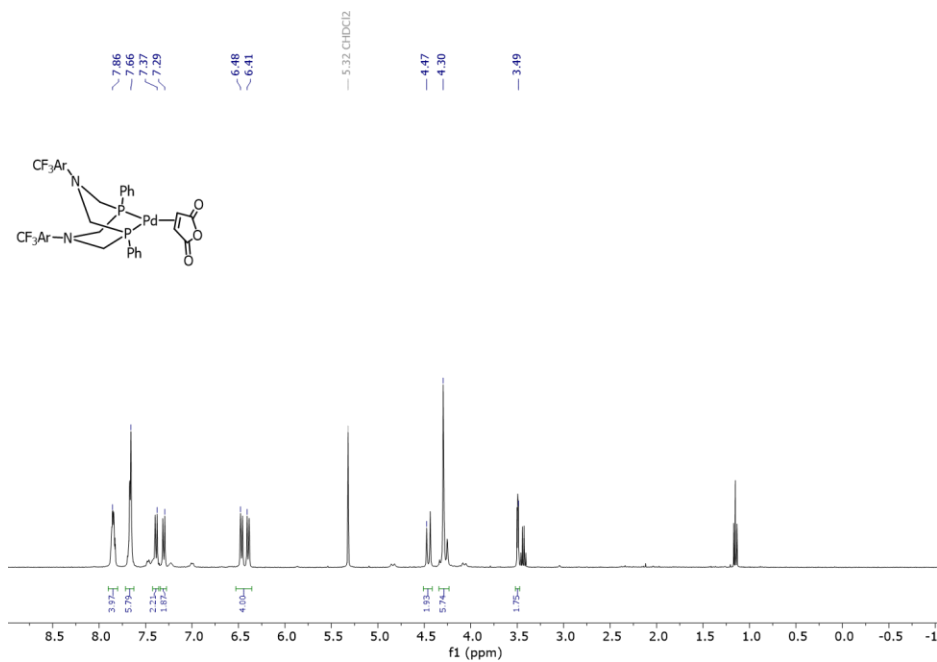


**Figure D-1.**  $^1\text{H}$  NMR spectrum of  $\text{Pd}(\text{P}^{\text{Ph}}_2\text{N}^{\text{ArCF}_3})_2(\text{MAH})$  (**5-3a**) (600 MHz,  $\text{CD}_2\text{Cl}_2$ ).

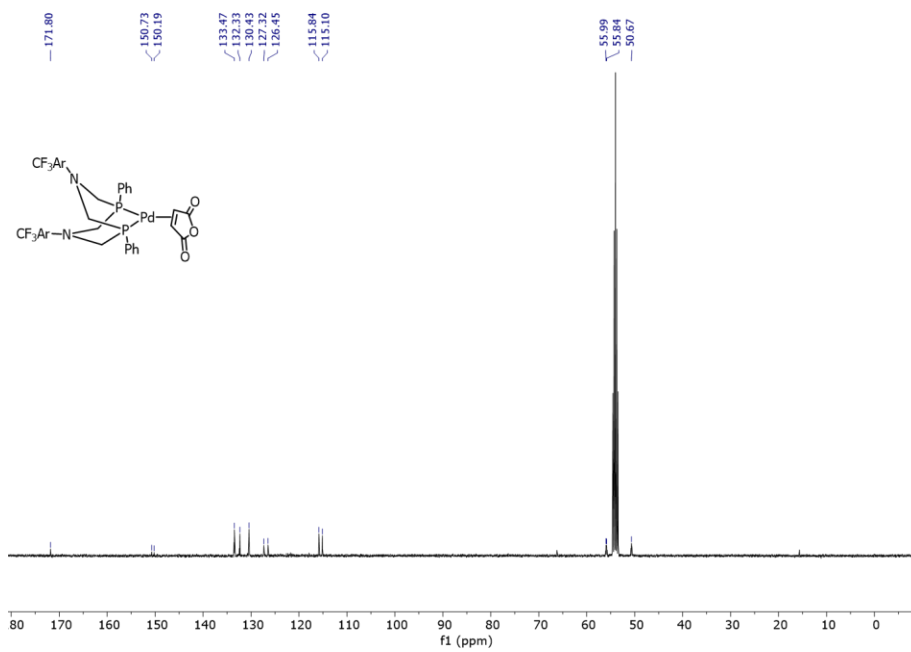


**Figure D-2.**  $^{13}\text{C}\{^1\text{H}\}$  NMR spectrum of **5-3a** (151 MHz,  $\text{CD}_2\text{Cl}_2$ ).

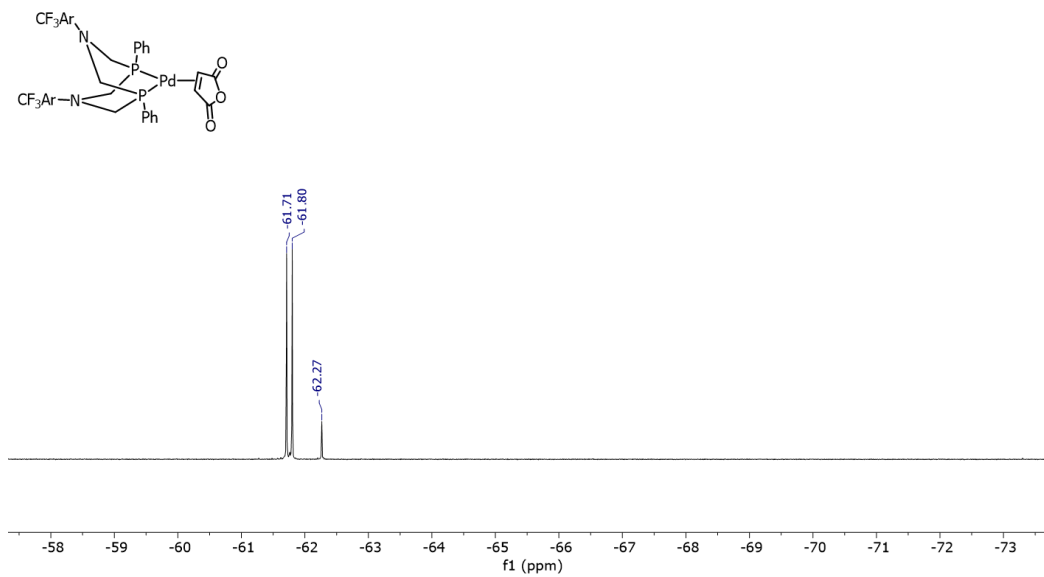


**Figure D-3.** <sup>19</sup>F NMR spectrum of **5-3a** (565 MHz, CD<sub>2</sub>Cl<sub>2</sub>).

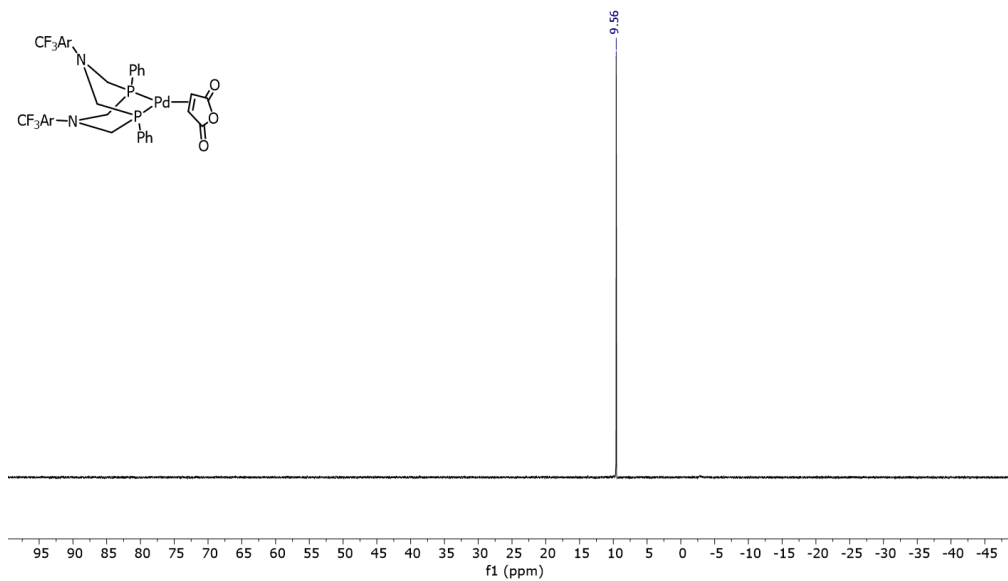


**Figure D-4.** <sup>31</sup>P{<sup>1</sup>H} NMR spectrum of **5-3a** (243 MHz, CD<sub>2</sub>Cl<sub>2</sub>).

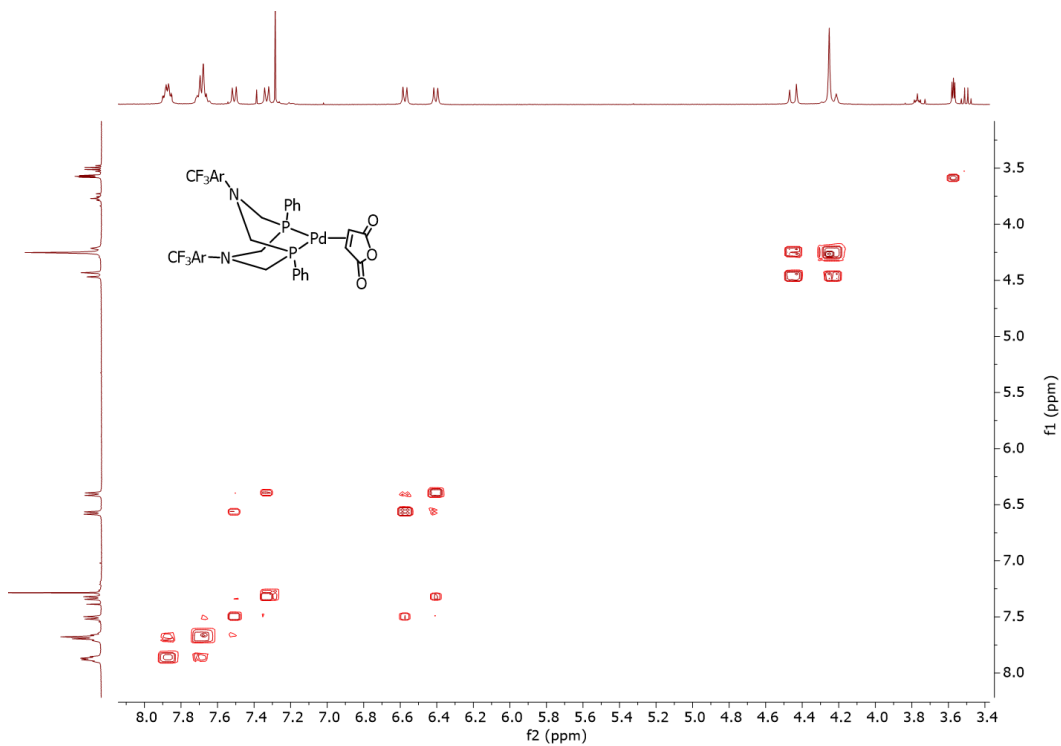


**Figure D-5.**  $^1\text{H}$ - $^1\text{H}$  COSY NMR spectrum of **5-3a** (400 MHz,  $\text{CD}_2\text{Cl}_2$ ).

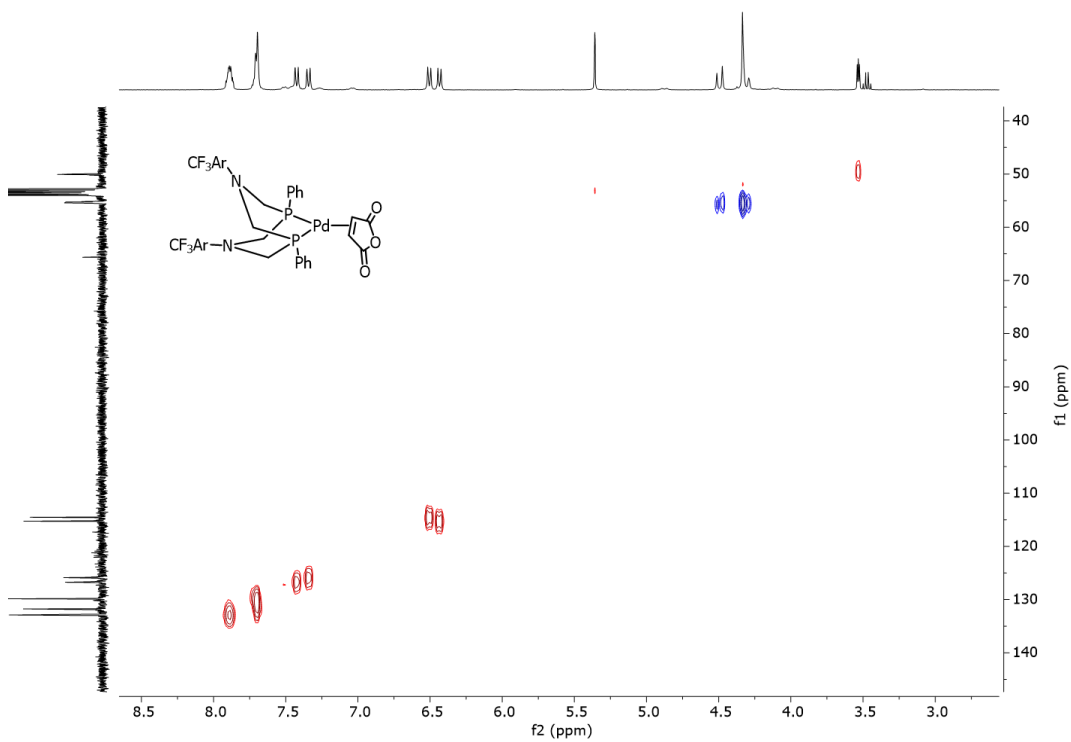


**Figure D-6.**  $^1\text{H}$ - $^{13}\text{C}\{^1\text{H}\}$  HSQC NMR spectrum of **5-3a** (400 MHz,  $\text{CD}_2\text{Cl}_2$ ).

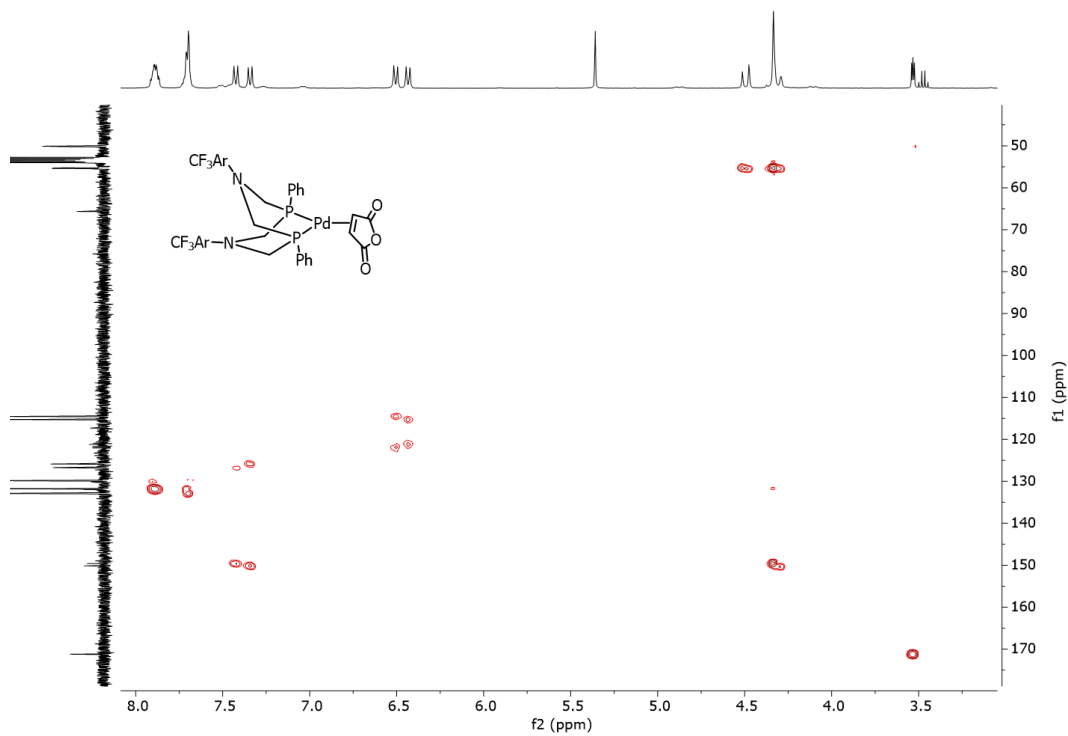


**Figure D-7.**  $^1\text{H}$ - $^{13}\text{C}\{^1\text{H}\}$  HMBC NMR spectrum of **5-3a** (400 MHz,  $\text{CD}_2\text{Cl}_2$ ).

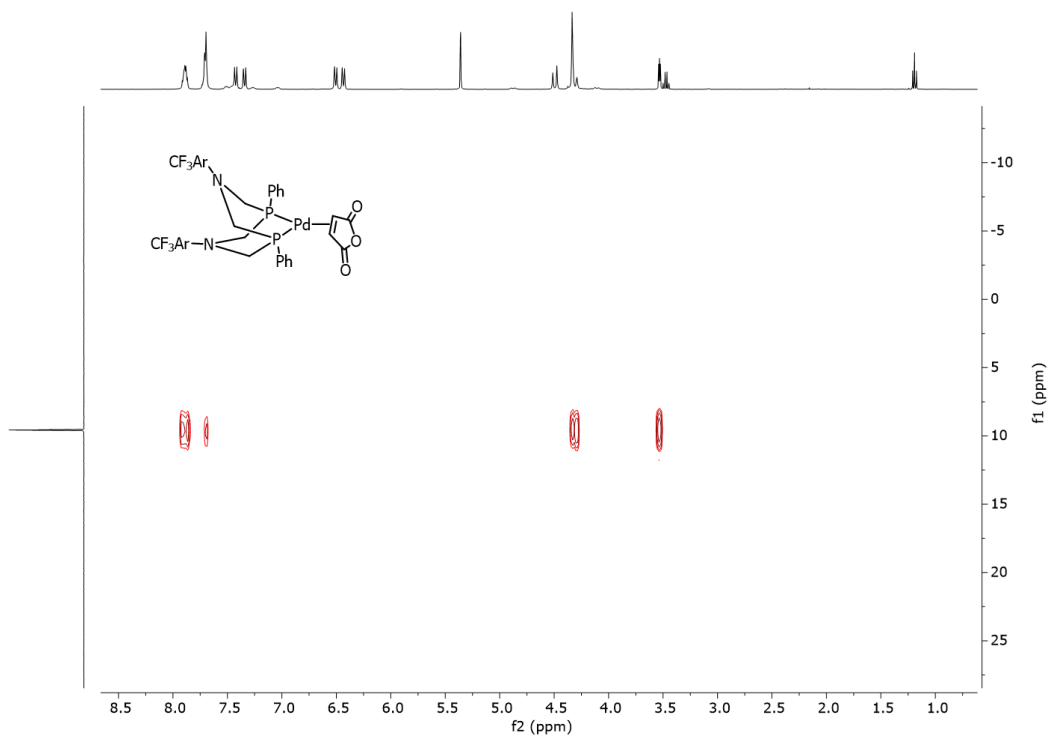


**Figure D-8.**  $^1\text{H}$ - $^{31}\text{P}\{^1\text{H}\}$  HMBC NMR spectrum of **5-3a** (400 MHz,  $\text{CD}_2\text{Cl}_2$ ).

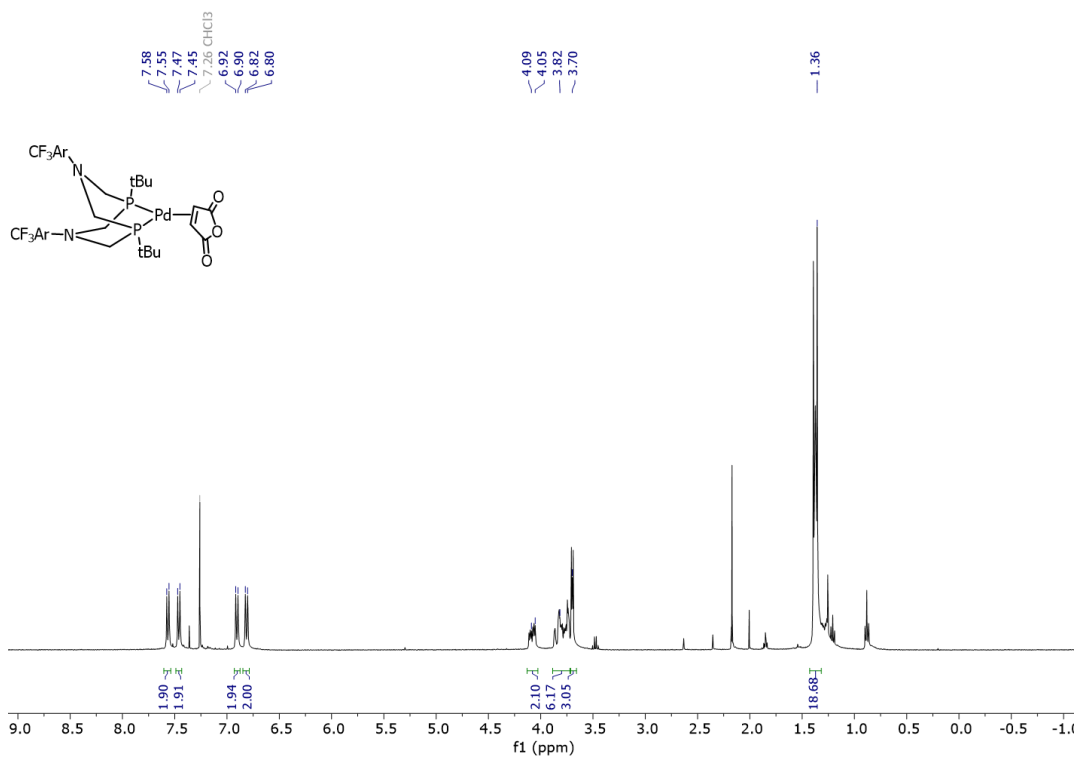


**Figure D-9.** <sup>1</sup>H NMR spectrum of  $\text{Pd}(\text{P}^t\text{BuN}^{\text{ArCF}_3})_2(\text{MAH})$  (**5-3b**) (600 MHz, CD<sub>2</sub>Cl<sub>2</sub>).

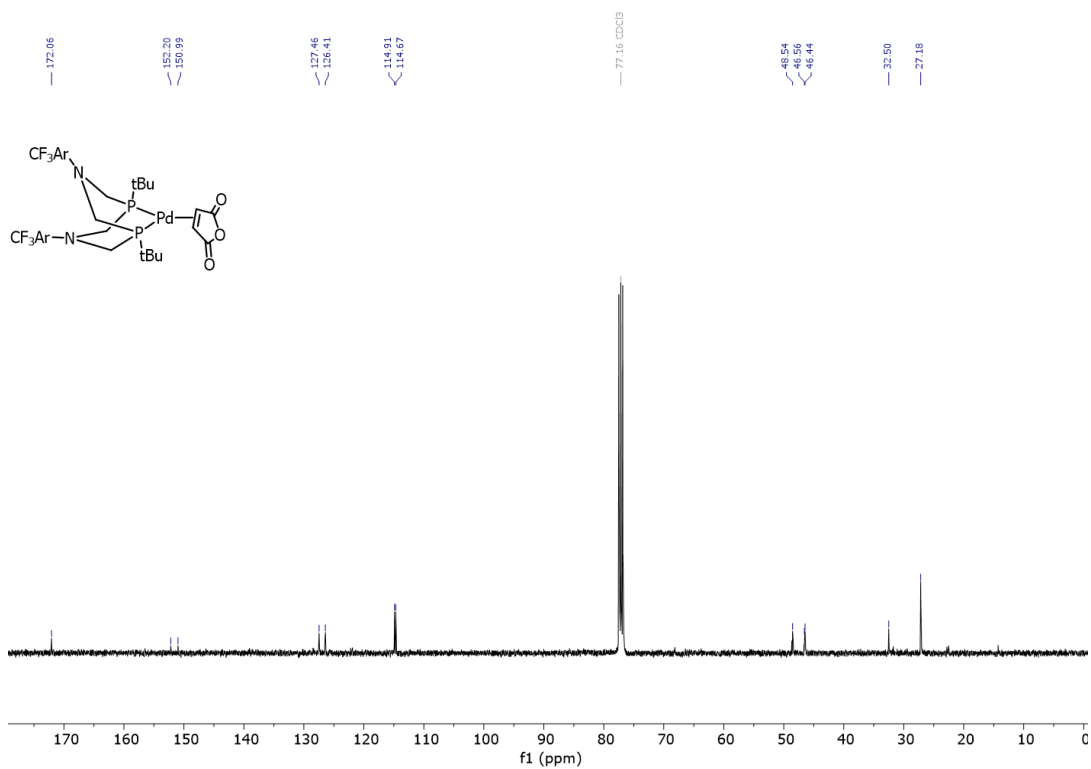


**Figure D-10.** <sup>13</sup>C{<sup>1</sup>H} NMR spectrum of **5-3b** (151 MHz, CD<sub>2</sub>Cl<sub>2</sub>).

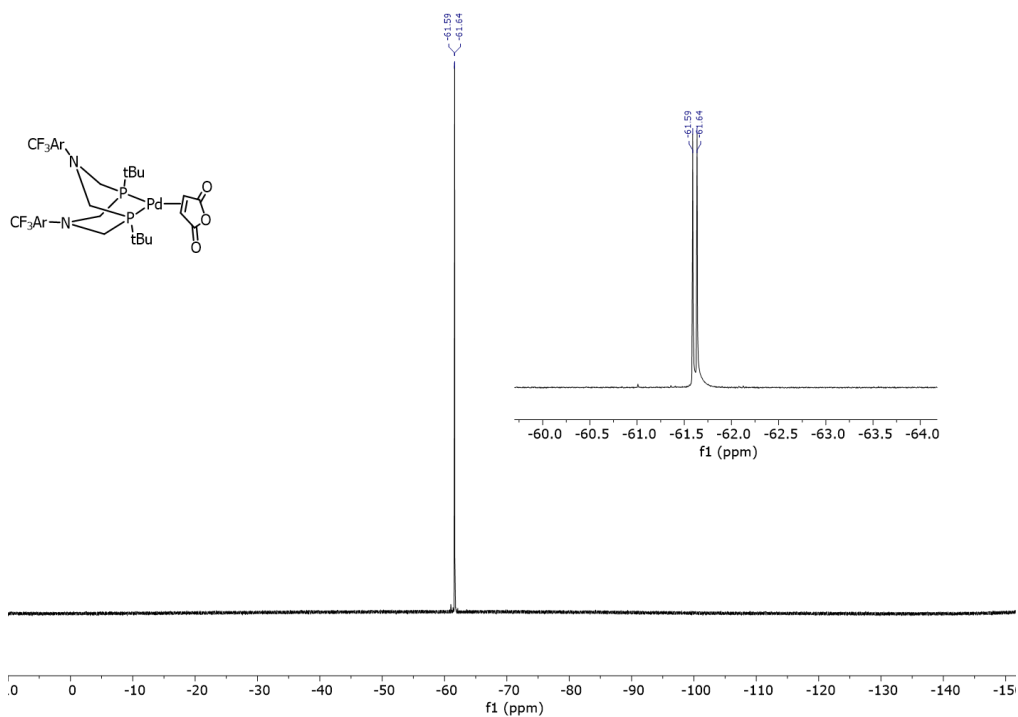


**Figure D-11.**  $^{19}\text{F}$  NMR spectrum of **5-3b** (565 MHz,  $\text{CD}_2\text{Cl}_2$ ).

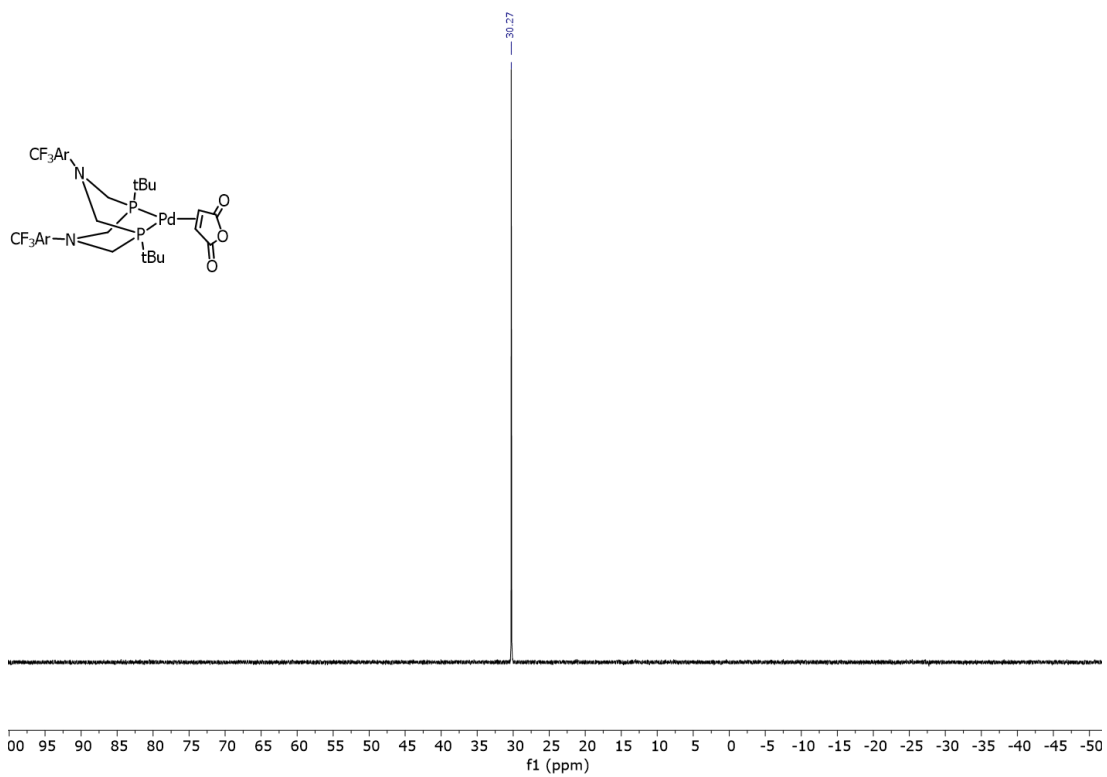


**Figure D-12.**  $^{31}\text{P}\{^1\text{H}\}$  NMR spectrum of **5-3b** (243 MHz,  $\text{CD}_2\text{Cl}_2$ ).

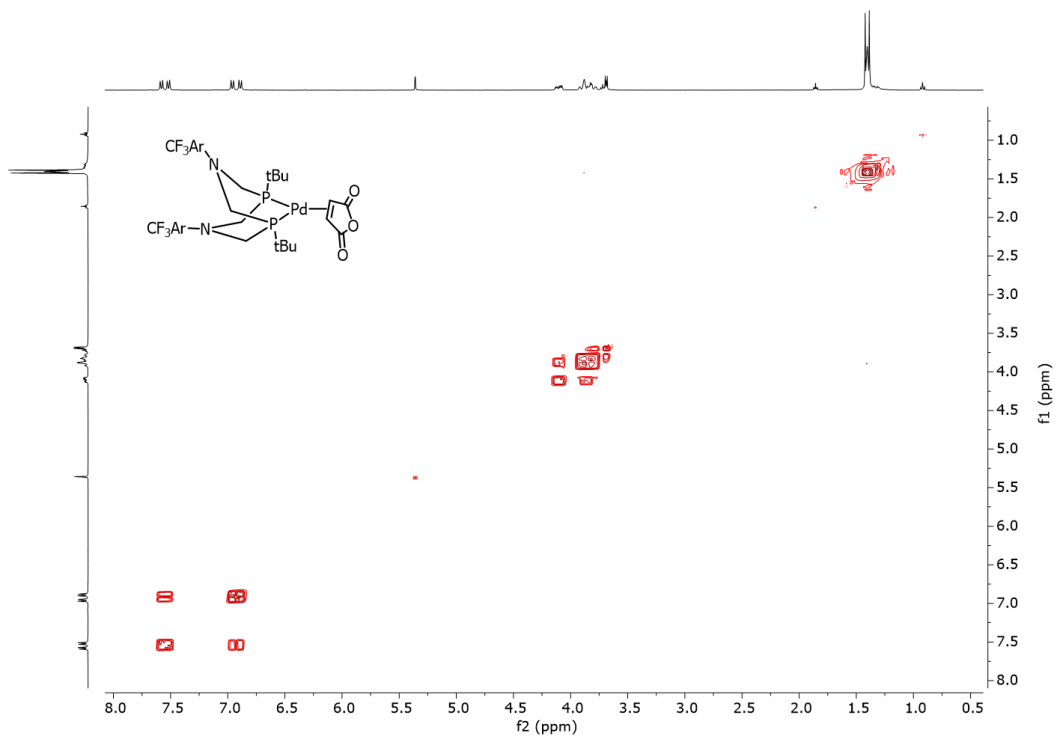


**Figure D-13.**  $^1\text{H}$ - $^1\text{H}$  COSY NMR spectrum of **5-3b** (400 MHz,  $\text{CD}_2\text{Cl}_2$ ).

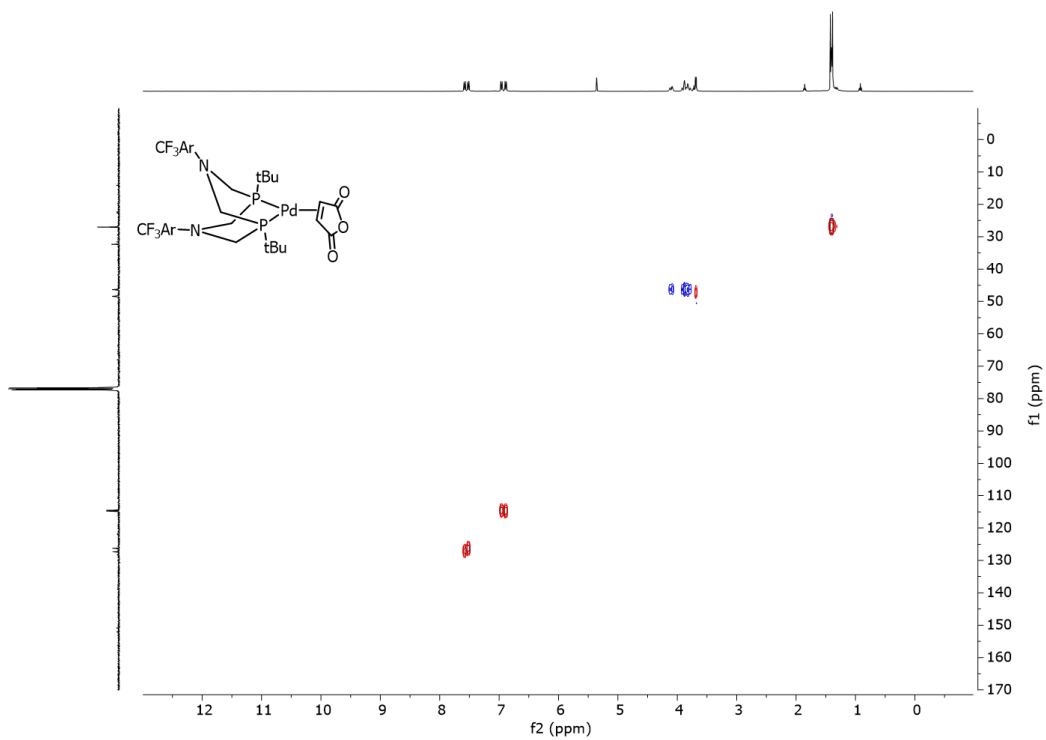


**Figure D-14.**  $^1\text{H}$ - $^{13}\text{C}\{^1\text{H}\}$  HSQC NMR spectrum of **5-3b** (400 MHz,  $\text{CD}_2\text{Cl}_2$ ).



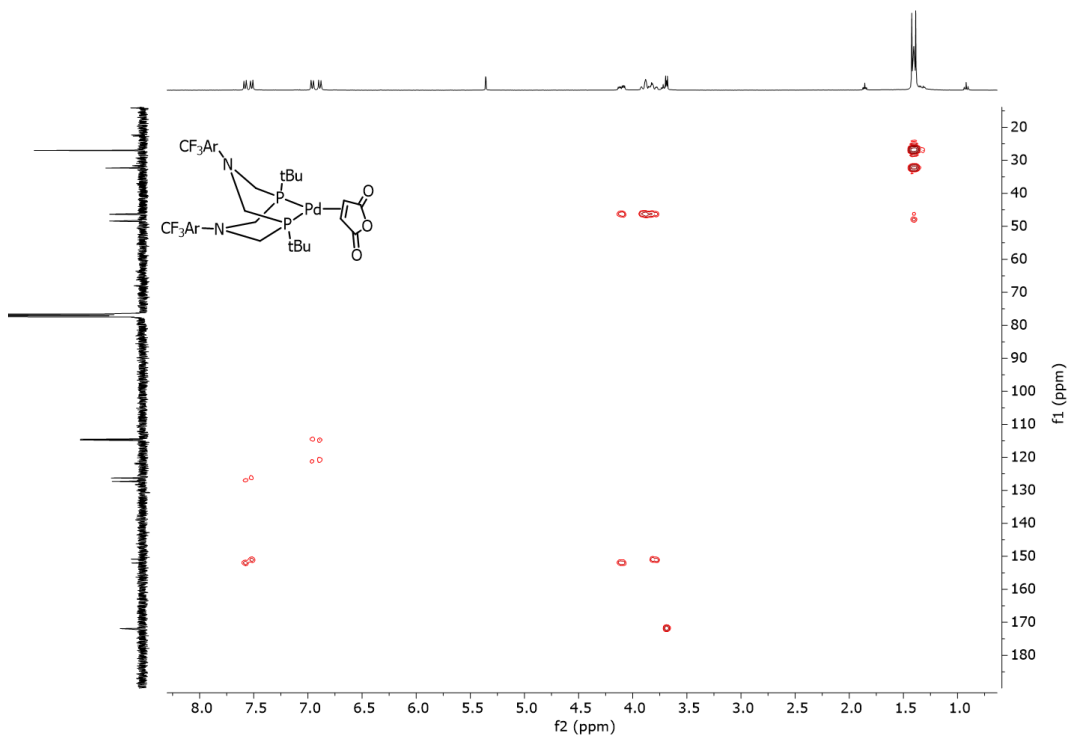


**Figure D-15.**  $^1\text{H}$ - $^{13}\text{C}\{^1\text{H}\}$  HMBC NMR spectrum of **5-3b** (400 MHz,  $\text{CD}_2\text{Cl}_2$ ).

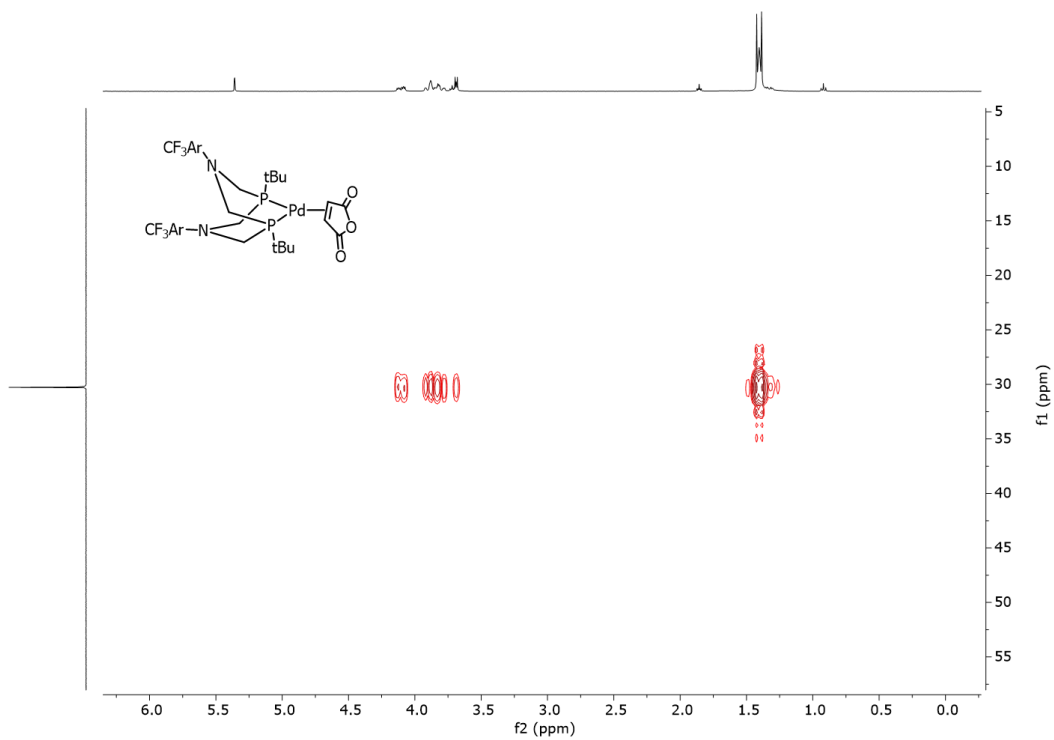


**Figure D-16.**  $^1\text{H}$ - $^{31}\text{P}\{^1\text{H}\}$  HMBC NMR spectrum of **5-3b** (400 MHz,  $\text{CD}_2\text{Cl}_2$ ).

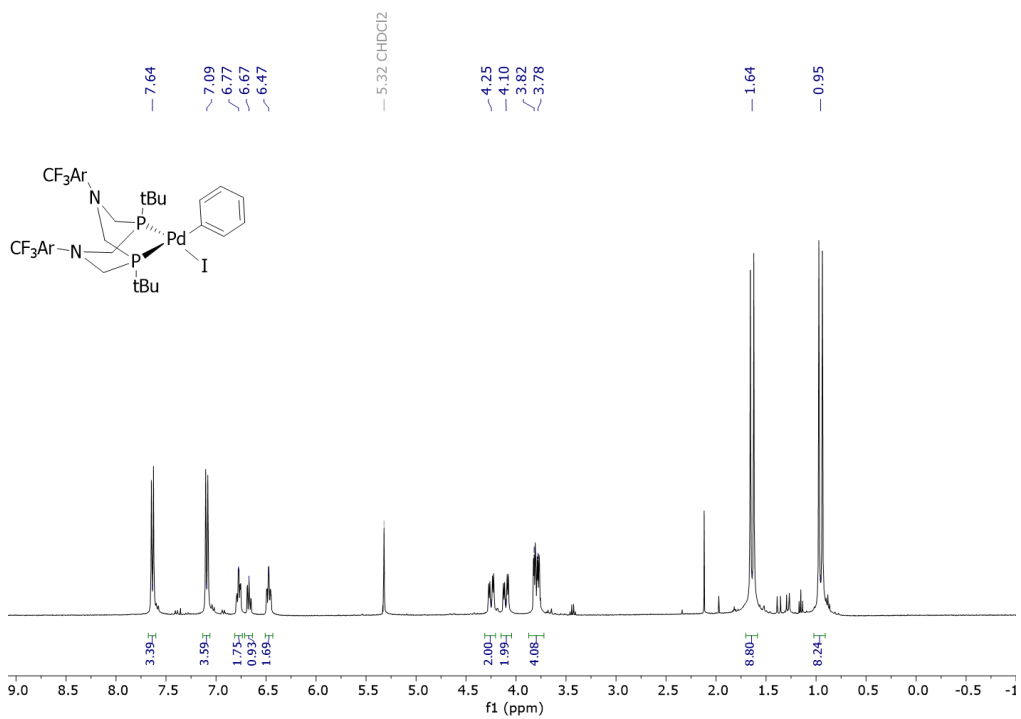


**Figure D-17.**  $^1\text{H}$  NMR spectrum of  $\text{Pd}(\text{Ph})(\text{I})(\text{P}(\text{tBu})_2\text{N}(\text{ArCF}_3)_2)$  (**5-5b**) (400 MHz,  $\text{CD}_2\text{Cl}_2$ ).

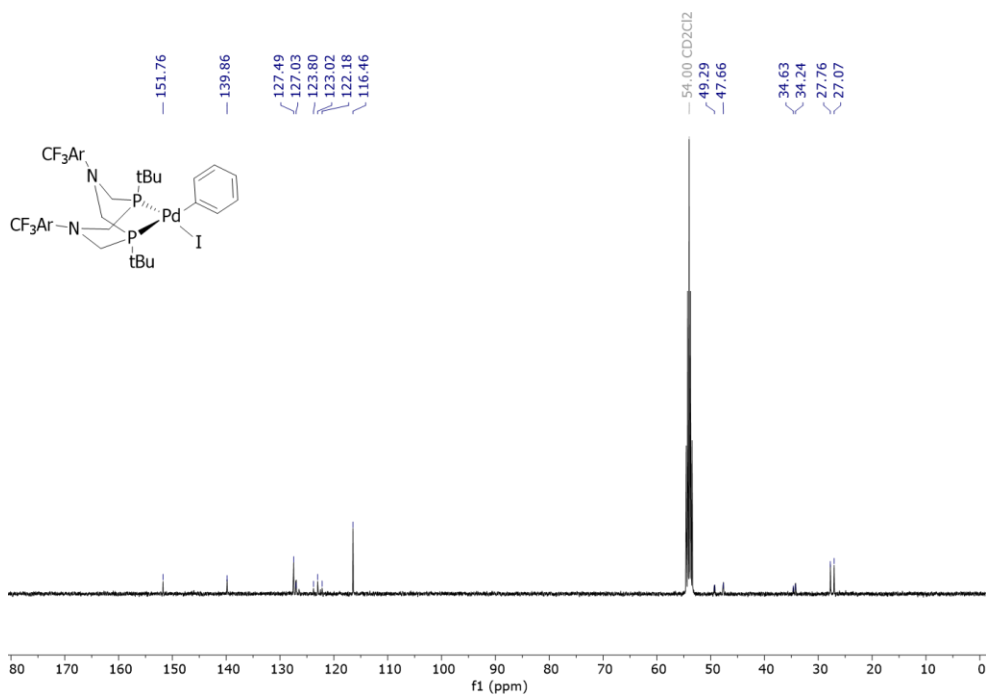


**Figure D-18.**  $^{13}\text{C}\{^1\text{H}\}$  NMR spectrum of **5-5b** (101 MHz,  $\text{CD}_2\text{Cl}_2$ ).

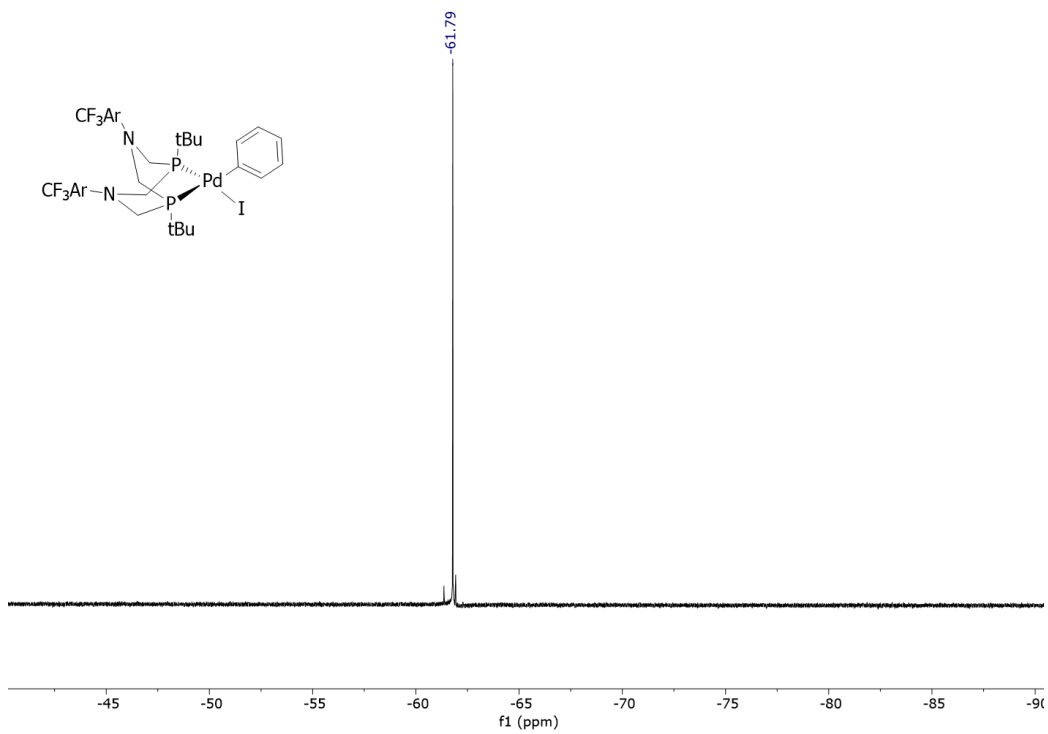


**Figure D-19.** <sup>19</sup>F NMR spectrum of **5-5b** (376 MHz, CD<sub>2</sub>Cl<sub>2</sub>).

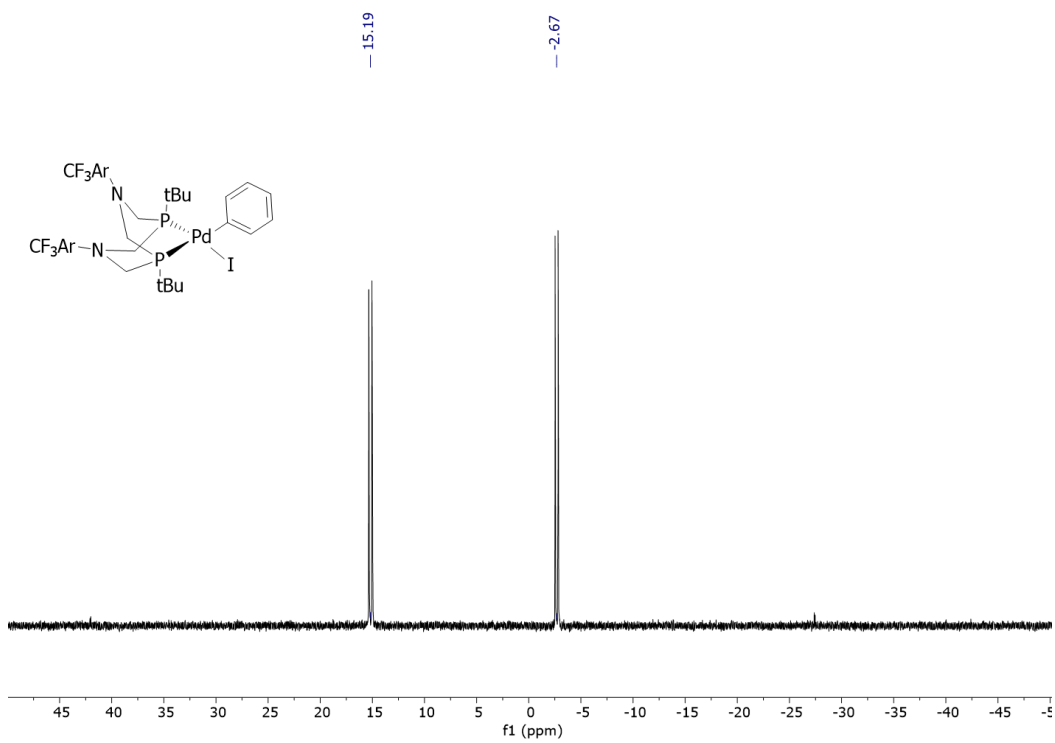


**Figure D-20.** <sup>31</sup>P{<sup>1</sup>H} NMR spectrum of **5-5b** (162 MHz, CD<sub>2</sub>Cl<sub>2</sub>).

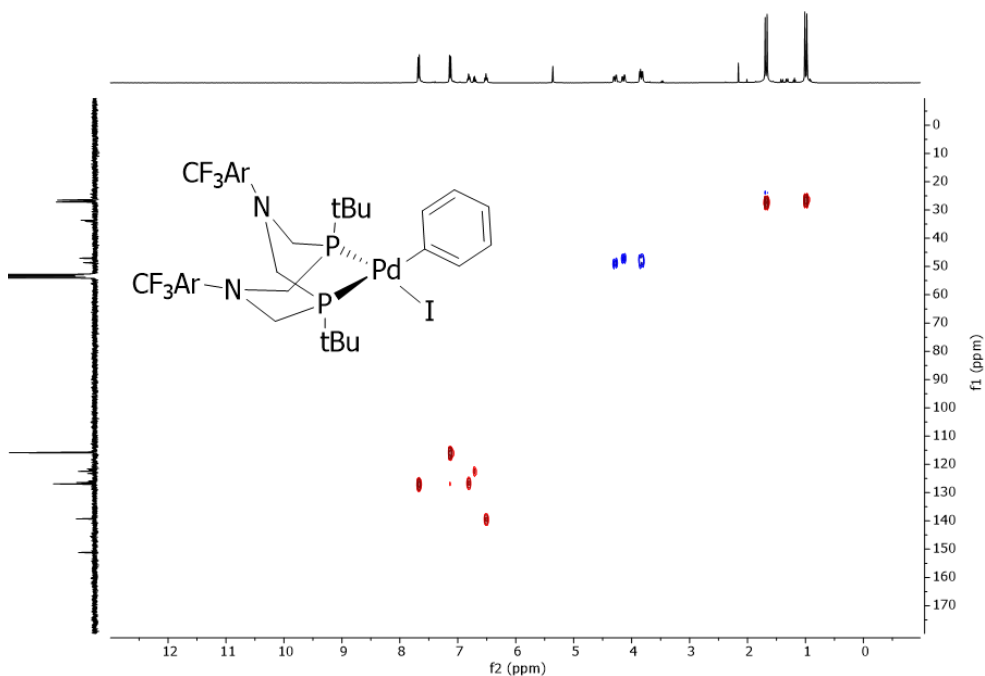


**Figure D-21.**  $^1\text{H}$ - $^{13}\text{C}\{^1\text{H}\}$  HSQC NMR spectrum of **5-5b** (600 MHz,  $\text{CD}_2\text{Cl}_2$ ).

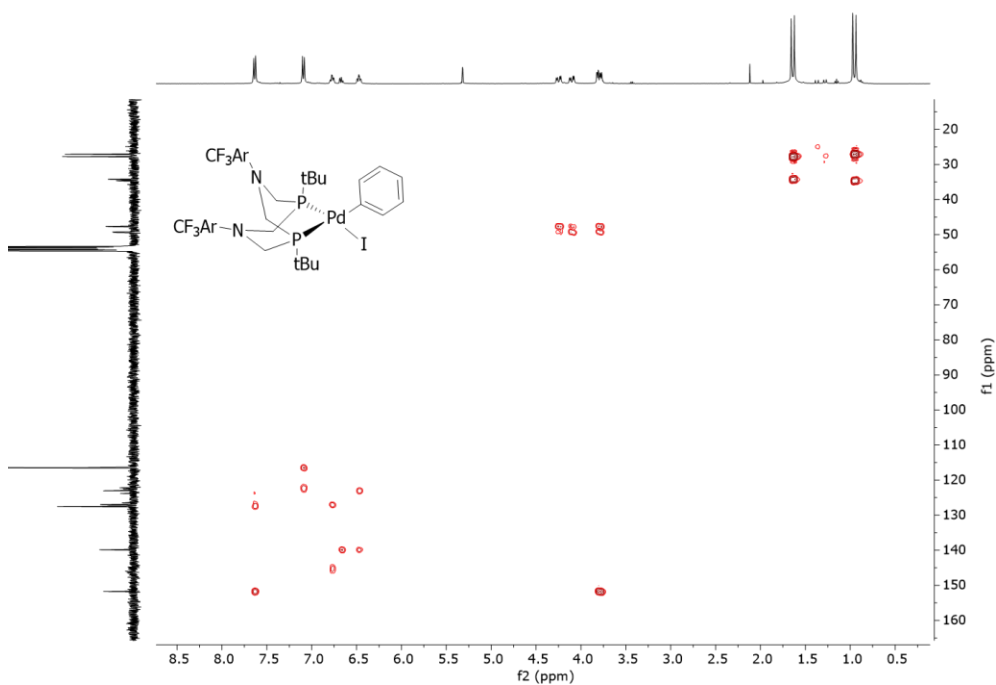


**Figure D-22.**  $^1\text{H}$ - $^{13}\text{C}\{^1\text{H}\}$  HMBC NMR spectrum of **5-5b** (600 MHz,  $\text{CD}_2\text{Cl}_2$ ).

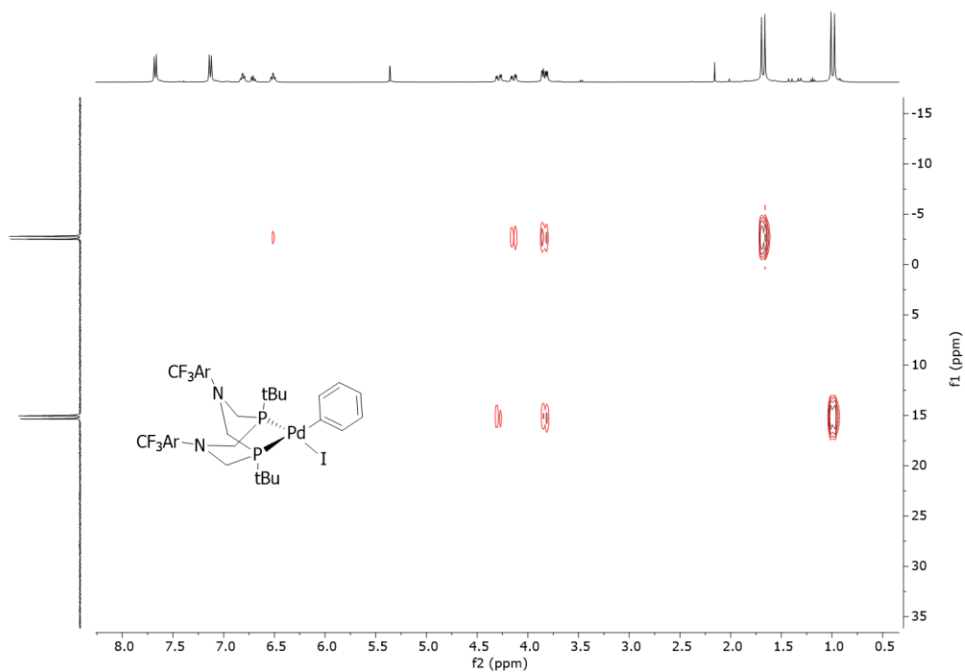


**Figure D-23.**  $^1\text{H}-^{31}\text{P}\{^1\text{H}\}$  HMBC NMR spectrum of **5-5b** (600 MHz,  $\text{CD}_2\text{Cl}_2$ ).

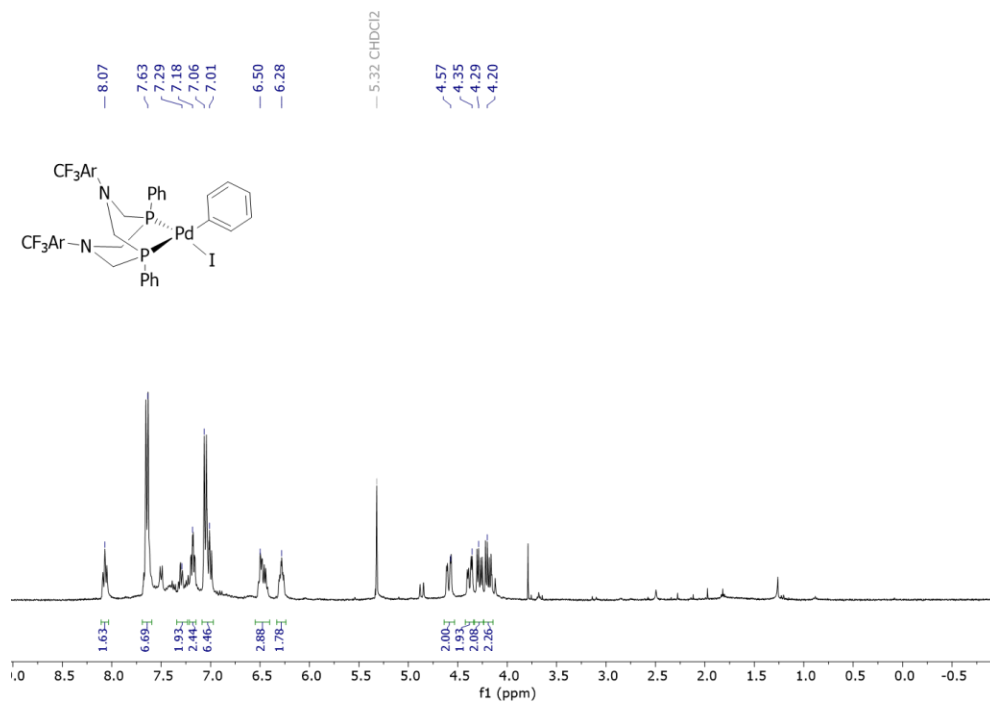


**Figure D-24.**  $^1\text{H}$  NMR spectrum of  $\text{Pd}(\text{Ph})(\text{I})(\text{P}^{\text{Ph}}\text{N}^{\text{Ar}}\text{CF}_3)_2$  (**5-5a**) (400 MHz,  $\text{CD}_2\text{Cl}_2$ ).

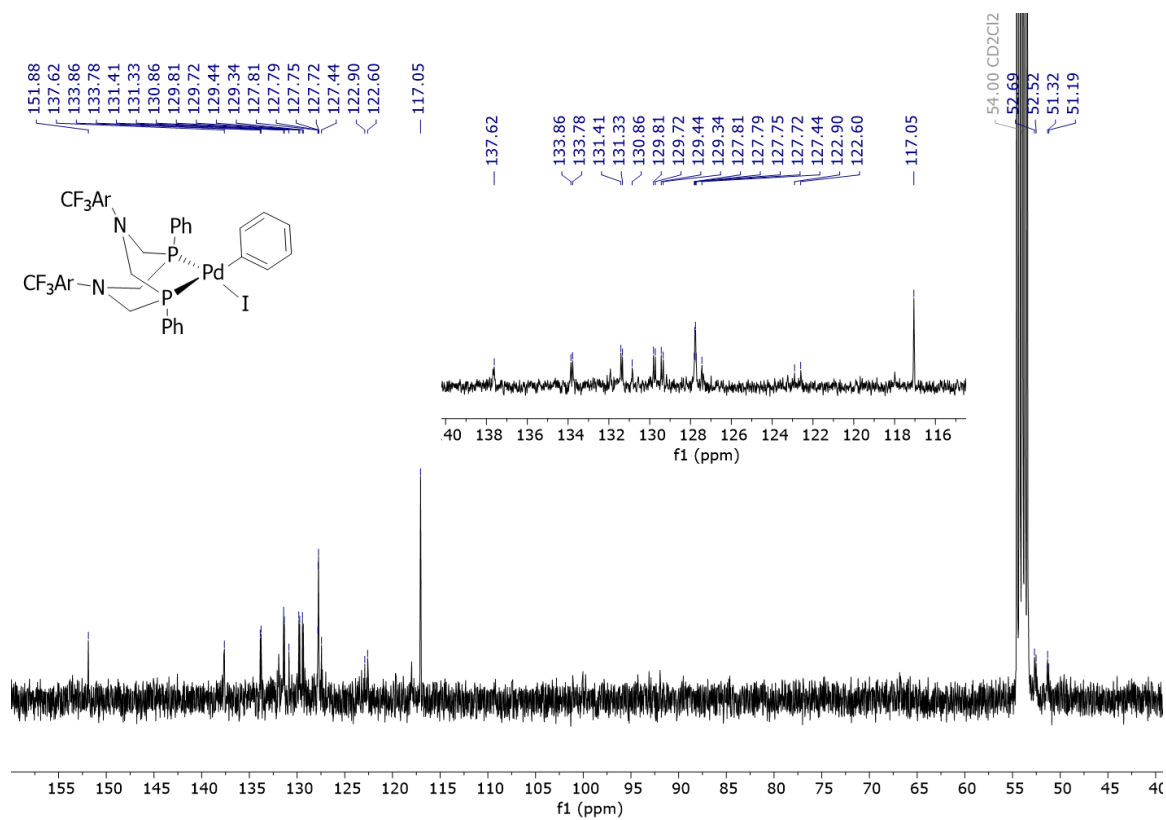


**Figure D-25.**  $^{13}\text{C}\{^1\text{H}\}$  NMR spectrum of **5-5a** (101 MHz,  $\text{CD}_2\text{Cl}_2$ ).

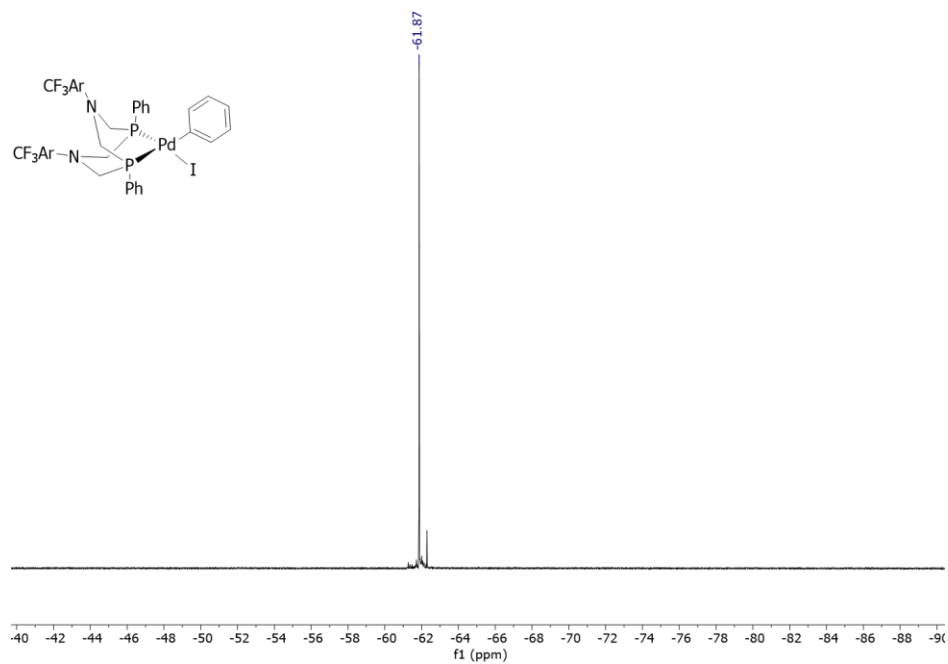


**Figure D-26.**  $^{19}\text{F}$  NMR spectrum of **5-5a** (565 MHz,  $\text{CD}_2\text{Cl}_2$ ).

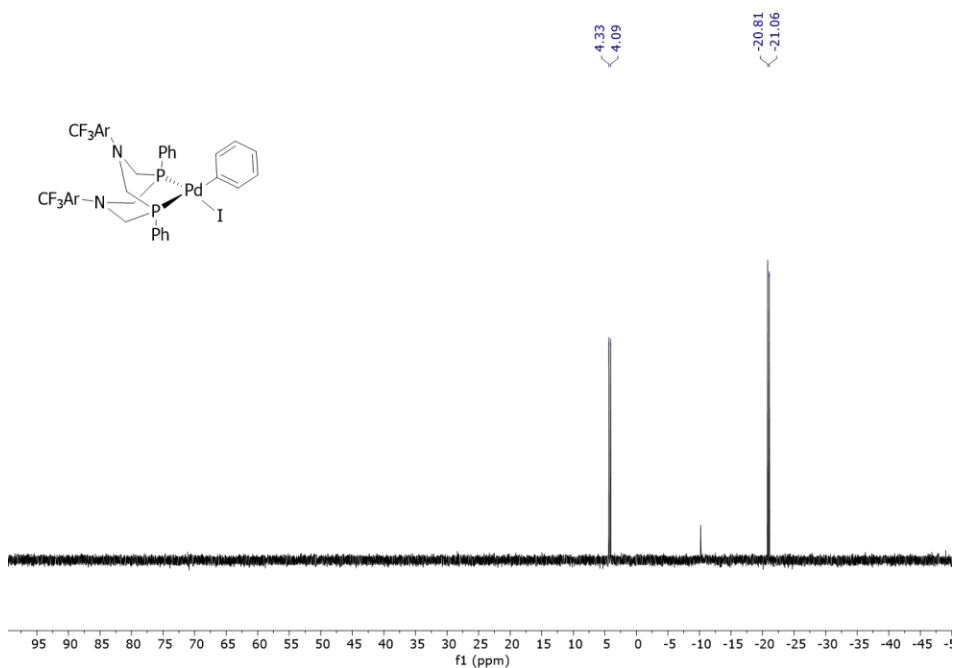


**Figure D-27.**  $^{31}\text{P}\{^1\text{H}\}$  NMR spectrum of **5-5a** (243 MHz,  $\text{CD}_2\text{Cl}_2$ ).

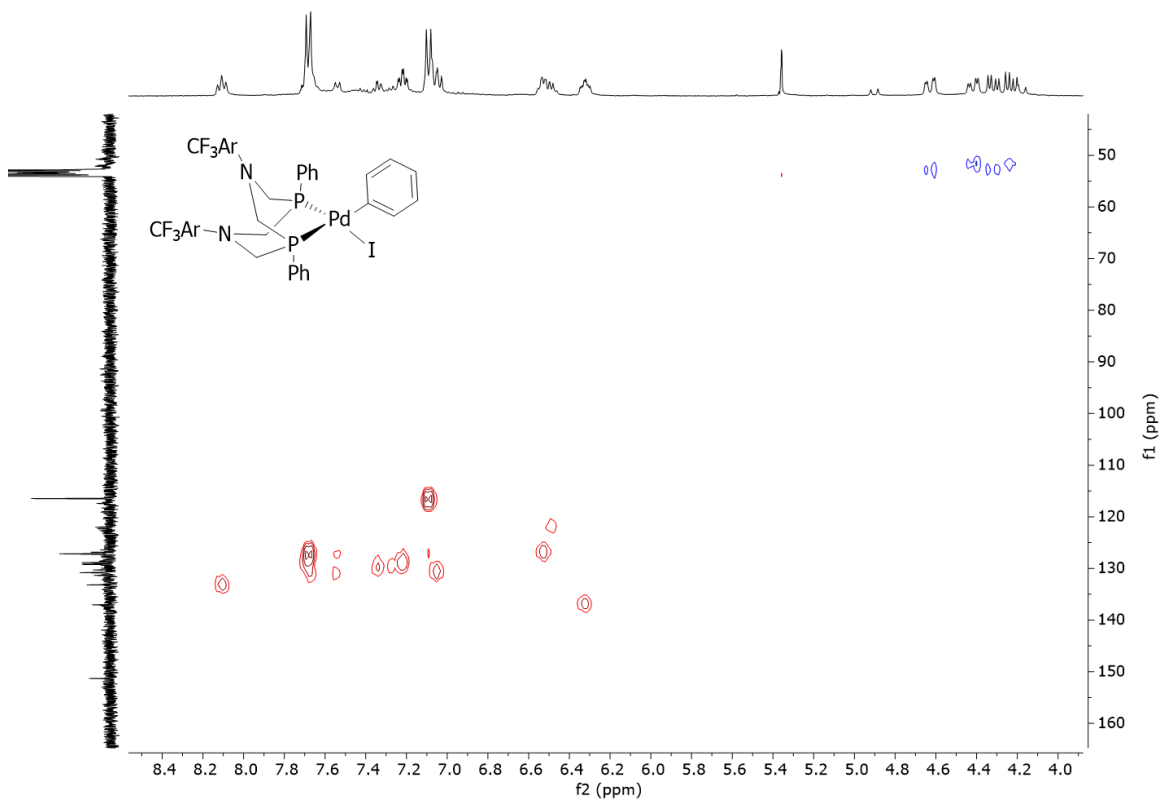


**Figure D-28.**  $^1\text{H}\text{-}^{13}\text{C}\{^1\text{H}\}$  HSQC NMR spectrum of **5-5a** (400 MHz,  $\text{CD}_2\text{Cl}_2$ ).

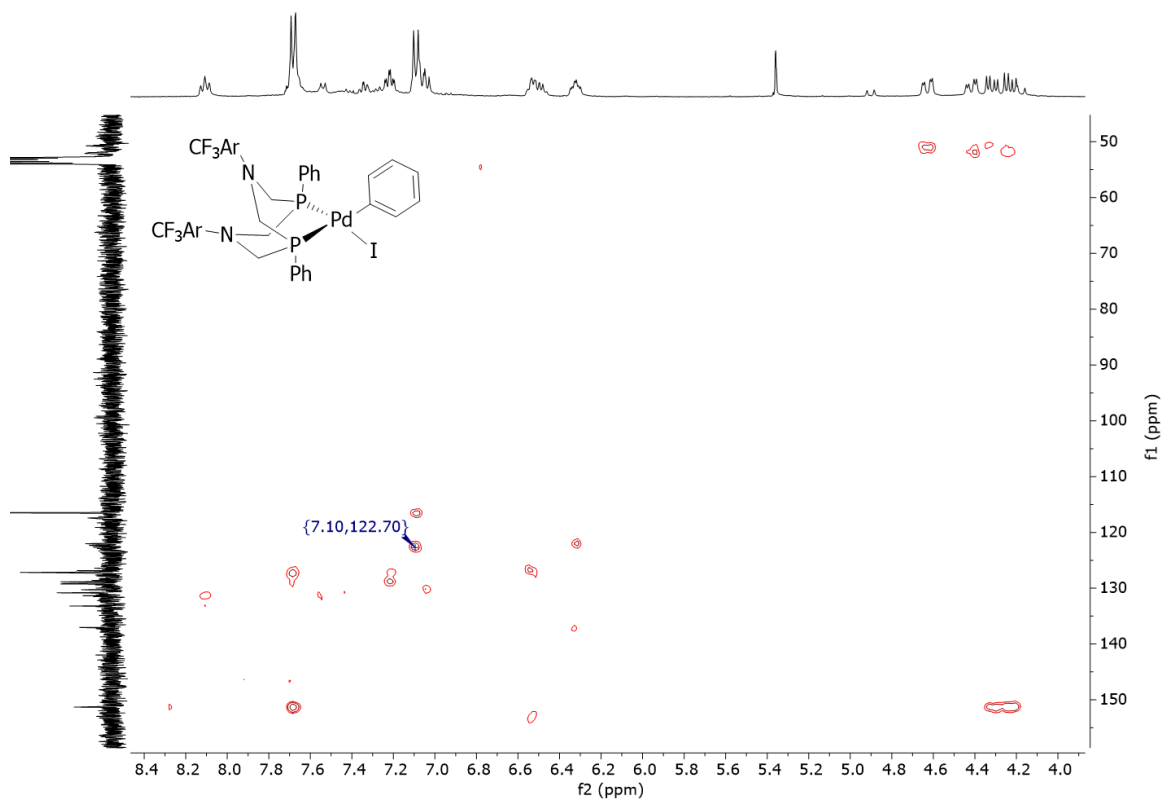


**Figure D-29.**  $^1\text{H}$ - $^{13}\text{C}\{^1\text{H}\}$  HMBC NMR spectrum of **5-5a** (400 MHz,  $\text{CD}_2\text{Cl}_2$ ).

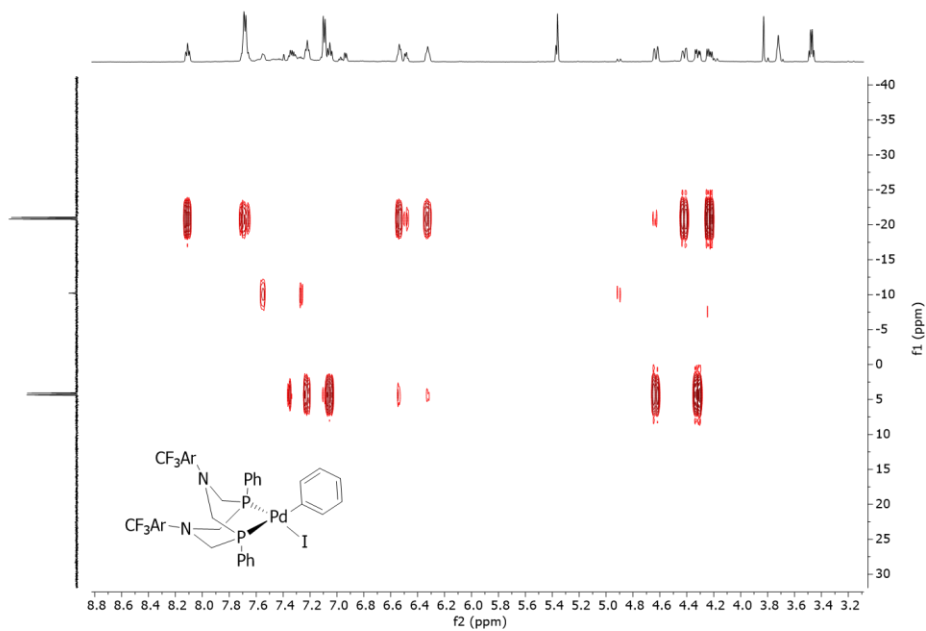


**Figure D-30.**  $^1\text{H}$ - $^{31}\text{P}\{^1\text{H}\}$  HMBC spectrum of **5-5a** (400 MHz,  $\text{CD}_2\text{Cl}_2$ ).



## IR Spectra

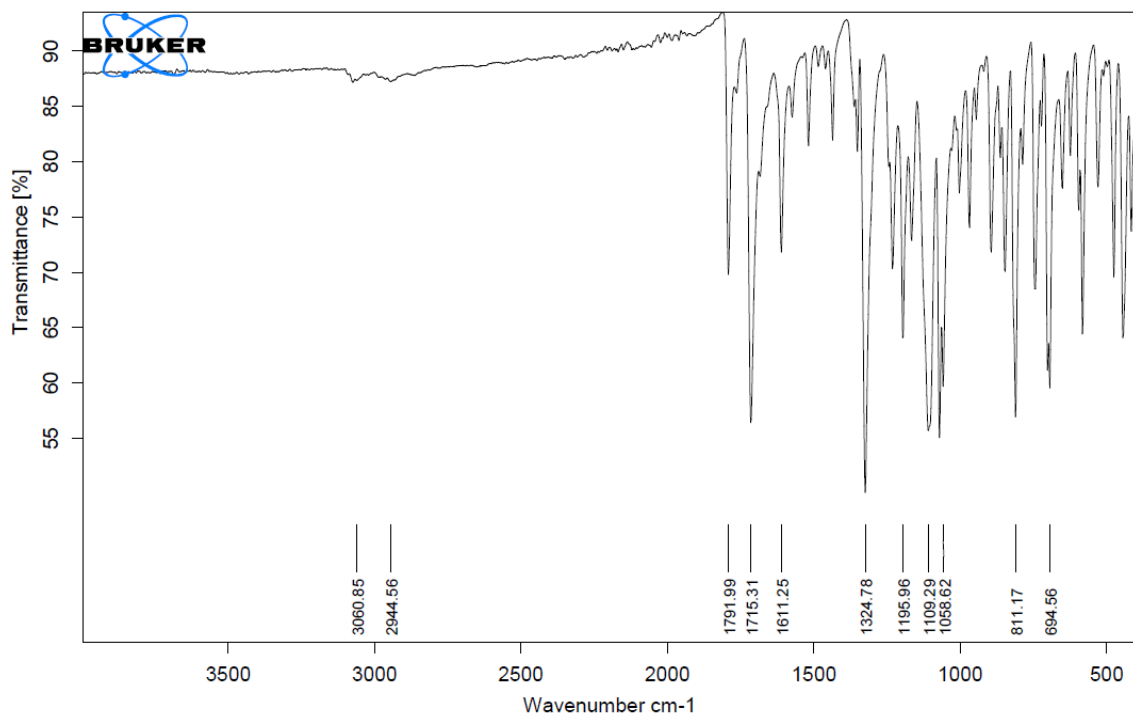


**Figure D-31.** ATR-FTIR spectrum of solid **5-3a**.

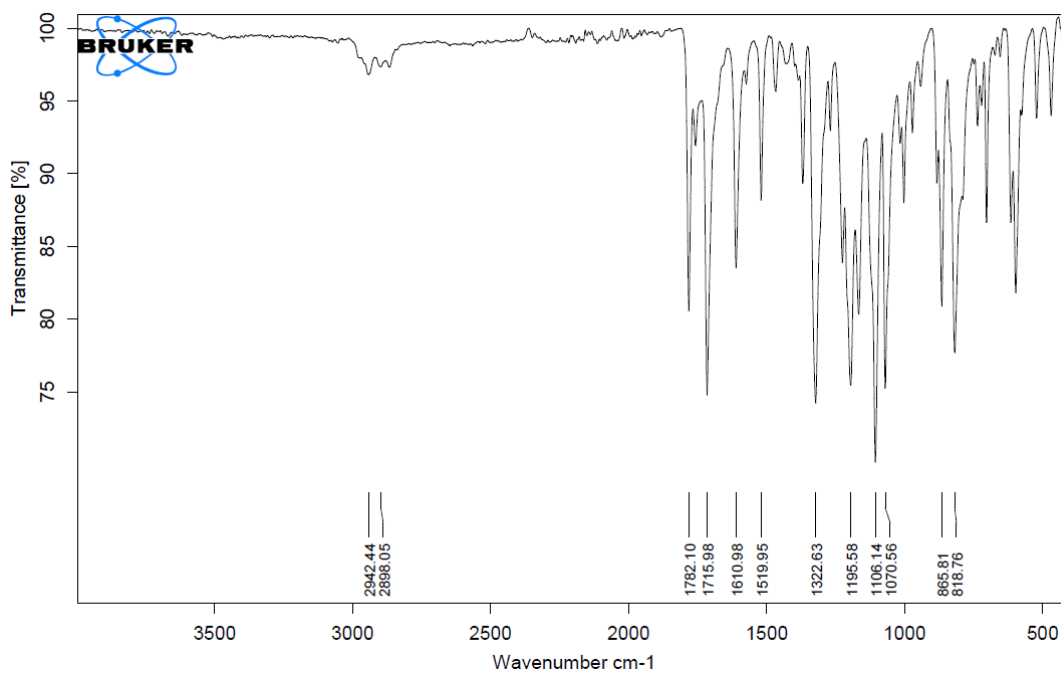


**Figure D-32.** ATR-FTIR spectrum of solid **5-3b**.

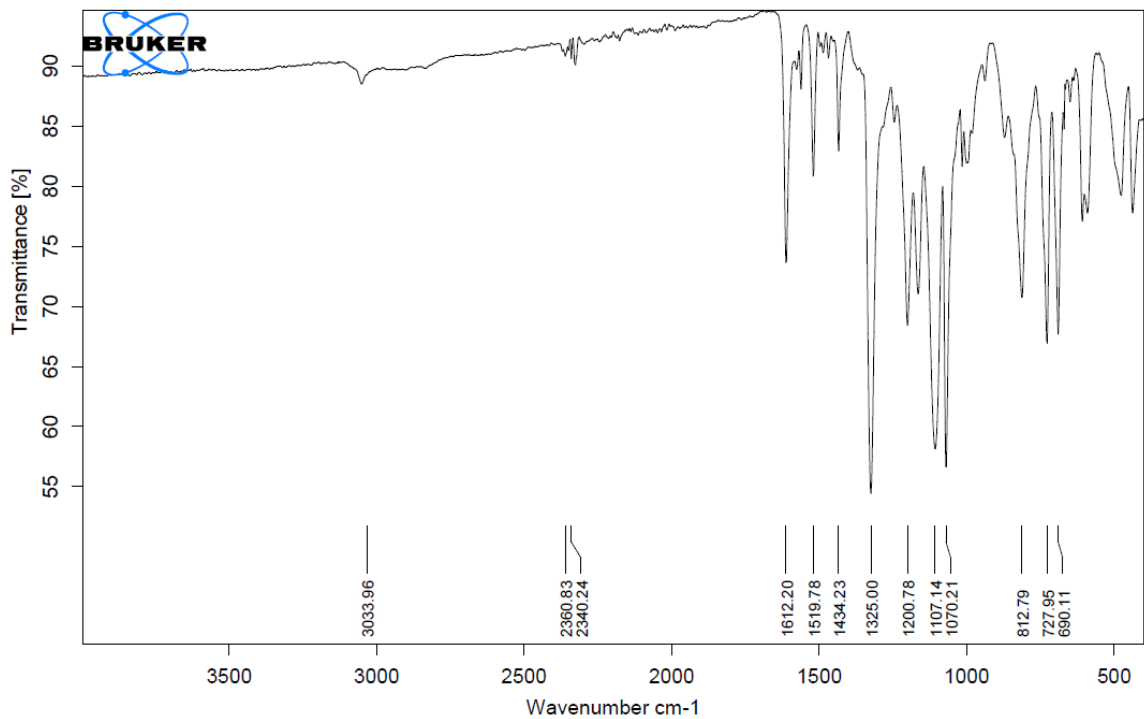


**Figure D-33.** ATR-FTIR spectrum of solid **5-5a**.

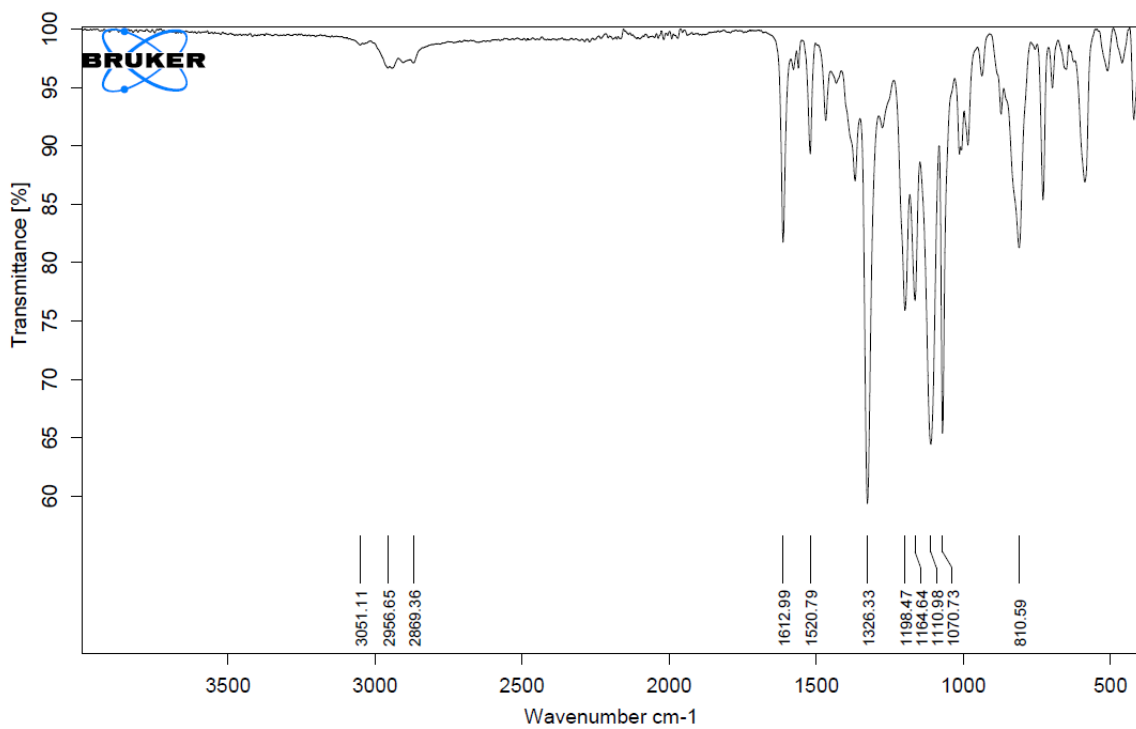


**Figure D-34.** ATR-FTIR spectrum of solid **5-5b**.

## MALDI

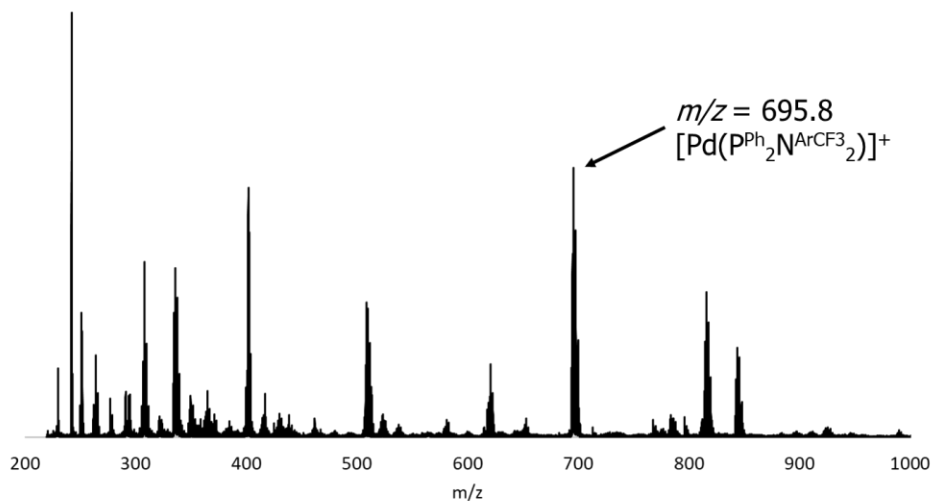


**Figure D-35.** MALDI-TOF mass spectrum of **5-3a** with pyrene as the matrix (1:20 molar ratio)

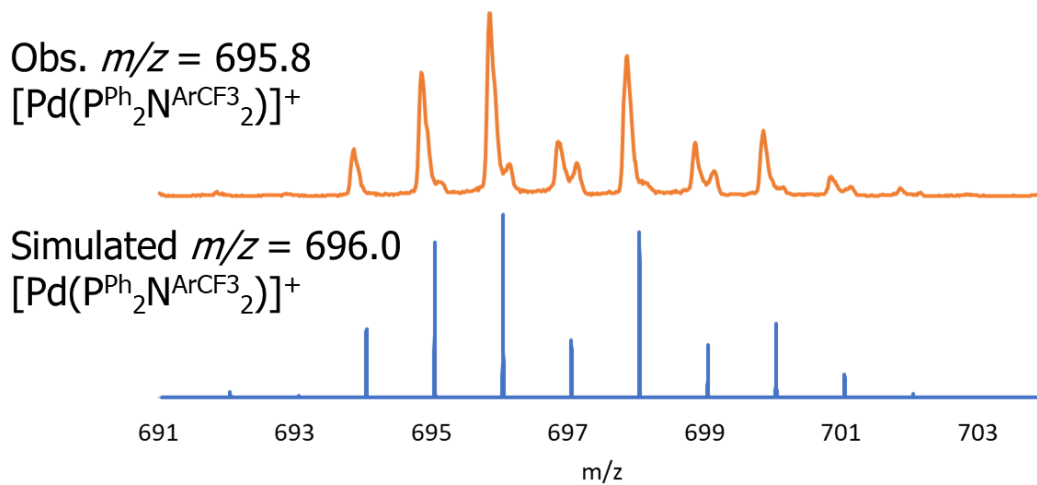


**Figure D-36.** Zoom-in of the observed MALDI-TOF mass spectrum signal of  $[\text{Pd}(\text{P}^{\text{Ph}}_2\text{N}^{\text{ArCF}_3}_2)]^+$  (top) at  $m/z = 695.8$ ; and simulated signal (bottom) with  $m/z = 696.0$  for  $[\text{Pd}(\text{P}^{\text{Ph}}_2\text{N}^{\text{ArCF}_3}_2)]^+$ .

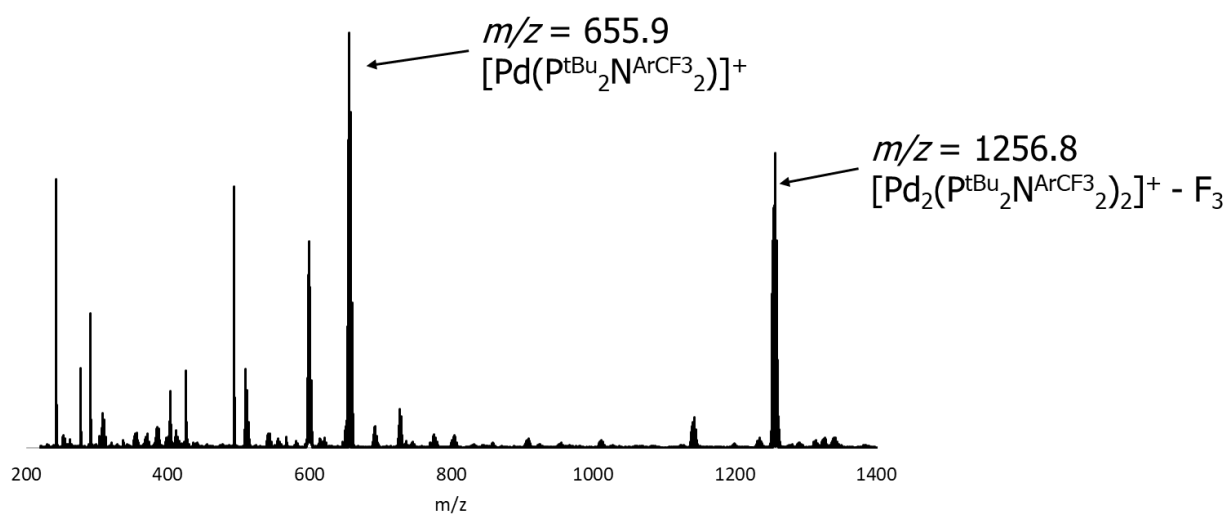


**Figure D-37.** MALDI-TOF mass spectrum of **5-3b** with pyrene as the matrix (1:20 molar ratio)

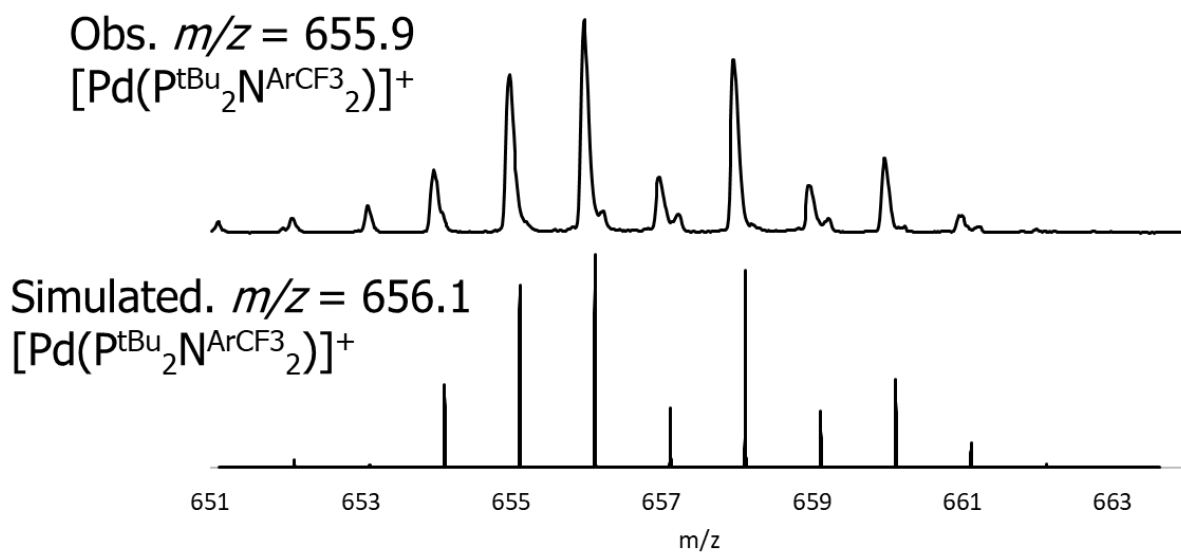


**Figure D-38.** Zoom-in of the observed MALDI-TOF mass spectrum signal of  $[\text{Pd}(\text{P}^{\text{tBu}}_2\text{N}^{\text{ArCF}_3}_2)]^+$  (top) at  $m/z = 655.9$ ; and simulated signal (bottom) with  $m/z = 656.1$  for  $[\text{Pd}(\text{P}^{\text{tBu}}_2\text{N}^{\text{ArCF}_3}_2)]^+$ .

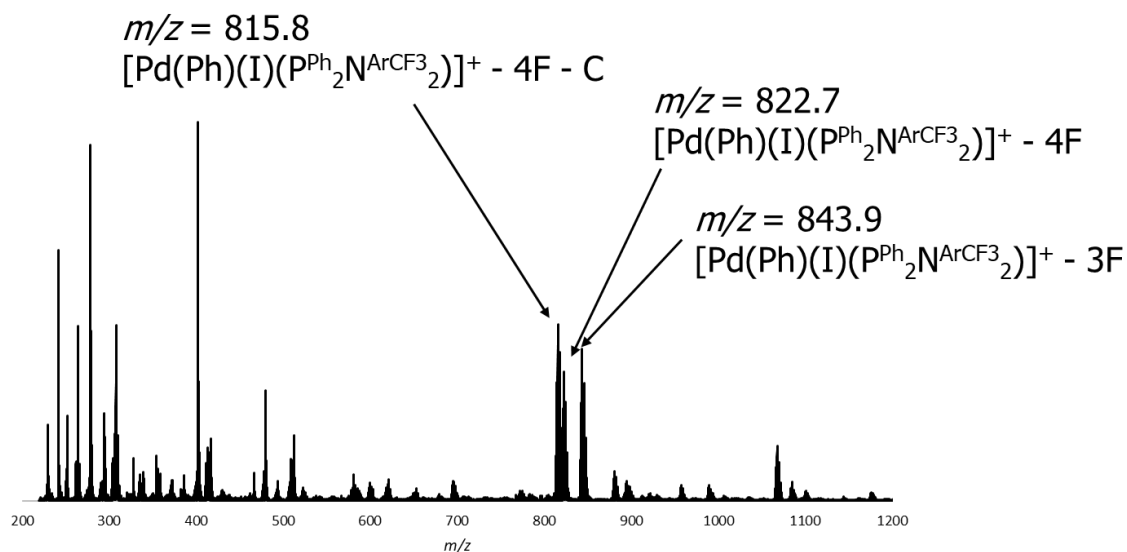


**Figure D-39.** MALDI-TOF mass spectrum of **5-5a** with pyrene as the matrix (1:20 molar ratio)

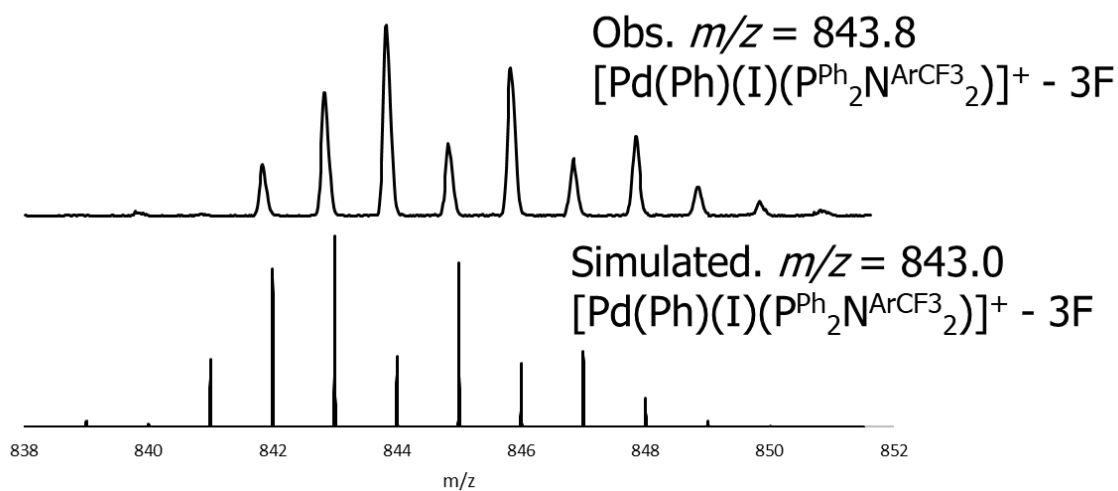


**Figure D-40.** Zoom-in of the observed MALDI-TOF mass spectrum signal of  $[\text{Pd}(\text{Ph})(\text{I})(\text{P}^{\text{Ph}}_2\text{N}^{\text{ArCF}_3}_2)]^+ - 3\text{F}$  (top) at  $m/z = 843.8$ ; and simulated signal (bottom) with  $m/z = 843.0$  for  $[\text{Pd}(\text{Ph})(\text{I})(\text{P}^{\text{Ph}}_2\text{N}^{\text{ArCF}_3}_2)]^+ - 3\text{F}$ .

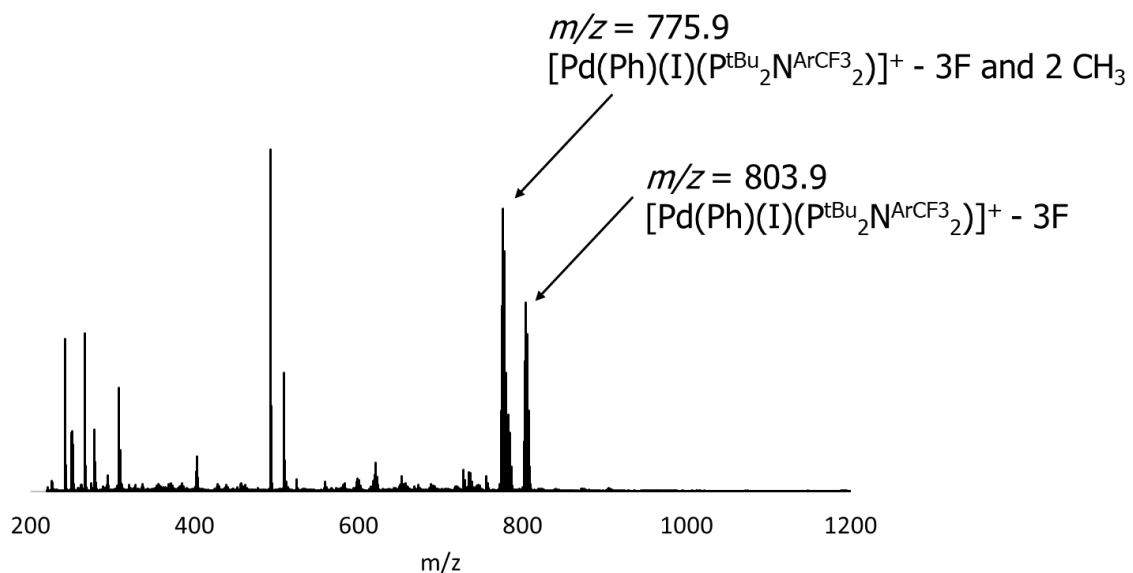


**Figure D-41.** MALDI-TOF mass spectrum of **5-5b** with pyrene as the matrix (1:20 molar ratio)

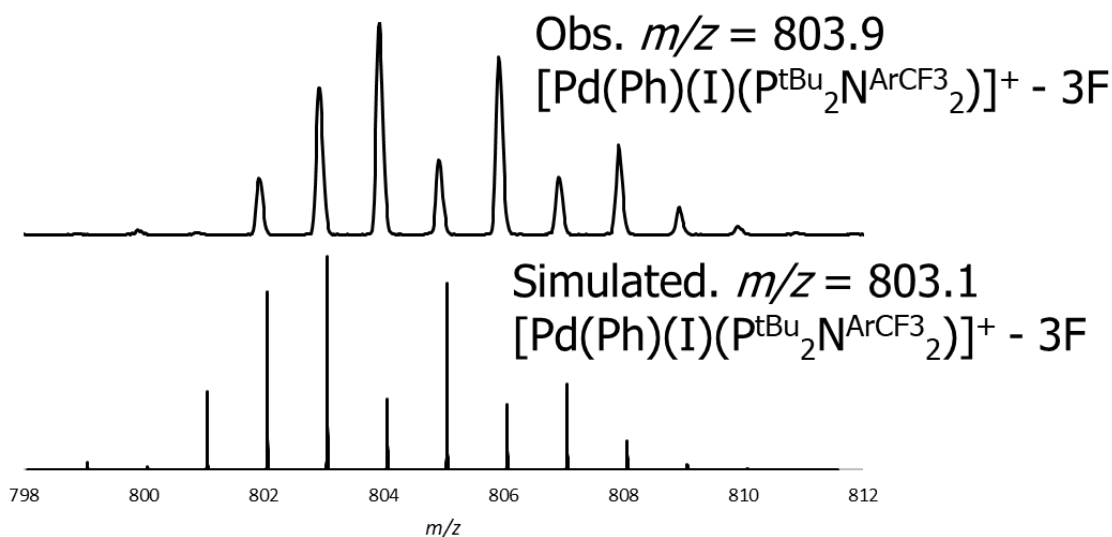


**Figure D-42.** Zoom-in of the observed MALDI-TOF mass spectrum signal of  $[\text{Pd}(\text{Ph})(\text{I})(\text{P}^{\text{tBu}}_2\text{N}^{\text{ArCF}_3}_2)]^+ - 3\text{F}$  (top) at  $m/z = 803.9$ ; and simulated signal (bottom) with  $m/z = 803.1$  for  $[\text{Pd}(\text{Ph})(\text{I})(\text{P}^{\text{tBu}}_2\text{N}^{\text{ArCF}_3}_2)]^+ - 3\text{F}$ .

## Crystallographic Details

*Data Collection and Processing.* Sample of **5-2a**, **5-5-3a**, **5-3b**, and **5-5a** were mounted on a Mitegen polyimide micromount with a small amount of Paratone N oil. All X-ray measurements were made on a Bruker Kappa Axis Apex2 diffractometer at a temperature of 110 K. The data collection strategy was a number of  $\omega$  and  $\phi$  scans which collected data up to  $2\theta_{\max}$  as listed in Table D-X. The frame integration was performed using SAINT.<sup>1</sup> The resulting raw data was scaled and absorption corrected using a multi-scan averaging of symmetry equivalent data using SADABS.<sup>2</sup>

*Structure Solution and Refinement.* The structure for **5-3a** was solved by using a dual space methodology using the SHELXT program.<sup>3</sup> Most non-hydrogen atoms were obtained from the initial solution. The remaining atomic positions were obtained from difference Fourier maps. The hydrogen atoms were introduced at idealized positions and were allowed to ride on the parent atom. Both CF<sub>3</sub> groups were disordered. The occupations for the predominant rotamers refined to values 0.759(10) and 0.72(2) for the CF<sub>3</sub> groups contains atoms C21{F1,F2,F3} and C34{F4,F5,F6} respectively. The CH<sub>2</sub>Cl<sub>2</sub> of solvation was also disordered by rotation about the C35-C11 bond to give two distinct positions for the Cl2 atom. The occupancy for the predominant orientation refined to a value of 0.512(8). The structural model was fit to the data using full matrix least-squares based on  $F^2$ . The calculated structure factors included corrections for anomalous dispersion from the usual tabulation. The structure was refined using the SHELXL program from the SHELX suite of crystallographic software.<sup>4</sup> Graphic plots were produced using the Mercury program suite.<sup>5</sup>

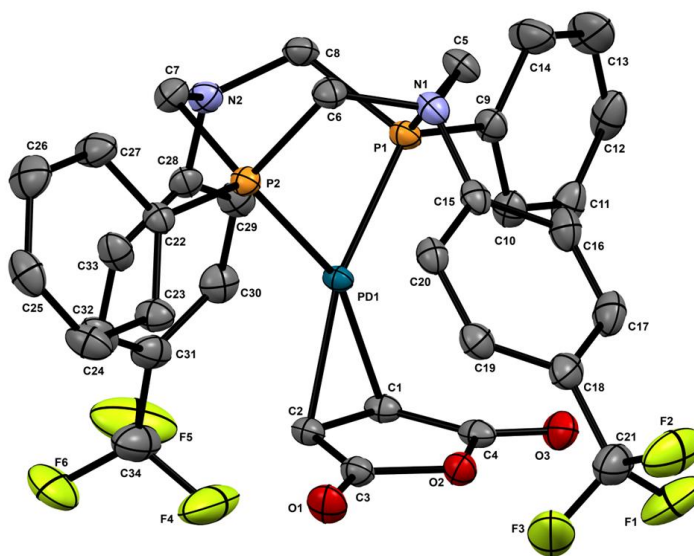


**Figure D-43.** ORTEP drawing of **5-3a** showing naming and numbering scheme. Ellipsoids are at the 50% probability level and hydrogen atoms and disordered fluorine atoms were omitted for clarity.

*Structure Solution and Refinement.* The structure of **5-3b** was solved by using a dual space methodology using the SHELXT program.<sup>3</sup> Most non-hydrogen atoms were obtained from the initial solution. The remaining atomic positions were obtained from subsequent difference Fourier maps. The hydrogen atoms were introduced at idealized positions and were allowed to ride on the parent atom. The CF<sub>3</sub>-aryl group bound to atom N2 was disordered over two positions. The disorder could be described as a small rotation about an axis passing through N2 and running perpendicular to the C6-C8-C16 plane. The angle subtended from N2 to the *para* carbon positions (C19 and C19') was 6.75°. The occupancy factor for the major component refined to a value of 0.501(8). The asymmetric unit also included a 0.5 of CH<sub>2</sub>Cl<sub>2</sub> molecule which resided on a crystallographic glide plane. In addition, another CH<sub>2</sub>Cl<sub>2</sub> molecule was fractionally occupied and disordered across a glide as well. The occupancy for this second CH<sub>2</sub>Cl<sub>2</sub> molecule refined to a value of 0.175(3). The structural model was fit to the data using full matrix least-squares based on  $F^2$ . The calculated structure factors included corrections for anomalous dispersion from the usual tabulation. The structure was refined using the SHELXL program from the SHELX suite



of crystallographic software.<sup>4</sup> Graphic plots were produced using the Mercury program suite.<sup>5</sup>

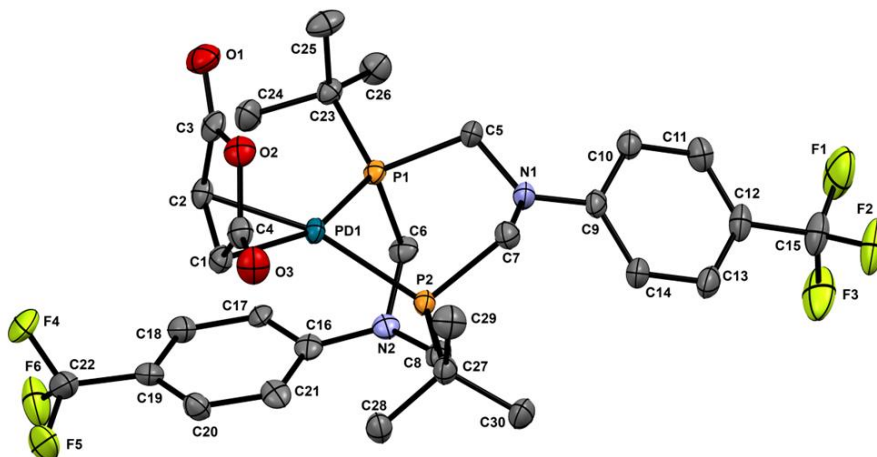


**Figure D-44.** ORTEP drawing of **5-3b** showing naming and numbering scheme. Ellipsoids are at the 50% probability level and hydrogen atoms were omitted for clarity. The minor component of the disordered CF<sub>3</sub>-aryl group was also omitted for clarity.

*Structure Solution and Refinement.* The structure of **5-2a** was solved by using a dual space methodology using the SHELXT program.<sup>3</sup> All non-hydrogen atoms were obtained from the initial solution. The asymmetric unit contained four symmetry independent complexes and their corresponding anions as well as several CH<sub>2</sub>Cl<sub>2</sub> molecules of solvation. Some of the solvent molecules were disordered over several sites. For this reason, the solvent contributions to the X-ray scattering subjected to a solvent masking procedure as implemented by the SQUEEZE routine included in the PLATON program.<sup>6</sup> The hydrogen atoms were introduced at idealized positions and were allowed to ride on the parent atom. The structural model was fit to the data using full matrix least-squares based on  $F^2$ . The calculated structure factors included corrections for anomalous dispersion from the usual tabulation. The structure was refined using the SHELXL program from the SHELX suite of crystallographic software.<sup>4</sup> Graphic plots were produced using the Mercury program.<sup>5</sup>

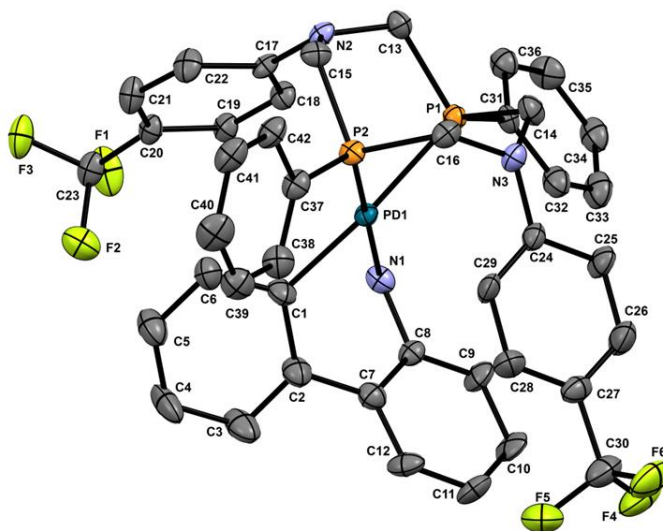


**Figure D-45.** ORTEP drawing of **5-2a** representative cation showing naming and numbering scheme. Ellipsoids are at the 50% probability level and hydrogen atoms were omitted for clarity.

*Structure Solution and Refinement.* The structure of **5-5a** was solved by using a dual space methodology using the SHELXT program.<sup>3</sup> Most non-hydrogen atoms were obtained from the initial solution. The remaining atom positions were recovered from subsequent difference Fourier maps. The hydrogen atoms were introduced at idealized positions and were allowed to ride on the parent atom. The compound exhibited a number of disorders. The sample crystal was compositionally disordered between (L)(I)Pd-C<sub>6</sub>H<sub>5</sub> and (L)PdI<sub>2</sub>. The phenyl derivative was the predominant component and its occupancy refined to a value of 0.8306(16). In addition to the compositional disorder, the molecule also exhibited two orientational disorders. The first orientational disorder involved the CF<sub>3</sub> group containing atom C30. The occupancy of the predominant orientation of the CF<sub>3</sub> group refined to a value of 0.853(7). The second orientation disorder occurred in the phenyl ring containing atom C31. The two orientations were rotated by approximately 43° relative to one another. The occupancy of the predominant orientation refined to a value of 0.832(9). The structural model was fit to the data using full matrix least-squares based on  $F^2$ . The calculated structure factors included corrections for anomalous dispersion from the usual tabulation. The structure was refined using the SHELXL program from the SHELX suite of crystallographic software.<sup>4</sup> Graphic plots were produced using the Mercury program.<sup>5</sup>

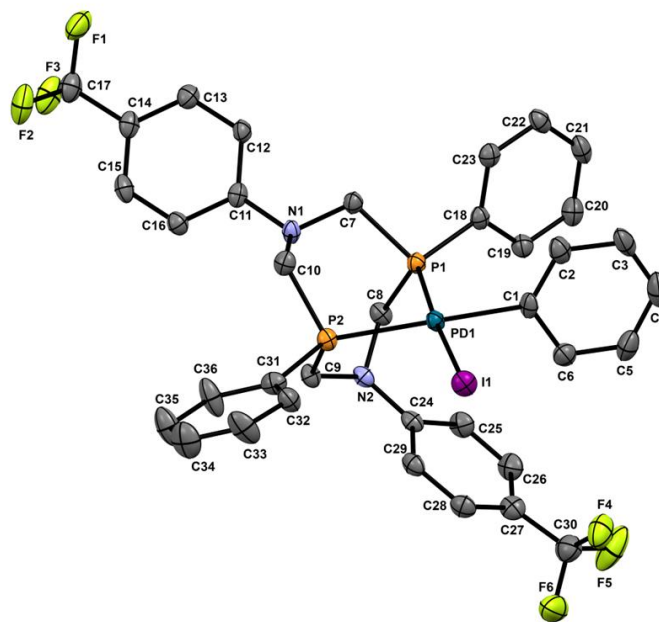


**Figure D-46.** ORTEP drawing of **5-5a** with disorder omitted showing naming and numbering scheme. Ellipsoids are at the 50% probability level and hydrogen atoms were omitted for clarity.

**Table D-1.** Summary of crystal data for **5-3a**, **5-3b**, **5-2a**, and **5-5a**.

Compound	<b>5-3a</b>	<b>5-3b</b>	<b>5-2a</b>	<b>5-5a</b>
Formula	$C_{35}H_{30}Cl_2F_6N_2O_3P_2Pd$	$C_{30.67}H_{37.35}Cl_{1.35}F_6N_2O_3P_2Pd$	$C_{43}H_{39}F_6N_3O_3P_2PdS$	$C_{34.98}H_{30.15}F_6I_{1.17}N_2P_2Pd$
Formula Weight (g/mol)	879.85	812.27	960.17	909.29
Crystal Dimensions (mm)	$0.216 \times 0.196 \times 0.086$	$0.297 \times 0.282 \times 0.074$	$0.427 \times 0.160 \times 0.061$	$0.305 \times 0.048 \times 0.036$
Crystal Color and Habit	gold prism	colourless prism	colourless prism	pink needle
Crystal System	orthorhombic	orthorhombic	monoclinic	monoclinic
Space Group	$Pbc_a$	$Ab_a2$	$P2_1$	$C2/c$
Temperature, K	110	110	110	110

$a$ , Å	16.698(5)	15.726(6)	17.517(11)	21.236(8)
$b$ , Å	18.013(5)	24.110(10)	25.515(13)	17.185(6)
$c$ , Å	23.117(8)	18.032(7)	20.026(9)	18.627(10)
$\alpha$ , °	90	90	90	90
$\beta$ , °	90	90	90.619(13)	93.403(4)
$\gamma$ , °	90	90	90	90
$V$ , Å <sup>3</sup>	6953(4)	6837(5)	8950(8)	6786(5)
Number of reflections to determine final unit cell	9988	9766	9267	9903
Min and Max $2\theta$ for cell determination, °	4.52, 52.48	5.18, 59.56	4.7, 52.76	4.74, 50.14
$Z$	8	8	8	8
$F(000)$	3536	3299	3904	3568
$\rho$ (g/cm <sup>3</sup> )	1.681	1.578	1.425	1.780
$\lambda$ , Å, (MoK $\alpha$ )	0.71073	0.71073	0.71073	0.71073
$\mu$ , (cm <sup>-1</sup> )	0.852	0.809	0.599	1.767
Diffractometer Type	Bruker Kappa Axis Apex2	Bruker Kappa Axis Apex2	Bruker Kappa Axis Apex2	Bruker Kappa Axis Apex2
Scan Type(s)	phi and omega scans	phi and omega scans	phi and omega scans	phi and omega scans
Max $2\theta$ for data collection, °	59.262	64.174	53.544	52.948
Measured fraction of data	0.999	0.998	0.999	0.999

Number of reflections measured	343830	182173	356858	112658
Unique reflections measured	9788	11956	38053	6976
$R_{\text{merge}}$	0.0930	0.0547	0.0917	0.0875
Number of reflections included in refinement	9788	11956	38053	6976
Cut off Threshold Expression	$I > 2\sigma(I)$	$I > 2\sigma(I)$	$I > 2\sigma(I)$	$I > 2\sigma(I)$
Structure refined using	full matrix least-squares using $F^2$	full matrix least-squares using $F^2$	full matrix least-squares using $F^2$	full matrix least-squares using $F^2$
Weighting Scheme	$w=1/[\sigma^2(F_o^2)+(0.0294P)^2+12.3341P]$ where $P=(F_o^2+2F_c^2)/3$	$w=1/[\sigma^2(F_o^2)+(0.0331P)^2+9.6025P]$ where $P=(F_o^2+2F_c^2)/3$	$w=1/[\sigma^2(F_o^2)+(0.0458P)^2+40.6095P]$ where $P=(F_o^2+2F_c^2)/3$	$w=1/[\sigma^2(F_o^2)+(0.0176P)^2+26.1518P]$ where $P=(F_o^2+2F_c^2)/3$
Number of parameters in least-squares	526	527	2130	509
$R_1$	0.0330	0.0300	0.0538	0.0308
$wR_2$	0.0754	0.0709	0.1306	0.0583
$R_1$ (all data)	0.0479	0.0347	0.0643	0.0496
$wR_2$ (all data)	0.0843	0.0734	0.1363	0.0643
GOF	1.016	1.050	1.065	1.050
Maximum shift/error	0.002	0.004	0.001	0.002

Min & Max peak heights on final  $\Delta F$  Map ( $e^{-\Delta}$ )

-1.376, 0.777	-1.158, 1.016	-1.025, 1.286	-1.045, 0.838
---------------	---------------	---------------	---------------

Where:

$$R_1 = \frac{\sum (|F_o| - |F_c|)}{\sum F_o}$$

$$wR_2 = \left[ \frac{\sum (w(F_o^2 - F_c^2)^2)}{\sum (w F_o^4)} \right]^{1/2}$$

$$GOF = \left[ \frac{\sum (w(F_o^2 - F_c^2)^2)}{(\text{No. of reflns.} - \text{No. of params.})} \right]^{1/2}$$

## References

1. Bruker-AXS, SAINT version 2013.8, **2013**, Bruker-AXS, Madison, WI 53711, USA
2. Bruker-AXS, SADABS version 2012.1, **2012**, Bruker-AXS, Madison, WI 53711, USA
3. Sheldrick, G. M., *Acta Cryst.* **2015**, *A71*, 3-8
4. Sheldrick, G. M., *Acta Cryst.* **2015**, *C71*, 3-8
5. Macrae, C. F.; Bruno, I. J.; Chisholm, J. A.; Edington, P. R.; McCabe, P.; Pidcock, E.; Rodriguez-Monge, L.; Taylor, R.; van de Streek, J. and Wood, P. A. *J. Appl. Cryst.*, **2008**, *41*, 466-470
6. Spek, A. L., *Acta Cryst.* **2015**, *C71*, 9-18

## Appendices E: Copyright Material and Permissions

### Chapter 2 :

Alkyne Hydrofunctionalization Mechanism Including an Off-Cycle Alkoxy carbene Deactivation Complex

Author: Devon E. Chapple, Megan A. Hoffer, Paul D. Boyle, et al



Publication: Organometallics

Publisher: American Chemical Society

Date: Jun 1, 2022

Copyright © 2022, American Chemical Society

#### PERMISSION/LICENSE IS GRANTED FOR YOUR ORDER AT NO CHARGE

This type of permission/license, instead of the standard Terms and Conditions, is sent to you because no fee is being charged for your order. Please note the following:

- Permission is granted for your request in both print and electronic formats, and translations.
- If figures and/or tables were requested, they may be adapted or used in part.
- Please print this page for your records and send a copy of it to your publisher/graduate school.
- Appropriate credit for the requested material should be given as follows: "Reprinted (adapted) with permission from {COMPLETE REFERENCE CITATION}. Copyright {YEAR} American Chemical Society." Insert appropriate information in place of the capitalized words.
- One-time permission is granted only for the use specified in your RightsLink request. No additional uses are granted (such as derivative works or other editions). For any uses, please submit a new request.

If credit is given to another source for the material you requested from RightsLink, permission must be obtained from that source.

**Chapter 3:**

**JOHN WILEY AND SONS LICENSE  
TERMS AND CONDITIONS**

Aug 16, 2022

---

---

This Agreement between Mr. Devon Chapple ("You") and John Wiley and Sons ("John Wiley and Sons") consists of your license details and the terms and conditions provided by John Wiley and Sons and Copyright Clearance Center.

License Number 5370800608318

License date Aug 16, 2022

Licensed Content  
Publisher John Wiley and Sons

Licensed Content  
Publication ChemCatChem

Licensed Content Title Origin of Stability and Inhibition of Cooperative Alkyne Hydrofunctionalization Catalysts

Licensed Content Author Devon E. Chapple, Paul D. Boyle, Johanna M. Blacquiere

Licensed Content Date Jul 12, 2021

Licensed Content  
Volume 13

Licensed Content Issue 17

Licensed Content Pages 12

Type of use Dissertation/Thesis

Requestor type Author of this Wiley article

Format Electronic

Portion Full article

Will you be translating? No

Title Origin of Stability and Inhibition of Cooperative Alkyne Hydrofunctionalization Catalysts

Institution name Western University

Expected presentation date Oct 2022

Publisher Tax ID           EU826007151  
Total                         0.00 CAD  
Terms and Conditions

## TERMS AND CONDITIONS

This copyrighted material is owned by or exclusively licensed to John Wiley & Sons, Inc. or one of its group companies (each a "Wiley Company") or handled on behalf of a society with which a Wiley Company has exclusive publishing rights in relation to a particular work (collectively "WILEY"). By clicking "accept" in connection with completing this licensing transaction, you agree that the following terms and conditions apply to this transaction (along with the billing and payment terms and conditions established by the Copyright Clearance Center Inc., ("CCC's Billing and Payment terms and conditions"), at the time that you opened your RightsLink account (these are available at any time at <http://myaccount.copyright.com>).

### Terms and Conditions

- The materials you have requested permission to reproduce or reuse (the "Wiley Materials") are protected by copyright.
- You are hereby granted a personal, non-exclusive, non-sub licensable (on a stand-alone basis), non-transferable, worldwide, limited license to reproduce the Wiley Materials for the purpose specified in the licensing process. This license, **and any CONTENT (PDF or image file) purchased as part of your order**, is for a one-time use only and limited to any maximum distribution number specified in the license. The first instance of republication or reuse granted by this license must be completed within two years of the date of the grant of this license (although copies prepared before the end date may be distributed thereafter). The Wiley Materials shall not be used in any other manner or for any other purpose, beyond what is granted in the license. Permission is granted subject to an appropriate acknowledgement given to the author, title of the material/book/journal and the publisher. You shall also duplicate the copyright notice that appears in the Wiley publication in your use of the Wiley Material. Permission is also granted on the understanding that nowhere in the text is a previously published source acknowledged for all or part of this Wiley Material. Any third party content is expressly excluded from this permission.



- With respect to the Wiley Materials, all rights are reserved. Except as expressly granted by the terms of the license, no part of the Wiley Materials may be copied, modified, adapted (except for minor reformatting required by the new Publication), translated, reproduced, transferred or distributed, in any form or by any means, and no derivative works may be made based on the Wiley Materials without the prior permission of the respective copyright owner. **For STM Signatory Publishers clearing permission under the terms of the [STM Permissions Guidelines](#) only, the terms of the license are extended to include subsequent editions and for editions in other languages, provided such editions are for the work as a whole in situ and does not involve the separate exploitation of the permitted figures or extracts,** You may not alter, remove or suppress in any manner any copyright, trademark or other notices displayed by the Wiley Materials. You may not license, rent, sell, loan, lease, pledge, offer as security, transfer or assign the Wiley Materials on a stand-alone basis, or any of the rights granted to you hereunder to any other person.
- The Wiley Materials and all of the intellectual property rights therein shall at all times remain the exclusive property of John Wiley & Sons Inc, the Wiley Companies, or their respective licensors, and your interest therein is only that of having possession of and the right to reproduce the Wiley Materials pursuant to Section 2 herein during the continuance of this Agreement. You agree that you own no right, title or interest in or to the Wiley Materials or any of the intellectual property rights therein. You shall have no rights hereunder other than the license as provided for above in Section 2. No right, license or interest to any trademark, trade name, service mark or other branding ("Marks") of WILEY or its licensors is granted hereunder, and you agree that you shall not assert any such right, license or interest with respect thereto
- NEITHER WILEY NOR ITS LICENSORS MAKES ANY WARRANTY OR REPRESENTATION OF ANY KIND TO YOU OR ANY THIRD PARTY, EXPRESS, IMPLIED OR STATUTORY, WITH RESPECT TO THE MATERIALS OR THE ACCURACY OF ANY INFORMATION CONTAINED IN THE MATERIALS, INCLUDING, WITHOUT LIMITATION, ANY IMPLIED WARRANTY OF MERCHANTABILITY, ACCURACY, SATISFACTORY QUALITY, FITNESS FOR A PARTICULAR PURPOSE, USABILITY, INTEGRATION OR NON-INFRINGEMENT AND ALL SUCH

WARRANTIES ARE HEREBY EXCLUDED BY WILEY AND ITS LICENSORS AND WAIVED BY YOU.

- WILEY shall have the right to terminate this Agreement immediately upon breach of this Agreement by you.
- You shall indemnify, defend and hold harmless WILEY, its Licensors and their respective directors, officers, agents and employees, from and against any actual or threatened claims, demands, causes of action or proceedings arising from any breach of this Agreement by you.
- IN NO EVENT SHALL WILEY OR ITS LICENSORS BE LIABLE TO YOU OR ANY OTHER PARTY OR ANY OTHER PERSON OR ENTITY FOR ANY SPECIAL, CONSEQUENTIAL, INCIDENTAL, INDIRECT, EXEMPLARY OR PUNITIVE DAMAGES, HOWEVER CAUSED, ARISING OUT OF OR IN CONNECTION WITH THE DOWNLOADING, PROVISIONING, VIEWING OR USE OF THE MATERIALS REGARDLESS OF THE FORM OF ACTION, WHETHER FOR BREACH OF CONTRACT, BREACH OF WARRANTY, TORT, NEGLIGENCE, INFRINGEMENT OR OTHERWISE (INCLUDING, WITHOUT LIMITATION, DAMAGES BASED ON LOSS OF PROFITS, DATA, FILES, USE, BUSINESS OPPORTUNITY OR CLAIMS OF THIRD PARTIES), AND WHETHER OR NOT THE PARTY HAS BEEN ADVISED OF THE POSSIBILITY OF SUCH DAMAGES. THIS LIMITATION SHALL APPLY NOTWITHSTANDING ANY FAILURE OF ESSENTIAL PURPOSE OF ANY LIMITED REMEDY PROVIDED HEREIN.
- Should any provision of this Agreement be held by a court of competent jurisdiction to be illegal, invalid, or unenforceable, that provision shall be deemed amended to achieve as nearly as possible the same economic effect as the original provision, and the legality, validity and enforceability of the remaining provisions of this Agreement shall not be affected or impaired thereby.
- The failure of either party to enforce any term or condition of this Agreement shall not constitute a waiver of either party's right to enforce each and every term and condition of this Agreement. No breach under this agreement shall be deemed waived or excused by either party unless such waiver or consent is in writing signed by the party granting such waiver or consent. The waiver by or consent of a party to a breach of any provision of

this Agreement shall not operate or be construed as a waiver of or consent to any other or subsequent breach by such other party.

- This Agreement may not be assigned (including by operation of law or otherwise) by you without WILEY's prior written consent.
- Any fee required for this permission shall be non-refundable after thirty (30) days from receipt by the CCC.
- These terms and conditions together with CCC's Billing and Payment terms and conditions (which are incorporated herein) form the entire agreement between you and WILEY concerning this licensing transaction and (in the absence of fraud) supersedes all prior agreements and representations of the parties, oral or written. This Agreement may not be amended except in writing signed by both parties. This Agreement shall be binding upon and inure to the benefit of the parties' successors, legal representatives, and authorized assigns.
- In the event of any conflict between your obligations established by these terms and conditions and those established by CCC's Billing and Payment terms and conditions, these terms and conditions shall prevail.
- WILEY expressly reserves all rights not specifically granted in the combination of (i) the license details provided by you and accepted in the course of this licensing transaction, (ii) these terms and conditions and (iii) CCC's Billing and Payment terms and conditions.
- This Agreement will be void if the Type of Use, Format, Circulation, or Requestor Type was misrepresented during the licensing process.
- This Agreement shall be governed by and construed in accordance with the laws of the State of New York, USA, without regards to such state's conflict of law rules. Any legal action, suit or proceeding arising out of or relating to these Terms and Conditions or the breach thereof shall be instituted in a court of competent jurisdiction in New York County in the State of New York in the United States of America and each party hereby consents and submits to the personal jurisdiction of such court, waives any objection to venue in such court and consents to service of process by registered or certified mail, return receipt requested, at the last known address of such party.

## **WILEY OPEN ACCESS TERMS AND CONDITIONS**

Wiley Publishes Open Access Articles in fully Open Access Journals and in Subscription journals offering Online Open. Although most of the fully Open Access journals publish open access articles under the terms of the Creative Commons Attribution (CC BY) License only, the subscription journals and a few of the Open Access Journals offer a choice of Creative Commons Licenses. The license type is clearly identified on the article.

### **The Creative Commons Attribution License**

The [Creative Commons Attribution License \(CC-BY\)](#) allows users to copy, distribute and transmit an article, adapt the article and make commercial use of the article. The CC-BY license permits commercial and non-

### **Creative Commons Attribution Non-Commercial License**

The [Creative Commons Attribution Non-Commercial \(CC-BY-NC\) License](#) permits use, distribution and reproduction in any medium, provided the original work is properly cited and is not used for commercial purposes.(see below)

### **Creative Commons Attribution-Non-Commercial-NoDerivs License**

The [Creative Commons Attribution Non-Commercial-NoDerivs License](#) (CC-BY-NC-ND) permits use, distribution and reproduction in any medium, provided the original work is properly cited, is not used for commercial purposes and no modifications or adaptations are made. (see below)

### **Use by commercial "for-profit" organizations**

Use of Wiley Open Access articles for commercial, promotional, or marketing purposes requires further explicit permission from Wiley and will be subject to a fee.

Further details can be found on Wiley Online Library <http://olabout.wiley.com/WileyCDA/Section/id-410895.html>

**Other Terms and Conditions:**

**v1.10 Last updated September 2015**

# Curriculum Vitae

**Name:** Devon Chapple

## Education

**Doctorate of Philosophy in Chemistry**, Western University

2017 – Present

Doctoral Thesis: Mechanistic Elucidation of  $M-P^{R_2}N^{R'_2}$  Catalysts for Hydrofunctionalization and Cross Coupling Reactions

Supervisor: Professor Johanna M. Blacquiere

**Bachelor of Science, Honours Specialization in Chemistry**, Western University

2012 – 2016

Undergraduate Thesis: Metal-Ligand Cooperative Catalysis for the Synthesis of Nitrogen Heterocycles

Supervisor: Johanna M. Blacquiere

## Publications

4. Devon E. Chapple, Megan A. Hoffer, Paul D. Boyle, Johanna M. Blacquiere\*. Alkyne Hydrofunctionalization Mechanism Including an Off-Cycle Alkoxycarbene Deactivation Complex. *Organometallics* **2022**, 41(12), 1532-1542.

3. Devon E. Chapple, Paul D. Boyle, Johanna M. Blacquiere\*. Origin of Stability and Inhibition of Cooperative Alkyne Hydrofunctionalization Catalysts. *ChemCatChem* **2021**, 13(17), 3789-3800.

2. Soheil Hajirahimkhan<sup>a</sup>, Devon E. Chapple<sup>b</sup>, Ghazale Gholami<sup>b</sup>, Johanna M. Blacquiere<sup>b</sup>, Chunbao (Charles) Xu<sup>a</sup>, and Paul J. Ragogna<sup>b,\*</sup>. “Lignophines”: Lignin-Based Tertiary Phosphines with Metal-Scavenging Ability. *Chem. Commun.* **2020**, 10357-10360.

1. James M. Stubbs, Devon E. Chapple, P. D. Boyle, J. M. Blacquiere\*. Catalyst Pendant-base Effects on Cyclization of Alkynyl Amines, *ChemCatChem*, **2018**, 10, 3964-3702.

## Conferences (OP – Oral Presentation, PP – Poster Presentation; Presenter)

OP3: Devon E. Chapple, Johanna M. Blacquiere\*. ‘Scope and Mechanism: Ru-P<sub>2</sub>N<sub>2</sub> Mediated Hydrofunctionalization to Generate Heterocycles’. IUPAC, 104<sup>th</sup> Canadian Chemistry Conference and Exhibition, Virtual, August 2021.

OP2: Devon E. Chapple, Johanna M. Blacquiere\*. ‘Mechanistic Insight of Ru-P<sub>2</sub>N<sub>2</sub> Catalysts for Intramolecular Hydroamination’. 102<sup>nd</sup> Canadian Chemistry Conference and Exhibition, Quebec City, June 5<sup>th</sup>, 2019.

PP2: Devon E. Chapple, James M. Stubbs, and Johanna M. Blacquiere\*. ‘Primary Coordination Sphere Optimization of Ru-P<sup>R</sup><sub>2</sub>N<sup>R'</sup><sub>2</sub> Catalysts for Alkynyl Amine Cyclization’. Inorganic Discussion Weekend, Waterloo, November 2018.

PP1: James M. Stubbs, Devon E. Chapple, Johanna M. Blacquiere\*. ‘Systematic Ligand Tuning of Metal-Ligand Cooperative Catalysts for the Cyclization of Alkynyl Amines’ 21st International Symposium on Homogeneous Catalysis, Amsterdam, July 2018.

OP1: Devon E. Chapple, Johanna M. Blacquiere\*. Metal-Ligand Cooperative Catalysis for the Synthesis of Nitrogen Heterocycles. 45<sup>th</sup> Southern Ontario Undergraduate Student Chemistry Conference, York University, Toronto, ON, March 2017.

### Awards and Scholarships

- Robert and Ruth Lumsden Award 2022

### Mentoring/Volunteering

**4491 Thesis Mentor**, Western University  
2017 – Present

- Provided guidance and taught laboratory skills to three 4491 students.

**Laboratory Teaching Assistant (Head TA 2022 for 2281)** 2017-2022  
Western University

- Chemistry 2213A: Organic Chemistry for Life Sciences
- Chemistry 2223B: Organic Chemistry of Biological Molecules
- Chemistry 2271A: Structure and Bonding in Inorganic Chemistry
- Chemistry 2281G: Inorganic Chemistry of the Main Group Elements

**102<sup>nd</sup> Canadian Chemistry Conference and Exhibition Volunteer** 2019  
Quebec City, Quebec

- Assisted in the setup of the conference workshops
- Provided technical support to presenters

### Courses

9503R – Advanced NMR Spectroscopy I – 92%; 9507Q – Advanced Chemical Communications – 86%; 9521S – Catalysis – 80%; 9603S – Advanced NMR Spectroscopy II – 90%; 9563Q – Total Synthesis – 93%; 9651S – Organometallic Chemical Bond Activation – 87%; 9671T – Synthesis with Organometallics – 88%; 9823R – Heterocycles – 92%; 9648B – Computational Quantum Chemistry – AUD.

